NASA Conference Publication 2076

FOURTH NATIONAL AERONAUTICS AND SPACE ADMINISTRATION WEATHER AND CLIMATE PROGRAM SCIENCE REVIEW

The proceedings of a review held January 24-25, 1979
at the NASA Goddard Space Flight Center,
Greenbelt, Maryland

Edited by
Earl R. Kreins
Sponsored by
The National Aeronautics and Space Administration
Office of Space and Terrestrial Applications

Prepared at Goddard Space Flight Center

NASA
National Aeronautics and
Space Administration

Goddard Space Flight Center
Greenbelt, Maryland 20771

NASA Conference Publication 2076

FOURTH NATIONAL AERONAUTICS AND SPACE ADMINISTRATION WEATHER AND CLIMATE PROGRAM SCIENCE REVIEW

The proceedings of a review held January 24-25, 1979
at the NASA Goddard Space Flight Center,
Greenbelt, Maryland

Edited by
Earl R. Kreins
Sponsored by
The National Aeronautics and Space Administration
Office of Space and Terrestrial Applications

Prepared at Goddard Space Flight Center

NASA
National Aeronautics and
Space Administration

Goddard Space Flight Center
Greenbelt, Maryland 20771

FOREWORD

This Document contains the proceedings of the Fourth NASA Weather and Climate Program Science Review. This was the fourth in a series of annual reviews of the principal meteorological research results conducted under the Weather and Climate Program of the NASA Office of Space and Terrestrial Applications. The purpose of the review was two-fold. First, it provided a means for evaluating program progress and a basis for justifying future activity. And, secondly, it promoted information exchange with the meteorological community. To aid in this exchange, representatives from the National Oceanic and Atmospheric Administration, Department of Defense, Department of Energy, National Academy of Sciences, and the National Science Foundation were invited to attend. The science review was held at the NASA Goddard Space Flight Center, Greenbelt, Maryland, on January 24-25, 1979.

The NASA Weather and Climate Program has two major thrusts. The first involves the development of experimental and prototype operational satellite systems, sensors, and space facilities for monitoring and understanding the atmosphere. The second thrust involves basic scientific investigations aimed at studying the physical and chemical processes which control weather and climate. These major aspects of the program focus on exploiting the capabilities of space technology for: (1) detection, monitoring, and prediction of severe storms; (2) the improvement of global weather forecasting; and (3) the monitoring and prediction of climate and climate change. This fourth science review concentrated on the scientific research rather than the hardware development aspect of the program.

These proceedings contain 65 papers covering the three general areas: Severe Storms and Local Weather Research, Global Weather, and Climate. Thirty-seven of the papers were presented orally during the review. They are denoted by an asterisk in the Table of Contents. To expedite the publication of these proceedings, papers were submitted in camera ready format. Each author assumes full responsibility for the content of his paper

Earl R. Kreins
Science Review Coordinator
NASA Meteorology Program Office
Goddard Space Flight Center

Page intentionally left blank

TABLE OF CONTENTS

SESSION 1

SEVERE STORMS AND LOCAL WEATHER RESEARCH

Session Moderator – Earl R. Kreins

*Presented at the Review

SESSION 2

GLOBAL WEATHER RESEARCH

Session Moderator – Robert M. Rados

SESSION 3

CLIMATE RESEARCH

Session Moderator – Leland L. Dubach

Paper No. 1

THUNDERSTORM/ENVIRONMENT INTERACTIONS THAT AFFECT SUBSEQUENT CONVECTION

R. A. Maddox and L. R. Hoxit, *NOAA, Environmental Research Laboratories, Boulder, Colorado*

ABSTRACT

Mesoscale kinematics and thermodynamics of severe thunderstorm-baroclinic zone interactions, and the development and evolution of mesoscale pressure systems associated with strong convective storms, are being studied in an ongoing research project.

INTRODUCTION

Four intensive case study days were selected - 24 April and 6 May 1975; 4 April and 27 May, 1977. All available conventional data sets have been analyzed for these days. In addition to extensive subjective analyses, computer generated objective analyses have been performed on selected data fields.

The kinematics of severe thunderstorm baroclinic zone interactions are being considered in the 24 April and 6 May cases. On both days intense tornadic development occurred as severe thunderstorm cells approached strong baroclinic zones to the east of surface moisture and thermal ridges. A review of other intense, but relatively isolated, tornado events indicates that this scenario is not unusual. Detailed time series, both of surface and sounding data, seem to indicate that horizontal and vertical wind shears within the planetary boundary layer play important roles in the concentration of mesoscale vorticity in the storm region.

The 27 May case is being used to study the temporal evolution of PBL wind fields near such a thermal boundary. At midmorning a thunderstorm outflow boundary was situated just south of the NSSL mesonet in Oklahoma and instrumented tower time series data are being utilized.

The 4 and 24 April cases have provided an opportunity to study the development and evolution of two distinctly different types of mesoscale low pressure systems. In the 4 April case at least two meso-β scale lows are detectable and the thunderstorms associated with these pressure systems produced significant severe weather. Upper-air data are being analyzed and important interactions between the storms and the larger scale flow fields have been detected. On 24 April a meso-α scale

cyclonic circulation persisted and intensified during the afternoon helping to trigger storm development within a somewhat hostile larger scale environment. In the one case a mesosystem developed in conjunction with, or in response to, intense thunderstorms, while in the other case a pre-existing meso-pressure system acted to initiate storm development.

The following sections present some preliminary results of this study.

MESOSCALE VORTICITY FIELDS AND SATELLITE IMAGERY

Adler and Fenn (1977) and Peslen (1977) have related satellite data (IR cloud-top temperatures and derived wind fields) to the severity of the 6 May storms. In the present study objectively computed kinematic parameters (divergence, relative vorticity, etc.) for the surface wind fields were considered relative to GOES imagery. It was noted that most fields maximized in regions where severe storms subsequently occurred.

Barnes (1978) suggested that a tornado cyclone's ability to produce vortices in the friction layer depended upon ambient vorticity exceeding a threshold of 10^{-3} S^{-1} on scales of about 25 km. Although features on such small scales are not detectable in routine surface data, it is hypothesized that analyses of meso-β scale ambient vorticity fields might indicate the likelihood of the required vorticity threshold being reached at smaller scales. To investigate this hypothesis a vorticity time parameter was defined:

$$VTP = \frac{10^{-3} - (\xi+f)}{\{-(\xi+f)\ \nabla\cdot V - V\cdot\nabla(\xi+f)\}} S$$

Smaller values of VTP (negative values are not allowed) may indicate that mesoscale ambient conditions are more favorable for occurrence of intense tornadic storms. Objective analyses were accomplished utilizing an analysis scheme developed by Barnes (1973). This method employs an exponential weight function and produces a gridded and smoothed field in only one iteration. The filter response for the examples shown retained >90% of the amplitude of waves longer than 200 km. Analyses are also being considered for stronger filter responses.

A mesoanalysis of surface conditions at 2200 GMT 24 April 1975 is shown in Fig. 1. The VTP is contoured in regions of $5X10^{4}S$ and less and 2230 GMT thunderstorm areas, from GOES imagery, are cross-hatched. The thunderstorm in NE Oklahoma was the only storm coincident with favorable mesoscale kinematic fields and it generated destructive tornadoes at 0000 and 0040 GMT. Contoured VTP fields are shown for 2000 GMT 6 May 1975 in Fig. 2 and two favorable (low value) VTP regions are superposed on a 2000 GMT GOES image in Fig. 3. One favorable area existed behind the surface front in a region where very dry air was being pulled

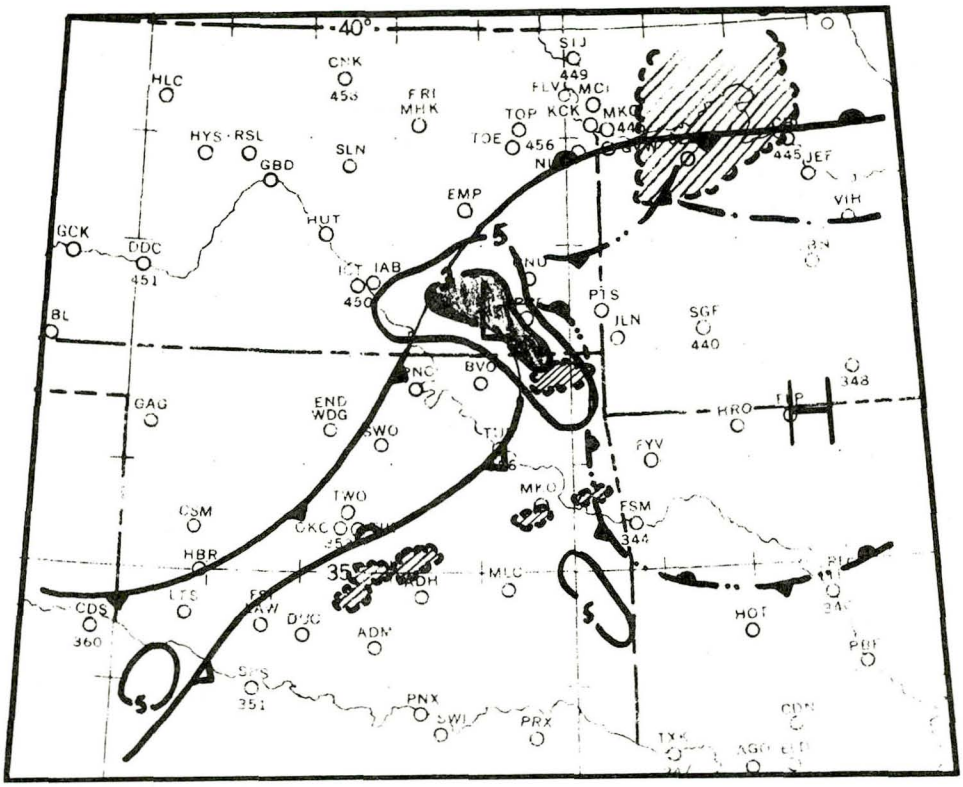

Fig. 1. Mesoanalysis of surface features at 2200 GMT 24 April 1975. VTP values are contoured and thunderstorm areas, from 2230 GOES imagery, are cross-hatched.

into a low pressure circulation. No thunderstorms existed in this dry zone; however, destructibe tornadoes occurred during the next 90 minutes in both favorable regions shown on Fig. 3.

Although only two cases have been examined, the results are encouraging and indicate that fields derived from conventional observations might be used in conjunction with satellite data to specify regions where the threat of intense tornadic events is maximizing. The short term forecast and warning applications could be valuable once such a technique is tested in many situations. An interactive data processing and analysis system, such as AOIPS, would be of great use in developing and displaying these types of data blends.

BOUNDARY LAYER WIND FIELDS NEAR THERMAL BOUNDARIES

Individual soundings and NSSL tower data, along with observational and theoretical boundary layer studies (e.g. Hoxit, 1974,

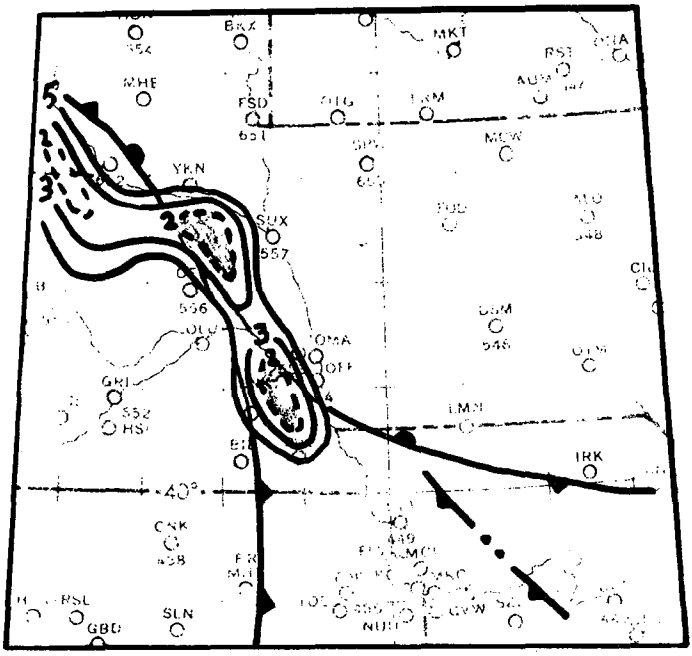

Fig. 2. Mesoanalysis of surface features at 2000 GMT 6 May 1975. VTP values of $\leq 5X10^4$ S are contoured.

Fig. 3. Regions of VTP $\leq 2X10^4$ S within the moist air mass superposed on the 2000 GMT 6 May 1975 GOES visible image.

and Cattle, 1971), have been utilized to develop a physical model of sub-cloud wind profiles near thermal boundaries. Figure 4 shows a schematic representation of wind profiles in the lowest kilometer for three different air masses within a meso-α pattern often associated with severe thunderstorms. At point A, within a warm, dry and well mixed airmass, the wind veers slightly with height and the speed increases slowly. In the hot, moist and conditionally unstable airmass (point B) warm thermal advection and surface friction produce a wind profile which veers and increases in speed with height. At point C, in a cool, moist thunderstorm outflow region, the cold low-level thermal advection acts to decrease the veering. Winds at this point have maximum speeds near the surface and veer little with height until a transition occurs into the warmer airmass above. Within this cool, moist airmass the cross-isobaric flow is greater than in the other two airmasses.

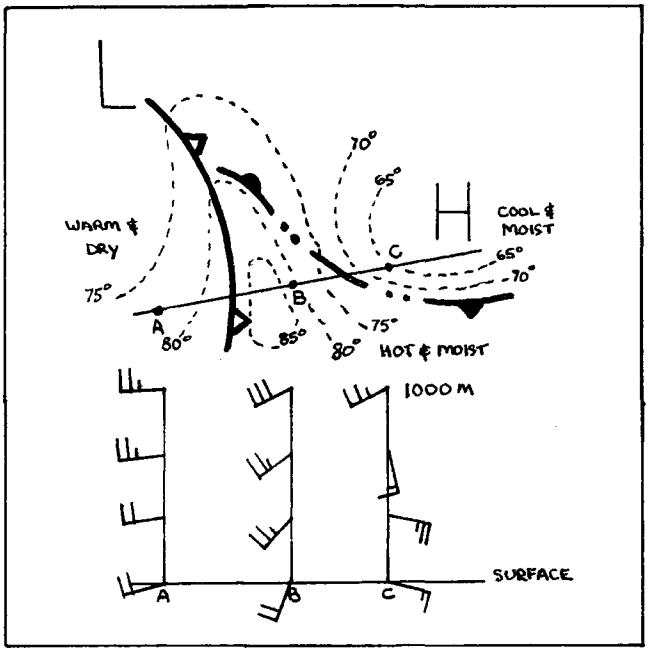

Fig. 4. Schematic representation of boundary layer wind profiles within a typical severe thunderstorm producing surface pattern. Surface features and isotherms (^{o}F) are indicated.

The Fig. 4 cross-section of wind profiles indicates that the vertical wind profiles are modified in a manner which acts to maximize convergence and cyclonic vorticity within a narrow

zone along the thermal boundary between B and C. Such systematic perturbations in planetary boundary layer wind profiles may, in part, explain why storms often reach maximum intensity and become tornadic as they approach thermal boundaries. Satellite imagery and satellite derived low level wind fields might, on some occasions, be utilized to locate wind shear zones associated with thermal boundaries.

ACKNOWLEDGMENTS

This research is being partially supported by NASA Grant RC-7705.

REFERENCES

Adler, R.F., and D. D. Fenn, 1977: Satellite-based thunderstorm intensity parameters. Preprints Tenth Conf. on Severe Local Storms, AMS, Omaha, Neb., 8-15.

Barnes, S. L., 1978: Oklahoma thunderstorms on 29-30 April 1970. Part II: Radar-observed merger of twin hook echoes. Mon. Wea. Rev., 106, 685-696.

_____, 1973: Mesoscale objective map analysis using weighted time-series observations. NOAA Tech. Memo. ERL NSSL-62, 60 pp.

Cattle, H., 1971: The terrestrial low latitude boundary layer. Ph.D. dissertation, Imperial College of Science and Technology, 201 pp.

Hoxit, L.R., 1974: Planetary boundary layer winds in baroclinic conditions. J. Atmos. Sci., 31, 1003-1020.

Peslen, C. A., 1977: A satellite interpretation of the dynamics of a severe local storms area using 5 minute interval SMS data. Preprints Tenth Conf. on Severe Local Storms, AMS, Omaha, Neb., 1-7.

Paper No. 2

THUNDERSTORM VERTICAL VELOCITIES AND MASS FLUX ESTIMATED FROM SATELLITE DATA

Robert F. Adler, *Laboratory for Atmospheric Sciences, Goddard Space Flight Center, NASA, Greenbelt, Maryland* and Douglas D. Fenn, *GE/MATSCO, Beltsville, Maryland*

ABSTRACT

Infrared geosynchronous satellite data with an interval of five minutes between images are used to estimate thunderstorm top ascent rates on two case study days. A mean vertical velocity of 3.5 ms^{-1} for 19 clouds is calculated at a height of 8.7km. This upward motion is representative of an area of approximately 10km on a side. Thunderstorm mass flux of approximately 2 x 10^{11} gs^{-1} is calculated, which compares favorably with previous estimates. There is a significant difference in the mean calculated vertical velocity between elements associated with severe weather reports ($\bar{w}$= 4.6 ms^{-1}) and those with no such reports (2.5 ms^{-1}).

Calculations were made using a velocity profile for an axially symmetric jet to estimate the peak updraft velocity. For the largest observed w value of 7.8 ms^{-1} the calculation indicates a peak updraft of approximately 50 ms^{-1}.

1. INTRODUCTION

In the current paper we present the results of using a simple method to estimate thunderstorm cloud-top vertical velocity from SMS/GOES rapid-scan (5 minute interval) window channel infrared (IR) data. Time rate of change of cloud-top minimum equivalent blackbody temperature (T_{BB}) is converted to vertical velocity w by

$$w = \left(\frac{\partial T}{\partial z} \right)^{-1} \frac{dT_{BB}}{dt}, \qquad (1)$$

where the lapse rate is determined from rawinsonde data. In the following sections the calculated vertical velocities are compared for clouds with associated severe weather reports and for those with no such reports, and the computed values are also compared with previous estimates of thunderstorm vertical velocities.

2. DESCRIPTION OF ANALYSIS TECHNIQUE

The analysis of the digital satellite data was performed on the Atmospheric and Oceanic Information Processing System (AOIPS), an interactive image analysis system described by Billingsley (1976). Sequences of images are enhanced, elements are isolated and identified, and their maximum gray level (minimum T_{BB}) recorded. The analysis of the thunderstorms used in this study (on April 24, 1975 and May 6, 1975) was part of a larger effort (see Adler and Fenn, 1978). On each

of these study days an area of convection was monitored during a set period of time (approximately 4 hours). Thunderstorm elements were defined by the technique described by Adler and Fenn (1976, 1978) and time histories of each element were determined.

It should be emphasized here that not all thunderstorms can be observed at middle tropospheric heights. This is because they are often hidden by dense cirrus clouds produced by previous convection. In the two case studies that will be described here, of the thunderstorm elements defined above 10km (T_{BB} = 226K), only about 25-30% could be detected at lower heights.

3. VERTICAL VELOCITY ESTIMATES

a. Sources of Error

The vertical velocity estimates presented in this paper are subject to error because of errors in the satellite radiance measurements and possible unrepresentativeness of the data. A possible source of error is in the cloud emissivity. For thick water clouds such as we are dealing with, the emissivity (ϵ) is very close to unity. In order to use T_{BB} in place of T in Equation (1), $\epsilon = 1$ must be assumed. For ice clouds, especially thin cirrus clouds, emissivity can be substantially less than 1.0. As the thunderstorm top glaciates, the change from water to ice may reduce the cloud top emissivity and T_{BB} will be larger than T, the cloud top temperature. This effect, however, appears to be small and will not affect the vertical velocity calculations. This conclusion is based on calculations made with the help of tables presented by Hunt (1973) and on results presented by Cox (1977).

The most serious source of error stems from the satellite data itself. The IR channel has an instantaneous field of view (IFOV) of 8km on a side at the subsatellite point and approximately 10km at 40N. As noted by Negri, et al., (1976) the use of SMS/GOES IR temperatures to determine thunderstorm height results in underestimates, especially for small elements. In comparison with radar measurement of thunderstorm tops, the satellite underestimation is approximately 2km. This effect is related to two factors. First, the satellite, because of its rather large IFOV, is averaging over an area approximately $100 km^2$ compared with the radar observation, which is applicable to an area closer to $1 km^2$. Thus the radar will be identifying smaller, higher features, because of its better resolution. The second factor is inadequate sensor response when going from a warm (low) to a cold (high) target (Negri, et al., 1976). In general, the bias in the estimation of storm height will not affect the vertical velocity calculation. However, it may affect the height to which the velocities are assigned.

Other errors might arise from the use of inaccurate lapse rates in Equation (1). In the calculations to follow we use a smooth profile which is a mean of the ambient and the moist adiabatic lapse rate. The calculations can be shown to be rather insensitive to variations in the lapse rate. Using either the moist adiabatic or the ambient lapse rate instead of the average of the two produces only 10% differences in the calculated velocities. The final validation of the calculated vertical velocities must come through a careful comparison with radar, aircraft or satellite stereo observations.

b. Vertical Velocity Results

Fourteen elements on May 6, 1975 and ten on April 24, 1975 were analyzed. Minimum T_{BB} as a function of time for each element was plotted and dT_{BB}/dt

values were calculated. The warmest or lowest of the monitored elements was at T_{BB} = 260K (about 6km). Not all thunderstorms could be observed from that point upward through the remainder of the troposphere. Some elements were blocked out by other storms; other elements were not detected until they penetrated middle level cloud fields.

Vertical velocities were calculated every 5K in the vertical for each cloud element or thunderstorm using Equation (1) and a lapse rate halfway between ambient and moist adiabatic. The mean w was then calculated for various categories of clouds to produce composite profiles. The results for the May 6 case are shown in Figure 1. Profiles are shown for thunderstorms associated with severe weather reports (based on National Severe Storms Forecast Center logs) and those with no accompanying reports. The numbers in parentheses indicate the number of cases constituting each mean or composite vertical velocity. The mean profile of all cases is also shown.

The vertical velocities in Figure 1 and the calculated divergence noted above are applicable to an area of about 10km on a side. The calculated vertical velocities do not represent updraft core velocities, which could be an order of magnitude larger when measured on a horizontal scale of 1 km (see Section 5).

A similar diagram for April 24, 1975 case is given in Figure 2. The convection of interest on this day was centered in southwestern Missouri. The composite w profiles for three categories are displayed. The additional category is for weak elements which did not reach a height of 10km (as determined by the T_{BB} values). In the layer from 7 to 9km the average w is approximately 1.5 ms^{-1} for those storms. This is significantly lower than the composite for "non-severe" elements in either Figure 1 or 2.

The 235-240K level (~8.7km) is representative of the layer of relatively large vertical velocities on both days. Figure 3 shows the frequency distribution of the 19 elements or clouds for these two days. The hatched portion of the histogram contains the values for the severe weather elements. The average w for all 19 cases is 3.5 ms^{-1}. The severe and non-severe elements have average values of 4.6 and 2.5 ms^{-1}, respectively. The severe thunderstorms dominate the high end of the distribution where six out of seven cases with $w > 4 ms^{-1}$ are associated with severe weather reports.

c. Mass Flux Calculation

Because of the values of w calculated in the last section are representative of an area larger than a typical thunderstorm updraft, vertical volume or mass flux calculations can be simply made through the formula,

$$F_m = \rho A w, \qquad (2)$$

where F_m is the vertical mass flux, ρ is the density, and A is the area. For the 235-240K layer (~8.7km) ρ is assumed to be 5 x $10^{-4} gcm^{-3}$, and A is assigned a value of 100km^2 for the area of the satellite IFOV.

With the given values for ρ and A the mean w for all storms of 3.5 ms^{-1} is converted to a mass flux of 1.8 x $10^{11} gs^{-1}$. The mean w of severe elements (4.6 ms^{-1}) is equivalent to a mass flux of 2.3 x $10^{11} gs^{-1}$. These magnitudes are for the mass flux through a given layer associated with a growing thunderstorm top. The calculated values compare favorably with results presented by other investigators. Kropfli and Miller (1976) calculate a value of 1.9-2.0 x $10^{11} gs^{-1}$ between 8-9km for a northeast Colorado storm calculated using vertical velocity

inferred from dual-Doppler radar data. Auer and Marwitz (1968) present results of the cloud base mass flux into 18 hailstorms on the high plains deduced from aircraft measurements. Their average value is 2.3 x 10^{11} gs^{-1}. Therefore, it appears that the upward flow deduced from the satellite observations is of a reasonable magnitude when compared to calculations and observations on approximately the same scale. Inferences about the magnitude of the maximum updraft are presented in Section 5.

4. EXAMPLE OF INTENSE THUNDERSTORM

On April 24, 1975 a severe thunderstorm complex developed over extreme northeastern Oklahoma in the late afternoon and moved into southwestern Missouri around sunset. The most significant severe weather associated with the system was the Neosho, Mo. tornado which touched down at approximately 0040 GMT, April 25. By following the evolution of the storm system backwards in time, the initial intense convection can be detected and its associated rapid cloud top growth calculated.

The Neosho cloud system was designated cloud 18 as part of a larger study of this day. Figure 4 exhibits minimum cloud top T_{BB} as a function of time for cloud 18 in its early stages. The temperature drops precipitously between 2200 and 2220GMT with a maximum calculated rate of 4K min^{-1}. The drop in temperature between 260K and 220K takes only a little more than 15 minutes. This type of rapid change emphasizes the importance of short interval data to study and monitor thunderstorm activity.

Using a lapse rate varying from 7.8km^{-1} at 260K, to 8.6Kkm^{-1} at 240K, to 8.0Kkm^{-1} at 215K the vertical velocity was calculated using Equation (1). The maximum calculated w is 7.8ms^{-1} at about 9km.

5. INTERPRETATION OF CALCULATED VERTICAL VELOCITIES IN TERMS OF MAXIMUM UPDRAFT

The vertical velocities presented in the previous sections of this paper are mean velocities over an area equivalent to the satellite instantaneous field of view (IFOV), which in this case is approximately 100km^2. In the temperature range 235-240K (~8.7km) the 19 observed w's based on the satellite data ranged from 1.2 to 7.8 ms^{-1}, with a mean of 3.5ms^{-1}. Although these are very large values when compared to typical synoptic-scale w's, they are small when compared to maximum thunderstorm updraft magnitudes. Thunderstorm updrafts can reach magnitudes of 10ms^{-1} very easily and are typically 30ms^{-1} in supercell thunderstorms (Browning, 1977; Davies-Jones, 1974). These large updraft values are probably representative of an area approximately 1km^2. Thus there are two orders of magnitude difference in the area covered by the estimated w's obtained from the satellite data in this study and the area covered by the peak updraft velocity.

Assuming axial symmetry and a knowledge of the shape and size of the radial profile of vertical velocity, one can make an estimate of the maximum updraft magnitude. The formula chosen in this study, based on Kyle et al., (1976) and Schlichting (1978) is

$$w = w_o \, e^{-a(r/R)^2}, \qquad (3)$$

where w_o is the peak w, r is the radial distance, R is the radius of the updraft, and the constant a = 2.3.

Integrating Equation (3) over a circular area of radius r_1, and dividing the result by the area of the integration produces an expression for the mean w over the area, i.e.,

$$\bar{w} = \frac{w_o}{a} \left(\frac{R}{r_1}\right)^2 [1 - e^{-a(r_1/R)^2}]. \quad (4)$$

The size of thunderstorm updrafts is highly variable (Browning, 1977). Based on the discussion of updraft sizes by Browning (1977) and an examination of cross-sections by Kropfli and Miller (1976) and Ray (1976) of thunderstorm vertical motions deduced from Doppler radar data, an updraft radius of 3km is reasonable.

For an area of 100km^2 (approximately equal to the IFOV), the equivalent radius of integration is 5.6km. Thus with R = 3km and r_1 = 5.6km,

$$\bar{w} = 0.12\ w_o. \quad (5)$$

Thus, with all the assumptions as to profile shape and updraft size, Equation (5) indicates that the mean $\bar{w}$ of 3.5ms^{-1} is equivalent to a w_o of 29ms^{-1} and the 7.8 ms^{-1} value from the Neosho storm (Section 4) is equivalent to a w_o of 65ms^{-1}.

For an R of 3.5km, instead of 3km, the 65ms^{-1} value in the largest paragraph would drop to 46ms^{-1}. It is obvious that the calculated w_o is sensitive to the size of the updraft.

Despite the variability and sensitivity of the w_o calculations, it is evident that the satellite observations on a scale of 10km are producing $\bar{w}$ of up to approximately 8ms^{-1}, and this can be interpreted as being roughly equivalent to a maximum updraft of 50ms^{-1} in intense thunderstorms.

6. SUMMARY

Rapid-scan (5 minute interval) SMS/GOES IR data have been used to estimate thunderstorm top ascent rates for severe and non-severe thunderstorms on two case study days. On both days examined (May 6 and April 24, 1975) the thunderstorm elements with associated severe weather reports have larger average w's. The severe and non-severe elements had mean w's of 4.6 and 2.5ms^{-1}. Intensity of convection appears to be correlated with the occurrence of severe weather, and the satellite data appear to be capable of quantifying the convection intensity.

The calculated vertical velocities are representative of an area (100 km^2) roughly equivalent to the satellite instantaneous field of view (IFOV). Mass flux estimates of approximately 2 x 10^{11}gs^{-1} are calculated, which are reasonable in comparison with other estimates.

Calculations were performed to estimate the peak updraft velocity from the satellite based values (averages over 100 km^2 areas). With a reasonable value of R (3-3.5km), the $\bar{w}$ of 7.8ms^{-1} for the Neosho storm produces an estimate of approximately 50ms^{-1} for w_o.

REFERENCES

Adler, R. F. and D. D. Fenn, 1976: Thunderstorm Monitoring from a geosynchronous satellite. In Preprints of 7th Conference on Aerospace and Aeronautical Meteorology, 307-311.

Adler, R. F., and D. D. Fenn, 1978: "Satellite-based Thunderstorm Intensity Parameters," NASA TM 78094 (also submitted to J. Appl. Met.; Preliminary version of paper in Tenth Conference on Severe Local Storms, October 1977), 42 p.

Auer, A. H. and J. D. Marwitz, 1968: Estimates of air and moisture flux into hailstorms on the high plains. J. Appl. Met., 7, 196–198.

Billingsley, J. B., 1976: Interactive image processing for meteorological applications at NASA/Goddard Space Flight Center. In Preprints of 7th Conference on Aerospace and Aeronautical Meteorology and Symposium on Remote Sensing from Satellites, 268–275.

Browning, K. A., 1977: "The Structure and Mechanisms of Hailstorms," In Hail: A Review of Hail Science and Hail Suppression, A.M.S., Meteorological Monographs, 16, No. 38, 1-43.

Cox, S. K., 1977: Satellite derived cloud cluster cloud-top heights. 11th Technical Conference on Hurricanes and Tropical Meteorology, Miami Beach, Florida, 355-356.

Davies–Jones, R. P., 1974: Discussion of measurements inside high-speed thunderstorm updrafts. J. Appl. Met., 13, 710–717.

Hunt, G. E., 1973: Radiative properties of terrestrial clouds at visible and infrared thermal window wavelengths. Quart. J. R. Met. Soc., 99, 346–369.

Kropfli, R. A. and L. J. Miller, 1976: Kinematic structure and flux quantities in a convective storm from dual-Doppler radar observations. J. Atmos. Sci., 33, 520–529.

Kyle, T. G., W. R. Sand, and D. J. Musil, 1976: Fitting measurements of thunderstorm updraft profiles to model profiles. Mon. Wea. Rev., 104, 611–617.

Negri, A. J., D. W. Reynolds, and R. A. Maddox, 1976: Measurements of cumulonimbus clouds using quantitative satellite and radar data. In Preprint Volume of Seventh Conference on Aerospace and Aeronautical Meteorology, 119–124.

Ray, P. S., 1976: Vorticity and divergence fields within tornadic storms from dual-Doppler observations. J. Appl. Met., 15, 879–890.

Schlichting, H., 1968: Boundary Layer Theory. McGraw–Hill, Chap. 24.

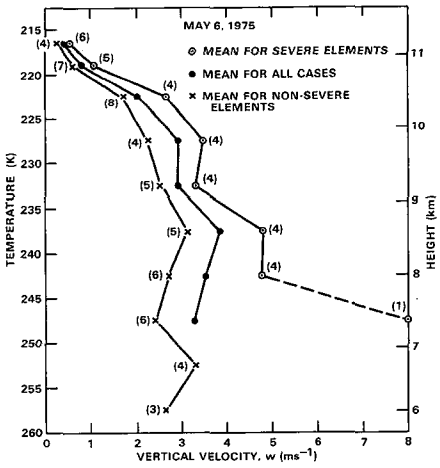

Fig. 1–Composite vertical velocity profiles for May 6, 1975. Numbers in parentheses are the number of cases.

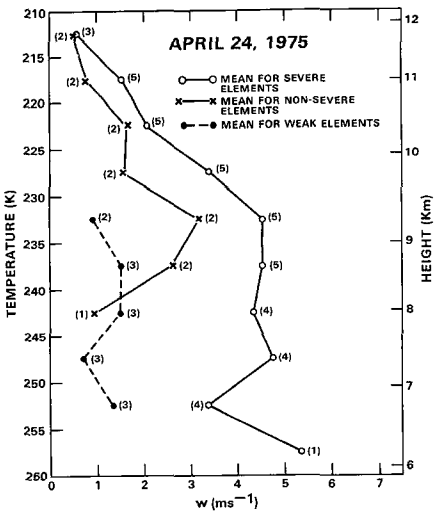

Fig. 2–Composite vertical velocity profiles for April 24, 1975.

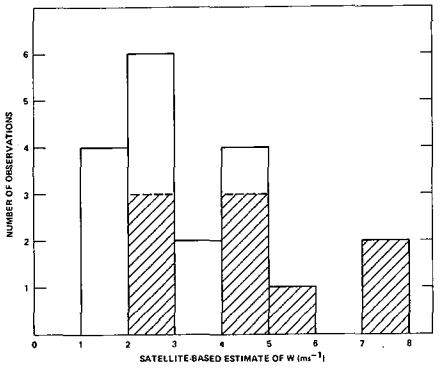

Fig. 3–Frequency distributions of estimated vertical velocities at 8.7 km for clouds on April 24 and May 6, 1975. Hatched portion of histogram indicates thunderstorms with accompanying severe weather reports.

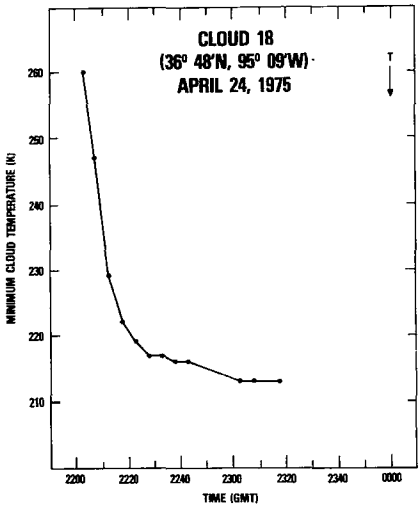

Fig. 4–Minimum equivalent blackbody temperature (T_{BB}) as a function of time for cloud 18 on April 24, 1975.

Page intentionally left blank

Paper No. 3

THUNDERSTORM FORMATION AND INTENSITY DETERMINED FROM A THREE-DIMENSIONAL SUBSYNOPTIC-SCALE TRAJECTORY MODEL

G. S. Wilson, *Marshall Space Flight Center, Alabama*

ABSTRACT

A diagnostic trajectory model has been used to provide a better understanding of the interrelationships between synoptic- and convective-scale systems. Results indicate that synoptic scale systems exert a strong controlling influence over the formation and intensity of small mesoscale convective circulations.

INTRODUCTION AND DATA

NASA's fourth Atmospheric Variability Experiment (AVE IV) was conducted from 0000 GMT 24 April to 1200 GMT 25 April 1975 primarily to further establish the variability and structure of the atmosphere in regions of convective storms, and to investigate the poorly understood interrelationships between these storms and their environment. AVE IV data provide a unique opportunity to evaluate these relationships and scale interactions since two severe lines of thunderstorms occurred during the experiment. Special rawinsonde soundings were taken at 3- or 6-h intervals in AVE IV over the U.S. east of 105°W longitude and all available surface, radar (from Manually Digitized Radar (MDR) data (Foster and Reap, 1973)), and satellite data were used in the diagnostic analyses.

This paper presents results aimed at providing a better understanding of the interrelationships between synoptic- and convective-scale systems obtained by following individual air parcels, embedded within the macro-scale flow pattern, as they traveled within the convective storm environment of AVE IV. A three-dimensional trajectory model was used to objectively calculate parcel paths while MDR data was used to locate convective activity of various intensities and to determine those trajectories that traversed the storm environment.

THE TRAJECTORY MODEL

To develop data for the trajectory model, the u, v, θ, and ϕ variables of the AVE IV data were interpolated from randomly-spaced rawinsonde stations to equally-spaced grid points. Therefore, all input data for the model were contained on 18x18 grid arrays ($\Delta x=\Delta y=158$ km) at 18 pressure levels from the surface up

to 100 mb for all times of the AVE IV Experiment and were stored on computer disk.

From these basic analyzed fields, vertical velocities were calculated for every grid point so that u, v, and ω components of the wind vectors were defined three-dimensionally over the experiment area. The method used in determining the vertical velocities follows exactly the technique used by Wilson and Scoggins (1976) and Wilson (1976). The technique is basically kinematic and extensive comparative research shows this method to be far superior to all other calculating techniques when results are compared to the observed weather.

All trajectories in AVE IV were computed backward in time to insure that air parcels would terminate their paths exactly at a given grid point on a given pressure surface. The mathematical procedure used to calculate trajectories from wind fields defined in Eulerian space is given by Collins (1970).

Figure 1 uses a specific plotting technique (after Reap, 1972) to show five air parcel trajectories passing over a severe squall line in AVE IV ending at the 300-mb level. Three-hour MDR composite charts, including data ±1 h surrounding a given release time, were prepared for all nine periods of AVE IV. The 0600 GMT data is superimposed in the figure (maximum MDR value was chosen in each block for the composite chart and MDR values ≥ 4 are usually considered thunderstorms). The location of each parcel at the last four consecutive time periods (between 2100 GMT 24 April and 1200 GMT 25 April) is shown with tick marks and the vertical location is indicated in millibars (subsiding and rising parcels are shown in dashed and solid lines, respectively).

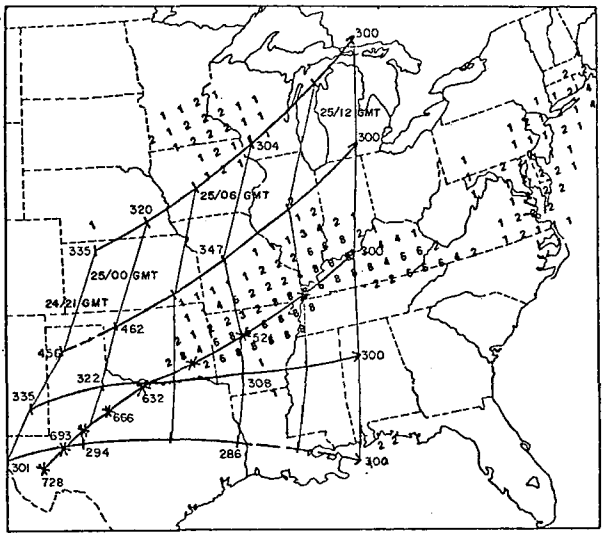

Fig. 1. Plotted trajectories for five air parcels passing over a severe squall line (MDR data superimposed) in AVE IV at 0600 GMT 25 April. All parcels terminate at 300 mb with the vertical location (mb) shown at each time period (tick marks).

Of particular interest is the extreme diverging of the air parcels between 2100 GMT (over the Southern Plains) and 1200 GMT (over the Eastern U.S.) as they traveled over the squall line, indicating the large magnitude of the upper-level divergence. In response to this divergence, the air parcel traveling from southwest Texas northeastward across Arkansas and Kentucky rises from 728 to 300 mb (a-372-mb net vertical displacement (NVD) in 15 h) while the other three air parcels change their pressure less than 50 mb during the same time period.

Reap (1972) has developed a technique for translating results from a trajectory model into an Eulerian framework. A quantity called net vertical displacement (NVD) was developed by Reap which, when translated into the Eulerian grid, resulted in a spatial distribution of dp/dt for all air parcels ending their trajectories at all grid points in the grid array. The rate of pressure change along the parcel's path is actually calculated from $\Delta p/\Delta t$ where Δp represents the pressure change observed by the parcel as it moved three-dimensionally in space over a time period of 12 h (Δt). Using the 3- and 6-h data available in the AVE IV experiment, NVD's were computed in a similar manner as was previously described except Δt was 3 or 6 h. The increased temporal resolution of the data produced a NVD distribution that related well to the location and intensity of convective activity.

NET VERTICAL DISPLACEMENTS, PARCEL ENERGY INDICES, AND CONVECTIVE STORM DELINEATION

Figure 2 shows the average vertical profiles of NVD (mb/3h) as a function of precipitation intensity (from MDR data) from all nine time periods of AVE IV. "No precipitation" areas had small positive NVD's at most levels while negative values occurred in

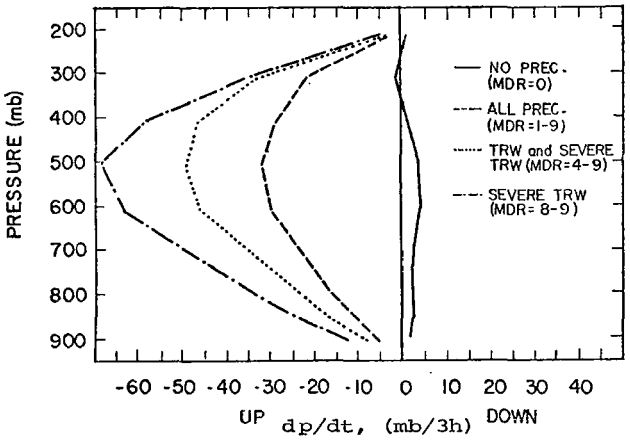

Fig. 2. Average profiles of dp/dt or NVD as a function of pressure and MDR coded precipitation intensity. (Maximum MDR value was assigned to a grid point within 1/2 grid distance (≈80 km) in MDR 3-h composite charts).

precipitation areas with the maximum upward values located around 500 mb. The magnitudes of the average values of NVD's were larger at all pressure levels in areas containing more intense convective activity so that a value of -70 mb/3h was associated with severe TRW in AVE IV.

Figure 3a shows examples of the gridded trajectory data (NVD's at 850 and 500 mb) for 0600 GMT April 25 when a severe squall line was located in the middle of the network. The NVD fields of AVE IV not only exhibited good spatial and temporal continuity but correlated highly with both the location and intensity of precipitation as revealed by the radar observed convection for Fig. 3a (see Fig. 1 for MDR composite chart) and Fig. 2. Negative (rising air parcels) NVD centers were associated with all major precipitation areas and subsidence (positive NVD's) usually separated these systems.

To accurately parameterize the static stability of the atmosphere in AVE IV, a method was developed to objectively calculate both the amount of buoyant energy (ergs/g) necessary to be added to a parcel to make it hydrostatically unstable (negative buoyant energy or NBE) and the amount available to be converted into kinetic energy of the upward vertical velocity (positive buoyant energy or PBE) or "updraft" if the parcel were to become unstable. For each time period, the basic gridded temperature and moisture fields were used to produce spatial fields of NBE and PBE. NBE was calculated by summing all negative buoyant energy up to 500 mb over each grid point. PBE resulted from summing all positive energy up to 100 mb. Smaller NBE values should correlate with the increasing occurrence of TRW while larger PBE should relate to the increasing intensity of convective activity.

Figure 3b presents the NBE and PBE spatial fields (10^4ergs/g) for the same period as Fig. 3a. Convective precipitation (MDR$\geq$2) usually occurred where NBE values were $<200. \times 10^4$ ergs/g, while thunderstorms and severe convection were associated with values $<100. \times 10^4$ergs/g. While the location of the convective activity was accurately delineated with the NBE fields, the PBE fields related well to the intensity where most MDR$\leq$4 were associated with PBE values $<500. \times 10^4$ergs/g. In contrast, heavy and severe TRW (MDR$\geq$6) occurred with higher PBE values ($>500. \times 10^4$ergs/g).

Since both a dynamic lifting mechanism and weak static stability are both usually needed for convective storm development, NVD's (at 9 pressure levels from 900 mb to 100 mb) and the NBE and PBE stability measurements were combined, using multiple linear regression, in an attempt to spatially delineate the location and intensity of convection for all AVE IV time periods. Correlations were computed with grid point data where the predictand was the MDR intensity categories (MDR$<$2, 2$\leq$MDR$<$4, 4$\leq$MDR$<$8, MDR$\geq$8) calculated in the manner explained in Fig. 2. A linear correlation coefficient of 0.6 was obtained for these increasing intensity categories of convection with the most important parameters (in order) being NVD (500 mb), NVD (850 mb), NBE, and PBE (these parameters accounted for 98% of the total explained variance). This linear regression delineates (with 80% accuracy) between non-convective (MDR$<$2) and convective areas (MDR$\geq$2) but it only determines the correct intensity category 50% of the time.

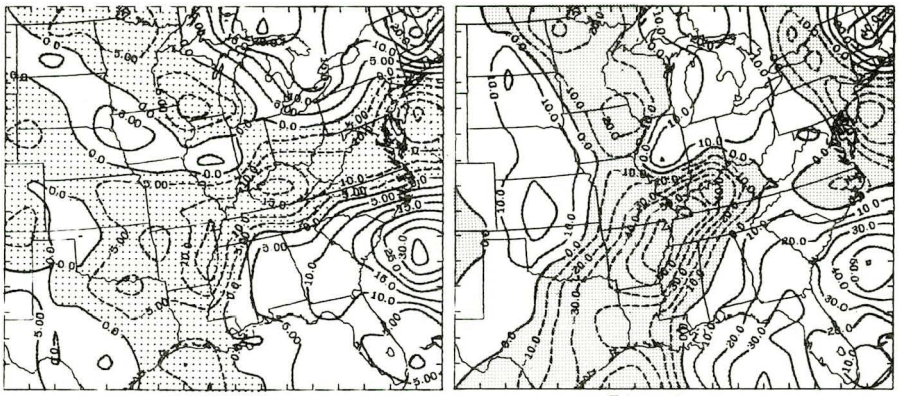

850 mb 500 mb

a. Net vertical displacements (mb/3h)

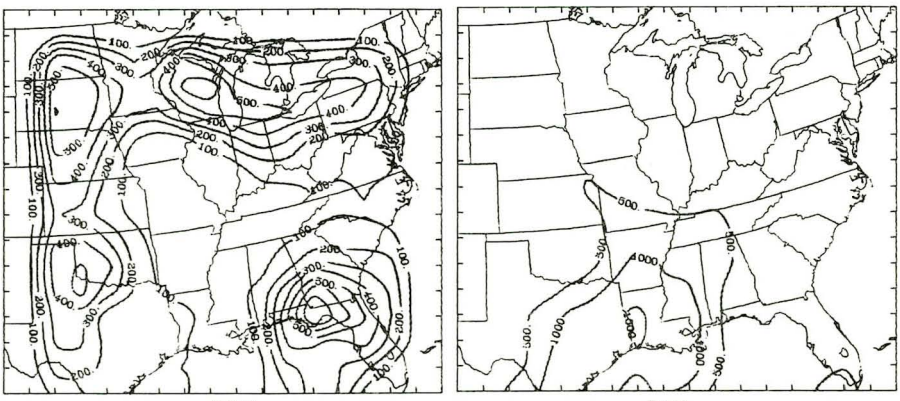

NBE PBE

b. Parcel energy indices (10^4 ergs g^{-1})

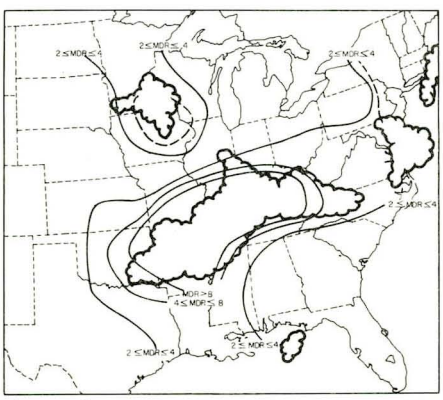

c. Diagnostic delineation of convective storm location and intensity

Fig. 3. Analyses of a) net vertical displacements, b) parcel energy indices, and c) diagnostically determined intensity categories of convection (scalloped areas are MDR≥2) for 0600 GMT April 25, 1975.

Figure 3c is an example of the diagnostic delineation of convective storm location and intensity for 0600 GMT 25 April. These results demonstrate the remarkably high degree of scale interaction between synoptic- and convective-scale systems which are separated (in scale length) by approximately three orders of magnitude.

CONCLUSIONS

A three-dimensional trajectory model has been used to both parameterize and dynamically explain the interactions between convective storms and their environment using data from NASA's AVE IV Experiment. By combining NVD's with an advanced measure of static stability (PBE and NBE), using multiple linear regression, convective activity of various intensities can be spatially determined. Convective and non-convective areas can therefore be delineated with 80% accuracy, which demonstrates the high degree of scale interaction between synoptic- and convective-scale systems.

ACKNOWLEDGMENTS

The author wishes to thank Miss Karen Cobbs for typing the manuscript. This research was sponsored by the National Aeronautics and Space Administration under Contract NAS8-31773, Aerospace Environment Division, Space Sciences Laboratory, NASA Marshall Space Flight Center, Alabama.

REFERENCES

Collins, R. W., 1970: AFGWC multilevel cloud model. AFGWC Tech. Mem. 70-10, 35 pp.

Foster, D. S., and R. M. Reap, 1973: Archiving of Manually Digitized Radar data, Techniques Development Laboratory Office Note 73-6, National Weather Service, Silver Springs, Md., 10210, 12 pp.

Reap, R. M., 1972: An operational three-dimensional trajectory model. J. Appl. Meteor., 11, 1193-1202.

Wilson, G. S., 1976: Large-scale vertical motion calculations in the AVE IV experiment. Geophys. Res. Letters, 3, 735-738.

_____, and J. R. Scoggins, 1976: Atmospheric structure and variability in areas of convective storms determined from 3-h rawinsonde data. NASA CR-2678, NASA Marshall Space Flight Center, Huntsville, Alabama, 118 pp.

Paper No. 4

KINETIC ENERGY BUDGET STUDIES OF AREAS OF CONVECTION

Henry E. Fuelberg, *St. Louis University, St. Louis, MO*

ABSTRACT

Synoptic-scale kinetic energy budgets are being computed for three cases when large areas of intense convection occurred over the Central United States. Major energy activity occurs in the storm areas.

INTRODUCTION

Kinetic energy budget studies have been performed mostly on synoptic-scale systems such as cases of cyclogenesis; few studies have dealt with mesoscale phenomena. Fuelberg (1977) and Fuelberg and Scoggins (1978) studied the energy variability of the synoptic-scale flow in which convection was imbedded. Large areas of intense thunderstorms seemed to influence the surrounding synoptic-scale environment. The present research involves additional studies of synoptic-scale kinetic energy variability during periods of intense thunderstorms.

THEORY

The kinetic energy equation in isobaric coordinates is:

$$\frac{\partial K}{\partial t} = \int_{\sigma}\int_{p} -\vec{V}\cdot\vec{\nabla}\phi - \int_{\sigma}\int_{p} \vec{V}\cdot k\vec{V} - \int_{\sigma}\int_{p} \frac{\partial \omega k}{\partial p} + \int_{\sigma}\int_{p} \vec{V}\cdot\vec{F}$$

(a) (b) (c) (d) (e)

where $\int_{\sigma}\int_{p} = \frac{1}{g}\iiint dx\,dy\,dp$, $\vec{F}$ is the frictional force, k is horizontal kinetic energy per unit mass, and A is the area of computation σ. Local changes in kinetic energy for a fixed volume, term (a) above, are due to four processes. Term (b) represents kinetic energy generation due to cross contour flow. Terms (c) and (d) are horizontal and vertical flux divergence of kinetic energy. Term (e), called the dissipation term, represents a transfer of energy between resolvable and unresolvable scales of motion.

PROCEDURES

Rawinsonde data are objectively analyzed onto a grid system that encloses the area of study. Gridded fields of the input data are obtained at the surface, and then at 50 mb intervals up

to 100 mb. Vertical motions are computed using the kinematic method. By using finite difference techniques, values of the budget terms are computed at individual grid points at 50 mb intervals. Grid point fields of the budget terms are related to storm location, and the grid point values can be averaged in various ways.

Three case studies are being investigated--the first and second Atmospheric Variability and Severe Storm Experiments (AVSSE I, 27-28 April 1975; and AVSSE II, 6-7 May 1975) and the seventh Atmospheric Variability Experiment (AVE VII, 2-3 May 1978).

RESULTS

Kinetic energy budgets have already been computed for the AVSSE I and II periods. Brief results of these studies will be described.

a. The AVSSE II Period. During AVSSE II, intense thunderstorm activity formed in the Midwest and in central Texas along a dry line. To isolate energy processes near the convection from processes in non convection areas, grid point budget values were averaged to give kinetic energy budgets over small areas that just enclosed the convection. The budget areas moved as the convection moved.

Thunderstorm activity began near 1500 GMT 6 May 1975, reached peak intensity (18.6 km tops) and areal coverage near 2100 GMT, and had dissipated by 0300 GMT 7 May. The pressure-time cross-section of Fig. 1 indicates that average synoptic-scale vertical motion within the area was a maximum upward value ($\omega<0$) at 2100 GMT and later changed to downward motion. The literature suggests that diabatic heating associated with convection is probably responsible for inducing these changes. Fig. 1 also reveals that kinetic energy from the lower and middle troposphere is transported to higher levels of the atmosphere.

Dramatic changes in the kinetic energy budget also occur. Destruction of kinetic energy by cross contour flow (- values) near the level of the jet stream changes to strong generation of kinetic energy near 2100 GMT and then tapers off and changes sign (Fig. 2). Fuelberg and Scoggins (1978) observed similar variations in energy generation during AVE IV. Using mesoscale data, Tsui and Kung (1977) found that periods of active convection were times of strong generation of kinetic energy, but that destruction of kinetic energy was dominant near the time of storm passage.

The profile of horizontal flux divergence of kinetic energy at peak storm intensity (2100 GMT) is considerably different from that at earlier and later times (Fig. 3). Strong upper level export of energy (+ values) is dominant at 2100 GMT. The fluctuations in the transport term seen in the present case are similar to those observed during the AVE IV squall lines (Fuelberg and Scoggins, 1978).

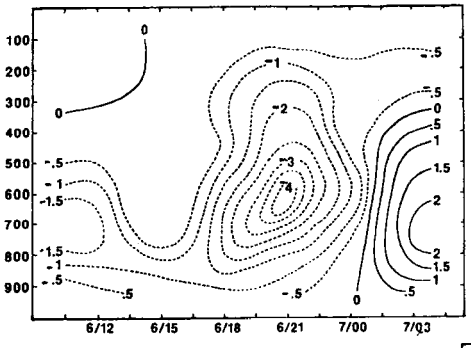

Fig. 1. Pressure-time cross section of vertical motion (ω) for the Texas convection area. $\mu b\ s^{-1}$.

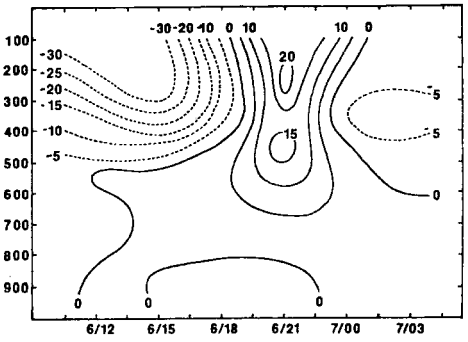

Fig. 2. Pressure-time cross section of term $-\vec{V}\cdot\vec{\nabla}\phi$ for the Texas convection area. W m^{-2}(100 mb)$^{-1}$

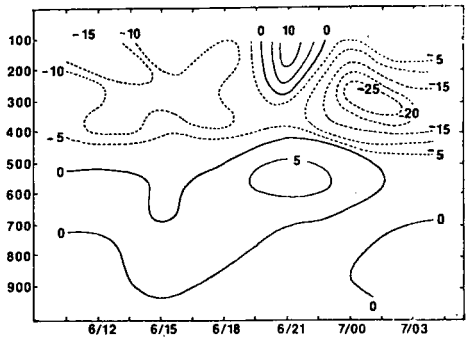

Fig. 3. Pressure-time cross section of term $\vec{V}\cdot k\vec{V}$ for the Texas convection area. W m^{-2}(100 mb)$^{-1}$.

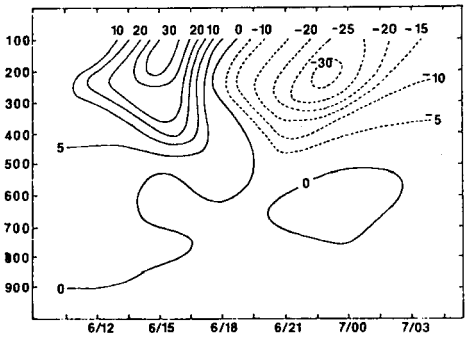

Fig. 4. Pressure-time cross section of the dissipation term for the Texas convection area. W m^{-2}(100 mb)$^{-1}$.

The dissipation term reveals that energy transfer between resolvable and unresolvable scales of motion is large in the synoptic-scale environment of the storms (Fig. 4). The net effect of all motions is a transfer of energy from resolvable to unresolvable scales (- values) after 1800 GMT. Before maximum storm intensity, the unresolvable scales of motion are a source of synoptic-scale kinetic energy.

A tabulated kinetic energy budget of this convection area is given in Table 1. Generation of kinetic energy by cross contour flow and dissipation to subgrid scales of motion are the two most important processes. The magnitudes of the energy processes occurring in the synoptic-scale environment of the convection are larger than those observed near many mature cyclones.

Table 1. Average kinetic energy budget for the limited area enclosing the convection in Texas at 2100 GMT 6 May 1975. The area is 1.5 x 10^{11} m^2.

Layer (mb)	K ($10^5 Jm^{-2}$)	$\partial K/\partial t$ (Wm^{-2})	$\vec{\nabla}\cdot k\vec{V}$ (Wm^{-2})	$\partial \omega k/\partial p$ (Wm^{-2})	$-\vec{V}\cdot\vec{\nabla}\Phi$ (Wm^{-2})	D (Wm^{-2})
Sfc-700	0.5	-0.9	-1.2	2.0	1.0	-1.1
700-400	6.5	8.5	10.0	8.4	31.8	-4.9
400-100	24.1	2.6	5.9	-10.4	52.4	-54.4
Total	31.1	10.2	14.7	0.0	85.2	-60.4

b. The AVSSE I Period. A line of severe thunderstorms stretching from Nebraska into Texas formed along a cold front during the AVSSE I period. The results of this section demonstrate a different procedure by which the kinetic energy budget of storm areas is being investigated.

Values of Manually Digitized Radar (MDR) data are assigned to each grid point at each observation time. The average of each budget term is computed for various categories of MDR intensity by combining all observation times.

The average budget for grid points having no convection during AVSSE I is given in Table 2A while the average budget for grid points of moderate and intense convection (MDR 4-9 of the old MDR scheme) is given in Table 2B. Energy processes occurring during convection are much larger than those observed for non convection. The grid points associated with convection are characterized by strong destruction of kinetic energy by cross-contour flow and by transfer of energy from subgrid to grid-scale motions (positive dissipation).

c. Other Studies. Beside the results presented in this brief report, spatial fields of the energy budget terms are being examined for continuity and their relation to storm activity and other map features. Energy budgets for individual times of each case study are being compiled and examined for temporal var-

Table 2-A. Average kinetic energy budget for grid points having no convection during AVSSE I (26-27 April 1975). The number of grid points is 138.

Layer (mb)	K ($10^5 Jm^{-2}$)	$\partial K/\partial t$ (Wm^{-2})	$\vec{\nabla}\cdot k\vec{V}$ (Wm^{-2})	$\partial \omega k/\partial p$ (Wm^{-2})	$-\vec{V}\cdot\vec{\nabla}\phi$ (Wm^{-2})	D (Wm^{-2})
Sfc-700	2.7	-1.2	0.7	0.6	2.4	-2.3
700-400	7.1	1.5	8.1	0.6	9.2	1.0
400-100	14.4	4.4	-8.1	-1.2	-13.2	8.3
Total	24.2	4.7	0.7	0.0	-1.6	7.0
B. Kinetic energy budget for MDR 4-9 (43 grid points).						
Sfc-700	2.7	-0.8	0.0	2.6	-3.9	5.7
700-400	9.9	7.0	-7.6	9.4	-2.8	11.6
400-100	19.1	9.4	-4.8	-12.1	-35.6	28.1
Total	31.7	15.6	-12.4	0.0	-42.3	45.4

iability. Results of the AVE 7 period (May 2-3, 1978) also are being compiled.

CONCLUSIONS

The synoptic-scale kinetic energy budget of large areas of intense convection is considerably different from that of areas of non convection. Time series analysis of some budget terms suggests that the energy variability is closely related to the life cycle of the storms.

ACKNOWLEDGEMENTS

This research is sponsored by NASA under Contract NAS8-32838 and is under the auspices of the Aerospace Environment Division, NASA Marshall Space Flight Center.

REFERENCES

Fuelberg, H. E., 1977: Atmospheric energetics in regions of intense convective activity. NASA CR-2826 Marshall Space Flight Center, Alabama, 136 pp.

_____, and J. R. Scoggins, 1978: Kinetic energy budgets during the life cycle of intense convective activity. Mon. Wea. Rev., 106, 637-653.

Tsui, T. L., and E. C. Kung, 1977: Subsynoptic-scale energy transformations in various severe storm situations. J. Atmos. Sci., 34, 98-110.

Page intentionally left blank

Paper No. 5

THE DISTRIBUTION OF BAROCLINITY WITHIN THE ATMOSPHERE

D. A. Barber and M. Wai, *Dept. of Atmospheric Sciences, Oregon State University*

ABSTRACT

A three dimensional numerical interpolation scheme which resolves frontal gradients with high fidelity has been developed and is being applied to the study of atmospheric upper baroclinic zones.

INTRODUCTION

The aim of our research is to improve understanding of the structure and evolution of atmospheric fronts. Achievement of this goal requires the representation of frontal intensity with a dynamically significant parameter for which we have selected the baroclinity,

$$\vec{B} = \frac{g}{\theta} \vec{\nabla}_p \theta \qquad (1)$$

where $\vec{B}$ is the baroclinity vector, g the acceleration of gravity, and θ and $\vec{\nabla}_p\theta$ are the potential temperature and its isobaric gradient. Furthermore, we may define local frontogenesis to be the local tendency of the baroclinity which may be shown to be (to good approximation)

$$\frac{\partial \vec{B}}{\partial t} = \frac{g}{\theta} \vec{\nabla}_p \left[\frac{d\theta}{dt} - \vec{\nabla}_p \cdot (\vec{v}\theta) - \frac{\partial}{\partial p} (\omega\theta) \right] \qquad (2)$$

where $\omega = \frac{dp}{dt}$.

Because of the small horizontal scale of fronts compared with the spacing of sounding stations the magnitude of the baroclinity may be considerably underestimated in the vicinity of intense fronts if only horizontal or isobaric data are utilized. This difficulty may be largely obviated through use of cross-section analyses which effectively apply the high resolution information available in the vertical over each sounding station to improvement of horizontal resolution. (Shapiro, 1970).

METHOD

The considerable expenditure of effort required for manual analysis of cross-sections has led to the development of successful numerical interpolation schemes for cross-section analysis (Shapiro and Hastings, 1973 and Whittaker and Petersen, 1975); however, these are two dimensional techniques from which one can obtain isobaric analyses only by laborious combination of many independently analysed cross-sections. We propose instead to apply a fully three dimensional scheme based on a straight forward extension of the Barnes (1973) horizontal method.

We extend the Barnes scheme by redefining his weight as

$$W_i = \frac{1}{4\pi kD} \exp\left[\frac{-d_i^2}{4k} - \frac{Z_i^2}{4D}\right] \qquad (3)$$

where W_i is the weight factor for the i^{th} observation, d_i and Z_i are the horizontal and vertical distances between the observation and a given grid point, and k and D are weight parameters controlling the smoothness of the output. To facilitate selection of k and D, we have coded a two dimensional cross-section analysis method based on (3) having a horizontal grid spacing of one latitude degree (111 km) and a vertical spacing of 50 mb.

The resulting potential temperature analysis on a cross section through the complex hyperbaroclinic zone studied by Frank and Barber (1977) is shown in Fig. 1 together with the component of the baroclinity in the plane of the cross-section estimated by finite difference method. For comparison, Fig. 2 reproduces the careful manual analysis of Frank and Barber. The numerical scheme has reproduced not only the gross features, but also most of the details with considerable fidelity. Further improvement would be possible (at the expense of more computer time) if the vertical resolution were increased.

A quantitative demonstration of the efficacy of the cross-section scheme is illustrated in Fig. 3. The baroclinity estimated from the cross section at the 500 and 800 mb levels is shown by the dashed lines. The solid lines are the results obtained through application of a horizontal Barnes analysis on a one latitude degree by one longitude degree grid. The magnitude of the baroclinity estimated from the cross-section program is fifty to one hundred percent greater in the hyperbaroclinic zones than that obtained from the isobaric analyses.

CURRENT WORK

We are now coding the full three dimensional scheme for application to the AVE II data. Furthermore, we intend to demonstrate its usefulness through application to operationally available

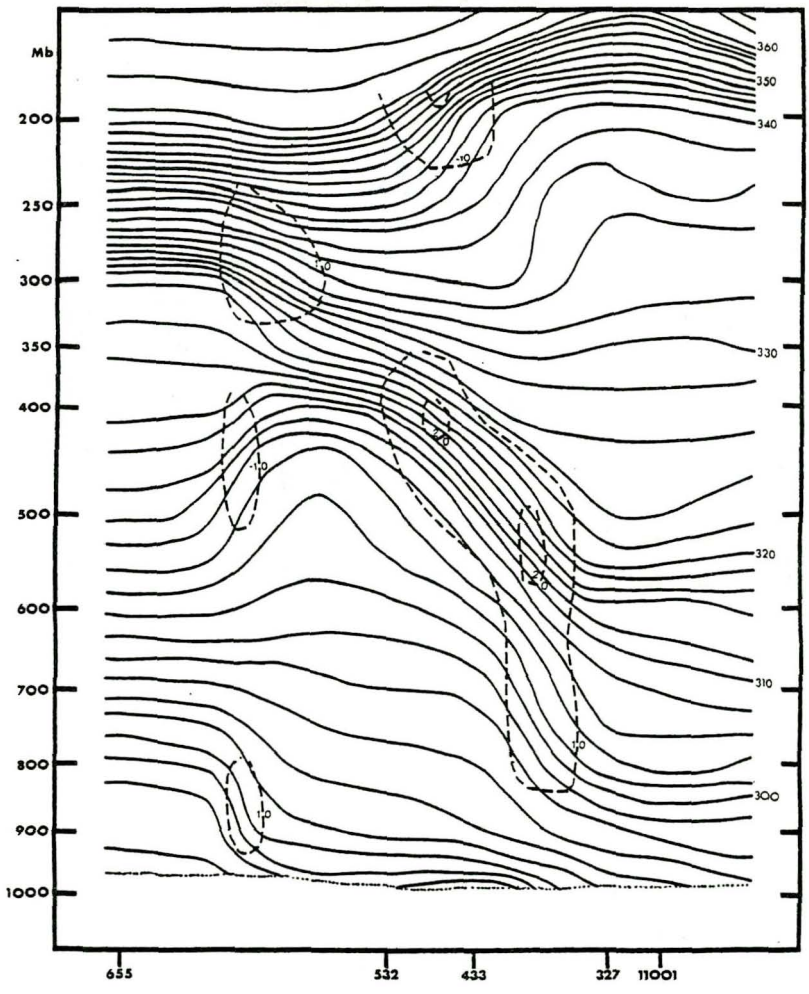

Fig. 1. Objectively analyzed cross-section through hyperbaroclinic zone. Isentropes (κ) solid and baroclinity (10^{-7} s^{-2}) dashed. 1115 uT, 12 May 1974.

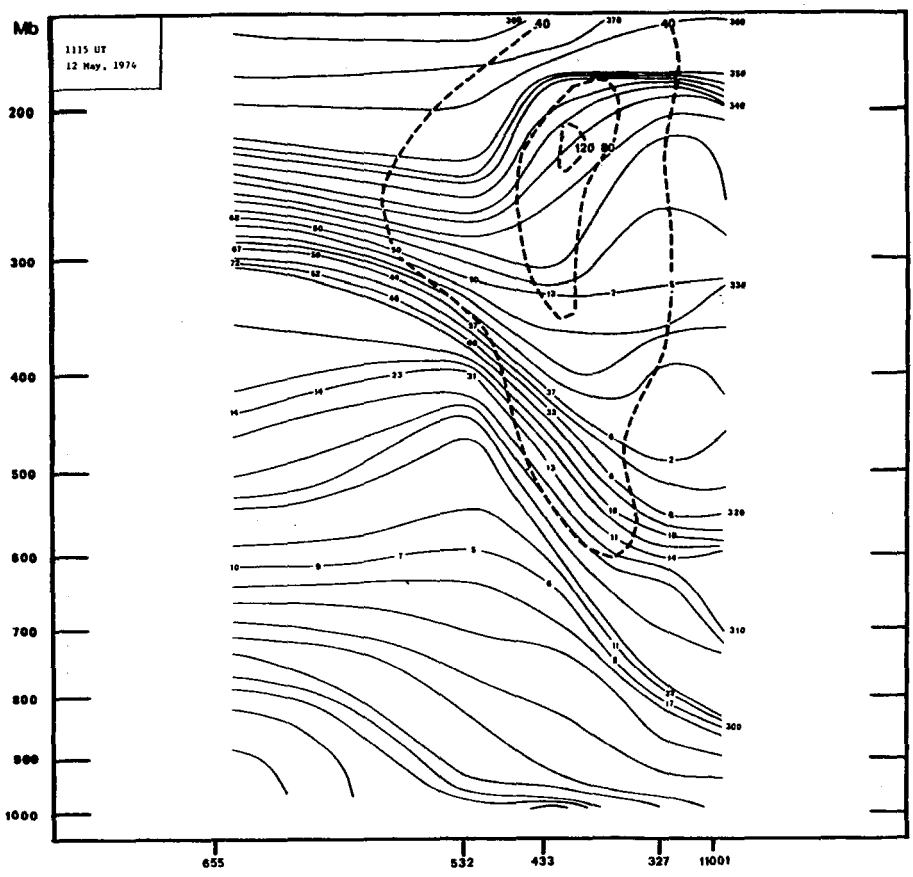

Fig. 2. Manually analyzed cross-section along same line as Fig. 1. Isentropes (κ) solid and isotachs (κt) dashed of flow normal to section (Frank and Barber, 1977).

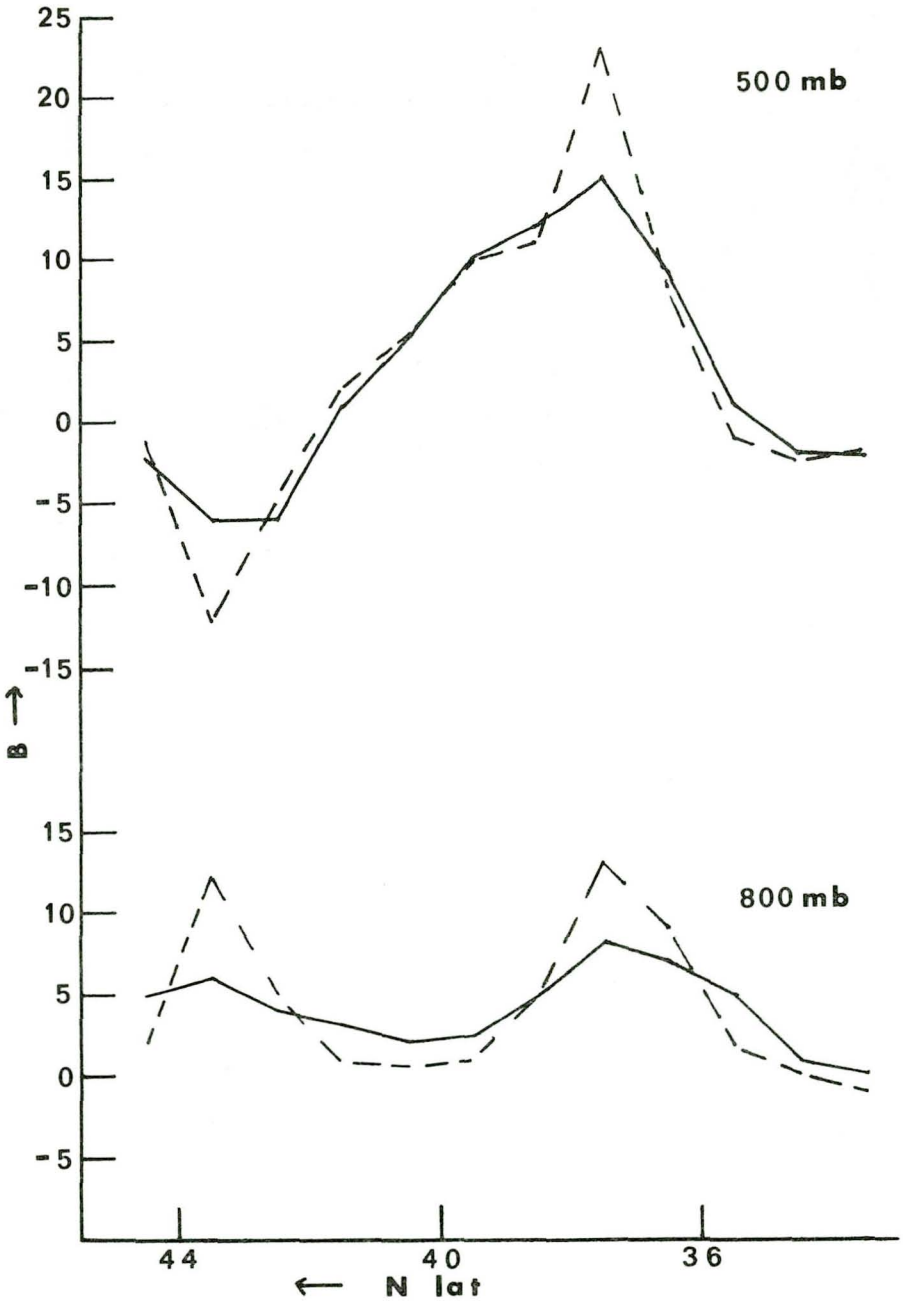

Fig. 3. Baroclinity (10^{-7} s^{-2}) from objective isobaric analysis (solid) and from objective cross-section (dashed) as a function of latitude along line of Fig. 1.

teletype data and comparison with National Weather Service analyses.

In addition to depicting the full three dimensional baroclinity distribution, we plan to apply the method to the wind field. In the case of the wind field, some smoothing of the vertical wind field is desirable (see Schmidt and Johnson, 1972). Therefore, a different set of weight parameters (k and D) will be appropriate.

Finally, we shall apply the improved three dimensional wind and temperature analyses to the evaluation of terms in the frontogenesis equation (2).

REFERENCES

Barnes, S., 1973: Mesoscale objective map analysis using weighted time-series observations. NOAA Tech. Memo. ERL NSSL - 62, Norman, OK, 60 pp.

Frank, A. and D. Barber, 1977: Fronts and frontogenesis as revealed by high time resolution data. NASA Ref. Publ. 1005, Marshal Space Flight Center, Alabama.

Schmidt, P. and D. Johnson, 1972: Use of approximating polynomials to estimate profiles of wind, divergence, and vorticity. Mon. Wea. Rev., 100, 345-353.

Shapiro, M.A., 1970: On the applicability of the geostrophic approximation to upper-level frontal-scale motions. J. Atmos. Sci., 27, 408-420.

Shapiro, M.A. and Hastings, 1973: Objective cross-section analyses by Hermite polynomial interpolation on isentropic surfaces. J. Appl. Meteor., 12, 753-762.

Whittaker, T. and R. Petersen, 1975: Objective cross-section analysis incorporating thermal enhancement of the observed winds. In Project Report: Meteorological Applications of Satellite Indirect Soundings. L.H. Horn, Principal Investigator. Dept. of Meteorology, University of Wisconsin, Madison.

Paper No. 6

A COMPARISON BETWEEN GOES-1 IR DIGITAL DATA AND RADAR DATA FOR THE 4 APRIL 1977 SEVERE STORMS OUTBREAK

C. A. Peslen, *Laboratory of Atmospheric Sciences, Goddard Space Flight Center* and Richard Anthony, *GE/MATSCO, Beltsville, Maryland*

ABSTRACT

The 4 April 1977 severe storms outbreak over Georgia and Alabama provided an excellent opportunity to examine the complementary characteristics between satellite and radar data.

INTRODUCTION

On 4 April 1977, an old thunderstorm boundary provided an environment conductive to the development of an intense mesosystem over Alabama and Georgia. Tornadoes, funnel clouds, large hail, and high winds were associated with severe local storms which developed along two parallel lines of activity between 1200 GMT and 2300GMT. A Southern Airways DC-9 crashed WNW of Atlanta, Georgia at 2117GMT after penetration of a mesolow – associated supercell. This event provided an opportunity to compare satellite and radar capabilities in examining features associated with severe thunderstorm cells.

PROCEDURE

GOES-1 infrared digital image data were displayed on the Atmospheric and Oceanographic Information Processing System (AOIPS) to infer cloud top heights and to examine line deformation, merging cells, and enhanced localized areas of mid to upper level cloudiness.

Hourly PPI reports of radar echo heights were compared to the corresponding satellite-derived cloud top heights of the coldest areas of the thunderstorm cells. When it was possible, satellite cloud top heights were acquired at 3 minute intervals and compared to the radar echo heights on the half hour to examine the relationship between the two techniques.

RESULTS

Figures 1 and 2 are examples of the enhanced infrared GOES-1 images for 1930GMT and 2100GMT. They were selected from the 44 image set to explain how areas of potential severe weather can be located using both conventional and satellite data. According to conventional analyses (Miller, 1978), a mesocyclone is intensifying in an area located between 33°00'N, 88°00'W and 34°30'N, 86°30'W. Increased local convergence and strong surface winds are contributing to strong vertical cell development. This development can be seen at 1930GMT in the aforementioned area. Satellite data show cloud top heights of 16.6km and 13.4km for the two coldest equivalent black body temperature areas. New cell growth can be seen along the southwest flank of the line due to strong moisture advection and

local convergence. By 2100GMT (Fig. 2), the original cold areas have greatly expanded between 34°00'N, 87°00'W and 35°30'N, 84°00'W. Cloud top heights have decreased from their maximum peak values. The Birmingham tornado (33°31'N, 86°49'W) has occurred and the Rome, Ga. (34°14'N, 85°11'W) mesolow is increasing in intensity. By 2112GMT, these two cold areas appear to merge and a tornado has occurred at Rome. The examination of a series of enhanced infrared images assisted in locating areas of potential severe weather in this case study.

Additional interesting features in the infrared data are enhanced areas of upper level cloudiness which are located at (36°00'N, 90°00'W), (36°30'N, 88°00'W) and (38°00'N, 86°00'W) on the 1930GMT image. Preliminary investigation shows that these features are moving northeastward at 67m $sec^{-1}$and are located between 9 and 11km. These features appear to be reflections of upper tropospheric wind maxima which are moving at twice the speed of the thunderstorm cells moving along the Birmingham - Rome axis. Convective activity appears to intensify along this axis as these features move northeastward. Additional research is required to determine whether these features are associated with upper level divergence and positive vorticity advection (PVA) and whether they play a significant role in the production of severe weather along the Birmingham - Rome axis.

This case study also presented an excellent opportunity to examine the complementary characteristics of satellite and radar data. Table 1 shows 18 cases where satellite-derived cloud top heights were matched exactly in time to their radar echo tops. A local sounding (Centerville, Ala.) was used to convert IR black body temperature to height. The mean difference between the two methods was .775km with slightly higher satellite cloud top heights. Previous studies by Smith and Reynolds (1976) and Maddox et al. (1976) indicated that radar heights were consistently higher than the IR tops derived from an environmental sounding. Inadequate IR resolution was noted as a reason for this difference. Also, cumulonimbus tops are not necessarily at ambient temperature. There were also some differences among the three studies: (1) radar and satellite times were not coincident in the Smith & Reynolds paper, (2) different types of clouds were measured, and (3) the statistical samples varied for each study. On the assumption that there is no satellite calibration problem, the satellite cloud top heights may be higher than the radar tops since: (1) the coldest areas in the satellite data may not necessarily be the area of precipitation reflected by the radar echo, and (2) the radar operator may not stop the Range Height Indicator at the cell's highest point.

Comprehensive studies of the relationship between radar echo heights and satellite cloud top heights are needed to resolve any ambiguities in data interpretation. Since height variations of overshooting tops can be detected in rapid scan (3 - 5 minute interval) geostationary satellite images (Adler and Fenn, 1978), it is important to understand what these height variations mean in the terms of thermodynamic and physical processes and what role they play in the production of severe weather.

CONCLUSIONS

An attempt was made to emphasize the unique and complementary characteristics of conventional and satellite data in examining areas of potential severe local storm development. The enhanced IR data assisted conventional and radar reports in locating the most likely area of severe weather on 4 April 1977 in Alabama and Georgia. A comparison between satellite cloud top heights and radar echo heights showed small differences in reported heights.

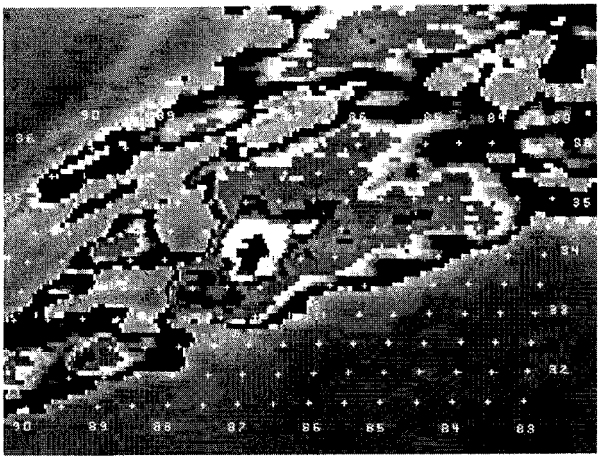

Figure 1. Enhanced IR digital image for 1930GMT on 4 April 1977.

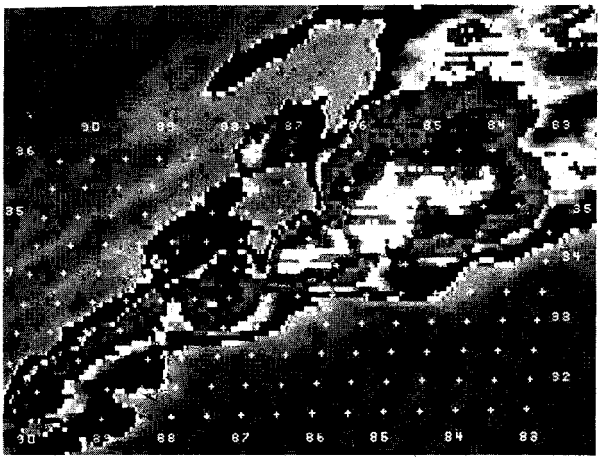

Figure 2. Enhanced IR digital image for 2100GMT on 4 April 1977.

Table 1
A Comparison Between Radar Heights
and Satellite-Derived Cloud Top Heights

Coldest Area	Radar Height (km)	Satellite-Derived Height (km)	Satellite Height – Radar Height (km)
1	15.2	16.2	+1.0
2	15.2	14.8	-0.4
3	12.5	14.1	+1.6
4	15.2	16.4	+1.2
5	14.0	13.4	-0.6
6	11.9	13.3	+1.4
7	13.7	13.3	-0.4
8	14.3	16.2	+1.9
9	15.2	16.2	+1.0
10	12.8	15.1	+2.3
11	12.2	15.1	+2.9
12	13.1	13.1	0.0
13	14.0	13.3	-0.7
14	12.2	15.2	+3.0
15	14.0	15.4	+1.4
16	13.1	13.3	+0.2
17	13.7	13.3	-0.4
18	12.8	13.1	+0.3

REFERENCES

Adler, R. F. and D. D. Fenn, 1978: Satellite – Based Thunderstorm Intensity Parameters. NASA Technical Memorandum 78094, Goddard Space Flight Center, 44 pp.

Maddox, R. A., A. J. Negri, and T. H. Vonder Haar, 1976: Comparison of Severe Storm Cloud Top Heights Derived from Satellite and Radar Observations. Prepared for 1976 Fall Annual Meeting of the American Geophysical Union.

Miller, R. C., 1978: Severe Convective Weather from the Jet Airliner – A study of Southern Airways Flight 242. Preprints from the Conference on Weather Analysis and Aviation Meteorology, Oct. 16-19, 1978, p. 279-283.

Smith, E. A., and D. W. Reynolds, 1976: Comparison of cloud top height determinations from three independent sources: Satellite IR measurements, Satellite viewed cloud shadows, Radar. Paper presented at COSPAR 19th Plenary Meeting, Philadelphia, PA, June 1976, 17 pp.

Paper No. 7

FORMULAS FOR DETERMINING STORM MOVEMENT FROM THE SURROUNDING FIELDS

R. C. Costen, *Langley Research Center, Hampton, Virginia*

ABSTRACT

Formulas are given for determining a conserved property of a storm and its centroid from any scalar field that has a tendency equation. The velocity of the centroid is also given. These formulas depend only on fields that are external to the storm.

INTRODUCTION

The propagation of storms may be characterized by the movement of local disturbances in many fields, such as density, moisture, internal energy, vorticity, divergence, pressure, stability, convection, etc. It is appropriate, then, to attempt to define a centroid for the disturbance in each of these fields and to characterize the movement and dynamics of a storm by the velocities and relative velocities of these centroids. The purpose of this paper is to show that this can be done for any scalar meteorological quantity s that satisfies a tendency equation of the form

$$\frac{\partial s}{\partial t} + b = 0 \tag{1}$$

where b represents the remaining terms. We shall also show that the centroid and its velocity are determined completely from fields that are outside the disturbance. This is a significant feature since measuring fields within a storm, either in situ or remotely, is often more difficult than measuring the fields that surround a storm. The scalar s may also represent the Cartesian components of vector quantities, such as the convection, and the vertical component of vorticity.

Approach-Throughout this paper, a disturbance in a field is defined by $\partial(\text{field})/\partial t \neq 0$; and a local disturbance is a disturbance that is surrounded by a layer of finite thickness where $\partial(\text{field})/\partial t = 0$. Instead of treating the scalar field s directly, we shall consider its Laplacian

$$L = \nabla^2 s \tag{2}$$

the source of the field s. A storm may be considered as a local disturbance in L, since $\partial L/\partial t$ is much larger within a storm, due to the movement and growth or decay of the storm, than in the quiescent surroundings.

Take V to be the volume of the storm, or, more specifically, the volume of the local disturbance in L, as illustrated in fig. 1. Within V, the disturbance

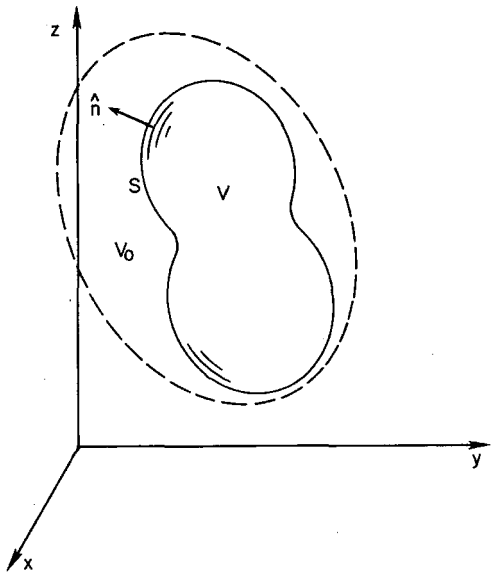

Fig. 1-Volume V that contains a local disturbance in L. Within V, the disturbance $\partial L/\partial t = -\nabla^2 b$ is generally nonzero; in the surrounding layer V_o of finite thickness $\partial L/\partial t = -\nabla^2 b = 0$. Also shown is the closed interface S between V and V_o with its outward unit normal $\hat{n}$.

$\partial L/\partial t = -\nabla^2 b$ is generally nonzero; however, V is surrounded by a layer V_o of finite thickness where $\partial L/\partial t = -\nabla^2 b = 0$. The volumetric integral of L in V is conserved and is termed the efflux E. Its centroid $\vec{R}_E$ may be regarded as a centroid of the storm, and the centroidal velocity $\dot{\vec{R}}_E$ may be regarded as a propagation velocity of the storm.

Centroidal Equations-In a previous paper (ref. 1), the movement of a local disturbance in a vector field $\vec{v}$ was treated, where $\vec{v}$ satisfied the equation $\partial\vec{v}/\partial t + \vec{f} = 0$. The vector field $\vec{v}$ was characterized by its curl and its divergence, as the scalar field s is now characterized by its Laplacian. The scalar formulation can be derived from the previous vector formulation by taking the gradient of eq. (1), and making the identifications $\vec{v} = \nabla s$ and $\vec{f} = \nabla b$ in the previous vector formulas. This gives for the

conserved efflux

$$E = \iiint \nabla^2 s \, dV = \oiint \frac{\partial s}{\partial n} \, dS \tag{3a}$$

its centroid

$$\vec{R}_E = E^{-1} \iiint \vec{r} \nabla^2 s \, dV = E^{-1} \oiint (\vec{r} \frac{\partial s}{\partial n} - \hat{n} s) dS \tag{3b}$$

and the velocity of the centroid

$$\dot{\vec{R}}_E = E^{-1} \oiint \hat{n}(b - \chi) dS \tag{3c}$$

where χ is a scalar field that must be constructed by solving Laplace's equation

$$\nabla^2 \chi = 0 \quad (\text{in} \quad V) \tag{3d}$$

with the Neuman boundary condition

$$\frac{\partial \chi}{\partial n} = \frac{\partial b}{\partial n} \quad (\text{on} \quad S) \tag{3e}$$

where S is the surface that encloses volume V and has an outward unit normal $\hat{n}$, as shown in fig. 1.

According to these formulas, it is only necessary to know s, $\partial s/\partial n$, b, and $\partial b/\partial n$ on the enclosing surface S in order to determine the conserved efflux E, its centroid $\vec{R}_E$, and the centroidal velocity $\dot{\vec{R}}_E$. This contrasts with the previous vector formulation (ref. 1), which included volume integrals that could not be transformed to surface integrals.

Classical Center of Mass- Eqs. (3) also contrast with the classical formulas for the center of mass and its movement, as derived from the continuity equation

$$\frac{\partial \rho}{\partial t} + \text{div} \, \rho \vec{u} = 0 \tag{4}$$

where ρ is the density and $\vec{u}$ is the fluid velocity. The classical formulas apply to an arbitrary volume τ and give for the conserved mass

$$M = \iiint \rho d\tau \tag{5a}$$

for the center of mass

$$\vec{R}_M = M^{-1} \iiint \vec{r} \rho d\tau \tag{5b}$$

and for the centroidal velocity

$$\dot{\vec{R}}_M = M^{-1} \iiint \vec{\rho u} d\tau \tag{5c}$$

The volumetric integrals in eqs. (5) cannot, in general, be transformed to surface integrals. Therefore, in order to determine the center of mass and its movement, we must know ρ and $\vec{u}$ throughout the volume τ.

Comparative Example-Since eq. (4) has the same form as eq. (1), we may apply eqs. (3) to the volume V of a local disturbance in the Laplacian of the density field ρ by making the identifications $s = \rho$ and $b = \text{div } \rho\vec{u}$, as follows:

$$E = \oiint \frac{\partial \rho}{\partial n} \, dS \tag{6a}$$

$$\vec{R}_E = E^{-1} \oiint (\vec{r} \frac{\partial \rho}{\partial n} - \hat{n}\rho) dS \tag{6b}$$

$$\dot{\vec{R}}_E = E^{-1} \oiint \hat{n}(\text{div } \rho\vec{u} - \chi) dS \tag{6c}$$

where χ satisfies

$$\nabla^2 \chi = 0 \quad (\text{in } V) \tag{6d}$$

$$\frac{\partial \chi}{\partial n} = \frac{\partial}{\partial n} \text{ div } \rho\vec{u} \quad (\text{on } S) \tag{6e}$$

Only surface integrals appear in eqs. (6), in contrast to eqs. (5) where volume integrals occur. Also, E represents the conserved efflux of $\nabla\rho$ for a storm, $\vec{R}_E$ its centroid, and $\dot{\vec{R}}_E$ its propagation velocity. Caution is appropriate, however, for although ρ is positive, $\nabla^2\rho$ may take on positive and negative values, and the centroid may conceivably lie or move outside the storm.

CONCLUSION

Any scalar meteorological quantity for which a tendency equation exists may be used to define a conserved property of a storm and its centroid. The movement of each such centroid is determined wholly from fields that are external to the storm.

REFERENCE

1. Costen, R. C.: General solutions for the movement of storms. NASA CP 2029, 1977, pp. 219-223.

Paper No. 8

A MESOSCALE NUMERICAL MODEL AND THE DEVELOPMENT OF A SEVERE STORM PREDICTION SYSTEM

M. L. Kaplan, *Management and Technical Services Company, Langley Research Center, Hampton, Virginia*

ABSTRACT

This paper deals with the use of a mesoscale numerical model for predicting preferred zones of severe storm development. A 60 consecutive day real-time test of the prediction system during the spring of 1978 proved useful in determining the problems and potentialities of such a system. A case study of severe storm development from this test period is described and compared to the model forecast fields.

INTRODUCTION

During the period from mid-April to mid-June 1978, a 60 consecutive day test of a mesoscale numerical model was performed. This was done to determine the feasibility of its use in a real-time environment for the prediction of preferred zones of severe local storm development. This test was run at NASA Langley Research Center, and all model integrations were performed on the CDC STAR-100 computer system. Initial data were received daily from the National Meteorological Center through the Bureau of Reclamation in Denver, Colorado. This initial data consisted of 1200 G.m.t. Limited Area Fine Mesh (LFM) analyses of geopotential height, temperature, and dewpoint at 190 km grid mesh intervals. These data were then interpolated to a 60 x 48 x 12 level three-dimensional matrix of 38 km grid mesh interval. After running a numerical 24-hour forecast (typically requiring 20 minutes of "wall-clock" time on the STAR-100 computer), a mesoscale severe storm index was disseminated for daily use and evaluation to the National Severe Storms Laboratory, Air Force Global Weather Central, and Goddard Space Flight Center.

The numerical hydrostatic (primitive equation) model utilizes sixth-order space advection, the Euler backward time marching scheme, and a sixth-order spatial diffusion operator. The system is presently adiabatic and ignores surface friction. For the spring test period, vertical levels ranged from 1150 to 12,000 m elevation. The boundary conditions were fixed in time with respect to the lateral boundaries.

The 60-Day Real-Time Test-The 60-day test period during the spring of 1978 permitted the achievement of several goals for the

mesoscale numerical model: (1) The model was run in real-time with a standard meteorological data base on a daily basis for the first time; (2) the model simulated the development of and interaction between sub-synoptic and mesoscale waves with reasonable fidelity; (3) the model provided a useable forecast of the preferred mesoscale areas of convective activity; and (4) problem areas where the model could be improved were revealed. Before discussing these problems and future plans for dealing with them, we shall present an example of a model forecast.

Example of Forecast-Severe weather erupted over southwestern Oklahoma and northwestern Texas during the late afternoon and evening of May 18, 1978. At approximately 6 p.m. c.s.t. (0000 G.m.t. May 19, 1978), Post, Texas, reported 2 cm hail. During the next 2 hours (0000 to 0200 G.m.t.), a 19 km swath from southwest of Grassland, Texas, to near Post, Texas, received hail up to 4.5 cm in diameter and nearly 6.4 cm of rain. In addition, at approximately 6:30 p.m. c.s.t. (0030 G.m.t.), Hollis, Oklahama, reported hail as large as 7 cm in diameter.

Later in the night, the severest convective activity shifted slightly to the southwest. At 1:24 a.m. c.s.t. May 19, 1978 (0724 G.m.t.), Slaton, Texas, reported hailstones up to 4.5 cm in diameter.

The 1200 G.m.t. May 18, 1978, surface weather situation presents a familiar pattern for the central and western plains. A north-south trough extends from eastern Montana southward to western Texas. A cold front is placed along the trough axis over the Oklahama Panhandle eastward to Georgia. Warm, very moist air is found to the east of the cold front and south of the stationary front. Surface dewpoints near 24°C (75°F) were observed over southeastern Texas with 21°C (70°F) dewpoints extending as far north as Dallas, Texas. Meanwhile, to the west of the cold front, surface dewpoints were mostly below -1°C (30°F) over extreme western Texas, New Mexico, and Colorado.

The 1200 G.m.t. May 12, 1978, 500 mb flow exhibits the characteristics of an omega blocking pattern over the United States. A difluent pattern in the wind field and height field is present over the central and southern plains. By 1200 G.m.t. May 19, 1978, the surface and 500 mb flow patterns show little change throughout this region. Integrating the numerical model with increased vertical resolution in the lower troposphere yields a very impressive forecast when one compares the 750 m σ_E (moist static stability) and 400 m divergence fields with the radar summaries presented in figs. 1-4.

By 10 hours into the forecast (2200 G.m.t.), the model has organized a zone of convergence from central Kansas southwestward through west central Oklahoma into west central Texas. A moderately strong convergence maximum ($-4 \times 10^{-5} s^{-1}$) is located over central Kansas at this time. The forecasted σ_E distribution also has an axis of moderately low values from central Kansas southward to north central Texas.

Over the next 2 hours (2200 to 0000 G.m.t. May 19, 1978), the area of maximum convergence is forecasted to move to the southwest and increase in magnitude to -5.6×10^{-5} s^{-1}. The minimum σ_E axis is also forecasted to increase in strength and shift slightly to the west during this 2 hour period. Thus, by 12 hours (0000 G.m.t.), the maximum 400 m convergence and minimum 750 m σ_E are nearly superimposed over southwestern Oklahoma. It was at about this time that the first reports of severe weather were received from Hollis, Oklahoma, and Post, Texas.

During the next 2 hours (0000 G.m.t. to 0200 G.m.t.), the model forecasts a southwestward movement and growth of the convergence band. The area of maximum convergence has moved into the vicinity of Childress, Texas, and Hobart, Oklahoma. The magnitude has reached nearly -10^{-4} s^{-1}. The minimum values of σ_E have again decreased in response to the low level moisture convergence associated with the zone of wind velocity convergence. The 0135 G.m.t. radar summary shows a southwest to northeast squall line which is nearly coincident with the model's band of superposition of strong low level convergence and minimum σ_E values. In fact, the area of maximum convergence between 12 and 14 hours of the model forecast is also the location of the most intense radar-observed activity. For example, the highest radar-reported echo (18.9 km) is located just to the southwest (toward lower σ_E) of the model-forecasted convergence maximum.

By 16 hours (0400 G.m.t.) the model-forecasted convergence maximum has moved southwestward into the vicinity of Lubbock, Texas. During the 2 hours from 0200 G.m.t. (14 hours) to 0400 G.m.t. (16 hours), the low level moisture convergence has continued to force a decrease in the 750 m σ_E values over southwestern Oklahoma and extreme north central Texas. One should note that by the 16 hour mark, a portion of the western flank of the convergence band has become superimposed upon high values of σ_E ($\sigma_E > 1.0$). Thus one would expect the majority of the convective activity to occur on the northeastern side of the convergence band, and this is observed on the late evening radar summaries.

The 10 to 16 hour convergence forecasts have clearly indicated a southwestward movement in the preferred zone of convective development, and the same trend is observed in the real world. The convective activity in southwestern Oklahoma diminishes during the night while the activity in northwestern Texas continues through 1035 G.m.t.

Problems Encountered-Several technical problems were encountered during the test: (1) The limited size of the model domain prevented the proper handling of synoptic wavelengths greater than 2000 km for time periods in excess of 8 hours; (2) poor initial low level data over high terrain regions due to the fictitous build-down of data to the lower boundary caused the model to erroneously create or amplify areas of convergence or potential instability near these high terrain regions; (3) the geostrophic initialization of momentum often caused unrealistic wave developments during the first few hours of the forecast; (4) the model

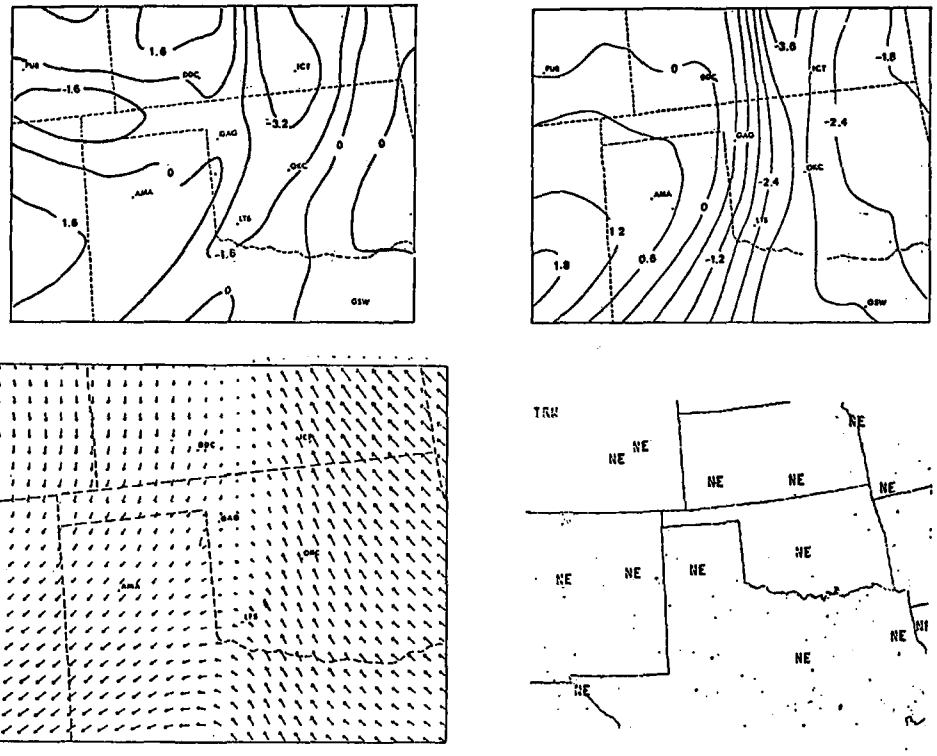

Fig. 1– Ten hour 400 m model forecast valid at 2200 GMT 18 May 1978.
Upper left: Divergence at intervals of 1.6×10^{-5} s^{-1}.
Upper right: 750 m σ_E at intervals of 0.6.
Lower left: Wind vectors.
Lower right: National Weather Service radar summary for 2035 GMT 18 May.

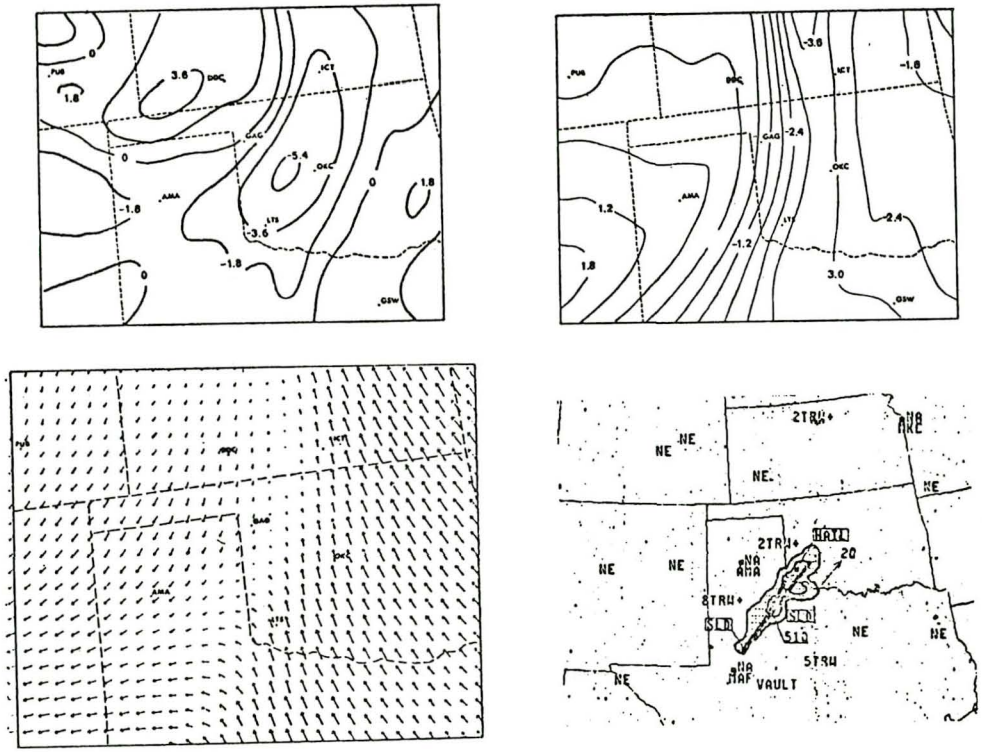

Fig. 2- Twelve hour 400 m model forecast valid at 0000 GMT 19 May 1978.
Upper left: Divergence at intervals of 1.8×10^{-5} s^{-1}.
Upper right: 750 m σ_E at intervals of 0.6.
Lower left: Wind vectors.
Lower right: National Weather Service radar summary for 2335 GMT 18 May.

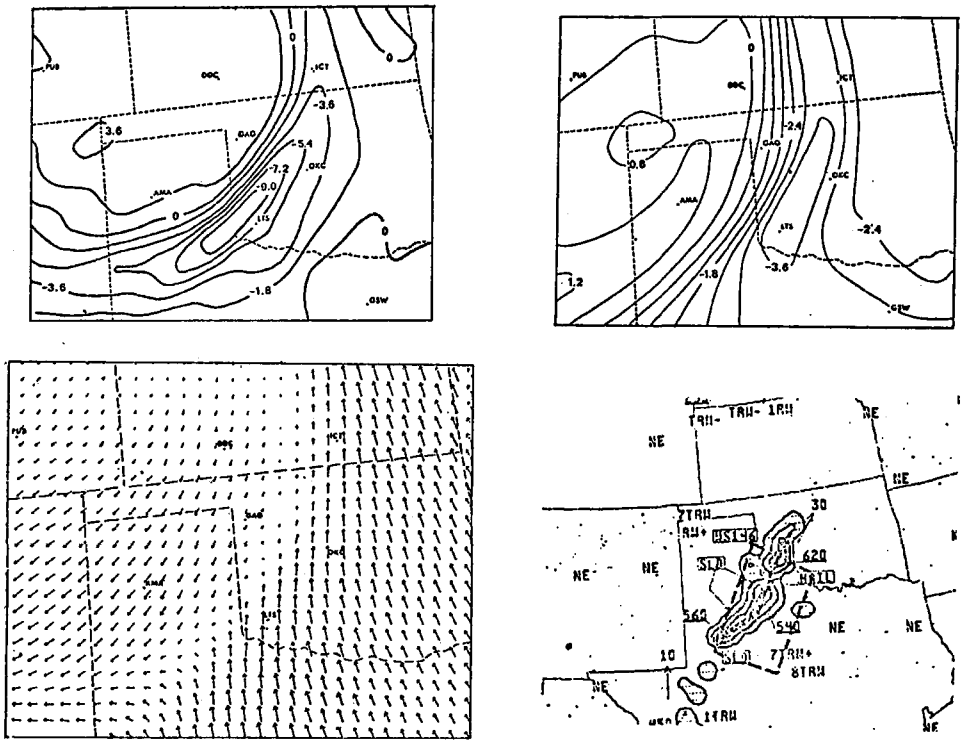

Fig. 3- Fourteen hour 400 m model forecast valid at 0200 GMT 19 May 1978.
Upper left: Divergence at intervals of 1.8×10^{-5} s^{-1}.
Upper right: 750 m σ_E at intervals of 0.6.
Lower left: Wind vectors.
Lower right: National Weather Service radar summary for 0135 GMT 19 May.

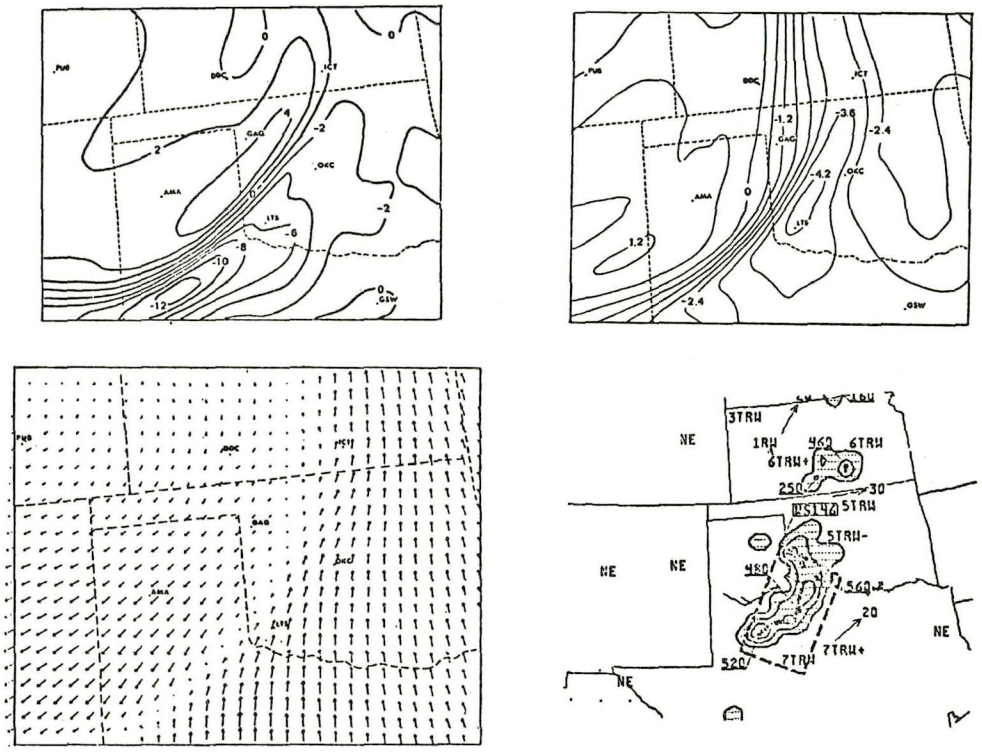

Fig. 4– Sixteen hour 400 m model forecast valid at 0400 GMT 19 May 1978.
Upper left: Divergence at intervals of 2×10^{-5} s^{-1}.
Upper right: 750 m σ_E at intervals of 0.6.
Lower left: Wind vectors.
Lower right: National Weather Service radar summary for 0335 GMT 19 May.

vertical resolution in the lower troposphere may have been insufficient to capture the complete dynamical process associated with the generation and amplification of the mesoscale convergence zones; and (5) because of telecommunications limitations, only the distribution of a preliminary index (with values 0 to 10) could be made available to users on a real-time basis, and much information was lost by condensing the entire model forecast into this index.

Improvements Being Implemented-The following improvements are expected to alleviate these problems and substantially improve the forecasts: (1) Because of available improvements in STAR system software and hardware, the model horizontal domain will be expanded from 60 x 48 to 90 x 64 points in 1979, and by 1980, a horizontal matrix size of 134 x 84 will be possible; (2) terrain-following lower levels will be incorporated into the model to eliminate the build-down problem in the mountains; (3) additional vertical resolution will be added to the lower tropospheric region of the model (several cases (e.g., May 18, 1978) have already been rerun using levels at 400, 750, 1150, 1650, and 2275 m instead of the 1150, 2275, and 3400 m levels used during the spring 1978 test period); (4) the geostrophic initialization scheme will be replaced by a dynamical balancing scheme which will represent the initial wind field with greater realism without distorting the observed pressure field; (5) additional scales of motion will be simulated by employing several smaller scale nested grids in addition to the 38 km grid; and (6) if increases become available in telecommunications hardware, future disseminated forecasts will include actual dependent variables of the model in order to give the users a more comprehensive picture of the model forecast.

SUMMARY

A mesoscale numerical model was run in real-time for a 60 consecutive day test period during the spring of 1978. Model output parameters were used to predict preferred zones of severe storm potential. The test revealed that the model captured a substantial number of subsynoptic and mesoscale dynamical processes with fidelity. However, problem areas were also noted, and corrective measures are being implemented to improve the performance of the model for the spring 1979 severe storm season.

Paper No. 9

NUMERICAL PREDICTION EXPERIMENTS SIMULATING THE IMPACT OF MESOSCALE SATELLITE DATA*

Carl W. Kreitzberg, *Drexel University, Philadelphia, Pennsylvania*

ABSTRACT

Recent developments in mesometeorology are summarized to place this research in perspective. Recent advances in computer analysis and forecast system development that provide the basis for the simulation tests are discussed. The impact of NIMBUS-6 humidity data on analyses off the West Coast are shown and incorporation of geopotential gradient data is discussed. Experiments to demonstrate the feasibility of incorporating satellite-derived wind fields in mesoscale severe storm models are mentioned briefly.

INTRODUCTION

A revolution in mesometeorology is taking place because of recent advances in meteorological satellites, large and small computers, and data communication and display systems (Kreitzberg, 1976). The greatest impact has been made by the GOES visible and infrared image data because of the high resolution in both space and time, and because the data are available in real-time to many meteorologists. Forecast applications are numerous and considerable research is underway to extend the applicability of the data. For example, detailed precipitation rates and wind fields can be deduced by those with adequate image analysis systems.

The launch of TIROS-N marks the beginning of a new era in mesoscale meteorology because of the multitude of remote sounding data available from the TOVS system. At the same time, digitized weather radar data are becoming available with the installation of digital video integration processor (DVIP) equipment on National Weather Service network radars. The urgency of the need for such information on an operational basis is demonstrated by actions of the Federal Aviation Administration (FAA). DVIP data from several radars are displayed in color in real-time at Air Route Traffic Control Centers (ARTCC) and Enroute Flight Advisory Service (EFAS) locations. They will put 150 high resolution color radar displays into service at 20 ARTCC and 44 EFAS locations during the next 18 months to complement the laser facsimile GOES image data.

* Semiannual progress report, NASA Grant NSG-5162, and contribution to the Fourth NASA Weather and Climate Program Science Review, January 24 & 25, 1979.

The mesoscale data explosion from ground-based sensors is just beginning. The National Weather Service is moving rapidly toward automation of surface observations (Klein and Haggard, 1978) and experimental networks of sensors around airports are being developed by both National Weather Service and Air Weather Service. Networks of environmental data stations and automatic data acquisition systems are being installed by the power industry (Tennessee Valley Authority, for example) and the Forest Service. Digital weather stations are available to individuals for several hundred dollars. Computer dial-up systems can collect data from these digital networks and stations, and such data can be communicated on the State and National Data Circuits associated with AFOS.

The hardware required to manipulate the mesoscale data fields has been developed in NASA's AOIPS system, University of Wisconsin's McIDAS system, and the NESS VISSR Image Registration and Gridding System (VIRGS). The communication of ground-based point observations can be handled by AFOS and the digital radar and satellite data can be communicated by land lines or communication satellites (Bristor, 1978).

Numerical weather prediction research has moved toward higher resolution numerical models (Perkey, 1976; Kreitzberg, 1978; Anthes and Warner, 1978). It has been demonstrated that these models develop more detailed patterns during the forecast than exist at the initial time. Fig. 7, p. 359, in Chang and Kreitzberg (1977) shows the detail with which squall lines can be depicted. This forecast had been initialized using only the 1200 GMT rawinsonde data and a remarkably detailed and accurate squall line is shown from 7 h to 12 h into the forecast. The papers of Perkey and Chang demonstrate further that short-range forecasts of convective precipitation amounts are often very accurate, but they are also rather sensitive to the initial relative humidity fields.

It is clear that the limiting factor on reliable detailed short-range forecasts is the initial analysis. Equally clear is the fact that much more data are being collected than are being used in weather prediction. Currently, the weak link is the composite data analysis system that uses a dynamic prediction model to provide for four-dimensional data assimilation. A very large effort has gone into data assimilation research on the large scale for the Global Weather Experiment (FGGE Advisory Panel, 1978). None of this effort has been concerned with moisture analyses, including relative humidity and cloud water concentration. The mass and motion adjustment is known to have important differences on the scale of detailed prediction models compared with hemispheric and global models.

The goal of the NASA supported research by Drexel University's Atmospheric Sensing and Prediction Project is to expand the regional scale numerical prediction model towards a prediction system that includes the composite data analysis function. This has been a small effort over several years, having begun at MSFC in 1975 and transferred to GSFC in 1977.

The principal effort during this past year has been to upgrade the set of data processing, analysis, prediction, and

diagnostic computer codes into a system of codes called Limited Area and Mesoscale Prediction System (LAMPS). This system includes a preprocessor and a library of data manipulation codes, together called FLOTRAN, which has been developed in collaboration with Daniel Anderson at the National Center for Atmospheric Research. FLOTRAN has the power and flexibility to take concise, simple code that is relatively easy to write correctly, document internally, and read, and then generate FORTRAN code from it that can be compiled by most computer systems. Therefore, it is relatively easy to change when doing complex research experiments and easy to maintain in spite of its size. It is portable to other computer systems. The dynamic prediction model is the heart of LAMPS but only comprises 15% of the code (5,000 out of 35,000 statements).

Model nesting experiments have been performed to demonstrate the sensitivity of forecasts to grid resolution and the use of forecasts on a larger grid to initialize forecasts on a smaller grid. Results reported in Kreitzberg and Chang (1978) demonstrate the need for moisture profiles over the Gulf of Mexico and document the ability of smaller grid models to generate narrower, more intense squall lines using the same data as lower resolution models. It is clear that more vertical resolution near the tropopause is necessary for 35-km horizontal resolution models to reach their full potential; otherwise, convective cloud tops are limited to the model tropopause instead of the real tropopause.

DATA IMPACT STUDIES

The urgent requirement for satellite humidity data over the offshore waters lead us to investigate the potential of the NIMBUS-6 sounder data off the U. S. West Coast on August 18, 1975. Our standard relative humidity analysis scheme uses the National Meteorological Center analysis as the first guess field. The rawinsonde data averaged over the model layer (1 km in this example) and centered at the model level (as shown in Fig. 1a) is then used to refine the analysis. Our analysis with the first guess and the rawinsonde data is given in Fig. 1b. Satellite soundings from NIMBUS-6 provided by the University of Wisconsin are located at points shown in Fig. 1c. The analysis from the first guess plus the satellite and rawinsonde data is shown in Fig. 1d.

Clearly, the density of satellite data, collected between 0800 GMT and 1000 GMT, is exactly what we need off the West Coast. The satellite analysis in Fig. 1d is drastically different from the rawinsonde analysis in Fig. 1b (which is the same over the ocean as the first guess because there are no rawinsonde data there). The satellite analysis is qualitatively reasonable in view of the visible and infrared image data in this storm.

The forecast with and without satellite data will be shown at the NASA Program Review. The cloud and precipitation forecasts will be greatly different, but the gross synoptic forecasts will not be too different after 24 h.

Much more remains to be done on this NIMBUS-6 case in terms of detailed validation of the humidity analyses compared with the

cloud image data. Also important will be quantitative comparison of the forecasts with and without the satellite humidity data. The most significant results will be those comparing the two forecasts with the observed evolution of cloudiness as the storm develops and moves onshore, and those comparing the forecast with the observed precipitation along the coast.

The geopotential height gradients from NIMBUS-6 are used in the pressure field and wind analyses in LAMPS. The impact of these data on the analyses and the forecasts will be examined separately and then combined with the satellite humidity analyses. It is expected that some tests and tuning will be required to properly mix the satellite geopotential gradient and the first guess geopotential data. Problems may arise along the coast where observation types change.

The insertion of wind fields derived from GOES image data is the third problem. We will be inserting real data from the Neasho and Omaha tornado cases and the May 20, 1977, severe storm case (AVE-IV, AVSSE-II, SESAME '77 cases). To demonstrate feasibility and to demonstrate dynamic response as a function of grid resolution, perturbation scales, and amplitude, a series of experiments with idealized perturbations is being conducted.

REFERENCES

Anthes, R. A. and T. T. Warner, 1978: Development of hydrodynamic models suitable for air pollution and other mesometeorological studies. Mon. Wea. Rev., 106, 1045-1078.

Bristor, C. L., 1978: The case for an expanded digital WEFAX. Bull. Amer. Meteor. Soc., 59, 1145-1149.

Chang, C. B. and C. W. Kreitzberg, 1977: Severe weather prediction studies. Preprints, 3rd Conference on Numerical Weather Prediction (Omaha), AMS, Boston, pp. 354-361.

FGGE Advisory Panel, 1978: The Global Weather Experiment--Perspectives on Its Implementation and Exploitation. NAS, Washington, D.C., pp. 104.

Klein, W. H. and W. G. Haggard, 1978: Automation in meteorology. Preprints, Conference on Atmospheric Environment of Aerospace Systems and Applied Meteorology (New York, NY), AMS, Boston, pp. 174-179.

Kreitzberg, C. W. and C. B. Chang, 1978: Sensitivity of precipitation forecast to grid resolution (data and density). GARP Programme on Numerical Experimentation Report No. 18, pp. 81-84.

_____, 1978: Progress and problems in regional numerical weather prediction. Computational Fluid Dynamics, SIAM-AMS Proceedings, Vol. XI, Amer. Math. Soc., Providence, RI, pp. 32-58.

_____, 1976: Interactive applications of satellite observations and numerical modeling. Bull. Amer. Meteor. Soc., 57, 679-685.

Perkey, D. J., 1976: A description and preliminary results from a fine-mesh model for forecasting quantitative precipitation. Mon. Wea. Rev., 104, 1513-1526.

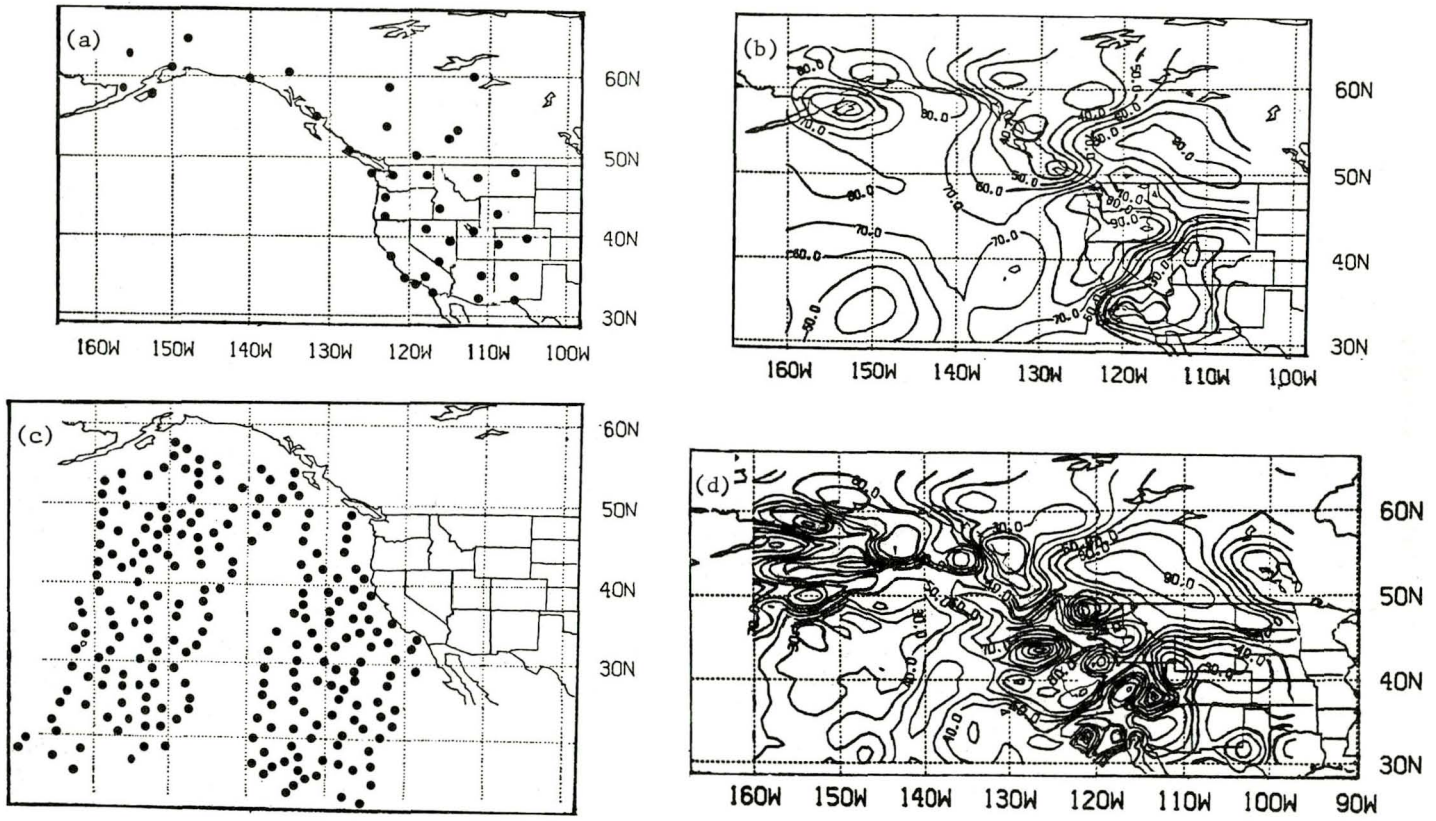

Fig. 1--Impact of relative humidity data on analyses: (a) rawinsonde data points; (b) analysis with first guess and rawinsonde data; (c) satellite data points; (d) analysis with all data.

Page intentionally left blank

Paper No. 10

NASA ACTIVITIES AND INTERESTS IN THE 1979 REGIONAL AND STORM SCALE EXPERIMENT

Robert E. Turner and Kelly Hill, *Marshall Space Flight Center, MSFC, AL 35812*

ABSTRACT

A brief overview is presented of NASA's planned involvement in an interagency severe storms field measurement program

INTRODUCTION

During the past decade or more, a major concentration of research has gone into the large and small ends of the atmospheric scales of motion, leaving a gap in the understanding of phenomena associated with the middle (mesoscale) scale. This gap includes the important processes involved with the onset and development of severe storm systems. It is widely acknowledged that our lack of knowledge about the organization of mesosystems forms one of the greatest obstacles to developing a general understanding of the mechanisms of severe local storms and the parameterization of them in numerical and statistical models.

To learn more about mesoscale systems and their mechanisms, NASA will conduct an Atmospheric Variability Experiment (AVE) in the Spring of 1979 and start planning for a larger field experiment in the early 1980's. This effort is directed toward the acquisition of correlative data sets for application to investigations of storm initiation and development. NASA's objectives for the field experiments include:

(1) Improve the understanding of the mechanisms associated with the development of severe weather, especially those which might be observable from satellite sensors.

(2) Determine to what extent satellite data can be used to detect and monitor the development of severe storms.

(3) Obtain a better diagnostic understanding of the coupling between synoptic and mesoscale processes associated with severe storm systems.

Plans are for the 1979 NASA AVE experiment to be part of an interagency cooperative mesoscale field experiment and research project called Little SESAME. The involvement depends upon the degree of sponsorship and resources made available by other governmental agencies for the basic Little SESAME Project.

The primary objective of the 1979 AVE experiment is to acquire correlative sets of rawinsonde, satellite, and radar data during periods of severe weather. The data will be used in studies of meso-synoptic processes responsible for the formation and development of severe convective activity associcated with phenomena such as tornadoes, damaging winds, hail, floods, turbulence, etc., that affect the property and personnel safety. The secondary objective is to compile a data set for investigating atmospheric variability, and associated severe storm development with emphasis on the determination of mechanisms for the formation of severe storms.

EXPERIMENTS

The meso-, regional, local, and convective scales involve very complex physical processes including important contributions from the underlying geography, intense heat release and non-linear interactions between the larger and smaller scales. Because the important physical processes, scientific methods/techniques and the state of knowledge are all scale dependent, two experiments will be conducted during the period of April to July, 1979. One will be on a regional scale and one on a storm scale.

The regional scale experiment shown in Figure 1 will consist of three 24-hour periods and will involve 23 National Weather Services (NWS) rawinsonde sites and 20 supplemental rawinsonde sites taking measurements at 3-hour intervals during a severe outbreak of weather. Rapid scan visual and infrared imagery recorded by the GOES satellite at 3-5 minute intervals will be made. Weather radar data will be obtained from photographs of the scope taken every 15 minutes during severe outbreaks from stations located in the experiment area.

The storm scale experiment will consist of three 24-hour periods and will involve 23 National Weather Service rawinsonde sites (same as regional scale) taking measurements at 3-hour intervals, and 20 supplemental rawinsonde sites taking measurements at 90 minute intervals during severe weather (Figure 2). GOES satellite rapid scan visual and infrared imagery

recorded at 3-5 minute intervals will be obtained. Weather radar data in the form of photographs of the storm cells as displayed on the scope will be obtained from sites near or in the experiment area.

Rawinsonde data will be reduced by the NASA-AVE technique which will include a quick-look assessment and documentation of each experiment. The data obtained from the experiment will be made available to all investigators and the scientific community by hard copy or on magnetic tape.

POTENTIAL RESEARCH

The number of potential scientific studies that could be conducted using the data available from these experiments are numerous. Some possibilities are:

(1) Examination of conditions which lead to the severe and unusual weather events throughout the experiment day. This would include vertical motion (lifting mechanisms), kinematic parameters, convective instability, air structure, etc.

(2) Perform studies of budgets of energy (transformations included), moisture, and vorticity to determine the source of energy for the storms and the mechanisms responsible for the release of the latent energy.

(3) Relate satellite observations to results from various analyses to determine what can be learned from satellite data about the conditions established from 3-hour and 1½ hour rawinsonde data.

(4) Investigate the role of the jet stream in the formation of convective activity.

(5) Develop improved storm forecast capability through the development of models of severe storms and their environment which use space technology and conventional ground based data sources.

(6) Perform correlative analyses of the satellite and ground measurements to determine the critical atmospheric variables or storm severity indicators which may be required for future sensor system developments.

These are only a few of the possibilities. Research results from the utilization of these experimental data in studies relating to the understanding and knowledge of severe weather will be documented and made available to the scientific community.

CONCLUSION

In 1980, using the results of the 1979 field experiment, NASA will conduct applied research on severe storms dynamics and the atmospheric environment to determine the conditions which lead to severe storm development in order to improve the understanding of storm initiation. NASA will develop and demonstrate the utility of the analysis and interpretation technique/method for severe storms data where measurements from space sensors are combined with conventional measurements of atmospheric parameters. Participation with the Convective Storms Division of NCAR is planned on a research study scheduled for the Summer of 1980 under the sponsorship of NSF. Sponsorship of electrical field and lightning measurements, selected ground based sensing and satellite data acquisition, plus possible aircraft sensor contributions, is anticipated.

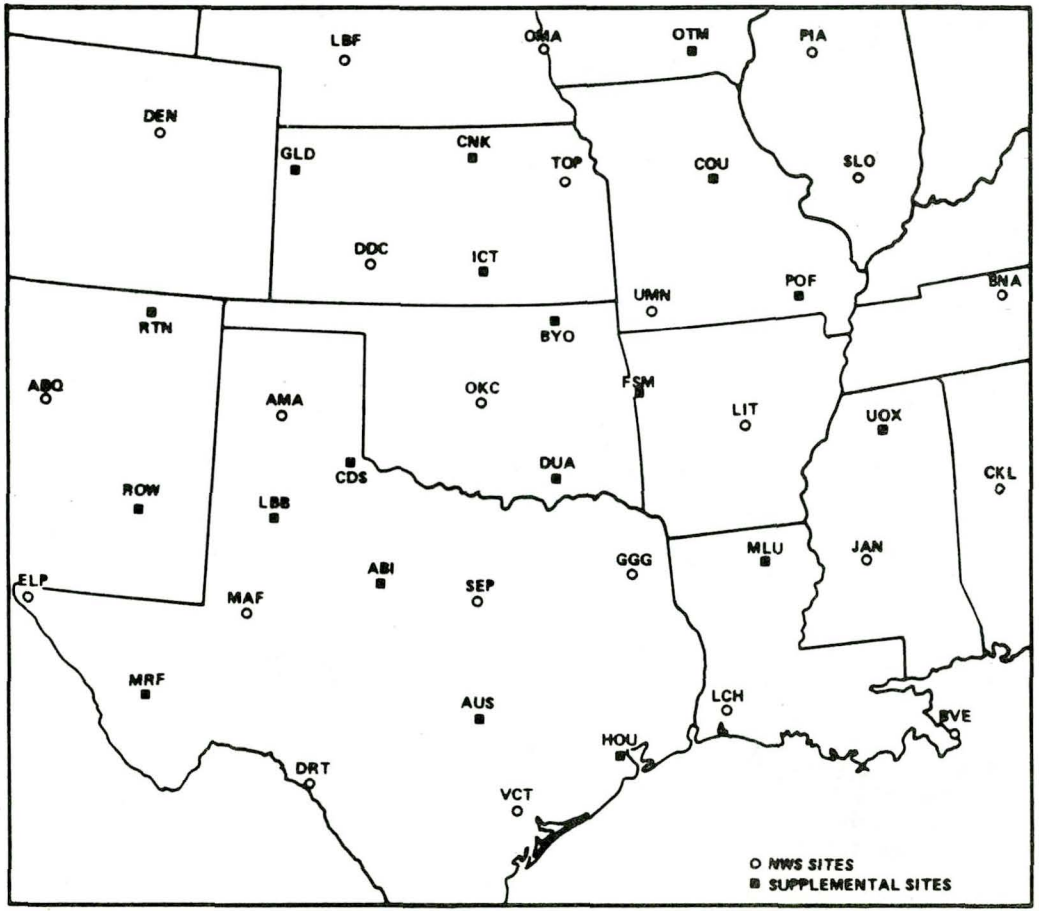

FIGURE 1 '79 REGIONAL SCALE SOUNDING PROGRAM NETWORK

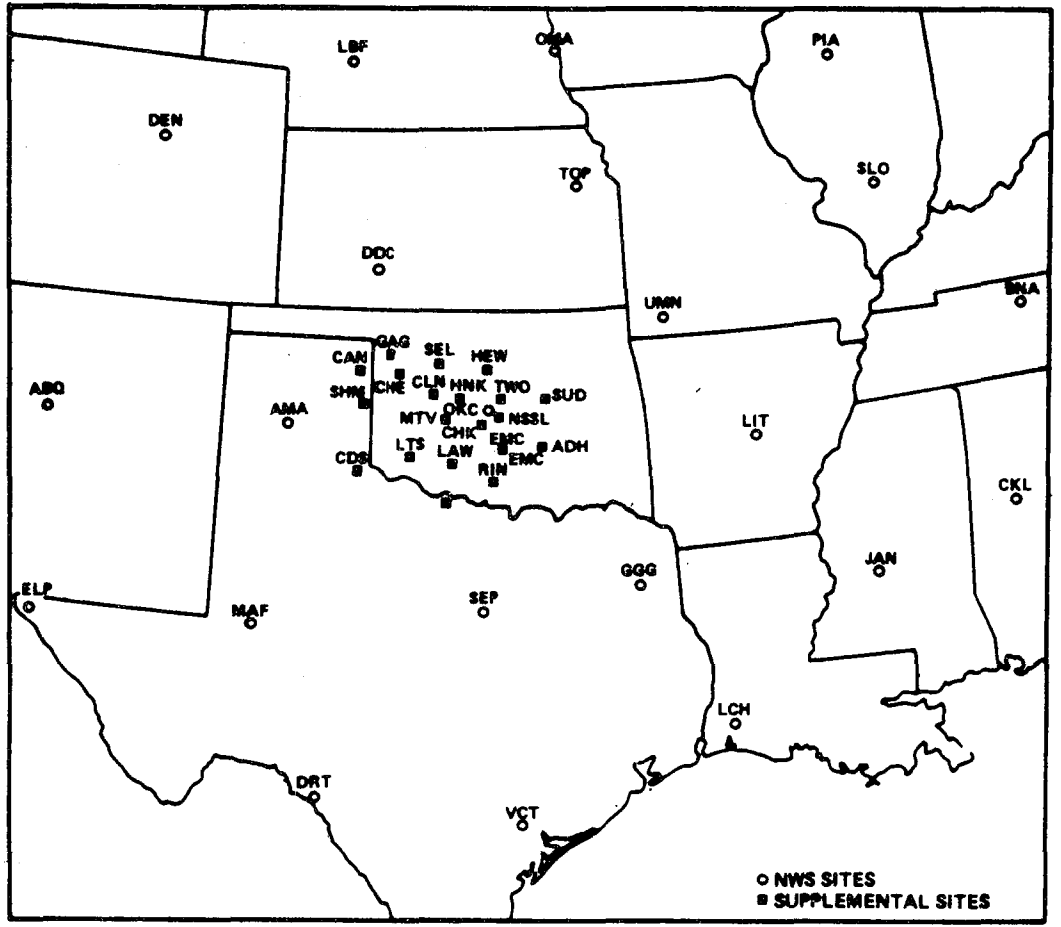

FIGURE 2 '79 STORM SCALE SOUNDING PROGRAM NETWORK

Paper No. 11

STEREOGRAPHIC CLOUD HEIGHTS FROM THE IMAGERY OF TWO SCAN-SYNCHRONIZED GEOSTATIONARY SATELLITES

R. A. Minzner, *Goddard Space Flight Center, Greenbelt, Maryland*
R. D. Teagle, *Defense Mapping Agency Topographic Center, Washington, D. C.*
J. Steranka, *General Electric Co., MATSCO, Beltsville, Maryland*
W. E. Shenk, *Goddard Space Flight Center, Greenbelt, Maryland*

Scan synchronization of the sensors of two SMS-GOES satellites yields imagery from which cloud heights can be derived stereographically with a theoretical two-sigma random uncertainty of ±0.25 km for pairs of satellites separated by 60° of longitude. Systematic height errors due to cloud motion can be kept below 100 m for all clouds with east-west components of speed below hurricane speed, provided the scan synchronization is within 4 seconds at the mid-point latitude, and the spin axis of each satellite is parallel to that of the earth.

BACKGROUND

In mid February 1975, while SMS 2 was in its test phase, and still under the control of Goddard Space Flight Center, the spin-scan imaging system of this satellite was synchronized with that of SMS 1 to produce consecutive pairs of stereo images. That is, the spin-scan camera of one satellite was adjusted so that both satellites scanned corresponding portions of a common field of view within a few seconds of each other, for each of a number of pairs of images. For this set of stereo image pairs, SMS 1 was located at a longitude of 75°W, while SMS 2 was located at longitude 107°W, resulting in a 32-degree difference in viewing angle (a 32° convergence angle). The resulting stereographic pairs of hard-copy images were analyzed photogrammetrically by a specially designed optical-mechanical instrument to yield cloud heights with a 2-sigma uncertainty of 500 m (Minzner et al., 1977).

Portions of these same image pairs have also been remapped digitally and combined into two-color anaglyph imagery which, when viewed with anaglyph spectacles, produce 3-D images from hard-copy prints or from the cathode-ray tube of an interactive system, the Atmospheric and Oceanographic Information Processing System (AOIPS).

A second stereo test was accomplished on May 26, 1978, when the two GOES satellites had a longitudinal separation of 60°. The increased separation of the satellites produced no apparent degradation in the stereo imagery, and decreased the uncertainty in the measured cloud heights. The effective area of stereo coverage along the equator was reduced, however, from about 100° to 70° as seen in Figure 1.

UNCERTAINTY ANALYSIS

The study of uncertainty in cloud heights obtained from stereographic pairs is limited in this report to two major sources, image distortion due to each of two causes, and the ability of the eye or other sensor to resolve apparent height differences in the stereo model under various conditions. The word "model" in this paper

signifies the scaled-down system of a pair of stereo images which faithfully reproduce the original viewing parameters of the two GOES VISSR systems. The scale of a model in which the image resolution of one pixel (0.9 km) equals the eye's resolving ability (38 μm) is about 1:24,000,000.

Fundamental to the entire stereo analysis are the concepts of base-to-height ratio (B/H) and vertical-deformation ratio (VDR). Base-to-height ratio is simply explained in a flat-earth model as the ratio of the separation between the two stereo cameras to the height of the cameras above the reference plane. An example of base-to-height ratio AB/H is shown in each of two simple flat-earth models of Figure 2. In each of these models, the convergence angle between the nadir-looking rays of the two cameras, one at A' and one at B', is zero.

The concept of vertical-deformation ratio is only slightly more sophisticated than that of B/H. In the simple model of Figure 2, VDR is nearly the reciprocal of B/H, and more exactly is equal to (H-h)/A'B', where (H-h) is the height of the cameras less the target height h which is being measured. It is clear from Figure 2 that (H-h)/A'B' = h/CD, where CD is the apparent horizontal displacement of the image of target T between the two superimposed stereo images. A comparison of the two models of this figure shows that for a fixed target height h, the X-displacement CD, parallel to the base line AB, increases as the B/H increases. The X-displacement CD is the quantity which provides the apparent vertical relief in the model, and hence permits the recovery of the target height h from the imagery of the two cameras. Any distortion of the apparent horizontal displacement CD introduces a corresponding relative distortion in the measured value of h.

The models of Figure 2 are unrealistically simple when compared with the situation of two geostationary satellites separated by 60° of longitude, each viewing about 1/3 of the surface of a spherical earth. The nadir-looking rays of the two satellites are no longer parallel, as in Figure 2, but rather, form a convergence angle V at the earth's center. This convergence angle is equal to the difference in the longitudinal positions of the two satellites. For a spherical-earth model the B/H is a function of convergence angle. When the sphericity of the earth, the height of the satellites, and the convergence angle V are all considered, one obtains values of VDR shown in the three-dimensional graph of Figure 3.

Figure 3 shows that for any one convergence angle, VDR maximizes at the midpoint longitude between the two subsatellite points. The greatest maximum of VDR plotted in this figure is 4.9 for a convergence angle of 10°. As the convergence angle increases successively from 10° to 60°, the corresponding maximum values of VDR decrease from 4.9 to 0.71. For a unit target height h, it is evident that the X-displacement CD measured along a spherical-earth model increases with increasing convergence angle, and hence provides an improved basis for the determination of model height (h).

For any single convergence angle, e.g., 60°, the VDR decreases as the radial distance between the target and the midpoint longitude (ML) increases along any direction from the ML. Figure 3 shows this decrease only along the equator. The value of VDR becomes very small, about 0.02, at a longitudinal distance (80-V/2) degrees from the ML. This graph shows that for a unit model height h, the related X-displacement distance CD along the model sphere at this longitude becomes very large, i.e., 50 units. A longitudinal distortion of one unit at this longitude along the equator of the model sphere would introduce a distortion of only 2% in h. A longitudinal distortion of one unit at the ML would introduce a distortion of 141% in h. (The longitudinal distortion is measured in terms of longitudinal position along the equator of a hypothetical model sphere, and not in terms of a linear distance along the image plane.)

There are two possible sources of serious error in cloud-height determination due to errors or distortions in ground-scale position of the cloud. The first of these is due to remapping distortions; the second is due to possible cloud motion occurring between the sensing of corresponding pairs of stereo images by the two satellites.

Since each satellite views a given land mass, e.g., North America, from very different locations, the image of the land mass viewed from one satellite does not conform with that viewed from a second satellite. In order to perform the photogrammetrical analysis for cloud heights, it is necessary to properly remap a region of interest on one satellite image to the same region of interest on the other satellite image. This remapping is required so that all sea-level features of one image are congruent with those of the other image. The higher land features and the cloud features will then show horizontal displacements proportional to the value of the VDR at the location of the features. If the remapping introduces east-west distortions in any particular target, the related target height will be in error in the amount of the local VDR times the east-west distortion.

For the hard-copy photogrammetrical analyses, it has been found desirable to remap imagery so as to compress image information rather than to stretch image information. Thus, for analyses of areas east of the ML, the imagery of the eastern satellite is remapped and compressed to fit that of the western satellite. This procedure retains the model resolution of the western satellite image, and increases the model resolution of the eastern satellite image. A related procedure applies to areas west of the ML.

An error in equatorial cloud height due to cloud motion may occur when some time increment Δt exists between the scanning of a particular cloud feature, first by the sensor of one satellite, and then by the sensor of the second satellite. The magnitude of the height error may be calculated by multiplying Δt by u, the east-west component of the cloud motion, and multiplying this result by the VDR for the particular equatorial longitude.

By a reversal of the above procedure, a set of values of longitudinal departure from the ML, and the corresponding set of values of VDR were used to calculate a related set of values of Δt which would produce a constant cloud-height error of 100 meters, for each of four east-west cloud speeds. These data are longitudinally symmetrical about the ML, and one half of each of these four data sets is plotted in Figure 4. These curves all show a minimum value at the ML, which for the current GOES East and GOES West satellites, lies at 105°W. The successive minima for east-west cloud speeds of 10, 20, 30, and 40 m/s are seen to be 14, 7.0, 4.7, and 3.5 seconds respectively.

When the separation between exposure times is less than 3.5 seconds at the ML, any clouds at the ML which have an east-west speed of less than 40 m/s will have a height error of less than 100 m due to cloud motion. For clouds at latitudes remote from the ML, the 100 m error limit will be retained with much larger time separations, provided the spin axis of both satellites are sufficiently well aligned with that of the earth. For east-west cloud speeds less than hurricane speeds (33 m/s), a time separation of 4 seconds at the ML will guarantee cloud-height errors of less than 100 m at all locations, when the spin-axis alignment is suitable.

The limiting factor in the determination of the target height in the stereo model is the ability of the sensor or operator to correlate the two images of the target in the model by converging the corresponding rays at the model height h of the target, and then to measure h with an appropriate scale. In the analysis of hard-copy pairs of stereo images, this process consists of having the operator move a floating dot from the reference level to the apparent height of the target in the model. The accuracy with which this process can be accomplished depends upon a number of

factors: (1) the operator's eye resolving ability, (2) the base-to-height ratio of the model, and (3) the linearity and smoothness of motion of the floating-dot reference mark.

The mean value of the eye's resolving ability (era) expressed at the two-sigma level is about 38 μm at 10 inches from the image (Sidgwick, 1961). Figure 2, which was used above to illustrate B/H, also illustrates the relationship of the eye's resolving ability to the model-height uncertainty $2\delta h$ for each of two values of B/H. The two-sigma value of era implied in Figure 2 also implies a two-sigma value for $2\delta h$. It is apparent that for a fixed value of era, the value of $2\delta h$ decreases as B/H increases. A graph of the two-sigma value of $2\delta h$ as a function of B/H is shown in Figure 5. This graph, which was developed from the geometrical relationship shown in Figure 2, also shows the relationship between B/H and convergence angle for pairs of geostationary satellites. One can see that $2\delta h$, the two-sigma value of uncertainty in the perception of the vertical height of the model has been decreased from about .043 mm to .022 mm by increasing the convergence angle of the satellite pair from 32° to 60°. The relationship between $2\delta h$ and B/H applies independently of image resolution as long as the image resolution is equal to or below the value of era.

With the two images of a target feature merged at the model height h, it is necessary to measure this model height accurately with an appropriate scale. In hard-copy stereography, this process is accomplished by means of a floating dot somewhere in the optical train. This dot is attached to a precision lead screw which serves as a scale. The dot is designed to be moved continuously and smoothly, with a high degree of linear precision along this scale which provides a measure of the distance between the apparent position of the reference surface and the apparent target height in the model. The ground-scale height of the target feature is then obtained by multiplying both the measured model height h and its uncertainty $2\delta h$ by the viewing scale of the imagery. For satellites separated by 60 and 32 degrees, the theoretical uncertainty $\pm\delta h$ is found to be ± 0.25 km and ± 0.48 km, respectively. The latter value is in agreement with measured uncertainty values (Minzner et al., 1978).

Image contrast and continuity of the target are also important factors in the ability of the eye or other sensor to determine the model height of the feature. No attempt is made to discuss these topics in this limited paper.

CONCLUSIONS

Theoretical considerations as well as actual measurements show that random cloud-height uncertainty and effective area of stereo coverage both decrease with an increase in longitudinal separation of the scan-synchronized satellites. For the present 60° separation, the theoretical two-sigma height uncertainty is about ± 0.25 km even though the finest resolution of the GOES imagery is about 0.9 km. The present location, 135°W, of the western member of the scan-synchronous pair of satellites eliminates from effective stereo coverage a large region which includes a significant portion of northeastern United States. The coverage for this important area of our country could be restored to an operational stereo cloud-height system, while retaining the coverage of the remainder of the contiguous United States, by either of two methods: (1) move the western satellite eastward by 15°, or (2) place a third active GOES satellite either at 120°W or 30°W. Each of these approaches would have its own set of advantages and disadvantages, none of which are discussed in this paper because of space limitations.

For the current satellite locations, a scan synchronization within four seconds at the midpoint latitude would keep systematic cloud-height errors due to cloud

motion within 100 m for all clouds with an east-west component of speed below hurricane speed, provided the spin axis of each satellite is nearly parallel to that of the earth.

REFERENCES

Minzner, R. A., W. E. Shenk, R. D. Teagle, and J. Steranka, Stereographic Cloud Heights from SMS/GOES Imagery, *Paper No. 42 Third National Aeronautics and Space Administration Weather and Climate Program Science Review*, Nov. 29-30, 1977.

Minzner, R. A., W. E. Shenk, R. D. Teagle, and J. Steranka, Stereographic Cloud Heights from SMS/GOES Satellites, *Geophysical Research Letters* 5, 21-24, 1978.

Sidgwick, J. B., *Amateur Astronomers' Handbook*, Faber and Faber, London, 2nd Ed. 1961.

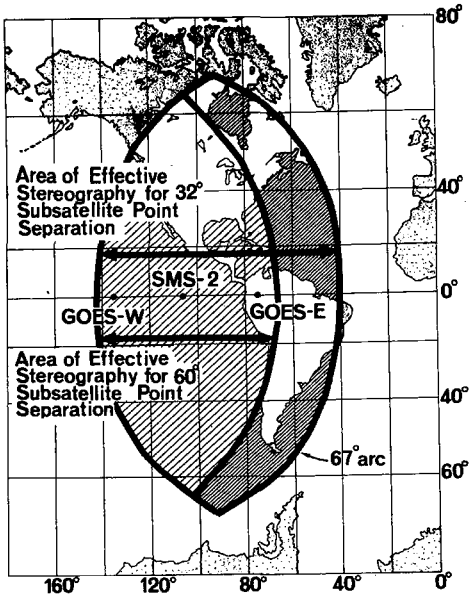

FIGURE 1

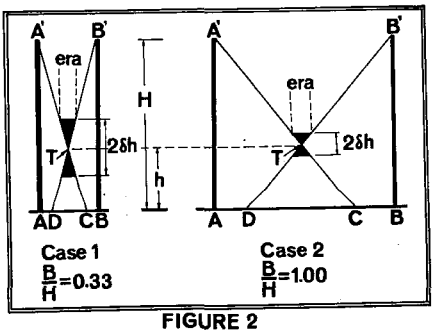

FIGURE 2

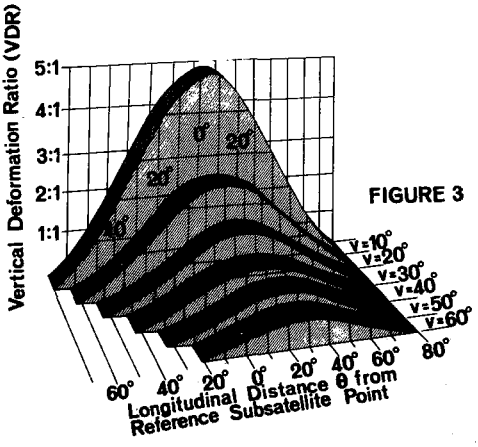

FIGURE 3

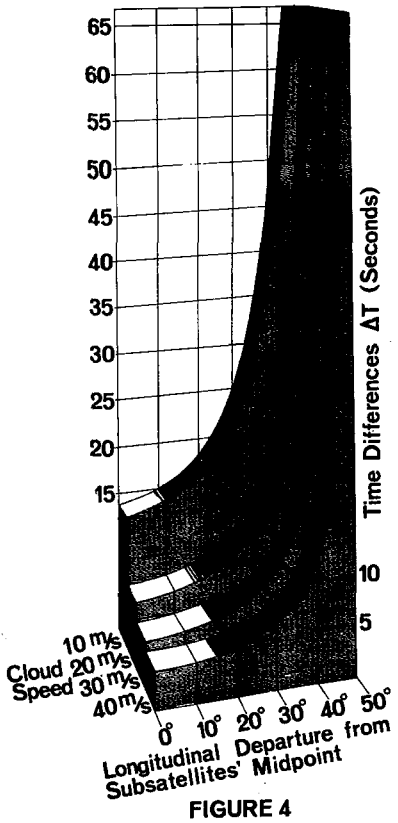

FIGURE 4

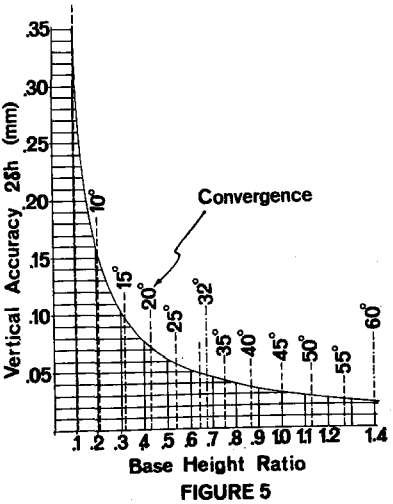

FIGURE 5

Paper No. 12

FOUR DIMENSIONAL OBSERVATIONS OF CLOUDS FROM GEOSYNCHRONOUS ORBIT USING STEREO DISPLAY AND MEASUREMENT TECHNIQUES ON AN INTERACTIVE INFORMATION PROCESSING SYSTEM

A. F. Hasler, M. desJardins, W. E. Shenk, *Goddard Space Flight Center, Greenbelt, Maryland*

ABSTRACT

Simultaneous Geosynchronous Operational Environmental Satellite (GOES) 1 km resolution visible image pairs can provide quantitative three dimensional measurements of clouds. These data have great potential for severe storms research and as a basic parameter measurement source for other areas of meteorology (e.g. climate). These stereo cloud height measurements are not subject to the errors and ambiguities caused by unknown cloud emissivity and temperature profiles that are associated with infrared techniques. Previous work by Minzner et al. (1978a) has demonstrated the validity of stereo measurements from geostationary satellites using techniques based on conventional analogue stereography. This effort describes the display and measurement of stereo data using digital processing techniques.

Computer remapping of digital GOES image pairs allows the interactive display (on the Atmospheric and Oceanographic Information Processing System, AOIPS) of time sequences of stereo images: a true four dimensional representation of cloud structures. A description of similar work at the University of Wisconsin is given by Bryson (1978). Interactive manual and semi-automatic height measuring techniques have also been developed on AOIPS. Capabilities under development include: 1) measurement of multilevel wind fields with accurate height assignment; 2) estimation of thunderstorm intensity from horizontal and vertical cloud growth rates; and 3) measurement of four dimensional cloud structure for comparison with numerical models and radar observations. Stereo height verification and error analyses were conducted using computer crosscorrelation on AOIPS. Accuracies of ±0.5 km appear to be possible for geographical features and clouds with precisions (relative accuracies) approaching ±0.1 km.

INTRODUCTION

The quantitative three-dimensional geometric descriptions of cloud structure as a function of time is extremely important in severe storm research as well as other areas of meteorology. A few of the many uses include: 1) height assignment for satellite cloud winds; 2) cloud growth rate measurements for storm intensity estimation; and 3) input and verification for radiation models. This paper describes the stereo display and measurement of the four dimensional cloud

structure using digital data on an interactive image processing system (AOIPS) which has many inherent advantages over previously used techniques.

The only method routinely used over the U.S. for measuring cloud heights at frequent intervals depends on infrared equivalent blackbody temperatures (T_{BB}'s) from the Geosynchronous Operational Environmental Satellites (GOES). Stereo cloud height measuring techniques have the following advantages over the infrared techniques: 1) The GOES visible resolution is 8 times greater than the IR resolution, making it possible to measure the height of much smaller clouds and cloud features. 2) The infrared techniques require a knowledge of cloud emissivity which cannot be determined accurately from GOES images so that thin clouds (especially cirrus) often have large height errors. 3) The infrared techniques require an atmospheric temperature profile which is generally not available and in the case of isothermal layers cannot be accurately used for height assignment. 4) The stereo representation allows the operator to scan large areas while observing height differences, whereas with infrared techniques, height is generally shown only as a T_{BB} change which is not as easily interpreted. 5) Multilevel height determination is possible using stereo including measurements beneath thin cirrus which are impossible using the infrared.

Previous stereo analyses from geostationary satellites by Minzner et al. (1978a, 1978b) involves the use of hard copy images and optical mechanical systems. The processing techniques used in this work operate directly on the digital data in its most pure form. The measurements made directly from the digital data do not differ from the degradation and inaccuracies inherent in all image display systems and optical mechanical devices. Computer remapping of the images gives a three dimensional view of a large area with no apparent distortion. When time sequences of remapped stereo image pairs are displayed on AOIPS the 3-dimensional evolution of clouds can be observed: a true 4-dimensional representation. The unique image shift capabilities of AOIPS allow the interactive manual measurements of height as well as automatic computer cross correlation height measurement and interactive image enhancement.

Another paper in this volume by Minzner et al. (1978b) describes: 1) The useful area of coverage for the two operational GOES satellites; 2) Stereo cloud height errors caused by imprecise image pair scan synchronization; and 3) Theoretical error limits for satellites with various longitude separations.

TECHNIQUES

Basic Remapping, Display and Height Measurement

Image sequences from the two GOES satellites are precisely navigated. A 512 X 512 visible picture element (pixel) area of interest from one satellite is chosen. A somewhat larger area from the second GOES satellite is then remapped digitally* into the coordinate system of the first satellite such that sea level features are superimposed. Features above or below sea level will be displaced to the left or right. This parallax gives a three-dimensional view when the image pair is projected through the red and green channels of a color television system and viewed through red and green glasses. The magnitude of the parallax is a function

*See Moik (1977) for remapping programs used on the IBM 360-91.

of the altitude and is used to calculate the height. Time sequences of remapped image pairs are then displayed on AOIPS. The heights are measured on AOIPS using the following procedure: a cursor or box is moved under joystick control to the cloud or geographical feature to be measured. One of the images is shifted also using the joystick (a unique AOIPS function) until the parallax for that feature is eliminated. Observed through the stereo glasses the cursor appears to move up or down until it is at the height of the feature. This manual measurement of the parallax can only be made to the nearest pixel, therefore a cross correlation algorithm must be used when subpixel accuracy is required. The parallax is used to calculate the height taking into consideration the positions and attitudes of the satellites.

Cloud Motion and Height Measuring Techniques

Software is under development at GSFC on AOIPS to allow the measurement of cloud motion and height simultaneously from stereo image sequences. Observation of three-dimensional cloud motion fields makes it much easier to measure winds at many levels and to minimize confusion between cloud tracers, because even small altitude differences between cloud layers are observed. This software will also aid in the measurement of cloud height variations as a function of time. Methods are also being developed to contour cloud height as a function of time on AOIPS. These methods will be adapted for the cloud growth techniques used to estimate vertical velocities and storm intensity which is now done using infrared techniques by Adler & Fenn (1978a, 1978b).

STEREO HEIGHT VERIFICATION AND ERROR ANALYSIS

Measurements of the altitude of known geographical features, repeatibility studies on cloud heights, and stereo vs. IR height comparisons have been made to evaluate the stereo cloud height accuracy. The altitude of the coastline over a 5° latitude by 5° longitude area of the Gulf of Baja California was measured to determine bias errors and to estimate altitude measurement variability. The average bias error was $\overline{Z}$ = -0.67 km with a standard deviation σ_Z = 0.29 km as shown in Table 1. Over a small 5 x 5 pixel area the standard deviation σ_Z = 0.10 km. The coastline altitude bias error was also measured in central California and near Lake Titicaca in South America where $\overline{Z}$ = 0.11 km and 0.26 km respectively (also shown in Table 1).

Also, the altitude of several lakes in and near California, and Lake Titicaca were used for verification. The differences between the stereo heights and the known (map) altitudes ranged from 0.01km to 0.29 km once the sea level bias error was removed. Although we have no rigorous verification of cloud top height we conclude from these terrestrial data comparisons that the absolute accuracy of the cloud height measurements is about ±0.5 km and if a feature of known altitude is available in the image, measurements of precision approaching ±0.1 km are possible (relative accuracy). The absolute accuracy is dependent upon having a very accurate navigation solution. Repeatibility measurements of heights of various cloud types indicate that cloud layer altitudes can be measured within about 0.1 km even for very thin cirrus as shown by the standard deviation values ranging from σ_Z = 0.08 to σ_Z = 0.19 in Table 2. Repeatibility over a few pixels (σ_Z local) is also excellent. All measurements were made using a crosscorrelation algorithm which can measure to subpixel precision. For maximum precision it is necessary to have a fairly large, high contrast feature oriented in a north south direction.

Table 1. AOIPS digital stereo error analysis based on geographical feature height verification from GOES East (75°W) and GOES West (135°W)

	Altitude (km)				
	Z_{MAP}	$\overline{Z}$	$\overline{Z}_{CORRECTED}$	σ_Z	$Z_{MAP} - \overline{Z}_{CORRECTED}$
BAJA (1 km ≈ 1.5 pixels)					
5° Lat. X 5° Long. area	0	-0.67		0.29	
5 X 5 pixel area	0	-0.46		0.10	
CALIFORNIA (Lake Tahoe Area/ 1 km ≈ 2 pixels)					
Coast Line	0	0.11		0.25	
Walker Lake	1.21	1.03	0.92	0.17	0.29
Pyramid Lake	1.16	1.20	1.09		0.07
Lake Tahoe	1.90	2.0	1.89		0.01
Mono Lake	1.95	2.0	1.89		0.06
SOUTH AMERICA (Lake Titicaca area/ 1 km ≈ 5 pixels)					
Coast Line	0	0.26	–	0.11	
Lake Titicaca	3.82	4.21	3.95	0.19	0.13

Table 2. AOIPS digital stereo error analysis based on cloud height measurements from GOES East (75°W) and GOES West (135°W)

	(km)				
	$\overline{Z}$	σ_Z	σ_Z (LOCAL)	Z_{IR}	$\overline{Z} - Z_{IR}$
REPEATIBILITY (Baja area/1 km ≈ 1.5 pixels)					
Stratocumulus	1.2	0.19	0.01		
Cirrus	8.2	0.12	0.06		
Very Thin Cirrus	7.8	0.08			
STEREO/IR COMPARISON (Florida area/1 km ≈ 3 pixels)					
Stratocumulus	0.7			0.1	0.6
Middle Level Cumulus	4.9			4.9	0.0
	5.8			6.1	-0.3
Small Cumulonimbus Tower	9.1			10.6	-1.5
Cumulonimbus Cirrus Anvil	11.1			12.4	-1.3

Manual measurements made on the 1 km resolution displays used for this study and on features of about 1 pixel area can be made only to the nearest pixel. For the four areas used in this study the ratio of horizontal parallax to vertical resolution ranged from 1.5 to 5 pixels per km. Therefore measurements to 1 pixel would give precision ranging from 0.67 to 0.2 km. For large features where the cross correlation was used subpixel measurements with precision of 0.15 to 0.5 pixels would be required to give the approximately 0.1 km vertical resolution indicated by the data. Comparison of stereo cloud height with IR cloud height on high emissivity clouds show agreement to approximately 1 km as shown in Table 2. Since only a climatological atmospheric temperature profile was used for determining the infrared derived heights this gives only an order of magnitude verification.

RECOMMENDATIONS AND FUTURE WORK

Tests using 8 km resolution infrared images from GOES indicate that stereo techniques work equally well in the infrared, but since the resolution is low it is likely that little useful height information may be obtained over other methods. It is recommended that future geosynchronous satellites have an infrared resolution of 1 km so that this extremely powerful stereo technique is available 24 hrs/day.

It is also extremely important that 5 minute interval synchronized stereo image pairs be obtained in the future, since this is required for cloud growth and motion measurements in the complicated weather situations where stereo has its greatest impact. These intervals are needed because many clouds and cloud features have such short lifetimes that the continuity provided by 5 minute intervals is absolutely necessary to measure their motion or growth.

Techniques are proposed to display mesoscale and submesoscale numerical model results on AOIPS in a graphical four-dimensional manner. When combined with the four-dimensional representation of cloud structures from the GOES sattellites this should provide a powerful diagnostic tool for understanding the model output and comparing it with observed weather.

REFERENCES

1. Adler, R. F., and D. D. Fenn, 1978a: "Thunderstorm Vertical Velocities Estimated from Satellite Data", Conference on Weather Forecasting and Analysis and Aviation Meteorology, Oct. 16-19, 1978, Silver Spring, MD, AMS.
2. Adler, R. F., and D. D. Fenn, 1978b: "Satellite-Based Thunderstorms Intensity Parameters", NASA Technical Memorandum 78094, May 1978, NASA/GSFC. Submitted to Journal of Applied Meteorol.
3. Bracken, P. A., J. T. Dalton, J. B. Billingsley, J. J. Quonn, 1978: Atmospheric and Oceanographic Information Processing System (AOIPS) System Description, March 1977, NASA/GSFC X-933-77-148.
4. Bryson, W. 1978: Cloud Height Determination from Geosynchronous Satellite Images. University of Wisconsin, Ph.D. Thesis.
5. Minzner, R. A., W. E. Shenk, and T. Steranka, 1978a: Stereographic Cloud Heights Heights from Images of SMS/GOES Satellites, Geophysical Research Letters, Vol. 5, No. 1, pp. 21-24.
6. Minzner, R. A., R. D. Teagle, J. Steranka, and W. E. Shenk, 1978b: Stereographic Cloud Height from the Imagery of Two Scan-Synchronized Geostationary

Satellites, 4th NASA Weather and Climate Program Science Review, NASA Conf. Pub. in printing.
7. Moik, J. G., 1977: Users Guide for Batch Operation of the SMIPS/VICAR Image Processing System, NASA/GSFC X-933-76-114.

Paper No. 13

ANALYTIC STUDIES ON SATELLITE DETECTION OF SEVERE, TWO-CELL TORNADOES

George F. Carrier, *Harvard University, Cambridge, Massachusetts*
Paul Dergarabedian and Francis E. Fendell, *TRW, Inc., Redondo Beach, California*

ABSTRACT

It is argued that a two-cell structure is likely to be the unique property, and potentially satellite-accessible observable, of the exceptionally severe tornado. Analysis elucidating the dynamic, thermodynamic, and geometric properties of this two-cell structure is described. The analysis ultimately will furnish instrumentation requirements.

INTRODUCTION

The goal of this research is to identify and to characterize a unique property of the exceptionally severe tornado that might permit its detection by future passively instrumented geosynchronous meteorological satellites with highly refined resolution. Such a tornado tends to have long path length ($\sim$100 km) and long life span ($\sim$1 hr), such that early detection makes possible worthwhile warning. Since the exceptionally severe 2% or so of tornadoes effect about 98% of tornado-associated destruction (Darkow 1977), these special cases deserve emphasis. Of course, the inability of passive satellite detectors to penetrate the highest-level cloud layer is a serious restriction in achieving the goal.

One would prefer to forecast the onset of tornadoes. Current satellite indicators [midtropospheric minimum in the vertical profile of the total static enthalpy (Darkow 1967, Negri 1977), or low cloud-top temperature with rapid cloud-area increase (Adler 1977)] cannot specify whether, when, or in what form, severe weather will arise. In fact, despite Adler's success for one specific event, Negri finds for another event that the minimum cloud-top temperature occurred hours after an intense hailstorm, and that explosive cloud-top growth was absent for a concomitant devastating tornado. Intuitively, inferring the existence of significant convective activity is distinct from detecting a specific unerring indicator of severe-tornado occurrence (see Darrah 1978). Thus, here attention is confined to satellite use for severe-tornado detection, as opposed to forecasting.

IDENTIFICATION OF AN OBSERVABLE ACCESSIBLE TO A SATELLITE

Funnel-cloud-length interpretation (Dergarabedian and Fendell 1973) permits one to establish instantaneously and accurately the peak swirl speed, relative to the axis of rotation, of any sighted tornado; in practice, these speeds are found to reach, but never to exceed, about 110 m/s. Examination of a very large number of atmospheric soundings taken in close spatial and temporal proximity to tornadoes (Dergarabedian and Fendell 1977) readily establishes that the ground-level horizontal pressure deficits from ambient achievable by moist-adiabatic ascent are at most about 1-2 kPa (10-20 mb). By the cyclostrophic balance, such deficits are equivalent to peak swirls on the order of 50 m/s. The 10-kPa (100-mb) pressure deficits consistent with 100-m/s peak swirl are achievable thermohydrostatically only by having a central dry-adiabatically compressed downdraft of nonrotating, originally tropopause-level air. In short, the same evolution from one-cell to two-cell structure that marks the evolution of a tropical storm to a very dangerous typhoon (Fendell 1974), also marks the evolution of a mesocyclone to a dangerous-tornado-bearing supercell (Dergarabedian and Fendell 1977), although vastly different horizontal scales characterize the two types of vortical storms. There must exist a well-developed "eye" (nonrotating, descending core) within an "eye wall" (annulus of swirling updraft), with the "eye"/"eye wall" interface sloping appreciably away from the axis of rotation with height, from simple conservation-of-angular-momentum considerations in an atmosphere with density decreasing with altitude. Otherwise, peak swirl speeds, relative to the axis of rotation, of 110 m/s are thermohydrostatically inexplicable, and no plausible alternative mechanisms have been identified.

Thus, the "eye" furnishes a unique characteristic of the severe tornado and an observable possibly accessible to passively instrumented meteorological satellites. Elucidation of the typical geometric dimensions, dynamic properties, and thermodynamic states of the "eye"/"eye wall" interface becomes the goal of this research.

INPUT FROM OVERFLIGHTS OF THUNDERSTORMS

Descriptions from aircraft overflights of anvil clouds (Anonymous 1977) report observations of "cumulonimbus collapse" and "hole formation" in the cirrus shield of thunderstorms one-quarter to one-half hour before onset of a destructive tornado. The inference drawn here is that compressional heating associated with "eye" insertion is being observed; of course, the nascent "eye" may not extend the depth of the troposphere, so "hole formation" does not imply a severe tornado inevitably follows. Incidentally, it is probably a misconception that cumulonimbi "overshoot" (Fujita et al. 1975) their level of neutral stability; such momentum build-up in so subsonic an atmospheric flow as buoyancy-driven ascent of a cumulonimbus (typified by speeds of 10 m/s, with gusts of 25 m/s) is unlikely. As a rotating thunderstorm spins up, entrainment into cumulonimbi decreases (Emmons and Ying 1967),

especially in the lower troposphere, such that later cumulonimbi transcend the neutral stability level (i.e., the tropopause) established by earlier, more diluted cumulonimbi.

INPUT FROM MODELING

One would prefer to concentrate immediately on the upper-tropospheric flow in a severe tornado, because this portion of the flow is accessible to passive satellites. However, there are crucial constraints on mass, momentum, and heat flux, into and out of the upper-tropospheric flow, posed by the lower-tropospheric flow. In fact, a logical analytic procedure is to follow the flow through the same sequential "path" as air is "processed" in the tornado.

The severe tornado is here modeled as a closed vertical quasisteady axisymmetric system of four subregions (Dergarabedian and Fendell 1970); in each of the four subdivisions significantly distinct physical processes enter. The bulk of the system is a potential vortex, in which little axial variation occurs in the dynamics and in which radial flow is negligible. Air slowly sinks from the potential vortex, in cyclostrophic equilibrium, into a near-ground inflow layer, in which angular-momentum-dissipating frictional forces upset the cyclostrophic balance to permit radial influx ("teacup effect"). A critically important, but rarely appreciated, characteristic of the high-swirl portion of the inflow layer is that it is inviscidly controlled, such that the role of friction is confined to a very-near-ground sublayer (Carrier 1971; Burggraf et al. 1971; Carrier and Fendell 1978). The swirling radial influx erupts into an annulus of swirling updraft, that conveys lower-tropospheric fluid to the upper troposphere; the annulus consists of three components: a turnaround or corner flow, an "eye wall", and an upper-tropospheric outflow -- these three regions together are considered the third subdivision of the tornado. The fourth subdivision, unique to the severe tornado, is the "eye" (see Figure 1).

RECENT RESULTS FROM MODELING

In the past, solution for the potential vortex and for the near-ground inflow layer has been available. However, the turnaround flow, which tends to be an elliptical domain bounded by two streamsurfaces of initially unknown position, has proved an intractable free-boundary problem for analysts. Here solution for the turnaround flow has been furnished by method-of-lines integration of a turnaround-flow formulation, which is rendered of parabolic-like character by transformation of variables (Carrier, Dergarabedian and Fendell 1978). Results show that accelerations from streamline curvature during separation of the inflow give but a 10% augmentation in swirl in the turnaround over peak swirl speeds in the potential vortex. More importantly, displacement of the annular swirling updraft from the axis of rotation is now characterized for the lower troposphere.

CONCLUDING REMARKS: DIRECTIONS FOR FURTHER WORK

In view of results just enumerated, it now seems possible to proceed logically to the characterization of the thermodynamic, dynamic, and geometric properties of mid- and upper-tropospheric "eye"/"eye wall" configurations. This information will furnish the resolution and sensitivity required for meteorological-satellite instrumentation dedicated to detection of severe tornadoes. The only alternative to pursuing and exploiting this knowledge is to grasp at correlations without established meteorological bases.

REFERENCES

Adler, R. F. 1977, Third NASA Wea. & Climate Program Sci Rev., Greenbelt, MD.: Goddard Space Flight Center, NASA.

Anonymous 1977, Bull. Amer. Meteorol. Soc. 58, 608-609.

Burggraf, O. R., Stewartson, K. & Belcher, R. 1971, Phys. Fluids 14, 1821-1833.

Carrier, G. F. 1971, J. Fluid Mech. 49, 133-144.

Carrier, G. F. & Fendell, F. E. 1978, EPRI Proj. 308, Rept. NP-748, pp. A-1 - A-45. Palo Alto, CA: Electric Power Res. Inst.

Carrier, G., Dergarabedian, P. & Fendell, F. 1978, NASA Contractors Report (in preparation).

Darkow, G. L. 1977, Proc. Symp. on Tornadoes: Assessment of Knowledge & Implications for Man, pp. 243-247. Lubbock, Tex.: Inst. for Disaster Res., Texas Tech. U.

Darkow, G. L. 1967, Preprints of Papers Presented at the Sixth Conference on Severe Local Storms, pp. 218-221. Boston, Mass.: Amer. Meteorol. Soc.

Darrah, R. P. 1978, Mon. Wea. Rev. 106, 1332-1339.

Dergarabedian, P. & Fendell, F. 1977, NASA Contractors Rept. CR-2830.

Dergarabedian, P. & Fendell, F. 1973, J. Astronaut. Sci. 21, 26-31.

Dergarabedian, P. & Fendell, F. 1970, J. Astronaut. Sci 17, 218-236.

Emmons, H. & Ying, S.-J. 1967, Eleventh Symp. (Intern.) on Combustion, pp. 475-486. Pittsburgh: Combustion Inst.

Fujita, T. T., Forbes, G. S. & Umenhofer, T. A. 1975, Weatherwise 29, 116-131.

Negri, A. J. 1977, Atmos. Sci. Paper 278. Fort Collins, Colo.: Dept. Atmos. Sci., Colo. St. U.

THE FOUR-PART STRUCTURE OF A MATURE QUASISTEADY AXISYMMETRIC VORTEX (CLOSED SYSTEM)

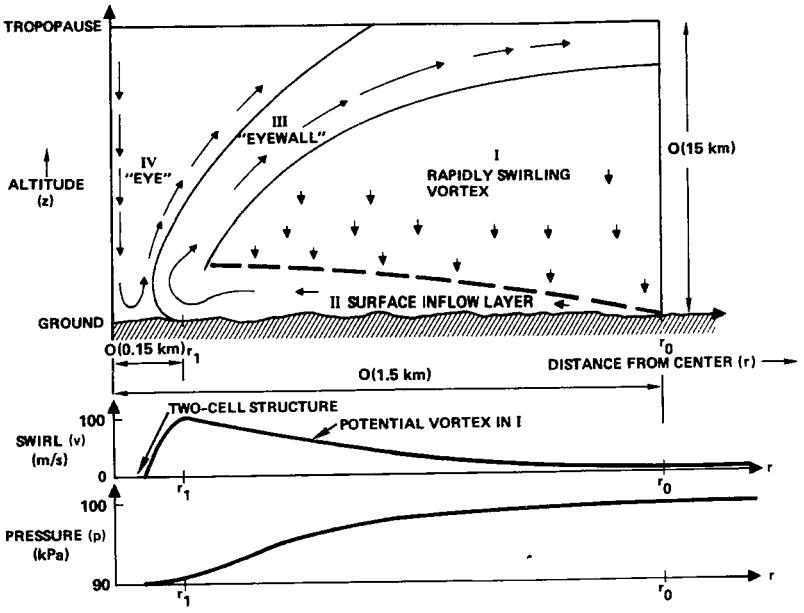

Fig. 1. A schematic, not to scale, of the structure of a tornado, with 100-m/s peak swirl relative to the axis of symmetry. The radial profile of the swirl, at midtropospheric altitude, reveals a nonrotating central "eye" joined to a nearly potential vortex. The pressure deficit from ambient, at ground level, may reach about 10 kPa; the outwardly sloped "eye"/"eye wall" interface permits fluid in the potential-vortex portion of the tornado to achieve swirl speeds consistent with this pressure deficit.

Page intentionally left blank

Paper No. 14

MEASUREMENT OF HURRICANE WINDS AND WAVES WITH A SYNTHETIC APERTURE RADAR

O. H. Shemdin and D. B. King, *Jet Propulsion Laboratory, Pasadena, CA*

ABSTRACT

This paper presents an analysis of data collected in a hurricane research program. The data were collected with a Synthetic Aperture Radar (SAR) during five aircraft flights in the Atlantic in August and September, 1976.

Work has been conducted in two areas. The first is an analysis of the L-Band SAR data in a scatterometer mode to determine the surface windspeeds in hurricanes, in a similar manner to that done by an X-Band scatterometer. The data available is limited but sufficient for demonstrating that this technique is feasible and has certain advantages over X-Band scatterometers. However, further refinement and experimentation is necessary.

The second area of our work has been to use the SAR to examine the wave patterns in hurricanes. The wave patterns in all of the five storms are similar and show a marked radial asymmetry. The dominant waves propagate ahead of the storm in a broad arc that has an apparent center in a region of confused sea to the right and rear of the hurricane eye. The asymmetry in the wave patterns is attributed to the forward motions of the storms. The wave directions throughout the storms do not show a sensitive dependence on the forward speed of the storms or on their maximum wavespeeds. However, there is an increase in peak wavelength with increasing windspeed and forward velocity.

INTRODUCTION

Hurricane waves play a controlling factor in the design of permanent structures along the Gulf and East Coasts of the United States and in other parts of the world. In spite of their importance, they are poorly understood and often not adequately

predicted. This lack of understanding is due in a large part to the difficulties involved in accurate data collection under the extreme conditions. It is shown that remote sensing techniques provide extremely valuable data sources in such situations.

Data Collection

In August and September 1976, the Jet Propulsion Laboratory (JPL) participated in a hurricane research program with a number of other NASA research centers and with the NOAA-National Hurricane and Environmental Meterological Laboratory. JPL collected information on the directional properties of hurricane waves using Synthetic Aperture Radar (SAR) onboard a NASA CV-990 research aircraft. The five flights were made into Tropical Storm Emmy on August 24 (designated as Emmy 1 in this paper), Hurricane Emmy on August 25 (Emmy 2), Hurricane Frances on August 31 (Frances), Tropical Storm Gloria on September 28 (Gloria 1), and Hurricane Gloria on September 30 (Gloria 2). These storms were all in the western Atlantic. Approximately 700 minutes of data were collected in these five storms.

Hurricane Wind Measurements

The technique of using airborne and spacecraft radar-scatterometers to measure ocean surface wind magnitudes and directions has been demonstrated and documented primarily with frequencies near 14 GHz. This report discusses the use of microwaves at L-band frequency of 1.215 GHz. The L-Band instrumentation was an adaption of a SAR whose primary function was to obtain high resolution images of the large gravity waves generated in the hurricane (Elachi, Thompson and King, 1977). The usual form for the data is a two dimensional high resolution image of the surface reflectivity with resolution cell sizes of approximately 25 by 25 meters. We employed a different method of signal processing to yield a measure of the average reflectivity (backscattered radar cross section/unit area) over a much larger area. This technique is called the "scatterometer" mode of the instrument since it receives and continuously monitors the averaged power backscattered by an area on the surface (about 4.0 by 0.5 km) that is viewed at an angle of 20° off nadir. Thus the variations of the surface reflectivity (proportional to the surface roughness caused by the wind stress) can be measured along a straight line segment (at constant altitude) parallel to the aircraft flight path.

Three SAR passes across the eye and eyewall of Hurricane Gloria were analysed. These corresponded to times when there

were reasonably simultaneous passes of the same regions by low level aircraft to obtain low level wind speeds. The data showed that the relative changes in radar cross sections followed closely the large variations in wind speed that were measured in the storm. The size of the observed area on the surface (footprint) was sufficiently small so that the velocity structure in the eye walls was resolveable to a smaller scale than for that of the presently designed scatterometers. All three passes had the largest backscatter from the eye wall regions, with a well defined minimum in the eye. As expected, the radar cross section then diminshed with increasing radial distance from the eye, corresponding to the lower wind speeds at the larger distances from the center.

Based on work done at X-Band, we then examined modifications of the SAR signal to account for wind direction. The wind speeds were modified by multiplying them by a factor of $[1+0.5\mathrm{Cos}(2\emptyset)]$, $\emptyset$ being the angle between the radar beam axis and the wind. These results showed an improved correlation when the direction factor is included. The effect of rainfall was also examined and was shown to depress the signal intensity.

Other effects were also examined. The signal does not appear to saturate up to sustained wind speeds of ninety knots. Also, there does not appear to be any correlation between the scatterometer signal and the presence of large gravity waves.

The analysis conducted here was preliminary in nature due to the limited amount of ground truth available but does show that the technique of using L-Band to measure surface windspeeds is potentially useful. It has advantages over X-Band scatterometer of having significantly finer resolution and of being able to penetrate rainfall (abet with a modified signal). Its major disadvantage is a decrease in the sensitivity of widespeed fluctuations compared with X-Band.

Hurricane Wave Measurements

Figure 1 shows processed SAR wave imagery at selected locations throughout Gloria 2. Each wave image is enlarged ten times relative to the hurricane scale. The direction of hurricane forward motion is to the top of the figure. For comparison, all the hurricane flights were oriented in this manner, regardless of the direction of true north. These images are placed in their proper location relative to the moving eye of the hurricane.

The striking feature of Figure 1 is the pronounced asymmetry in the wave field. There is an arc of waves which extends

from the right front quadrant through the left front and into the left rear storm center. The hurricane winds are blowing in a counterclockwise spiral and thus the dominant waves in much of the storm are traveling at 90° or more with respect to the local wind direction. The arc appears to have its center in right rear quadrant but there is no distinct origin. Instead, the wave patterns in this area suggest a confused sea. The Fourier transforms show multiple dominant peaks which are traveling in different directions.

The pronounced asymmetry in the wave field is caused primarily by the forward motion of the hurricane. The counterclockwise winds (for northern hemisphere storms) blow faster on the right hand side of a moving hurricane than on the left due to the added speed of the storm. This causes larger waves to be generated in this area. However, more importantly, these waves tend to travel with the storm and so stay in the generation region much longer. These dominant waves then propagate throughout most of the storm depending on the group velocities and directions of propagation.

The other hurricanes were then compared with Gloria II and found to have similar overall wave patterns. The variations in these patterns corresponded with variations in the storms forward velocity and maximum wind speeds. The faster moving storms and those with higher wind speeds had longer wave lengths in front of the storms but there was little change in wave propagation direction, except in the confused right rear quadrant.

Summary and Conclusions

This paper presents work done on the analysis of hurricane wind and wave data collection with a SAR. We have shown that a SAR has useful potential as an instrument to measure wind but that more analysis needs to be done before the procedure becomes operational. We have also analysed directional wave data in hurricanes and found them to be very different from predicted results and have attempted to explain the dominant mechanics involved.

REFERENCES

Elachi, C., T. Thompson and D. King (1977), "Observation of the Wave Pattern Under Hurricane Gloria with Airborne Synthetic Apperture Radar", Science, Vol. 198, pp. 609-610.

King, D., and Shemdin, O.H. (1978), "Radar Observations of Hurricane Wave Directions", Proc. 16th Int'l Conf. Coastal Eng., Hamburg.

Weissman, D. and King, D., (1978), "Relationship Between Hurricane Surface Winds and L-Band Radar Backscatter from the Sea Surface." Submitted to J. Atmos. Sciences.

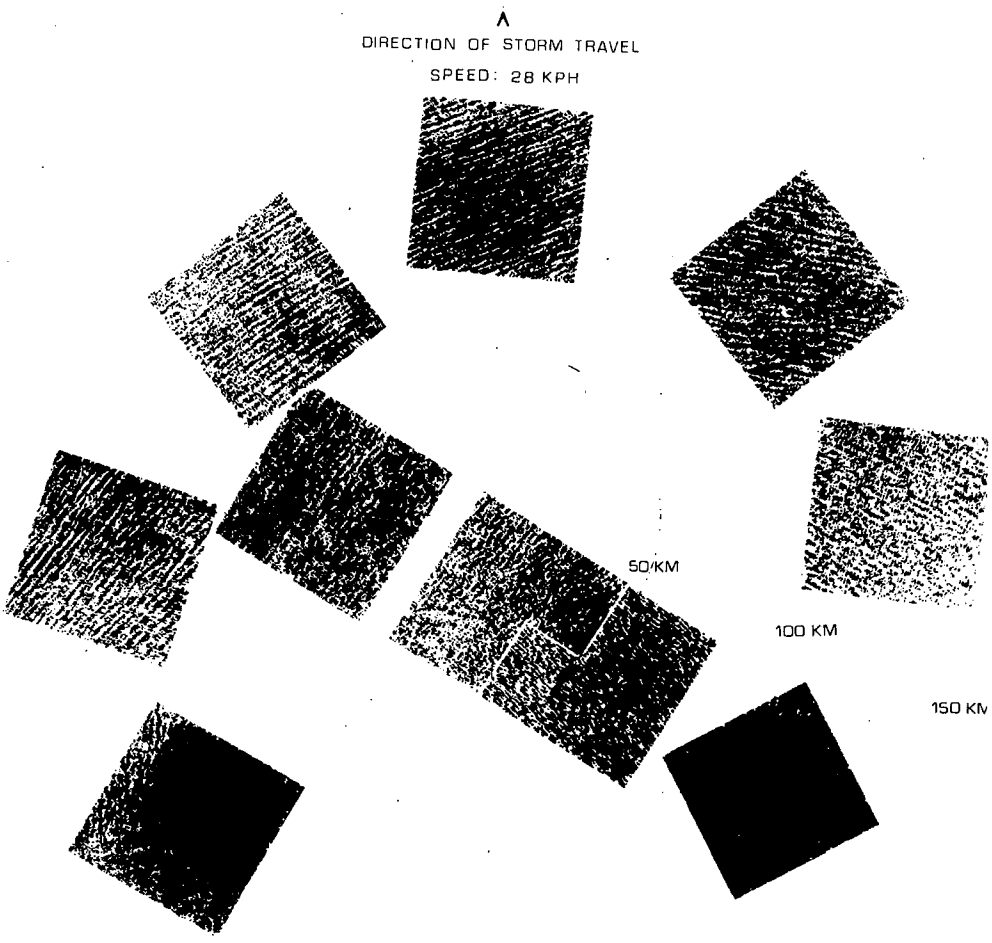

FIGURE 1. SAR Wave Patterns in Hurricane Gloria II.

Page intentionally left blank

Paper No. 15

ESTIMATING TROPICAL CYCLONE OUTER SURFACE WINDS FROM SATELLITE MICROWAVE DATA

Stanley Q. Kidder, *Department of Atmospheric Science, Colorado State University, Ft. Collins, Colorado*

ABSTRACT

Warm temperature anomalies over tropical cyclones are sensed by the 55.45 GHz channel of the Nimbus 6 Scanning Microwave Spectrometer (SCAMS). Radial brightness temperature gradients are related to radial surface pressure gradients through the hydrostatic and radiative transfer equations. Surface wind speeds outside of the radius of maximum wind are calculated from the pressure gradients and compared with observations.

1. INTRODUCTION

One of the most important measurements to be made on tropical cyclones is that of surface wind speed. In this paper a simple technique for estimating outer surface winds using data from the 55.45 GHz channel of the Nimbus 6 Scanning Microwave Spectrometer (SCAMS) or from the 54.96 GHz channel of the Tiros-N Microwave Sounding Unit (MSU) is proposed. The advantages of the technique are that it is physically based, it requires little computation time, and it is not affected by clouds.

2. THEORY

The brightness temperature measured by a satellite-borne radiometer is given by

$$T_B = \epsilon T_s \tau_o + \int_o^H W(z)T(z)dz \qquad (1)$$

where ϵ is surface emittance, T_s surface temperature, τ_o transmittance from the surface to the satellite, T(z) atmospheric temperature, and W(z) a weighting function (Fig. 1). For a frequency such as 55.45 GHz (SCAMS) or 54.96 GHz (MSU) which have a vanishingly small τ_o, the brightness temperature is a weighted mean upper tropospheric temperature. Coincidentally, tropical cyclones are driven by upper tropospheric warm temperature anomalies (Fig. 2). Because these temperature anomaly curves have very similar shape,

$$T'(r,z) \approx \alpha(r)\hat{T}(z), \qquad (2)$$

where $\hat{T}(z)$ is a standard anomaly profile, a relationship between brightness temperature gradient and surface pressure gradient can be derived, assuming hydrostatic balance (see Kidder, 1979):

$$\frac{\partial T_B}{\partial r} = -A \frac{\partial \ell n P_S}{\partial r}, \tag{3}$$

where A is given by

$$A = \frac{\frac{g}{R}\int_0^H \frac{\hat{T}(z)}{T_o^2(z)}\,dz}{\int_0^H W(z)\hat{T}(z)dz}, \tag{4}$$

and $T_o(z)$ is the temperature profile of the storm's environment. In the western North Pacific A is 0.95×10^{-2} K^{-1} and 0.84×10^{-2} K^{-1} for 55.45 GHz and 54.96 GHz, respectively. In the Atlantic the values are 1.02×10^{-2} K^{-1} and 0.61×10^{-2} K^{-1}, respectively.

The surface wind speed is related to the radial surface pressure gradient by

$$\frac{v^2}{r} + f\, v\sec\beta = \frac{1}{\rho}\frac{\partial p}{\partial r} = -ART_s \frac{\partial T_B}{\partial r} \tag{5}$$

where R is the gas constant and β is the inflow angle, roughly 22.5° on the average (Frank, 1977). Friction is implicit in this equation. Because there is noise in the brightness temperature field (±0.5 K) it is useful to know the functional form of the wind to use as a smoothing tool. Such a function, suggested by Hughes (1952), Riehl (1954, 1963), and others, is

$$V = Cr^{-X}. \tag{6}$$

Inserting Equation (6) into (5) and integrating holding, A, f, β, C, and X constant gives

$$T_B(r) - T_C = (ART_S)^{-1}\left[-\frac{C^2}{2X}\, r^{-2X} + \frac{f\sec\beta}{1-X}\, Cr^{1-X}\right], \tag{7}$$

where T_C is an integration constant. To calculate wind speeds, one calculates the average brightness temperature in radial bands around the center of the storm. Then one calculates the C for a given X, which gives the least squares best fit to the observed brightness temperatures. The wind at any radius (outside the radius of maximum wind) is given by Equation (6).

It is important to note that clouds and precipitation have virtually no effect at the two frequencies mentioned here (Kidder, 1979); thus, these measurements can be made regardless of weather conditions.

3. OBSERVATIONS

Two types of data were used to examine the theory. First simulated satellite data was calculated using soundings constructed from multi-level aircraft penetrations. Figure 3 shows the calculated surface wind speed and the observed vortex average relative wind at 95 kPa for hurricane Inez on 28 September, 1966 (Gray and Shea, 1976). In this calculation, X was set equal to 0.5 which has been shown

to be the best value for low level winds in the inner core region by Riehl (1963) and Shea and Gray (1972). Because the wind of the surface is less than at 95 kPa, the calculated surface winds are somewhat too high, but the shape of the curve is good, and some sort of correction could produce accurate surface winds.

The second type of data used was from the 55.45GHz SCAMS channel. The brightness temperatures were averaged in 56km bands about the storm center, and the radius of $15 ms^{-1}$ (30kt) and $26 ms^{-1}$ (50kt) winds were calculated for eight typhoons during 1975 using X = 0.7 which is a reasonable choice for r greater than 100km (Kidder, 1979). These data are compared with best track estimates in Figure 4. There are, unfortunately, very few data points, but there does seem to be a relationship between the observed and predicted radii. That the slopes of the regression lines are less than one is somewhat disturbing, but it may be explained in part by the inclusion of "safety factors" in official estimates. The uncertainty (one standard deviation) in estimates made from the regression line is 63km for the radius of $26 ms^{-1}$ winds and 82km for $15 ms^{-1}$ winds.

4. CONCLUSIONS

While this technique is not ready for operational use, it shows enough promise that more research should be undertaken. The first step in this process should be testing the technique using Tiros-N MSU data. Because of the smaller A for 54.96 GHz, the MSU data give about a 70% greater signal for an individual storm than the SCAMS data. Also, aircraft observations could be useful.

5. ACKNOWLEDGEMENT

Supported by NASA (NSG-5258).

REFERENCES

Frank, W. M., 1977: The Structure and Energetics of the Tropical Cyclone. I. Storm Structure. Mon. Wea. Rev., 105, 119-1135.

Gray, W. M., and D. J. Shea, 1976: Data Summary of NOAA's Hurricane Inner-Core Radial Leg Flight Penetrations 1957-1967, and 1969. Colorado State University Atmospheric Science Paper No. 257, Fort Collins, Colorado, 219 pp.

Hughes, L. A., 1952: On the Low Level Wind Structure of Tropical Cyclones. J. Meteorol., 9, 422-428.

Kidder, S. Q., 1979: Determination of Tropical Cyclone Surface Pressure and Winds from Satellite Microwave Data. Colorado State University, Ph.D. Thesis, in preparation.

Riehl, H., 1954: Tropical Meteorology. McGraw-Hill, New York.

_____, 1963: Some Relations Between Wind and Thermal Structure of Steady-State Hurricanes. J. Atmos. Sci., 20, 276-287.

Shea, D. J., and W. M. Gray, 1972: The Structure and Dynamics of the Hurricane's Inner Core Region. Colorado State University Atmospheric Science Paper No. 182, Fort Collins, Colorado, 134 pp.

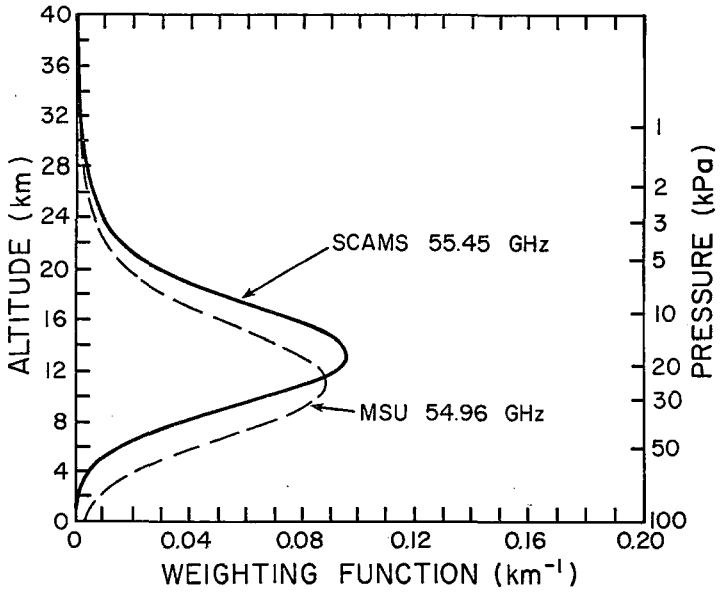

Fig. 1–Weighting functions.

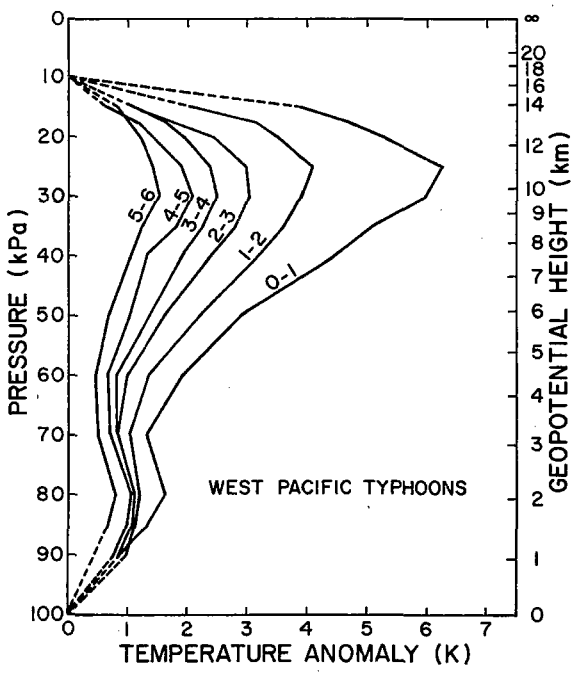

Fig. 2–Temperature anomalies (difference from environment) for the mean typhoon in one degree radial bands.

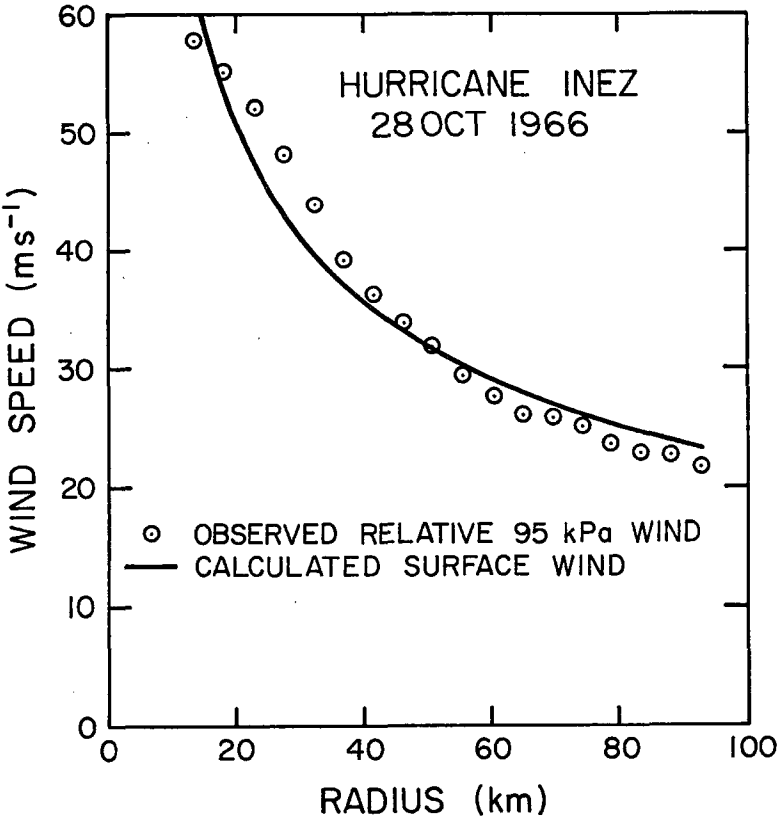

Fig. 3–Observed 95 kPa wind speeds compared with surface winds calculated from simulated satellite data.

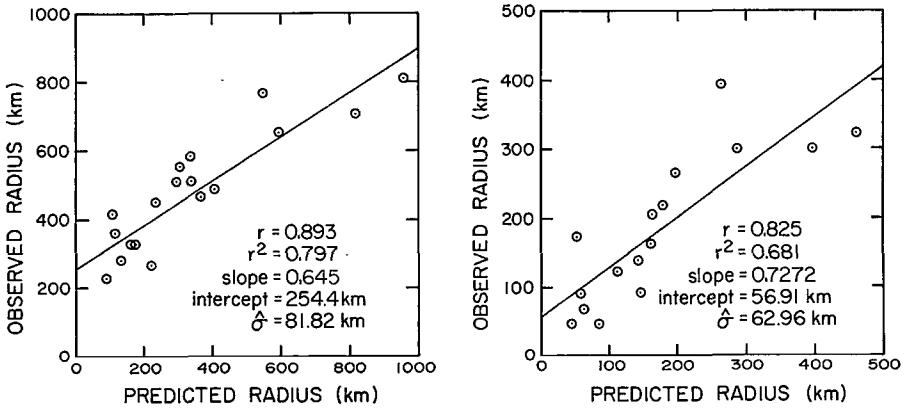

Fig. 4–Radii of (a) 15 ms^{-1} (30 kt) and (b) 26 ms^{-1} (50 kt) wind calculated from SCAMS 55.45 GHz data compared with observations.

Page intentionally left blank

Paper No. 16

RAIN OBSERVATIONS IN TROPICAL STORM CORA

T. T. Wilheit, A. T. C. Chang, J. L. King, and E. B. Rodgers, *Goddard Space Flight Center,* R. A. Nieman, B. M, Krupp, and H. Siddalingaiah, *Computer Sciences Corporation,* B. C. Diesen, *U.S. Air Force,* and J. Stratigos, *Georgia Institute of Technology*

Passive microwave observations were made in tropical storm Cora at 19.35 and 94GHz. These observations suggest that 94GHz is appropriate for mapping the extent of rain over either land or ocean backgrounds and that some rainfall intensity measurement is also possible.

INTRODUCTION

With the launch of the Electrically Scanned Microwave Radiometer (ESMR) aboard the Nimbus–5 satellite, it became possible to map rain over the oceans globally (Wilheit et al. 1977). The technique depends on observing rain in emission against cold space as reflected off the ocean. Thus, the ESMR depends on the large and predictable reflectivity of the ocean surface for mapping rain and cannot be so–used over land, a severe limitation for many applications. Appropriate measurement frequencies for this approach to rain mapping are in the 10–20GHz (3–1.5cm) range.

Figure 1 shows brightness temperature calculated according to the model discussed by Wilheit et al. (1977) for 19.35GHz over both typical land and water surfaces and for both horizontal and vertical polarizations. For rain measurements over ocean, one would use horizontal polarization which gives good sensitivity to rain from about 1 to 20mm/hr. Over land, on the other hand, there is little sensitivity in either polarization to rain intensity over this same dynamic range. When one allows for the extreme variability of land backgrounds, it becomes obvious that the use of radiometry at this frequency for rain mapping over land is hopeless.

The use of higher frequencies for mapping of rain over land was suggested by Savage and Weinman (1975). This approach depends on the scattering of microwave radiation by the larger hydrometeors and causes rain areas to appear colder than the non–raining background. A detailed study of the Nimbus–6 Electrically Scanned Microwave Radiometer (ESMR) data by Rodgers et al. (1978) has demonstrated this possibility in a quantitative manner but the results must be considered marginal for operational applications. Still higher frequencies might well provide a useful tool for the measurement of rain over land. Also the use of higher frequencies makes possible high resolution which in the 10–20 GHz range is difficult from low Earth orbit and prohibitive from geosynchronous orbit. Thus, in order to address both these problems, rain over land and spatial resolution, airborne measurements at 94GHz have been initiated.

OBSERVATIONS

During the summer of 1978, the NASA CV-990 aircraft was equipped with a complement of microwave radiometers which included a 94GHz radiometer which viewed 45° to the right hand side of the aircraft and the aircraft ESMR which scans from 50° to the left, through nadir to 50° to the right in 39 discrete steps and measures microwave brightness temperature at 19.35GHz. Other measurement frequencies ranged from 6.6 to 183GHz. Relevant systems routinely carried aboard the 990 include an inertial navigation system, a nadir viewing 10μ infrared radiometer and an atmospheric temperature probe.

The best opportunity to observe rain with this system came on August 11, 1978. Tropical Storm Cora had passed the Lesser Antilles and was decaying off the coast of Venezuela. The Convair 990 flew out of San Juan, P.R. and flew the pattern indicated in Figure 2. The storm was entered from the north at about 1700GMT and a north-to-south traverse was flown across the reported eye followed by a clockwise octagon pattern around the reported eye position. The aircraft then proceeded to the northern sector, where the most intense rain had been found, to observe individual rain cells. The triangles indicate the direction of flight at two minute intervals and the flight level winds are indicated by conventional meteorological symbols. As can be seen here, the storm no longer had a closed circulation and was only an open wave with about 30kt winds at the 13km flight level. Figures 3 and 4 show observations for two short time segments during the period in which the aircraft was overflying individual rain cells. The calibrations are preliminary and could be off by as much as 20°K, but, nevertheless, qualitative relationships are detectable. There is a clear tendency for increases in the 19.35 GHz brightness to be related to decreases in the 94GHz brightness. That is, an increase in rain intensity as indicated by the ESMR is accompanied by a decrease in the 94GHz brightness caused by scattering in the upper portions of the rain cell. The relationship is not precisely one-to-one but a general trend holds. Because the two sensors observe the rain in different manners and because of imperfections in the experimental situation, one would not expect a one-to-one relationship.

The data of Figures 3 and 4 and from another similar time segment were combined and displayed in Figure 5. Here the 94GHz brightness temperature is plotted as a function of the corresponding 19.35GHz brightness temperature for each observation. When the data are so displayed, a general relationship as indicated by the line segments A, B, and C becomes obvious. It may be interpreted as follows:

A. These data represent a no-rain situation. The choice of vertical polarization causes the 94GHz brightness temperature to be fairly high and constant. A land background would be similar or even warmer. The 19 GHz brightness shows more variability due to variation in cloudiness and surface winds.

B. This is a transition from no rain to rain. Non-raining clouds have few particles with greater than 50μ radius. As the dropsize grows toward the 100μ to 1 mm range, typical of rain drops, scattering begins to occur at 94GHz while the drops are still small enough to be within the Rayleigh absorption (cloud-like) region for 19GHz.

C. This is rain. The increase in brightness temperature at 19.35GHz with increasing rain rate has been well documented (Wilheit et al. 1977). It appears that there is a concommitant decrease in the 94GHz brightness. This may permit the use of 94GHz for the mapping of rain intensity but there may be too little accuracy for the intensity estimates to be useful. This remains to be settled.

D. This group of points clearly does not follow the overall trend observed in the rest of the data, yet they appear to cluster in a self-consistent manner suggesting a meteorological phenomenon rather than experimental errors. Further investigation, hopefully, will identify the phenomonon. Given the calibration uncertainties, it could be explained by large concentrations ($\gtrsim 0.1\,gm/cm^2$) of supercooled water.

Although these observations were made over water, they suggest the usefulness of 94GHz measurements for mapping rain over land. With any non-trivial rain rate ($\gtrsim 1\,mm/hr$) the rain column will be opaque at 94GHz and the background, land or water, will not influence the observed brightness temperature directly. It is possible, however, that drop size distributions are significantly different in land and ocean rain. If the cluster of points at D in Figure 5 does, in fact, turn out to be large concentrations of supercooled water, the combination of 19 and 94GHz measurements planned for the NASA B-57 aircraft would be useful indeed.

REFERENCES

Rodgers, E., H. Siddalingaiah, A. T. C. Chang and T. Wilheit, "A Statistical Technique for Determining Rainfall Over Land Employing Nimbus-6 ESMR Measurements" NASA-TM-79631, (1978) Submitted to J. App. Met.

Wilheit, T. T., A. T. C. Chang, M. S. V. Rao, E. B. Rodgers and J. S. Theon, 1977: "A Satellite Technique for Quantitatively Mapping Rainfall Rates Over the Oceans." J. Appl. Meteor., 16, pp. 551-560.

Savage, R. C., and J. A. Weinman, 1975: "Preliminary Calculations of the Upwelling Radiance from Rain Clouds at 37.0 and 19.35 GHz." Bull. Amer. Meteor. Soc., 56, 1272-1274.

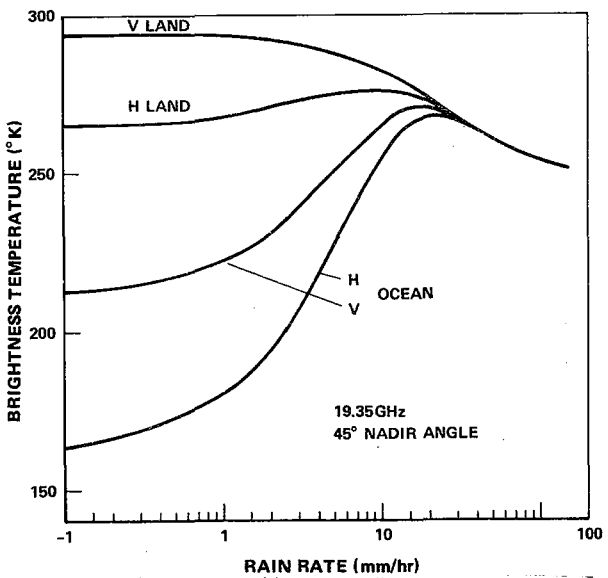

Fig. 1-Brightness temperature as a function of rain rate for ocean and land backgrounds viewed at 45° calculated according to Wilheit et al. (1977)

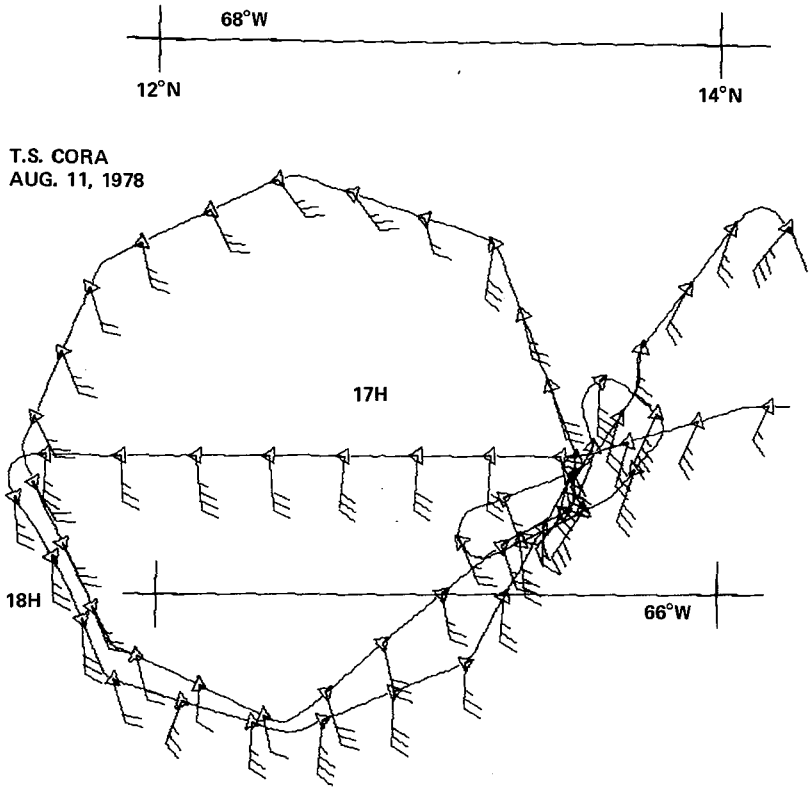

Fig. 2–Plot of CV–990 aircraft flight path through tropical storm Cora at 13 km altitude with wind barbs

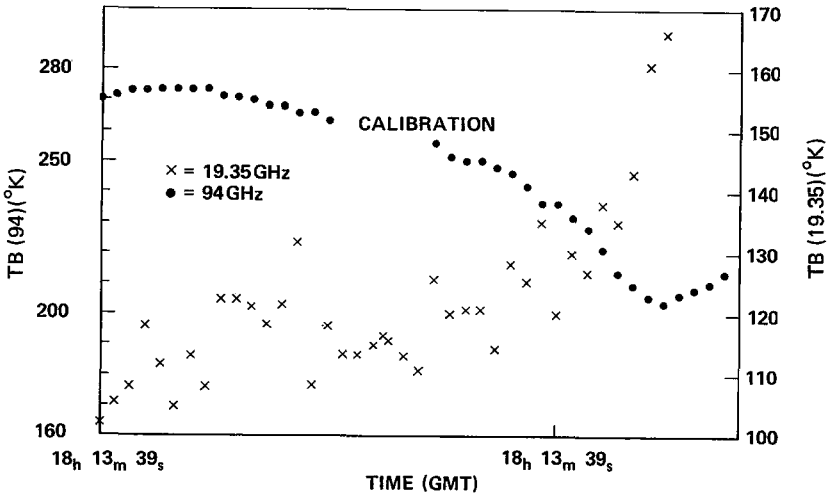

Fig. 3–Brightness temperature observations at 19.35 and 94GHz in tropical storm Cora

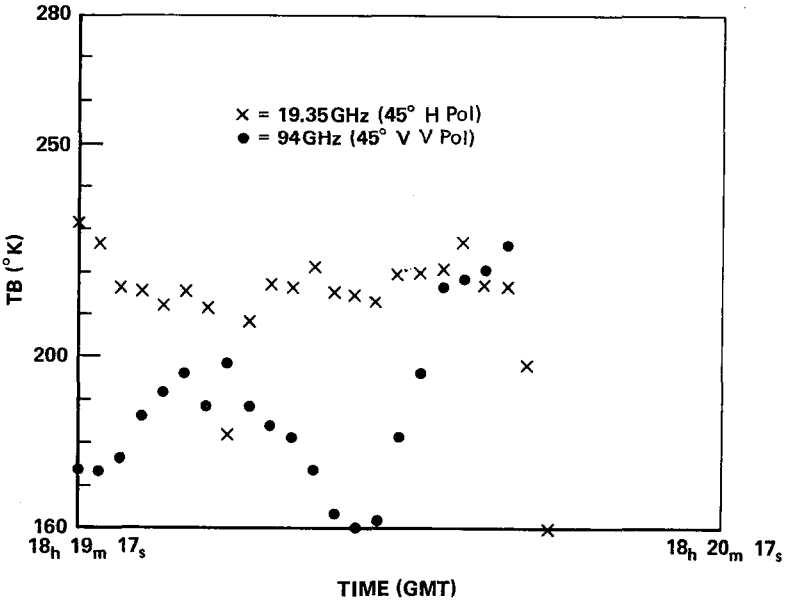

Fig. 4–Brightness temperature observations at 19.35 and 94GHz in tropical storm Cora

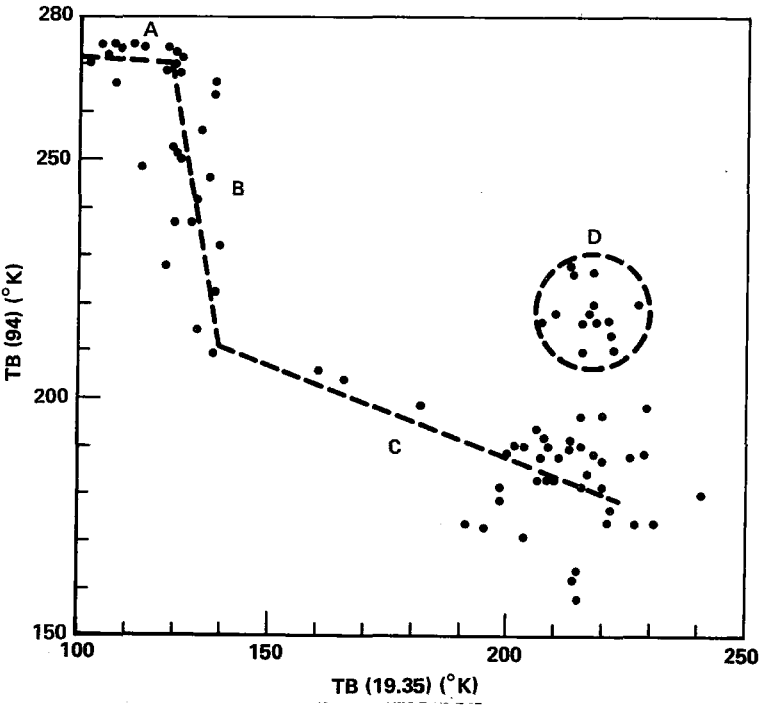

Fig. 5–Simultaneous observations 7 19.35 and 94GHz brightness temperature

Page intentionally left blank

Paper No. 17

AN OBJECTIVE METHOD FOR FORECASTING TROPICAL CYCLONE INTENSITY AND MOTION USING NIMBUS-5 ESMR MEASUREMENTS AND NON-SATELLITE DERIVED DISCRIPTORS

H. E. Hunter, *ADAPT Services Corporation, Reading, Massachusetts*
E. B. Rodgers and W. E. Shenk, *Goddard Space Flight Center, Greenbelt, Maryland*

An empirical analysis program, based on finding an optimal representation of the data, has been applied to 120 observations of 29 1973 and 1974 North Pacific tropical cyclones. Each observation consists of a field of Nimbus-5 Electrically Scanning Microwave Radiometer radiation measurements at 267 grid points covering and surrounding the tropical cyclone plus nine other non-satellite derived discriptors. Forecast algorithms to estimate storm intensity and motion at 12, 24, 48, and 72 hours after each observation have been developed using an independent eigen screening analysis. These algorithms were based on best track data. Independent testing of these algorithms showed that the performance of most of these algorithms were better than persistence and the algorithms forecasting 24, 48, and 72 hour maximum wind speed were better than those made operationally by the Joint Typhoon Warning Center for 1973 and 1974 that did not use best track data.

INTRODUCTION

The release of latent heat (LHR) through condensation and precipitation processes is essential to the development and maintenance of tropical cyclones. With the advent of the Nimbus-5 Electrically Scanning Microwave Radiometer (ESMR-5), it has been possible to remotely measure tropical cyclone rainfall characteristics (i.e. LHR, maximum rainfall rate, rainfall rate distribution) and to relate these to storm intensity (Adler and Rodgers, 1977). To more thoroughly examine this relationship and to see whether there also exists a relationship between ESMR-5 derived tropical cyclone rainfall characteristics and storm motion, an empirical analysis method developed by the ADAPT Corporation was used to relate the ESMR-5 derived tropical cyclone rainfall characteristics to both storm intensity and movement.

ADAPT APPROACH

The general concept of the ADAPT approach is to take the data from the original high dimensional data space and transform it to a lower dimensional optimal analysis space. This is accomplished by applying a conventional transformation (i.e. Karhunen-Loeve, Eigenvector, or Principal Component) on a large number of data vectors such as those found from satellite imagery (Andrews, 1972 and Watanabe, 1965). Algorithms are then developed in the lower dimensional optimal analysis space by using an independent eigen screening technique. This technique is related to classical screening regression but differs in that the screening is performed in eigen vector space where the orthogonality eliminates all the redundancy problems

associated with classical screening. The screening decision is based on an independent test (Lachenbrach and Mickey, 1968). The algorithms were developed using ESMR-5 data and the nine non-satellite derived discriptors (described in the data sampling section). The algorithms that were developed using both the satellite and non-satellite data used the non-satellite data in two ways. The first way was to use the non-satellite discriptors to bias the transformation to the optimal space so that the ESMR-5 values in the first terms of the transformation carried the same information as the non-satellite discriptors. The second way was to use the non-satellite discriptors to append the non-satellite data to the end of the ESMR-5 derived radiation values. Analysis of the derived algorithms showed that the biased ESMR-5 values were the most efficient in carrying all the information (information derived from both satellite and non-satellite variables) for these algorithms.

Since the transformation is orthogonal, the results of the algorithm can be transformed back to the original data space (i.e. the satellite imagery). Thus, the relative importance of each data vector as obtained from the satellite image will be known. In the case of the ESMR-5 observations of tropical cyclones, the transformation will tell which regions of the storms are most important for forecasting storm intensity and motion.

DATA SAMPLING

To obtain independent data, a grid consisting of a rectangular array (13° latitude x 10° longitude) of 267 points was used to extract data vectors from a "Bull's Eye" projection (Shenk et al., 1971) of the ESMR-5 brightness temperatures (T_B). The storm center was located approximately in the middle of the grid. Spacing between the inner grid points are .63° latitude and 1.25° latitude for the outer grid points. In addition to the ESMR-5 measurements there are nine non-satellite derived discriptors used for independent data. They are:

1. Day of the year.
2. Observation time.
3. Latitude of storm at the time of observation.
4. Longitude of the storm at the time of observation.
5. Maximum winds at the observation time.
6. Latitude change of storm in 12 hours.
7. Longitude change of storm in 12 hours.
8. 12 hour change in maximum winds ending at the observation time.
9. Time difference between time of observation and satellite pass.

These nine non-satellite variables were explicitly selected to be used in conjunction with satellite data.

The dependent data consist of the 12, 24, 48, and 72 hour change in maximum winds and movement that were obtained by extrapolating the 12 hour best track information for each interval. Best track data was the only objective data available for these cases.

FORECAST ALGORITHMS

Regression algorithms were developed to forecast 12, 24, 48, and 72 hour tropical cyclone maximum winds and latitude and longitude displacement using the two data combinations. The results of independently testing these algorithms are shown in Tables 1 and 2. These tables summarize the performance of the algorithms by comparing the mean error made by persistence forecast calculated from best track and the Joint Typhoon Warning Center (JTWC) operational forecast (not based on best track) with the mean error made by the algorithms. The JTWC forecast were not for the same storms used in this study but were for the same period.

Table 1
Performance of Wind Speed Forecast Algorithms

Algorithm	Persistence	JTWC	Satellite Alone	Satellite plus Conventional
Max Wind Forecast	Kts	Kts	Kts	Kts
12 hr	6.8	9.2	15.1	6.1
24 hr	20.0	14.0	15.1	10.3
48 hr	39.0	19.0	18.3	13.0
72 hr	55.0	23.0	19.2	16.6

Table 2
Performance of Position Forecast Algorithms

Algorithm	Persistence	Satellite Alone	Satellite plus Conventional
Latitude Forecast	NM	NM	NM
24 hr	57.0	65.4	53.1
48 hr	132.0	132.0	110.0
72 hr	220.0	183.0	168.0
Longitude Forecast	NM	NM	NM
24 hr	63.0	86.8	56.5
48 hr	157.0	190.0	142.0
72 hr	275.0	279.0	220.0

Columns 1 through 5 in Table 1 respectively delineate the algorithm, mean errors made by persistence, JTWC, the satellite alone, and the combination of satellite plus non-satellite data. The format in Table 2 is the same except that there is no information on the JTWC forecast. The persistence forecast for the longer time periods are too large since the best track data for the past 12 hours were used to determine these forecast.

ANALYSIS OF ALGORITHMS

Examination of the tables reveal that the performance of the wind speed algorithms are showing the greatest improvement. This is not surprising since ESMR-5 is measuring latent heat release in a tropical cyclone (an index of storm intensity) and that current and 12 hour maximum wind speeds are part of the non-satellite data. A significant result apparent from examining these tables is that the satellite derived algorithms out performed the persistence maximum wind forecast for 24, 48, and 72 hours as well as the JTWC operational maximum wind forecast for 48 and 72

hours. In addition, by adding the non-satellite derived discriptors, which are easily obtainable for most storms, the performance is substantially greater for all algorithms. Even better performance should be realized for these satellite algorithms if more ESMR-5 observations of tropical cyclones were available. Similar results were found by Gentry et al. (1978) when the results from their 24 hour tropical cyclone maximum wind regression equations were compared with persistence. The regression equations were developed to forecast tropical cyclone 24 hour maximum wind speeds utilizing satellite measured infrared equivalent blackbody temperature of the storm (an index of LHR) alone and together with the changes in maximum winds during the preceding 24 hours and the current maximum winds (both obtained from best track).

An important ADAPT output for understanding the physics behind an algorithm is the relative importance map obtained by transforming the algorithm from the lower dimensional space back to the original data space. Figure 1 is such a plot. On this figure, the 19 x 19 array represents the grid that was used to sample the ESMR T_B (center of the storm represented by a box with an X inside). The higher the number the greater the importance for each data space variable (Blank is least

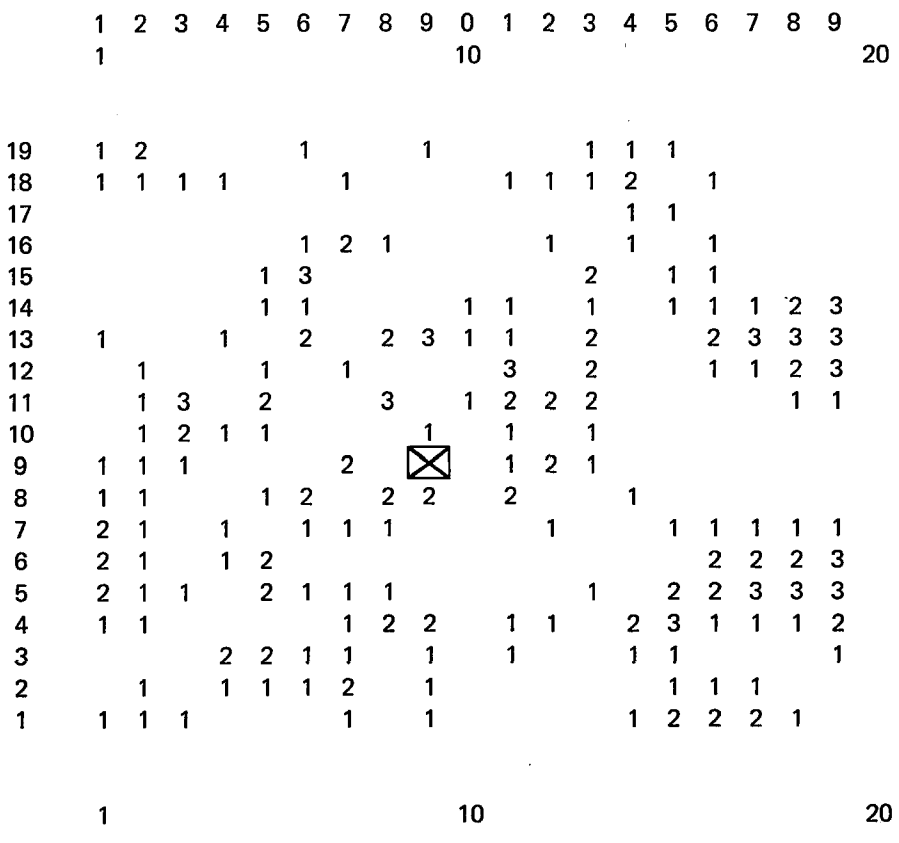

Fig. 1—The importance of the 267 data space variables to estimate the 24 hour maximum winds.

important). The cluster of the larger values in the grid indicates that the importance of these areas of the storm in estimating 24 hour wind speed are probably related to the configuration and intensity of the rain bands around the center. There appears to be more information (greater number of 2's and 3's) east of the center.

SUMMARY

The application of the ADAPT representation and the independent screening regression technique to derive tropical cyclone intensity and movement forecast algorithms have shown encouraging results towards improving the accuracy of wind forecast relative to persistence and the JTWC operational forecast and long term position forecasts relative to persistence. With an increase in the number ESMR observations of tropical cyclones, a further improvement in the performance of these forecast algorithms would be expected.

REFERENCES

Adler, R. F., and E. B. Rodgers, 1977: Satellite Observed Latent Heat Release in a Tropical Cyclone, Mon. Wea. Rev. 105, pp 956-963.

Andrews, H. C., 1972: Introduction to Mathematical Techniques in Pattern Recognition, John Wiley & Sons, Inc.

Gentry, R. C., E. Rodgers, J. Steranka, and W. E. Shenk, 1978: Predicting Tropical Cyclone Intensity Using Satellite Measured Equivalent Blackbody Temperatures of Cloud Tops, NASA TM-79645, pp 34.

Lachenbrach, P. A., and M. R. Mickey, 1968: Estimation of Error Rates in Discriminate Analysis, Technometrics Vol. 10, pp 11.

Shenk, W. E., H. Powell, V. V. Salomonson, and W. B. Bandeen, 1971: Meteorological Uses of the Stereographic Map Projection, J. Appl. Meteor, 10, 582-589.

Watanabe, S., 1965: Karhunen-Loeve Expansion and Factor Analysis Theoretical Remarks and Predictions, Transaction of the 4th Prague Conference, 635-660.

Page intentionally left blank

Paper No. 18

A STATISTICAL TECHNIQUE FOR DETERMINING RAINFALL OVER LAND EMPLOYING NIMBUS-6 ESMR MEASUREMENTS

E. Rodgers, *Goddard Space Flight Center,* H. Siddalingaiah, *Computer Sciences Corporation, Silver Spring, Maryland 20910,* A. T. C. Chang and T. Wilheit, *Goddard Space Flight Center, Greenbelt, Maryland.*

ABSTRACT

An empirical method has been employed to deliniate synoptic scale rainfall over land utilizing Nimbus-6 ESMR measurements.

INTRODUCTION

Savage et al. (1976) demonstrated theoretically that at 37.0GHz, the frequency at which the Nimbus-6 ESMR (ESMR-6) sensor measures upwelling radiance, the scattering by hydrometeors is strong enough to render a qualitative interpretation of rain over land. Furthermore, Weinman and Guetter (1977) demonstrated from theoretical considerations that the upwelling radiation at 37.0GHz emerging from hydrometeors is essentially unpolarized. This in contrast to wet land surface whose reduced emissivity (due to surface moisture) becomes highly polarized when viewed obliquely. Thus, it is reasonable to conclude from these theoretical considerations that rain over dry land surfaces can be at least qualitatively monitored employing 37.0GHz radiometer measurements from ESMR-6.

It is the purpose of this study to substantiate the above conclusions and to arrive at an algorithm which detects rain over land by statistically analyzing ESMR-6 data. This statistical analysis will be performed by first sampling three categories of ESMR-6 brightness temperatures (T_B's) (representing rain over land, wet land surfaces without rain, and dry land surfaces), then testing these populations for uniqueness, and finally developing a classification algorithm to delineate rain over land.

THE ESMR-6 SYSTEM

The ESMR-6 system flown aboard Nimbus-6 (Wilheit, 1975) receives the thermal radiation upwelling from the earth's surface and atmosphere in a 250MHz band centered at 37.0GHz. The antenna beam scans electrically in 71 steps an arc of 70° ahead of the spacecraft along a conical surface with a constant incidence angle of 50° to the earth's surface every 5.3 seconds with a nominal resolution of 20km crosstrack and 45km down track. The instrument measures both horizontal and vertical polarization components by using two separate radiometric channels. The data are calibrated using warm (instrument ambient) and cold (cosmic background) inputs to the radiometer. The T_B as observed from the satellite are dependent upon the emission from the earth's surface modified by the intervening

atmosphere. The emissivity, being a function of the dielectric constant, is variable over land surfaces (depending on vegetation, surface roughness, and soil moisture) and generally large (ca,.9). In a raining atmosphere, three constituents contribute to the absorption: molecular oxygen, water vapor, and liquid droplets. Water droplets are the only source of scattering at this frequency. Ice crystals are essentially transparent.

DATA SAMPLING

In order to develop an algorithm which classifies a given ESMR-6 instantaneous field of view (IFOV) as rain over land, dry land surface, or wet land surface, simultaneous ground stations and radar measurements of rain and ESMR-6 T_B were needed. Eight daytime synoptic scale rainfall cases over the Southeastern United States were used where surface rain rate data taken from stations reporting hourly rainfall amounts and from the WSR-57 radar coincided with the Nimbus-6 overpass to within 5 minutes. The surface temperature in each of these cases was not less than 5°C. Rain areas were sampled within areas delineated as rain by the WSR-57 radar (rain rates $\geq$ 2.5 mm hr^{-1}) and/or the station reporting hourly rainfall amounts. Wet land surfaces were sampled in areas where rain had fallen within 3 hours and upstream and adjacent to the raincells observed on the WSR-57 radar. Dry land surfaces were sampled over areas where rain had not fallen within a 24 hr. period previous to the Nimbus-6 pass.

STATISTICAL ANALYSIS

Figure 1 presents the scatter plot of the sampled data. The C's represent the mean points of the populations. Each of the frequency concentration ellipses encompasses 68 percent (one standard deviation) of the data from the respective populations. These ellipses reveal the extent of scattering of the data from each population, the correlation between the variables T_H and T_V in each population (the higher the correlation the larger the eccentricity of the ellipse), and the extent of overlap among the populations. It can be seen that the largest overlap is between the populations representing rain areas and wet land surfaces. This ambiguity may be attributed to the fact that an ESMR-6 IFOV (pixel) partially filled with moderate to heavy rain or completely filled with very light rain is influenced by the wet surface background and consequently produces a signature somewhat similar to that of wet land surfaces.

The three concurrent lines drawn in this figure are the Fisher discriminant lines. These lines separate two-by-two the ensemble of points representing rain over land, dry land surfaces, and wet land surfaces.

Table 1 shows the elementary statistics of the sampled data. It can be seen from Figure 1 and Table 1, that the T_B representing rain over land are colder than those representing dry land surfaces. However, this will not always be the case. Since the surface emission is given by ϵT_s (ϵ is the surface emissivity and T_s is the surface thermodynamic temperature), there is an influence of T_s on ESMR-6 measured dry land surface T_B. A decrease in T_s results in a decreased ESMR-6 T_B of dry land surfaces and consequently in the reduced T_B contrast between dry land surfaces and rain over land.

It can also be seen from this table that the difference in the means of the horizontal and vertical polarized T_B (6.5°K) representing rain over land is much smaller when compared to the corresponding mean difference (16.1°K) representing wet land surfaces. This in accordance with the theoretical findings that hydrometeors are not polarized (Weinman and Guetter, 1977) whereas wet land surfaces are highly polarized.

Table 1
Rain Over Land

	Rain Area		Dry Ground		Wet Soil	
Sample Size: N	216		189		66	
	T_{HR}	T_{VR}	T_{HD}	T_{VD}	T_{HW}	T_{VW}
Mean: μ	254.53	260.98	271.46	278.18	252.05	268.86
Standard Deviation: d	7.21	5.81	6.18	7.2	9.41	7.64
Sample Correlation Coefficient Between T_H And T_V: ρ	0.55		0.37		0.82	

Prior to employing these data for the development of classification algorithms, an examination was made to verify whether the three populations were statistically distinguishable from one another. To accomplish this, tests were carried out first to determine the significance of the differences between the means of any two classes and second to estimate the simultaneous confidence intervals for the differences of the means of any two populations. It was found that the differences between the means of any two classes were highly significant and that the probability that the mean vectors of any two populations coincide was less than 1 in 100. The simultaneous confidence intervals computed according to Scheffe's procedure showed that none of the intervals contained zero except the one for the differences between the means of horizontal polarized T_B's for wet land surfaces and rain over land. However, the three populations are distinguishable from one another when the dual polarization information is taken into account simultaneously. It should be noted that the lower bounds for the differences of the means of the T_B's for rain over land and wet land surfaces are very small when compared to those of the other two pairs of the populations. Hence, it will be more difficult to detect rainfall over land from wet land surfaces. Since the populations were found to be statistically distinguishable and satisfied the Gaussian frequency distribution, the Bayesian pattern recognition technique was employed to develop a classification algorithm to detect and delineate active rainfall areas from wet and dry land surfaces. (Rodgers, et al., 1978.)

ERROR ANALYSIS

An error estimate was made in order to evaluate the performance of the classification algorithm. The error rates were computed according to the asymptotic formulas given by Okamoto (1963). The results are seen in Table 2 which shows that the chances of incorrectly classifying wet or dry land surfaces as rain over land is nearly 23 percent. But when a given ESMR-6 pixel is classified as rain over land and each of the eight contiguous pixels clustered around it is also classified as rainfall over land, then the chance of misclassification of that central pixel is reduced to 7.7×10^{-6} percent assuming each pixel is independently classified. Table 3 displays the actual probabilities that the classification algorithm classifies the sampled data into various populations as indicated. The average accuracy is computed by taking the mean of the diagonal elements of the corresponding error matrices. The apparent average accuracy compares well with the estimated average.

Table 2
Probabilities of Misclassification: Theoretical Computation

Known \ Classified	Rain	Dry	Wet
Rain	77.15	6.66	16.19
Dry	6.67	82.08	11.25
Wet	16.28	11.29	72.43

Average Accuracy: 77.22 Percent

Table 3
Bayesian Classification Error Matrix

Known \ Classified	Rain	Dry	Wet
Rain	89.35	6.02	4.63
Dry	7.41	91.53	1.06
Wet	27.27	15.15	57.58

Average Accuracy: 79.49 Percent

ALGORITHM EVALUATION

A case not previously used was tested to verify qualitatively the performance of the Bayesian Classification algorithm. This case consisted of a synoptic scale rain pattern over the Southeastern United States (14 September, 1976) which was observed by the ESMR-6 sensor (surface thermodynamic temperature $\geqslant 15°C$). Rainfall as delineated by the WSR-57 radar and stations reporting hourly rainfall amounts is seen in Figure 2. The approximate time of the radar PPI images was 1630 GMT (within 5 minutes of the Nimbus-6 pass). The reporting times of the stations reporting rain amounts were 1500, 1600, and 1700 GMT. The shaded areas within the WSR-57 radar PPI range (46 km) are rain rates greater than 2.5 mm hr^{-1}. The radars were located at Waycross and Macon, Georgia; Charleston, South Carolina; and Wilmington and Cape Hatteras, North Carolina. Surface station data were taken at 1800 GMT. Dots, together with the hourly amounts of rain (see model in figure) if any, denote hourly rainfall reporting stations.

The Bayesian classification map is seen in Figure 3. Areas of clouds delineated by the Nimbus-6 Temperature Humidity Infrared Radiometer (THIR) 11.5 μm channel (equivalent blackbody temperatures (T_{BB}) $\leqslant 270°K$) are shown on the map. Rain areas in the absence of clouds or in areas of low clouds are misclassifications. Only regions covered by clusters of contiguous pixels classified into a single individual class are shown, since the probability of misclassifying clusters is much less than that of a single pixel.

A comparison of Figure 2 with Figure 3 shows good agreement between areal distribution of ESMR-6 derived rain over land and observed rain (no attempt was made to verify wet surfaces areas). However, the classified area of rainfall over North Carolina and Southwestern Georgia is contrary to ground observations. The

rainfall indicated by ESMR-6 over North Carolina may be suspended liquid water in the clouds ahead of the rain area (the area of rain was moving NE towards North Carolina). On the other hand, the ESMR-6 delineated rain over Southwestern Georgia, which was upstream from the rain area, may be due to wet land surfaces produced by the rain that fell a few hours prior to the Nimbus-6 pass.

The Bayesian classification algorithm was applied to another case (1645 GMT August 27,1976, surface thermodynamic temperatures $\geqslant 15°C$) over the same geographical area as the previous case in order to determine whether the surface characteristics (vegetation, soil moisture, and surface roughness) had influenced the classification algorithm performance in the previous case. During this period, the area in question was under the influence of a Bermuda high and there was only convective rainfall in the area, particularly along the Gulf States. Results showed that the only areas classified as rain over land were along the Gulf Coast. The regions in the previous case where the algorithm showed rainfall were classified as dry land surfaces. Hence, there was no influence of extraneous surface characteristics on the outcome of the previous case study.

However, contradicting results occurred when the Bayesian classification algorithm was applied to a night time Nimbus-6 pass over the same geographical area (0525 GMT, September 13, 1976, surface thermodynamic temperature $\geqslant 15°C$) where there was no synoptic scale rainfall reported. Almost all pixels were classified by the algorithm as rain over land. Examining the ESMR-6 T_B showed that the temperatures were below 0°C. This anomaly may be attributed to the change in the surface emissivity caused by the presence of dew on the vegetation. Therefore, the pattern classification algorithm trained by data sampled from Nimbus-6 daytime passes can be employed only when dew is absent.

CONCLUSIONS

Statistical analyses were performed on the sampled ESMR-6 data for the purpose of detecting rainfall areas over land from dry and wet land surfaces. It was found from these studies that synoptic scale rainfall over land, where surface thermodynamic temperatures were greater than 5°C and the vegetation was bereft of dew, could indeed be delineated despite the large ESMR-6 IFOV. However, there was some ambiguity in distinguishing between rainfall areas and wet land surfaces.

REFERENCES

Duda, R. O. and P. E. Hart, 1973: Pattern Classification and Seen Analysis, pp. 10-36, John Wiley and Sons, New York, NY.

Okamoto, M., 1973: An Asymptotic Expansion of the Distribution of the Linear Discriminant Function. Ann. Math. Statist., 34, 1286-1301.

Rodgers, E. B., H. Siddalingaiah, A. T. C. Chang, and T. Wilheit, 1978: A Statistical Technique for Determining Rainfall Over Land Employing Nimbus-6 ESMR Measurements, NASA TM 79631, pp. 33.

Savage, R. C., P. J. Guetter, and J. A. Weinman, 1976: The Observation of Rain Clouds over Land in Nimbus-6 Electrically Scanned Microwave Radiometer (ESMR-6) Data. Preprint Vol. 7th Conf. on Aerospace and Aeronautical Meteorology and Symposium on Remote Sensing from Satellite, 131-136.

Weinman, J. A. and P. J. Guetter, 1977: Determination of Rainfall Distribution from Microwave Radiation Measured by the Nimbus-6 ESMR. J. Appl. Meteor., 16, 437-442.

Wilheit, T. T., 1975: The Electrically Scanning Microwave Radiometer (ESMR) Experiment. Nimbus-6 User's Guide NASA Goddard Space Flight Center, 87-108.

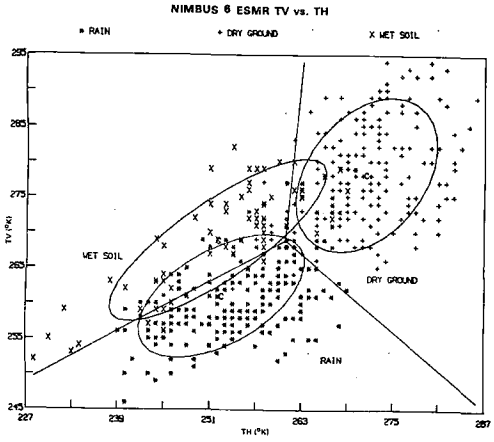

Fig. 1—Vertical polarized vs. horizontal polarized ESMR-6 T_B

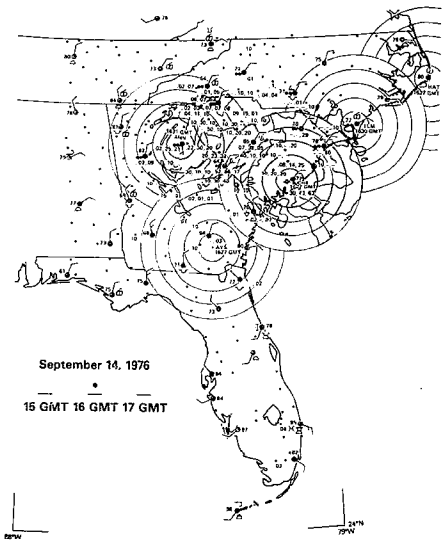

Fig. 2—Rainfall over the Southeast United States is delineated by the WSR-57 radar and hourly rainfall reporting station. Time of data is approximately 1630 GMT September 14, 1976. Shaded areas represent WSR-57 observed rain (rain rates $\geq$ 2.5 mm hr.). Dots represent hourly rainfall reporting stations.

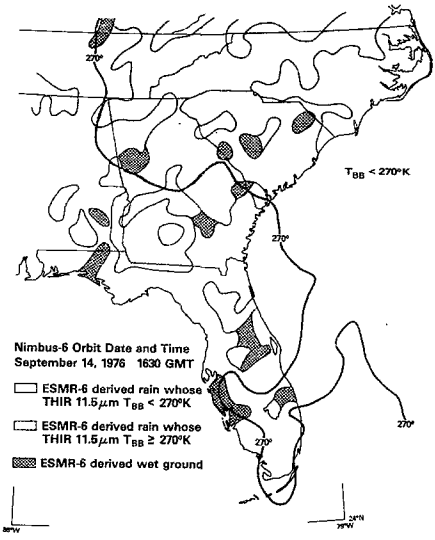

Fig. 3—ESMR-6 derived rainfall distribution using the Bayesian classifier. Dark curve depicts equivalent blackbody temperatures (T_{BB}) of 270°K as measured by the Nimbus-6 THIR 11.5 channel. Areas that have $T_{BB} \leq 270$°K represent cloud cover. Time of Nimbus-6 pass 1630 GMT September 14, 1976.

Paper No. 19

MIE DISDROMETER FOR IN SITU MEASUREMENT OF DROP SIZE DISTRIBUTIONS

H. G. Loos, *Laguna Research Laboratory, Laguna Beach, California*

ABSTRACT

Test results are shown for a disdrometer breadboard which uses Mie scattering and incoherent optical correlation for in situ measurement of drop size distributions in a cloud chamber.

INTRODUCTION

Certain expansion cloud chamber experiments planned for the Atmospheric Cloud Physics Laboratory (ACPL) payload for Spacelab III require in situ measurement of drop size distributions inside the chamber. With joint ONR-NASA MSFC support, an instrument has been breadboarded and tested which may provide the drop size distribution measurement capability required for the ACPL, as well as for other settings.

The instrument processes in parallel fashion the light scattered by all drops in a sizeable portion of the illuminating collimated light beam, and utilizes the details of the scattered light intensity versus scattering angle in a technique which combines incoherent optical correlation by means of spatial filters with digital data processing. Besides providing a proof of concept, the breadboard was built and tested in order to obtain experimental information about certain noise features of the instrument, so that these could be compared with theoretical results in an effort to check our understanding of the signal to noise degradation suffered inthe data reduction process. Such understanding is indispensable for successful design of a practical instrument of this type.

The statistical noise measurements require that repeated measurements be made on the same cloud. Therefore, we chose as test object a cloud of latex spheres, which are small enough so that gravitational settling does not present a problem. Repeated measurements were made on monodispersed as well as polydispersed clouds, using latex spheres of .30, .36, .40, .55, and 1.01 micrometers radius.

Description of the instrument breadboard

A two-color collimated light beam is used to illuminate part of the cloud in the chamber. Light scattered by the cloud drops in a certain range of angles passes through a chamber

window and is processed by the detector which is mounted outside the chamber. The detector consists of a wide-angle 35mm camera lens, in the focal plane of which there is a color transparency which acts as a spatial filter; the light which passes through the color slide falls on a photomultiplier tube. The PMT signal is measured with a number of different filters in place; in the present breadboard, 11 filters are arranged on a disc which can be turned by a stepper motor. The 12th "filter" is opague and serves to measure the dc offset to be subtracted. Each of the filters is a color slide with green and red transmittances which vary with location on the slide. The PMT signal is proportional to the sum of the correlations, in the green and in the red, of the light intensity function incident on the filter, and the filter transmittance function. Hence, in the linear regime of the PMT, the subtracted PMT outputs are linear functionals of the drop size distribution. If the drop size distribution is a linear combination of at most 11 basis functions, the drop size distribution can be calculated by executing a fixed linear transformation on the 11- dimensional subtracted PMT output vector, and by using the resulting numbers as coefficients in a linear combination of basis distribution functions. This data reduction is done digitally. Near shot-noise limited operation is obtained by following each measurement (for each filter) by a calibration, using an LED. This makes it possible to eliminate the effects of all gain drifts in the system, except for the drift due to temperature change of the differential spectral quantum efficiency of the PMT photocathode. The breadboard is completely controlled by an HP 9825A desc calculator, and data acquisition is done by an HP 3437A system voltmeter which interfaces with the HP 9825A. The scattering angle ranges from 20 to 80 degrees. The 11 filters used in the breadboard are rather crude and are far from optimal; consequently, the signal to noise ratio degradation in the data reduction is much larger than need be. A process to produce better filters is under development. For simplicity, we used as basis functions the very sharply peaked size distributions of Dow-Chemical latex spheres of radii .30, .36, .40, .55, and 1.01 microns. The background scattering in the chamber is considered as a separate scattering object, whose intensity is allocated a separate axis in size space.

Noise considerations

Let $\vec{n}$ be the vector whose components are the expansion coefficients of the drop size distribution in terms of the basis size distribution functions; $\vec{n}$ is here called a size vector and the space spanned by the size vectors is called the size space. Let $\vec{s}$ be the vector whose components are the (dc offset-subtracted) PMT outputs with the different filters in place. For linear PMT operation and incoherent superposition of the light scattered by the different drops one has

$$\vec{s} = M \vec{n}, \qquad (1)$$

where M is a linear transformation, represented by a matrix. M is here called the Mie mapping or the forward mapping. If M is not singular, there exists an inverse mapping

$$\vec{n}=C\vec{s}, \tag{2}$$

such that either $\vec{n}$ of (2) is a solution of (1) or else the forward map (1) applied to $\vec{n}$ of (2) gives a result $\vec{s}$ which differs minimally from the measured data vector. These cases occur respectively if the data space dimension is equal to or larger than the size space dimension."Minimal difference" is meant here as minimal Euclidean norm of the difference vector, and is equivalent to a least squares fit. The matrix C is determined once and for all, and is stored in the instrument microcomputer (here, the HP9825A). The measured data vector has a noise part $\Delta\vec{s}$, which through (2) gives rise to a noise part

$$\Delta\vec{n}=C\Delta\vec{s} \tag{3}$$

in the size vector.The ratio

$$\beta\equiv\frac{|\Delta\vec{n}|/|\vec{n}|}{|\Delta\vec{s}|/|\vec{s}|}=\frac{|C\Delta\vec{s}|}{|\Delta\vec{s}|}\cdot\frac{|\vec{s}|}{|C\vec{s}|} \tag{4}$$

depends on the directions of $\Delta\vec{s}$ and $\vec{s}.\vec{s}$ lies in the image of the non-negative cone in size space, whereas the direction of $\Delta\vec{s}$ is unrestricted. In practice, we are interested in some appropriate average$\langle\beta\rangle$, which expresses the degradation of signal to noise ratio suffered in the data reduction (2). For $\Delta\vec{s}$ in the direction of $\vec{s}$, one has $\beta=1$; the associated $\Delta\vec{n}$ is in the direction of $\vec{n}$ and therefore causes an apparent fluctuation in cloud density. $\Delta\vec{s}$ perpendicular to $\vec{s}$ causes a vector $\Delta\vec{n}$ with components $\Delta\vec{n}_{\parallel}$ and $\Delta\vec{n}_{\perp}$, respectively in the direction of $\vec{n}$ and perpendicular to $\vec{n}$. $\Delta\vec{n}_{\perp}$ causes a change in the direction of $\vec{n}$, resulting in an apparent fluctuation of the normalized measured size distribution. In practice, the "angle noise" $|\Delta\vec{n}_{\perp}|/|\vec{n}|$ of the size vectors sets the instrument resolution. There is angle noise $|\Delta\vec{s}_{\perp}|/|\vec{s}|$ in data space as well, and the ratio

$$\gamma=\frac{\langle|\Delta\vec{n}_{\perp}|/|\vec{n}|\rangle}{\langle|\Delta\vec{s}_{\perp}|/|\vec{s}|\rangle} \tag{5}$$

of average angle noises in size space and data space is a useful expression for the degradation due to data reduction.

There are contributions to $\Delta\vec{s}$ from "counting"errors in the sensitive experimental volume (SEV), from nonuniformities of the drop densities in the SEV, from quantum effects in the scattering, from PMT shot noise, from changes in the quantum efficiency of the PMT photocathode, and from post-detection noise. For the better runs the measurement turns out to be nearly PMT-shot-noise limited . For shot noise, the standard deviation of the vector component $(\Delta\vec{s})_j$ is proportional to $\sqrt{s_j}$, and therefore, the surfaces of constant noise probability in data space are hyperellipsoids with an aspect ratio and an orientation which depends on the data vector $\vec{s}$. In the noise calculation, a conservative simplification was made, in which these shot noise ellipsoids are replaced by spheres with a radius equal to the rms value of the shot noise vector components. For an ensemble of normalized noise vectors $\Delta\vec{s}$ with uniformly random directions, β of (4) was calculated, together with

the maximum value of β, the directions $\Delta\vec{s}$ and $\vec{s}$ for the maximum, and the ratio of rms values

$$\langle\beta\rangle = \frac{\text{rms} \mid C\Delta\vec{s}\mid / \mid\Delta\vec{s}\mid}{\text{rms} \mid C\vec{s}\mid / \mid\vec{s}\mid} \quad , \qquad (6)$$

where $\vec{s}$ is determined from (1) and $\vec{n}$ runs over an ensemble of normalized vectors with non-negative components but otherwise uniformly random directions. The degradation $\langle\beta\rangle$ of (6) depends on the range of scattering angles seen by the detector, the basis size distribution functions, the number of instrument channels, and the filter transmittance functions. Choosing these items in such a manner that the degradation $\langle\beta\rangle$ has an acceptable value is one of the main concerns in the instrument design.

Measurements

We measured 33 clouds consisting of latex spheres of .30, .36, .40, .55, and 1.01 microns radius, with either a single particle size or mixtures. For each cloud, 20 complete measurements were made (a full revolution of the filter wheel constitutes one complete measurement). Concentrations ranged from about 30 to several hundred particles per cm^3. For each ensemble of 20 measurements the ratio of noise to shot noise, the average data vector, and the rms angle noise in the data vector were calculated. For each data vector the corresponding size vector was calculated, using an inverse mapping computed from the forward mapping obtained from the ensemble average of measured forward mappings; from these results, the average size vector for the ensemble and the rms angle noise of the size vector was obtained. From the rms angle noises the degradation γ of (5) was calculated. Also, to provide further insight into the mapping M, the angles between data vectors in a few data subspaces were calculated for several monodispersed clouds.

Results

19 to 25 of the 33 runs had a ratio of noise to shot noise below 2, depending on the choice of basis and data subspace. Poor runs resulted from large powerline fluctuations which sometime plague our laboratory.

The rms angle noise in the data vector and in the size vector, as well as the ratio of these two angle noises has been calculated from the data for the forward mapping M, for two choices A and B of basis and data subspace. Choice A has been made to investigate the instrument resolution at the small particle end; we use as basis for the mapping M the background, and monodispersed clouds with spheres of .30, .36, and .40 microns radii, together with a 5-dimensional data subspace. In choice B, the .36 micron particle is dropped in favor of two particles of .55 and 1.01 micron radius, and a 6-dimensional data subspace is used. Table I shows the rms value $\langle\gamma\rangle$ of the ratio γ of rms angle noise of size vector and data vector, for the collection of all runs, including the bad runs with noise / shot noise ≥ 2, for the choices

A and B, together with the theoretical results for the maximum value of β, and the average value $\langle\beta\rangle$ of (6), calculated from an ensemble of random vectors in the manner discussed above.

measured:	choice A	choice B
$\langle\gamma\rangle$	5.1	10.9
standard deviation in γ	2.1	8.1
theoretical:		
β_{max}	19.7	100.0
$\langle\beta\rangle$	8.7	43.0

Table I

Comparison of measured and theoretical results for the degradation suffered in the data reduction process.

It is seen that, as expected, the calculated degradation $\langle\beta\rangle$ is conservative for both choices A and B, but much more so for B. The theoretical overestimation of the degradation is due to the simplification discussed above, in which the shot noise ellipsoids in data space are replaced by spheres. The very large overestimation of the degradation in case B suggests that for the design of a practical shot-noise-limited instrument with an appreciable number of channels the noise analysis should be refined to take into account the ellipsoidal shape of the surfaces of constant probability in data space.

For monodispersed clouds, the instrument capability to recognize clouds of single-size particles among the radii of .30, .40, .55, and 1.01 microns may be expressed in terms of the total electric energy W supplied to the illuminating lamp during the measurement, and the visible range R of the cloud. From the data it follows that correct identification of a .40 micron particle cloud with a confidence level of 99.7 % requires

$$W/R \geq 1.0 \times 10^{-3} \text{ Joules/Meter.} \qquad (7)$$

Instrument resolution for polydispersed clouds may be expressed in terms of W, R, and the rms angle noise $\Delta\phi$ in size space. From the data we find for a polydispersed cloud consisting of particles of radii .30, .36, and .40 microns

$$\Delta\phi = A\sqrt{R/W} \quad \text{degrees,} \qquad (8)$$

where A=.46 for the worst run, and A= 8.5×10^{-2} for the best run. In (8), W is the electric energy to the lamp in Joules, and R is the visible range in Meters. The results (7) and (8) hold as long as measurements are shot-noise-limited, and for serial operation. For parallel operation, the right hand sides must be divided by the number of instrument channels.

Page intentionally left blank

Paper No. 20

ADVANTAGES OF ICE CRYSTAL GROWTH EXPERIMENTS IN A LOW GRAVITY ENVIRONMENT

B. J. Anderson and V. W. Keller, *MSFC, AL;* J. Hallett, *DRI, Reno, NV*

ABSTRACT

The effects of convective fluid motions and mechanical supports on ice crystal growth in experiments conducted on earth can be inferred from studies conducted in their absence in a low-gravity environment. Current experimental results indicate the effects may be significant.

INTRODUCTION

Discussions on studies of crystal growth in low-gravity usually emphasize the absence of two variables in such an environment, convective fluid motions and a support for the growing crystal. Theoretical estimates of the magnitudes of these effects are difficult to obtain, primarily because of the primitive state of our knowledge of crystal growth mechanisms. However, the experimental results reported here and by other workers shed some light on the problem.

Convective Fluid Motion

Most experiments designed to study the effect of convective fluid motion on ice crystals growing from the vapor are conducted in a cold chamber in which a cloud of supercooled water droplets is artifically "seeded" to produce ice crystals which then grow and fall out of the cloud. As the crystals grow, they deplete the vapor supply and thus lower the ambient supersaturation. To maintain a constant ambient environment near water saturation, droplets must be added to the cloud. The simultaneous presence of droplets and ice crystals makes the "effective" supersaturation near the crystals difficult to determine and even more difficult to control. Although these studies may closely simulate the crystal growth conditions encountered in a natural cloud, they do not allow close observation of the growing crystals, long growth times (maximum of about 200 seconds), constant environmental growth conditions, or separation of the effects on crystal growth of droplets and ventilation velocity.

Recent studies were conducted in a dynamic thermal diffusion chamber to investigate the effect of ventilation on ice crystals grown from the vapor in the absence of water droplets. Partial

results of this work were reported earlier; (Keller and Hallett, 1978) a complete description is in preparation. This experimental chamber employed two horizontal, ice coated, parallel plates, 1.2 m in length and separated by a distance of 2.5 cm. Air was circulated between the plates past ice crystals which nucleated and grew from a 250 micron diameter glass fiber suspened vertically between the two plates. This chamber allowed crystals to be closely observed for extended periods of time and to be grown at selected and well controlled ambient conditions of temperature, supersaturation, and ventilation velocity. However, neither the effect of the mechanical support on the nucleation and initial growth of the crystals nor the effect of natural convection on the subsequent crystal growth was fully known. Using the measurements from a large number of crystals grown in this chamber under a variety of ambient conditions, the composite effect of the ambient conditions of temperature, supersaturation, and ventilation velocity on the linear growth rates of ice crystals was compiled. Figure 1 shows isopleths of the ventilation velocity (cm s^{-1}) for an ambient temperature of -14.5°C.

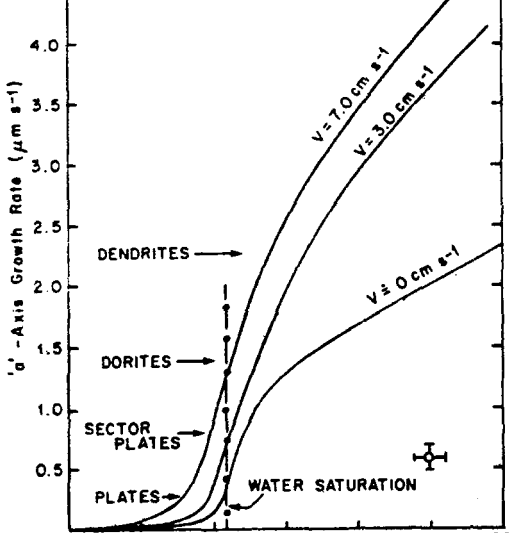

Figure 1. Isopleths of ventilation velocity (cm s^{-1}) for an ambient temperature -14.5°C show the relationship between the 'a'-axis growth rate and the ambient vapor density excess. Water saturation is indicated by a dot-dash line.

The various crystal shape regimes at this temperature are indicated by name. The shape regime boundaries as a function of 'a'-axis growth rate are not sharp, but can vary somewhat from one crystal to the next depending upon the crystal thickness. The most obvious effect shown by this figure is that the introduction of a ventilation velocity reduces the ambient supersaturation necessary to sustain the same linear growth rate. That is, increasing the ventilation velocity is roughly equivalent to increasing the ambient supersaturation. Other results show that for a fixed ambient temperature and ambient supersaturation, the linear 'a'-axis growth rate is directly proportional to the square root of the ventilation velocity provided that the crystal shape does not change significantly. Furthermore, the crystal shape transitions from plate to dendrite and column to needle occur at a lower ambient supersaturation as the ventilation velocity is increased.

It should be noted that the ventilation velocity specified in Fig. 1 as $v \triangleq 0$ cm s^{-1} actually had a magnitude of a few mm s^{-1} due to the gravity induced natural convection associated with the release of latent heat from the growing crystals. The magnitude of this convection velocity increases with increasing growth rates. The effect of this small convection velocity on the growing crystals can not presently be quantitatively evaluated. When natural convection is greatly reduced, such as in the low gravity environment available on the Spacelab, Atmospheric Cloud Physics Laboratory (ACPL) flights, its effect on earth-based experiments can be inferred. It is anticipated that the effect of greatly reducing the natural convection velocity will be primarily observed on the habit transitions of ice rather than in terms of any substantial decreases in water vapor transfer. These habit transitions occur at -3, -8 and -25°C, where plate-like habit alternates with column-like habit as the temperature falls. Ice at supersaturations normally encountered in the atmosphere has been shown in recent laboratory studies to grow primarily by surface nucleation processes, one or another low index face being favored depending on the temperature. At somewhat lower supersaturations, there is an effect of emergent crystal dislocations on growth, and the laboratory studies strongly suggest that the transition is influenced by quite small local convective velocities. In other words, in the absence of convection, different crystal habits could occur. A knowledge of this transition, coupled with information on the relative mass fluxes, will yield information on surface molecular processes.

Mechanical Supports

The effects of a mechanical support on ice crystals growing from the vapor have also been difficult to ascertain. Most of the information on these effects is deduced indirectly from experiments such as the study of ice crystal growth reported by Schaefer and Cheng, 1968. In that study ice crystals were

nucleated by six different mechanisms, under similar conditions in a supercooled water cloud at -20°C. Sometimes the crystals were nucleated on particulates such as silver iodide, lead iodide, or soil particles, and sometimes by rapid cooling from the injection of dry ice particles, or the expansion that occurs when a plastic bubble of packing material is compressed and "popped." In each case the crystals grew as they fell through the supercooled cloud. The structures of the resulting crystals apparently varied with the nucleating mechanism in a way that persisted to crystal sizes at least as large as 100 microns. Whereas, simple featureless plates were produced by adiabatic expansion and dry ice nucleation, complex and irregular crystals grew on volcanic dust and glacial clay particles.

These results suggest that the strain field produced by the nucleating particle (or by a mechanical support if one were introduced) could have a significant influence on the subsequent crystal growth. An indication of the magnitude of this effect can be obtained from recent studies of the epitaxial growth of ice on AgI and CuS single crystal substrates (Anderson and Hallett, 1979). These ice crystals were grown from the vapor in a precisely controlled temperature and vapor density environment and examined by photography through a microscope with a long working distance objective and vertical white light illumination. Under these circumstances the crystals grow as thin plates, the basal surface of the ice against the exposed basal surface of the substrate crystal. The crystals exhibit "thin film" white light interference patterns so that the thickness of a crystal can be determined from its color. Radial growth along the substrate usually predominates because the substrate forms an efficient heat sink for the growth interface. Frequently, crystals will grow radially only, without any discernible thickening.

Comparison of ice crystal growth on the two substrates, AgI and CuS, at the same environmental conditions, demonstrates the potential influence of a mechanical support. First, non-thickening crystals do not appear at warm temperatures (above -7°C) on either substrate. On CuS they form 10 to 20 percent of the crystal population as the temperature is lowered to -16°C; at and below -20°C the fraction may exceed 30 percent. These numbers are not precise because the flatness of the substrate also plays a role. On AgI, some crystals thicken very slowly at the warmer temperatures, but non-thickening plates do not begin to appear until about -15°C. The percentage of non-thickening crystals then increases rapidly with decreasing temperature and is comparable to the percentage for CuS below -20°C. A comparison of crystal growth rates at -15.2°C for non-thickening crystals on CuS and slowly thickening crystals on AgI shows that ice grows radially three times faster on AgI than on CuS (see Figure 2). This is interesting because examination of the radial growth rate of a non-thickening crystal, on either AgI or CuS, which subsequently begins to thicken shows that the thickening

face adsorbs much of the available vapor and retards the radial growth. It must be noted that the quantitative information gained from these studies applies only to crystals less than 2 microns thick.

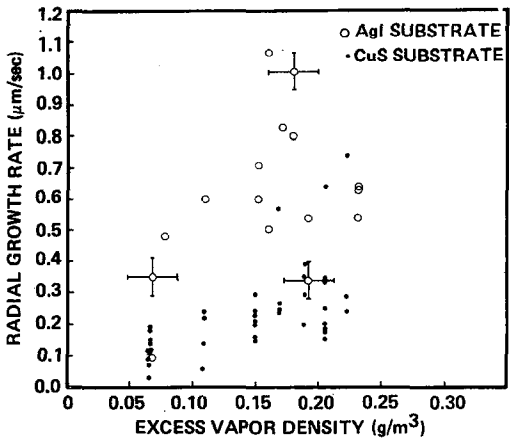

Figure 2. Ice crystal growth rates normal to the prism face on CuS and AgI (T = -15.2 C).

These results imply that the strain introduced into the epitaxially grown ice crystals is larger for CuS than for AgI. A comparison of crystallographic lattice dimensions in the basal plane shows that the lattice mismatch at the crystal-substrate interface is smaller between ice and AgI than between ice and CuS. This mismatch may be the primary source of the strain. Although comparisons such as these of radial growth rates for ice crystals growing epitaxially on different substrates give some assessment of the interface induced crystal strain, a thorough understanding of the effects introduced by a mechanical support on crystal growth must take into account such parameters as heat transfer along the support, trace contamination, asymmetric crystal growth, competition between adjacent crystals, and pertubations to the surrounding vapor and temperature fields.

Discussion

The initial ACPL ice crystal growth experiment is

specifically designed to study the effect of greatly reduced natural convection. The utilization of a support fiber in this initial experiment simplifies the experiment but, more importantly, it allows the results to be more readily interpreted and compared to similar experiments conducted on earth. Later ACPL ice crystal growth experiments will study the combined effect of removing both natural convection and the mechanical support from the experimental system.

References

Anderson, B. J. and J. Hallett, 1979: Influence of environmental saturation and electric field on growth and evaporation of epitaxial ice crystals. Accepted for publication in the Journal of Crystal Growth.

Keller, V. W. and J. Hallett, 1978: The influence of the carrier gas velocity, diffusivity, and thermal conductivity on ice crystal habit. IN: Proceedings of the Conference on Cloud Physics and Atmospheric Electricity, Issaquah, Washington, 109-113.

Schaefer, V. J. and R. J. Cheng, 1968: The effect of the nucleus on ice crystal structure. IN: Proceedings of the International Conference on Cloud Physics, Toronto, Canada, 255 - 259.

Paper No. 21

FUTURE FREEZE FORECASTING

J. F. Bartholic, R. A. Sutherland, *Institute of Food and Agricultural Sciences, University of Florida, Gainesville, Florida*

Florida

ABSTRACT

Real time GOES thermal data acquisition, an energy balance minimum temperature prediction model and a statistical model are incorporated into a minicomputer system. These components make up the operational "Satellite Freeze Forecast System" being used to aid NOAA, NWS forecasters in developing their freeze forecasts. The general concept of the system is presented in this paper. Specific detailed aspects of the system can be found in the references cited.

INTRODUCTION

Better weather information is becoming increasingly important with high energy costs. The computerized "Satellite Freeze Forecast System" is a new forecasting tool which will aid the National Weather Service (NWS) forecasters significantly in providing better freeze forecast information for Florida and ultimately other areas in the United States. The present development activities grew out of research started in 1972. It became clear as the program progressed that remotely sensed aircraft and satellite information was an extremely valuable tool on freeze nights. In January 1976, the first nearly real time use of surface temperature satellite data was undertaken. The many groups involved NASA with financial, technical and personnel support; NOAA personnel from the Environmental Sciences Service Center at Auburn, Alabama; from the National Environmental Satellite Services (NESS); from the NWS in Ruskin, Florida and from the Institute of Food and Agricultural Sciences, University of Florida [Bartholic and Sutherland (1976), Sutherland and Bartholic (1977)]. The results of this intense satellite study on a freeze night showed clearly a potential for developing an operational satellite freeze forecast system. Development of that system officially started in May 1977 when NASA provided equipment and a contract to support development of this system at the University of Florida. The hardware was delivered to Gainesville on 1 July 1977. The system was first tested this past winter at Ruskin with the National Weather Service to aid them in developing their freeze forecasts. An updated version is being used to aid forecasters this winter.

Growers of citrus, vegetables, ornamentals, cattle, and

nearly all home owners in Florida take freeze protection action. Citrus growers alone can burn from 4 to 6 million dollars of fuel in a single, very cold night. Growers can make better decisions and frequently may fire for fewer hours on freeze nights with the improved information and, subsequently, better forecasts provided by this "Satellite Freeze Forecast System" (SFFS).

New Freeze Forecast Methods

The software (programs) used in the system to allow the computer to aid the forecaster will be discussed, then the hourly sequence of events that occur on a cold night as the satellite freeze forecast is developed will be described and finally, how this system will aid forecasters and, consequently, those needing better freeze forecast information will be discussed.

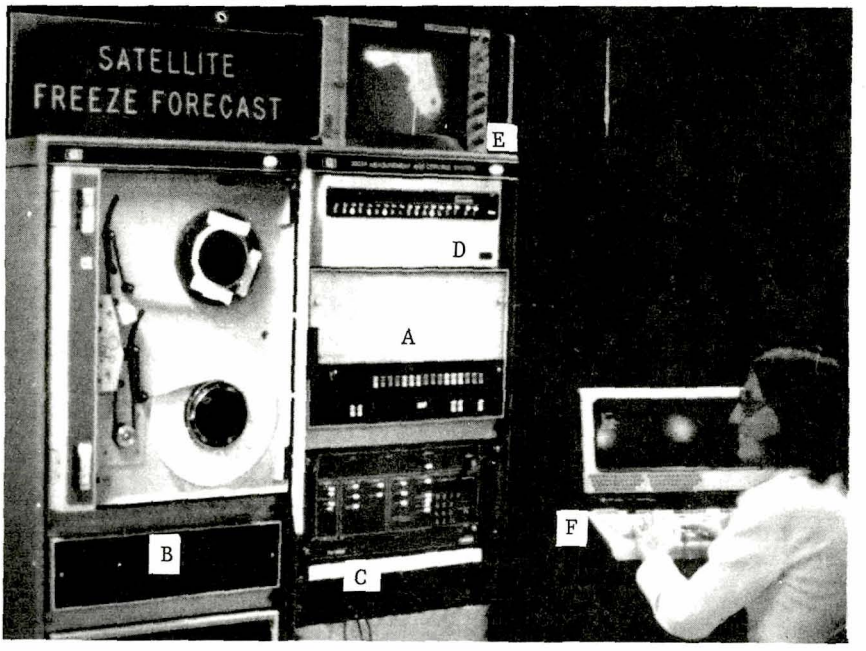

Figure 1. A photograph of the system.

A. the Hewlett-Packard 2100 MX Minicomputer
B. the random access disc storage
C. the electronic equipment that converts the amplitude modulated satellite signal as it comes over the phone lines to a voltage that can be converted by an A to D converter in the computer
D. the modem complex which allows a number of people to call the system and input to receive data over the phone lines
E. the color display which shows satellite derived temperature patterns of Florida in vivid colors
F. the terminal that allows the forecaster to interact with the system: (Jane Langford, a Computer Programmer is at the console)

Computer Programs

The system is capable of running a number of programs. Some are called up automatically on a time base such as those to handle the satellite data. Numerous others can be called easily from the terminal by the forecaster (Figure 1). These programs all reside on discs so they are rapidly accessible. The programs can be modified in real time, if necessary. This means that the system can easily continue to evolve over the next few years.

Forecasting Sequence

The system and forecaster will follow the following process during each hour from approximately 6 p.m. on. The satellite scans the surface of the earth with a heat-sensing detector. The signal that comes from that detector is sent to antennas in Washington. The signal is then taken into computers where it is corrected for temperature calibration and satellite orbit considerations. In the present case, the signal goes over phone lines from Washington to Miami, then to the freeze forecast system in Ruskin, Florida. The satellite scans over a period of approximately 20 minutes. The SFFS at Ruskin continually monitors the line to detect the signal when it starts. It then automatically keeps track of the signals that come across the phone line -- over 1,200 scan lines in all. The lines are counted until the area with Florida is obtained. Then, the signal is digitized and stored. The forecaster then sees the satellite temperautre picture of the Georgia, Alabama, and Florida area in color on his TV screen. Each color represents approximately 2°F (Sutherland, et al 1979). Thus, he has a complete temperature picture for the entire surface of the southeast at approximately 20 minutes after the hour.

The forecaster sits at the terminal and receives information from 12 key locations around the state while information is automatically going into the computer. This information from around the state includes inversion air temperatures, soil temperatures, wind speed and direction, dew point and net radiation. These are typed onto a form which automatically appears on the CRT tube of the display. These temperatures are then entered into the computer and used in a physical heat balance model. A model is used to calculate the temperatures expected for the rest of the night at each of the 12 key locations. These predictions are portrayed back on the terminal for the forecaster to get his first updated predictions at the 12 locations. Now, the system has information on the latest temperature patterns across the state of Florida, as well as the present temperature at 12 locations and predicted temperatures for the 12 locations for the rest of the night. (See Figure 2). The system predicts temperature maps of the entire surface of the state for each hour of the rest of the night, using the predicted temperatures, the last satellite temperature picture and correlation coefficients between the key stations and 3,000 locations in the state (Sutherland and Bartholic, 1977 A).

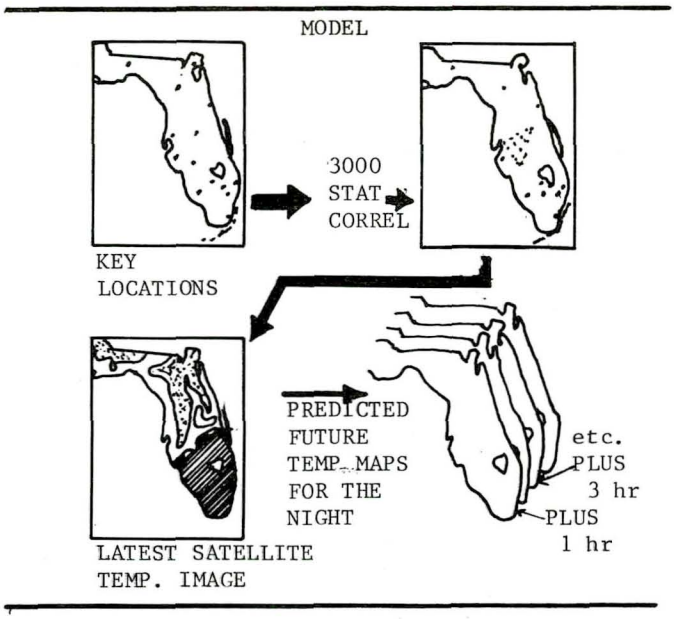

Figure 2. Flow diagram showing the sequence of steps required to develop predicted temperature maps.

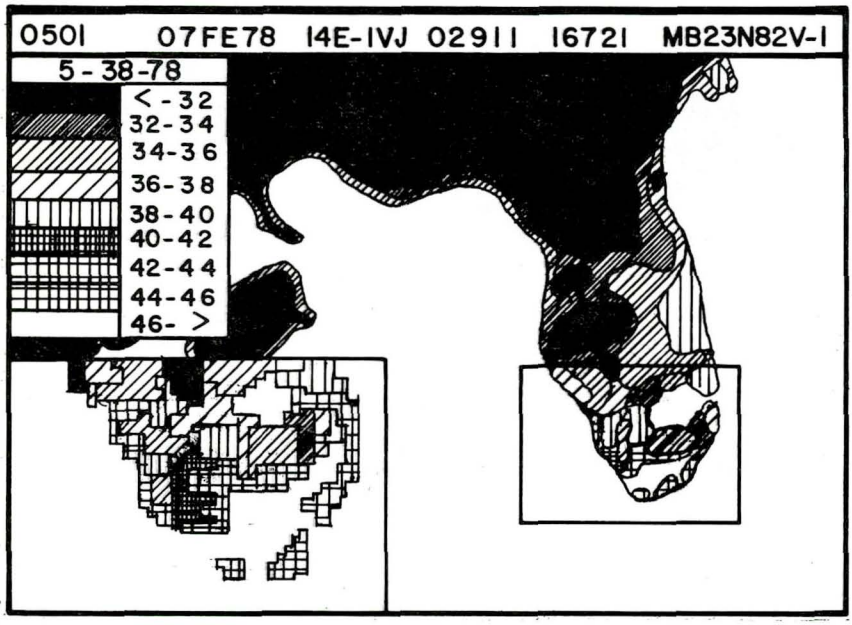

Figure 3. Black and white rendition of GOES Thermal Data from the Satellite Freeze Forecast System color TV screen.

The system develops a new forecast each hour for the entire surface of the state for the remaining hours of the night and thus, vital information needed by growers and those making freeze protection decisions is provided.

The physical model (for the 12 key stations) was operational during this past winter and was run on many of the cold nights by the forecasters. Evaluation of the 152 runs for the 1977-78 winter showed:

96% of predicted minimum temperature values were within $\pm$ 5°F
91% " " " " " " " $\pm$ 4°F
83% " " " " " " " $\pm$ 3°F
64% " " " " " " " $\pm$ 2°F
42% " " " " " " " $\pm$ 1°F

of the actual minimum measured. The second model was run but enough data has not yet been collected to produce satisfactory statistical coefficients relating the 3000 points to the 12 key locations. Work is continuing to develop new coefficients. A larger GOES data base from cold nights is being acquired from which to develop the new coefficients for use in the system.

The color data, of course, cannot be reproduced in this paper, so a black and white rendition is shown. Geostationary Orbiting Environmental Satellite (GOES) thermal data acquired and displayed by the SFFS is shown in Figure 3. These GOES data are obtained with the system every hour. Thus, temperatures, temperature trends, and cloud movement can be easily determined and followed.

Forecast Output

This winter the satellite freeze forecast system will be run in parallel with the traditional way of forecasting freeze temperatures. More frequent updates of the forecast and more detailed forecasts of the areas of the state are now available from the forecast office because of the SFFS. This improved frequency and smaller resolution information is of assistance in itself. However, certainly the written description of the color picture loses much in its translation.

TV stations and new means for communicating present temperature prediction pictures will be seen in coming years. Certainly, a grower could quite easily pick out his particular area with a satellite picture in front of him. He would have the most detailed temperature information technically possible at this time by observing the changes taking place.

CONCLUSION

Freezing temperatures can completely destroy a crop in a few hours. There are a number of possible methods for moderating these minimum temperatures but most methods are relatively costly and they are energy intensive. The grower needs to know detailed present temperatures and future temperature predictions for his specific area to make the best use of freeze protection devices.

The "Satellite Freeze Forecast System" will provide this type of information for the grower so that he can make better decisions for protecting the valuable food resource he has responsibility for providing.

REFERENCES

Bartholic, J.F. and R.A. Sutherland 1976: Cold climate mapping using satellite high resolution thermal imagery. 7th Conf. on Aerospace and Aeronautical Meteorology and Symposium on Remote Sensing from Satellites. Nov. 16-19. Am. Met. Soc.

Sutherland, R.A. and J.F. Bartholic 1977A: Afreeze forecasting model based upon meteorological satellite data. Thirteenth American Met. Society Conf. on Ag. and Forest Met., Purdue Univ., West Lafayette, Indiana, April 4-6.

Sutherland, R.A. and J.F. Bartholic 1977B: Significance of Vegetation in Interpreting Thermal Radiation from a Terrestrial Surface. J. App. Met. 16-8 August.

Sutherland, R.A., J.L. Langford, J.F. Bartholic and R.G. Bill, Jr. 1979: A real time satellite data acquisition, analysis and display system - a practical application of the GOES network. Accepted for publication, J. App. Met. March.

Paper No. 22

REMOTE SENSING APPLIED TO THE EVALUATION OF CROP FREEZE PROTECTION DEVICES

R. A. Sutherland, *Institute of Food and Agricultural Sciences, University of Florida, Gainesville, Florida 32611*

ABSTRACT

Thermal images from an aircraft-mounted scanner are used to evaluate the effectiveness of crop freeze protection devices. Fuel oil heaters, wind machines and irrigation systems are evaluated from flights at an altitude of 450 m over an experimental citrus grove of 1.5 hectares.

INTRODUCTION

In the past it has been difficult to determine the effectiveness of various measures that are taken in order to prevent freeze damage to crops. This difficulty is caused in great part by the fact that temperature measurements made with conventional sensors such as thermocouples or thermisters are limited to a small number of discrete points. Usually, it has been through trial and error that methods were learned.

In recent years, however, infrared technology has advanced to the point where remote sensing in the 8-14μ "thermal" radiation region has become a common and reliable research tool. This provides a new perspective on evaluating freeze protection methods because measurements can be made from a scanning aircraft giving a spacially continuous overview of surface radiation patterns of a relatively large area. The full impact of the technology lies in the fact that under most conditions the magnitude of the emitted radiation is directly related to the surface (or crop) temperature (Sutherland and Bartholic, 1977). The data, when properly reduced give a temperature "picture" of an entire area as opposed to the more conventional ground measurements of a few discrete points. A major purpose of this paper is to report progress made by using the remote sensing technique.

Description of apparatus and test site

The test site is an experimental citrus grove located in Northern Florida near the University of Florida (~29.5°N, 53 m.a.s.l.). An aerial photograph of the grove is shown in Fig. 1. The trees in the northern 2/3 of the grove are approximately 4 m in height. Those in the southern 1/3 are shorter (3 m). Tree spacings are 3.05 m east-west (rows) and 4.88 m north-south.

Except for a few missing trees, the grove is homogeneous in the east-west direction. The grove is located on flat terrain of Kanapaha Fine Sand.

Figure 1. Aerial photograph of the test site.

A computerized data acquisition facility for ground truth measurements is located near the southwest corner. The grove is equipped with two heater types, Spots and Scheu on alternate rows spaced at every other tree along rows. The undertree irrigation sprinkler heads are in every row, centered in the row and spaced at every other tree. The irrigation pump is a 20 Kw electric motor and pumps well water (21°C) from a depth of approximately 30 m. The pump valve was adjusted to give a deposition rate at the sprinkler heads of 0.2 cm min^{-1}. The wind machine is 10 m high with a single propeller 4.7 m in length, is driven by a gasoline engine and rotates about a vertical axis once every 5 min.

The overall spacial resolution of the aircraft scanner is approximately 1.25 m^2 which is sufficient to resolve individual trees. The data which is recorded on magnetic tape as an analog signal aboard the aircraft was later digitized at a rate which maintained this resolution. In this paper the term pixel will be applied to this area. A more detailed description of the aircraft and scanner can be found elesewhere (Sutherland and Bartholic, 1975). A linear approximation was used to convert the scanner signal to surface temperature and emissivities are approximated as unity. Errors due to these approximations for the scanner bandpass of 8-14μ are small (Sutherland, et. al., 1978)

Results

Fig. 2 shows a typical thermal image of the test site which was taken during a time when the grove was in the natural (unprotected) condition. In Fig. 2, lighter areas are warmer and

darker areas the colder. The entire range of the data is -8.9 to +0.56°C. The darker (colder) rows in the grove are the tree tops and the lighter (warmer) rows are bare soil.

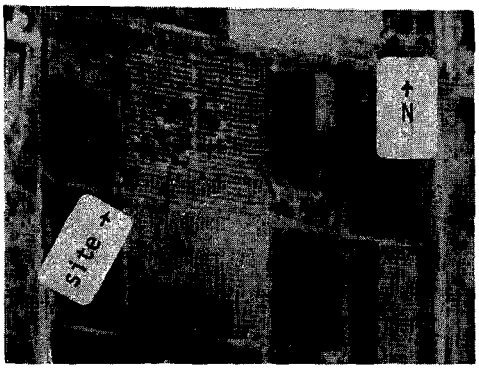

Figure 2. Typical thermal image of the test site taken when the grove was in the unprotected condition.

The digitized data used to produce the image of Fig. 2 was further analyzed by sectoring off only the area containing the grove and calculating the number of pixels (16000 total) found in the scene between various temperature intervals (i.e. histograms).

For evaluation of the wind machine the entire unprotected grove was considered the control then the data from a previous flight when the wind machine was operating is compared. For the heaters and irrigation the west half of the grove was considered control while the east half was first irrigated then heated.

All of the flights reported here were made on the night of 22-23 Feb. 1978. This was a calm night with no detectable wind. The experiments were started near midnight after most cooling had occured. Flights were then made approximately every two hours during which time nocturnal cooling was occuring at a nearly steady rate of 0.15°C/hour.

The resultant histograms of the thermal images are shown in Fig. 3. The mean temperatures of the distributions are marked along the x axis.

The results of Fig. 3a and 3b show the overall effectiveness of the wind machine, based upon the mean temperature of the grove to be 1.06°C. The broader distribution for the wind protected grove is indicative of the fact that the amount of protection provided by the wind is a function of distance from the machine which is located near the southwest corner of the grove. This was borne out in the accompanying thermal images (not shown).

The results of Fig. 3c and 3d show the overall effectiveness of the undertree irrigation, based upon mean temperatures only, to be 2.1°C. This mean, however, could be somewhat misleading since it is influenced by temperatures of the irrigation water itself, which was pumped in at elevated temperature. This is apparent from the bimodal distribution of Fig. 3d where the second peak at a higher temperature is certainly due to this fact. Perhaps a more accurate assessment of the effectiveness of the irrigation technique is the low temperature cut-off which by subtracting the lower thresholds gives an effectiveness of 0.78°C.

The results of Fig. 3e and 3f show the effectiveness of the heaters to be 1.5°C based upon means. This is again somewhat misleading for the same reason as before since some of the higher temperatures are the heaters themselves. By subtracting the lower thresholds, however, the effectiveness of the heaters is approximately 0.63°C, about the same as the irrigation technique. This latter observation is somewhat complicated by the fact that it was necessary to operate the wind machine during the heater experiment in order to protect the control portion of the grove from killing freeze damage. Perhaps a better direct comparison between irrigation and heating is to use the result of Fig. 3c as control for both. Viewed this way, the effectiveness of each is about the same.

Conclusions

The technique of remote sensing has been shown to be useful in evaluating freeze protection methods. Although more data is desired it can be concluded from the results shown that the technique of undertree irrigation competes effectively with that of heating. The economic significance of this latter conclusion lies in the fact that the cost of heating is about $20 per acre per hour while undertree irrigation is $.75 per acre per hour.

References

Sutherland, R. A. and J. F. Bartholic: 1974, "Aircraft-Mounted Thermal Scanner to Determine Grove Temperatures During Freeze Conditions," Proceedings of the Florida State Horticultural Society. 87, 65-69.

Sutherland, R. A. and J. F. Bartholic: Significance of Vegetation in Interpreting Thermal Radiation from a Terrestrial Surface," Journal of Applied Meteorology. 16, 759-763.

Sutherland, R. A., J. F. Bartholic and J. F. Gerber: 1978, "Emissivity Correction for Interpreting Thermal Radiation from a Terrestrial Surface," Journal of Applied Meteorology. In review.

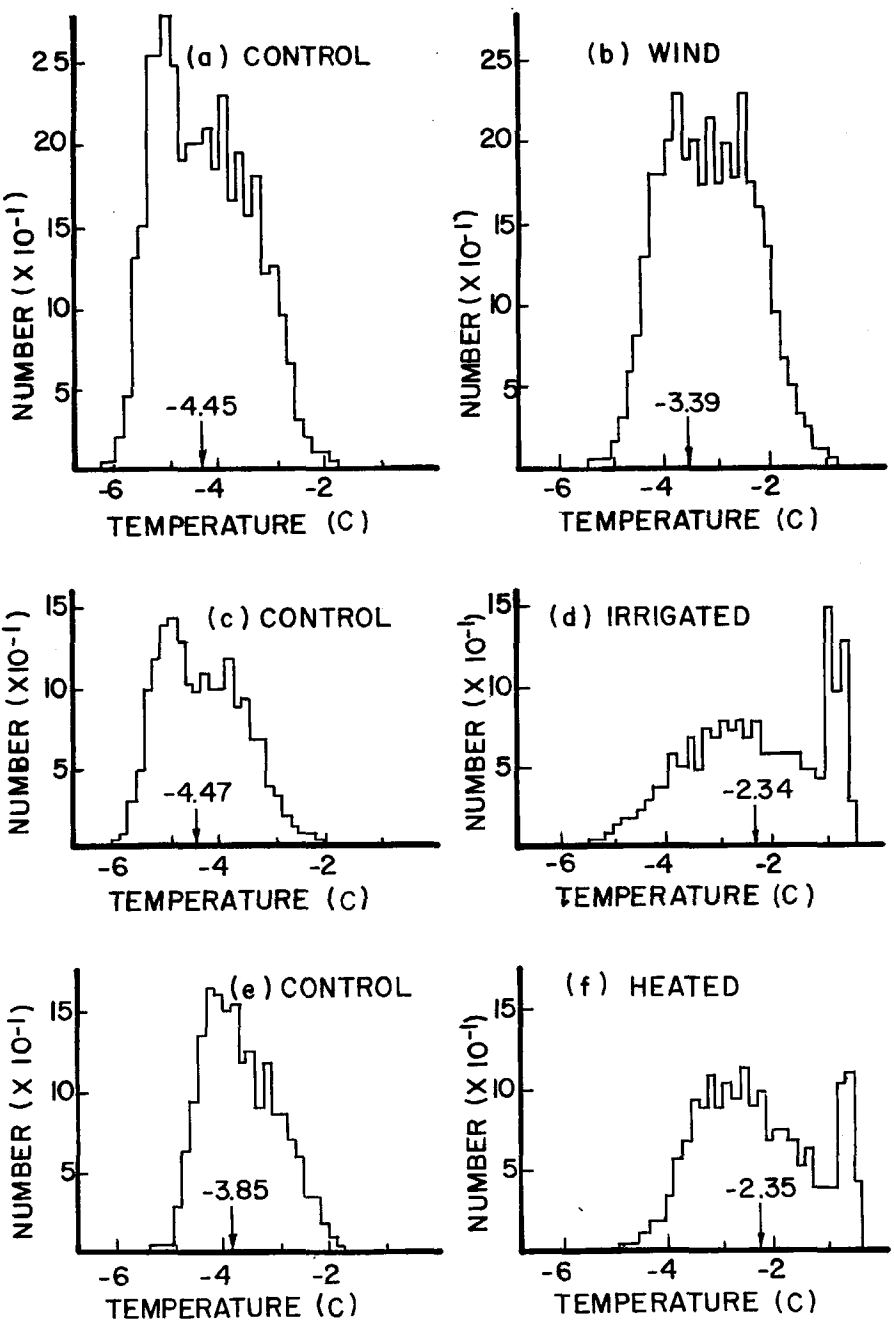

Figure 3. Histograms of the thermal images.

Page intentionally left blank

Paper No. 23

SENSITIVITY OF FORECAST SKILL TO DIFFERENT OBJECTIVE ANALYSIS SCHEMES

W. E. Baker, *National Research Council, Washington, DC and Goddard Space Flight Center, Greenbelt, Maryland*

ABSTRACT

Numerical weather forecasts are characterized by rapidly declining skill in the first 48 to 72 h. Recent estimates of the sources of forecast error indicate that the inaccurate specification of the initial conditions contributes substantially to this error.

The sensitivity of the forecast skill to the initial conditions is examined by comparing a set of real-data experiments whose initial data were obtained with two different analysis schemes. Results are presented to emphasize the importance of the objective analysis techniques used in the assimilation of observational data.

INTRODUCTION

The current skill of numerical weather forecast degrades rapidly in the first 48 to 72 h due to inaccurate initial conditions as well as model deficiencies. Recent estimates of the sources of forecast error (e.g., Miyakoda, 1975; Robert, 1976; Somerville, 1976) indicate that inaccurate initial data may contribute substantially to the rapid error growth. Errors in the specification of the initial conditions are due to both inadequacies in the observing systems and data analysis techniques. In this paper we examine the importance of the objective analysis techniques by comparing a set of real-data experiments forecast from initial data obtained with two different analysis schemes.

Data Analysis and Model Initialization

Two different analysis schemes were utilized to obtain the initial conditions for a pair of 72 h forecasts begun from 0000 GMT 11 February 1976. The two analysis schemes are similar in that they apply successive corrections to a first guess field (Cressman, 1959). The Laboratory for Atmospheric Sciences (GLAS) general circulation model (Somerville et al., 1974) was utilized as the forecast model.

One analysis scheme (hereafter referred to as Scheme A) is described in Halem et al. (1978) and will not be discussed in detail here. A second scheme (Scheme B), recently developed, differs in several respects from Scheme A as outlined below.

Successive corrections are made to a first guess geopotential height field in Scheme B, whereas, a temperature analysis is performed in Scheme A. A vertically consistent height analysis is maintained in Scheme B through the use of the hydrostatic equation. Substantially larger scanning radii are used in the successive correction procedure in Scheme B than in Scheme A. In Scheme B, the number of scans and size of the scanning radii vary depending on the particular field analyzed and the number of observational points available in a given radius.

In the data assimilation, Scheme A was applied every 12 h with the GLAS model. Scheme B was applied every 6 h with a model provided by the National Meteorological Center (Stackpole, 1976). No balancing of the mass and velocity fields was performed in either analysis procedure.

Evaluation of the Analysis Techniques

To illustrate the differences in the two analysis schemes, we present in Fig. 1a the 500 mb geopotential height field obtained using Scheme A for 0000 GMT 11 February 1976. The 500 mb geopotential height values for Scheme B are shown in Fig. 1b, and those obtained by the National Meteorological Center (NMC) using the Hough analysis (Flattery, 1971) are illustrated in Fig. 1c.

The differences in the two analysis schemes are reflected in the differences between Fig. 1a and 1b. A nine-point smoother was incorporated into Scheme B, whereas no smoothing was applied in Scheme A. This accounts for the differences in smoothness of the contours in the two plots. In general, Fig. 1b more closely resembles the NMC analysis (Fig. 1c) than does Fig. 1a, particularly in the high latitudes. This is due in large part to the larger scanning radii used in Scheme B in the successive correction procedure.

To illustrate the improvement in forecast skill, the 72 h sea level pressure RMS and S1 statistics over North America are shown in Table 1. The smaller values with Scheme B indicate an improvement in forecast skill.

The refinements in the analysis procedure (Scheme B) are responsible for this improvement and indicate the importance of the objective analysis techniques used in the assimilation of observational data.

(a) Scheme A for 0000 GMT 11 February 1976

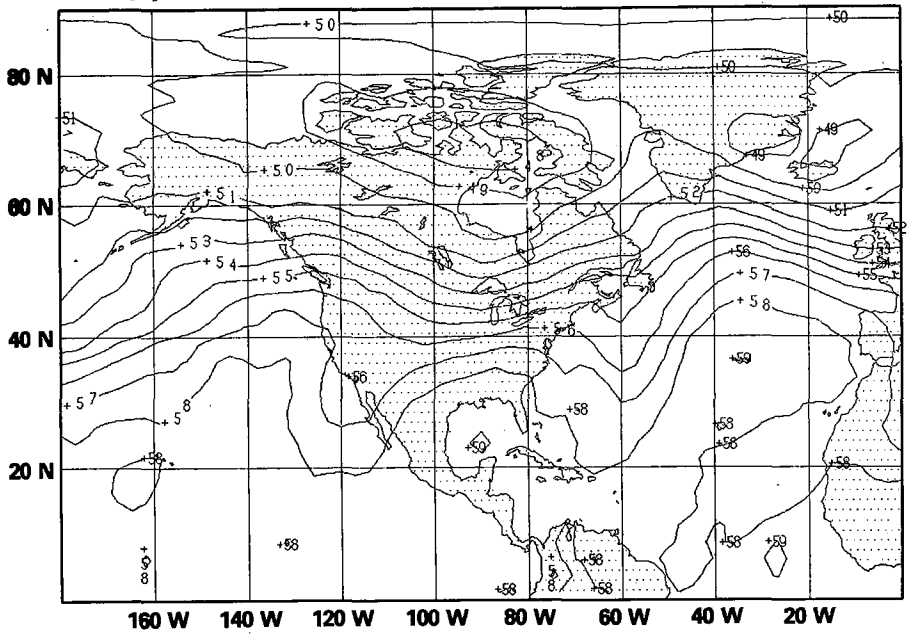

(b) Scheme B for 0000 GMT 11 February 1976

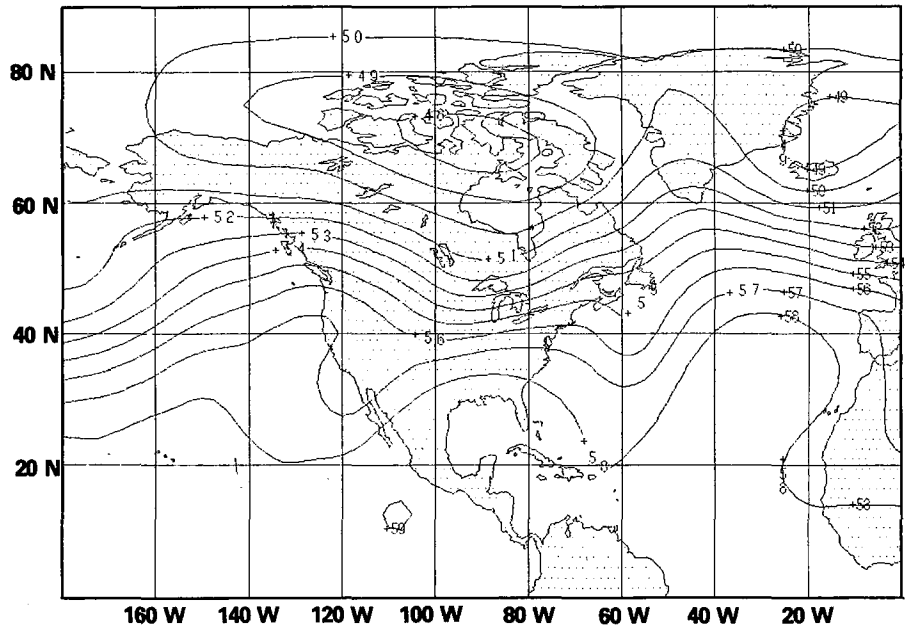

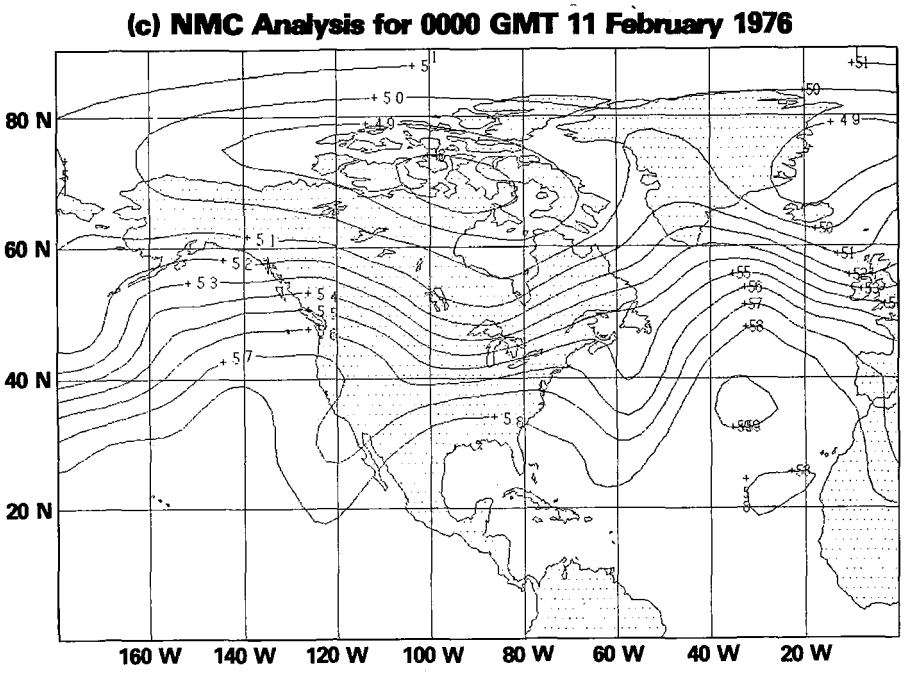

Fig. 1. 500 mb geopotential height in units of 10^2m.

Table 1. 72 h sea level pressure RMS and S1 statistics over North America for 0000 GMT 14 February 1976.

A		B	
RMS	S1	RMS	S1
8.4	75.7	5.6	67.2

ACKNOWLEDGMENTS

This research was conducted while the author was supported by a National Research Council Resident Research Associateship.

The programming and technical assistance provided by Mr. D. Edelmann, Mr. D. Han, and Mr. M. Iredell are sincerely appreciated. The encouragement and support of Dr. M. Halem is gratefully acknowledged.

The NMC staff patiently answered questions regarding the implementation of Scheme B. The author particularly acknowledges the assistance of Mr. J. McDonell, Dr. R. McPherson, and Dr. J. Stackpole. Dr. Stackpole also provided the model used in the assimilation and the vertical interpolation program used in Scheme B.

REFERENCES

Cressman, G. P., 1959: An operational objective analysis system. Mon. Wea. Rev., 85, 367-374.

Flattery, T. W., 1971: Spectral models for global analysis and forecasting. Air Weather Service Tech. Rep. 242, 42-54.

Halem, M., M. Ghil, R. Atlas, J. Susskind, and W. J. Quirk, 1978: The GISS sounding temperature impact test. NASA Tech. Memo. 78063, Goddard Space Flight Center, Greenbelt, Maryland, 421 pp.

Miyakoda, K., 1975: Weather forecasts and the effect of the subgrid scale processes. Seminars on Scientific Foundation of Medium Range Weather Forecasts, European Centre for Medium Range Weather Forecasts, Reading, England, 380-593.

Robert, A., 1976: Sensitivity experiments for the development of NWP models. Proc. Eleventh Stanstead Seminar, Publ. Meteor. No. 114, McGill University, 68-81.

Somerville, R. C. J., 1976: Sensitivity of large-scale numerical weather forecasts to deficiencies in models. Ann. Meteor. (NF), 11, 266-268.

_____, P. H. Stone, M. Halem, J. E. Hansen, J. S. Hogan, L. M. Druyan, G. Russell, A. A. Lacis, W. J. Quirk, and J. Tenenbaum, 1974: The GISS model of the global atmosphere. J. Atmos. Sci., 31, 84-117.

Stackpole, J. D., 1976: The National Meteorological Center nine-layer global forecast model. Preprints Conf. on Wea. Forecasting and Anal., Albany, NY, Amer. Meteor. Soc., 112-116.

Page intentionally left blank

Paper No. 24

NONLINEAR INITIALIZATION OF THE GLAS MODEL

F. Baer, *University of Maryland, College Park, Maryland*

ABSTRACT

A simplified version of the GLAS model is linearized and the normal modes extracted. These modes show the necessary separation for nonlinear initialization.

INTRODUCTION

The finite difference form of the GLAS model is exceptionally difficult to put into normal mode form. A procedure is outlined which will allow a simplification of the model and still incorporate the essential ingredients for nonlinear initialization so that the high frequency components may be slowed. A small version of the simplified system is presented, linearized, and the normal modes described. Some form of this system will ultimately be initialized and tested in the GLAS model.

INITIALIZATION

The procedure for nonlinear initialization has been presented by Baer and Tribbia (1977). The system equations should be written in the form,

$$\frac{d\chi}{dt} + \underset{\sim}{A}\chi = \varepsilon\, G(\chi,\chi) \tag{1}$$

where χ is a vector of dependent variables (grid point values of the flow field and physical variables, for example), $\underset{\sim}{A}$ is a matrix of fixed quantities dependent on the system, and ε is small parameter, usually the Rossby number. Since most systems of this sort are exceptionally complicated, as in the GLAS model, let us rewrite (1) in the form

$$\frac{d\chi}{dt} + \hat{\underset{\sim}{A}}\chi = \varepsilon\, G + (\hat{\underset{\sim}{A}}-\underset{\sim}{A})\chi \tag{2}$$

where $\hat{\underset{\sim}{A}}$ is a "simpler" matrix, and $\| S^{-1}(\hat{\underset{\sim}{A}}-\underset{\sim}{A})S \|$ is of order ε. Here $\underset{\sim}{S}$ is the modal matrix which diagonalyses $\underset{\sim}{A}$.

We shall find the modes of $\hat{\underset{\sim}{A}}$, a simple version of the GLAS model so that we may separate the frequencies into fast and slow, a procedure essential to the nonlinear initialization scheme. Thus we will find,

$$\hat{\underset{\sim}{A}} = \underset{\sim}{S} \begin{pmatrix} \varepsilon\Lambda_x & 0 \\ 0 & \Lambda_y \end{pmatrix} \underset{\sim}{S}^{-1} \tag{3}$$

where clearly the scaled frequencies $\varepsilon\lambda_x << \lambda_y$.

GLAS MODEL NORMAL MODES

We begin the simplification of the GLAS model from the non-forced version (see Somerville, et. al., 1974) described as follows:

$$\begin{aligned}
&\frac{\partial \mathbb{V}}{\partial t} + \mathbb{V} \cdot \nabla\mathbb{V} + \hat{f}\mathbf{k}\times\mathbb{V} = -\nabla_\sigma\Phi + \sigma\alpha\nabla_\sigma\pi \\
&\nabla_\sigma \cdot \mathbb{V} + \frac{\partial \dot{\sigma}}{\partial \sigma} = -\frac{d}{dt}\,\ell n\,(\rho\,\frac{\partial\Phi}{\partial\sigma}) \\
&\frac{\partial\Phi}{\partial\sigma} = -\alpha\pi \\
&\frac{\partial \ell n\theta}{\partial t} + \mathbb{V} \cdot \nabla\ell n\theta + \dot{\sigma}\,\frac{\partial \ell n\theta}{\partial\sigma} = 0 \\
&P = P_t + \sigma\pi \ , \ \pi = P_s - P_t
\end{aligned} \tag{4}$$

Symbol definitions may be found in the above reference. We now linearize this system about a state of rest, let $\pi \to \pi(x,y,t) + \Pi$ and $\alpha \to \alpha(x,y,\sigma,t) + A(\sigma)$ where $\pi << \Pi$ and $\alpha << A$. We include the following definition where ϕ is the perturbation of Φ ,

$$\psi \equiv \phi + \sigma A\pi \ , \ \omega \equiv \dot{\sigma} + \frac{\sigma}{\Pi}\frac{\sigma\pi}{\partial t} \ , \ \mathbb{V} = (u,v) \ . \tag{5}$$

The resulting linearized system then becomes,

$$\begin{aligned}
&\frac{\partial \mathbb{V}}{\partial t} + \hat{f}\mathbf{k}\times\mathbb{V} + \nabla_\sigma\psi = 0 \\
&\frac{\partial}{\partial t}\,\psi_\sigma + N^2(\sigma)\omega = 0 \\
&\nabla_\sigma \cdot \mathbb{V} + \omega_\sigma = 0
\end{aligned} \tag{6}$$

If we now assume a solution in longitude of periodic form, e^{ikx} , we get,

$$\begin{aligned}
u_t - fv + ik\psi &= 0 \\
fu + v_t + \psi_y &= 0 \\
iku + v_y + \omega_\sigma &= 0 \\
\psi_{\sigma t} + N^2\omega &= 0
\end{aligned} \tag{7}$$

Now to separate the vertical dependence from the latitudinal, let

$$(u,v,\psi) = G(\sigma)\ (\hat{u},\hat{v},\hat{\psi})\ (y,t)$$
$$\omega = H(\sigma)\ \hat{\omega}(y,t) \tag{8}$$

Substitution of (8) into (7) yields the result that

$$\hat{\psi}_t = C^2(ik\hat{u} + \hat{v}_y) \tag{9}$$

$$H_{\sigma\sigma} = \frac{N^2}{C^2} H \ ; \ G_{\sigma\sigma} = (\ell n N^2)_\sigma \ G_\sigma + \frac{N^2}{C^2} G \tag{10}$$

and application of the boundary conditions that $\dot{\sigma} = 0$ at $\sigma = 0,1$, gives the conditions that $H(\sigma=0) = 0$ and $H_\sigma(\sigma=1) = -(\Pi|C^2)A(1)H(1)$. These conditions applied to the solution of (10) yield the required separation constants C^2, which are also denoted as "equivalent depths".

The first two equations of (7), together with (9) allow for a solution of the latitudinal structure and generate the normal modes and frequencies. We have,

$$\frac{\partial \chi}{\partial t} + i\hat{\underset{\sim}{A}}\chi = 0 \ ; \ \chi^T \equiv (\hat{u},i\hat{v},\hat{\psi})$$
$$\hat{\underset{\sim}{A}} = \begin{pmatrix} 0 & f & k \\ f & 0 & \frac{\partial}{\partial y} \\ -kC^2 & C^2\frac{\partial}{\partial y} & 0 \end{pmatrix} \tag{11}$$

To better understand these modes in a simplified framework, let us solve (11) in a channel extending from $-60° \leq \theta \leq 60°$ latitude with rigid walls so that $\hat{v}(\pm 60) = 0$. Equations (11) also show that $\hat{v}_{yy}(\pm 60) = 0$ and give equations on the boundaries for $\hat{\psi}$ and $\hat{u}$. For additional simplification, we assume the channel to be broken into $2N + 1$ equally spaced grid-points such that $Y = N\Delta y$ and $-Y \leq y \leq Y$, with $y = n\Delta y$. We also use centered differences to replace derivatives. In the finite-difference form, system (11) becomes,

$$\frac{d\chi}{dt} + i\hat{\underset{\sim}{A}}\chi = 0 \quad \chi^T = (U,V,\Phi)$$
$$U^T = (\hat{u}_{N-1}\cdots\hat{u}_0\cdots\hat{u}_{1-N}) \quad (2N-1) \text{ values}$$
$$V^T = i(\hat{v}_{N-1}\cdots\cdots\hat{v}_{1-N}) \tag{12}$$
$$\Psi^T = (\hat{\psi}_{N-1}\cdots\cdots\hat{\psi}_{1-N})$$

and $\hat{\underset{\sim}{A}}$ is a $3(2N-1)$ square matrix. The roots of $\hat{\underset{\sim}{A}}$ represent the frequencies of the reduced system as specified in (3) and will represent an approximation of the GLAS model.

STRUCTURE OF MODES AND FREQUENCIES

For pilot experiments, we have chosen to break up the atmosphere into three equal σ-layers. Finite difference solution of H from (10) then yields the following three equivalent depths in units of geopotential height;

$$C_1^2 = -8.402*10^4$$

$$C_2^2 = -4.235*10^3$$

$$C_3^2 = -8.012*10^2$$

The corresponding structures of vectors H_1, H_2 and H_3 may be seen on Figure 1. They have the expected distribution for this resolution. For the latitudinal structure, we have taken $\Delta y = 5°$ and $\Delta y = 10°$. For the former case, we generate 69 modes for each equivalent depth (C^2) and for each planetary wave (k). For the latter case, the number reduces to 33 modes. In either case, many of the modes are computational and presenting their structures would be overwhelming. Fig. 2 gives some indication of the structure of the latitudinal modes. We have plotted the 49th vector for the case of $\Delta y = 5°$, showing the distribution for waves 1, 6, 15 and 30 for both the external and first internal modes. Note that the vector for wave one and the external mode shows some truncation properties which are not apparent for the internal mode. The other vectors all have a very similar structure. These vectors reflect Rossby type oscillations with periods in excess of 40 hours.

In Table 1 we describe the distribution of eigenvalues for the $\Delta y = 10°$ truncation. We denote the number of modes which fall into the "high" frequency as compared to the "low" frequency for selected wave numbers and the three vertical structures. Note that all but wave number one have very strong separation between the gravity and rotational modes; i.e., there are twenty two "fast" modes and eleven "slow" ones. Separation in wave one, although not pronounced, is apparent. This difficulty with long waves has been seen in other experiments.

SUMMARY

The data presented indicate that normal modes may be extracted from a simplified version of the GLAS model, and mode separation is evident to allow for nonlinear initialization. Tests must now be performed which will determine how important the approximations to the true numerical model are, and how effective initialization with the simplified model will be.

An interesting observation of the study to date shows that some of the modes are strongly affected by truncation. Devices for removing the amplitudes of these modes (if they have slow frequency) are under investigation. The high frequency computational modes may be removed by the nonlinear initialization technique.

References

Baer, F., J. T. Tribbia, 1977: On complete filtering of gravity modes through nonlinear initialization. Mon. Wea. Rev., 105, 1536-1539.

Somerville, R. C. J., et. al., 1974: The GISS model of the global atmosphere. J. Atmos. Sci., 31, 84-117.

TABLE 1: Periods in hours for all frequencies for model with $\Delta y = 10°$ and for selected wave numbers. Values in parentheses indicate the number of modes in the specified range.

WAVE NUMBER	EXT. MODE	FIRST INT.	SECOND INT.
1	$6 \leq T \leq 16$ (19)	$15 < T < 56$ (22)	$15 < T < 60$ (20)
	$23 \leq T \leq 45$ (7)	$T > 170$ (11)	$T = 102$ (2)
	$T > 189$ (7)		$T > 393$ (11)
6	$4.1 < T < 6.5$ (22)	$13 < T < 29$ (22)	$15 < T < 43$ (20)
	$T = 18.2$ (2)	$T > 103$ (11)	$T = 65.6$ (2)
	$T > 85$ (9)		$T > 140$ (11)
15	$2.3 < T < 2.6$ (22)	$8.9 < T \leq 11.4$ (22)	$13 < T < 26.3$ (22)
	$T = 31.9$ (2)	$T > 201$ (11)	$T > 238$ (11)
	$T > 198$ (9)		
30	$1.24 < T \leq 1.28$ (22)	$5.3 \leq T \leq 5.7$ (22)	$10 < T < 13.2$ (22)
	$T = 58.8$ (2)	$T > 312$ (11)	$T > 420$ (11)
	$T > 390$ (9)		

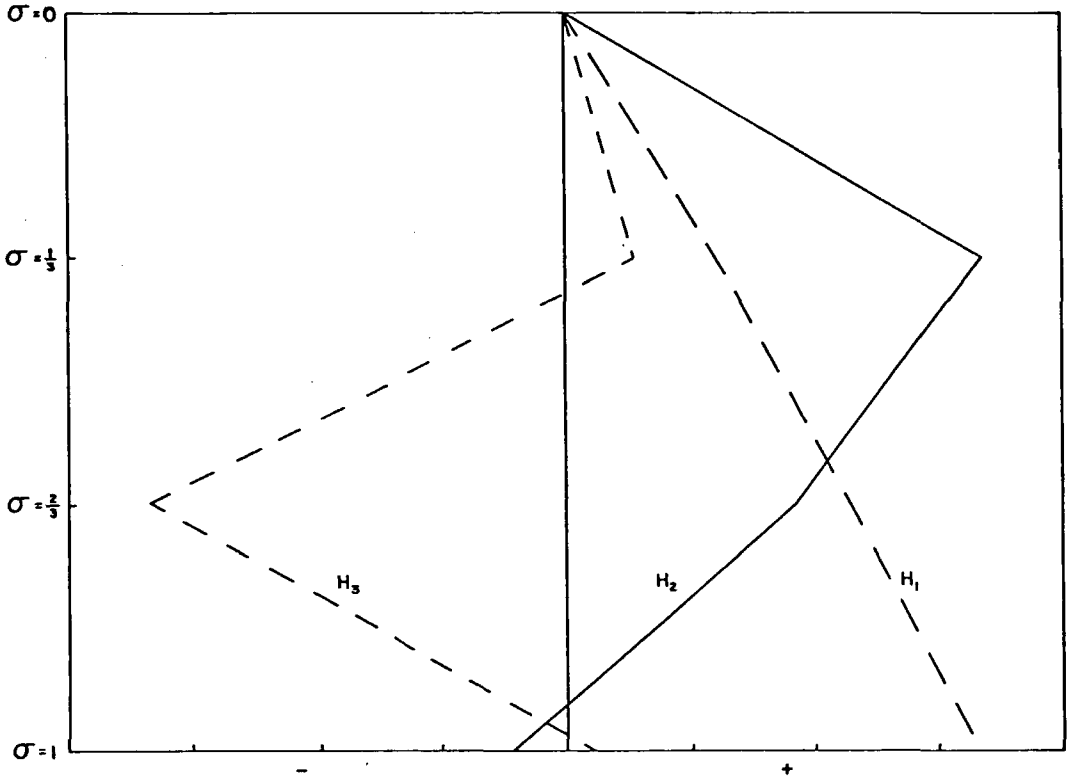

Figure 1: Vertical structures for the external and two internal modes of the simplified model. The vectors are not normalized.

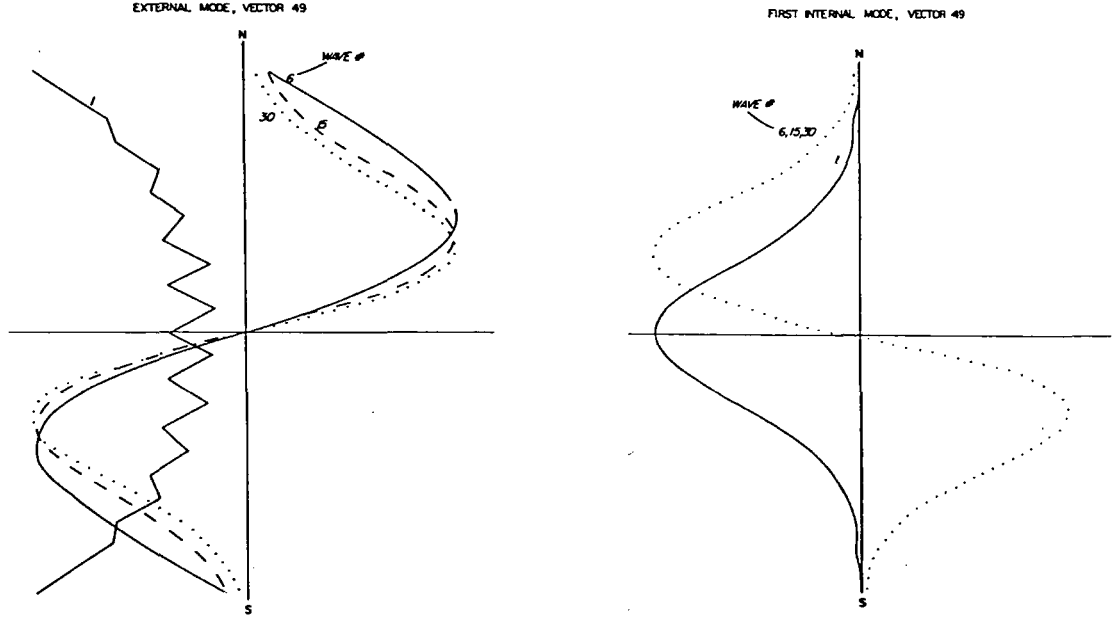

Figure 2: Latitudinal structure of the 49th vector (a Rossby mode) of the stream function for the external and first internal mode, for wave numbers 1, 6, 15 and 30. The ordinate represents the N-S width of the channel and the vectors are not normalized.

Page intentionally left blank

Paper No. 25

CASE STUDIES OF MAJOR DST-6 SOUNDING IMPACTS WITH THE GLAS MODEL

R. Atlas, *Goddard Space Flight Center, Greenbelt, Maryland*

ABSTRACT

Two case studies of DST-6 sounding impacts are presented. In each of these cases, major improvements to the GLAS model's forecasts of specific synoptic features resulted from including satellite-sounding data in the initial analysis.

INTRODUCTION

A detailed subjective evaluation of the impact of satellite-derived temperature soundings on synoptic forecasts with the high resolution (2½°lat.x3°long.) version of the GLAS GCM has been carried out for eleven of the forecasts from the February 1976 DST period. Following the procedures of Atkins and Jones (1975), qualified weather forecasters were asked to judge the relative utility of prognostic charts generated from SAT and NOSAT initial conditions, without actually knowing which forecasts had utilized satellite-derived sounding data. This evaluation showed the overall impact of the satellite data assimilation to be modest and beneficial, supporting the conclusions of our statistical evaluation (Ghil et al., 1978) and revealed no cases in which major negative impacts occurred. Two cases in which major improvements to GLAS model forecasts resulted from the inclusion of satellite-derived temperature soundings will be presented in the following sections.

72-h Forecast from 0000GMT, 19 February 1976

This was a case in which a significant improvement to the predicted displacement of an intense winter storm occurred in the latter half (36-h period) of the forecast period. The initial conditions for this forecast showed a moderately intense low pressure system, associated with an upper level short wave trough, located off the northwest coast of the U. S. As this system moved inland, a new low developed along an already existing stationary front and became the dominant feature by 1200GMT on 19 February. During the next 24 h, the cyclone moved southeastward and intensified, after which time it recurved and then accelerated toward the northeast. The storm produced heavy snow, blizzard, or near-blizzard conditions in Colorado, Kansas, Nebraska, Iowa, Michigan, and

Wisconsin. Tornadoes or severe thunderstorms were reported in Kansas, Oklahoma, Texas, Arkansas, Missouri, Illinois, Louisiana, and Mississippi. The majority of the severe weather occurred toward the end of the forecast period after recurvature of the cyclone to the northeast.

Fig. 1a and 1b depict the 72-h sea-level pressure prognoses, and predicted track of this cyclone, for the SAT and NOSAT cases, respectively, while the corresponding analysis and observed track is depicted in Fig. 1c. Fig. 1d shows the NMC operational 72-h forecast.

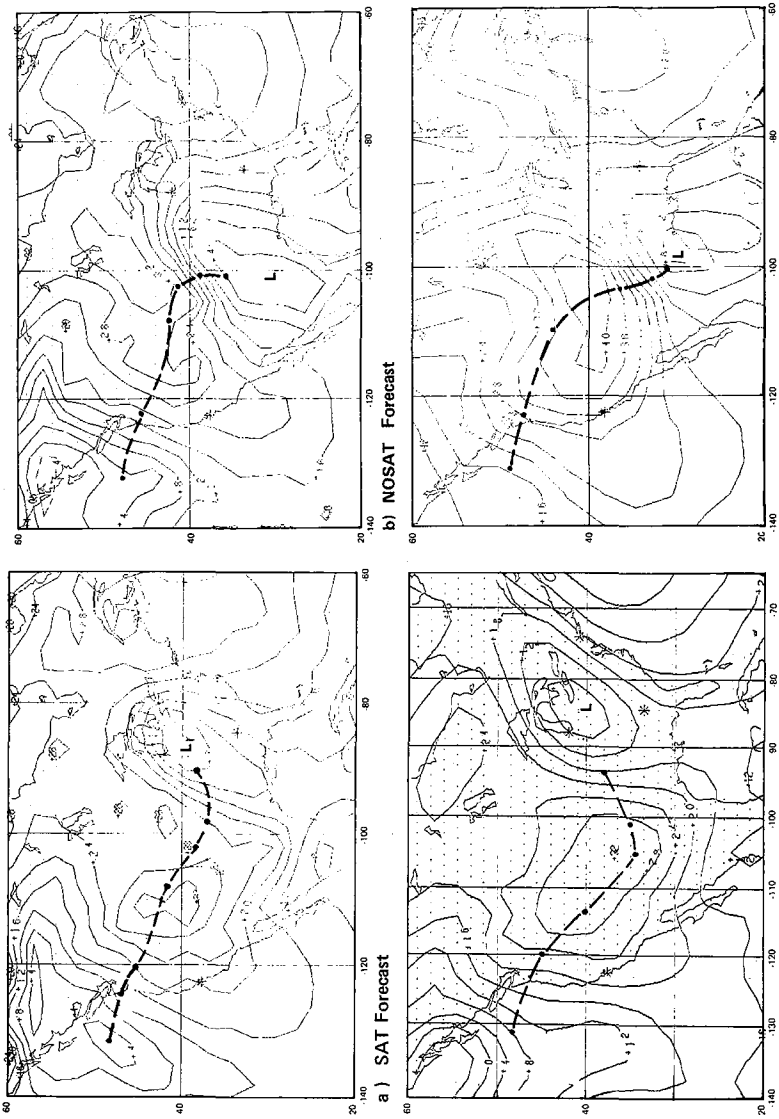

Fig. 1a shows the 72 h forecast from SAT initial data at 0000GMT 19 February 1976; Fig. 1b the corresponding NOSAT forecast; Fig. 1c shows the verification analysis (operational NMC analysis), and Fig. 1d the NMC operational 72 h forecast. Dots represent past positions of low at 12 h intervals.

A comparison of these charts reveals the very significant improvement in the model prediction that included satellite-sounding data. During the first 36 h of the forecast, only slight differences exist between the SAT and NOSAT sea-level prognoses as both predict the intensification and southeastward movement of the low. After 36 h, however, major differences in the predicted track are evident. The NOSAT system forecasts the low to move south-southeastward, while the SAT system forecasts the low to continue southeastward for 12 h and then recurve to the northeast such that the 48, 60, and 72-h forecast positions of the low are in excellent agreement with observations.

Since most of the severe weather associated with this low occurred during the last 30 h of the forecast, it is clear that significantly improved local weather forecasts could have resulted from the use of the SAT prognoses in this situation. In order to investigate this point further, the SAT and NOSAT predictions of local convective instability and destabilization by differential equivalent potential temperature advection were compared. It was found that a 51 percent reduction in RMS errors of convective instability and a 22 percent reduction in RMS errors of differential advection occurred in the prediction which included satellite sounding data.

An evaluation into the nature of the impact in this case has been partially completed. Results from this study indicate that differences in the initial thermal advection patterns off the west coast of the U. S. between SAT and NOSAT analyses amplified with time as the cyclone moved inland and contributed significantly to the differing displacements after 36 h. The effects of additional initial state differences are also being investigated.

72-h Forecast from 0000GMT, 11 February 1976

In this case, a weak cyclone formed along a stationary front in southwest Canada, moved southeastward while intensifying during the first 40 h of the period, and then recurved to the east-northeast. While the predicted tracks of this low are similar for both the SAT and NOSAT systems, major differences in the intensification of this low were evident on all prognoses after 36 h. In each case the SAT system forecast a more intense cyclonic circulation in better agreement with observations.

Fig. 2a and 2b depict the 72-h sea-level pressure prognoses for the SAT and NOSAT cases, respectively, while the corresponding analysis is depicted in Fig. 2c. Fig. 2d shows the NMC operational 72-h forecast.

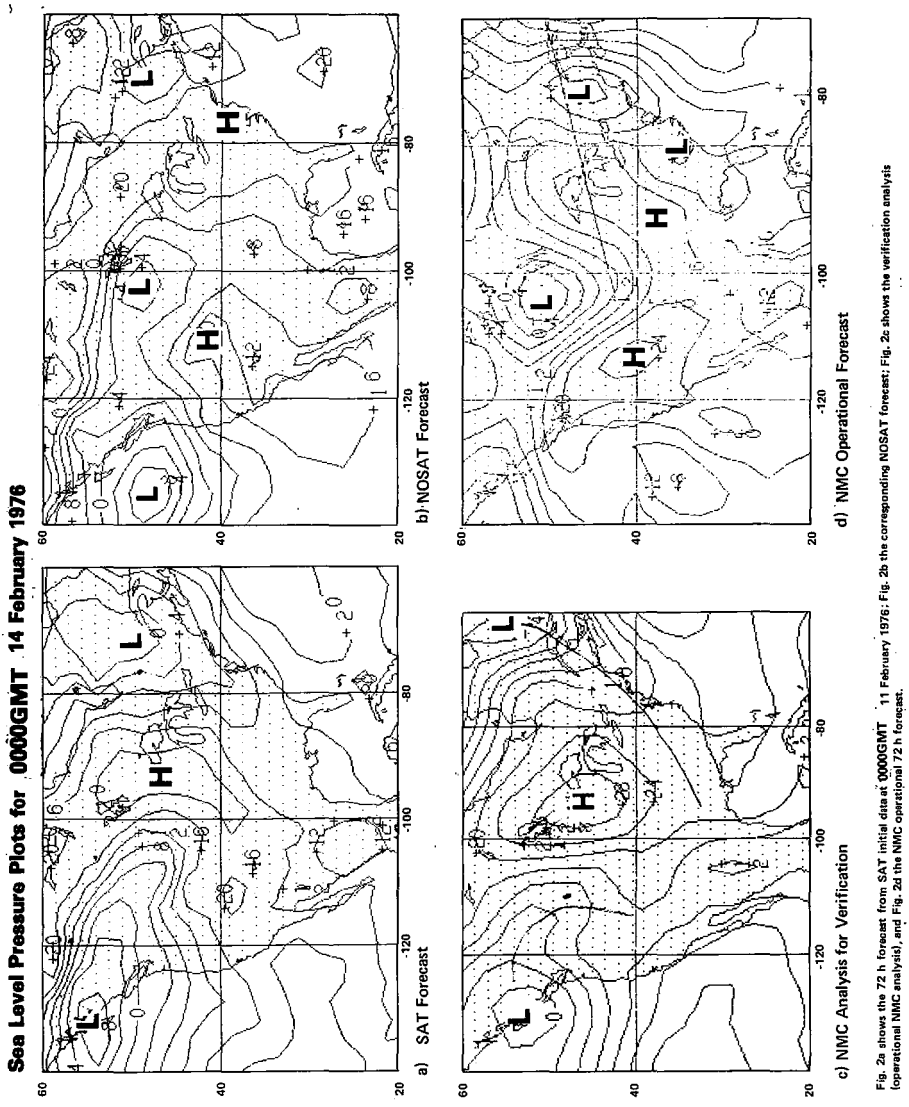

Fig. 2a shows the 72 h forecast from SAT initial data at 0000GMT 11 February 1976; Fig. 2b the corresponding NOSAT forecast; Fig. 2c shows the verification analysis (operational NMC analysis), and Fig. 2d the NMC operational 72 h forecast.

A comparison of these figures reveals that the SAT prognoses is substantially better than the NOSAT in its prediction of the cyclonic circulation over southeastern Canada and the northeastern U. S., as well as the anticyclone approaching the Great Lakes and the pressure trough extending southeastward from southwest Canada. Improvements relative to the NMC prognoses are also evident.

ACKNOWLEDGMENTS

The author wishes to acknowledge R. Rosenberg and M. Eaton for their assistance in the evaluation of satellite-sounding impact; D. Sakal for providing computer and graphics support; Dr. M. Halem, Manager of the Goddard Modeling and Simulation Facility, for his guidance and encouragement; and the staff of the NMC Development Division for supplying us with the forecasts from their 6L PE model.

REFERENCES

Atkins, M. J., and M. V. Jones (1975). An experiment to determine the value of satellite infrared spectrometer (SIRS) data in numerical forecasting. Meteor. Mag., 104, 125-142.

Ghil, M., M. Halem, and R. Atlas: Effects of sounding temperature assimilation on weather forecasting: model dependence studies. Remote Sensing of the Atmosphere from Space, H. J. Bolle, ed., Pergamon Press, 1979.

Page intentionally left blank

Paper No. 26

SOME ASPECTS OF THE NEW UCLA GENERAL CIRCULATION MODEL

M. J. Suarez, *Department of Atmospheric Sciences, UCLA*

ABSTRACT

A potential enstrophy conserving scheme and a modified σ-coordinate have been coded in the UCLA general circulation model. The new model is being tested with global simulation experiments.

Introduction

During the past year we have modified several aspects of the UCLA general circulation model. Major changes are:

---- The inclusion of a potential enstrophy conserving advection scheme in the equation of motion;

---- reformulation of the vertical differencing based on a modified σ-coordinate in which the predicted PBL top is a coordinate surface;

---- the inclusion of the turbulent entrainment parameterization reported by Randall at the Third NASA Weather and Climate Program Review.

Other changes include: a potential temperature conserving horizontal advection scheme, a modified upstream scheme for advection of moisture, and inclusion of the ice phase in the cloud model used in the cumulus convection parameterization.

The potential enstrophy conserving scheme

Large truncation errors produced by poorly resolved steep topography can in a non-linear system affect large-scale waves. The convergence of the solution as the grid size is reduced will be slow unless the numerical scheme can prevent the false cascade of energy to small scales. In a purely two dimensional flow, governed by conservation of absolute vorticity, η, a false cascade may be prevented by using a scheme that conserves enstrophy, $\frac{1}{2}\eta^2$, and kinetic energy. In the presence of topography

a two-dimensional barotropic flow is governed by conservation of absolute potential vorticity, $q = \eta/\pi$, where π is the surface pressure. In this case a numerical scheme that conserves potential enstrophy and total energy will guarantee an upper bound on the absolute enstrophy and once again prevent the cascade to small scales.

As reported by Arakawa at last year's NASA Weather and Climate Program Review, a preliminary study using shallow water equations with steep topography showed that a potential enstrophy conserving scheme was superior to a conventional scheme when the grid size was comparable to the scale of variation of the topography. These ideas have been extended to the general circulation model equations in the following way: The equation of motion and continuity in a σ-coordinate may be written in the form

$$\frac{\partial \vec{V}}{\partial t} = \eta\, \vec{k} \times \vec{V} - \dot{\sigma} \frac{\partial \vec{V}}{\partial \sigma} - \nabla(\phi + \tfrac{1}{2}\, \vec{V}\cdot\vec{V}) - \sigma\alpha\nabla\pi$$

$$\frac{\partial \pi}{\partial t} = -\nabla\cdot(\pi \vec{V}) - \frac{\partial}{\partial \sigma}(\pi\dot{\sigma})$$

These equations guarantee conservation of $\overline{\tfrac{1}{2}q^2\pi\Delta\sigma} = \overline{\tfrac{1}{2}\eta^2/\pi\Delta\sigma}$ for a layer between two material surfaces separated by an amount $\Delta\sigma$, provided V is independent of σ within the layer, $\nabla\alpha \times \nabla\pi = 0$, and the vorticity is defined in terms of gradients at constant σ. The numerical scheme guarantees conservation under these constraints when the material surfaces coincide with its σ-coordinate surfaces.

The modified σ-coordinate system

A major deficiency noted in the previous version of the UCLA general circulation model was a lack of organization in fields strongly influenced by the planetary boundary layer. Precipitation in the tropics, for example, was less sensitive to sea surface temperature than in either nature or earlier versions of the model. This was thought to be due to the indirect way in which the general circulation and the parameterized PBL were coupled.

In the old model layers were defined by conventional σ-coordinate surfaces, as indicated by the heavy lines in the upper half of figure 1. The well-mixed planetary boundary layer, whose depth was predicted, was then allowed to occupy any fraction of the lower atmosphere. Typically, it was confined to a part of the lowest general circulation layer, as shown on the right of the figure, but it could also penetrate to higher

layers, as shown on the left. Coupling between this PBL and the general circulation model was handled by writing prognostic equations for the magnitude of the discontinuities at the top of the PBL and diagnostic relations for PBL properties.

We felt that the difficulties arising from the weak coupling between PBL and general circulation model in this scheme may be overcome by making the top of the PBL a coordinate surface. We therefore redefined the vertical coordinate as follows:

$$\sigma = \frac{p - p_I}{p_B - p_I} \qquad p_I \leq p \leq p_B$$

$$\sigma = \frac{p - p_B}{p_s - p_B} + 1 \qquad p_B \leq p \leq p_s$$

where p_I is a constant pressure above which we use pressure coordinates, p_B is the pressure at the PBL top, and p_s is the surface pressure. The PBL top then corresponds to $\sigma = 1$ and the earth's surface to $\sigma = 2$. This coordinate allows us to make the PBL the lowest GCM layer, and PBL quantities become the prognostic variables from which the jumps at the PBL top are defined. To improve the accuracy of the jumps, vertical resolution is increased immediately above the PBL. The model is being run with the 9-level (15-level when the stratosphere is included) structure shown in figure 2.

These changes have been coded into the new version of the UCLA general circulation model. The model has been tested for an idealized limited domain and is now being tested with global simulation experiments.

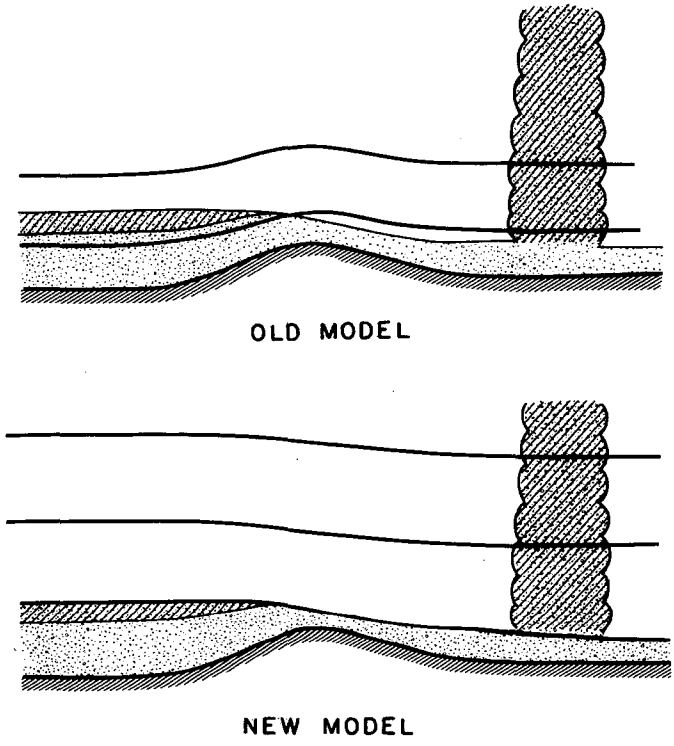

Figure 1 - Schematic of the model's layers near the ground in the old and new σ-coordinates. Note that in the new version the PBL coincides with the lowest layer

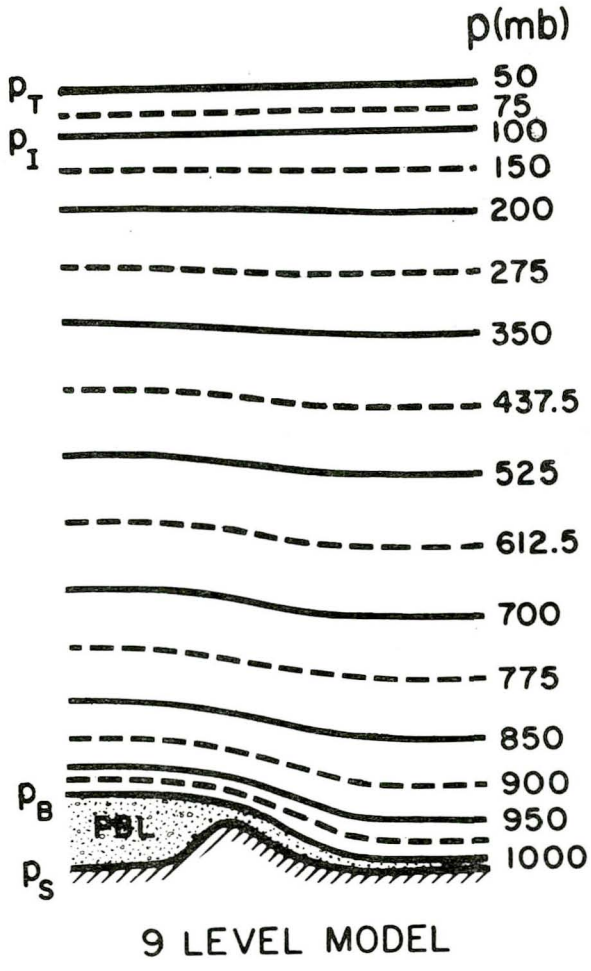

Figure 2 - Vertical structure of the new 9-level model. Pressures refer to the case when the PBL top is at 1000mb.

Page intentionally left blank

Paper No. 27

THE EFFECT OF CLOUDS ON THE EARTH'S RADIATION BALANCE

G. F. Herman, *University of Wisconsin, Madison, Wisconsin,*
M. L. Wu, *National Research Council, Washington, DC, and*
W. T. Johnson, *Sigma Data Services Corporation, c/o Goddard Space Flight Center, Greenbelt, Maryland*

ABSTRACT

The effect of global cloudiness on the radiation balance at the top of the atmosphere is studied in general circulation model experiments. Wintertime simulations were conducted with clouds that had realistic optical properties, and were compared with simulations in which the clouds were transparent to either solar or thermal radiation. Clouds increase the net balance by limiting longwave loss to space, but decrease it by reflecting solar radiation. It is found that the net result of cloudiness is to maintain net radiation which is less than would be realized under clear conditions: Clouds cause the net radiation at the top of the atmosphere to increase due to longwave absorption, but to decrease even more due to cloud reflectance of solar radiation.

1. INTRODUCTION

The role that clouds play in maintaining the global radiation budget is complicated and poorly understood. Clouds affect fluxes and flux divergences by absorbing and scattering solar radiation, and by absorbing, scattering, and emitting thermal radiation. At the same time, the occurrence of clouds depends on surface and atmospheric temperature, both of which are determined in part by the radiation field. Attempts to deduce the role of clouds from observations (e.g., Ellis, 1978), from simplified models (e.g., G. Hunt, 1977), or from global circulation models (e.g., B. Hunt, 1978) have led to conflicting conclusions because of the variety of physical processes that actually were investigated.

We present here a preliminary analysis of the results of GLAS (Laboratory for Atmospheric Sciences) general circulation model experiments that were designed to demonstrate the potential role that clouds play in determining mean monthly climate through their interaction with the radiation field. Attention is focused on the net radiation of earth-atmosphere system (RNEA) as it is affected by cloud interacting with short- and long-wave components, respectively.

2. SUMMARY OF EXPERIMENT

The GLAS General Circulation Model

A version of the model was used that was similar to those described by Somerville et al. (1974), Stone et al. (1977), and Herman and Johnson (1978). It differed in its use of the Wu et al. (1978) longwave radiation code, which was called every 5 hours, sea surface temperatures which varied smoothly during the experiment, Shapiro filtering of wind, temperature, moisture and sea level pressure fields, and fixed snow line. The initial state was defined from the 1 January 1975 0000GMT National Meteorological Center (NMC) global analysis. The integration period was 30 days.

The control was a standard January simulation with fully active short- and long-wave radiation calculations, and fully active cloud formation processes, i.e., convection and supersaturation. In the control, both the cloud and radiation computations are completely consistent with the model's other hydrodynamic and thermodynamic processes.

In one experiment ("solar transparency") all cloud and radiation calculations were carried out as in the control, but the cloud fraction was fixed at zero in the solar radiation calculation (cf. Lacis and Hansen, 1974). Thus, clouds formed, liberated latent heat, and emitted longwave radiation, but were otherwise transparent to the streams of solar radiation. The second experiment ("thermal transparency") specified zero cloud fraction in the Wu longwave calculations, but retained the model-generated cloudiness in all calculations, including solar radiation. We deduce the cloud effect by comparing the control with the "transparent" simulations, and attribute differences in the model climatology to the absence of thermal or solar radiative interactions with global clouds.

3. RESULTS AND DISCUSSION

Cloud affects the terrestrial radiation balance in the solar spectrum by reflecting radiation to space, thus decreasing solar radiation available to the earth-atmosphere system, or by increasing absorption path lengths by multiple scattering, thus increasing solar heating. In longwave regions of the spectrum, clouds absorb radiation emitted from the atmosphere's lower layers ("greenhouse effect") diminishing the total longwave loss to space. Cloud effects are illustrated in Table 1, which shows the effect of solar and thermal cloud transparency on various components. For comparison, the observational results of Raschke et al. (1973) also are included.

When clouds do not interact with thermal radiation (column C) the net longwave loss at the top of the atmosphere increases by

Table 1. Radiation balance for real and transparent cloud conditions (Wm^{-2}).

	(A) Control	(B) Solar transparency	(C) Thermal transparency	(D) Observations
1. Net thermal at top				
N. hemisphere	-207	-215	-236	-232
S. hemisphere	-213	-223	-253	-239
Global	-210	-219	-244	-235
2. Solar absorption (earth-atmosphere)				
N. hemisphere	165	199	159	174
S. hemisphere	332	429	327	330
Global	249	314	243	252
3. Albedo (earth-atmosphere)				
N. hemisphere	.29	.13	.31	.27
S. hemisphere	.31	.13	.33	.29
Global	.30	.13	.33	.28
4. Net radiation (thermal loss minus absorbed solar)				
N. hemisphere	- 42	- 16	- 77	- 56
S. hemisphere	119	206	74	91
Global	39	95	- 1	17

34 Wm^{-2} (16%) globally, and by comparable values in the northern and southern hemispheres. The solar radiation absorbed by the earth-atmosphere system is essentially unaffected, as might be surmised from purely radiative arguments. Similarly, there is no significant change in the planetary albedo, which suggests that the maintenance of global cloudiness is largely independent of cloud longwave radiative processes. The net radiation at the top of the atmosphere in the northern and southern hemisphere, and globally, decreases by 35, 45, and 40 Wm^{-2}, respectively. The effect of clouds on the longwave radiation is therefore comparable to the net radiation itself during the winter.

The role of clouds in the solar radiation balance is shown in column B. When clouds are transparent to solar radiation, thermal radiation at the top of the atmosphere becomes slightly more negative because of warmer surface and atmospheric temperatures. Solar radiation absorbed by the earth-atmosphere system increases by 34 Wm^{-2} (21%) in the northern hemisphere, 97 Wm^{-2} (29%) in the southern hemisphere, and 65 Wm^{-2} (26%) globally.

The predominant effect of cloudiness in the radiation balance is in determining the planetary albedo. In general, clouds maintain the planetary albedo near its observed value of 33% as compared with an albedo of 13% with non-interacting clouds.

The net cloud effect is seen in row 4. During the winter in the northern hemisphere, the difference between the solar and thermal cloud effect is -9 Wm^{-2}, i.e., the balance would become 35 Wm^{-2} more negative due to longwave effects, by only 26 Wm^{-2} more positive due to solar effects. The trend is reversed in the southern hemisphere; Longwave effects would decrease the net radiation by 45 Wm^{-2}, but this would be more than compensated by the solar increase of 87 Wm^{-2}. On a global basis, the solar effect (56 Wm^{-2}) dominates the longwave effect (40 Wm^{-2}).

Evidently, clouds affect the radiation balance mainly through their effect on the planetary albedo. This result is in agreement with the observational analysis of Ellis (1978), where it was concluded that the cloud effect on solar radiation dominated that on longwave radiation at almost all latitudes during all seasons studied. G. Hunt (1978) reached a similar conclusion based on one-dimensional radiative transfer calculations.

It has frequently been argued (cf. Cess, 1976) that the greenhouse effect of clouds would dominate or cancel the cloud effect on solar radiation. While this hypothesis may be valid on a regional basis, such as the Arctic, it is not supported by the results obtained here.

REFERENCES

Cess, R. D., 1976: J. A. S., 33, 1831-1843.

Ellis, J. S., 1978: Ph.D. Thesis, Colorado State Univ.

Herman, G. F., and W. T. Johnson, 1978: M. W. R., 106.

Hunt, G. E., 1977: J. Q. S. R. T., 18, 295-307.

Hunt, B. G., 1978: Q. J. R. M. S., 104, 91-102.

Lacis, A. A., and J. E. Hansen, 1974: J. A. S., 31, 118-133.

Raschke, E., et al., 1973: NASA TN D-7249.

Somerville, R. C. J., et al., 1974: J. A. S., 31, 84-117.

Stone, P. H., et al., 1977: M. W. R., 105, 170-194.

Wu, M. L., et al., 1978: Third Conf. Atmos. Rad., Davis, CA.

Paper No. 28

A TEST OF A CUMULUS PARAMETERIZATION MODEL USING THE GATE DATA

D. Rodenhuis, *Meteorology Program, University of Maryland, College Park, MD 20742*

ABSTRACT

Two parametric, ensemble cloud models have been tested with data obtained during GATE (1974). The first model is an adaption of the Arakawa-Schubert scheme which uses an entraining jet to represent individual cumulus cloud types. The second model consists of an ensemble of cylindrical cells to represent the convective cloud field.

INTRODUCTION

An important feature of synoptic-scale numerical prediction models and for planetary-scale general circulation models is the parameterization of cumulus convection. For integrations over short time periods, it is possible to treat subgrid-scale convection in an extremely artificial way, or ignore it altogether. However, when the period is large, and especially in the tropics, convection is an important mechanism for the vertical transport of heat, moisture and momentum. Even when the period is short ($\gtrsim$1 day) and the large-scale flow is not influenced by convective activity, the prediction of convective rainfall and cloudiness are still important objectives of the local weather forecast and climate of a region.

In preparation for a study of parameterized convection in a predictive model where physical processes are not free to be chosen arbitrarily, we have studied several parameterization models in a diagnostic sense, using observations of synoptic-scale variables to determine the characteristics of convection rather than the reverse. If these models give reasonable results, their ultimate application will be in a prediction scheme in NWP and GCM models.

The first part of the study investigates the sensitivity of the Arakawa-Schubert parameterization method. Lord (1978) has completed a more extensive study using a different numerical procedure ("overadjustment"). We have also compared our more limited results with those obtained using an overadjustment procedure by Schubert and Silva-Diaz (personal communication).

The second part of the study is a test of an ensemble of cellular convective elements (Cheng, 1978; Rodenhuis and Cheng, 1979). The results of this model are compared to those of Nitta (1977) who also used the entraining jet cloud model of Arakawa and Schubert (1974) to explain the residual term in a budget calculation.

RESULTS

Sensitivity Tests of the Entrainment Model

Figure 1 shows the results of computing the detrainment level for each cloud type which is identified by a constant entrainment coefficient, λ. The input data is the composite of Nitta (1977) for unorganized convection in GATE (6 September 1974). (The radiational heating rate, Q_R=0 for these studies.) Three cases are shown corresponding to different conditions at the cloud base:

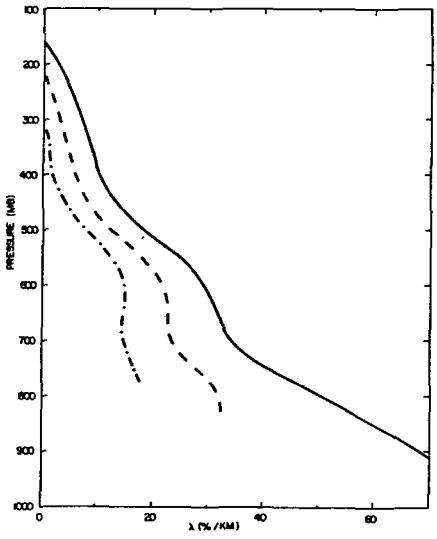

Fig. 1. The detrainment level of model clouds as a function of the detrainment rate (λ). Case 1 (solid); Case 2 (dashed); Case 3 (dash-dotted).

Case 1: Cloud base and top of the mixed layer all identical; cloud elements are neutrally buoyant at cloud base.

Case 2: Cloud base is identical with Case 1, but the top of the mixed layer is assumed to be 25 mb below; cloud elements have the properties of the environment within the mixed layer.

Case 3: Cloud base and the top of the mixed layer are identical; cloud elements have the same properties as the environment at the cloud base ($\Delta h = \Delta s_v = 0$).

These rather small changes in conditions which are applied at the cloud base strongly influence the spectra of convective cloudiness as shown in Fig. 2. Only in Case 1 is there a large number of small cumuli which are considered to be so essential for the moisture budget of an atmosphere with imbedded deep convection.

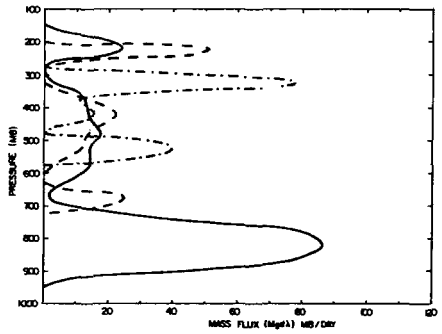

Fig. 2. The cloud mass flux spectrum as a function of detrainment level for the three cases shown in Fig. 1.

Figure 3 shows a comparison of our results (University of Maryland [UM]) with those from a calculation of W. Schubert and P. Silva-Diaz (Colorado State University [CSU]; personal communication). For this comparison, identical input data was used. The differences are due almost entirely to the method of integration in the calculation of $\lambda(z)$:

$$\overline{h^*} = h_c(z,\lambda) = \frac{1}{\eta(z,\lambda)} \left[h_c(z_B,\lambda) + \lambda \int_{z_B}^{z} \eta(z',\lambda)\overline{h}(z')dz' \right] \quad (1)$$

where $\overline{h^*}$ and h_c are the moist static energy in the environment and cloud, respectively. The * indicates scattered values.

$\eta(z,\lambda)$ is specified exponential function of height and λ.

z_B is the height of the cloud base.

Note that there is a gap in the spectrum of the CSU results between 875 and 925 mb (dashed line) which does not occur in the UM calculation.

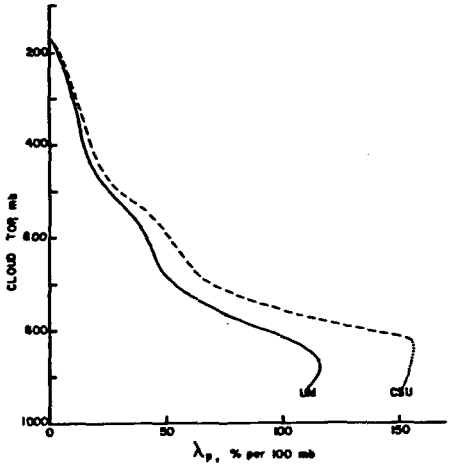

Fig. 3. The detrainment level of model clouds as a function of detrainment rate (λ) computed with two different methods.

This discrepancy accounts for some of the differences in the cloud spectra seen in Fig. 4. In addition, the UM results have been simply minimizing the residual term in the equation (the equilibrium hypothesis):

$$\frac{dA}{dt} = \int K(\lambda,\lambda') \, M_B \, d\lambda + \overline{F} \doteq 0 \qquad (2)$$

where A is the cloud work function

$\underline{K}$ is the cloud:cloud interaction matrix

$\overline{F}$ represents the large-scale forcing function

and M_B is the cloud base mass flux.

However, Schubert uses a different method (described by Lord, 1978), which modifies $\overline{F}$ to accommodate changes in A which occur over a small arbitrary period of time, Δt. Thus, Schubert's results depend on Δt, as can be seen in Fig. 4 for the 2 cases of CSU results.

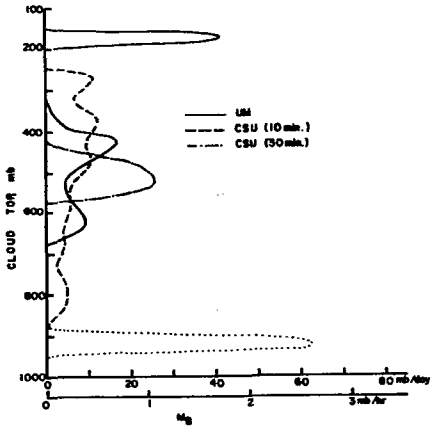

Fig. 4. The cloud mass flux spectrum as a function of detrainment level for three cases.

Note that the UM results do not prohibit low cloud types (Fig. 3), but they are not required for the solution of (2). However, we do require high clouds detraining at 175 mb. By way of control, the CSU results of 875 mb (dotted curve) prohibit cloud tops at that level, but not more shallow clouds. Therefore, a large number of shallow clouds are required to satisfy the equilibrium condition, at least for Δt=10 min.

Comparison with the Cellular Model

Figure 5 (top) shows the results of cloud spectra obtained by using an ensemble of cellular convective elements (Rodenhuis and Cheng, 1979). This result also differs from those in Figs. 2 and 4, because an entirely different method is used to compute the cloud number density and mass flux. Rather than imposing the equilibrium hypothesis (2), the net-heating-and-moisture-deficit budget is satisfied:

$$Q_1 - Q_2 - Q_R = -\frac{\partial}{\partial p}(F_\theta) - L\frac{\partial}{\partial p}(F_q) \qquad (3)$$

where Q_1 = net cumulus heating
Q_2 = net cumulus moisture deficit
Q_R = radiational heating rate
F_θ = net cumulus heat flux
F_q = net cumulus moisture flux.

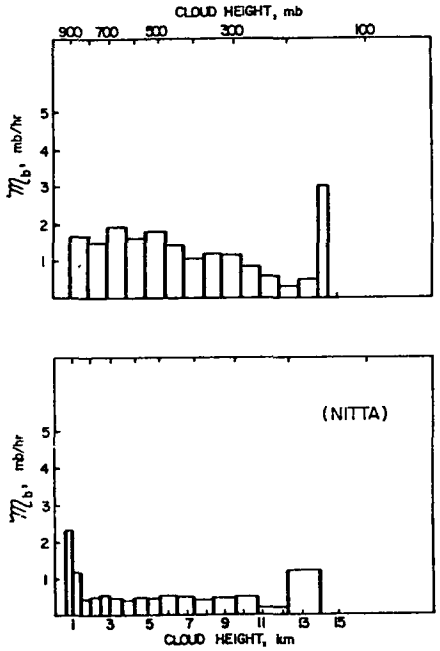

Fig. 5. A comparison of cloud base mass flux determined from the cellular model (upper) and determined by Nitta (1977). Input data (6 September 1974, GATE) for both results are identical.

Although there are some similarities between Figs. 2, 4, and 5, there are serious discrepancies in every case. (Some differences are due to different values of Q_R.)

Comparison with the Entrainment Model

The entrainment cloud model has also been used with (3) by Nitta (1977) to determine the cloud spectra. These results are shown in Fig. 5 (lower). The relatively large number of lower cloud agrees (perhaps fortuitously) with Case 1 of Fig. 2. There is some similarity between the upper and lower parts of Fig. 5, but the bimodal distribution does not occur with the cellular model because of the increased mass flux of middle-level clouds.

CONCLUSIONS

The spectra of the cloud base mass flux has been calculated by two different methods: (1) by an application of the equilibrium hypothesis, equation (2), and (2) by using the bulk budget method, equation (3). In each cse we have shown two independent calculations using different computational schemes (UM and CSU),

or using different models (entrainment model and the cellular model). Our results using the equilibrium hypothesis show that the spectra are very sensitive to the conditions at the cloud base. Furthermore, the results depend on the computational scheme which is used. Finally, the spectra do not agree very well with those calculated from the budget method, although differences in Q_R account for some of this discrepancy.

When the cellular model is used with the budget method, the results are in general agreement with Nitta's spectra, although there is not a strong bimodal mass flux distribution. The rainfall estimate with the model is 10.21 mm/day, as compared to 10 mm/day from the average of the shipboard observations during the period. Other evidence (Cheng, 1978) shows that the cellular model behaves reasonably over a wide range of conditions.

In addition, the ensemble cellular cloud model can diagnose the cloud areal fraction and number density of each cloud type. Figure 6 shows these new spectra for the same period of analysis as has been used throughout this study. These results may be used to compare with independent, direct measurements of cloud dimensions from radar or satellite radiometers. This is an extremely useful link between cloud parameterization in numerical models and direct observations of clouds, especially from satellite platforms.

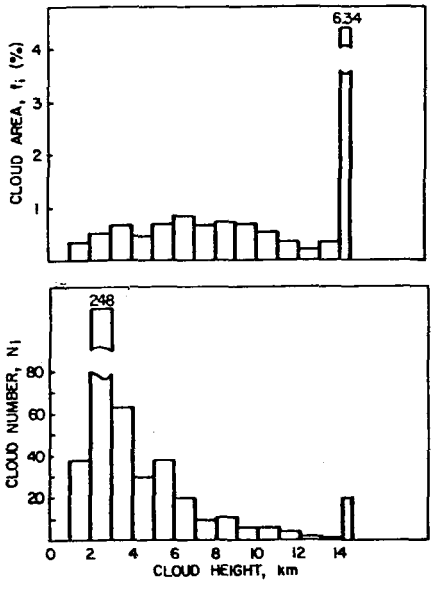

Fig. 6. Spectra of cloud areal fraction and number density as a function of closed height determined from the ensemble cellular model.

REFERENCES

Arakawa, A., and W. H. Schubert, 1974: Interaction of a cumulus cloud ensemble with the large-scale environment, Part I. J. Atmos. Sci., 31, 674-701.

Cheng, C-S, 1978: Diagnostic study fo tropical cumulus intensity using a cellular convection model. Ph.D. dissertation, Univ. of Md., 173 pp.

Hack, J. J., and W. H. Schubert, 1976: Design of an axisymmetric primitive equation tropical cyclone model. Atmos. Sci. Paper No. 263, Colo. State Univ., 70 pp.

Lord, S. J., 1978: Development and observational verification of a cumulus cloud parameterization. Ph.D. dissertation, Univ. of Calif., 358 pp.

Nitta, T., 1977: Response of cumulus updraft and downdraft to GATE A/B-Scale motion systems. J. Atmos. Sci., 34, 1163-1186.

Rodenhuis, D., and C-S Cheng, 1979: An ensemble model of cellular convective elements. In preparation.

Paper No. 29

EFFECT OF A PACIFIC SEA SURFACE TEMPERATURE ANOMALY ON THE CIRCULATION OVER NORTH AMERICA

J. Shukla and B. Bangaru, *Massachusetts Institute of Technology, Cambridge, Massachusetts, Sigma Data Services Corporation, c/o Goddard Space Flight Center, Greenbelt, Maryland*

ABSTRACT

During the fall and winter of 1976-77, sea surface temperature (SST) in the north Pacific was characterized by abnormally cold temperatures in the central and western portions of the north Pacific with a warm pool located off the west coast of the U. S. (Figure 1). Namias (1978) has suggested that the north Pacific SST anomalies may have been one of the multiple causes of the abnormally cold temperatures in eastern North America during the 1976-77 winter. This study attempted to test this hypothesis by conducting a numerical experiment with the GLAS general circulation model.

INTRODUCTION

The model used in the present study is the one described earlier by Somerville et al. (1974) and Stone et al. (1977). A modified version of the model has also been presented in the proceedings by Halem et al. (1978). The experiments were performed by first integrating the GLAS GCM for 45 days with the climatological mean SST and the observed initial conditions valid for January 1, 1975. This integration is referred to as the Control run (C). The climatological SST field was then changed by adding a time invariant anomaly field and therefore, although the climatological SST varied with season, the imposed anomaly field remained constant with time. The structure of the imposed SST anomaly was the same as shown in Figure 1, but the numerical values were exaggerated by considering them in °C rather than °F. The model was integrated again for 45 days and will be referred to this run as the Anomaly run (A).

Control Run C and Anomaly Run A were further repeated with their respective boundary conditions in SST but the initial conditions in u, v, T, and surface pressure were randomly perturbed. The spatial variation of the random perturbations corresponded to Gaussian distributions with zero means and standard deviations of 1°C in temperature, 4 m/s in horizontal wind components and 3 mb in surface pressure over land points and 2°C in temperature, 8 m/s in horizontal wind components, and 6 mb in surface pressure over ocean points.

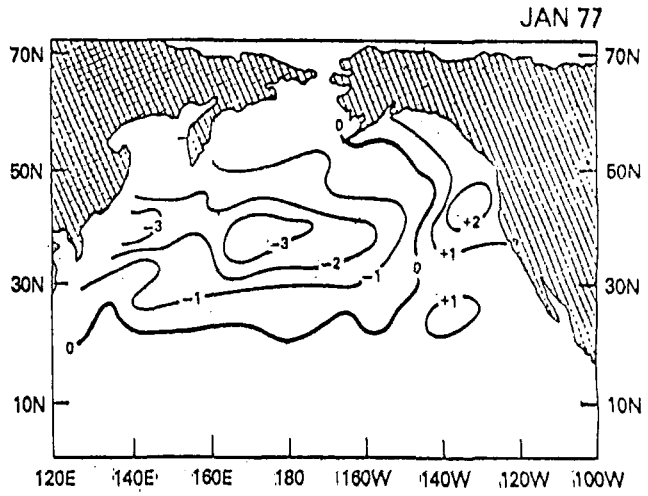

Fig. 1. Observed sea surface temperature anomaly (°F) during January 1977.

These runs are referred to as Initial Condition Perturbation Runs C_1 and A_1 for Control (C) and Anomaly (A), respectively. Four additional Initial Condition Perturbation Runs were already made by Spar et al. (1978) which are referred to as C_2, C_3, C_4, and C_5. The atmospheric parameters for the six runs are referred to as C, C_1, C_2, C_3, C_4, C_5, as the mean control (Cm) and the average of two anomaly runs A and A_1 as mean anomaly (Am). In order to assess the response of the imposed SST anomaly on the atmospheric circulation, the differences between the mean control and the mean anomaly runs averaged for the period between day 15 through day 45 are examined and the magnitude of the differences is compared with respect to the standard deviation among the mean monthly values for the six control runs for this period.

Figure 2a shows the differences between the mean anomaly and the mean control runs for the 700 mb temperature. The largest differences are found along the International Date Line, which is the longitude of maximum negative anomaly in SST, and the eastern parts of Canada, and the northern U. S. A positive anomaly is found over Greenland. Occurrence of colder 700 mb temperatures over the cold anomaly and warmer 700 mb temperatures over the warm anomaly can be explained by considering the radiative, sensible and latent heat fluxes. A detailed examination of the model-generated heat fluxes showed that the evaporation and convective cloudiness decreased over the cold anomaly. Reductions in the moisture and the sensible heat flux, which reduces the convective clouds, causes a reduction in the latent heat of condensation and this can also cause cooling of the atmospheric temperatures. Consistent with the decrease in the convective

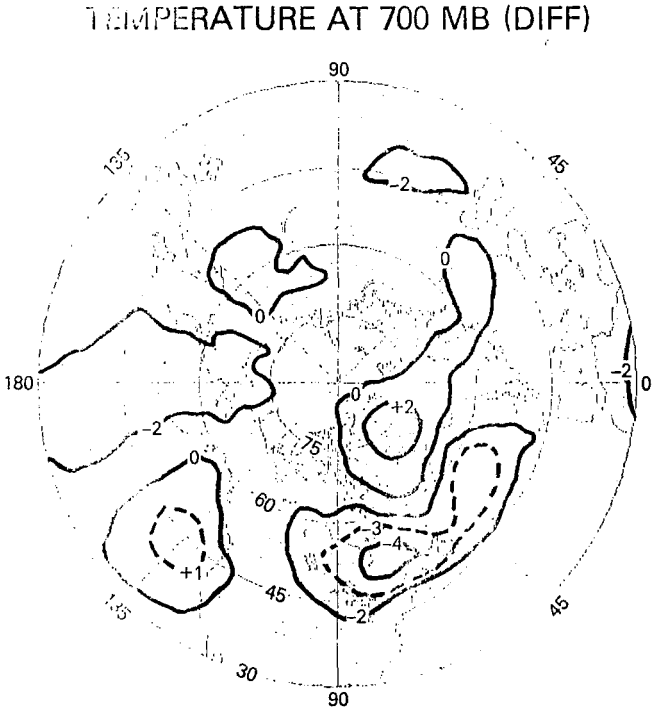

Fig. 2a. Temperature at 700 mb (Difference).

cloudiness, it was also found that the solar flux at the surface increased but the long wave flux at the surface decreased. Since the sea surface temperatures were prescribed, this feedback does not operate in the model. It should be noted, however, that the net effect of these diabatic heat sources and sinks is such that the heat source (sink), which is initially confined to the lower boundary, finally extends into the troposphere.

The most interesting feature in this figure is the coldest 700 mb temperatures centered around 50N, 75W. This is clear evidence of the downstream response of the model to the SST anomalies in the Pacific. Figure 2b shows the ratio of the differences and the standard deviations among the six control runs. These ratios are the signal-to-noise ratio. Two areas of maximum signal to noise are found, one over the anomaly itself and the other centered around 50N, 75W. The positive temperature anomalies over Greenland were found to have a signal-to-noise ratio less than two.

In the earlier numerical experiments with the NCAR model (Kutzbach et al. [1977], Chervin et al. [1976]) no significant downstream effect was noticed. Although the two general circulation models are not identical (especially with regard to

their simulation of the transient eddies), in GLAS' opinion, the primary reason a downstream effect was observed in the GLAS model was due to the nature of the spatial structure of the SST anomaly.

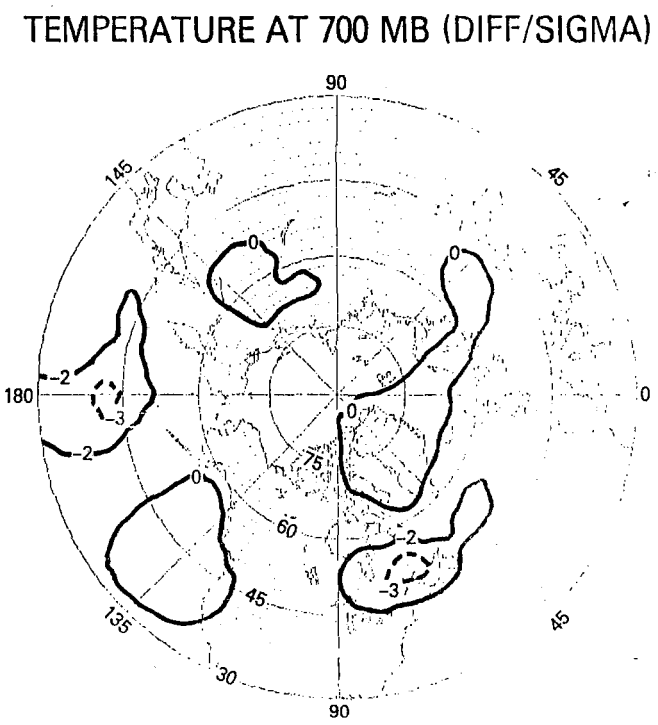

Fig. 2b. Temperature at 700 mb (Difference/Standard Deviation).

The results of these numerical experiments support the hypothesis by Namias that the SST anomalies over the Pacific during the 1976-77 winter may be one of the contributing factors towards very cold temperatures over the northeast U. S. and warm temperatures over the Alaska region. Since this was not a coupled ocean-atmosphere model, SST anomalies were assumed to persist for the whole period of integration. This assumption is justified byu the observed fact that the SST anomalies do persist for a time period ot several months.

These results show clear evidence of a downstream response of the model atmosphere to the imposed SST anomalies over the Pacific. It is interesting to note that for some levels the downstream effect away from the anomaly is more than the effect over the anomaly itself. Since the natural variability of the mid-latitude atmosphere is rather large, the standard deviation among six predictability runs was calculated and the ratios of the mean differences to the standard deviations indicated that the downstream effects are indeed significant.

The results of the present study suggest that the downstream orographic barriers may contribute to amplify the SST-generated atmospheric perturbations. In other words, an orographically forced atmospheric flow regime may be more sensitive to further modification by the perturbations generated by the SST anomalies. This qualitative conjecture is suggested by those numerical experiments in which it is found that the effects of the north Pacific SST anomalies are most prominent on the western and the eastern sides of the North American continent. This is of special significance for the winter of 1976-77 because, as pointed out by Namias (1978), the anomalous flow pattern over North America was in phase with the normal winter flow pattern. Therefore, this was interpreted as an inphase amplification of the normal winter circulation, which is orographically and thermally forced by the mountains and the mean heat sources and sinks. The purpose of this numerical experiment was not to simulate the actual events of the 1976-77 winter but only to examine the effects of similar SST anomalies on the model atmosphere. It should be noted that the atmospheric conditions in the mean control run corresponded to the winter of 1975.

Detailed examination of the model-simulated daily charts indicated that in general the anomaly runs did not show a persistent blocking pattern near the west coast of the U. S. as observed during the 1976-77 winter. However, there were periods of 3-5 day duration in which the ridge over the west coast of the U. S. was highly intensified and such events were more frequent in the anomaly run compared to the control run. Blocking situations do occur but they do not last too long. It is not clear whether this is a manifestation of some model deficiency or it is because the model integrations are not performed long enough for several interannual cycles.

References

Chervin, R. M., W. M. Washington, and S. H. Schneider, 1976: Testing the statistical significance of the response of the NCAR general circulation model to north Pacific Ocean surface temperature anomalies. J. Atmos. Sci., 33, pp. 413-423.

Halem, M., J. Shukla, Y. Mintz, M. L. Wu, R. Godbole, and Y. Sud, 1978: Climate comparisons of a winter and summer numerical simulation with the GLAS general circulation model. Proceedings at the JOC Study Conf. on Climate Models, April 3-7, Washington, DC.

Kutzbach, J. E., R. M. Chervin, and D. H. Houghton, 1977: Response of the NCAR general circulation model to prescribed changes in ocean surface temperature, Part 1: Mid-latitude changes. J. Atmos. Sci., 34, pp. 1200-1213.

Namias, J., 1978: Multiple causes of the North American abnormal winter 1976-77. Mon. Wea. Rev., 106, pp. 279-295.

Somerville, R. C. J., P. H. Stone, M. Halem, J. E. Hansen, J. S. Hogan, L. M. Druyan, G. Russell, A. A. Lacis, W. J. Quirk, and J. Tenenbaum, 1974: The GISS model of the global atmosphere. J. Atmos. Sci., 31, pp. 84-117.

Spar, J., J. J. Notario, and W. J. Quirk, 1978: An initial state perturbation experiment with the GISS model. Mon. Wea. Rev., 106, pp. 89-100.

Stone, P. H., S. Chow, and W. J. Quirk, 1977: The July climate and a comparison of the January and July climates simulated by the GISS general circulation model. Mon. Wea. Rev., 105, pp. 170-194.

Paper No. 30

SENSIBLE AND LATENT HEATING OF THE ATMOSPHERE AS INFERRED FROM DST-6 DATA

G. F. Herman and S. D. Schubert, *University of Wisconsin, Madison, WI 53706* and W. T. Johnson, *Sigma Data Services Corp., c/o NASA/Goddard Space Flight Center, Greenbelt, MD 20771*

ABSTRACT

The average distribution of convective latent heating, boundary layer sensible heat flux, and vertical velocity are determined for the winter 1976 DST period from GLAS model diagnostics. Key features are the regions of intense latent heating over Brazil, Central Africa, and Indonesia; and the regions of strong sensible heating due to air mass modification over the North Atlantic and North Pacific Oceans.

1. INTRODUCTION

Radiative transfer, latent heat release, and sensible heating at the earth's surface are the principal sources of heating in the atmosphere. According to the zonally-averaged values of Newell et al. (1974), latent heating during the winter is a maximum in the mid-troposphere between 30N and 30S, with smaller maxima centered at 55N and 55S; radiation cools the troposphere everywhere except in the high latitudes of the Southern Hemisphere; and the transport of heat to the atmosphere from the underlying surface ("boundary layer fluxes") occurs everywhere outside of the polar regions, and is largest at 40° in the northern hemisphere, and 30° in the southern hemisphere. There have been numerous estimates of atmospheric radiative heating (cf. Hunt, 1977, for summary) but very little is known about the global distribution of either boundary layer heating or latent heating. Frequently boundary layer fluxes are deduced as a residual from the surface energy balance (e.g., Budyko, 1963), and average latent heating is estimated from precipitation measurements at the surface (e.g., Newell et al., loc cit).

We present here selected results from our diagnostic analysis of the winter 1976 Data Systems Test (DST) dataset which span the period 29 January to 4 March 1976. The analysis represents a synthesis of the comprehensive DST data with assimilation and forecast calculations carried out with the GLAS general circulation model. It will be demonstrated that GCM assimilations and forecasts for sufficiently short periods provide an internally consistent basis for estimating state variables in data sparse regions, and estimates of vertical fluxes and latent heat

release-quantities that normally are impossible to measure in nature.

2. SUMMARY OF ANALYSIS

The GLAS assimilation without satellite data ("NOSAT-7578") formed the basic global dataset. At an interval of 6 h throughout the duration of the DST period, boundary layer fluxes, and convective heating and vertical velocity (ω) at each grid point in the vertical were computed and stored along with approximately 21 other diagnostic quantities that were routinely calculated during the model integration. Here boundary layer flux refers to the flux of sensible heat from the surface, which may have either fixed or variable temperature, into the bottom layer of the model as computed by an empirical surface drag law. Latent heating refers only to the latent heat release from the parameterization of moist convection; it does not include the latent heat released when supersaturation occurs as a result of non-convective processes. Vertical velocity is computed from model-generated state variables, and is fully consistent with the model's thermodynamic calculations.

Averages were constructed for the entire period 29 January to 4 March, excluding the period 3-6 February which was deleted because of missing data.

3. RESULTS AND DISCUSSION

Figure 1 illustrates the average distribution of convective latent heating at level 5 in the model. Virtually all heating occurs in a band between 20N and 20S, and the largest values are found over northeast Brazil, equatorial Africa, and over Indonesia, and the southwestern tropical Pacific. In an independent analysis of DST-6 wind data, Paegle et al. (unpublished manuscript) computed the mean upper level flow divergence, and areas of maximum divergence correlate very well with the regions of maximum latent heating computed here. This correlation between heating and divergence illustrates the strong coupling between the latent heating and large-scale dynamics of the tropics, and supports the hypothesis that the large-scale dynamics in the tropics are in fact forced by the latent heating that occurs over Brazil, Africa, and Indonesia. Evidently, the largest latent heating rates occur over land, where heating rates are 4-6°C per day, as compared with 1-3°C per day over oceanic regions.

The average boundary layer flux of sensible heat (watts per square meter) is illustrated in Figure 2. The largest fluxes over land occur over southern South America, South and Central Africa, India, and Australia. Still larger fluxes of sensible heat (in excess of 150 Wm^{-2}) occur in the North Atlantic between Newfoundland and Iceland. Values in excess of 50 Wm^{-2} occur in the Barents Sea, the Sea of Okhotsk, and in the North Pacific

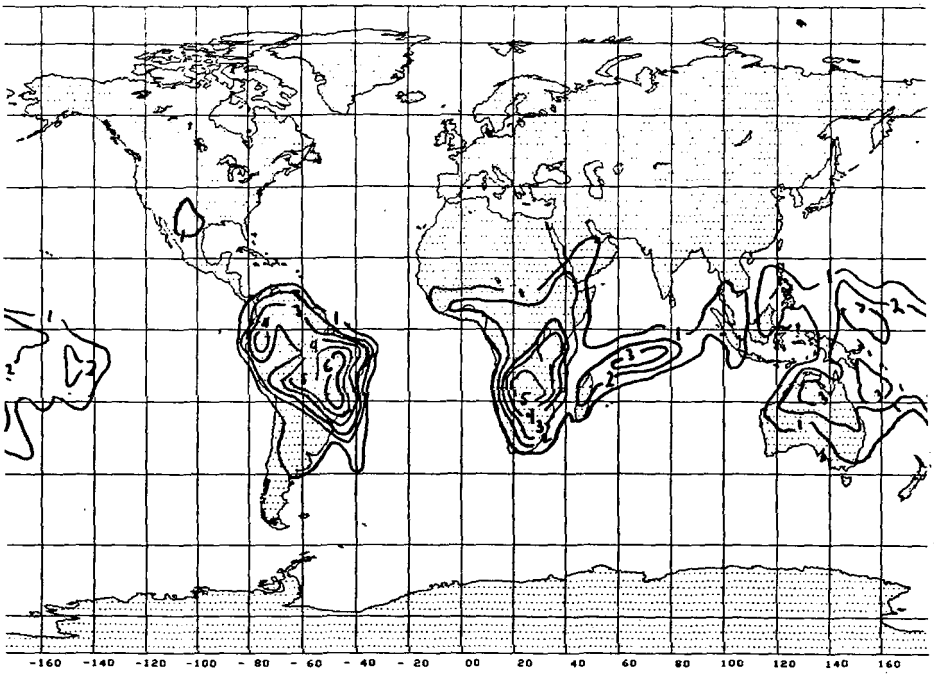

Fig. 1. Convective Latent Heating ($^{0}C\ Day^{-1}$).

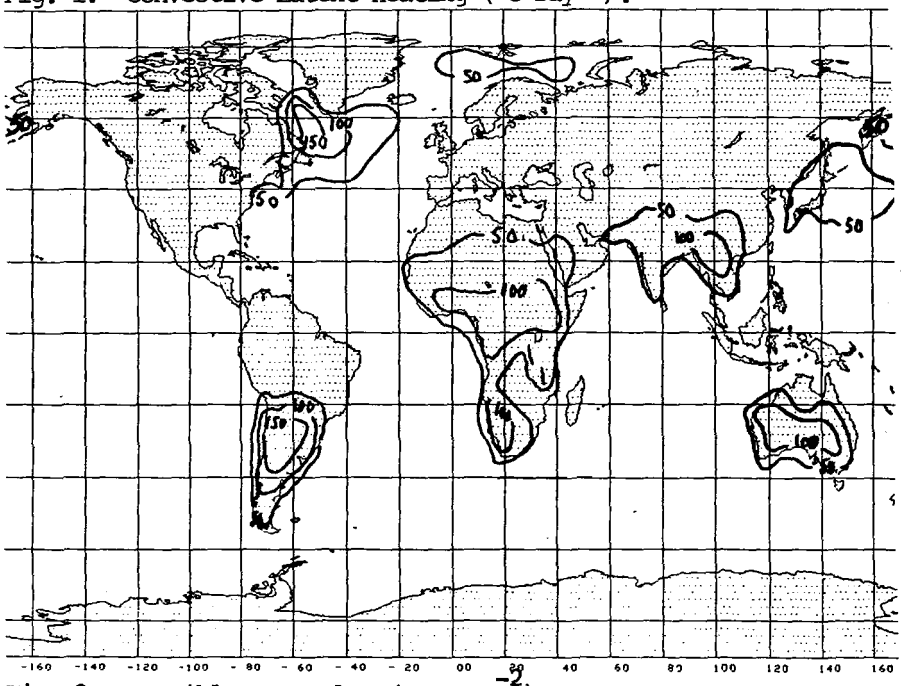

Fig. 2. Sensible Heat Flux (Watts m^{-2}).

between Siberia and the Aleutian Islands. These large fluxes in the high latitudes of the North Atlantic and North Pacific occur as a result of the strong and frequent air mass modification that occurs in these regions. During the winter cold Arctic air masses stream off the Canadian, Greenland, and Siberian continents over the relatively warmer waters of the Gulf Stream or Kuroshio. The large air sea temperature difference causes extensive convective heating in the lower layers of the air masses. (The simultaneous adjustment of ocean surface temperature is not calculated in the model at the present time.)

It has been recently demonstrated (Herman and Johnson, 1978) that the sea ice content of these same regions of the North Atlantic and North Pacific plays a key role in the wintertime climate of the northern hemisphere through its effect on sensible and latent heat fluxes. Sea ice extent and air mass modification obviously combine in a complicated way to determine the net diabatic heating in the high latitudes.

The average vertical velocity field at level 5 of the model (in microbars per second) is shown in Figure 3. The global field is, of course, very complicated. It is worth noting, however,

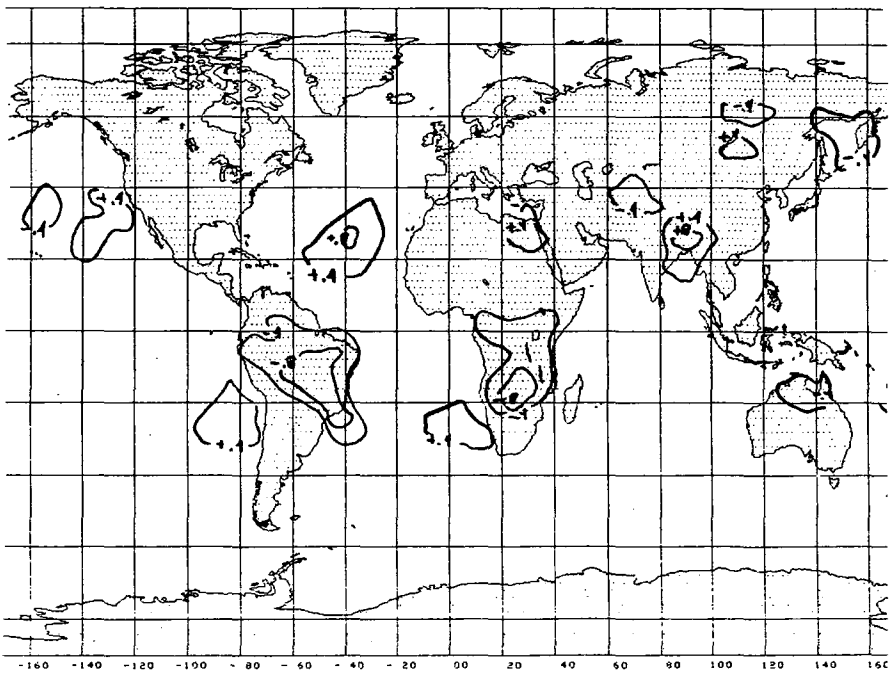

Fig. 3. Vertical Velocity (microbars sec^{-1}).

the strong and well defined regions of rising motion (ω negative) that occur in conjunction with the convective activity over Brazil and Africa; rising motion associated with air mass modification is found over the Sea of Okhotsk, and the regions of strong subsidence over the subtropical Atlantic and Pacific are also evident.

4. ACKNOWLEDGMENTS

This work was supported by NASA Grant NSG-5223 to the University of Wisconsin.

5. REFERENCES

Budyko, M. I., 1963: Thermal Balance of the Earth. Gidrometeo iz dat.

Herman, G. F., and W. T. Johnson, 1978: MWR, 106.

Hunt, G. E., 1977: J.Q.S.R.T., 18, 295-307.

Newell, R. E., et al., 1974: The General Circulation of the Tropical Atmosphere. MIT Press.

Page intentionally left blank

Paper No. 31

NUMERICAL METHODS FOR METEOROLOGY AND CLIMATOLOGY

E. Isaacson, D. Marchesin, G. Zwas, *Courant Inst. of Math'l Sciences, New York University*

ABSTRACT

Efficient numerical methods for long term weather forecasting are developed. One implicit and one explicit scheme are compared as to accuracy.

INTRODUCTION

It has been estimated that about 30% of the error in meteorological forecasts is attributable to the inaccuracy of numerical schemes currently used. In order to minimize this error, we have developed and tested two new numerical methods. These schemes are particularly designed to perform long term integrations for climatological purposes, since they conserve the global quantities: total mass, total energy, and total potential enstrophy of the flow. One of the schemes is implicit, while the other one is explicit. The greater inherent efficiency of the implicit scheme, for fine spatial grid calculations arises from the fact that its time step Δt may be an integer multiple of $\Delta X/U$, and is not required to be less than $\Delta X/(C+U)$ as is the case for explicit schemes, where ΔX is the smallest spatial interval size, U is the maximum speed of propagation of the flow, while C is the much larger maximum speed of sound waves in the flow. In other words, a much larger time step is permitted for implicit schemes. But, in order to derive this benefit it is essential that the amount of computer time used to solve the implicit equations at any time step, be a small multiple of the time needed to make one time step with an explicit scheme. Our application of these schemes indicates that indeed the implicit scheme requires less computer time than does the explicit scheme, for fine grid sizes.

In section 2, both the implicit and explicit methods are used to solve the shallow water equations

for a single-layered atmosphere over a smooth earth and comparisons of the solutions and of the computer time are made. In section 3, with orography present, a comparison is made of the solutions produced by the explicit scheme both with and without the conservation of the global quantities. Here it is observed that the solution produced while conserving the global quantities, is smoother and more accurate. In section 4, a brief description is given of the numerical schemes.

Application of schemes

The technique for devising an implicit scheme and the method for modifying both implicit and explicit schemes so as to conserve the global quantities were applied to the solution of the nonlinear shallow water equations for a single layered, incompressible fluid over a spherical earth. As initial conditions, three subtropical highs were centered symmetrically in each hemisphere on latitudes $\pm$ 30°, and at longitudes 0°, 120°E, 240°E. The initial wind speed is found geostrophically from the initial height field. The initial hydrostatic "pressure" (i.e. density·height) rose from 1036 (corresponding to 8500 meters) to 1046 at the center of the highs. The maximum of the initially geostrophic velocity is about 13 meters/sec. Contour levels of the initial "pressure" field are plotted, on a stereographic chart of the Northern Hemisphere, along with arrows indicating the initial wind speed and direction in Fig. 1. After 24 hours, we exhibit in Fig. 2, appropriately scaled height fields produced on one third of the Northern Hemisphere with a fine spherical grid using $\frac{360}{128}$ ° in both longitude and latitude. Fig. 2a was produced by the explicit scheme, while Fig. 2b was produced by the implicit scheme. Note how closely the "high" cells resemble each other after 24 hours. The left most column of numbers represent longitudes, that is row 73 corresponds to longitude $73\frac{360}{128}$ °. The rightmost column corresponds to the latitude nearest the equator and the second column from the left corresponds to the latitude nearest the North Pole.

For the explicit scheme a time step of 3 minutes was used, while in the implicit scheme an interval of 15 minutes was used. The table below lists the computing times (CPU) required on a 60 bit machine, the CDC-6600, for each method with both the fine grid and a coarse spherical grid of $360/64^{\circ}$ for latitude and longitude.

	explicit scheme	implicit scheme	revised implicit scheme
coarse grid	3 min	9 min	3 min
fine grid	24 min	36 min	12 min

Computing Times on CDC-6600

Note that the time step of 15 minutes was used in the implicit scheme for both the fine and coarse grids; whereas in the explicit scheme, 6 minutes was used for the coarse grid and 3 minutes was used for the fine grid. Both schemes produced solutions with comparable accuracy. Furthermore, we have observed that it is possible to revise the implicit scheme to take advantage of the special form of the hydrodynamic equations, so as to cut the computing time of the implicit scheme in half. This feature of the equations of motion is also present in the full hydrodynamic equations used for general circulation models. With this improvement the implicit scheme would run in less time than the explicit scheme, for fine grids.

Orography effects

A major source of computational errors is found to be the way in which current numerical methods treat flow over and around high and extensive mountain ranges, e.g. Rocky Mountains, Andes Mountains, Himalayan Mountains, etc. In order to eliminate this difficulty, Arakawa has advocated using difference schemes that conserve the total potential enstrophy, total energy, and total mass. We have found it possible to modify any difference scheme, so as to make the new scheme conserve these global quantities. In particular, we show the effect that this conservative modification has when we introduced orography into the shallow water model previously described in section 2. That is, we introduced three identical mountain ridges centered respectively along the three longitudes $60^{\circ}E$, $180^{\circ}E$, and $300^{\circ}E$. The maximum height

above sea-level of the mountain ridge is $\frac{8500}{16}$ meters, at the equator. The mountain height decreases to zero at the poles. The initial velocity is again found from geostrophic balance on the sphere. The fluid tends to flow around the ridges, by veering to the pole. In Fig. 3a, we see that the solution produced after 24 hours without the conservation of the global quantities has larger velocities and steeper height gradients near the pole, than does the solution shown in Fig. 3b, which is produced with the conservation of total mass, total energy, and total potential enstrophy. In the Table below we indicate the relative change from the initial values of these global quantities, after t=24 hours and after t=48 hours, for the explicit scheme. In the first column the larger relative deviations are found without the use of the conservative modification method; whereas the smaller relative deviations in the second column are produced with the use of the conservative modification method.

quantity	without conservative modification	with conservative modification
total mass (24 hours)	$140 \cdot 10^{-6}$	$0.2 \cdot 10^{-6}$
total energy (")	$203 \cdot 10^{-6}$	$0.5 \cdot 10^{-6}$
total pot.enstrophy	$5766 \cdot 10^{-6}$	$10.0 \cdot 10^{-6}$
total mass (48 hours)	$235 \cdot 10^{-6}$	$0.5 \cdot 10^{-6}$
total energy (")	$260 \cdot 10^{-6}$	$1.1 \cdot 10^{-6}$
total pot.enstrophy	$17,750 \cdot 10^{-6}$	$16.0 \cdot 10^{-6}$

Relative errors in total quantities.

The Numerical Schemes

The explicit scheme is a so-called leapfrog scheme in which the solution is advanced from $(t-\Delta t)$ and t to the time $(t+\Delta t)$. The first order time derivatives are replaced by differences centered at time t while the first order spatial derivatives in latitude and longitude, are replaced by fourth order, five point, centered difference expressions. At the latitudes closest to the pole, the values of the solution determined by this difference scheme are smoothed by using the fast Fourier transform. This

program has been adapted from the ideas of Kreiss and Oliger [4] and Williamson and Browning [6], and is described in Isaacson and Stoker [5].

The implicit scheme is roughly speaking a Crank-Nicolson type scheme in which the solution is advanced from time t to time $(t+\Delta t)$. Here the fourth order accuracy is obtained by using a Padé rational fraction in the spatial difference operators. After clearing fractions, by multiplying all terms by the denominator, we obtain a compact three point spatial difference expression. The resulting simultaneous difference equations are simplified by writing the spatial operator as the product of a longitudinal factor and a latitudinal factor. These factors have a block tri-diagonal matrix representation, that is easily invertible. This idea and its implementation were proposed by A. Harten based on the methods used by Beam and Warming [1,2] in aerodynamics. Considerable effort was needed to find an efficient and stable factorization method. Finally, it was found necessary to use a fourth order Shapiro filter at each time step in order to maintain stability.

The conservative modification method is described in general terms in Isaacson [3]. Here the work involved in modifying the solution found at time $(t+\Delta t)$ is of the order of the amount of calculation used in one time step of the explicit scheme.

---

*Acknowledgement: The authors were supported in part under NASA grant, NSG-5034. The first author was supported in part under DOE contract EY-76-C-02-3077. The DOE computing facility at the Courant Inst., with a CDC 6600, was used for most of the numerical experiments. The computing facility of the Laboratory for Atmospheric Sciences at NASA-Goddard Space Flight Center, including an Amdahl computer system, was used for the rest of the numerical experiments. The third author is on leave from Tel-Aviv University, Israel.

References

1) Beam, R.M. and Warming, R.F., J. of Comp. Phys., v.22, 1976, pp. 87-110.

2) Beam, R.M. and Warming, R.F., AIAA Third Computational Fluid Dynamics Conference, Albuquerque, New Mexico, June 1977, pp.1-11.

3) Isaacson, E., Advances in Computer Methods for PDE, II, IMACS-AICA, 1977, pp. 251-255.

4) Kreiss, H.O. and Oliger, J., GARP Publ., no. 10, Feb. 1973.

5) Stoker, J. and Isaacson, E., Courant Institute Report, IMM-407, Jan. 1975.

6) Williamson, D.L. and Browning, G.L., J. of Appl. Meteorology, v. 12, No. 2, March 1973,pp. 264-274.

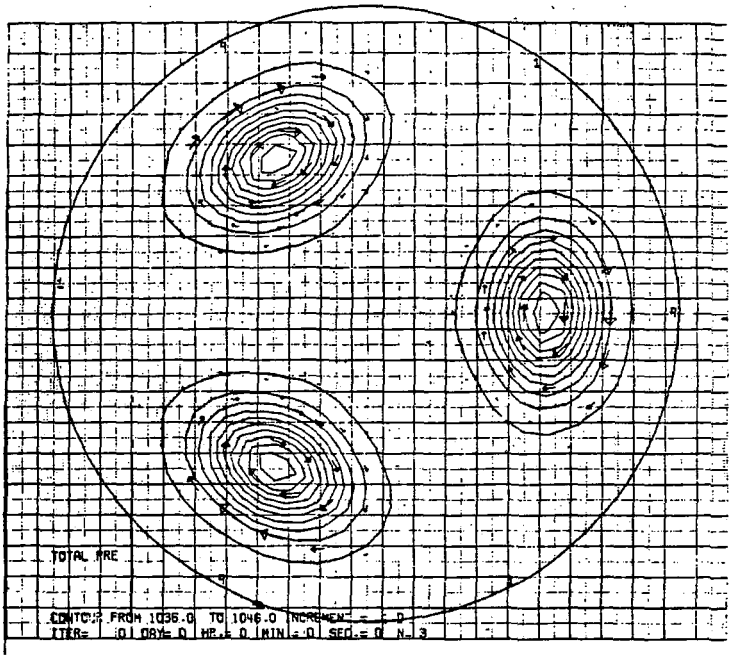

Fig. 1. Contour levels of the initial pressure field.

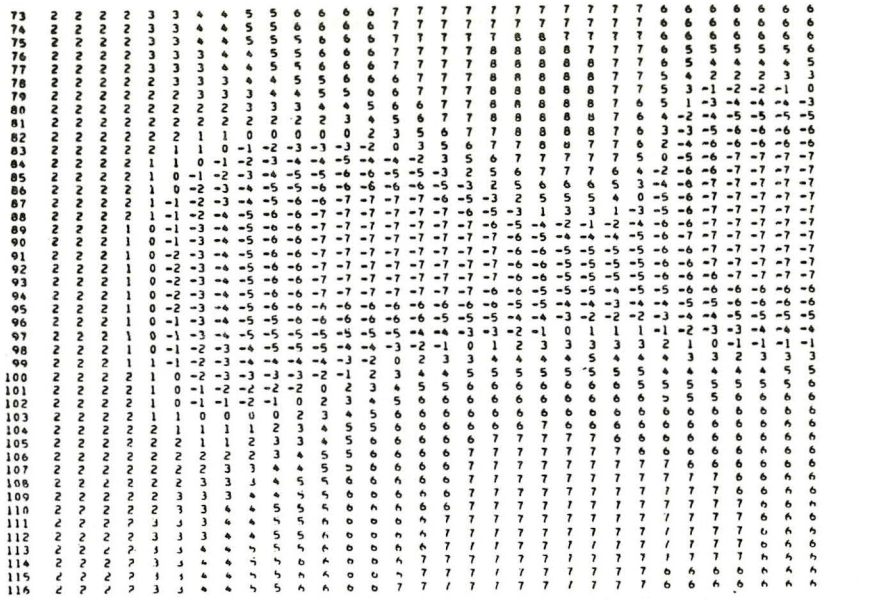

Fig. 2a. Height field after 24 hours - explicit scheme

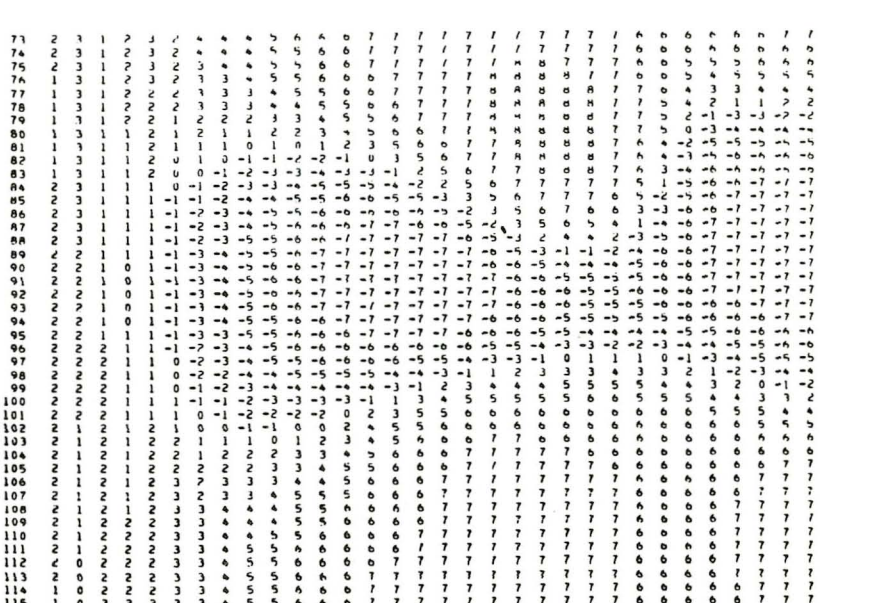

Fig. 2b. Height field after 24 hours - implicit scheme

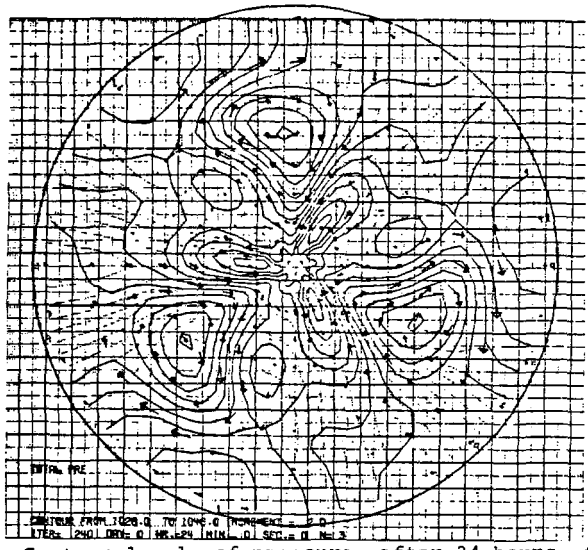

Fig. 3a. Contour levels of pressure, after 24 hours, found without the conservation of the total mass, total energy, and total potential enstrophy.

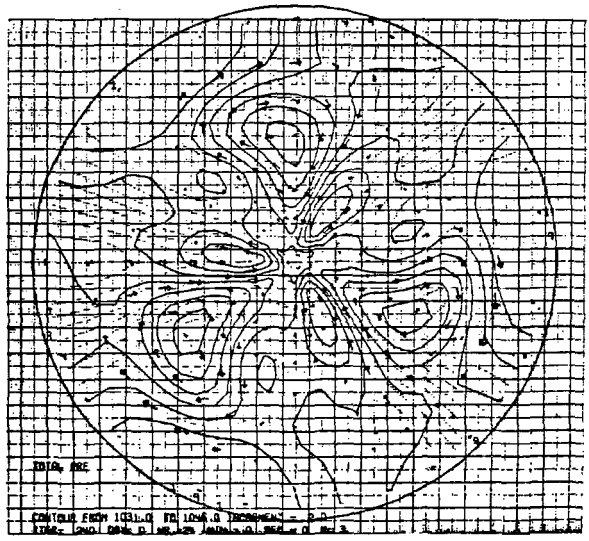

Fig. 3b. Contour levels of pressure after 24 hours, found with the conservation of the total mass, total energy, and total potential enstrophy.

Paper No. 32

ADVANCED METEOROLOGICAL TEMPERATURE SOUNDER (AMTS) SIMULATIONS

J. Susskind, *Goddard Space Flight Center, Greenbelt, Maryland,* A. Rosenberg, *Sigma Data Services Corporation, c/o Goddard Space Flight Center, Greenbelt, Maryland* and L. D. Kaplan, *Goddard Space Flight Center, Greenbelt, Maryland*

ABSTRACT

This is a report of simulation studies on temperature retrievals from AMTS and their effect on atmospheric analysis. Observations are simulated from radiosonde reports and observed cloud cover. Temperature retrievals are performed and RMS temperature and thickness errors are calculated relative to the radiosonde profiles and compared to similarly generated HIRS statistics. Significant improvement over HIRS is found throughout the atmosphere but especially in the stratosphere and lower troposphere.

INTRODUCTION

The AMTS is a next generation passive IR temperature-humidity sounder currently being designed for use on space shuttle or free flyer in a joint Goddard-JPL project. This sounder uses narrow spectral band passes in order to select spectral regions whose atmospheric absorption characteristics have pressure and temperature dependence which produce sharp temperature weighting functions (Kaplan et al., 1977). The multi-purpose sounder consists of 28 channels, shown in Table 1, which have spectral band passes ranging from 0.5-2.5 cm^{-1} and are designed to sound atmospheric temperature profile, humidity profile, surface temperature, cloud height, and cloud amount. The weighting functions for 12 temperature sounding channels are shown in Fig. 1, together with a comparable set for HIRS. The AMTS weighting functions are all considerably sharper than those of HIRS, with the exception of the channel at 635.77 cm^{-1}, peaking at 280 mb, which is of comparable sharpness to the analogous HIRS channel. The simulation study employed these channels as well as two 15μm channels in both AMTS and HIRS for cloud filtering.

SIMULATION STUDY

A simulation study was performed to assess the impact of improved temperature sounding on atmospheric analyses. Significant level temperature profiles from 73 radiosonde reports over the U. S. at 16 February 1976 were used to generate the true atmosphere. Observations for both HIRS and AMTS were simulated in two adjacent fields of view for each radiosonde station, using

Table 1. Advanced meteorological sounder spectral bands.

Channel number	Center wavelength $\nu(cm^{-1})$	$\lambda(\mu m)$	Resolution $\Delta\nu(cm^{-1})$	Main function
1	606.95	16.476	0.5	Cloud filtering
2	623.20	16.046	0.5	Cloud filtering
3	627.80	15.929	0.5	Cloud filtering
4	635.85	15.727	0.5	Temperature
5	646.60	15.466	0.5	Temperature
6	652.75	15.320	0.5	Temperature
7	666.25	15.009	0.5	Temperature
8	666.85	14.996	0.5	Temperature
9	669.25	14.942	0.5	Temperature
10	667.90	14.972	0.5	Temperature
11	1203.00	8.313	1.0	Windows and
12	1231.80	8.118	1.0	cloud filtering
13	1772.00	5.643	1.5	Humidity
14	1844.50	5.422	1.5	Humidity
15	1889.57	5.292	1.5	Humidity
16	1809.50	5.526	1.5	Humidity
17	1839.40	5.437	1.5	Humidity
18	1850.90	5.403	1.5	Humidity
19	1930.10	5.181	1.5	Humidity
20	2384.00	4.1946	2.0	Temperature
21	2386.10	4.1909	2.0	Temperature
22	2388.20	4.1873	2.0	Temperature
23	2390.20	4.1837	2.0	Temperature
24	2392.35	4.1800	2.0	Temperature
25	2394.50	4.1762	2.0	Temperature
26	2424.00	4.1254	2.5	Surface
27	2505.00	3.9920	2.5	temperature
28	2616.50	3.8219	2.5	

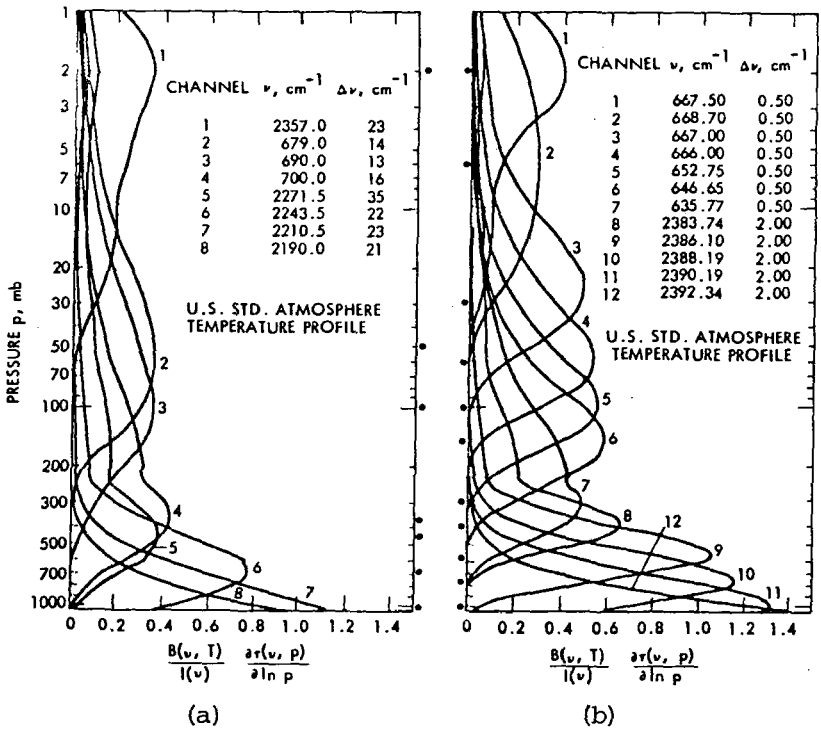

Fig. 1. Normalized weighting functions of HIRS (Fig. 1a) and AMTS (Fig. 1b) temperature sounding channels for nadir viewing.

the radiosonde profile, observed cloud cover, and a .2°C brightness temperature random noise in all channels. The observed (single layer) cloud heights and cloud fractions for each field of view were derived from HIRS/SCAMS observations over the U. S. at that time period using the dual field of view technique described in Halem et al. (1978). Temperature differences between the ground and the surface air were included in the simulation to the extent that they were included in the radiosonde significant level temperature profile. Additional surface effects such as non-unit emissivity and reflected solar radiation were not included in the simulation. Also, the effect of humidity and ozone on the transmittances were ignored though the temperature dependence of the transmittances was taken into account. Effects of humidity and ozone, non-unit emissivity, reflected solar radiation, and surface air-ground temperature discontinuities all tend to degrade the quality of actual soundings close to the ground. Thus, simulated soundings in the lower troposphere will be somewhat better than actual soundings for both HIRS and AMTS. These factors can be partially accounted for by observations in supplementary channels. However, it is expected that the effects neglected in the simulation will degrade actual AMTS lower tropospheric sounding relative to the simulation less than those of HIRS for the following reasons: First, AMTS has more water vapor sounding channels with sharper weighting functions than HIRS. Second, AMTS has three 4.0μm channels designed for use in determining ground temperature, surface emissivity, and reflected solar radiation while HIRS has one and HIRS 2 on TIROS N has two. Finally, unlike HIRS, AMTS soundings are unaffected by ozone.

RESULTS

Given the set of observations, retrievals were performed for both HIRS and AMTS, using the Chahine (1970) relaxation method and cloud filtering technique (Chahine, 1974). For comparison purposes, a climatology initial guess was used for both AMTS and HIRS. Table 2 shows RMS temperature errors of the retrieved profiles versus mandatory level radiosonde temperatures for the HIRS and AMTS retrievals. Significant improvement is seen between 500 mb and the surface and above 200 mb.

As a result of the sharpness of the AMTS weighting functions, it is also possible to perform AMTS retrievals using only the observed brightness temperatures to generate the initial guess without the benefit of any a-priori information whatsoever. This procedure uses the empirical finding that brightness temperature for AMTS channels closely approximates actual temperatures at channel-dependent characteristic pressures for a wide variety of profiles. Observed brightness temperatures are then used as initial guess temperatures at the characteristic levels. The temperature profile is obtained by linear interpolation of T ln ln P between the characteristic pressures in all segments except one in which a discontinuity in apparent lapse rate occurs.

Table 2. RMS temperature errors (°C) at mandatory levels.

Pressure (mb)	HIRS	AMTS guess	
		Climatology	Characteristic pressure
50	3.14	2.17	2.22
70	4.26	2.07	1.83
100	3.06	1.65	1.58
150	2.34	1.48	2.11
200	4.76	4.01	2.45
240	2.47	2.52	2.45
300	1.90	1.91	2.69
400	1.77	1.65	1.63
500	1.73	1.36	.88
700	2.32	1.55	1.45
850	2.08	1.54	1.60
1000	.92	.69	.72
Overall	2.77	2.04	1.89

The temperature profile in this segment, assumed to contain the tropopause, is determined by triangulation from adjacent segments. The intersection of the adjacent segments provides a good measure of the tropopause and agrees in height with the actual tropopause to better than 1 Km.

Results of AMTS retrievals using characteristic pressure guess including triangulations are shown in the last column of Table 2. These retrieved temperatures are at least as good over all as those using the climatology guess, though temperatures at 300 mb are somewhat worse due to the relative broadness of the 300 mb weighting function.

The effects of the higher resolving power of the AMTS over HIRS is demonstrated by a sample retrieval shown in Fig. 2. Fig. 2a shows the radiosonde profile together with the retrieved HIRS profile using a climatology guess. While general agreement is good, detailed changes in lapse rate in the lower troposphere and tropopause region are poorly represented in the solution. The same radiosonde station is compared to the AMTS profile retrieved using the characteristic pressure guess. Agreement of the retrieved profile with the radiosonde profile is substantially better than for HIRS, particularly in the lower troposphere and tropopause region. The derived tropopause agrees to within 3 mb with the actual tropopause pressure.

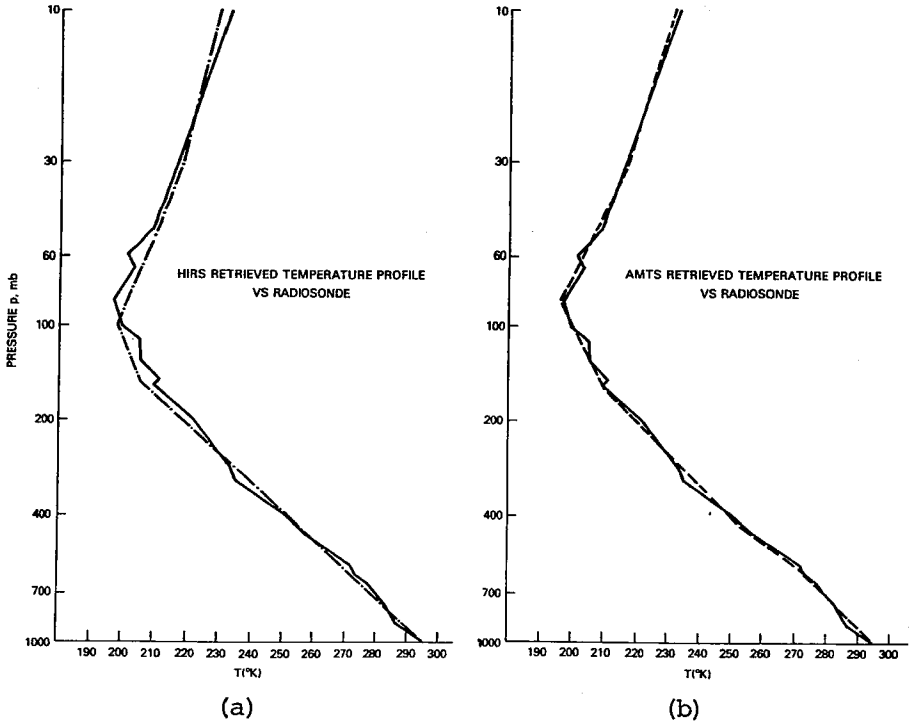

Fig. 2. Sample radiosonde significant level temperature profile with superimposed retrieval of HIRS and AMTS.

Table 3 shows RMS errors of retrieved slab-averaged temperatures between the mandatory pressure levels as compared to slab-averaged radiosonde temperatures. These thickness errors are more significant meteorologically than point temperature differences. As with the temperature errors, the thickness errors are in all cases smaller in AMTS than HIRS when a climatology guess is used. Use of the characteristic pressure guess produces further substantial improvement in the middle troposphere, but degradation around 300 mb. Work is still being done to improve results in this region.

Table 3 also shows RMS errors of the mean temperatures between 500 mb and the surface relative to radiosonde. These are approximately 1°C in HIRS, .5°C in AMTS with climatology guess, and .25°C in AMTS with characteristic pressure guess, corresponding to mean errors of 20, 10, and 5 meters in 500 mb heights, respectively. The significance of these errors can best be seen in contours of 500 mb heights constructed from radiosonde temperatures and compared to those constructed from the AMTS and HIRS retrievals. While HIRS agreement is good, the AMTS

duplicates almost all structure of the radiosonde 500 mb height field. These fields, as well as those of thickness and tropopause, will be shown in the oral presentation.

Table 3. RMS slab average temperature errors (°C).

Slab (mb)	HIRS	AMTS guess	
		Climatology	Characteristic pressure
1-50	2.06	.58	.15
50-100	3.36	1.05	1.01
100-200	2.00	1.24	1.37
200-300	1.44	1.29	1.87
300-400	1.67	1.45	1.88
400-500	1.54	1.35	.97
500-700	1.18	.98	.62
700-850	1.76	.91	.86
850-Surface	1.46	1.05	1.14
Overall (mass weighted)	1.65	1.10	1.09
500-Surface	.96	.47	.23

REFERENCES

Chahine, M. T., 1970: Inverse problems in radiative transfer determination of atmospheric parameters. J. Atmos. Sci., 27, 960-967.

_____, 1974: Remote sounding of cloudy atmospheres, I. The single cloud layer. J. Atmos. Sci., 31, 233-243.

Halem, M., M. Ghil, R. Atlas, J. Susskind, and W. J. Quirk, 1978: The GISS Sounding Temperature Impact Test. NASA TM 78063.

Kaplan, L. D., M. T. Chahine, J. Susskind, and J. E. Searl, 1977: Spectral band passes for a high precision satellite sounder. Appl. Opt., 16, 322-325.

Paper No. 33

REMOTE SENSING OF CLOUD DISTRIBUTION

M. T. Chahine, *Jet Propulsion Laboratory, California Institute of Technology, Pasadena, California*

ABSTRACT

Day and night mapping of the global distributions of the horizontal cloud-cover and the corresponding cloud-top pressure levels can be derived from the same infrared data used to derive clear column temperature profiles. Application to the 15 μm VTPR data are given. Extension of this approach for the determination of the radiative transfer properties of clouds are presented and the possibility of using such information to infer cloud types is discussed.

1. INTRODUCTION

The most important atmospheric parameters of interest in studying radiative transfer in cloudy atmospheres are the clear-column vertical temperature profiles, the amounts, heights, and radiative transfer properties of clouds. Clouds play a major role in the radiative processes in the earth atmospheres both in the absorption and reflection of solar radiation and in the emission of thermal energy. A knowledge of the vertical location, the horizontal distribution and the optical properties of clouds provides information on the heat sources and sinks, storage rates and transport phenomena in the atmosphere. Such information play a critical role in determining the drives for motions in the atmosphere and oceans.

Visible and infrared pictures of clouds indicate the existence of clouds, but do not give information about their altitudes or their radiative transfer parameters which are essential for the estimate of their types. By contrast, infrared temperature sounding data permit the determination of the horizontal and vertical distribution of clouds provided that all the sounding channels observe the same field of view at the same time. The requirement of simultaneous observations is necessary because clouds are usually a very inhomogeneous medium both vertically and horizontally.

2. APPROACH

The upwelling radiance from a planetary atmosphere is a function of the thermal state of the atmosphere, the concentration of radiatively active gases, and the extents, heights, and radiative

transfer properties of clouds and aerosols. Thus, in principle, it should be possible to recover useful information about the physical and chemical structure of an atmosphere from analysis of the upwelling radiance. However, the problem in analyzing such data lies in finding ways to uncouple the effects of these variables and retrieve the true values of each unknown separately. *By treating the cloud effects as short term oscillations over the clear-column upwelling radiance,* an analytical method was developed by Chahine (1974) to retrieve clear-column vertical temperature profiles from radiance measurements made in the presence of clouds. The method requires radiance data measured in two spectral regions and over two adjacent fields of view having different amounts of clouds. The uncoupling of the effects of clouds is carried out without any a priori information about the amounts, heights and optical properties of the clouds in the fields of view. Once the clear-column temperature profiles are determined the same radiance data could then be used to determine the heights, amounts, and radiative transfer properties of clouds.

Formulation of this approach is straightforward. It will be carried out here in two steps:

First, we consider the radiance $\tilde{I}(\nu)$ measured at frequency ν in the presence of clouds, and define the corresponding clear-column radiance $I(\nu)$ as

$$I(\nu) = B(\nu,T_s)\,\tau(\nu,p_s) + \int_{\ln p_s}^{\infty} B[\nu,T(p)\,\frac{\partial\tau(\nu,p)}{\partial \ln p}\,d \ln p \qquad (1)$$

where $\tau(\nu,p)$ is the transmittance of a clear-column of gaseous absorbers between pressure level p and the sounder. B is the blackbody Planck function and T(p) is the clear-column vertical temperature profiles. Next we express the difference between $I(\nu)$ and $\tilde{I}(\nu)$ in terms of an expansion function $G(\nu,p)$ and an expansion coefficient N as

$$I(\nu) - \tilde{I}(\nu) = NG(\nu,p_c, \ldots) + N'G'(\nu,p_c \ldots) \qquad (2)$$

In this first step we don't need to define the form of $G(\nu,p)$ because we aim to eliminate it. Detailed discussion of this approach is given by Chahine (1977). For simplicity we take here one expansion team only and consider observations made over two adjacent fields of view (subscripts 1 and 2) having different amounts of clouds, such that $\tilde{I}_1 \neq \tilde{I}_2$ and write Eq. (2) as

$$\begin{aligned} I_1(\nu) - \tilde{I}_1(\nu) &= N_1\, G(\nu,p, \ldots) \\ I_2(\nu) - \tilde{I}_2(\nu) &= N_2\, G(\nu,p, \ldots) \end{aligned} \qquad (3)$$

Now, if the two fields of view are continguous we can assume that $I_1(\nu) \simeq I_2(\nu)$ and drop their subscripts. Equation (3) becomes then

$$I(\nu) = \tilde{I}_1(\nu) + \eta[\tilde{I}_1(\nu) - I_2(\nu)]$$
$$\text{where} \quad \eta = \frac{N_1}{N_2 - N_1} = \text{constant} \tag{4}$$

Determination of $T(p)$ and $I(\nu)$ could be carried out according to the methods described by Chahine (1974, 1975, 1977).

In the second step we substitute the value of $I(\nu)$ into Eq. (3) and write

$$N_1 \, G(\nu, p_c, \ldots) = I(\nu) - \tilde{I}_1(\nu) \tag{5}$$

for each sounding frequency ν_j. The left-hand side of Eq. (5) contains all the radiative transfer properties of the clouds and the terms on the right-hand side are all known. We need now to formulate or model the expansion function $G(\nu, p \ldots)$.

3. CLOUD MODELING

To deduce the properties of clouds one is faced with the problem of solving the complete equation of transfer in a Mie scattering medium. This sort of approach is not practical here because of the small number of available measurements. Thus we are confined to use simple black or nonblack cloud models consisting of one, two or three layers.

For the types of data currently available from infrared sounders observations made in the range between 3.7 μm and 15 μm, we need consider only one layer cloud models. We could express $G(\nu, p, \ldots)$ in terms of only a small set of cloud parameters such as the fractional cloud cover N_c, the mean cloud top pressure level p_c, the cloud emissivity ε_c, transmissivity t_c, and reflectivity ρ_c.

a. Single Layer of Black Clouds

In most radiation models it is assumed for simplicity purposes that all clouds, except cirrus, are sufficiently thick and dense to be treated as black clouds with emissivity $\varepsilon_c = 1$. Low stratus and cumulus water clouds have emissivities which are close to unity. Yamamoto et al. (1970) have shown that for long-wave radiations dense water cloud absorbs more than 90% of infrared radiation within a depth of 50 m. Thus if we set the source function at the cloud level p_c to be the Planck function value $B[\nu, T_c(p_c)]$ we can express $G(\nu,p)$ for $\varepsilon_c = 1$ as

$$G(\nu, p_c) = B(\nu, T_s) \, \tau(\nu, p_s) + \int_{\ln p_s}^{\ln p_c} B[\nu, T(p)] \frac{\partial \tau(\nu, p)}{\partial \ln p} \, d \ln p \tag{6}$$
$$- B[\nu, T(p_c)] \, \tau(\nu, p_c) \quad ,$$

where the only unknown on the right-hand side is the cloud top pressure level p_c.

Determination of p_c can be accomplished by considering two sounding frequencies, say ν_1 and ν_2 for which $\tau(\nu,p_s)$ is preferably small in order to minimize the effect of changes in earth surface emissivity. From Eq. (5) and Eq. (6) we write, for, say, the first field of view

$$\frac{G(\nu_1,p_c)}{G(\nu_2,p_c)} = \frac{I(\nu_1) - \tilde{I}_1(\nu_1)}{I(\nu_2) - \tilde{I}_1(\nu_2)} \tag{7}$$

and solve for p_c by trial and error in a manner similar to the approach described in Section 4.b by Chahine (1975).

The values of the expansion coefficient N in this case are the effective fractional cloud cover which is the product of the actual fractional cloud cover N_c and the actual cloud emissivity, $N \simeq N_c\ \varepsilon_c$. N can be readily derived from Eq. (5) using ν_1 or ν_2 as

$$N_1 = \frac{I(\nu_1) - \tilde{I}_1(\nu_1)}{G(\nu_1,p_c)} \tag{8}$$

Application of this model to the analysis of the VTPR sounder data has been carried out and the results will be discussed in Section 4.

b. Single Layer of Transmitting Clouds

The assumption of black clouds is attractively simple but its validity is questionable to say the least. Many common types of stratocumulus clouds do not become black until their thickness exceeds half a kilometer. The emissivity of middle-level and cirrus clouds remains less than one even when their thickness exceeds several kilometers. A useful procedure to treat non-black clouds is to assume the cloud to be transmitting but not reflecting with

$$\varepsilon_c(\nu) + t_c(\nu) = 1$$

By considering observations in two spectral regions, say $[\nu] = 4.3$ μm and $[\nu'] = 15$ μm CO_2 bands, we can derive an expression for the ratios of emissivities in the two bands as

$$\frac{\varepsilon_c(\nu)}{\varepsilon_c(\nu')} = \frac{I(\nu) - \tilde{I}_1(\nu)}{I(\nu') - \tilde{I}_1(\nu')} \frac{G(\nu',p_c)}{G(\nu,p_c)} \tag{9}$$

Since the cloud emissivity is frequently dependent and a strong function of the water content of clouds and their thickness, the ratios of the emissivity can be used for deducing the cloud optical thickness and identify their types. The determination of N, $\varepsilon(\nu)/\varepsilon(\nu')$ and p_c is carried out simultaneously by the method

of trial and error starting with $p_c \leq p_s$ in a manner slightly more elaborate than the one followed for black clouds. Numerical simulations of this approach are currently under way and the results will be applied to the HIRS II data.

4. APPLICATION OF BLACK CLOUD MODEL TO VTPR DATA

Satellite verification of this approach has been carried out and the results are shown in Figs. 1, 2, and 3. The computations were carried out, in collaboration with M. Halem, J. Susskind, and J. Forkash, using 15 μm VTPR data from the NOAA 4 satellite. The determination of the clear column radiance for the VTPR (i.e. the clear column temperature profile) requires the use of a priori assumptions about the surface temperature. The surface temperature here was obtained from the NOAA Analysis. The effects of errors in T_s on the retrieved values of p_c is small particularly for p_c < 700 m according to McCleese (1976).

The resulting sample of cloud distribution shown here corresponds to one week of VTPR data from January 1 - 7, 1975 averaged on the GSFC-GLAS model grid size of 4° latitude by 5° longitude.

The effective fractional cloud cover distribution varied between 0% and 89%. The graphical illustrations in Fig. 1 show

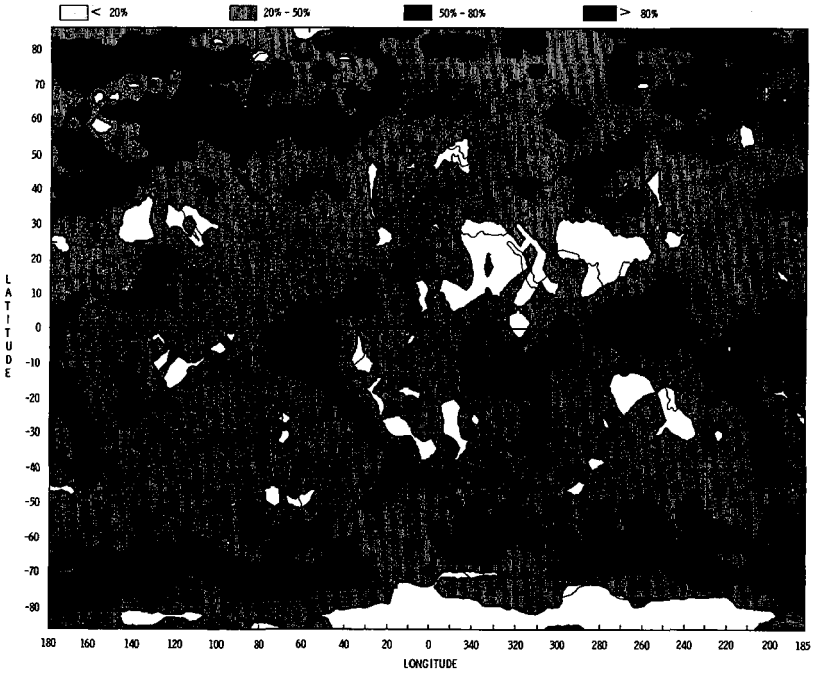

Fig. 1 — Map of effective infrared fractional cloud cover derived from the VTPR Sounder data for the period of January 1 - 7, 1975.

this distribution in four shades corresponding to the ranges less than 20%, 20% - 50%, 50% - 80%, and greater than 80%. The results obtained by this technique agree very well with the results obtained by J. C. Sadler of the University of Hawaii for the same period of time.

The cloud top pressure levels varied between surface and 145 mb and the results illustrated in Fig. 2 show the cloud top

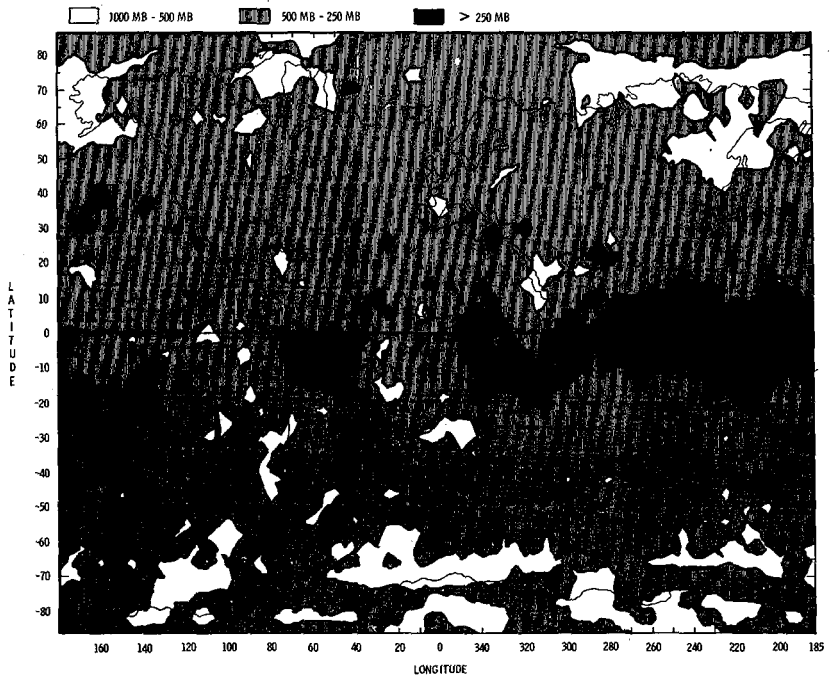

Fig. 2 — Map of effective cloud top pressure level distribution derived from VTPR Sounder Data for the period of January 1 - 7, 1975.

level distribution in three shades corresponding to surface-500 mb, 500 mb - 250 mb and above 250 mb. These results possess the basic features of the global circulation and compare well with the small amount of available information. Additional verifications are still required.

Statistical averages are presented in Fig. 3 which give the meridional profiles of zonally averaged cloud distribution, in fractions, and the cloud top pressure levels in mb: The Global average of the effective cloud cover as seen in the 15 μm band is shown to be 0.41, corresponding to 0.40 for the northern hemisphere and 0.42 for the southern hemisphere.

The standard deviation of the fractional cloud cover for the 4° wide zone is given also in Fig. 3. The average zonal standard deviation is 0.24 which is close to the value corresponding

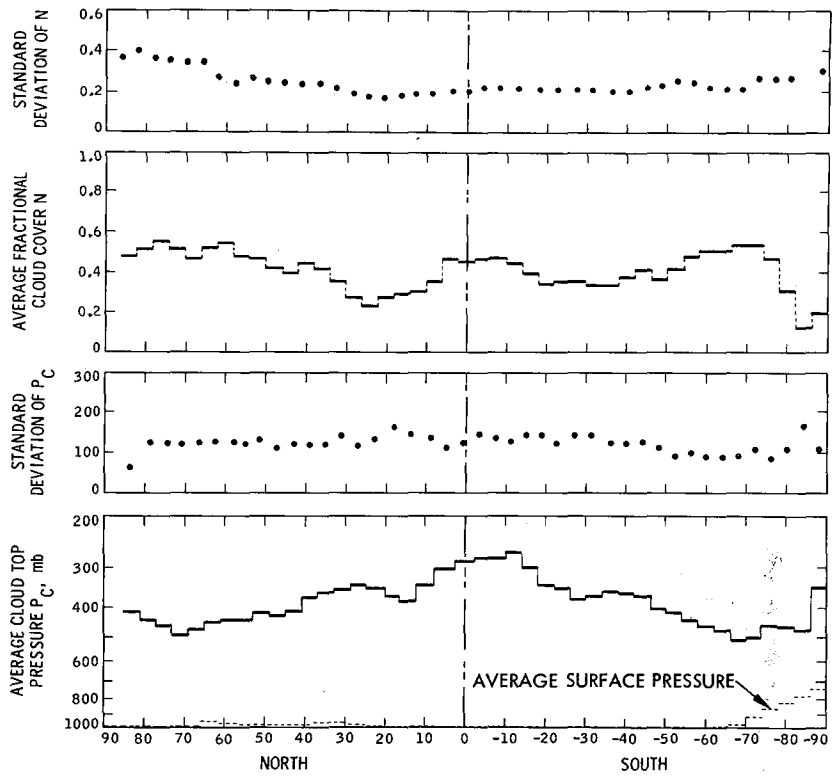

Fig. 3 — Meridional profiles of zonally averaged infrared cloudiness for January 1 - 7, 1975.

to a constant probability distribution p(X) = 1 on [0,1]. By contrast, the standard deviation of the meridionally averaged fractional cloud distribution is 0.1. Thus, the dispersion (variance) of the meridional distribution of clouds is six times larger than the zonal dispersion.

5. CONCLUSION

The results shown in Figs. 1, 2, and 3 demonstrate the capability of temperature sounding radiance data to yield meaningful information about the cloud distribution even under black cloud model assumptions. More extensive verifications still need to be carried out.

Extension of this technique to transmitting clouds will provide information about the true cloud distribution and emissivity. The emissivity could be used in conjunction with the cloud height and amount of yield information about the types of clouds.

Further extension of this technique to the cases of reflecting clouds and to multiple cloud layers is, in principle, possible,

but application of these cloud models to current sounder data is not meaningful because of the poor vertical resolution provided by current operational sounders.

REFERENCES

Chahine, M. T. (1974). Remote sounding of cloudy atmospheres. Part I. The single cloud layer. J. Atmos. Sci., 31, 233-243.

Chahine, M. T. (1975). An analytical transformation for remote sensing of clear-column atmospheric temperature profiles. J. Atmos. Sci., 32, 1946-1952.

Chahine, M. T. (1977). Remote sounding of cloudy atmospheres. Part III. Multiple cloud formations. J. Atmos. Sci., 34, 744-757.

McCleese, D. J. and Wilson, L. S. (1976). Cloud top heights from temperature sounding instruments. Quant. J. R. Met. Soc., 102, 781-790.

Yamamamoto, G., M. Tanaka and S. Asano (1970). Radiative transfer in water clouds in the infrared regions. J. Atmos. Sci., 27, 282-293.

Paper No. 34

VISIBLE FLUX VARIATIONS ACROSS FINITE CLOUDS

Frederick R. Mosher, *SSEC, Univ. of Wisconsin, Madison*

ABSTRACT

A new radiative transfer model has been developed to compute visible flux variations across and within finite clouds of varying shapes. The technique has much of the versatility of Monte-Carlo models, as well as the speed of the analytical finite cloud models.

INTRODUCTION

Quantitative and qualitative uses of visible satellite data have been hampered by the present deficiences of radiative transfer theories. An underlying explanation of what causes the brightness variations of clouds observed in satellite images is lacking. Much of the theoretical work dealing with cloud scattering of light has dealt with plane-parallel homogeneous clouds. However, satellite measurements of cloud brightness are contrary to the plane-parallel results. Monte-Carlo simulations by McKee and Cox (1974) using cubic clouds have shown that the three dimensional character of the cloud is important in the scattering of visible light. Reynolds et al. (1978) have shown the height to width ratio effect predicted by finite cloud models agrees with satellite observed cloud brightness. Wendling (1977) has shown that the striations on the cloud top can influence the amount of scattered light, while McKee and Klehr (1978) showed similar results for a turret on top of a cubic cloud.

The above studies used Monte-Carlo simulations of finite clouds. While the Monte-Carlo technique is well suited to studies with finite cloud boundries, it is a very expensive and time consuming method. Faster analytical finite cloud methods have been developed, such as the delta-Eddington approximation to the radiative transfer equation by Davies (1978), but these models are constrained to a limited number of homogeneous geometric shapes and cannot handle problems

such as cloud top texture or liquid water inhomogeneities within a cloud.

Building Block Finite Cloud Model

A new approach, conceptually similar to a three dimensional doubling or adding method, has been developed. The starting point of this model is the scattering properties of a small cuboid determined from a Monte-Carlo model. These initial cuboids are then stacked together, and the interaction between the cubes solved for. The simplest case of this method uses a Monte-Carlo simulation with an input flux illuminating one face of a cube to determine the percent of the input flux which exits the top, sides, and bottom surfaces. These initial cubes are then stacked together. The output fluxes from interior cubes are the input fluxes for their neighboring cubes. If there are N cubes, then a system of 6N linear equations are defined. By specifying the fluxes at the exterior boundries of the cloud, the equations can be solved using algebraic or iterative techniques. An iterative technique based on Newton's method was used in this study because of its speed and ease of solving large systems of equations. Running time of the model with a larger cloud formed from 1000 smaller cubes was approximately 30 seconds on a UNIVAC 1110. The non-vertical incidence of light was handled by decomposing the incident flux into vertical and horizontal components, and applying these fluxes normal to the top and side faces.

An error analysis of the model showed three main sources of error; the limited number of angles allowed, the discrete representation of gradients, and the convention of decomposing non-vertical incident flux into normal components. The errors associated with the discrete representation of gradients were shown to be small (generally less than 10%), but the limited number of angles caused significant problems in dealing with strong anisotropic scattering. Clouds with optical dimensions larger than 20 had errors of less than 10%, but smaller clouds had errors of up to 50%. While the building block model is not as accurate as Monte-Carlo models, it is generally comparable in accuracy with other rapid three dimensional multiple scattering models.

Model Results

The model has been used to investigate some of the finite cloud effects which can be associated with

cloud brightness patterns observed by satellites. For homogeneous cube-shaped clouds with optical dimensions of 100, the model showed a brightness variation across the cloud with sharp gradients near the edges and a reasonably uniform brightness pattern across the top center regions of the cloud. As the sun was shifted toward the side of the cloud, the brightest part of the cloud top shifted toward the sunlit side. The model was also used to investigate the possibility of developing correction factors for applying plane parallel solutions to finite cloud situations. The model showed that the center portions of a finite cloud show the most consistent correction factors because the center is farthest from the edge effects. However, even the center values of the cloud departed significantly from plane parallel solutions so that care must be taken in applying plane parallel solutions to any part of a cloud.

The model was used to investigate the effects of liquid water inhomogeneities within a cloud. A concentration of liquid water at the cloud top (but still maintaining a flat top) will affect the scattered light by showing up as a bright spot for the overhead sun case. For large solar zenith angles the liquid water inhomogeneity had very little effect on the scattered light. When the liquid water concentration was placed lower down into the cloud, the bright spot diminished rapidly. When the liquid water concentration was an optical thickness 25 (about a kilometer) below the cloud top, the bright spot completely disappeared.

The model was also used to investigate the effects of cloud structure. For an overhead sun a cloud top turret appeared darker than the parent cloud. When the sun was near the horizon, the turrets appeared as bright spots. Cloud shapes such as approximate cylinders, truncated spheres, inverted paraboloids, and cubes all showed varying albedo relationships to solar zenith angle. The figures with the smaller cloud top dimension (even though the maximum dimensions were the same) showed lower albedoes for the overhead sun. For larger solar zenith angles, the albedos of the different shapes showed a greater similarity than for the overhead sun. Attempts at trying to model aircraft flux measurements of clouds showed that simulations using geometric shapes which closely resemble the observed shapes gave the best representation of the observed flux patterns.

References

Davies, R., 1978: The Effect of Finite Geometry on the Three-Dimensional Transfer of Solar Irradiance in Clouds. J. Atmos. Sci., 35, 1712-1725.

McKee, Thomas B., and Stephen K. Cox, 1974: Scattering of Visible Radiation by Finite Clouds. Journal of the Atmospheric Sciences, 31, 1885-1892.

McKee, T. B., and J. T. Klehr, 1978: Effects of Cloud Shape on Scattered Solar Radiation. Mon. Wea. Rev., 106, 399-404.

Reynolds, David, T. B. McKee, and K. S. Danielson, 1978: Effects of Cloud Size and Cloud Particles on Satellite-Observed Reflected Brightness. J. of Atms. Sci., 35, 160-164.

Wendling, Peter, 1977: Albedo and Reflected Radiance of Horizontally Inhomogeneous Clouds. J. Atmos. Sci., 34, 642-650.

Paper No. 35

STUDIES OF SNOWPACK PROPERTIES BY PASSIVE MICROWAVE RADIOMETRY

A. T. C. Chang, D. K. Hall, J. L. Foster, A. Rango and T. J. Schmugge,
Goddard Space Flight Center, Greenbelt, Maryland

ABSTRACT

Research involving the microwave characteristics of snow was undertaken in order to expand the information content currently available from remote sensing, namely the measurement of snowcovered area. Microwave radiation emitted from beneath the snow surface can be sensed and thus permits information on internal snowpack properties to be inferred. The intensity of radiation received is a function of the average temperature and emissivity of the snow layers and is commonly referred to as the brightness temperature (T_B). The T_B varies with snow grain and crystal sizes, liquid water content and snowpack temperature.

The T_B of the 0.8 cm wavelength channel was found to decrease moreso with increasing snow depth than the 1.4 cm channel. More scattering of the shorter wavelength radiation occurs thus resulting in a lower T_B for shorter wavelengths in a dry snowpack. The longer 21.0 cm wavelength was used to assess the condition of the underlying ground. Ultimately it may be possible to estimate snow volume over large areas using calibrated brightness temperatures and consequently improve snowmelt runoff predictions.

INTRODUCTION

The use of remotely-acquired microwave data, in conjunction with essential ground measurements will most likely lead to improved information extraction regarding snowpack properties beyond that available by conventional techniques. Landsat visible and near-infrared satellite data have recently come into near operational use for performing snowcovered area measurements (Rango, 1975; 1978). However, Landsat data acquisition is hampered by cloud cover, sometimes at critical times when a snowpack is ripe. Furthermore, information on water equivalent, free water content, and other snowpack properties germane to accurate runoff predictions is not currently obtainable using Landsat data alone because only surface and very near-surfaces reflectances are detected.

Microwaves are mostly unaffected by clouds and can penetrate through various snow depths depending on the wavelength. Hence, microwave sensors are potentially capable of determining the internal snowpack properties such as snow depth and snow water equivalent (Hall et al., 1978; Rango, et al., 1978). However, operational use of remotely-collected microwave data for snowpack analysis is not imminent because of complexities involved in the data analysis. Snowpack and soil properties are highly variable and their effects on microwave emission are still being

explored. Nevertheless much work is being done to develop both active microwave (Hoekstra and Spangle, 1972; Ellerbruch, et al., 1977) and passive microwave techniques (Edgerton, et al., 1971; Schmugge et al., 1973; Schmugge, 1973; Linlor et al., 1974; and Chang et al., 1976) for analysis of snowpack properties. Passive microwave data obtained during recent flights by NASA aircraft and measurements made by University of Kansas in Colorado will be discussed. Recent results from analyzing the Nimbus Electrically Scanned Microwave Radiometer (ESMR) data with snowpack depth will also be discussed.

Passive Microwave Experiments

During the winter of 1976 and 1977 the NASA P-3 aircraft equipped with Multifrequency Microwave Radiometer (MFMR), cameras and other support instruments was flown over test sites near Steamboat Springs and Walden, Colorado. Ground truth which includes snow depth and temperature, free water content, density, structure and soil moisture was taken along the flight lines. In February and March 1977 a mobile microwave system was used to conduct a snow experiment in Steamboat Springs (Stiles et al., 1977). This experiment was supported by NASA Goddard Space Flight Center. The microwave equipment was mounted atop truck-mounted booms. Ground truth data were also taken during the experiment.

Passive microwave data from space have been available since December 1972 when Nimbus 5 was launched with the Electrically Scanning Microwave Radiometer (ESMR) onboard sensing at the 1.55 cm wavelength. Further data became available in June 1975 with the launch of Nimbus 6 with an ESMR instrument capable of receiving dual-polarized microwave radiation from the earth at 0.8 cm wavelength. Due to the coarse spatial resolution of these two instruments, a large homogeneous area in Canada was selected for analysis.

Interpretation of Microwave Emission from Snow

Snow particles act as scattering centers for microwave radiation. Computational results indicate that scattering from individual snow particles within a snowpack is the dominant source of upwelling emission in the case of dry snow. This type of radiation upwelling through snow is governed by Mie scattering theories for which a good description can be found in Chang et al. (1976). Microwave radiation emanating from snow originates from a depth of ~10-100 times the wavelength used (Chang et al., 1976). However, when the snowpack thickness is less than the microwave penetration, the underlying surface will contribute to the T_B (Chang and Gloersen, 1975).

Using the multifrequency analysis approach, one can make inferences regarding not only the thickness of the snowpack, but the moisture conditions and the condition of the underlying soil (wet versus dry). The shorter wavelengths such as the 0.8 cm, sense near-surface temperature and emissivity, and surface roughness. At the intermediate wavelengths, 1.4 and 1.7 cm, the radiation is less affected by the surface and more information is obtained on the characteristics of the mid-pack. Longer wavelengths such as 21 cm, represent greater penetration through a snowpack and receive a strong contribution of emission from the underlying ground. All of the above generalizations apply to the snow depths encountered at Steamboat Springs and Walden during the study period.

In addition to snow depths, snow grain and crystal sizes, ice lenses and layers within the snowpacks were measured in the snow pits. Grains, crystals, lenses and layers act as scatterers to the microwave radiation if their size is

comparable to the wavelength. Short wavelength radiation tends to be scattered by snow crystals and grains (~ 1 mm) which are comparable to the wavelength, as well as by the larger ones. Longer wavelengths are not affected by the very fine crystals and grains, but will be affected by lenses and layers, the result of snow metamorphism.

The presence of free water in the snowpack and the condition of the ground below the pack were also measured. Free water in snow (5%) will cause a sharp increase in the T_B (Chang and Gloersen, 1975). This is because the effects of scattering of individual snow particles are reduced when free water coats the crystals, and emission increases.

The condition of the ground beneath the snow will determine the intensity of the radiation incident from below. Dry or frozen ground has a high emissivity (~0.9–0.95) with a T_B of ~260°K whereas unfrozen wet ground has a much lower emissivity (~0.7) with brightness temperatures as low as 150°K. Knowledge of the condition of the ground underlying the snow is important for the interpretation of observed brightness temperatures and can generally be determined from the 21 cm observations.

Observational Results

Snow Depth. Table 1 shows the various snow depths and average wetness conditions of the snow encountered at the two sites in 1976 and 1977. When the snowpack is dry (< 1% free water present), the T_B should decrease with increased snow depth as shown in Figure 1. Figure 1 graphically illustrates the responses of the 0.8 and 1.4 cm channels of the MFMR to the various snow depths shown in Table 1.

The greater T_B decrease evident in the plot of the 0.8 cm channel (solid line in Figure 1) is due to the fact that more particles are present which can scatter the 0.8 cm radiation than the 1.4 cm radiation (dashed line) because of the size range of particles within a snowpack. A deep snowpack obviously has more crystals and/or grains than does a shallow pack. Crystals and grains large enough to scatter the 1.4 cm and longer wavelength emission are inherently fewer.

Table 1

Average Snow and Ground Conditions at the Study Areas

	depth cm	snow condition	ground condition
March 1976			
Steamboat Springs	75.4	dry	wet
Walden	10.5	moist	frozen
January 1977			
Steamboat Springs	36.1	dry	frozen
Walden	trace	N/A	frozen
March 1977			
Steamboat Springs	41.1	dry to moist	frozen
Walden	2.5	moist	wet

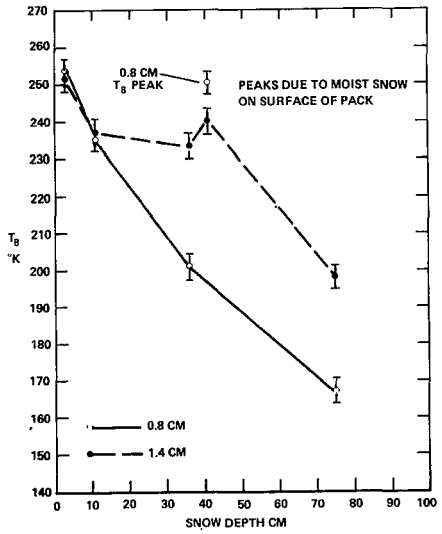

Figure 1. Horizontally Polarized Microwave T_B Responses to Snow Depths

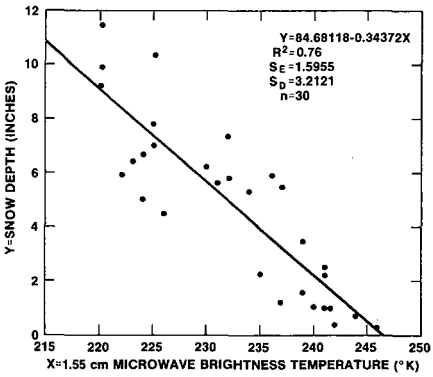

Figure 2. Nimbus 5 Microwave Brightness Temperature versus Snow Depth on the Canadian High Plains

Recently, a study has been performed to derive relationships between the snow depth and brightness temperature measured by ESMR on board the Nimbus 5 and 6 satellites. The area studied was a homogeneous area located on the Canadian high plains near southern Alberta and Saskatchewan. Figure 2 illustrates the snow depth versus brightness temperature data for Nimbus 5 and the resulting significant (at the .002 level) regression line and statistics. The Nimbus 5 data are from the nighttime pass on 14 March 1976 and the snow depth data are from 15 March 1976. Air temperatures prior to 15 March were well below 0°C with little chance of significant melting, and as a result, dry snow conditions were assumed. Figure 3 presents a comparable plot for snow depth and Nimbus 6 vertically polarized brightness temperature from the daytime pass on 15 March 1976. It does appear that in simple regression analysis that the Nimbus 6 data produce better relationships than the Nimbus 5 data. This most likely results from the fact that the emission from the relatively thin snowcover at 1.55 cm contains a more significant contribution from the variable underlying soil layer than at 0.81 cm.

Snowpack and Soil Moisture Conditions. The response of the MFMR data to snow moisture has also been analyzed. Snow wetness is very important to runoff forecasting, as is the condition (wet or dry) of the underlying ground. Variations in snow moisture have been measured using a freezing calorimeter technique during the 1976 and 1977 aircraft experiments and it has been found that free water in a snowpack will raise the 0.8 cm T_B. Note the peak in the response of the 0.8 channel to the 41.1 cm depth snow in Figure 1 (open circle ~250°K). This is the March 1977 snowpack at Steamboat Springs. The peak is apparently caused by surface moisture to which the 0.8 cm radiation is very sensitive. The longer wavelengths did not respond as markedly (i.e., show the sharp T_B increase) because they emanate from deeper, drier layers within the snowpack. If all wavelengths were to show the peak, theoretically the snowpack would be ripe.

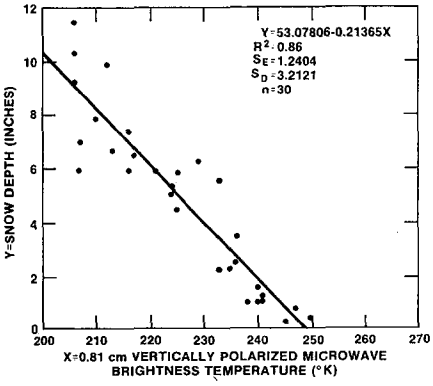

Figure 3. Nimbus 6 Vertically Polarized Microwave Brightness Temperature versus Snow Depth on the Canadian High Plains

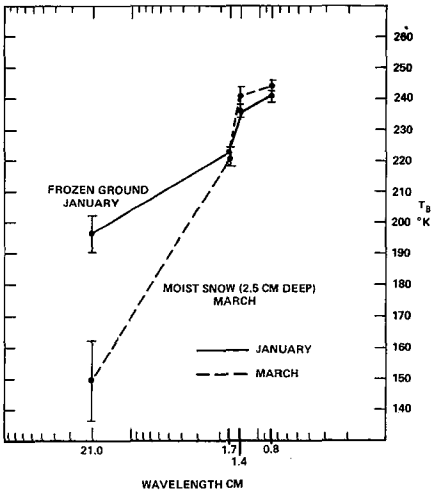

Figure 4. Variation of Microwave T_B with Radiometer Wavelength, Walden, Colorado, 1977

Figure 4 compares the responses of all four wavelengths over frozen ground in January, 1977 (solid line) to that over shallow (2.5 cm), moist snow and wet ground at Walden in March 1977 (dashed line). The shortest wavelengths, 0.8 and 1.4 cm, have slightly higher average brightness temperatures for moist snow (March) than for the frozen ground (January). The 1.7 cm channel shows approximately the same T_B for frozen ground and moist snow while the difference in the 21 cm T_B between moist snow and frozen ground is 47°K. The 21.0 cm radiation is apparently unaffected by the moist snow because the snow is so shallow. The low T_B of the 21 cm wavelength in March results from the wet ground beneath the snow.

Figure 5 shows the variation of brightness temperature as a function of time for 2.8 cm and 0.8 cm wavelengths (Stiles et al., 1977). When the free water content within the snow pack increased to approximately 4% the brightness temperature jumped from 140K to 260K at the 0.8 cm wavelength with 50° incidence angle. This is consistent with the aircraft measurements.

Summary and Conclusions

It has been demonstrated that there are differences in the microwave brightness temperatures for the snowpacks studied at Walden and Steamboat Springs, Colorado during the 1976 and 1977 experiments. An average T_B decrease for the shorter wavelengths (0.8, 1.4 and 1.7 cm) of 35°K has been shown to correspond with a 39.3 cm greater snow depth for the March 1976 as compared to the January 1977 Steamboat Springs snowpack. A T_B decrease of 50°K for the 21 cm wavelength is attributed to wet soil conditions in March 1976. Furthermore, a sharp rise, ~49°K, in the 0.8 cm T_B corresponds to moist snow on a surface of the Walden snowpack in March 1977 demonstrating the sensitivity of microwave

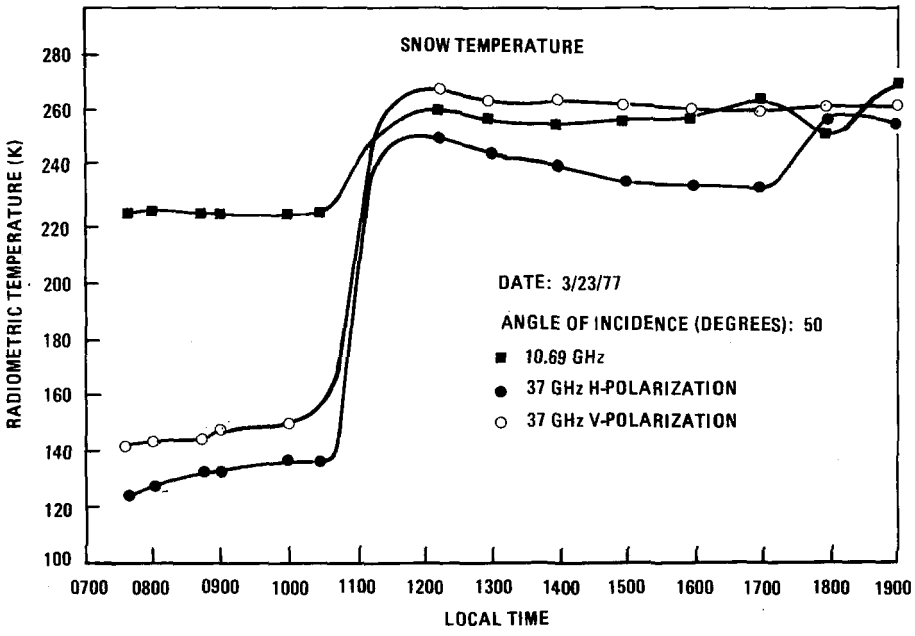

Figure 5. Microwave TB Variation with Time
(University of Kansas)

radiation to moist snow. Also, a greater T_B decrease for a given snowpack is evident for the short, 0.8 cm, as compared to the longer, 1.4 cm, wavelength. This is due to the fact that shorter wavelength radiation is scattered more so than longer wavelength radiation thereby resulting in a lower emissivity and a lower T_B for the short wavelengths. A dry snowpack has particle sizes typically < 0.1 cm. As the wavelength of the radiation approaches the particle size, the scattering will increase. This greater scattering lowers the T_B and the emissivity of a snowpack.

Snow depth, free water within the pack, and underlying conditions were addressed in this paper. Varying conditions of these parameters were encountered in the study areas and subsequent correlations made with the microwave data were consistent between different measurements. The challenge in the analysis of the microwave response to snowpack properties lies in the fact that snowpack conditions are complex and their interaction with microwave radiation is not completely understood. The fact that snowpack character can change so rapidly, and, is in fact constantly changing, adds a complicating factor to data analysis. It is believed that with additional measurements in the coming years a more quantitative relationship between brightness temperatures and snow depth will be possible for snowpacks of known wetness condition. The near-term goal is to understand the microwave emission from snow so that a system for improved snowpack monitoring from a remote platform can be defined.

References

Chang, T. C. and P. Gloersen, 1975: Microwave Emission from Dry and Wet Snow, in Operational Applications of Satellite Snowcover Observations, NASA SP-391, Washington, D.C., pp. 399-407.

Chang, T. C., P. Gloersen, T. Schmugge, T. T. Wilheit and H. J. Zwally, 1976: Microwave Emission from Snow and Glacier Ice, Journal Glaciology, V. 16, No. 74, pp. 23-39.

Edgerton, A. T., A. Stogryn and G. Poe, 1971: Microwave Radiometric Investigations of Snowpacks, Aerojet General Corp., Final Report 1285R-4.

Ellerbruch, D. A., W. E. Little, H. S. Boyne and D. D. Bachman, 1977: Microwave Characteristics of Snow, Proceedings of the 45th Annual Western Snow Conference, Albuquerque, New Mexico, pp. 68-74.

Hall, D. K., A. Chang, J. L. Foster, A. Rango and T. Schmugge, 1978: Passive Microwave Studies of Snowpack Properties. Proceedings of the 46th Annual Western Snow Conference, Otter Rock, OR, pp. 33-39.

Hoekstra, P. and D. Spanogle, 1972: Radar Cross Section Measurements of Snow and Ice, Cold Regions Research and Engineering Laboratory, Technical Report TR 235, Hanover, New Hampshire, 39 pp.

Rango, A. (ed), 1975: Operational Applications of Satellite Snowcover Observations, National Aeronautics and Space Administration, NASA SP-391, Washington, D.C., 430 pp.

Rango, A., 1978: Pilot Tests of Satellite Snowcover/Runoff Forecasting Systems, Proceedings of the 46th Annual Western Snow Conference, Otter Rock, Oregon, pp. 7-14.

Rango, A., A. T. C. Chang and J. L. Foster, 1978: The Utilization of Spaceborne Microwave Radiometers for Monitoring Snowpack Properties, Submitted to Nordic Hydrology.

Schmugge, T., 1973: Microwave Signature of Snow. Proceedings of the Annual Science and Technology Review GSFC, National Aeronautics and Space Administration, NASA SP-361, pp. 193-195.

Schmugge, T., T. T. Wilheit, P. Gloersen, M. F. Meier, D. Frank and I. Dirmhirn, 1974: Microwave Signatures of Snow and Fresh Water Ice, in Advanced Concepts and Techniques in the Study of Snow and Ice Resources, National Academy of Sciences, Washington, D.C. pp. 551-562.

Stiles, W. H., B. C. Hanson and F. T. Ulaby, 1977: Microwave Remote Sensing of Snow: Experiment Description and Preliminary Results, RSL Technical Report 340-1, University of Kansas, 110 pp.

Page intentionally left blank

Paper No. 36

MODELLED AND MEASURED ENERGY EXCHANGE AT A SNOW SURFACE

Isidore Halberstam, *Jet Propulsion Laboratory, Pasadena, CA.*

ABSTRACT

Results of a model developed at JPL for the energy interchange between the atmosphere and the snow are compared with measurements made over a snowfield during a warm period in March, 1978. Both model and measurements show that turbulent fluxes are considerably smaller than the radiative fluxes, especially during the day. The computation of turbulent fluxes for both model and data is apparently lacking because of problems inherent in the stable atmosphere.

INTRODUCTION

Snow surfaces in GCMs are generally treated as most other surfaces with high albedos with the exception, perhaps, of constraining the surface temperature to remain always at or below 0°C. Hydrology models of the snowpack give detailed analyses of the physical processes present in the snow, but the related, complex atmospheric processes are usually parameterized in bulk fashion. Neither of these two approaches can suffciently portary the interchange of energy at the surface, especially when turbulent fluxes are involved. To fill this gap, an investigation of the air-snow interface was undertaken with detailed measuring and modelling of both the atmospheric boundary layer and the snowpack.

THE MODELLING EFFORT

The model initially developed is one-dimensional (columnar) divided into a free atmospheric layer, an upper boundary layer (the Ekman layer, or, simply the upper layer), and a lower, constant flux layer (the surface layer). The snowpack lies below the atmosphere at an initial depth of 60 cm, where calculations are performed on a logarithmic grid to give very high resolution near the surface. Below the snow rests the ground which has an assumed constant temperature at a 20 cm depth. The equations for the upper layer predict winds, temperature and humidity assuming a constant pressure gradient and employing

variable eddy diffusivities calculated from the Hoffert and Sud (1976) parameterizations. The surface layer is then derived diagnostically from the Businger et al (1971) equations, given the calculated values of wind, temperature and humidity at the bottom of the upper layer and a derived surface temperature based on a flux balance equation. The fluxes present at the surface are net long-wave radiation, conduction to the snowpack, and sensible and latent heat convection. The turbulent convective processes are themselves dependent on the surface temperature, necessitating an iterative procedure for solution.

The snowpack equation involves the ordinary diffusivity equation with additional terms to account for internal heating due to short-wave (solar) radiation (the snow being translucent) and latent heat release due to melting and refreezing. The water that is produced by melting is assumed to leave the snowpack and enter the ground.

The modelling of the surface layer during stable conditions runs into a problem because the flux profile relationships are valid only for subcritical Richardson numbers ($Ri < .21$). When Ri approaches its critical value, the first-order turbulence is inhibited by strong buoyant forces. What happens in nature is that a laminar layer is created which effectively blocks momentum or heat transfer to the lower turbulent layer which continues to lose heat and momentum. When enough momentum has been lost to create sufficient shear between the laminar flow and the turbulent region, Ri decreases to subcritical values and a "burst" of heat and momentum, as described by Businger (1973), is delivered to the surface. These "burst" phenomena have been included in ad hoc fashion in the model.

DATA GATHERING IN A SNOW-COVERED FIELD

In support of the modelling effort, measurements were made over and in a snow-covered field in Lee Vining, CA. The area is about 8 km southwest of Mono Lake and is a fairly flat area until the Sierra Nevada range some 30 km west of the site. Measurements were made from 15-17 March 1978 during a period of high pressure and subsidence when daytime air temperature (at 2m) reached about 20° C while night-time readings dropped to near -9°C. The snowpack was some 0.75m deep initially with obvious melt taking place during the period.

Instruments were mounted with logarithmic spacing on an 8m mast connected to a recorder to obtain windspeed, temperature, and dew point at various heights averaged over 16 min. A net radiometer was used to measure surface temperature. Eight temperature probes were used in the snow to define the temperature profile. A field weather station was mounted 2m above the snow as a backup to the other instruments.

Once measurements were gathered, momentum and sensible and latent heat fluxes were computed for the period using a method described by Businger (]973). The method basically converts profile measurements, using a least-square fit, to flux data through the flux-profile relationships.

RESULTS

The model was run for 5 1/3 simulated days under conditions in qualitative agreement to the ones present at Lee Vining. The sky was assumed clear with the sun declination near 0°. Figs. 1 (a) - (b) show the bihourly averaged sensible and latent heat fluxes with the negative (positive) sign corresponding to negative (positive) stability. (Units are in cal cm^2 s^{-1} with 1 unit = 4.2×10^4 Wm^{-2}.) After an initial adjustment period, the heat flux is seen to be mostly directed toward the surface with but brief negative excursions right after solar noon (0 h corresponds to noon local time). The maximum positive flux is between 7 and 8 Wm^{-2} which is relatively small compared to radiative fluxes. The latent heat pattern is similar to the sensible heat record but achieves only about one half the magnitude. The noisy form of the record is probably due to the action of the parameterized bursts which occur intermittently.

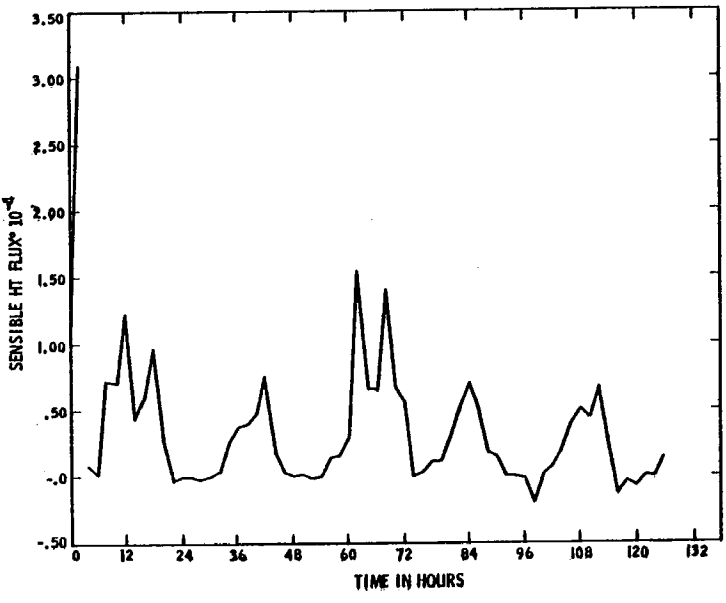

Fig. 1 (a) Computed sensible heat flux (in cal $cm^{-2}s^{-1}$) for 5 1/3 days beginning at noon.

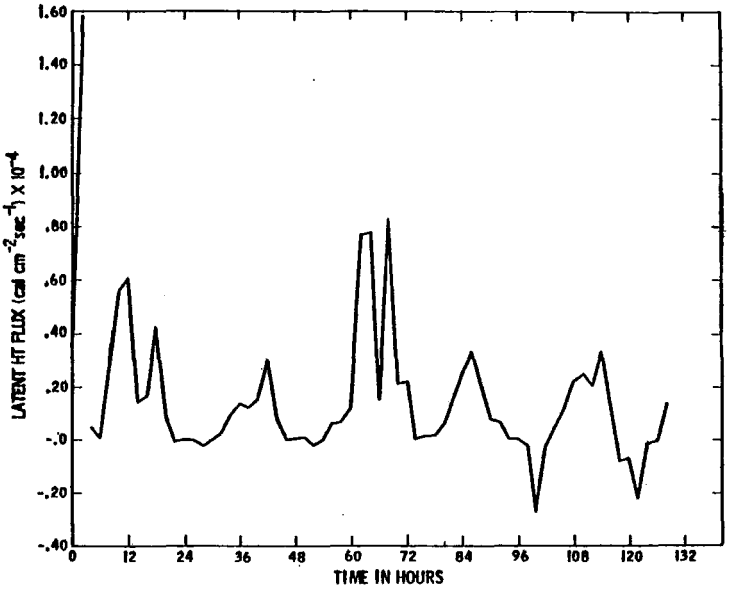

Fig. 1 (b) Computed latent heat flux for the same period.

Fig. 2 shows the sensible and latent heat fluxes calculated for the Lee Vining data. Here the fluxes were derived from 16 min averages of the heat and humidity profiles fitted by least squares to the similarity equations. The peak magnitudes are somewhat higher than the model values, but the noisy pattern, similar to the one produced by the model, is obvious throughout the night. The latent heat pattern, except for a brief departure around sunset, parallels the sensible heat record, again, in basic agreement with the model. A note of caution, however, must be inserted in the derivation of the heat fluxes from the profile data. A noontime profile measurement for the snow and atmosphere on 16 March, depicted in Fig. 3, shows an extremely large gradient ($\sim$ 16°C) between the snow surface and the atmosphere at 0.5m above the snow. The airflow is surprisingly laminar down to 0.5m (the wind data point at 6m should appear at 4m), with winds very light up to the top of the mast. With this kind of airflow, the surface layer is poorly defined, turbulent motion being suppressed to but a few centimeters above the snow. The matching of such profile data to well-developed turbulent structures becomes a highly dubious venture.

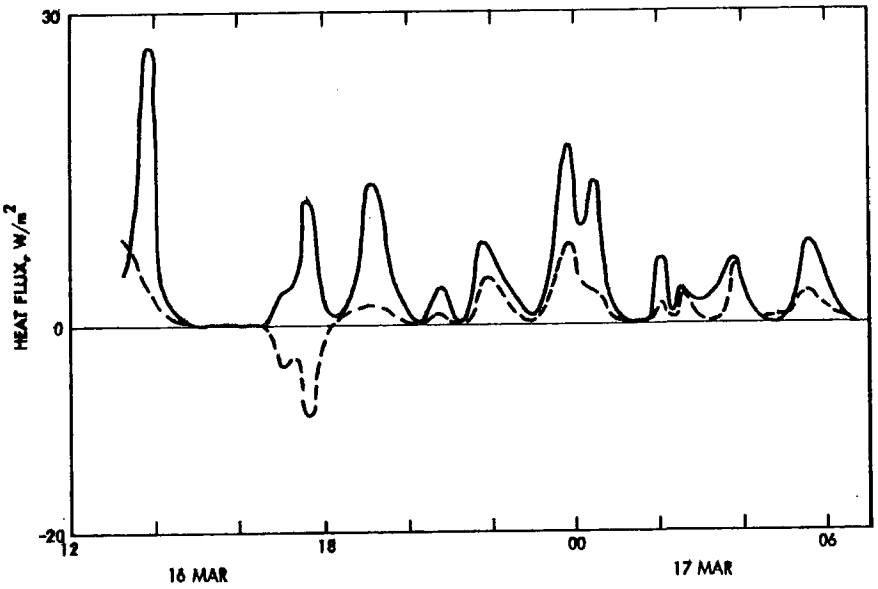

Fig. 2 Sensible (solid line) and latent heat (dashed line) fluxes at the surface based on measurements at Lee Vining from 1200 PST to 0600 PST, 16-17 March 1978.

CONCLUSIONS

The model apparently behaves well and predicts behavior which is at least in qualitative agreement with observed phenomena. A large gap remains in the understanding of the stable atmosphere, especially when Ri exceeds its critical value. Undertaking more measurements of this nature while continuing with the modelling effort will help in the re-evaluation of boundary layer theory for highly stable conditions.

REFERENCES

Businger, J.A., 1973: Turbulent transfer in the atmospheric surface layer. Workshop on Micrometeorology, Amer. Meteor. Soc., Boston, Mass., 67-100.

_____, J.C. Wyngaard, Y. Izumi, and E.F. Bradley, 1971: Flux-profile relationships in the atmospheric surface layer, J. Atmos. Sci., 28, 181-189.

Hoffert, M. and Y. Sud, 1976: Similarity theory of the Buoyant interactive planetary boundary layer with entrainment, J. Atmos. Sci., 33, 2136-2151.

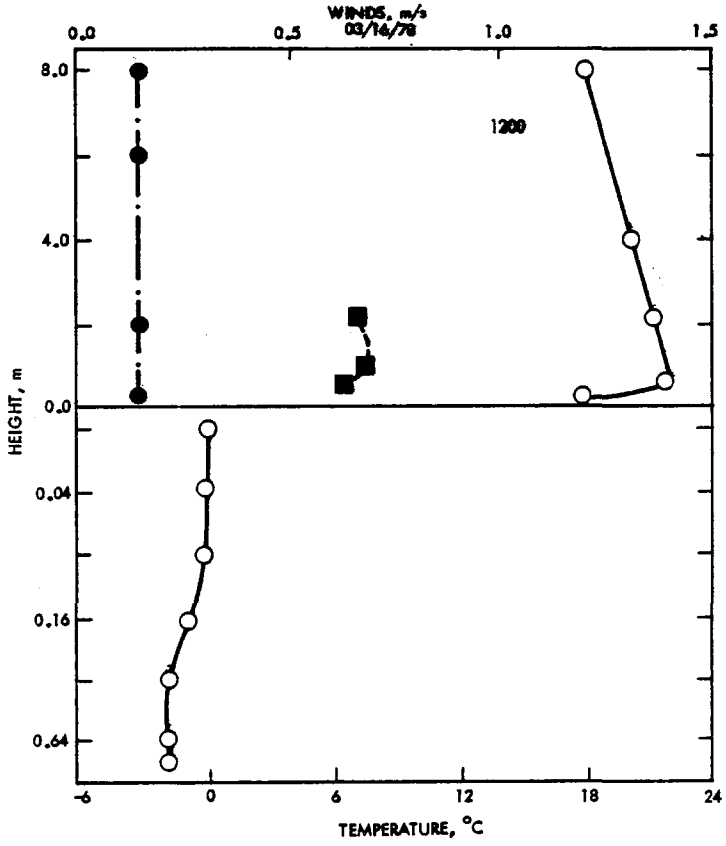

Fig. 3 Profiles of temperature (open circles, wind speed (black circles), and dewpoint (black squares) at 1200 PST on 16 March at Lee Vining. The solid line dividing upper and lower portions of the figure represents the snow surface, with logarithmically-spaced temperatures taken in the snow appearing below the line.

Paper No. 37

THE MICROWAVE RADIOMETER SIGNATURE OF ARTIFICALLY GENERATED SEA FOAM

B. M. Kendall and C. T. Swift, *Langley Research Center, Hampton, VA*

ABSTRACT

Microwave radiometer experiments have been undertaken to measure the thermal emission from artificially generated sea foam. This data will be used to quantify the physics of emission from the ocean to more accurately retrieve geophysical parameters of interest.

INTRODUCTION

There have been a series of aircraft measurements conducted by the Goddard group which unquestionably show that the microwave brightness temperature significantly increases with the percent foam coverage in the field of view of a radiometer. The discovery of this phenomenon suggested that microwave radiometers can be used to infer surface wind speed, since the percentage foam increases with increasing wind speed.

In order to conduct a comprehensive set of measurements, which would be extremely expensive if conducted from aircraft, a device was built which artificially generate foam. Measurements were then undertaken as function of radiometer frequency, viewing angle, and polarization with percent foam as a parameter.

The Foam Generator

The device is 4 x 4 feet square, and foam is generated by passing air through an array of porous glass "frits" and into a layer of saline water above the frits. The percent foam is controlled by regulating the air flow through the frits. The percent foam can be generated with good repeatibility, so that extensive radiometric measurements can be conducted a a function of viewing angle, frequency, and polarization over a known target.

Experimental Results

Measurements have been performed at X-band (10.69 GHz) and at S-band (2.65 GHz), and planning is underway to obtain measurements at K-band (37 GHz). Some of the initial S-band results are shown in the figures. Figure 1 shows absolute brightness temperature plotted vs angle with air flow, and hence, percent foam as a parameter for vertical polarization. The curve shows a

rather dramatic increase in brightness as the percentage foam increases, and reaches an emissivity of approximately 0.9 at the highest air flow rate (near 100% foam coverage). The curve also shows that the Brewster angle occurs at lower values of the angle of incidence as the flow rate increases. This suggests a lowering of the dielectric constant of the target. Figure 2 shows the corresponding curves for horizontal polarization. This polarization also shows a substantial increase in brightness temperature at all angles of incidence as the air flow rate is increased. Figure 3 shows the increased brightness temperature as a function of air flow for both polarizations at a viewing angle of 55°. This curve indicates that horizontal polarization is much more responsive to changes in the percent foam coverage than is the vertical polarization - particularly as the surface becomes completely covered with foam. Satellite systems should therefore utilize the horizontal polarization in order to infer high wind speed.

An analytical model for the emissivity of foam will be generated when data is reduced at other electromagnetic frequencies.

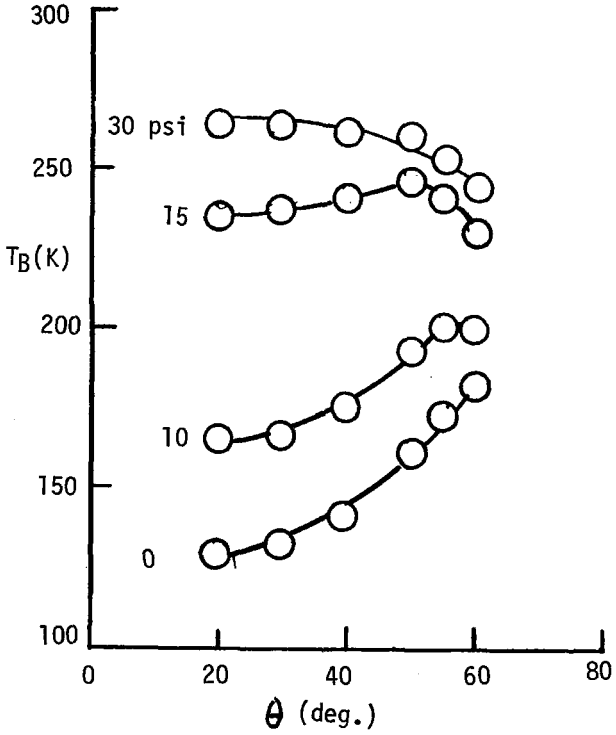

Fig. 1-Brightness temperature vs viewing angle (2.65 GHz, vertical polarization). Air flow in pounds per square inch.

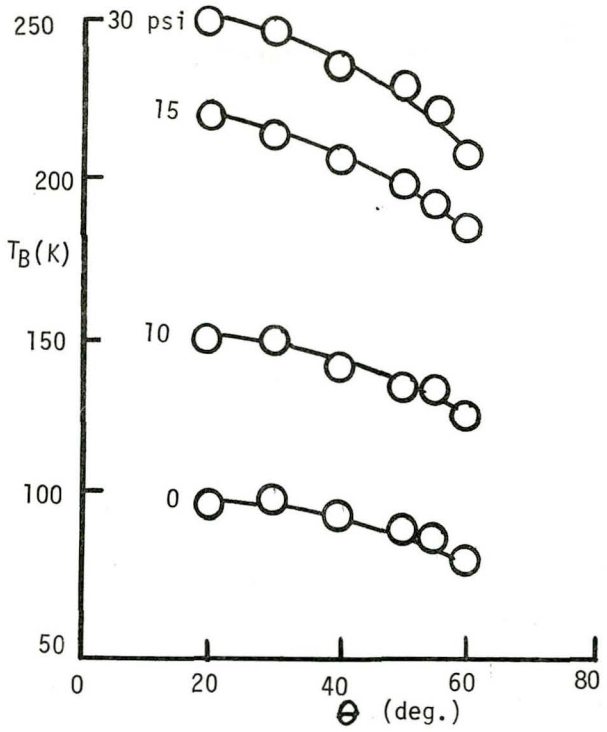

Fig. 2-Brightness temperature vs viewing angle (2.65 GHz, horizontal polarization). Air flow in pounds per square inch.

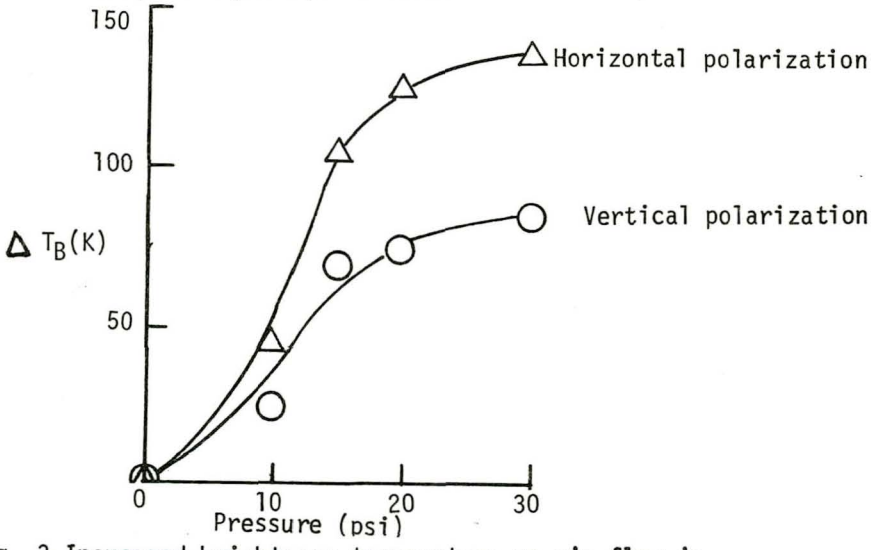

Fig. 3-Increased brightness temperature vs air flow in pounds per square inch (2.65 GHz, 55° viewing angle).

Page intentionally left blank

Paper No. 38

A MODEL FOR THE MICROWAVE EMISSIVITY OF THE OCEAN'S SURFACE AS A FUNCTION OF WIND SPEED

Thomas T. Wilheit, *Greenbelt, Maryland*

ABSTRACT

A quantitative model is presented which describes the ocean surface as an ensemble of flat facets with slopes distributed as per Cox and Munk (1955) partially covered with an absorbing nonpolarized foam layer. Experimental evidence is presented for this model.

INTRODUCTION

The launch in 1978 of the Scanning Multichannel Microwave Radiometer (SMMR) on both the Nimbus–7 and Seasat satellites has opened new possibilities for measurement of many geophysical observables, primarily the wind speed and water temperature at the ocean surface. Since the microwave brightness temperature observed in each of the SMMR channels is significantly affected by at least four variables, the liquid and vapor components of atmospheric water, sea surface temperature and surface wind, retrieval of the surface parameters is a non-trivial problem. The weak point in the physical understanding of these effects is in the effect of wind on the sea surface. Hopefully, the model presented here improves the situation somewhat. The model is clearly imperfect, but hopefully, will provide a framework and reference point for future refinements.

There have been two closely related programs supported by the Global Weather and GARP programs. The improved modeling of the microwave emissivity of the ocean surface, here reported, has been supported by Global Weather and is the key physical input to the algorithm for the retrieval of wind speed and sea surface temperature developed under the GARP Program. The approach taken here will be to present the model then to discuss several supporting observations.

THE MODEL

It is a straightforward problem to calculate the emissivity of a smooth water surface. The dielectric properties of sea water and saline solutions have been discussed by many authors. (Lane and Saxton (1952), Klein and Swift (1977), and Stogryn (1971)). We will use values derived from the Lane and Saxton (1952) measurements and expressed in an analytic form by Chang and Wilheit (1978). The formalism for calculating the emissivity for a given view angle and polarization is the so called Fresnel relations (Jackson 1962). The resulting emissivity as a function of view angle is shown in Figure 1 for a frequency of 10.7 GHz and a temperature of 285°K. Unfortunately, the ocean's surface is not a smooth surface; the wind roughens the surface, and, if it is blowing hard enough, partially covers the surface with foam. Cox and Munk (1955) have quantitatively described the distribution of surface slopes as a function of wind speed. They found that the

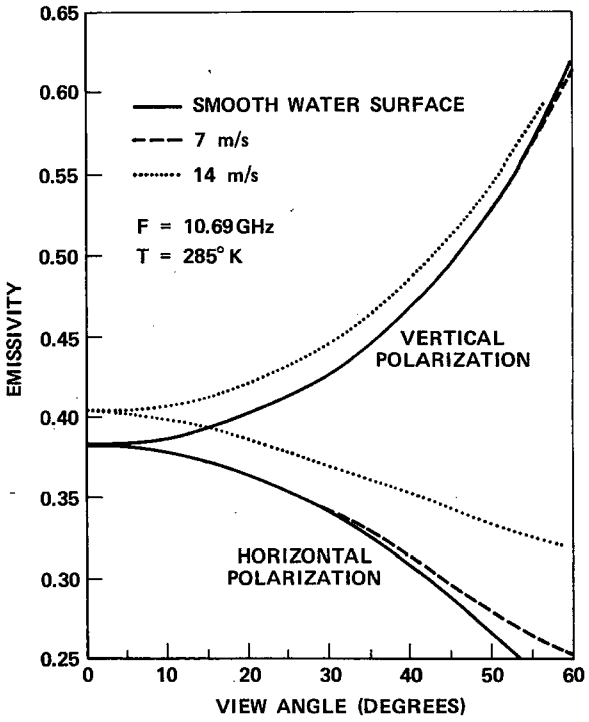

Fig. 1–Emissivity as a function of view angle for a smooth water surface and for the ocean surface with 7 and 14 m/s wind speed.

surface slopes were normally distributed with a variance, σ^2_{cm}, given by $\sigma^2 = .003 + .0048W$ where W is the wind speed in meters/second at 20m height. The factor multiplying W in the above equation is slightly different from that in the Cox and Munk (1955) paper because the winds were measured at 12.5M in their work; the conversion to 20m was done using the Cardone (1969) model for the atmospheric boundary layer assuming neutral stability.

The Cox and Munk (1955) measurements were made at visible wavelengths. Much of the roughness they observe is at scales very small compared to microwave wavelengths. This model requires only a fraction of the Cox and Munk roughness at the longer microwave wavelengths. Specifically, the slope variance observed at a given microwave frequency is:

$$\sigma^2(f) = (0.3 + 0.02\ f(GHz))\sigma^2_{cm} \qquad f < 35\,GHz$$

$$\sigma^2(f) = \sigma^2_{cm} \qquad f \geqslant 35\,GHz$$

To calculate a rough surface emissivity from this slope distribution, one simply averages the Fresnel relations (Jackson 1962) over the distribution of surface slopes. In doing so, one implicitly ignores surface curvature and all structure comparable to a wavelength and thereby reduces the problem to geometric optics. The

comparison with observations which follow will demonstrate that this is a surprisingly good approximation.

Wind also creates foam on the ocean's surface. Nordberg et al (1971) found a linear increase in brightness temperature with wind speed whenever the wind speed exceeded 7 m/s. They were viewing directly at the nadir which essentially eliminates the roughness effect leaving foam as the most reasonable explanation. In our model, we will treat foam as partially obscuring the surface in a manner independent of polarization. A non-reflecting material partially covering the surface would have this property as would an absorbing but partially transparent medium with the same temperature as the water. Either description alone would be inadequate, but a combination of the two descriptions would be closer to reality. The degree to which foam obscures the surface is frequency dependent and proportional to the amount by which the wind speed exceeds 7 m/s. A reasonable approximation to the available observations of the fraction, K, by which the surface reflectivity is reduced by foam is

$$K \cong a(1 - e^{-f/f_o})(W - 7\,m/s)$$

where f is the frequency

and a = .006 s/m

f_0 = 7.5 GHz

The primary available observations relevant to this are from the Bering Sea Expedition (BESEX) (Webster et al 1976) and from Cosmos 243 (Shutko 1978). These results, along with a plot of $\partial K/\partial W$ is given in Figure 2. The observations are difficult but nevertheless show reasonable self-consistency except possibly for the one BESEX point at 37 GHz.

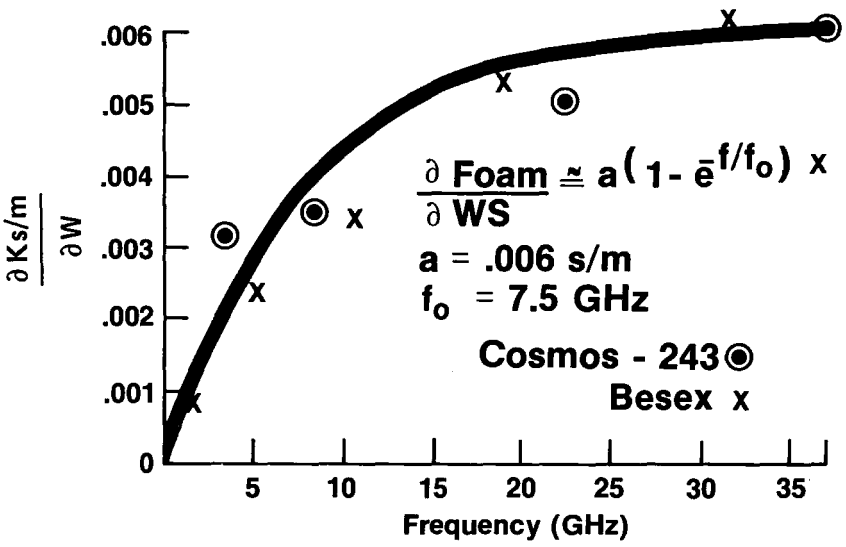

Fig. 2-Frequency dependence of reduction of reflectivity by foam.

Emissivities calculated according to this model for 7 and 14m/s are shown in Figure 1 for comparison with the emissivity of a smooth surface.

SUPPORTING OBSERVATIONS

Because the assumed foam model has no polarization character, dual polarized observations of the surface provide a test of the rough surface portion of the model. If one makes the approximation that the atmosphere and the surface have the same thermodynamic temperature T_1, then it is straightforward to show that for any given view angle

$$F_{T_1}(\theta) = \frac{T_H(\theta) - T_1}{T_V(\theta) - T_1} = \frac{R_H(\theta)}{R_V(\theta)}$$

Here $T_H(\theta)$ is the horizontal brightness temperature at an angle θ and $R_H(\theta)$ is the horizontally polarized reflectivity. $T_V(\theta)$ and $R_V(\theta)$ refer similarly to vertical polarization. Note that because $F_{T_1}(\theta)$ is the ratio of two reflectivities, it is independent of foam cover and thus provides a measurement of surface roughening. The data from the Electrically Scanned Microwave Radiometer (ESMR) on Nimbus-6 (37GHz, 50° view angle) have been so analyzed and compared with wind speeds derived from the operational data buoys (Wilheit, 1978). A summary of this comparison is given in Figure 3. The plotted data are for the most part, averages of

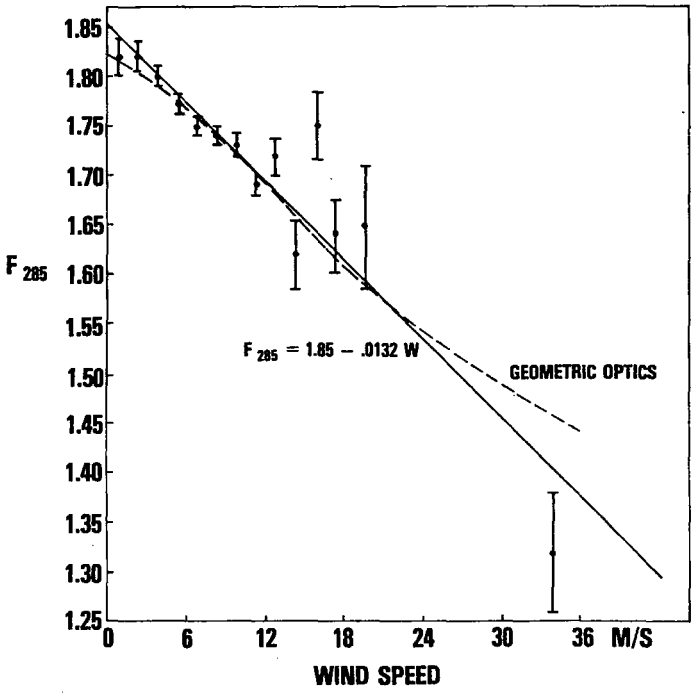

Fig. 3–Comparison between observed values of F_{285} and wind speed averaged over 1.5 m/s intervals.

many observations; a total of 264 observations are represented. In analyzing the data, it was found that a value of 285°K for T_1 worked best but that the improvement over any value in the range 280°K to 290°K was only marginal. Using the model described in the previous section the expected value of F_{285} has been calculated; the agreement with the observations is striking. A geometric optics model using the Cox and Munk sea surface slope distribution works extremely well at a wavelength of 0.8 cm and a view angle of 50°. Hollinger (1971) has made observations from a fixed platform at frequencies of 1.4, 8.36, and 19.34 GHz. He has filtered the data to remove most of the foam effect but application of an analysis technique similar to that applied to the Nimbus-6 ESMR data certainly removes the remainder. These data all can be interpreted in terms of the geometric optics model but with much less slope variance than the Cox and Munk values.

The fractions of the Cox and Munk slope variance required to account for the Hollinger data are plotted in Figure 4 along with the Nimbus-6 ESMR observation. These data form a picture consistent with the roughness required in our model (shown as a solid line).

CONCLUSION

A model has been presented for the microwave emissivity of a wind roughened, foam covered ocean. The roughness portion of the description is remarkably consistent with observations; the foam effects show somewhat more scatter. The strength of the foam cover effect at 6.6 and 10.7 GHz are important parameters in the interpretation of Nimbus-7 and Seasat SMMR data; the strength at higher frequencies, less so. In comparing the space observations with surface measurements of temperature and wind speed, it should be possible to adjust the foam effect at these two frequencies in order to fine-tune the retrieval algorithm.

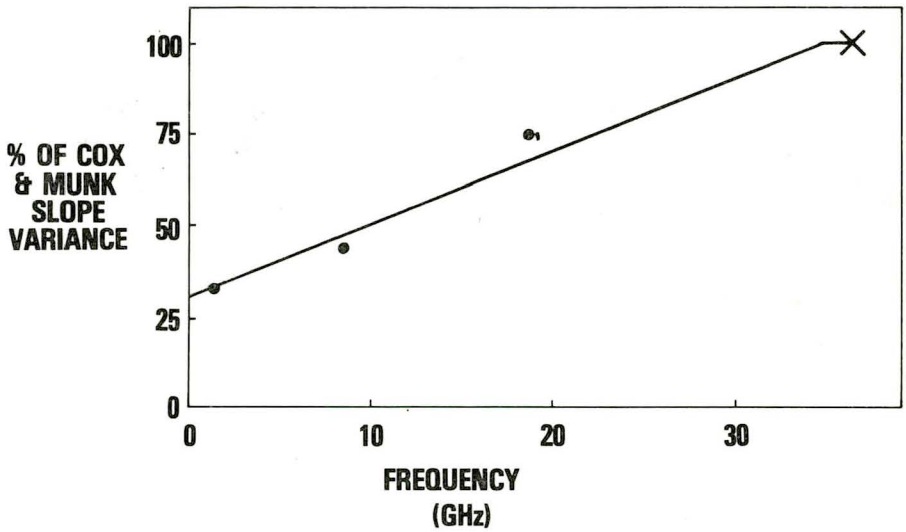

Fig. 4–Percentage of Cox and Munk (1955) slope variance required for a geometric optics model to explain the Nimbus-6 observations (X) and Hollinger (1971) (•) as a function of frequency.

REFERENCES

Cardone, V. J., "Specification of the Wind Distribution in the Marine Boundary Layer for Wave Forecasting," Ph.D Thesis, New York University, Department of Meteorology and Oceanography, 1969 (Available from NTIS Order No. AD702490).

Chang, A. T. C., and T. T. Wilheit, "Remote Sensing of Atmospheric Water Vapor, Liquid Water, and Wind Speed at the Ocean Surface by Passive Microwave Techniques From the Nimbus-5 Satellite," NASA TM-79568, June 1978 submitted to Radio Science.

Cox, C. and Munk, W., "Some Problems in Optical Oceanography," J. Marine Res. 14, 63-78 (1955).

Hollinger, J. P., "Passive Microwave Measurements of Sea Surface Roughness," Trans. IEEE Geoscience Electronics, GE-9, pp 165-169 (1971).

Jackson, J. D., "Classical Electrodynamics," John Wiley & Sons, Inc., New York (1962), p 216ff.

Kline, L. A., and C. T. Swift, "An Improved Model for the Dielectric Constant of Sea Water at Microwave Frequencies," Trans. IEEE AP-25 104-111 (1977).

Lane, J. A. and J. A. Saxton, "Dielectric Dispersion in Pure Polar Liquids at Very High Radio Frequencies," Proc. Roy. Soc., London A, 214, pp 531-545, (1952).

Nordberg, W., J. Conaway, D. B. Ross, and T. Wilheit, "Measurements of Microwave Emission from a Foam-Covered Wind Driven Sea," J. Atmos. Sci., 38, 429-435 (1971).

Shutko, A., "Report on Soviet Progress in Microwave Radiometry of the Ocean's Surface," presented at IUCRM Colloquium on Passive Radiometry of the Ocean's Surface, Patricia Bay, B.C., Canada, June 1978.

Stogryn, A., "Equations for Calculating the Dielectric Constant of Saline Water," Trans. IEEE, MTT-19 733-736 (1971).

Webster, W. J., Jr., T. T. Wilheit, D. B. Ross, and P. Gloersen, "Spectral Characteristics of the Microwave Emission from a Wind Driven Foam-Covered Sea," J. Geophys. Res. 81, 3095-3099 (1976).

Wilheit, T. T., "The Effect of Wind on the Microwave Emission From the Ocean's Surface at 37GHz," NASA TM-79588, July 1978 submitted to J. Geophys. Res.

Paper No. 39

APPLICATION OF NIMBUS-6 MICROWAVE DATA TO PROBLEMS IN PRECIPITATION PREDICTION FOR THE PACIFIC WEST COAST

W. Viezee and H. Shigeishi, *SRI International, Menlo Park, California,* and A. T. C. Chang, *Laboratory for Atmospheric Science, Goddard Space Flight Center, Greenbelt, Maryland*

1. INTRODUCTION

Reliable predictions of the rapid augmentation of mountain snowpack or of runoff in the Pacific Northwest westward of the Cascades depend largely on the extent to which pertinent percursor meteorological conditions can be diagnosed over the northeastern Pacific Ocean, where little or no conventional weather data exist. Although interpretations from satellite cloud-image data are increasingly used in weather forecast preparation, it is difficult to identify in advance those storm systems that produce surges of heavy precipitation over land, especially between October and April.

At present, the regional Limited-Area Fine-Mesh Model (LFM) of the National Meteorological Center (NMC) predicts precipitation for the West Coast. However, as pointed out by Fawcett (1977), the absence of observations over the eastern Pacific and the failure to model correctly atmospheric convection and complicated terrain effects on the atmosphere make the model less accurate over the western United States than for other geographic areas. Weather forecasters, therefore, must still depend on personal insight and experience in conjunction with numerical guidance when forecasting precipitation. The output of the numerical prediction models is currently complemented by objective precipitation forecasts from the Model Output Statistics (MOS) technique and the map-type PoPs (Klein and Glahn, 1974; Rasch and MacDonald, 1975); however, precipitation in moderate and heavy amounts remains one of the most difficult weather variables to predict.

Passive microwave sensors carried on satellite platforms provide measurements inside extensive storm cloud systems that the visible and infrared radiometers cannot obtain. For example, the electrically scanning microwave radiometer (ESMR) and scanning microwave spectrometer (SCAMS) instruments on the NIMBUS 5 and 6 satellites have provided data directly related to precipitable water, cloud liquid water, and rainfall over the ocean. This information should be exploited in research related to the precipitation prediction problems and the hydrology of the Pacific West Coast States, since conditions antecedent to significant precipitation and those with which numerical prediction models must be initialized develop over the ocean.

This paper reports on the preliminary results of a research study that emphasizes the analysis and interpretation of data related to total precipitable water and nonprecipitating cloud liquid water obtained from NIMBUS-6 SCAMS.

Sixteen cyclonic storm situations in the northeastern Pacific Ocean that resulted in significant rainfall along the west coast of the United States during the winter season October 1975 through February 1976 are analyzed in terms of their distributions and amounts of total water vapor and liquid water, as obtained from SCAMS data. The water-substance analyses for each storm case are related to the distribution and amount of coastal precipitation observed during the subsequent time period when the storm system crosses the coastline. Concomitant precipitation predictions from the LFM are incorporated into the study also. The overall objective of the research

is to explore techniques by which satellite microwave data over the ocean can be used to improve precipitation prediction for the Pacific West Coast states.

2. DATA ANALYSIS AND INTERPRETATION TECHNIQUE

Table 1 lists the 16 three-day periods for which storm cases over the northeastern Pacific Ocean were selected for analysis. In each case, the selected storm system moved eastward toward the West Coast.

The NIMBUS-6 SCAMS digital data tapes of vertically integrated water vapor and nonprecipitating cloud liquid water are used in the analyses. Two time periods of SCAMS data coverage (ascending and descending node) at intervals of 10 to 13 hours are available for each storm day.

Daily precipitation records were examined in conjunction with sequences of SMS-2 cloud images to determine the time period during which each selected storm system affected rainfall along the West Coast. For this time period (usually two to three successive days), rainfall observations at 27 coastal stations extending from Washington (48°N) to central California (34°N) were analyzed in terms of the latitude variation or distribution of coastal precipitation. This observed variation was then related to antecedent conditions of the storm's liquid water content over the ocean, as obtained from SCAMS.

The computer program used in analysis of the NIMBUS-6 SCAMS digital data and the coastal rainfall data has three major subroutines. One subroutine prints the satellite scan spot values for a given time period on a Mercator map extending from 30°N to 54°N latitude and 120°W to 168°W longitude. The second subroutine averages these data on a 1° mesh grid-point array (25 rows, 27 columns). For each time period, the third subroutine characterizes the storm (on the basis of the SCAMS data) in terms of the distribution of water vapor and liquid water as a function of latitude from north to south across the storm area.

Figures 1 and 2 illustrate the technique. Figure 1 shows the conditions of cloud liquid water associated with a major storm system over the ocean at 1045 GMT 7 Oct. 1975, and about 24 hours later, at 0915GMT 8 Oct. 1975. These

Table 1
Storm Cases in Northeastern Pacific Ocean Selected for Analysis

Case No.	Dates (PST)	Case No.	Dates (PST)
1	7 - 9 Oct 75	9	10 - 12 Dec 75
2	15 - 17 Oct 75	10	19 - 21 Dec 75
3	24 - 26 Oct 75	11	23 - 25 Dec 75
4	27 - 29 Oct 75	12	6 - 8 Jan 76
5	3 - 5 Nov 75	13	12 - 14 Jan 76
6	12 - 14 Nov 75	14	11 - 13 Feb 76
7	17 - 19 Nov 75	15	23 - 25 Feb 76
8	3 - 5 Dec 75	16	26 - 28 Feb 76

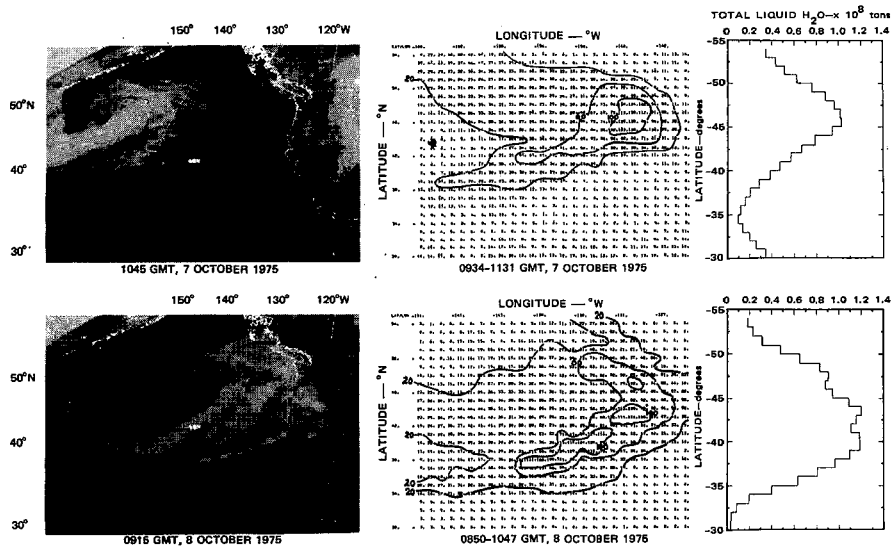

Fig. 1–SMS–2 infrared cloud image (left frame) and analysis of Nimbus–6 SCAMS cloud liquid water content (middle frame, units of mg/cm^2) for storm system at 1045GMT, 7 October 1975, and 24 hours later at 0915GMT, 8 October. Characteristic profiles of liquid water (right frames) are used to extract information on coastal rainfall distribution.

conditions are antecedent to the coastal rainfall shown in Figure 2, which indicates the observed distribution of 24-hour coastal rainfall for 8-10 Oct., and the 72-hour cumulative total for the three days. In Figure 1, the digital data of SCAMS liquid water (middle frames) are analyzed on the 1° mesh grid-point array. Each printed number represents the vertically integrated (columnar) liquid water, averaged over the grid square, expressed in units of 10^{-2} mm (mg/cm^2). The characteristic profiles of total liquid water (1° zonal strips across the grid-point area), expressed in units of 10^8 tons, are shown on the right side. Figure 1 shows that the SCAMS data:

- Have adequate quality for further analysis and interpretation.
- Reproduce the characteristic shape of the SMS–2 storm–cloud system.
- Reveal meaningful information on the space and time variations of cloud liquid water content not apparent in the image data.

Comparing the data of Figures 1 and 2 shows that the distribution of SCAMS cloud liquid water at about 0915GMT 8 Oct. has a maximum (>0.9 x 10^8 tons for 1° latitude intervals) between latitude 45°N and 37°N where coastal rainfall has a maximum on 9 Oct. and also in the three-day cumulative total. Thus, in this particular case, the distribution of the cloud liquid water content obtained from the NIMBUS–6 SCAMS contains information related to the distribution of coastal precipitation observed at a later time.

Analyses such as presented in Figures 1 and 2 were made for all 16 cases. Results of the research study are summarized below on the basis of representative case studies.

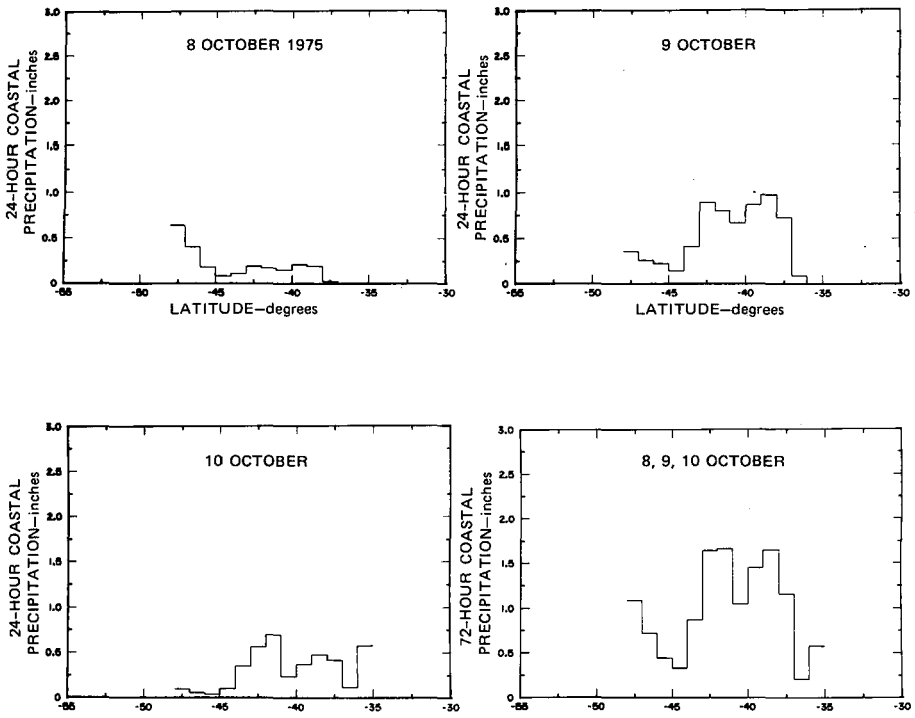

Fig. 2–Observed coastal rainfall distribution from Washington (48°N) to central California (34°N) during 3-day period in which storm system of Figure 1 affected weather conditions.

3. PRELIMINARY RESULTS

3.1 Discussion of Case Studies for December 1975

Table 2 summarizes the results for Cases 8 through 11 of Table 1. Two consecutive days of SCAMS data coverage are listed for each case. During these two days, the storm system moved eastward from about 145°W onto the West Coast. On each day, the area chosen for analysis is covered by SCAMS data from two consecutive descending-node (near local midnight) and two consecutive ascending-node (near local noon) NIMBUS–6 orbital passes. Each storm system is associated with approximately three consecutive days of coastal rainfall. At each listed time period t_0, the latitude (north to south) variation of SCAMS liquid water across the storm area is correlated with the distribution of the three-day (72-hour) cumulative coastal rainfall. The highest positive linear correlation coefficients are boxed: For these cases, the north-to-south distribution of storm-cloud liquid water at t_0 is quite similar to the distribution of the three-day total precipitation observed along the coast from Washington to central California at later time $t_0 + \Delta t$. The positive correlation increases when the two stations in Washington (Quillayute and Hoquiam), where rainfall is significantly affected by orography, are eliminated from the data sample.

Table 2
Linear Correlation Between SCAMS Liquid Water Distribution Over the Ocean at t_0 and Coastal 72-Hour Total Rainfall Distribution at $t_0 + \Delta t$

SCAMS Liquid Water Distribution			72-Hour Coastal Rainfall Distribution			
Case No.	Dates (Dec 75)	Time Period, t_0 (PST)	Δt (Hours)	Correlation Coefficient: With Washington: 48° - 34°N	Correlation Coefficient: Without Washington:* 46° - 34°N	Coastal Rainfall Dates (Dec 75)
8	3	0114-0312	96	+0.89	+0.88	4,5,6
		1130-1330	84	+0.90	[+0.92]	
	4	0033-0230	72	+0.69	+0.63	
		1047-1247	60	+0.28	+0.17	
9	10	0139-0333	96	+0.23	+0.27	11,12,13
		1201-1348	84	+0.39	+0.45	
	11	0052-0250	72	+0.63	[+0.71]	
		1107-1305	60	+0.47	+0.70	
10	20	0135-0332	72	-0.02	+0.15	20,21,22
		1151-1348	60	+0.34	+0.37	
	21	0051-0249	48	+0.62	[+0.71]	
		1107-1305	36	-0.54	-0.56	
11	24	0032-0228	96	+0.48	+0.03	25,26,27
		1233-1429	84	-0.41	-0.74	
	25	2347-0146	72	-0.61	-0.62	
		1150-1200	60	-0.10	[+0.53]	

*Boxed numbers indicate highest positive correlations, discussed in the text.

Figure 3 shows the information sets of the SCAMS cloud liquid water distribution over the ocean and the coastal precipitation distribution without the stations in Washington (46°N to 34°N) that correspond to the boxed correlations of Table 2. Table 2 shows that antecedent time periods (Δt) associated with the maximum (boxed) data correlations differ for each case, being 84 hours for Case 8 and 48 hours for Case 10. The reason is the difference in atmospheric circulation and storm movement.

The results for the storm cases examined in October and November 1975 showed that the distribution of the 72-hour cumulative coastal rainfall was highly correlated (linear correlation coefficients > 0.75) with the distribution of storm liquid water content over the ocean at a time period exclusively 60 to 72 hours earlier. The January and February cases showed results similar to those of Table 2, with variable antecedent time periods. The analyses results are straightforward when storms systems move from west to east, and our grid area (25° latitude x 26° longitude) encloses only one system at a time as was the case in October and November (see Figure 1). For December, January, and February, however, two frontal-wave systems were frequently present within the area of analysis, and a certain degree of discrimination must be exercised to separate the liquid water distributions.

3.2 Discussion of the LFM Data

We requested and received forecasts (printouts) of the amount of LFM precipitation corresponding to Cases 1 and 3 (October 1975) and Cases 5 and 7 (November 1975). Forecast periods up to 36 hours are available. Forecasts for longer time periods

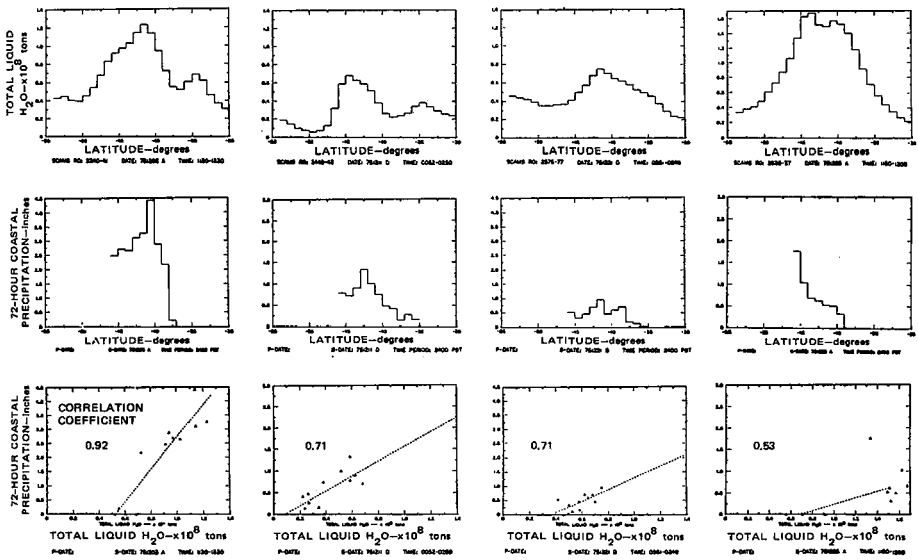

Fig. 3–Data sets of observed 72–hour coastal rainfall between 46°N and 34°N latitude, and of antecedent distribution of SCAMS liquid water over the ocean, that correspond to the high positive correlation coefficients of Table 2.

would have been preferable for comparison with the results of our October and November case studies, which showed high positive correlation between coastal rainfall distributions and the 60- to 72-hour antecedent SCAMS liquid water distributions over the ocean. From the available data, the LFM 24–hour precipitation predictions were selected for further analysis and interpretation in the following manner:

- The case studies for which LFM data are available were re–examined for high positive correlation between the distributions of observed coastal rainfall and of SCAMS data over the ocean at antecedent time periods less than the 60 to 96 hours considered previously (see Δt values in Table 2).
- For these "short-term" periods, our computer program analyzed the corresponding data sets of observed rainfall over land and antecedent total vapor and liquid water abundance over the ocean in a similar fashion, as shown in Figures 2 and 3. However, the coastal distributions of LFM 24-hour precipitation prediction closest in validation time to the time of observed precipitation (2400 PST) were included in the correlation.
- Values of LFM rainfall prediction at each location of the 27 coastal stations used in the study were obtained from the printouts by linear interpolation. These values provided the input to our computer program for correlation with the microwave sensor data.

An analysis sample is summarized in Figure 4 for Case 3 (25-27 Oct. 75). Available LFM 24-hour precipitation predictions, valid 1545 PST 25 Oct. and 0345 PST 26 Oct., are related to observed rainfall based on a midnight (2400 PST) observation time. In general, the distributions of SCAMS liquid water show a more

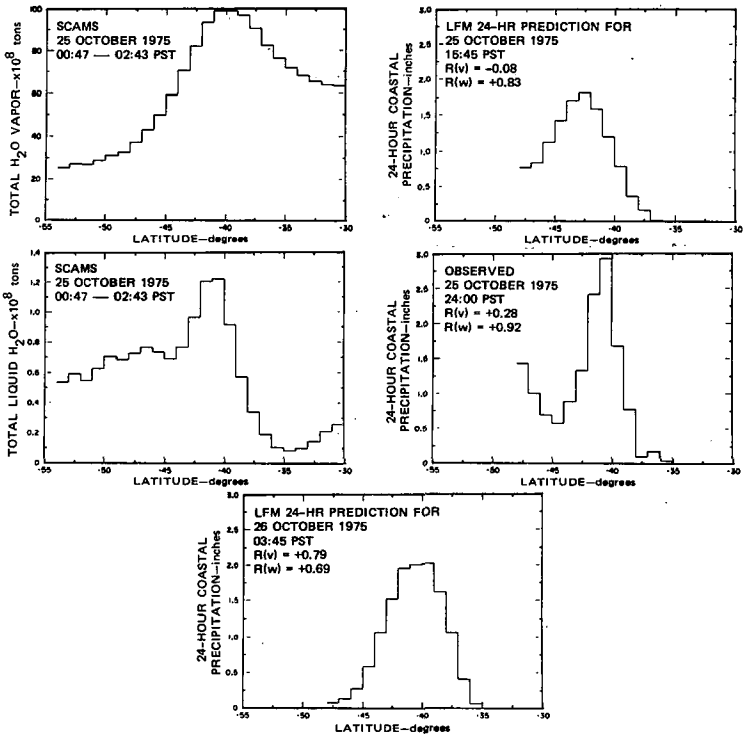

Fig. 4–Comparison between latitude variation of SCAMS–analyzed total vapor and liquid water abundance over the ocean, and the observed and LFM–predicted 24–hour cumulative coastal rainfall about 24 hours later. Degree of linear correlation of the latitude variation between the precipitation data sets and the SCAMS data is indicated by R(v) and R(w) for total vapor and liquid water, respectively (data refer to Case 3).

obvious relation than do the distributions of total vapor to observed and LFM-predicted rainfall at a later time. Most likely, total vapor would relate better if a background component of atmospheric water vapor, which results from the general increase in atmospheric temperature with decreasing latitude, were subtracted.

In Figure 4, the SCAMS liquid water distributions of 0047-0243 PST 25 Oct. 1975, shows a high positive correlation [R(w) = +0.92] with the distribution of coastal rainfall observed 24 hours later, and a somewhat lower positive correlation with the distributions of LFM-predicted rainfall about 15 hours later [R(w) = +0.83] and 27 hours later [R(w) = +0.69].

Analyses similar to those of Figure 4 were made for Cases 1, 5, and 7, and will be continued for other cases to explore the input of passive microwave remote sensor measurements of cloud liquid water to numerical prediction models.

4. CONCLUSIONS

Comparison and interpretation of information sets obtained from NIMBUS–6 passive microwave sensor data over the ocean and from precipitation records over

land indicate that rainfall along the coast of Oregon and California is related to antecedent conditions of remotely sensed storm-cloud liquid water content over the northeastern Pacific Ocean. Specifically, for each case examined, the distribution of SCAMS cloud liquid water across the storm system over the ocean foreshadows the relative distribution of coastal rainfall at a later time. Also, the antecedent SCAMS liquid water distributions over the ocean generally show a somewhat higher positive correlation with the observed coastal rainfall distributions than with the LFM-predicted distributions. This may indicate that the passive microwave remote sensor measurements contain information that can enhance the LFM predictions of coastal rainfall distribution.

REFERENCES

Fawcett, E. B., "Current Capabilities in Prediction at the National Weather Service's National Meteorological Center," Bull. Am. Met. Soc., 58, 143-149 (1977).

Klein, W. H., and H. R. Glahn, "Forecasting Local Weather by Means of Model Output Statistics," Bull. Am. Met. Soc., 55, 1217-1227 (1974).

Rasch, Glenn E., and Alexander E. MacDonald, "Map Type Precipitation Probabilities for the Western Region," NOAA Technical Memorandum, WR-96 (February 1975).

Paper No. 40

A STUDY OF THE EXPECTED EFFECTS OF LATITUDE-DEPENDENT ROTATION RATE ON LABORATORY GEOPHYSICAL FLOW EXPERIMENTS

J. E. Geisler, *Rosenstiel School of Marine and Atmospheric Science, University of Miami, Miami, Fla. 33149,* W. W. Fowlis, *Space Sciences Laboratory, Marshall Space Flight Center, Alabama 35512*

ABSTRACT

This paper reports results of a theoretical model study of some of the expected effects of spherical geometry on laboratory simulations of the type of geophysical flow that dominates the general circulation of the earth's troposphere.

INTRODUCTION

The traditional device for laboratory simulation of the general circulation of the atmosphere is an annular container of liquid situated on a rotating turntable (Hide, 1958; Fowlis and Hide, 1965). Fluid motion is driven by heating the outer wall of the annulus and cooling the inner wall, a crude analog of the observed fact that the earth's troposphere is heated in the tropics and is cooled in high latitudes. In the real atmosphere and in the laboratory annulus, the function of the motion field is to transport heat laterally from the heat source to the heat sink.

The annulus suffers from the defect that its geometry is far different from that of our spherical-shell atmosphere. Attempts to design a rotating spherical laboratory device have been frustrated by the presence of gravity, which acts vertically downward in the laboratory. This influence would be absent in a satellite. Atmospheric general circulation simulations in a spherical container with an electrostatic radial force field acting as "gravity" on a fluid with radially dependent dielectric constant have been proposed for Spacelab by Fowlis and Fichtl (1977). In this paper we report some results of a simple mathematical model study which isolates some of the expected differences between annulus flows and spherical shell flows.

THE MODEL

Consider a spherical shell of fluid rotating with constant angular velocity around a polar axis. The local vertical component of this rotation vector varies as the sine of the latitude, being zero for an equatorial observer and a maximum for a polar observer. As is generally well known, this latitudinal variation

of the local vertical component of rotation plays a significant role in the dynamics of the class of motions constituting the general circulation of the atmosphere (and laboratory simulations thereof). The simplest mathematical model which incorporates this effect is one in which the relevant equations are written in a Cartesian (rectangular) coordinate system rotating with respect to the vertical axis. This rotation rate is taken to be constant in the equations, except when it is differentiated with respect to the north-south coordinate. This local tangent-plane formulation of fluid motion on a sphere is generally known as the β-plane. If rigid walls are erected at two arbitrary latitudes in this model, we have a β-plane channel.

In its treatment of the dynamical effects of rotation, the β-plane channel is sort of midway between an annulus and a sphere. In our mathematical model study, we have subjected the β-plane channel to different degrees of cross-channel heating and different rotation rates, and noted the character of the resulting motion field. In particular, following the traditional description of the analogous flow patterns in the annulus, we distinguish between axially-symmetric motions and wave motions.

RESULTS

Figure 1, shows a so-called regime diagram (after Fowlis and Hide, 1965) showing the types of motion occuring in a typical annulus experiment.

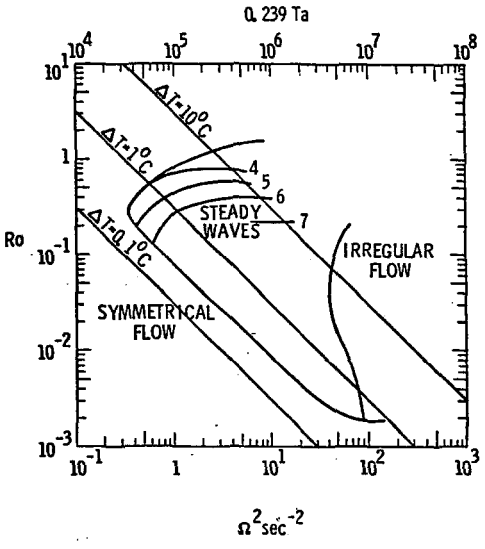

Figure 1
Experimentally determined regime diagram for annulus flow

The horizontal axis in the figure is the rotation rate squared; the vertical axis in the figure is a "thermal Rossby number", which varies directly with the imposed thermal contrast across the annulus and inversely as the square of rotation rate. We wish only to call attention to the fact that in this parameter space the region occupied by waves is bounded on the left by a convex, "knee-shaped" curve which we refer to as the stability boundary.

Figure 2 shows results of a simple mathematical model simulation of annulus flow (after Barcilon, 1964).

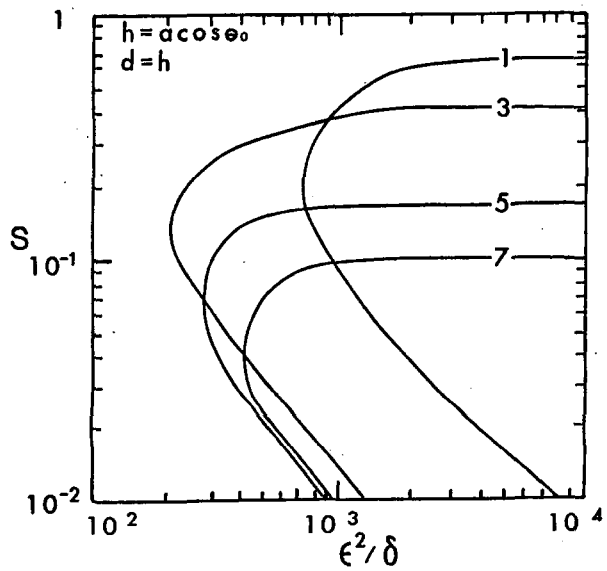

Figure 2
Theoretically determined regime diagram for annulus flow

The parameter space in this figure can be shown to be essentially identical to the parameter space in Figure 1. Each curve is the stability boundary for the zonal wavenumber shown. (Zonal wavenumber is formally equivalent to quantum number; that is, zonal wavenumber 1 means that the horizontal wavelength of the wave is exactly equal to the circumference of the annulus). The stability boundary for the system is the envelope of these curves. It is seen that this theoretically-obtained stability boundary has

essentially the same shape as the experimentally determined one (Figure 1).

Figure 3 shows results from our β-plane channel model when the dimensions of the channel are the same as the annulus in Figure 2.

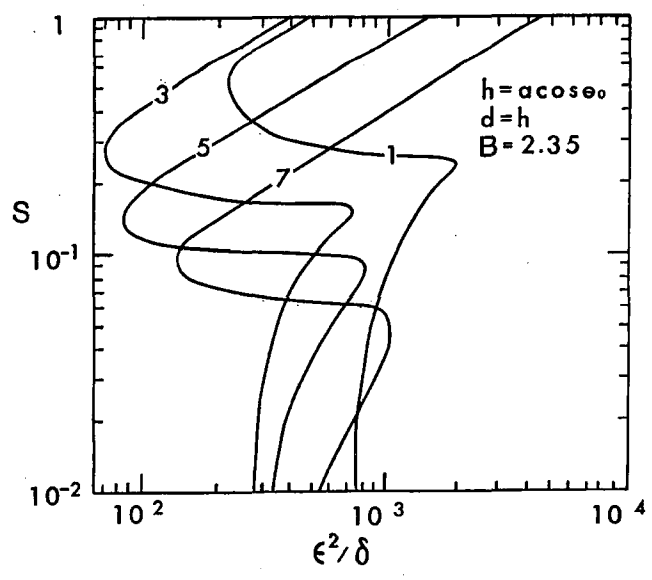

Figure 3
Theoretically determined regime diagram for β-plane channel flow

Again, the envelope of all these curves is by definition the stability boundary. In comparing this with Figure 2, it can be seen that the stability boundary has a considerably different shape and that it extends somewhat farther to the left. The conclusion here is that the β-effect (that is, the variation of local vertical rotation rate with latitude) results in more of parameter space being occupied by waves. Another interesting result, not discussed here, is that the β-effect produces a marked change in the vertical structure of the waves present and it also greatly changes the dependence of the results on the presence of a rigid lid upper boundary condition.

We have repeated these model simulations for a wide range of

channel dimensions and compared these results with simulations in annular geometry. These simulations support the general conclusion that the β-effect drives the stability boundary to the left in the parameter space diagram.

REFERENCES

Barcilon, V., 1964: Role of Ekman layers in the stability of the symmetric regime obtained in a rotating annulus. J. Atmos. Sci., 21, 291-299.

Fowlis, W. W. and Fichtl, G. H.: Geophysical Fluid Flow Model Experiments in Spherical Geometry. Proceedings of the Third NASA Weather and Climate Program Science Review. NASA Conference Publication 2029, Paper No. 32, 1977, p. 177.

Fowlis, W. W. and R. Hide, 1965: Thermal convection in a rotating annulus of liquid: effects of viscosity on the transition between axisymmetric and non-axisymmetric flow regimes. J. Atmos. Sci. 541-558.

Hide, R. 1958: An experimental study of thermal convection in a rotating liquid. Phil. Trans. Roy. Soc. Lond. A, 250, 441-478.

Page intentionally left blank

Paper No. 41

THE EFFECT OF SURFACE REFLECTION AND CLOUDS ON THE ESTIMATION OF TOTAL OZONE FROM SATELLITE MEASUREMENTS

R. S. Fraser, *Goddard Space Flight Center, Greenbelt, Maryland*
Z. Ahmad, *Systems and Applied Sciences Corporation, Riverdale, Maryland*

ABSTRACT

The total amount of ozone in a vertical column is being measured by Nimbus 4 and 7 observations of the intensity of ultraviolet sunlight scattered from the earth. The algorithm for deriving the amount of ozone from the observations uses the assumption that the surface reflects the light isotropically and the albedo is independent of wavelength. The effects of anisotropic surfaces and clouds on the estimate of total ozone are computed for models of the earth-atmosphere system.

INTRODUCTION

Nimbus 4 and 7 are making an important series of measurements of the total amount of ozone for most of the world over a period of many years. The amount of ozone is estimated from the intensity of the sunlight scattered from the earth in several bands within the 300 to 400 nm band. Since ozone absorbs light within this band, the intensity of the scattered light decreases as the amount of ozone increases. The algorithm for deriving the amount of ozone is based on a model of the earth-atmosphere system utilizing two assumptions: a) the surface reflects light isotropically according to Lambert's law; and, b) the surface reflectance, or albedo, is independent of wavelength.

Generally, these assumptions are not true, but methods have not been developed for improving the physical reality of the algorithm model. Nevertheless, advanced models of the earth-atmosphere system can be developed for computing the errors caused by these assumptions in estimations of the total amount of ozone. Results of computing the effects for strongly anisotropic surfaces will be discussed first, and then for clouds.

Anisotropic Reflection

The method for estimating the ozone error is to compute the intensity of ultraviolet light scattered by models of the earth-atmosphere system. The total amount of ozone in a vertical column is derived from the intensity by means of the same algorithm used for processing the Backscattered Ultraviolet Instrument measurements.

The effect of rough ocean surfaces is investigated first. The surface is assumed to be an ensemble of randomly oriented, small, reflecting facets. The reflection characteristics are computed according to the Cox-Munk theory (1954). Figure 1 shows how well the computed and measured values compare. The dots represent the intensities measured by Dr. Curran from the NASA Convair 990 aircraft at a height of 10.5 km. The abscissa gives the nadir angle of observation. The intensities are computed for 3 model atmospheres, each with a different aerosol model. The model containing haze L (index of refraction m=1.341-0.0i) agrees best with the measured values over an intensity range of an order of magnitude. The absolute accuracy of the computed intensity is not critical, but good precision is needed for computing changes in intensity associated with model perturbations. The precision of such computations are as good as the measured values -- namely, a few percent.

Table 1 gives the total ozone errors associated with wind speeds of 2 and 10 ms^{-1} and three solar zenith angles. The third column gives the albedo, or hemispherical reflectance for the model. The fourth column gives the albedo that is derived from the ozone algorithm on the assumption that the surface reflects light according to Lambert's law. The albedo is strongly overestimated when the nadir field-of-view is directed towards the bright solar glint. As the solar zenith angle increases and the glint pattern moves away from the nadir field-of-view, the derived albedo approaches the true value.

The total ozone errors in Dobson Units (DU) are given in the last column. They are -2% to -3% -- slightly less than the errors in the satellite values. The errors are small, because the algorithm utilizes the ratio of intensities in moderately and weakly absorbing bands. The effects of surface anisotropy on the reflected intensities is about the same in both bands.

TABLE 1

Model and derived surface albedos for λ380 nm. The last column gives the deviation in the derived amount of ozone from the model value of 240 DU.

Wind Speed (m/s)	Solar Zenith Angle (Degrees)	Surface Albedo Model	Surface Albedo Derived	Total Ozone Deviation (DU)	
2	0	0.04	0.23	-5	(-2%)
	28	0.04	0.08	-7	(-3%)
	58	0.08	0.08	-4	(-2%)
10	0	0.040	0.13	-8	(-3%)
	28	0.045	0.09	-6	(-2%)
	58	0.080	0.07	-4	(-2%)

Effects of deviations in the physical state of the atmosphere from the algorithm model tend to cancel in the ratio.

The effect of a snow-ice surface is discussed next. The measured and computed intensities of light reflected from a snow surface are shown for the principal plane containing the sun, the observer, and his zenith in Figure 2. The radial lines give the direction of travel of a photon. The parallel source of light ofπ units of flux is incident at an angle of 150° from the surface. The circular curves give the intensity of reflected light. The value of isotropic reflection is 1/2, independent of the angle. The values computed for a snow-ice surface are given by the continuous curve labeled as anisotropic. The dashed curve gives measured values. The magnitudes are not important, since they can be adjusted by varying the albedo within a large allowable range (O'Brien, 1977). The measured and anisotropic values are nearly isotropic for backward reflection; but show the strong forward scattering, similar to the solar glint pattern on water.

Table 2 gives the error in the derived amount of ozone, which is 16 DU out of a total of 342 DU. The error is the same when the surface reflects light isotropically, showing that the anisotropic effect is not the cause of the error. The error arises because the Antarctic region is modeled, and the surface is 3.6 km above sea level. When the surface reflectance exceeds 0.8, the algorithm calculates the total amount of ozone for a surface that is 7 km above sea level. The difference between the model and algorithm heights is the reason for the error.

TABLE 2

Surface albedos and total ozone deviations using the intensities at the top of the atmospheres with two surface characteristics. The total amount of ozone in the model is 342 DU. The solar zenith angle θ_o=58°. The surface is 3.6 km above sea level.

Surface Reflectance	Surface Albedo (λ380 nm) Model	Derived	(DU)
Isotropic	0.96	0.96	16 (5%)
Anisotropic	0.95	0.94	16

Clouds

There are no reliable observations of cloud albedo for the λ300 - 400 nm band. We have calculated the reflection and transmission characteristics of a cloud of water drops with an optical thickness τ_c=20 at λ380 nm. Its albedo increases slightly from 0.66 to 0.67 as the wavelength increases from 312 to 380 nm (the solar zenith angle θ_o=48°). Addition of 2 DU of ozone, appropriate for a cloud 1.5 km thick, does not change the albedo appreciably (see Figure 3).

The effect of the atmosphere and a ground surface at sea level on the albedo at the top of cloud is shown in Figure 3. The top of the cloud is placed at the pressure level of 0.4 atm and the base at 0.5 atm. The albedo at the cloud top is weakly dependent on the wavelength, when the surface albedo is small, as for oceans, bare and vegetated lands. On the other hand, when the surface albedo is high, as for snow and ice, the albedo at the cloud top increases significantly with wavelength (Figure 3).

Table 3 shows the deviation in the total amount of ozone in a vertical column caused by clouds. When the surface albedo is small, the error is small. When the surface albedo is large, the ozone errors become significant. The errors decrease with solar zenith angle, because the cloud reflectance increases, and less light is transmitted to interact with the lower atmosphere and ground. These results indicate that high clouds cause a small error in the derived amounts of ozone over surfaces of low reflectivity, but a moderate positive bias over snow surfaces.

TABLE 3

Deviation in the total amount of ozone (DU) caused by a layer of clouds whose upper surface is at pressure of 0.4 atm. The total amount of ozone is 350 DU.

surface albedo \ solar zenith angle	0°	68°
0.07	5 (1.47%)	1 (0.3%)
0.90	27 (7.7%)	11 (3.1%)

Summary

Surface anisotropy causes small errors in the amount of ozone estimated from satellite measurements of the intensity of scattered ultraviolet sunlight. The anisotropic effects for water and snow-ice are nearly independent of wavelength. The algorithm for estimating the total amount of ozone computes the ratio of intensities in moderate and weakly absorbing bands and compares this ratio with values computed for a model with Lambert reflectance. The difference in intensities between the Lambert and anisotropic models tends to cancel in the ratio, resulting in small ozone error.

Since the surface albedo of the algorithm model is independent of wavelength, variations from such a model cause ozone errors. A high cloud above a bright surface causes moderate ozone errors, but small errors above a dark surface.

References

Cox, C. and W. Munk, 1954: The measurement of roughness of the sea surface from photographs of the sun glitter. Jo. Opt. Soc. Amer., 44, 838-850.

Middleton, W.E.K. and A.G. Mungall, 1952: The luminous directional reflectance of snow. Jo. Opt. Soc. Amer., 42, 572-579.

O'Brien, H.W., 1977: Observations of the Ultraviolet Reflectance of Snow. Cold Regions Research and Engineering Laboratory, Hanover, New Hampshire, Report No. 77-27, 19p.

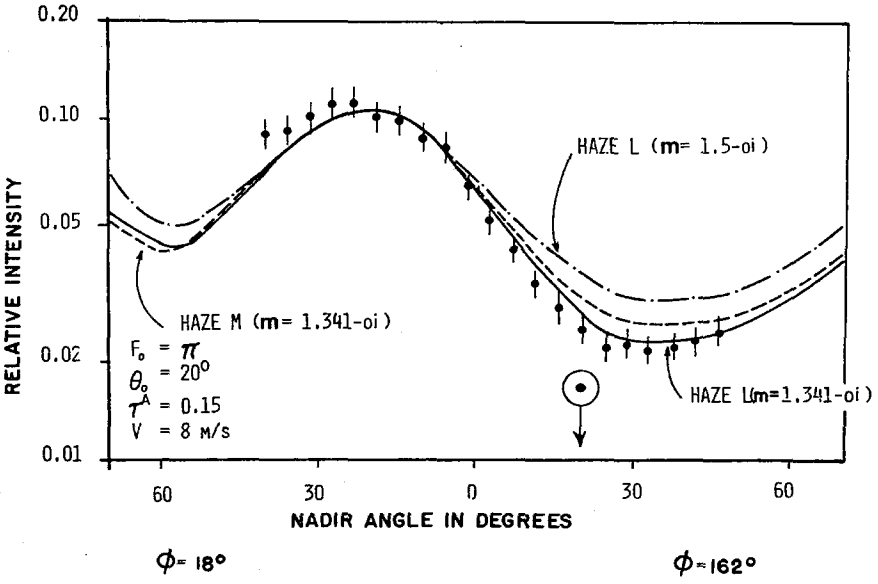

Fig. 1. Upwelling intensities at a height of 10.5 km. The dots give the measured values, and the lines give the values computed for model atmospheres.

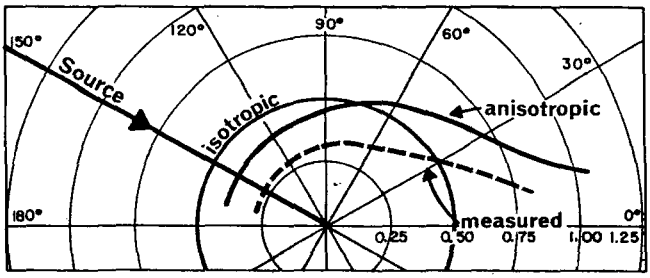

Fig. 2. The computed intensity of light reflected from model snow surfaces compared with values measured by Middleton and Mungall (1952) as a function of the angle from the horizon in the vertical plane containing the source of parallel light, which is located at a zenith angle of θ_o=60°. The source flux is π units. The model isotropic, model anisotropic, and measured intensities are represented respectively by the dot-dashed, continuous and dashed lines; their respective albedos are 1.0, 0.94, and 0.67.

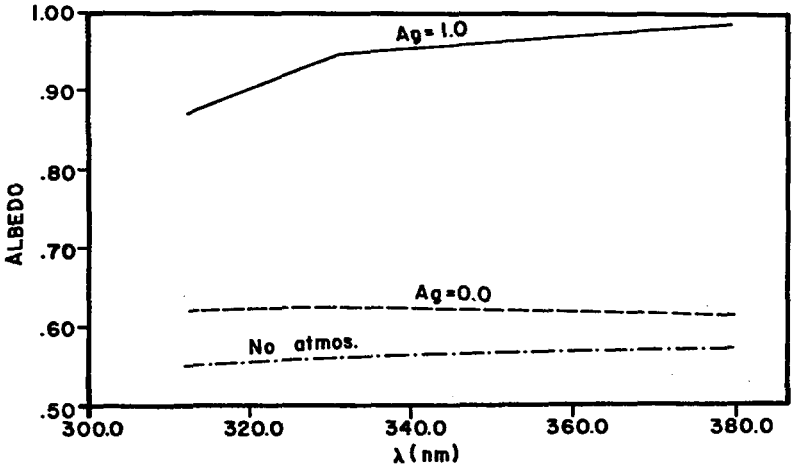

Fig. 3. The albedo at the upper cloud surface as a function of wavelength. The upper two curves are for ground albedos of 0.0 and 1.0. The lowest curve gives the cloud albedo in the absence of the earth's atmosphere and surface. The solar zenith angle is 0°.

Paper No. 42

APPLICATION OF A COUPLED AEROSOL FORMATION – RADIATIVE TRANSFER MODEL TO CLIMATIC STUDIES OF AEROSOLS

O. B. Toon, J. B. Pollack, *NASA-Ames Research Center, Moffett Field, California*

ABSTRACT

A sophisticated one-dimensional physical-chemical model of the formation and evolution of stratospheric aerosols has been used to predict the size and number concentration of the stratospheric aerosols as functions of time and altitude following: a large volcanic eruption; increased addition of carbonyl sulfide (OCS) or sulfur dioxide (SO_2) to the troposphere; increased supersonic aircraft (SST) flights in the stratosphere; and, large numbers of Space Shuttle (SS) flights through the stratosphere. A radiative-convective one-dimensional climate sensitivity study, using the results of the aerosol formation model, was performed to assess the ground level climatic significance of these perturbations to the stratospheric aerosol layer. Volcanic eruptions and large OCS or SO_2 increases could cause significant climatic changes. Currently projected SS launches and moderate fleets of SST's are unlikely to upset the stratospheric aerosol layer enough to significantly impact climate.

INTRODUCTION

Stratospheric sulfuric acid aerosols normally form an optically thin layer centered near 20 km. Observations of the aerosols show that significant optical depths occur after large explosive volcanic eruptions. Observations as well as theoretical calculations indicate that these enhanced optical depths can lead to significant climatic cooling because the aerosols backscatter solar energy to space (1, 2, 3). Observations of the aerosol optical properties after a volcanic eruption are very limited, severely complicating the difficulties in correctly, theoretically, evaluating the climatic impact of the volcanic aerosols. Hence we developed a 1-D physical-chemical aerosol model to calculate the aerosol optical properties beginning with the aerosol formation from gaseous precursors and considering all the microphysical and large scale processes affecting the aerosol's evolution (4, 5).

In our earlier work we applied the aerosol formation model, together with a 1-D radiative convective calculation of the Earth's vertical temperature profile to theoretically reassess the effects of volcanic aerosols on climate (6). We found that the volcanic aerosols significantly cooled the surface and warmed the stratosphere, in good agreement with observations.

The volcanic aerosols are short-lived ($\sim$2 years) and have significant latitudinal dependence so a proper evaluation of their climatic impact requires at least two-dimensional aerosol and climatic modeling. Such models are under construction. Other perturbation sources to the aerosol layer, such as SST, and SS flights, and increased levels of tropospheric OCS and SO_2 would be long-lived and globally homogeneous due to the continuous nature of the sources. Hence, we have proceeded with 1-D studies of the aerosol enhancement due to these sources.

Aerosol Changes Due to Space Shuttles and SST's

Space Shuttle engines will inject large numbers of small Al_2O_3 particles into the stratosphere. These particles are too small to directly enhance the optical depth of the aerosol layer, but sulfuric acid vapor could condense on these particles and so create larger acid particles which would be optically significant. In order to properly evaluate this possibility, a sophisticated aerosol model, such as the one described here, is a necessity. SST's inject both SO_2 and soot particles into the stratosphere. The SO_2 becomes photochemically converted into H_2SO_4 and directly augments the acid particles, while the soot could serve as nuclei for the growth of new acid aerosols.

Figure 1 illustrates the ambient aerosol size distribution at 20 km, the size distribution if 50 shuttle flights occur every year, and the size distribution that would result if 1 year's supply of Al_2O_3 from the shuttle engine was stored in the stratosphere. Evidently, the small shuttle particles are quickly lost by coagulating with the acid aerosols, few new acid aerosols are formed and the net effect on the aerosol layer is rather small. A similar situation is illustrated in Figure 2 which shows that neither the SO_2 nor the soot from 300 SST's flying 7½ hours per day in the stratosphere has a large effect on the aerosol layer.

The temperature changes due to the aerosol modifications illustrated by Figures 1 and 2 as calculated with the radiative convective model are on the order of 3×10^{-4} °K for 50 SS flights per year and on the order of 3×10^{-3} °K for the fleet of 300 SST's. These changes are undetectably small.

Aerosol Changes Due to Enhanced OCS and SO_2 Emissions

The background stratospheric aerosol layer is apparently maintained by tropospheric SO_2 and OCS diffusing into the stratosphere. Both these sulfur compounds are products of industrial processes and could therefore be significantly enhanced by man. OCS in particular has a relatively long lifetime in the atmosphere, its major source is unknown at present, and quantitative knowledge of its emission rate from industrial processes is not available.

Figure 3 illustrates the effects on the aerosol layer of removing SO_2 and OCS and of increasing SO_2 by a factor of 10 and OCS by factors of 5 and 10. Obviously, OCS provides most of the sulfate to the ambient layer, though SO_2 is significant at lower altitudes. Enhanced OCS or SO_2 significantly perturbs the aerosol layer, and may increase the aerosol mass by a factor of 2-4.

Using the 1-D radiative convective model we find that the Earth's surface temperature might decrease by a slightly more than $0.1^{\circ}C$ due to a tenfold enhancement of OCS. Within the aerosol layer the stratospheric temperature increased by about $0.1^{\circ}C$ due to an increase of OCS by a factor of 10. We have not yet completed the radiative calculations for an SO_2 enhancement by 10, but based on the aerosol model results, they should be comparable to those due to the OCS enhancement by a factor of 10. Wang et al's (7) results suggest that a tenfold increase in SO_2 might increase the temperature by about $0.1^{\circ}C$ due to an increased greenhouse effect. However, the SO_2 concentration drops sharply with altitude so a tenfold increase in the stratosphere could result without a corresponding increase in net tropospheric SO_2 by altering the upper tropospheric SO_2 sinks. Hence the net climatic impact of increased SO_2 depends on the circumstances of its alteration. No greenhouse calculations have been reported for OCS. However, OCS does have an absorption feature near 850 cm^{-1} so its greenhouse effect could be significant compared with the aerosol impact.

Temperature changes on the order of $0.1^{\circ}C$ are marginally significant climatic changes. So little is known about OCS that a factor of 10 increase in its abundance cannot be ruled out. Further information on the source of OCS, and on its greenhouse effect is important to obtain.

References

1. J.B. Pollack, O.B. Toon, A. Summers, B. Baldwin, C. Sagan, and W. Van Camp, "Stratospheric Aerosols and Climatic Change," Nature, 263, 551 (1976).

2. J.B. Pollack, O.B. Toon, C. Sagan, A. Summers, B. Baldwin, and W. Van Camp, "Stratospheric Aerosols and Climatic Change," Nature, 263, 551 (1976).

3. J.E. Hansen, W. Wang, and A. Lacis, "Mt. Agung Eruption Provides Test of Global Climatic Prediction," Science, 199, 1065 (1978).

4. R.P. Turco, P. Hamill, O.B. Toon, R.C. Whitten and C.S. Kiang, "A One-Dimensional Model Describing Aerosol Formation and Evolution in the Stratosphere--I, Physical Processes and Numerical Analogs," in press J. Atmos. Sci., (1978).

5. O.B. Toon, R.P. Turco, P. Hamill, R.C. Whitten, and C.S. Kiang, "A One-Dimensional Model Describing Aerosol Formation and Evolution in the Stratosphere--II, Sensitivity Studies and Comparison with Observations," in press J. Atmos. Sci., (1978).

6. J.B. Pollack and O.B. Toon, "Stratospheric Aerosols and Climatic Change," Third NASA Weather and Climatic Program Science Review, ed. E. Kreins, NASA Cp 2029, p. 159, (1977).

7. W.C. Wang, Y.L. Yung, A.A. Lacis, T. Mo, J.B. Hansen, "Greenhouse Effects Due to Man-Made Perturbations of Trace Gases", Science, 194, 685, (1976).

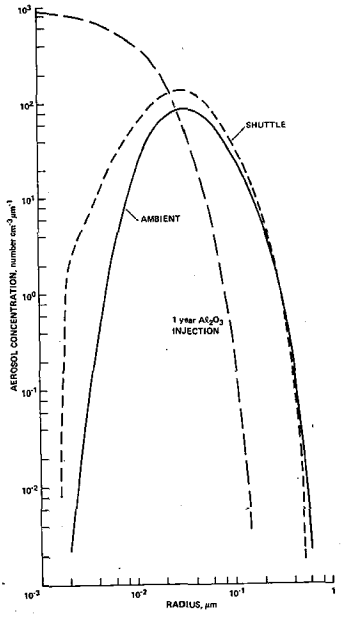

Fig. 1: Aerosol size distribution at 20 km under ambient and Space Shuttle perturbed conditions, as well as 1 year's Space Shuttle debris.

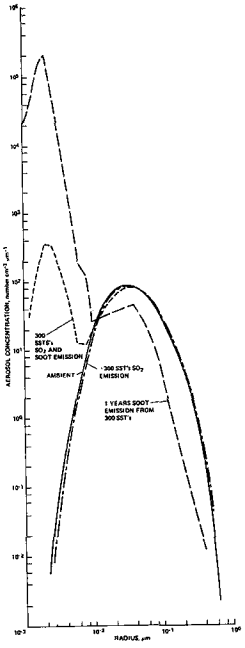

Fig. 2: Aerosol size distribution at 20 km under ambient and SST perturbed conditions as well as 1 year's SST soot emissions.

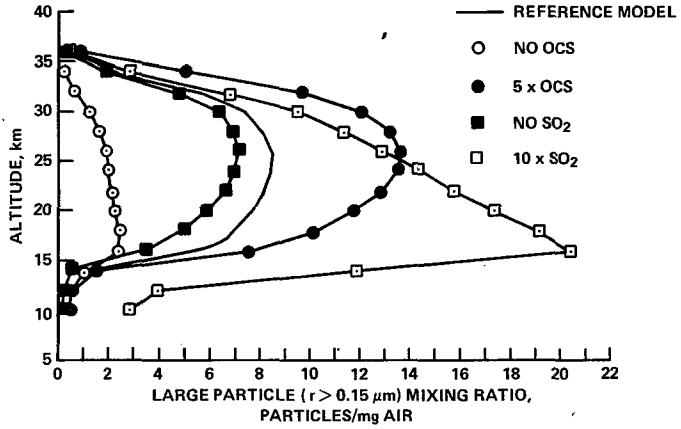

Fig. 3: Large particle mixing ratio under ambient conditions, and for altered ground level abundances of SO_2 and OCS.

Page intentionally left blank

Paper No. 43

PERTURBATION OF THE ZONAL RADIATION BALANCE BY A STRATOSPHERIC AEROSOL LAYER

Harshvardhan, *University of Maryland, College Park, Maryland*

ABSTRACT

The effect of stratospheric aerosols on the earth's monthly zonal radiation balance is investigated using a model layer consisting of 75% H_2SO_4, which is the primary constituent of the background aerosol layer.

INTRODUCTION

The role of stratospheric aerosols in enhancing the reflection of solar radiation has been investigated recently by numerous authors (e.g., Pollack, et al. 1976). Model calculations have shown that the dominant climatic effect of these aerosols is enhanced solar reflection with increased infrared opacity playing a smaller role. However, Herman, et al., (1976) have also pointed out that the degree of albedo enhancement is a strong function of the albedo of the underlying surface and the zenith angle of the incident solar radiation.

In this work, the effect of the aerosol layer at solar wavelengths will first be presented in terms of the albedo sensitivity, which may be defined as $d\alpha/d\tau$, where α is the unperturbed system albedo and τ is the optical depth computed at some reference wavelength, here $0.55\mu m$. The zonal variation of albedo sensitivity by month, together with the seasonal variation of solar irradiation yields the solar perturbation. With the inclusion of the effect of the stratospheric aerosol layer on the infrared radiation leaving the top of the atmosphere, the net energy deficit on a zonal basis is obtained.

AEROSOL LAYER

There is a persistent tenuous layer of submicron size aerosols in the stratosphere that is composed primarily of an aqueous solution of sulfuric acid. The number concentration of this aerosol layer increases after major volcanic events, and as the residence time of these aerosols is of the order of a year or more, radiative perturbations may be expected. Initially this enhanced concentration is limited to the vicinity of the explosion but in a matter of months may spread globally.

One result of this severe enhancement is the additional reflection of solar energy back to space. A radiative model of the aerosol is needed to compute the reflectivity of the layer. The aerosol composition is assumed to be 75% H_2SO_4 and a modified gamma size distribution is adopted. Since the optical depth of the aerosol layer is small (~ 0.1) even after major volcanic events, the optically thin approximation is used to compute the reflectivity of the layer. Use of the Henyey-Greenstein phase function yields analytical expressions for the planar albedo, $a(\mu_o)$,

and global albedo, $\bar{a}$, which are used here. The altered albedo of the earth–atmosphere system with the addition of a non-absorbing aerosol layer is

$$\alpha(\mu_o) = a(\mu_o) + \frac{\alpha'(\mu_o)\ [1 - a(\mu_o)]\ (1 - \bar{a})}{1 - \bar{a}\ \alpha'(\mu_o)} \tag{1}$$

where $\alpha'(\mu_o)$ is the unperturbed system albedo. A similar relationship exists for absorbing aerosols.

The albedo sensitivity averaged over the solar spectrum for the model aerosol layer is presented in Figure 1. Use has been made of the monthly zonal albedo given by Ellis and Vonder Haar (1976) to compute the sensitivity. The isopleths are in units of change in albedo in percent of incident solar energy for an optical depth perturbation of $\Delta\tau = 0.01$. In the optically thin limit, the response is linear and the effect of other layer thicknesses or non-uniform spread can be easily deduced. The dominant feature is seen to be the zenith angle dependence translated here in a monthly and latitudinal dependence. Over high latitudes the effect of surface reflectivity may also be noticed, such as the lower values of $\Delta\alpha/\Delta\tau$ in late winter and early spring when there is snow cover on the ground.

RADIATION BALANCE

The net zonal radiation balance is

$$D(\phi) = Q(\phi)\ [1 - \alpha(\phi)] - I(\phi) \tag{2}$$

where $Q(\phi)$ is the solar insolation at latitude ϕ, $\alpha(\phi)$ the albedo, $I(\phi)$ is the outgoing terrestrial infrared radiation. The presence of a stratospheric aerosol layer modifies α through increased reflectivity and I through an increased greenhouse effect acting in the opposite direction. The reduction in solar energy absorbed, $Q\Delta\alpha$, caused by a uniform stratospheric layer of $\tau_{vis} = 0.1$ is plotted in Figure 2 which follows from Figure 1 and the distribution of $Q(\phi)$ for each month.

The net loss in a column of the earth–atmosphere system, however, is $Q\Delta\alpha + \Delta I$ (note that ΔI is a gain, hence negative), which is the change in the radiation balance and it is necessary to compute the infrared greenhouse sensitivity of the aerosol layer. This is done for five model atmospheres using an atmospheric radiation model similar to the one by Harshvardhan and Cess (1978) in which an emissivity formulation has been used to calculate the infrared flux. When the infrared effect is combined with the solar perturbation, the net reduction in zonal radiation balance is obtained and is plotted in Figure 3.

The perturbation in the radiation balance can also be expressed as a change in the effective black-body radiative temperature of the atmosphere. This change is given by

$$\Delta T = -\frac{Q\Delta\alpha + \Delta I}{4\sigma T^3} \tag{3}$$

where σ is the Stefan–Boltzmann constant, T the effective black-body radiative temperature of the atmospheric column and $(Q\Delta\alpha + \Delta I)$ the decrease in the radiation balance. Figure 4 is a plot of ΔT in °K for $\tau_{vis} = 0.1$. It can be seen that the major radiative effect of the stratospheric aerosol layer occurs in the spring and fall when there is a pronounced change in the equator to pole radiative energy

gradient. As the results pertain to the entire atmospheric column, it is not possible to estimate the change in the diabatic heating at various levels of the atmosphere or estimate surface temperature changes. However, it appears from this analysis that a uniform layer of stratospheric aerosols would have only a small effect on the long term radiative regime equatorwards of 50° - 60°, if the change in turbidity corresponds to that caused by the Agung eruption.

REFERENCES

Ellis, J. and T. H. Vonder Haar, Atmos. Sci. Pap. 240, Colorado State Univ., Fort Collins, Co. (1976).

Harshvardhan and R. D. Cess, Tellus 28, 1 (1976).

Herman, B. M., S. R. Browning, and R. Rabinoff, J. Appl. Meteor. 15, 1057 (1976).

Pollack, J. B., O. B. Toon, C. Sagan, A. Summers, B. Baldwin and W. van Camp, J. Geophys. Res., 81, 1071 (1976).

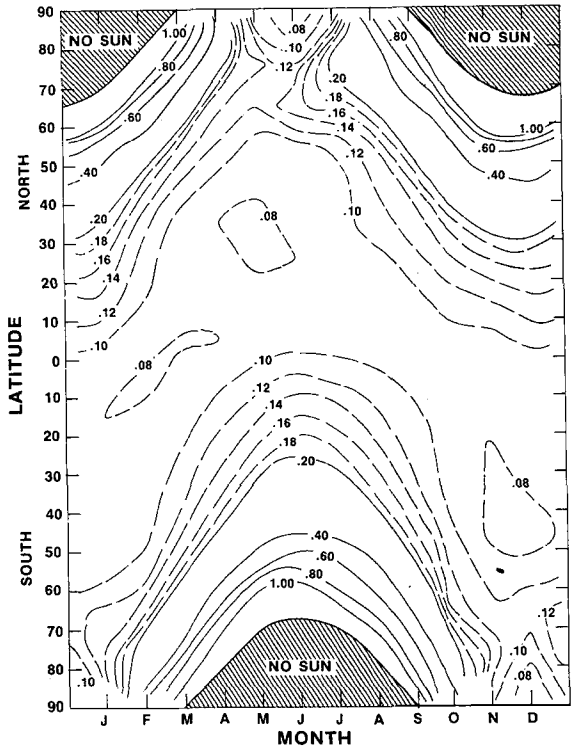

Fig. 1-Monthly zonal albedo sensitivity with solar averaged reflectivity.

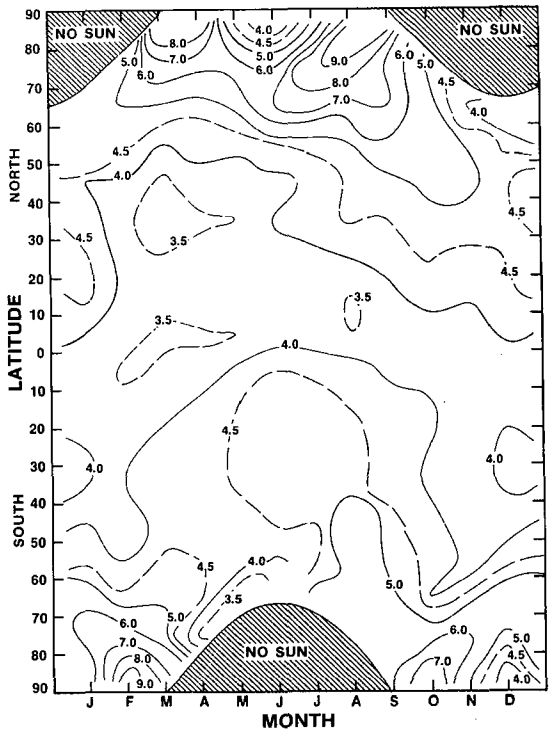

Fig. 2-Reduction in mean monthly solar energy absorbed in W/m^2 with addition of aerosol layer of $\tau_{vis} = 0.1$.

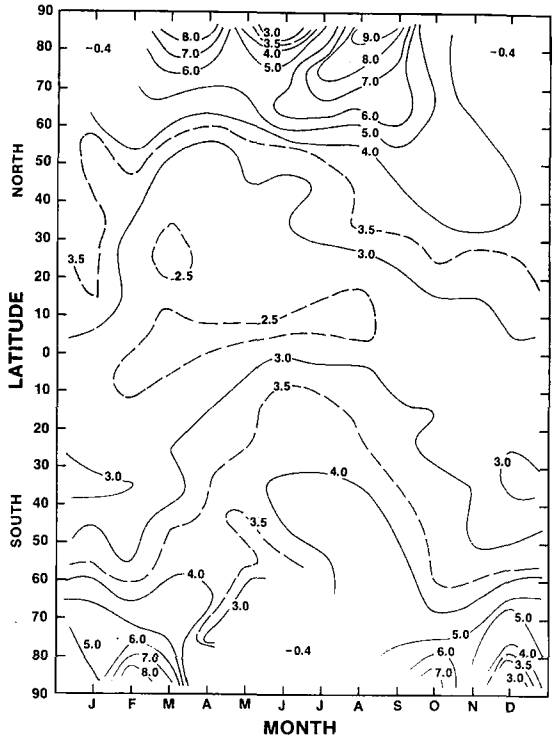

Fig. 3–Reduction in the zonal radiation balance in W/m^2 with addition of aerosol layer of $\tau_{vis} = 0.1$.

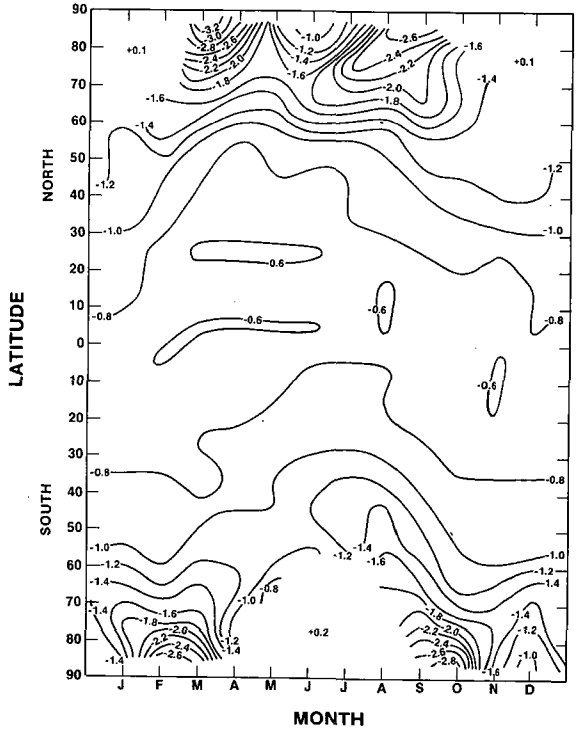

Fig. 4–Change in the effective black-body radiative temperature of the atmosphere in °K with addition of aerosol layer of $\tau_{vis} = 0.1$.

Page intentionally left blank

Paper No. 44

SCATTERING BY RANDOMLY ORIENTED ELLIPSOIDS: APPLICATION TO AEROSOL AND CLOUD PROBLEMS

Shoji Asano, Makoto Sato and James Hansen, *Goddard Institute for Space Studies, New York, NY 10025*

ABSTRACT

A program has been developed for computing the scattering and absoprtion by arbitrarily oriented and randomly oriented prolate and oblate spheroids. This permits examination of the effect of particle shape for cases ranging from needles through spheres to platelets. We discuss applications of this capability to aerosol and cloud problems. Initial results suggest that the effect of nonspherical particle shape on transfer of radiation through aerosol layers and cirrus clouds, as required for many climate studies, can be readily accounted for by defining an appropriate effective spherical particle radius.

Introduction. Many climate studies involve scattering or absorption of radiation by nonspherical particles. Examples include the climatic impact of natural or man-made changes in stratospheric and tropospheric aerosols and cirrus clouds. The nonspherical shape of such particles has generally been neglected, with the hope that spheres can adequately represent the results for other particles. With improvement of climate modeling capabilities and climate observations, it is becoming increasingly important to obtain a quantitative understanding of the effects of nonspherical particle shape and a prescription for defining the spheres which can be used to approximate nonspherical particles.

A general solution for scattering by infinitely long circular cylinders has been obtained and investigated (Kerker, 1969; Liou 1972), but that case is too special to provide an adequate test of particle shape effects. The next logical particle shape for analysis, in terms of practicality for obtaining a general solution analogous to the Mie solution for spheres, is the spheroid. In fact spheroids, formed by rotation of an ellipse about its major (prolate spheroid) or minor (oblate spheroid) axis, provide an excellent opportunity for investigation of the effect of nonspherical particle shape. As the ratio of the length of the major axis to length of the minor axis becomes large the particle becomes needle-like. At the other extreme it approaches the shape of a platelet. In between it passes through the special case of the sphere.

Asano and Yamamoto (1975) developed the scattering theory for a homogeneous spheroid. The objective of the work described here is to develop a program to implement that theory for particles all the way up to sizes which show the basic features of geometrical optics, and to apply this theory to climate studies.

Single arbitrarily oriented spheroid. Light scattering by a

spheroidal particle is specified by the following five physical quantities: 1) particle size relative to the wavelength of incident wave, 2) eccentricity, 3) complex refractive index $\tilde{m}$ relative to that of the surrounding medium, 4) orientation of particle to the incident wave, and 5) the observation direction.

We define the particle size parameter α by $\alpha = 2\pi a/\lambda$, where a is the semi-major axis of the ellipse and λ is the wavelength of the incident radiation. We specify the shape of the spheroid by the ratio of the semi-major axis a to the semi-minor axis b, which thus has a value greater than unity. We use the ratio a/b, rather than the eccentricity, since it is a more direct measure of the elongation of the spheroid.

Fig. 1 shows the geometry of scattering for a linearly polarized plane electromagnetic wave incident at an angle ζ to the z-axis. The origin of the coordinate system is taken at the center of the spheroid with the z-axis as the axis of rotation, i.e., as the major axis for a prolate spheroid and the minor axis for an oblate one. The spherical coordinate system (θ,ϕ) is adopted to represent the direction of a far-field observation point, where θ is the zenith angle measured from the positive z-axis and ϕ is the azimuth angle. The direction of incidence is assumed to be in the $\phi = 0$ plane (x-z plane) and is thus identified by $(\zeta,0)$.

The efficiency factor for scattering Q_{sca} is defined here as the ratio of the scattering cross section C_{sca} to the area of the geometrical shadow of the spheroid $G(\zeta)$ at the incidence angle ζ. In Fig. 2 Q_{sca} for prolate spheroids with $\tilde{m} = 1.50$ is plotted, as a function of the size parameter α, for various values of the shape parameter from a/b = 1.5 to 5. For small prolate spheroids, $\alpha < 4.0$, the scattering efficiency factors are greater for the spheroids which are closer to being spheres, i.e., for the smaller a/b. Q_{sca} (α) for a/b = 1.5 is very similar to that for spheres, with oscillations which damp out for large size parameters as Q_{sca} approaches the geometrical optics limit of 2. A striking feature is that with increase of a/b the first resonance maximum occurs at large size parameter and the peak value increases.

The major maxima and minima in Fig. 2 are due to interference of light diffracted with light transmitted by the particle. The phase shift for a light ray passing through the particle along the axis in the direction of incidence is $\rho = 2\alpha(\tilde{m}-1)$, which equals α or $2\pi a/\lambda$ for the case $\tilde{m} = 1.5$. Thus successive maxima, caused by constructive interference, occur at intervals of $\sim 2\pi$. The case of a/b = 3 is an exception; however, the average separation of the maxima would also be $\sim 2\pi$ if there were an additional maximum. The results for a/b = 3.5, shown by the dashed curve, in fact suggest that the expected second and third maxima have somehow combined into a single maximum for a/b $\sim$ 3.

Application of the anomalous diffraction approximation of van de Hulst (1957) to scattering by prolate spheroids at the parallel incidence gives extinction efficiency curves identical to those for spheres, without regard to a/b, but with the phase lag parameter $\rho = 2\alpha(\tilde{m}-1)$. However, in fact, the position and peak value of the first maximum of the scattering efficiency curves in Fig. 2 are strongly dependent on a/b. Furthermore, the mean periods of the major oscillations of the scattering efficiency curves are larger for the prolate spheroids than for spheres. These discrepancies from the expectation of the anomalous diffraction approximation can be attributed to effects of edge phenomena for grazing reflection,

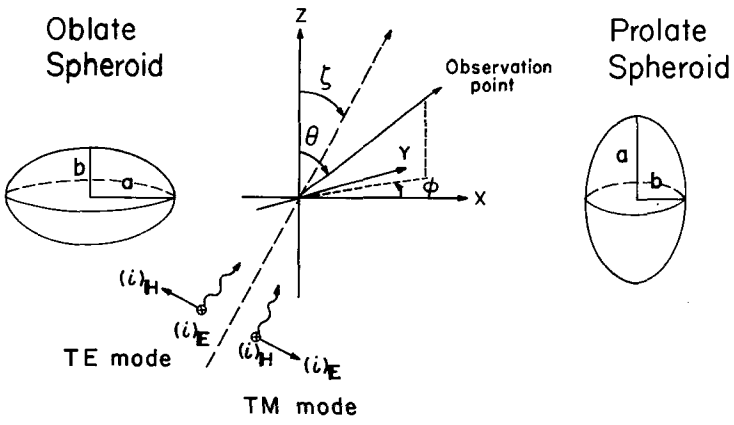

Fig. 1. Scattering geometry. A spherical coordinate system is adopted to represent the scattered field in the far-field zone. The origin of the coordinate system and the z-axis are the center and axis of revolution of the spheroid, respectively. The angle of incidence ζ is the angle in the plane of incidence (the x-z plane)between the direction of incidence and the z-axis.

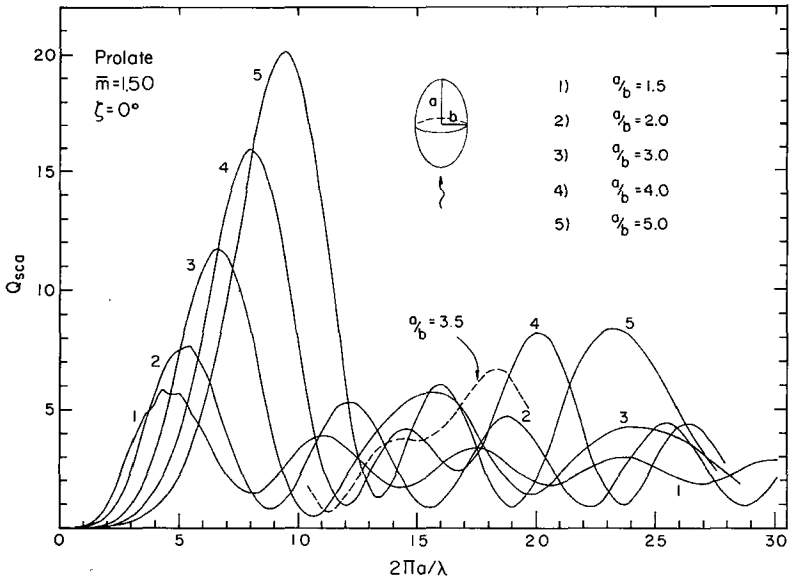

Fig. 2. Scattering efficiency factors Q_{sca} at $\zeta = 0$ as a function of the size parameter $2\pi a/\lambda$ for the prolate spheroids with $\bar{m} = 1.50$, for several values of the shape parameter a/b.

as discussed by Asano (1979).

Randomly oriented spheroids. Fig. 3 compares the scattering by randomly oriented prolate spheroids with scattering by spheres of equivalent size. For the spheres integration over a narrow distribution of particle sizes was performed in order to smooth out the oscillations which occur for a single size. For the spheroids this was not necessary since the integration over random orientations served the same function.

We define an equivalent spherical particle radius for any particle shape to be the radius of the circle which would give the same area as that of the particle's shadow. Since the complete scattering behavior of spheres is available in efficient subroutines (e.g. Hansen and Travis, 1974) this prescription represents a simple approximation for scattering by nonspherical particles.

Parts (a) and (b) of Fig. 3 compare the efficiency factor for scattering (Q_{sca}) and the asymmetry parameter of the scattering diagram ($<\cos\theta>$) for spheres and prolate spheroids. Two principal conclusions are: (1) spheres provide a good approximation for the nonspherical particles for these parameters which define the gross radiative properties, when the equivalent radius we have defined is employed, (2) there is no evidence that the nonspheres are less forward scattering than spheres.

Parts (c) and (d) of Fig. 3 compare the scattering diagram and linear polarization for spheres and prolate spheroids. It is apparent that the scattering at a specific angle is not in general well approximated by the simple prescription of using spheres of equivalent cross-sectional area. There is no evidence in the scattering by spheroids of this size parameter for special spherical particle geometrical optics features such as the rainbow and glory.

Discussion. These initial results are encouraging with regard to climate applications. The principal parameters defining the radiative transfer characteristics of aerosols and clouds are the efficiency factors for scattering and absorption and the asymmetry parameter. Our very limited sample of calculations for randomly oriented nonspherical particles suggests that it may be possible to accurately approximate these parameters with results for equivalent spheres. With regard to remote sensing applications which require knowledge of scattering behavior at a specific angle, the indications are that it will be necessary to take account of the specific particle shape involved. The calculations presented are only a small fraction of what will be needed to draw any firm conclusions; calculations are underway for larger sizes and for randomly oriented oblate spheroids.

Acknowledgements. During the course of this research S.A. held a NAS-NRC Post-doctoral Research Associateship at the Goddard Institute for Space Studies.

REFERENCES

Asano, S., Appl. Opt., 18 (in press), 1979.
Asano, S. and G. Yamamoto, Appl. Opt., 14, 29, 1975.
Hansen, J.E. and L.D. Travis, Light Scattering in Planetary Atmospheres, GISS Report, New York, 97 pp., 1976.
Kerker, M., Scattering of Light, Academic Press, NY, 666 pp., 1969.
Liou, K.N., Appl. Opt., 11, 667, 1972.
van de Hulst, H.C., Light Scattering by Small Particles, Wiley, New York, 470 pp., 1957.

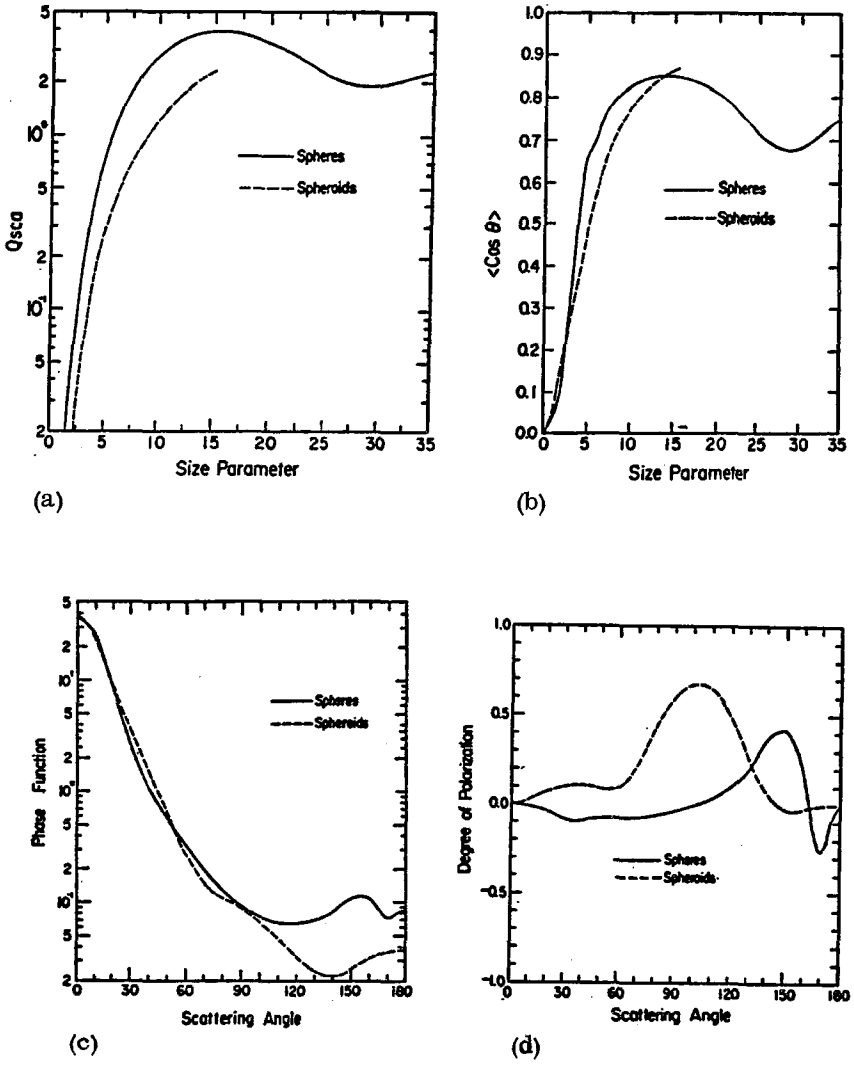

Fig. 3. Comparison of scattering by randomly oriented prolate spheroids with a/b = 5 with scattering by equivalent spheres. All calculations are for a real refractive index 1.33. (a) is the efficiency factor for scattering, (b) is the asymmetry parameter of the phase function, (c) is the phase function and (d) is the degree of polarization.

Page intentionally left blank

Paper No. 45

ERROR IN TOTAL OZONE MEASUREMENTS ARISING FROM AEROSOL ATTENUATION

Robert W. L. Thomas, *EG&G Washington Analytical Services Center, Inc., Riverdale, Maryland,* Reid E. Basher, *Department of Atmospheric Physics, Clarendon Laboratory, Oxford*

ABSTRACT

A generalized least squares method for deducing both total ozone and aerosol extinction spectrum parameters from Dobson spectrophotometer measurements has been developed. An error analysis applied to this system indicates that there is little advantage to additional measurements once a sufficient number of line pairs have been employed to solve for the selected detail in the attenuation model. It is shown that when there is a predominance of small particles (less than about 0.35 microns in diameter) the total ozone from the standard AD system is too high by about one percent. When larger particles are present the derived total ozone may be an overestimate or an underestimate but that serious errors occur only for narrow polydispersions.

INTRODUCTION

In estimating total ozone from the atmosphere's attenuation of solar radiation, it is necessary to use empirical methods to deal with the very variable and poorly known component of the attenuation due to scattering by particles, i.e., by dust, haze aerosols, etc. The current standard estimation method is the Dobson AD double bandpair method,[1] which is equivalent to assuming particulate attenuation to be spectrally linear.

As an intended advance on the standard method, Basher[2] proposed that the particulate attenuation spectrum be explicitly represented by a finite polynomial series. This concept was later generalized by Gardiner in terms of orthogonal polynomials but it was also shown by Gardiner that as one attempts to derive more information about the aerosol attenuation spectrum the result is to magnify the impact of other systematic measurement errors.

The objective of the work reported here was twofold. Firstly, we generalized the interpretation procedures in a new direction by defining solutions for overdetermined systems. This permitted goodness to fit estimates to be made giving some judgement as to when the detail of the aerosol attenuation model was excessive. Secondly, we developed estimates of actual errors in total ozone as

a function of aerosol particle size when each of the derived inversion procedures was applied. By means of these results, aerosol attenuation errors can be computed for arbitrary size distributions.

Generalized Multiple Line-pair Ozone Reduction System

When the particulate attenuation spectrum is represented by an arbitrary polynomial, the relative attenuation for the kth bandpair, at λ_1 and λ_2, is

$$\Delta\delta_k = \delta(\lambda_1) - \delta(\lambda_2) = \sum_{i=1}^{M} g_i G_i \qquad (1)$$

where

$$G_i = (\lambda_1 - \lambda_o)^i - (\lambda_2 - \lambda_o)^i \qquad (2)$$

and where λ_o is an arbitrarily chosen reference wavelength (λ_o=333.55 nm was chosen here), the g_i are the unknown coefficients of the polynominal representation and M is the chosen order of the representation. The bandpair's observation of ozone, X_k, can then be written

$$X_k = X + \Delta\alpha_k^{-1} \sum_{i=1}^{M} g_i G_i \qquad (3)$$

where X is the actual ozone value, and $\Delta\alpha_k$ is the bandpairs' relative ozone absorption coefficient. The set of N ($\geq$M+1) such linear equations in turn can be expressed in matrix form as

$$P = AQ \qquad (4)$$

where P is the column vector of the set of observed X_k, Q is the column vector of the quantities X and the g_i's to be estimated, and A is the matrix which relates the vectors as described by equation 3. A least squares technique is employed to solve these equations.

Results For Ozone Reduction Coefficients

The analysis was applied to the data cited by Basher[2]. In constructing the variance-covariance matrix, we assumed that the error in total ozone was inversely proportional to the ozone absorption cross-section difference $\Delta\alpha_k$, and the errors for different line pairs were uncorrelated. The numerical values of the parameters employed are summarized in Table 1. The ozone estimates are averages of large numbers of data and were given by Dobson and Normand[4].

Table 1. Parameters Employed In The Calculations

Line Pair	A	B	C	D
λ_1(n.m.)	325.4	329.1	332.4	339.8
λ_2(n.m.)	305.5	308.8	311.45	317.6
$\Delta\alpha_k$(atm.cm)$^{-1}$	1.744	1.157	0.809	0.356
X_k(atm.cm)	0.3526	0.3492	0.3461	0.3483

Solutions were obtained for all possible subsets of the line pairs A, B, C and D and the more interesting results are in Table 2.

TABLE 2. SUMMARY OF MULTIPLYING FACTORS REQUIRED TO ESTIMATE THE TOTAL OZONE AND RELATED RESULTS

N	M	LINE PAIRS USED	XA COEFF	XB COEFF	XC COEFF	XD COEFF	X ERROR(PC)
2	1	A B	2.860	−1.860	0.0	0.0	4.005
2	1	A C	1.788	0.0	−0.788	0.0	2.466
2	0	A D	0.960	0.0	0.0	0.040	0.980
2	1	A D	1.224	0.0	0.0	−0.224	1.644
2	1	B C	0.0	3.101	−2.101	0.0	6.509
2	1	B D	0.0	1.392	0.0	−0.391	2.842
2	1	C D	0.0	0.0	1.710	0.710	5.069
3	1	A B C	1.875	−0.151	−0.724	0.0	2.450
3	2	A B C	9.713	13.748	5.035	0.0	25.330
3	1	A B D	1.113	0.126	0.0	−0.239	1.627
3	2	A B D	5.498	−4.859	0.0	0.361	9.327
3	1	A C D	1.290	0.0	−0.091	−0.198	1.625
3	2	A C D	3.193	0.0	−2.752	0.558	7.272
3	1	B C D	0.0	1.296	0.118	−0.413	2.825
3	2	B C D	0.0	6.734	−6.566	0.832	17.889
4	0	A B C D	0.589	0.259	0.127	0.025	0.768
4	1	A B C D	1.156	0.182	−0.129	−0.209	1.594
4	2	A B C D	3.932	−1.558	−1.870	0.495	6.566

The results for the weighting coefficients are not only applicable to the estimate of total ozone, but are also the error magnification coefficients. Thus while the sum is always unity their magnitudes increase as M increases, confirming Gardiner's hypothesis of error magnification.

The parameter indicating expected percentage error was computed assuming a random error of 0.0035 (about 1%) in X_A. The propagated uncertainty for the quadratic M=2 cases varies considerably depending on the band combination, and is smallest for the ABCD and ACD combinations. Comparison of these combinations demonstrates the important point that the addition of the extra B bandpair to the ACD combination gives negligible reduction

in the propagated uncertainties in both ozone and particulate components. Comparison of the AD, ACD, and ABCD combinations for the linear M=1 cases shows a similar result. In other words, with respect to propagation of uncertainty there is virtually no advantage in using more than the minimum number of bandpairs needed for the given polynomial representation.

The choice of estimation method is essentially between the A bandpair with the constant M=0 particulate representation and a unit magnification of uncertainty, the AD combination with the linear M=1 representation and 1.6 magnification of uncertainty, and the ACD combination with the quadratic M=2 representation and a 6.8 magnification of uncertainty. The impact of any given level of X_k uncertainty on a particular ozone estimate can be directly determined from these magnifications.

Numerical Modeling

Empirical descriptions of particulate attenuation are needed because the physical parameters of atmospheric particulates upon which the attenuation depends vary very widely and are at best poorly known at a given place and time. There is, however, information available on the typical values and bounds of the parameters from which typical values and bounds of the attenuation can be assessed.

The procedure developed here is to describe the attenuation effects for a set of quasi-monodisperse distributions which span the particle size range of interest, with the understanding that the attenuation effects for actual atmospheric polydispersions can be found by simply integrating the computed effect, e.g., ozone error in X_{AD} for the quadratic method, over the appropriate size distribution. In this way the route along which the error generates is more clearly and usefully described.

The calculations of extinctions or attenuation used Mie theory applied to spherical particles of constant refractive index 1.55-0.005i, equivalent to spherical aerosols such as are found in hazes[3]. Averaging the extinctions over the Dobson slit transmittance functions was performed, but was found to have little effect owing to the ratio of slitwidth to center wavelength, at about 1/300, being so small.

A review of the reduction equations reveals that the residual between the estimate X_k and the true ozone, X, can be written approximately as

$$X_k - X = \frac{\Delta\delta_k}{\Delta\alpha_k} \qquad (5)$$

Thus if we compute $\Delta\delta_k$ using Mie theory the right hand side of equation (5) yields the actual error in the ozone estimate X_k. The related error in estimations for multiple line pairs can then be obtained by applying the appropriate coefficients given in Table 2 to these errors.

All the attenuations and ozone errors presented below are

normalized to an optical depth of 0.1 (base 10) at 305.5 nm. compatible with standard aerosol descriptions. Values for other optical depths are in simple proportion to the optical depth. Calculations were done for all possible bandpair combinations and polynomial representations, and for the observation variance model described earlier. The results for the A, B, C and D line pairs are given in Figure 1. It is clear that the error magnitudes are proportional to $\Delta\alpha_k^{-1}$, increasing from A to D. For small particles (less than 0.35 microns in diameter) an overestimate always occurs in agreement with the earlier analysis of Thomas and Holland. To compute the results for an arbitrary polydispersion, f(D), we must perform the integration

$$\epsilon = 10 \int_0^\infty \frac{f(D)}{N(D)} e(D)dD \qquad (6)$$

where N(D) is the column count required to produce unit optical depth (to base 10) and e(D) is the plotted error.

For the AD system we performed estimations for both the M=0 and M=1 (standard) case and the results are given in Figure 2. While the error for small particles is reduced from about 6% to 1% by fitting one aerosol coefficient, the error amplitude for larger particles is not significantly reduced. However the frequency of the oscillations increases for M=1 so that the effect of integrating these results over the polydispersions likely to occur in nature will be to reduce the resultant error.

Figure 3 presents results for the (A,B,C,D) combination with M=0, 1 and 2. It can be seen that for M=2 the effect is to increase the oscillation magnitude. However, the oscillation frequency also increases so that the actual error for a broad polydispersion may be smaller. For small particles, the M=2 solution reduced the error to only 0.1%.

CONCLUSIONS

The goodness of fit estimates that we have performed indicate that the data of Dobson and Normand[4] is compatible with the hypothesis of a quadratic spectral dependence of the aerosol attenuation and very low values of other systematic and random errors. However, the results can also be explained by simpler spectra if other systematic errors are present.

The evaluation of errors arising from spherical aerosol particles indicates that the practical application of a quadratic model would only be justified in the presence of aerosol with large optical depth or the presence of very narrow polydispersions with particle diameter greater than about 0.5 microns. The evaluation of the statistical characterization of aerosols at a Dobson site could, with the aid of the results developed, greatly clarify the magnitude of the errors in the total ozone arising from the aerosol attenuation spectrum.

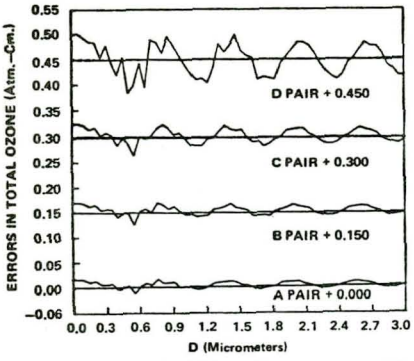

FIGURE 1. ERRORS IN TOTAL OZONE FOR SINGLE LINE PAIRS AS FUNCTION OF AEROSOL PARTICLE DIAMETER. (VERTICAL OPTICAL DEPTH TO BASE 10=0.1)

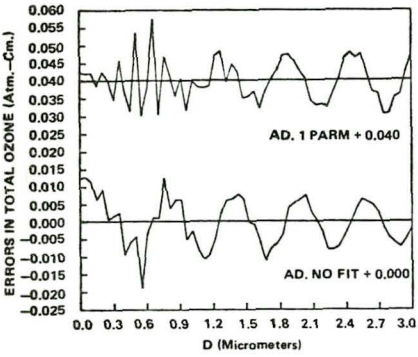

FIGURE 2. ERRORS IN TOTAL OZONE FOR MULTIPLE LINE PAIRS AND VARIOUS AEROSOL ATTENUATION MODELS AS FUNCTION OF AEROSOL PARTICLE DIAMETER. (VERTICAL OPTICAL DEPTH TO BASE 10=0.1)

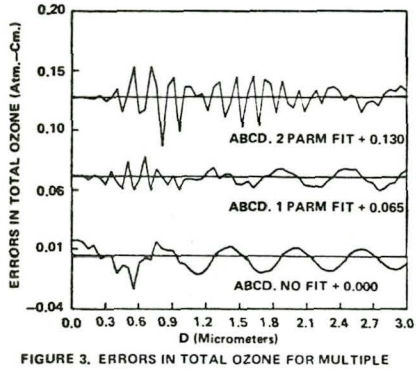

FIGURE 3. ERRORS IN TOTAL OZONE FOR MULTIPLE LINE PAIRS AND VARIOUS AEROSOL ATTENUATION MODELS AS FUNCTION OF AEROSOL PARTICLE DIAMETER. (VERTICAL OPTICAL DEPTH TO BASE 10=0.1)

REFERENCES

1. Dobson, G.M.B., Observers' Handbook for the Ozone Spectrophotometer, Ann. I.G.Y., 5, 46 (1957).

2. Basher, R.E., Quart. J.R. Met. Soc., 102, 667 (1976).

3. Gardiner, B.G., Quart. J.R. Met. Soc., 104, 623 (1978).

4. Dobson, G.M.B. and Normand, C.W.B., Ann. I.G.Y., 16, 161 (1962).

5. Perry, R.J., Hurst, A.J., and Huffman,D.R., Appl. Opt., 17, 2700 (1978).

6. "U.S. Standard Atmosphere," National Oceanic and Atmospheric Administration, Washington, D.C. (1976).

7. Elterman, L. and Toolin, R.B. in "Handbook of Geophysics and Space Environments," Shea L. Valley, ed., AFCRL publication (1965).

8. Thomas, R.W.L. and Holland, A.C., Appl. Opt. 16, 613 (1977).

Paper No. 46

THE SEASONAL AND INTERANNUAL VARIABILITY OF TOTAL OZONE AS REVEALED BY THE BUV NIMBUS-4 EXPERIMENT

Ernest Hilsenrath, *Goddard Space Flight Center, Greenbelt, MD*
Barry Schlesinger, *Systems and Applied Sciences, Riverdale, MD*

ABSTRACT

The initial study of the BUV/Nimbus-4 total ozone data is directed toward an analysis of the seasonal and interannual variability for the period April 1970 to April 1972. An objective analysis using a Fourier expansion shows the annual wave dominates at mid and high latitudes where the semiannual wave becomes significant in the tropics. A small interannual difference is detected and is most likely due to changes in the general circulation.

INTRODUCTION

The Nimbus-4 spacecraft was launched April 8, 1970 carrying the Backscattered Ultraviolet (BUV) Spectrometer for measurements of the columnar amount of ozone and the vertical distribution above 30 km. The BUV continued to operate until October 17, 1977 at which time it was turned off due to insufficient spacecraft power. The initial data was processed into ozone values and reported by Krueger (1974) Ghazi (1976) as well as by others. These early analyses used existing instrument calibrations, and orbital and engineering data. In addition, these analyses adjusted the satellite measured total ozone values to Dobson using a linear regression relationship developed from direct comparison of BUV measured values and Dobson values. Because of the recently recognized importance of the data, a task was initiated to reprocess the data and to continue processing the available data until the time the instrument was turned off. Generally, the objectives of the reprocessing activity were to: Establish a primary data base with screened, Earth located, and calibrated data for conversion to radiance values; improve the algorithms for processing the primary data base of radiance values to ozone values; and finally to validate the data and provide a consistent ozone data base. Details on satellite coverage, data quality checks, algorithm improvements, and validation tasks are being compiled and will be published elsewhere.

An extensive analysis of the comparability of BUV with the Dobson network has been conducted by Fleig, et al. (in preparation). This analysis shows from a comparison of nearly 4000 coincident measurements, using 00 code Dobson values and BUV

overflight values within 2° of the station, that the average difference changes by about 1 Dobson Unit (∿0.3%) over the two-year period studied here, indicating a high degree of stability in the spaceborne measurement.

The first two years of total ozone data discussed here covers the period April 1970 to April 1972 and contains about 300,000 total ozone values per year. The Nimbus-4 orbital parameters and the BUV instrument description are detailed in the Nimbus-4 User's Guide (1970) and not repeated here. The BUV measurement scheme has been previously described by Mateer et al. (1971) and is briefly summarized below. Total ozone is derived from a measurement of the solar irradiance, Fo, the backscattered radiance, I, at 312.5 nm, 317.5 nm, and 339.8 nm and the effective surface reflectance determined from the photometer. The measured backscattered radiances are compared to those computed from 21 standard profiles sorted into three latitude zones compiled from balloon and rocket data since the radiances are ozone profile dependent. Any total ozone value can then be obtained from the table of precomputed values containing the solar zenith angle dependence, θ, and reflectance by interpolation. A description of the standard profile compilation is given by Hilsenrath (1977).

This discussion of the total ozone is directed toward the interpretation of its seasonal and interannual variability as revealed by the spaceborne experiment over a two-year period. A convenient way of depicting a time varying globally distributed geophysical parameter is in terms of zonal means as a function of time. This analysis is appropriate for total ozone since its variability is dominated season and latitude. A rigorous analysis of the seasonal and interannual variations detected by the BUV is accomplished by a harmonic analysis of the zonal means as a function of time where the first two components represent the significant seasonal waves.

Time Latitude Cross Section

From ten degree wide latitude zones, a time latitude cross section, depicted in figure 1a, is generated from the monthly averaged daily zonal means. Total ozone is shown as contours in 20 Dobson Unit increments for the two year period (regions at high latitudes in winter have no contours). Figure 1b immediately below the cross section sharing the same absiscca is a calculation of the mean global ozone value where this mean value is computed for each month from the sum of the area weights of the zonal means using extrapolation from lower latitudes to include the polar night regions. (Note in proof, the values shown in this figure are not final. Final processing indicate small changes in absolute values, but the seasonal trends are essentially the same.)

The annual seasonal wave is clearly seen in the two hemispheres. There is an ozone high and low at mid to high latitudes in the spring and fall periods respectively in both years. However, there are distinctive differences in the seasonal trends for each hemisphere.

1. In the Northern Hemisphere the spring maximum occurs nearly simultaneously at mid and high latitudes with the maximum value occurring near the pole with total ozone amounts of about 500 D.U. and a standard deviation of about ± 50 Dobson Units.

2. In the Southern Hemisphere the spring maximum occurs first in September at 65°S with ozone values substantially lower than those in the Northern Hemisphere spring. The spring maximum values occur about one month later in the polar regions. The asymmetry of the winter buildups in the two hemispheres can be explained by the well known differences in the circulation features in the two hemispheres as described by Newell, et al.(1972), Dütsch (1974) and others. In the Northern Hemisphere, eddy processes associated with the intense winter planetary waves transport ozone poleward from mid latitudes. Whereas in the Southern Hemisphere the circulation is generally more zonal and poleward transport is delayed.

3. In the tropical regions, the total ozone amounts and the seasonal variation are considerably lower than at higher latitudes. The average value is about 250 ± 10 D.U. The ozone minimum is centered below the equator in April and moves northward as the year progresses. Also note the very rapid decrease in the northern tropics, that appears to coincide with the Southern Hemisphere spring maximum at 65°S in September, occurs in both years.

Global Mean Ozone

A more rigorous description of the total ozone seasonal variations for the two years will be given by the harmonic analysis and is discussed in the next section. However, at this point the seasonal and interannual difference in the global mean ozone amounts, shown in figure 1b, will be briefly discussed. In general, the ozone is shown to decrease when comparing the same months for the two year period. Analysis by Angell and Korshover (1978) as well as others show a comparable decrease over the same period using the Dobson network data. To some extent, however, satellite data suffers from the same uncertainties as those computed from the ground based data because of spatial and temporal coverage biases. BUV makes no observations in the polar night and in some cases coverage was not consistent from one year to the next. The subject of long-term trends in global means as determined from satellite and ground networks is being studied elsewhere (Heath, private communication) and is not pursued here.

The seasonal variation in the global mean, however, is clear from figure 1b. The global mean maximum occurs at the time of the Northern Hemisphere spring maximum (April) where the minimum occurs in December-January, after the Southern Hemisphere spring maximum and prior to the Northern Hemisphere winter buildup. The amplitude of the seasonal trend is about 20 D.U. (the day to day variations in the global means is about 1 D.U.). The seasonal amplitude presented here is about 5 times higher than that reported by Keating (1978) in his analysis of 9 monthly mean

global ozone amounts determined from the Nimbus-4 IRIS. In addition, no correlation of the BUV measured mean values could be found with solar activity associated with the 10.7 cm flux as was reported in Keating's analysis of IRIS.

Harmonic Analysis

In order to more objectively characterize the seasonal trends and the year to year differences in the global ozone,a harmonic analysis of the daily zonal mean data was performed. The procedure will be discussed elsewhere (in preparation) but the results are discussed below.

The annual wave or the first harmonic in the Fourier expansion is shown in figure 2a. The amplitude, given in Dobson Units, is the value of the first Fourier coefficient and the percent of the variance contributed by this harmonic is shown in the portion of this figure. Both values are plotted as function of latitude and both years are shown in the single figure to allow for a direct comparison. It should be clear that the data shown in this figure is a representation of information in figure 1a. The important features are:

1. In the Northern Hemisphere the amplitude of the annual wave increases with latitude. In addition, the variance is greater than 90% from subtropical latitudes to the pole. These features are essentially the same for the two years.

2. The amplitude of the annual wave is a minimum in the tropics and is only a few Dobson Units. The variance is nearly zero at the equator at least for the first year and the location of the minimum amplitude shifts about 10° southward in the second year.

3. In the Southern Hemisphere the amplitude of the annual wave is a maximum at mid-latitude and decreases towards the Southern Hemisphere pole. The percent variance of the annual wave is also very small near the pole indicating the south polar region does not undergo a significant seasonal variation in total ozone. At mid-latitudes there is a comparable 10° southward shift in the location of the maximum amplitude. This could be the result of year to year changes in the strength and location of the Hadley cell circulation in the Southern Hemisphere. Interannual changes in the strength of the Hadley cell have been demonstrated by Rosen and Wu (1976) in the Northern Hemisphere.

The second harmonic of the Fourier expansion of the daily zonal means provides information on the semiannual component in the seasonal ozone trend. A semiannual component would be expected because the Sun crosses the equator twice and a photochemical response may be detected in the tropics. On the other hand, a possible correlation may exist with the semiannual oscillation in the temperature and winds detected in the tropics in the upper stratosphere. Though these phenomena are of great interest and there may well be an ozone correlation found in a more detailed analysis that that performed here, it will be shown below the

semiannual component detected in the satellite measured total ozone for the two years studied here is the result of the inter-hemispheric influence of the annual wave whose phases are displaced by six months.

Figure 2b depicts the semiannual component in the same format as the previous figure except the ordinate for both the amplitude and the variance are half that of figure 2a. The important features are as follows:

1. In mid-latitude for both years the semiannual wave is small.

2. In the tropics this component becomes significant but less so in the second year. From 0 to 10°S the amplitude of the semi-annual component is comparable to the annual component and the variance is about 40% for the first year. Clearly this feature should be associated with the location and strength of the annual wave in the tropics, and further evidence of this association will be given below.

3. In the Southern Hemisphere the semiannual oscillation becomes important again and the amplitude is comparable to that of the annual wave. However, the significance of this feature should be regarded with some caution since nearly one-half of the values appearing in the highest latitude zone are the result of extrapolation from lower latitudes.

An additional solution to the harmonic analysis is the phase; where for this study represents the time of the maximum ozone value in each of the latitude zones for each harmonic component. Figure 4 shows the time of the maximum ozone value as a function of latitude for both the annual and semiannual waves for each year. The ordinate is given in month as well as day of the year. The significant aspects of the phase are summarized below. It should be noted this result is consistent with what was seen and interpreted from the time latitude cross section, figure 1.

1. In the Northern Hemisphere the time of the maximum of the annual wave occurs nearly simultaneously from mid to high latitudes.

2. In the Southern Hemisphere after going through 6 month phase shift at the equator the spring maximum occurs first at 40°S in September and then spreads poleward and equatorward reaching a maximum value in these regions in November.

3. With regard to the semiannual wave only the time of the first maximum is plotted at latitudes where the variance is greater than 2%. At low latitudes the first peak occurs about April which is coincident with the Northern Hemisphere spring maximum of the annual wave. The second maximum of the semiannual component occurs 6 months later or October which is coincident with the maximum of the annual wave in the Southern Hemisphere subtropics. This result does not exclude a possible response to the solar equatorial crossing but it seems more likely that the semiannual wave detected at low latitudes in the first year is the

influence of the annual waves at higher latitudes in the two hemispheres where the phases are six months apart.

Conclusion

A rigorous analysis of the seasonal and interannual variability of the total ozone measured by the BUV on Nimbus has been initially performed to:

1. Provide information on the relative role of chemistry and transport on the global distribution of ozone.
2. To help recognize transient phenomena in the stratosphere that may be important in Sun/weather relationships.
3. To better understand long-term trends associated with solar cycles, other climate parameters, and man's activities that may effect the environment.

This initial study has shown the BUV data for the period processed between April 1970 and April 1972 has sufficient accuracy and coverage to give a good description of the seasonal variability and reveal some interannual differences in the total ozone. These differences should eventually be correlated with changes in the general circulation. This study provides a starting point for ozone trend investigations from satellite measurements that are important in climate and environmental studies and a basis for studying the anomalous behavior of ozone.

Acknowledgment

The authors would like to acknowledge the remainder of the Ozone Processing Team which was directed by Dr. Albert Fleig at Goddard Space Flight Center. Special appreciation is given to Dr. James Gatlin who retraced the BUV instrument performance 7 years after it was flown and to Dr. Ashok Kaveeshwar who organized and implemented the data processing schemes used to produce the results given in this paper. Dr. Donald Heath is gratefully acknowledged for his encouragement and useful discussions in the interpretation of the data.

References

Angell, J. K., J. Korshover, 1978: "Global Ozone Variations: An Update into 1976," Monthly Weather Review, Vol. 106, page 725-737, May 1978.

Dütsch, H. U.: "The Ozone Distribution in the Atmosphere," Canadian Journal Chemistry, Vol. 52, No. 8, p. 1491-1504, 1974.

Ghazi, A., A. Ebel, D. F. Heath: "A Study of Satellite Observations of Ozone and Stratospheric Temperature During 1970-1971," Journal of Geophysical Research, Vol. 81, No. 30, pp. 5365-5376, 1976.

Hilsenrath, E., P. Dunn, C. Mateer, 1977: "Standard Ozone Profiles from Balloon and Rocket Data for Satellite Theoretical Model Input." Contributions Presented at the Joint Assembly CMUA Sessions IAOA/IAMAP, Seattle, Washington, August 1977.

Keating, G. M., 1978: "Relationship Between Monthly Variations of Global Ozone and Solar Activity," Nature, 274.

Krueger, A. J., 1974: "Behavior of Atmospheric Ozone Determined from Nimbus Satellite Backscattered Data," Proceedings of the International Conference on the Structure and Composition of the Upper and Lower Atmosphere, Melbourne, Australia, IAMAP, pp. 462-477, and NASA/GSFC X-Document 910-74-101.

Mateer, C. L., D. F. Heath, A. J. Krueger, 1971: "Estimation of Total Ozone from Satellite Measurements of Backscattered Ultraviolet Radiances," Journal of Atmospheric Sciences, 28, pp. 1307-1311.

Newell, R. E., J. U. Kidson, D. G. Vincent, G. J. Baer, 1972: The General Circulation of the Tropical Atmosphere and Interactions with Extratropical Latitudes, MIT Press, Cambridge, MA.

Nimbus Project, 1970: "The Nimbus-4 Users Guide," National Space Sciences Data Center, Greenbelt, MD, 214 pages.

Rosen, R. D. and M. Wu, 1976: "Observational Study of the Interannual Variability in Certain Features of the General Circulation," Journal of Geophysical Research, 81, pp. 6383-6389.

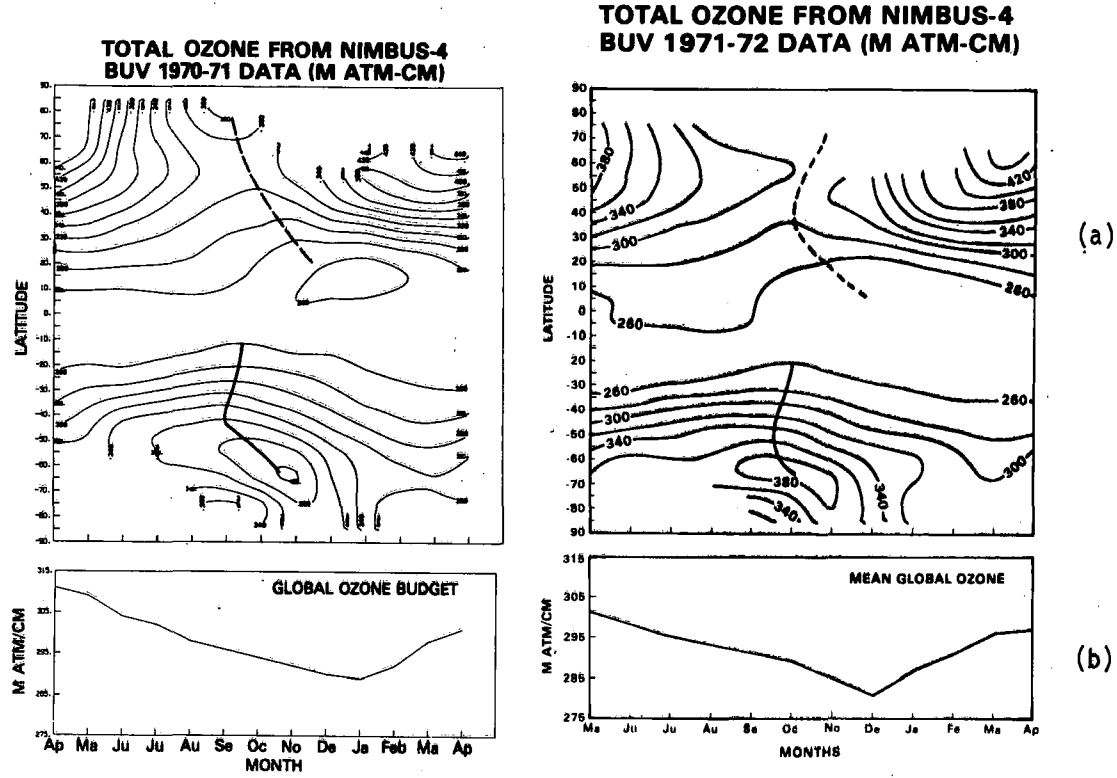

Figure 1a. Time latitude cross section for April 1970-April 1972.
2b. Global mean ozone calculated from area weights of zonal means.

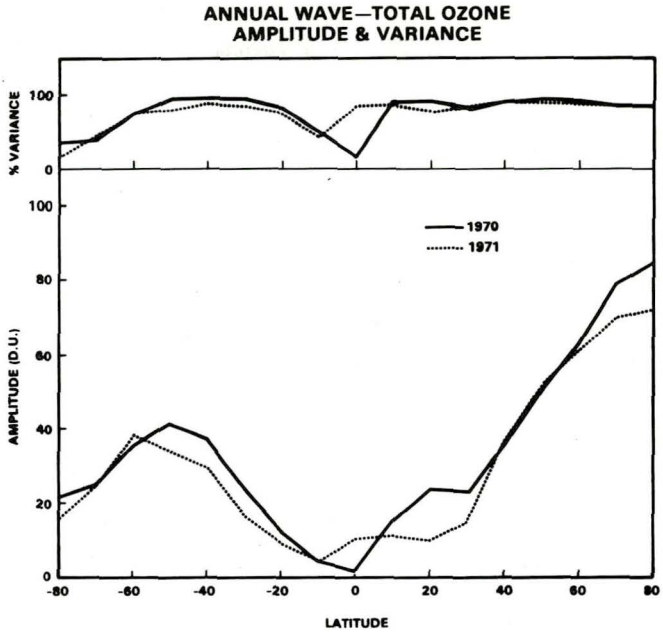

(a)

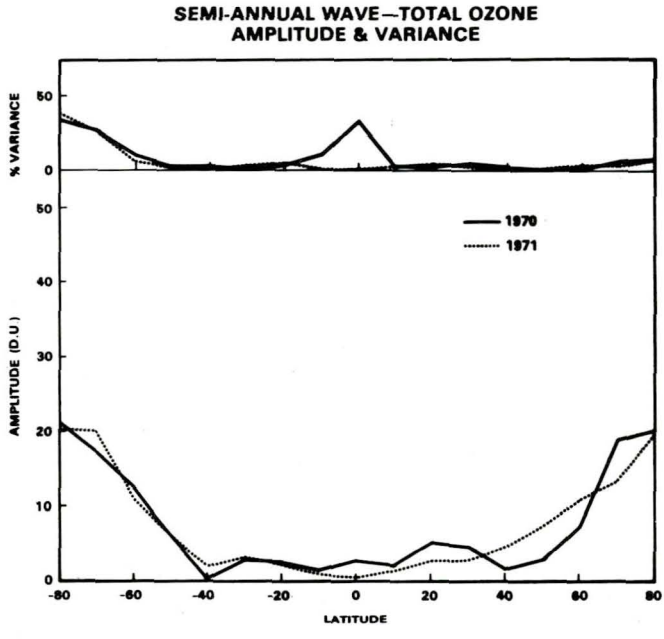

(b)

Figure 2. Solution to harmonic analysis. Annual (a) and semi-annual (b) wave correspond to first and second coefficient respectively.

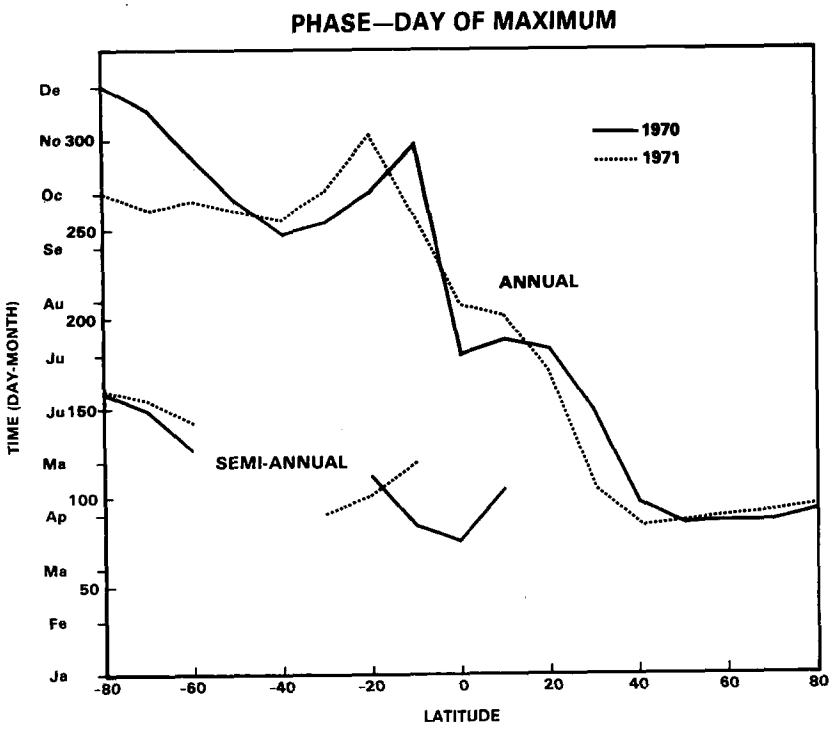

Figure 3. Phase of harmonics corresponding to day of maximum total ozone value. For semiannual wave, day of first maximum is indicated.

Paper No. 47

HOHENPEISSENBERG OZONESONDE INTERCOMPARISON

A. C. Holland and A. L. Torres, *Wallops Flight Center, Wallops Island, Virginia*

ABSTRACT

A series of dual-instrument vertical ozone soundings was carried out for the purpose of comparing the Electrochemical Concentration Cell Ozonesonde with different ozonesondes used by the international scientific community. Total ozone overburdens at the time of the soundings were also measured with a Dobson spectrophotometer.

INTRODUCTION

Soundings of the vertical ozone profile by balloon-borne instruments not only provide information on the detailed structure of the profile, but also complement and help validate data from remote-sensing methods. Since ozonesondes used by various international groups frequently differ, it is important that the instruments be brought together to determine their relative performance in measuring ozone. For this reason representatives of the USA, FRG, DDR, and Japan gathered in Hohenpeissenberg, FRG, during April of 1978 for such an intercomparison, organized by the WMO.

Ten dual-instrument soundings were carried out with the Electrochemical Concentration Cell (ECC) Ozonesonde. The ECC sonde was paired with a different ozonesonde during nine flights, while the tenth was made with two ECC sondes. At the time of this writing the WMO has not yet released the composite data set to the individual participants. Data is available concerning the agreement between ECC and Dobson measurements of total ozone, however, and is presented below. The result of the single sounding involving a pair of ECC ozonesondes is also given.

RESULTS

The total ozone overburdens as determined with the ECC ozonesonde are compared with the corresponding values obtained from Dobson instruments in Table 1. The mean percentage difference between the ECC and Dobson values was 5.6 ± 13.6, where the uncertainty represents one standard deviation. Two of the ECC values were inexplicably high and raised the mean difference and variation considerably. In general, however, the results are in keeping with those of an earlier study (1) in which a large

number of ECC sondes were calibrated relative to a UV standard. The latter work demonstrated a mean slope of near unity, but with a 6% variation (one standard deviation) about the mean.

Unlike the earlier work mentioned above (Reference 1) in which correcting ECC profiles with UV calibration data reduced the systematic errors between ECC and Dobson total ozone values (for a 30 sample set), correcting the present data had no significant effect. The UV-corrected data and the variations from the corresponding Dobson values are shown in the last two columns of Table 1. Use of the calibration data changed the mean percentage difference between the ECC and Dobson values from 5.6 ± 13.6 (uncorrected) to 5.8 ± 12.0 (corrected).

The dual-instrument sounding involving two ECC sondes was unusual in that the two sondes tracked one another very well up to about 70 mb. Above this height one of the sondes began indicating ozone concentrations as much as 45% higher than the other, although the general shapes of the two profiles were the same. The sonde indicating lower ozone readings gave a much closer total ozone value to that of the Dobson (1.9% difference) than did the other (19.3% difference). Inspection of the records failed to indicate any obvious source of the discrepancy.

REFERENCES

1. Torres, A. L., and A. R. Bandy, Performance Characteristics of the Electrochemical Cell Ozonesonde, J. Geophys. Res., in press.

TABLE 1. Comparison of total ozone values from ECC data (Ω_E), UV-corrected ECC data (Ω_{EUV}), and Dobson measurements (Ω_D).

DATE	Ω_E [a]	Ω_D [a]	$\frac{\Omega_E-\Omega_D}{\Omega_D}$ x100	Ω_{EUV} [a]	$\frac{\Omega_{EUV}-\Omega_D}{\Omega_D}$ x100
4/5/78	370	412	-10.3	374	-9.3
4/6/78	440	443	- 0.6	447	0.9
4/7/78	400	390	2.7	425	8.9
4/10/78	368	388	- 5.0	373	-3.9
4/11/78	410	388	5.7	403	3.8
4/12/78	462	426	8.6	477	11.9
4/14/78	430	418	3.0	426	2.0
4/17/78 [b]	433	425	1.9	440	3.7
	507	425	19.3	502	18.1
4/18/78	385	398	- 3.3	378	- 5.1
4/20/78	559	401	39.5	535	33.3

a units of m atm-cm

b pair of ECC ozonesondes flown together

Page intentionally left blank

Paper No. 48

THE REFLECTANCE CHARACTERISTICS OF SNOW COVERED SURFACES

E. S. Batten, *Jet Propulsion Laboratory, Pasadena, CA*

ABSTRACT

An analysis of field measurements of the reflectivity of an open snow field has been undertaken to assist in the interpretation of the NOAA reflectivity zones.

INTRODUCTION

The seasonal and year-to-year variations of the areal extent of ice and snow cover have an important effect on the heat balance of the Earth and hence on the weather and climate. Detailed monitoring of the snow and ice extent can be used to help predict future weather patterns and can be used to detect incipient climate changes. A better knowledge of the snow and ice extent of the past several years for which satellite data are available can help in the understanding of the mechanisms involved in weather and climate changes. The purpose of this study is to develop data analysis techniques to most efficiently use available satellite measurements to determine and understand components of the surface energy budget for ice and snow-covered areas. The emphasis here is placed on identifying the important components of the heat budget related to snow surfaces, specifically the albedo and the energy consumed in the melting process. Currently, weekly ice and snow charts are prepared by NOAA from satellite observations which map areas into three relative reflectivity zones. At the present time, about 10 years of this data are available. By quantifying the relative reflectivity zones, a unique albedo data base can be developed.

There are several problems encountered in determining the albedo of snow-covered surfaces from satellite measurements. First, the type, density, and height of vegetation will affect the albedo of the scene and produce temporal variations as the amount of vegetation showing through the snow changes with time. The NOAA reflectivity classes are to a degree a consequence of differences in the underlying vegetation. Second, the reflectivity of the snow changes as the snow ages, melts, refreezes, etc. necessitating repetitive coverage. Third, the reflectivity of a snow surface and more importantly a mixed snow-vegetation surface

is anisotropic and because the surface is viewed in a limited range of viewing angles and solar zenith angles, an algorithm must be derived to determine the total hemispheric reflectance from the measured bidirectional reflectance. Fourth, some satellite systems (NOAA, VHRR for example) measure radiance in only a small wavelength interval and the data must be extrapolated to the entire solar spectrum. Finally, measurements at the satellite include the effects of atmospheric scattering and absorption. If the surface albedo is desired, the data must be corrected for these atmospheric effects.

RESULTS

The correction for atmospheric effects was addressed previously (1) and quantitative estimates for the NOAA reflectivity zones were obtained from an analysis of NOAA 4 and 5 VHRR visible data. The albedo of the surface and atmosphere observed at the satellite was calculated from the radiance values obtained from the VHRR visible digital data. The "space" albedo clearly has a solar zenith angle dependence as can be seen from the values of the space albedo for areas which appeared to be completly snow covered in Fig. 1. This dependence was judged to be due to atmospheric attenuation. A simple correction was applied to the data to remove the atmospheric effects. It was assumed that the space albedo (As) can be expressed as:

$$As = Ag\ P_{\Delta\lambda}^{(m_{in} + m_{out})} \qquad (1)$$

where Ag is the surface albedo, $P_{\Delta\lambda}$ is the atmospheric transmission coefficient for the wavelength interval $\Delta\lambda$, and m_{in} and m_{out} are the air masses along the incoming and outgoing paths.

Applying Eq. 1 to the space albedos, estimates of the surface albedo were computed. Although the results are characteristic of only a limited wavelength band and still contain the effects of anisotropy, inspection of the sample scenes clearly show three brightness classes corresponding to NOAA ice and snow maps for the same period. Thus, for initial estimates of albedo values for the NOAA reflectivity zones, it is sufficient to assume that surface albedo for mixed scenes were obtained. Albedo values for the entire solar spectrum and for both pure snow and pure vegetation, estimates of the surface albedo for mixed scenes were obtained from this procedure are given below.

Zone 1: least reflectivity - albedo: 25 to 35%
Zone 2: moderate reflectivity - albedo: 35 to 55%
Zone 3: highest reflectivity - albedo: 60 to 70%

Reflectivity zone 3 corresponds to almost vegetation-free snow fields. The principal problem in determining the total

hemispheric reflectivity over all wavelengths from a surface with these characteristics lies in establishing the degree of anisotropy as a function of wavelength. From such information one may then extend satellite reflectance data viewed in a limited range of angles and narrow wavelength bands to provide estimates of surface albedo. To address this problem, field measurements of an open snow field using the JPL Portable Field Reflectance Spectrometer were conducted in March of 1977 and April of 1978. The data included measurements in the spectral range of 0.45 μm to 2.55 μm, and, for a variety of solar zenith angles, data were obtained for five inclinations from the vertical and five azimuths with respect to the sun. The data were averaged over 30 wavelength intervals each with a $\Delta\lambda$ of 0.05 μm. For each of these intervals, the ratio of the reflectance at a given viewing angle to the reflectance at nadir was determined and charts showing the angular distribution of the relative reflectivity for several wavelengths intervals prepared. The results have some irregularities in the patterns believed to be due to an uneven surface of irregularities in the snow condition. However, a clear pattern emerges of a wavelength dependence in the angular distribution of reflectance with the strongest anisotropy observed in the near IR. A sample of the results is given in Tables 1 through 3.

TABLE 1

The ratio of the reflectance at the given inclination and azimuth to the reflectance at nadir for the NOAA VHRR band.

INCLINATION FROM NADIR	AZIMUTH (0° TOWARD THE SUN)				
	0	45	90	135	180
30	1.016	1.020	1.007	.977	1.007
45	1.007	1.015	.983	1.032	1.015
60	1.034	.981	.939	.974	1.014
75	1.039	.958	.944	.938	.938

TABLE 2

The ratio of the reflectance at the given inclination and azimuth to the reflectance at nadir for λ = 0.8 μm.

INCLINATION FROM NADIR	AZIMUTH (0° TOWARD THE SUN)				
	0	45	90	135	180
30	1.025	1.036	1.017	.993	1.015
45	1.021	1.024	1.004	1.041	1.032
60	1.060	1.000	.966	.999	1.045
75	1.078	.986	.974	.969	.973

TABLE 3

The ratio of the reflectance at the given inclination and azimuth to the reflectance at nadir for λ = 1.1 μm.

	AZIMUTH (0° TOWARD THE SUN)				
	0	45	90	135	180
30	1.077	1.113	1.044	1.035	1.032
45	1.101	1.077	1.064	1.074	1.071
60	1.177	1.083	1.057	1.057	1.113
75	1.250	1.121	1.054	1.051	1.055

The greatest spatial and temporal albedo variations are found in relectivity zones 1 and 2. Within these zones, the vegetation density and shadows largely determine the spectral character of the albedo. During April of 1978, NC-130B overflights with the Modular Multiband Scanner were conducted in the Donner Pass and Benten areas. An analysis of these data is in progress aimed at determining the relationship between vegetation density over snow and the albedo of a mixed forest, shadow and snow scene.

REFERENCE

(1) Batten, E.S., M. Morrill, and J. Soho, 1977: The Albedo of Snow Covered Surfaces Determined from NOAA 4 and 5 Satellites, Presented at the Spring 1977 AGU Meeting, Washington, D.C.

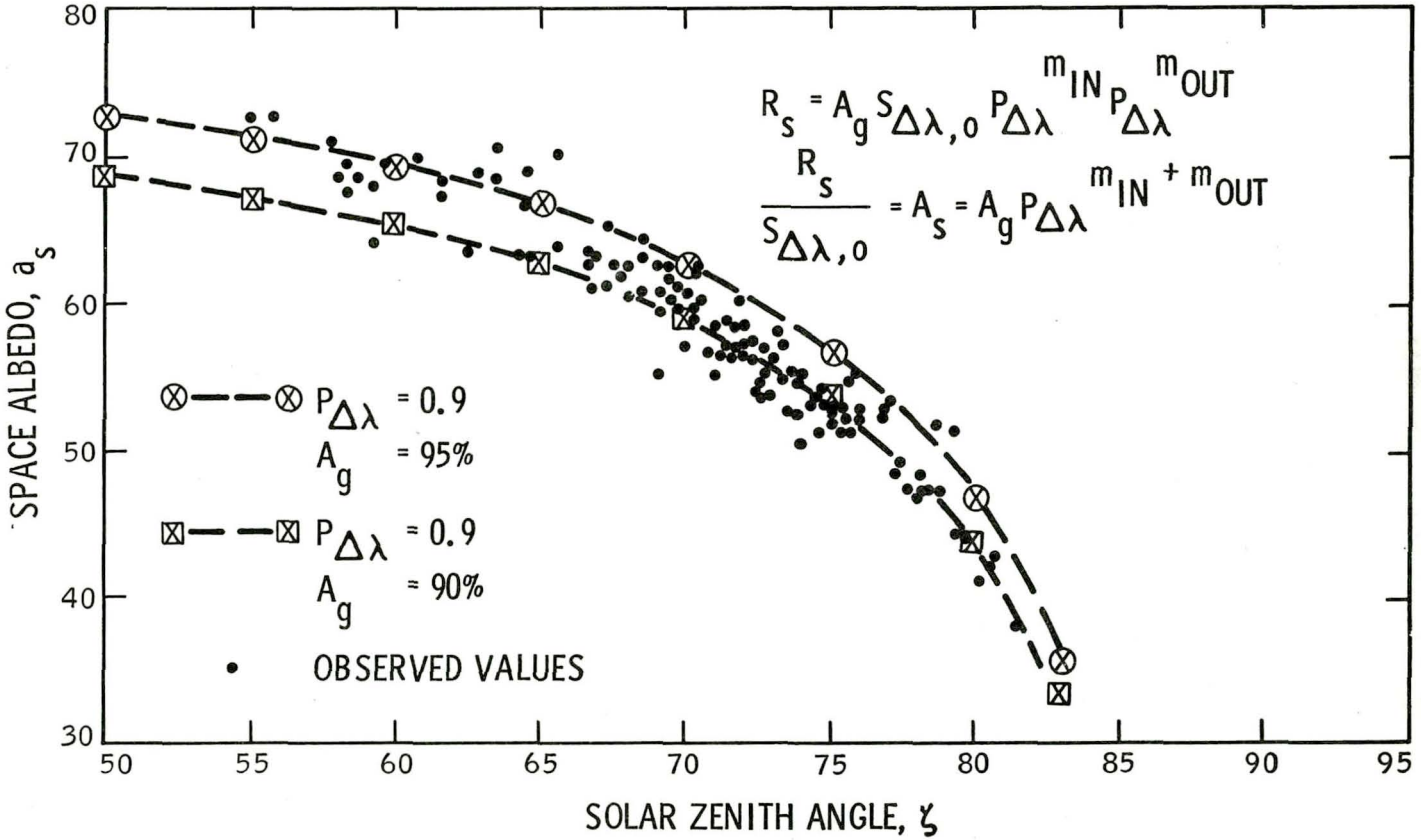

Fig 1 Observed and theoretical space albedo as a function of solar zenith angle as determined from NOAA 4 and 5 VHRR visible data.

Page intentionally left blank

Paper No. 49

THE ANNUAL CYCLE OF EARTH EMITTED RADIATION DISTRIBUTION

T. D. Bess and G. L. Smith, *Langley Research Center, Hampton, Virginia*

ABSTRACT

Measurements of longwave radiation from the Earth Radiation Budget (ERB) experiment aboard the Nimbus 6 spacecraft have been analyzed to show the annual cycle of the distribution of Earth emitted radiation

INTRODUCTION

The Earth Radiation Budget (ERB) instrument on the Nimbus 6 and Nimbus 7 spacecraft has provided a wealth of information about the Earth's radiation field (ref. 1). The instrument has wide-field-of-view (WFOV) radiometers for measuring total radiation leaving the Earth and shortwave (solar) radiation reflected by the Earth (ref. 2), so that longwave radiation emitted by the Earth can be determined. In this paper, results are presented for the annual cycle of longwave radiation distribution. The radiation field $q(\theta,\phi,t)$ at the top of the atmosphere may be described in the form

$$q(\theta,\phi,t) = \sum_{m,n} C_n^m(t)\ Y_n^m(\theta,\phi)$$

where θ is the colatitude, ϕ is the longitude of a point t is time. The coefficients $C_n^m(t)$ serve as a method of describing the time dependent distribution of emitted radiation. The $C_n^m(t)$ have been calculated from the ERB WFOV data.

Because the WFOV radiometers measure radiation flux incident from all directions onto a flat plate, the problem of relating these measurements to the radiation at the top of the atmosphere is one of resolution enhancement, or deconvolution. The theory of deconvolution has been developed for Earth emitted radiation (refs. 3 and 4) and has been applied to Nimbus 6 ERB data (refs. 5 through 7). The longwave deconvolution technique provides the C_n^m directly. For the results presented here the C_n^m were computed using a nominal limb darkening function.

RESULTS

The $C_n^m(t)$ have been computed for 1 month averages for 1 year of Nimbus 6 ERB data, from July 1975 through June 1976. The axisymmetric terms (m = 0) dominate up to n = 5, beyond which the pattern appears random. The magnitudes of $C_n^m(t)$ decrease rapidly with increasing n. The results are shown in figures 1 and 2 for $C_n^o(t)$ for n = 0 through 12.

Figure 1 shows the yearly cycle of $C_o^o(t)$, $C_1^o(t)$ and $C_2^o(t)$. The $C_o^o(t)$ term is the global average emitted radiation. The $C_1^o(t)$ term is a measure of hemispherical differences, or pole to pole differences. Its annual cycle is seen to have a nearly perfect sine shape, with a total range between its minimum and maximum values of 20 W/m^2. It does not oscillate about zero, but has a bias of 2-1/2 W/m^2. If the Earth were symmetric about the equator, one would expect the C_n^o terms for odd n values to have time histories which are symmetric about the time axis. Thus, the 2-1/2 W/m^2 bias in the annual cycle of C_1^o is due to land/ocean distribution differences between the Northern and Southern Hemispheres. The $C_2^o(t)$ term may be considered to be a measure of equator to pole gradient. It is seen to have an average value of approximately - 26 W/m^2, with a small variation which appears to be nearly semiannual.

The $C_n^o(t)$ for n = 3 through 12 are shown in figure 2. The C_3^o is nearly sinusoidal, with a total variation of 15 W/m^2 and a mean of approximately 4 W/m^2. As with C_1^o, this bias is a result of hemispheric differences of land/ocean distribution. The C_4^o term has a mean of approximately - 7 W/m^2 with variation of 5 W/m^2. Its shape is not so sinusoidal as the C_1^o or C_3^o histories. The C_5^o through C_{10}^o terms each have a significant annual sine component, and the C_6^o and C_8^o terms have a bias such that they do not change signs. The maximum absolute value decreases with increasing n until C_{11}^o and C_{12}^o, which are small and show little discernible pattern. Previous studies by Green and Smith (ref. 6) have indicated that twelfth degree is the limit of deconvolution for the orbit altitude of Nimbus 6. Whether the lack of pattern in the computed values of C_{11}^o and C_{12}^o is due to the nature of the atmosphere or due to the limitations of sampling and analysis is unclear at present.

CONCLUDING REMARKS

Analysis of 1 year of longwave data from the ERB instrument aboard Nimbus 6 shows a surprisingly simple variation with time of the longwave distribution. Analysis of other years of data will help to define the average annual cycle better, and to define the interannual variations. In order to complete the description of the radiation budget, work is ongoing at Langley Research Center to develop a technique for deconvolutiong short-wave WFOV data.

ACKNOWLEDGEMENT

The authors are grateful to Dr. Herb Jacobowitz and other members of the Meteorological Satellite Laboratory of NOAA for providing us with ERB data and for discussions with respect to the data.

REFERENCES

1. Jacobowitz, H.; Smith, W. L.; Howell, H. B.; Nagle, F. W.; and Hickey, J. R.: The First Eighteen Months of Planetary Radiation Budget Measurements from the Nimbus-6 ERB Experiment. Third Conference on Atmospheric Radiation, American Meteorological Society, Davis, CA, June 28-30, 1978.

2. Smith, W. L.; Hickey, J.; Howell, H. B.; Jacobowitz, H.; Hilleary, D. T.; and Drummond, A. J.: Nimbus-6 Earth Radiation Budget Experiment. Applied Optics, vol. 16, No. 2, Feb. 1977, pp. 306-318.

3. Smith, G. Louis and Green, Richard N.: A Technique for Analysis of Low Resolution Measurements of Earth Radiation Budget. Second Conference on Atmospheric Radiation, American Meteorological Society, Oct. 1975, pp. 111-114.

4. Smith, G. Louis and Green, Richard N.: Theoretical Analysis of Wide Field of View Radiometer Measurements of Earth Energy Budget. NASA paper presented at Fifth Annual Remote Sensing of Earth Resources Conference, Tullahoma, TN, March 29-31, 1976.

5. Green, R. N. and Smith, G. L.: Deconvolution of Earth Radiation Budget Data. Third National Aeronautics and Space Administration Weather and Climate Program Science Review, NASA CP-2029, 1977, pp. 299-303.

6. Green, R. N. and Smith, G. L.: Deconvolution Estimation Theory Applied to Nimbus-6 ERB Data. Third Conference on Atmospheric Radiation, American Meteorological Society, 1978, pp. 376-379.

7. Green, R. N. and Smith, G. L.: Parameter Estimation Applied to Nimbus-6 Wide-Angle Longwave Radiation Measurements, NASA TP-1307, Dec. 1978.

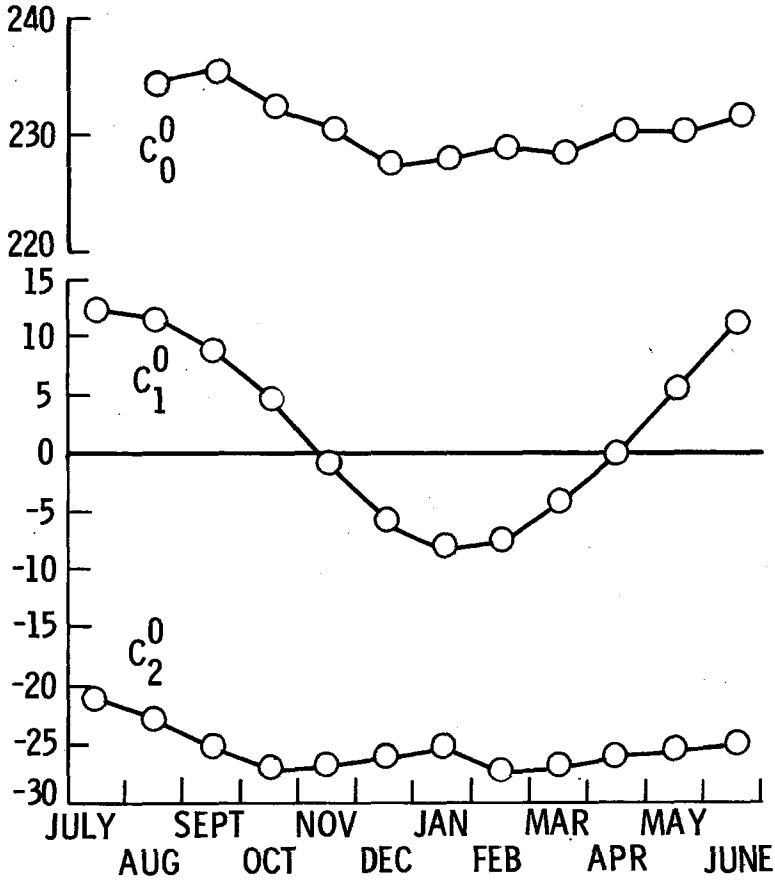

Figure 1. C_n^o histories for $n = 0, 1, 2$, for July 1975 through June 1976

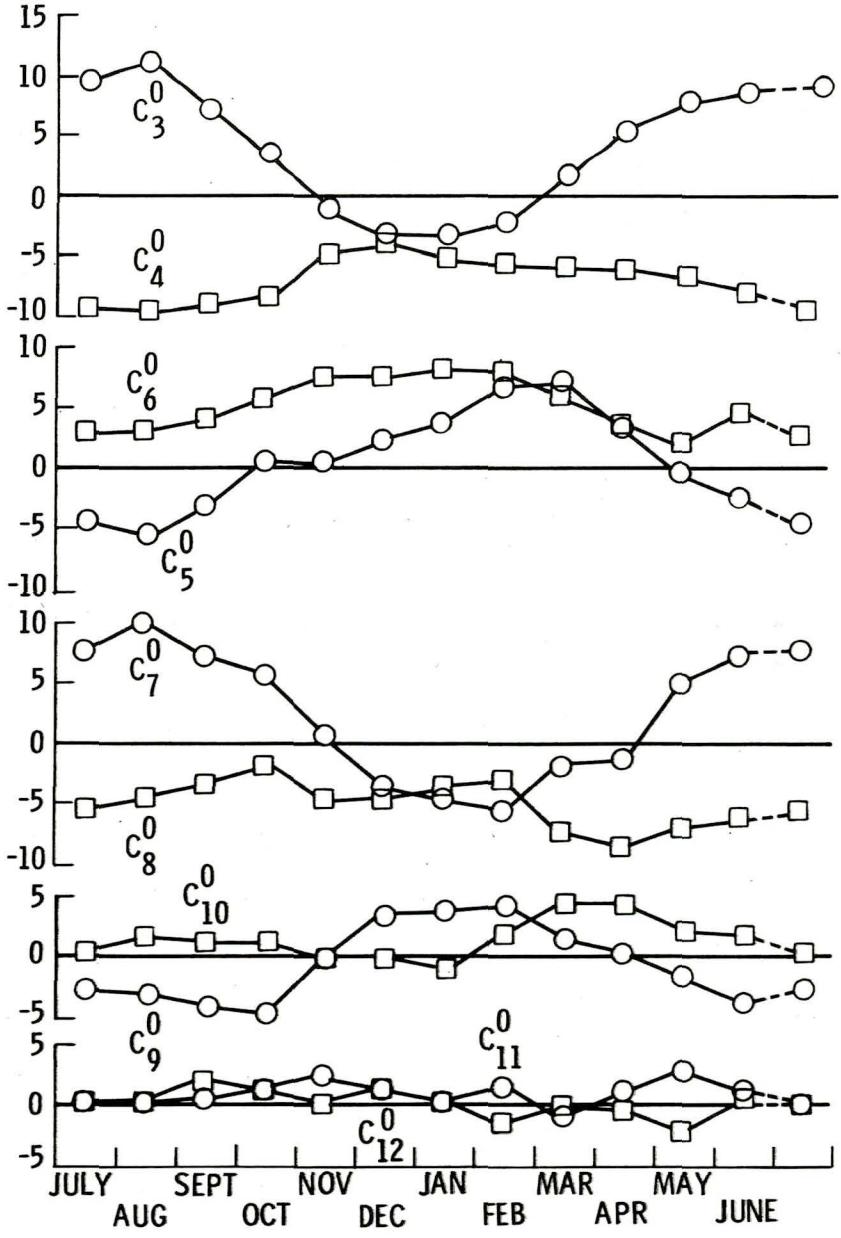

Figure 2. C_n^o histories for n = 3 through 12 for July 1975 through June 1976.

Page intentionally left blank

Paper No. 50

SPATIAL DISTRIBUTION OF EARTH FLUX DENSITY FROM UNRESTRICTED FIELD OF VIEW RADIATION MEASUREMENTS

W. L. Weaver, *Langley Research Center, Hampton, Virginia*

Abstract

A study was conducted in which simulated irradiances were reduced to Earth flux densities on different scales, and results are given from an analysis of Nimbus 6 data

INTRODUCTION

Measurements with unrestricted field of view (UFOV) flat plate radiometers can give very accurate estimates of global flux densities, provided the measurements are adequate in spatial and diurnal coverage. Simulation studies at Langley (Ref. 1 and 2) have shown that these detectors can also provide estimates of flux densities in latitude zones. This paper reports results of an analysis to determine if UFOV measurements can be used to estimate flux densities on scales smaller than the detector's Earth FOV. Simple geometric considerations were employed to reduce simulated irradiances to Earth flux densities. A spatial distribution of emitted flux density is also presented and discussed which was inferred from UFOV measurements of Nimbus 6.

SIMULATION STUDY

Simulated irradiance measurements from a satellite were calculated using a model of the Earth's emitted flux density which is based on Nimbus 3 data (Ref. 3). The Earth's surface was divided into 1654 flux regions, each with an area equal to a 5-degree latitude by 5-degree longitude region at the equator. The directional characteristics of the field were modeled either as lambertian or by a limb darkening function based on Nimbus 2 data (Ref. 3). A calculation was allowed to be influenced by all flux regions whose centers fell within the detector's Earth FOV. Measurement altitude was 600 km. A geometric shape factor was used to reduce the irradiances to estimates of flux density at the Earth's surface (Earth radius = 6371 km). These estimates of flux density were compared to model-derived average flux densities for concentric circles centered at the detector's FOV. A model-derived average flux density is the mean value derived directly from all 5-degree by 5-degree flux regions within the given circle.

Figure 1 shows results from two sets of measurements obtained in an equatorial orbit. One was obtained with a lambertian radiation model, and the other assumed the average limb darkening function (Ref. 3). Each data point (average measurement error) represents the average of the absolute errors between the estimated and the model-derived values of flux density for all measurements in the set. It is apparent that the results are not sensitive to the directional models. This is probably due to the fact that the detector gives much less weight to radiation from regions at the limb than to that near nadir. Flux densities inferred from the measurements are seen to be better estimates of modeled-derived flux densities over areas smaller than the detector FOV than over the detector's total Earth FOV. The area of best estimate appears to be for an area corresponding to an ECA of about 20 degrees. Such a circle encloses only about 15 to 20 percent of the detector's total Earth FOV, but the radiation from the area comprises about 80 percent of the measured irradiance.

Figure 2 shows results from individual measurements calculated every 10 degrees along the ground track of a Sun synchronous orbit having an inclination of 100 degrees. The directional model was assumed to be lambertian. Circles represent errors between estimated and model-derived flux densities for the detector's total Earth FOV. Squares show the errors when the estimated values are compared to model-derived values for a circle of ECA = 20 degrees. Estimates for the total FOV are seen to be in error by as much as 12 percent, and in almost all cases errors are less for the smaller circle. The average measurement error for the smaller scale is 60 percent less than that for the total FOV. Note that the errors can be either positive or negative; that is, the shape factor can overestimate or underestimate the average flux density. This was the reason for using the average of the absolute errors as a figure of merit in comparing results in figure 1. These results suggest that spatial distributions of estimated emitted flux densities derived from UFOV radiation measurements, using geometric shape factors, can be interpreted on scales smaller than the detector Earth FOV.

NIMBUS 6 DATA ANALYSIS

Longwave irradiances measured by the UFOV flat plate detectors on Nimbus 6 during August 1975 have been analyzed. Nimbus 6 is in a Sun synchronous orbit with a northward equatorial crossing of 12 noon local time. Irradiances were reduced, using shape factors, to estimates of flux density at an altitude of 30 km. Flux densities were averaged over 10-degrees latitude by 10-degree longitude regions. The spatial distribution of emitted flux density based on these averaged values is shown in figure 3.

These results are in good agreement with UFOV results reported in reference 4. Large-scale flux density patterns are identified in a latitude zone extending from 20 degrees south to 40 degrees north, where in some cases, longitudinal gradients are as strong as latitudinal gradients. The patterns, particularly over Africa, Europe, and Asia show details on a scale which appears to be much smaller than the detector FOV (ECA = 60 deg.).

CONCLUSIONS

A simulation study indicates that UFOV radiation measurements can be used to estimate Earth emitted flux densities on scales smaller than the detector FOV, and a spatial distribution of emitted flux density from Nimbus 6 data tend to confirm this result.

REFERENCES

1. Weaver, W. L.: Simulation Study of a Method for Analyzing Wide Field of View Radiometer Measurements from Satellites and Some Analysis of ESSA 7 Data. NASA CP 2029, Nov. 1977

2. Green, Richard N.: Simulation Studies of Wide and Medium Field of View Earth Radiation Data Analysis. NASA TP 1182, May 1978.

3. Raschke, Ehrhard; Vonder Haar, Thomas H.; Pasternak, Musa; and Bandeen, William R.: The Radiation Balance of the Earth-Atmosphere System from Nimbus 3 Radiation Measurements. NASA TN D-7249, April 1973.

4. Smith, W. L.; Hickey, J.; Howell, H. B.; Jacobowitz, H; Hilleary, D. T.; and Drummond, A. J.: Nimbus-6 Earth Radiation Budget Experiment. Appl. opt., vol. 16, no. 2, Feb. 1977, pp. 306-318.

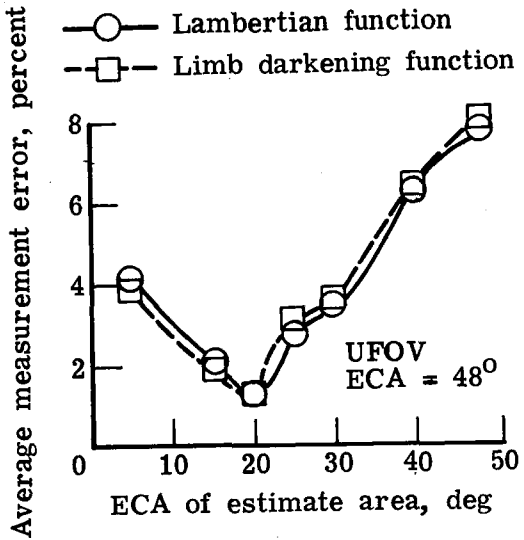

Fig. 1 - Errors in estimating flux density over circular regions smaller than the detector FOV. Altitude = 600 km.

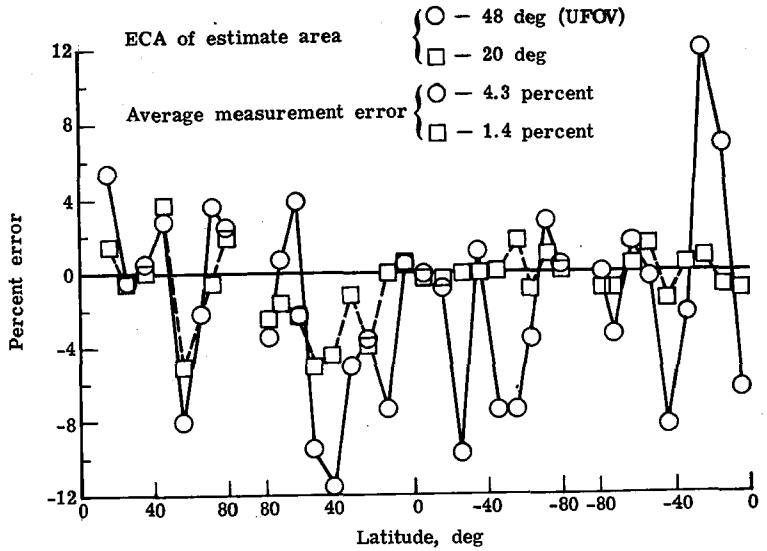

Fig. 2 - Errors in estimating flux density from individual measurements with UFOV detector. Altitude = 600 km, Lambertian model.

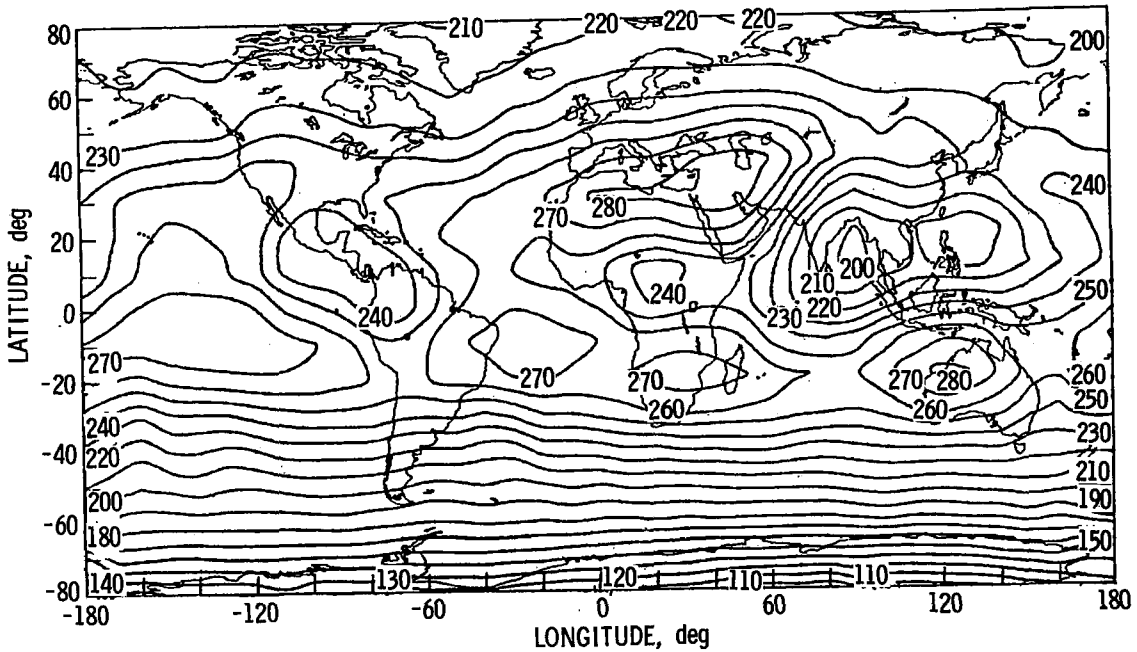

Fig. 3 - Spatial distribution of Earth emitted flux density for August 1975, from UFOV measurements on Nimbus 6. Units are W/m^2.

Page intentionally left blank

Paper No. 51

CORRELATED K-DISTRIBUTION METHOD FOR RADIATIVE TRANSFER IN CLIMATE MODELS: APPLICATION TO EFFECT OF CIRRUS CLOUDS ON CLIMATE

Andrew A. Lacis, Wei-Chyung Wang and James E. Hansen, *Goddard Institute for Space Studies, New York, NY 10025*

ABSTRACT

A radiative transfer method appropriate for use in simple climate models and 3-D global climate models has been developed. It is fully interactive with climate changes, such as in the temperature-pressure profile, cloud distribution and atmospheric composition, and it is accurate throughout the troposphere and stratosphere. The vertical inhomogeneity of the atmosphere is accounted for by assuming a correlation of gaseous k-distributions of different pressures and temperatures. Line-by-line calculations are made to demonstrate that the method is remarkably accurate. The method is then used in a 1-D radiative-convective climate model to study the effect of cirrus clouds on surface temperature. It is shown that an increase in cirrus cloud cover can cause a significant warming of the troposphere and the earth's surface, by the mechanism of an enhanced greenhouse effect. The dependence of this phenomenon on cloud optical thickness, altitude and latitude is investigated.

Introduction. Radiation calculations in climate models should be designed to be properly responsive to climate changes, such as in the atmospheric temperature and in the cloud, aerosol and gaseous atmospheric composition. The major difficulties are (1) accurately integrating over complex and sometimes overlapping absorption bands, which greatly change their characteristics with height, and (2) accurately including the effects of multiple scattering.

The basis of the approach we take for both solar and terrestrial radiation, which we call the correlated k-distribution method, is a generalization of the k-distribution method used by Lacis and Hansen (1974). In this generalization the vertical inhomogeneity of the atmosphere is approximately accounted for by assuming a simple correlation of k-distributions at different temperatures and pressures. By means of 'line-by-line' calculations we demonstrate that the method is remarkably accurate even for the notoriously difficult 9.6 μm ozone band.

There are several advantages to this radiative treatment, in addition to the fact that it includes all significant atmospheric constituents. Realistic spectral properties of clouds and aerosols are employed, based on Mie scattering computations with the best available composition and refractive index information; thus the treatments in the solar and thermal regions are self-consistent and we avoid crude assumptions such as black

or 'half-black' clouds. The accurate treatment employed for solar zenith angle effects is necessary for assuring proper latitude variations of radiative heating.

Correlated k-distribution method. The k-distribution f(k) for a given gas and frequency interval is the probability density function such that f(k) dk is the fraction of the frequency interval for which the absorption coefficient is between k and k + dk. The basic idea of grouping frequency intervals of gaseous spectra according to absorption coefficient strengths goes back at least to Ambartsumian (1936) who used it in estimating the influence of absorption lines in stellar atmospheres. Lacis and Hansen (1974) used k-distributions to include the effects of multiple scattering; they numerically derived a mean atmospheric k-distribution for water vapor absorption and scaled the gas amount as a function of pressure and temperature to crudely approximate the effect of atmospheric inhomogeneity.

Our generalization of the k-distribution method provides a more accurate treatment of the vertical inhomogeneity of the atmosphere; it is based on the assumption that the k-distributions at all altitudes are simply correlated in frequency space, i.e., the strongest absorption occurs at the same frequencies at all altitudes and similarly for the weakest absorption. This maintenance of the same relative rank of absorption coefficients over the entire pressure range of the atmosphere is rigorously correct for a single spectral line with a fixed center and for a uniform Elsasser (1942) band model. Fig. 1 is a schematic illustration of the k-distribution method.

For a real gaseous spectrum, we expect some blurring of the assumed correlation as a result of partial overlapping of lines with different line-widths and strengths and the fact that the temperature dependence of the line-strengths is not the same for all lines. To demonstrate that this has little impact on the overall accuracy of our method we show in Fig. 2 the thermal cooling rates computed with the correlated k-distribution method and with line-by-line calculations for the 9.6μm ozone band.

The computations for Fig. 2 were made for standard atmospheric temperature and ozone distributions with a 1 km vertical resolution (Lacis and Wang, 1979). The solid line was obtained by means of line-by-line computations using the line coefficients tabulated by McClatchey et al. (1973) with approximately 2×10^5 frequency intervals. The dotted curve was obtained by means of the correlated k-distribution approach with 5 probability intervals, i.e., 5 discrete values of k, each with an appropriate pressure-temperature dependence. Since the computing time is proportional to the number of frequency intervals or k values, the relative speed of the correlated k-distribution method is apparent.

The k-distribution is formally related to the transmission function by

$$T(u) = \frac{1}{\Delta\nu} \int_{\Delta\nu} e^{-k_\nu u} d\nu = \int_0^\infty f(k) e^{-ku} dk, \qquad (1)$$

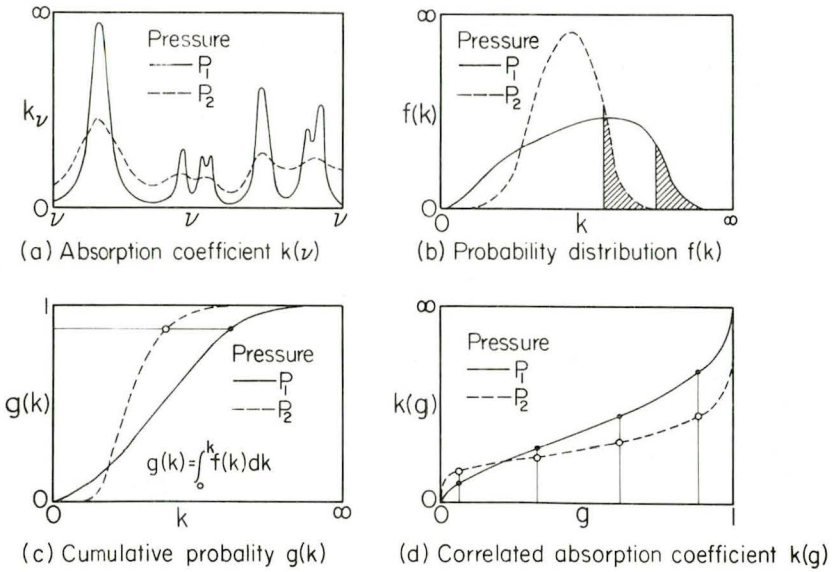

Fig. 1. Schematic illustration of the correlated k-distribution method. (a) is a schematic absorption line spectrum at two pressures. The greater pressure P_2 broadens the spectral features, but the line center positions remain fixed. (b) is the probability density of absorption coefficients. The broadened spectrum has a narrower k-distribution. The shaded areas depict the strongest absoprtion for both pressures and are assumed to refer to the same spectral intervals for both distributions. (c) is the cumulative probability density. This integrated k-distribution makes it possible to rank probability intervals according to relative absorption coefficient strength. (d) is the correlated k-distribution. Integration over g replaces integration over ν.

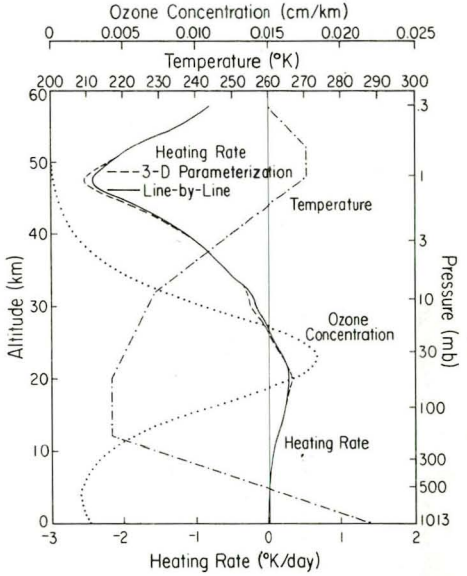

Fig. 2. Atmospheric cooling by the 9.6 μm ozone band. Computations are for a standard atmosphere temperature distribution and a standard mean ozone concentration (Lacis and Wang, 1978) using a 1 km vertical resolution. The solid line was obtained with explicit line-by-line integration using approximately 2×10^5 spectral intervals. The dashed line is the result obtained with the correlated k-distribution method using 5 probability intervals for the entire band.

where u is the gas amount. Because of its convenient mathematical properties, we choose the Malkmus (1967) model to represent T(u),

$$T(u) = \exp\{-\frac{\pi}{2} B[(1 + 4Su/\pi B)^{\frac{1}{2}} - 1]\} \quad (2)$$

where the two parameters, S and B, are the effective line strength and line width. Since f(k) is the Laplace transform of T(u) we obtain the k-distribution directly in terms of the Malkmus model parameters,

$$f(k) = \frac{1}{2} k^{-3/2} (SB)^{\frac{1}{2}} \exp[\frac{\pi}{4} B(2 - k/S - S/k)] . \quad (3)$$

The Malkmus model k-distribution is analytically integratable to yield the cumulative probability

$$g(k) = \int_0^k f(k')dk'. \quad (4)$$

This makes it convenient to rank intervals of Δg according to their relative absorption coefficient value. This procedure for ranking Δg retains an implicit frequency correlation with altitude and provides the basis for accurate computation of multiple scattering effects in an inhomogeneous atmosphere.

For a given gas and frequency interval, the k-distribution can be obtained in several different ways (Lacis and Wang, 1979). We use the tabulated line coefficients for H_2O, CO_2, O_3, CH_4 and N_2O compiled by McClatchey et al. (1973) to compute line-by-line absorption over homogeneous paths for pressures and temperatures over the range of values encountered in the stratosphere and troposphere. For each gas we obtain a table of S and B parameters by least square fitting of the Malkmus model to the line-by-line computations. This yields band model parameters which fit the line-by-line results within 1 or 2 per cent over a pressure-temperature range from the ground to a height of $\sim$70 km, where the assumption of local thermodynamic equilibrium begins to deteriorate. Note that the numerical approach for extracting band model parameters is not limited by the changing line shape with altitude; we can use the appropriate Voigt profile for each altitude and obtain a corresponding k-distribution in terms of its effective line strength and line width parameters.

Climatic effect of cirrus clouds. It is well known that clouds have two major competing effects on global climate: (1) they reflect solar radiation, which tends to decrease the surface temperature, and (2) they blanket thermal radiation from the earth's surface, reradiating at a lower temperature and thus tending to warm the surface temperature. The opinion of climatologists seems to be that a general increase in cloudiness would decrease the surface temperature, for example, according to Schneider (1972): "...the effect of a sustained increase in the average amount of cloud cover of the earth would be a decrease in the global-average surface temperature, provided that the cloud top height and cloud albedo remain unchanged."

It is recognized that cirrus clouds can present an exception to the expected cooling effect of clouds. For example, Fig. 3 (from Manabe and Strickler, 1964) shows that cirrus clouds at high altitudes can have a

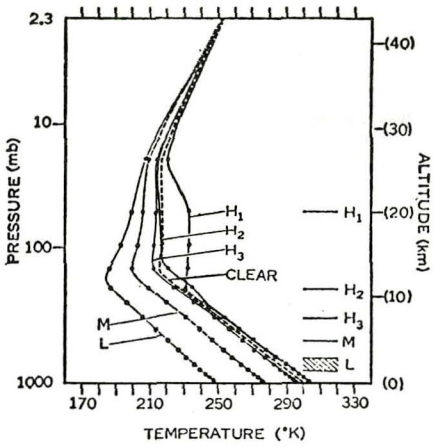

Fig. 3. Thermal equilibrium of various atmospheres with clouds. The height of overcast clouds used for each computation is shown by H_1, H_2 and H_3 for high clouds, M and L for middle and low clouds. The equilibrium curve of the clear atmosphere is shown by a thick dashed line. (After Manabe and Strickler, 1964).

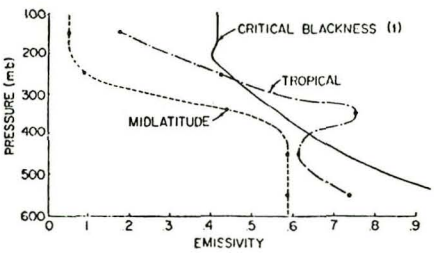

Fig. 4. Measured cirrus cloud infrared emissivities and the "critical blackness" curve from Manabe and Strickler (1964). (After Cox, 1971).

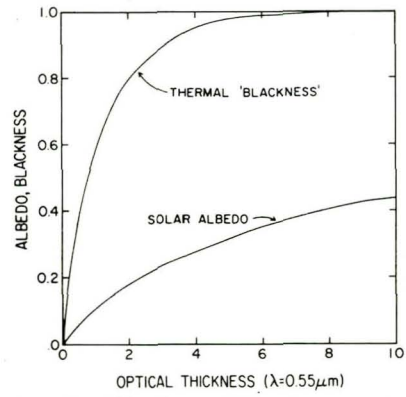

Fig. 5. Albedo and blackness of cirrus clouds as a function of optical thickness, computed for ice particles of 25 μm effective radius. The 'blackness' is the sum of the cloud absorbtivity and reflectivity for blackbody radiation of 250 K; the reflectivity contributes at most 0.05 to the blackness.

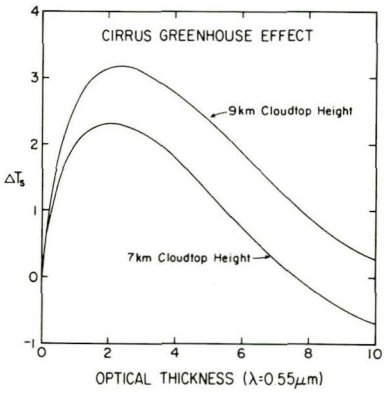

Fig. 6. Effect of cirrus clouds on surface temperature (in degrees K) as a function of the cirrus optical thickness and cloudtop height. The cirrus are assumed to cover 10% of the sky. Calculations are for a global average temperature profile, which is also similar to the mean profile at 30–40° latitude.

heating effect, though the magnitude is small compared to the cooling by other clouds. According to Manabe and Strickler (1964): "If the height of cirrus clouds is greater than 9 km and its blackness for infrared radiation is larger than 50 percent, cirrus has a heating effect on the temperature of the earth's surface." The cirrus infrared emissivities measured by Cox (1971) also suggest that a warming effect by cirrus is small and rather unusual, cf., Fig. 4 his measurements are interpreted as indicating that in the tropics only cirrus at altitudes 250-400 mb cause heating, and at midlatitudes all cirrus cause cooling.

However, the definition for blackness used by Cox (1971) differs from that of Manabe and Strickler (1964) which thus leaves the conclusions of Cox open to question. The nature of the calculations of Manabe and Strickler was to use a fixed cirrus albedo of 21% and to look at how the surface heating or cooling would change for different assumed infrared emissivities. In general the calculations of Manabe and Wetherald are extremely valuable,but in order to investigate the effect of cirrus on the temperature profile it is essential that the solar and thermal spectral regions be treated in a self-consistent fashion using spectrally dependent optical properties of water ice. The method described above permits this computation to be done with reliable accuracy.

Results for the solar albedo and thermal 'blackness' are shown in Fig. 5 as a function of optical depth. It is apparent that the thermal blackness (defined to be 1 minus the total transmission) is much more rapidly saturated than is the solar albedo. Typical cirrus cloud emissivities of ~ 0.4 to ~ 0.6 measured by Cox (1971) correspond to optical depths of ~ 0.5 to ~ 1.0 and should have corresponding albedos of $\sim 5\%$ to $\sim 10\%$ rather than the widely used value of 21% estimated by Haurwitz (1948). As shown in Fig. 6, cirrus clouds have a substantial warming effect on the surface temperature. It is only when the optical thickness becomes very large and the clouds appear at low altitudes that a cooling effect is experienced.

The most effective optical thickness for the heating (greenhouse) effect is approximately $\tau = 2$, for which the thermal blackness is nearly saturated while the solar albedo is still rather small. The warming effect is also sensitive to cloudtop height; thus high clouds, which reradiate the absorbed surface radiation at a lower effective temperature, provide greater warming than low clouds.

Discussion. These results, which were computed for mean global atmospheric conditions, show a substantial warming effect due to cirrus clouds. The same qualitative conclusion holds for tropical and polar latitudes. The magnitude of this greenhouse effect is sufficiently large to indicate the need for a careful reappraisal of the role of cirrus clouds in climate.

REFERENCES

Ambartsumian, V., Pub. de l'Obs. Astron. de Leningrad, 6, 7-18, 1936.
Cox, S.K., J. Atmos. Sci., 28, 1513-1515, 1971.
Elsasser, W.M., Harvard Meteor. Studies No. 6, Harv. U. Press, 1942.
Lacis, A.A., and J.E. Hansen, J. Atmos. Sci., 31, 118-133, 1974.
Lacis, A.A., and W.C. Wang, (in preparation), 1979.
Malkmus, W., J. Opt. Soc. Amer., 57, 323-329, 1967.
Manabe, S., and R.F. Strickler, J. Atmos. Sci., 21, 361-385, 1964.
McClatchey et al., AFCRL-TR-73-0096, Env. Res. Pprs. 434, 1973.
Schneider, S.H., J. Atmos. Sci., 29, 1413-1422, 1972.

Paper No. 52

WORLDWIDE CLOUD COVER MODEL

O. E. Smith, *Marshall Space Flight Center, Huntsville, Alabama,* and Paul N. Sommerville, *Florida Technological University, Orlando, Florida*

ABSTRACT

This is a first study effort aimed at modelling, i.e., classifying worldwide cloudiness into homogeneous regions, using a satellite data set containing Day IR, Night IR, Incoming, and Absorbed solar radiation measurements on a 2.5-degree latitude-longitude grid. The progress on the initial work to data and the methods of analysis are presented.

INTRODUCTION

The purpose of this investigation is to develop a model for worldwide cloud cover using a satellite data set containing infrared radiation measurements. Other cloud models exist [1 - 3]. These early cloud models used primarily ground-based cloud observations. The satellite data set containing Day IR, Night IR, Incoming, and Absorbed solar radiation measurements on a 2.5-degree latitude-longitude grid covering a 4-year period of record (with some missing months) has recently become available. There was originally a 2-year period of similar data on an NMC grid.[1] The first step is to convert these infrared data to estimates of cloud cover. The statistical analysis of classification of cloud region characteristics can then be performed.

There are several reasons for desiring a cloud model based on satellite data. The ground-based data are much more limited in scope. Some fairly large areas of the world have either no data or very sparse data, and models using ground-based observations necessitate a number of assumptions, including on occasion that a region is essentially like its antipodal location. A good worldwide cloud cover model is needed for the purpose of studying the relationship between cloudiness, precipitation, and the Earth radiation budget.

---

[1]The investigators gratefully acknowledge the efforts of Roy Jemne and his coworkers at NCAR for furnishing the data sets for this study.

CONVERSION OF SATELLITE IR MEASUREMENTS TO CLOUD COVER

A major initial task is to derive cloud cover estimates from the satellite infrared data. The method used in this investigation follows the suggestions obtained through personal communications with Tom Gray, National Environmental Satellite Services [4].

Albedo is defined as the reflective power, or the fraction of incident light that is reflected by a surface or body. Included in the satellite data are the amount of incoming solar radiation, I_{in}, and the amount of absorbed solar radiation, I_{ab}. The satellite observed albedo, A_{so}, is estimated by

$$A_{so} = (I_{in} - I_{ab}) / I_{ab} \quad . \tag{1}$$

If the Earth's surface absorbed all solar radiation, then the cloud cover might be taken simply as 1 minus albedo (assuming also that clouds reflect all solar radiation). Different parts of the Earth's surface, however, have differing radiances. For example, the albedo of the ocean is approximately 5 percent (95 percent of the solar radiation being absorbed), while the Sahara desert reflects approximately 40 percent of the solar radiation reaching it.

To determine cloud cover, we need to obtain the background radiation of the region of the Earth of interest. To do this, for a given month and a specified location, we calculate A_{so} from equation (1) for every day of a month and observe the minimum value, $A_{so_{min}}$. This minimum value should occur on the day of least (hopefully near zero) cloud cover. If $\underline{r}$ is the reflectance of the clouds and $\underline{n}$ is the fraction of cloud cover, then the basic formula may be written as

$$A_{so} = n * r + (1-n) * A_{so_{min}}$$

from which we have the fraction of cloud cover, $\underline{n}$, as:

$$n = \frac{A_{so} - A_{so_{min}}}{r - A_{so_{min}}} \quad . \tag{2}$$

This formula requires a knowledge of $\underline{r}$ which varies.

A way to estimate the cloud reflectance, r, is by observing the difference between the Earth's surface temperature and the temperature equivalent of the satellite-observed daytime infrared reading (denoted by IR_D). The radiance of the IR_D by Stefan's law is equal to $5.75 \times 10^{-8}\ T^4$ (watts/m^2), where T is the temperature equivalent in degrees Kelvin. Putting X = (surface temperature - T), (units degree Kelvin), the following relationship has been observed:

$$r = -0.000265\ X^2 + 0.0295\ X + 0.10\ . \qquad (3)$$

We propose to use a surface temperature of 30° C for latitudes within 25 degrees of the equator and -5° C for latitudes within 25 degrees of the pole. Interpolations will be used for intermediate latitudes.

Because this investigation is based on derived cloud cover estimates and may be subject to criticism, it is noted that ground-based cloud observations are also estimates as well as cloud cover obtained by satellite photography. We make this conjecture: Those variables which are not well defined in the IR to cloud cover conversion procedure will have small contributions to climatic modelling of the clouds over the entire month. For a specific day and area the preceding procedure may not be entirely satisfactory for synoptic cloud cover analysis.

MODELING FOR CLOUD COVER

We propose to obtain for each grid point (2.5× 2.5 latitude-longitude over the entire world to the extent the satellite infrared data are available) the mean and standard deviation of cloud cover for a specified month (beginning with the four January periods). Then we will use a nonparametric density estimate technique to estimate the joint probability density function of the mean and standard deviation of all the grid points so observed.

Visualize the following: A "plotted" joint probability density function will then show "hills" and "valleys." A discriminant method will be used to separate the hills, valleys, and plateaus in the joint probability density function. The grid locations corresponding to a particular region (e.g., hill) of the joint probability density function will be a region on the Earth's surface of similar cloud cover characteristics. We will thus be able to model cloud cover over the world for the specific month (say, January).

Similar analyses will be made for other months—say, April, July, and October. The result will be a division of the globe into distinct

regions based on cloud cover characteristics for each month. The statistical methods of classification are objective. These statistical methods could be applied to the original satellite infrared data.

To make a good climatological model a reasonably long record length is required. The satellite data available for this study comprise approximately 44 months. This is sufficient for some model development, but a longer period of record would be desirable.

REFERENCES

1. Barnes, J. C.; Glasen, A. H.; Sherr, P. E.; and Willand, J. H.: Worldwide cloud cover distribution for use in computer simulations. NASA Contractor Report CR-61226, June 1968.

2. Greaves, J. R.; Spiegler, D. B.; and Willand, J. H.: Development of a global cloud cover model for simulating Earth-viewing space missions. NASA Contractor Report CR-61345, April 1971.

3. Falls, L. W.: The beta distribution: a statistical model for world cloud cover. J. Geophys. Res., Vol. 79, No. 9, 1974, 1261-1264.

4. Gray, Tom: Personal communication, 1978.

Paper No. 53

PERIODIC VARIATIONS OF PRECIPITATION IN THE TROPICAL ATLANTIC OCEAN

M. S. V. Rao, *Systems & Applied Sciences Corporation, Riverdale, Maryland,*
J. S. Theon, *NASA Headquarters, Washington, DC*

ABSTRACT

Statistical analysis of the satellite-borne Electrically Scanning Microwave Radiometer data in the tropical Atlantic region reveals that the rainfall near local noon is higher both in frequency of occurrence and intensity than the rainfall in the same area near local midnight. Another striking feature that stands out from the analysis is an oscillation with a period of 3.3 days in rainfall occurrence and intensity. This periodicity is consistent with easterly waves traveling from the African continent to the region under study.

Quantitative rainfall maps for the tropical Atlantic region bounded by 25°N to 10°S and 95°W to 15°E were derived from satellite-borne Electrically Scanning Microwave Radiometer (ESMR) data. The basis of production of the maps is the selective response to liquid water in the atmosphere of ESMR operating at 19.35 GHz carried on board the Nimbus 5 satellite. Because the emissivity of water, ϵ_W, in the vicinity of 19 GHz is low ($\approx$0.4) and inversely proportional to the thermodynamic temperature T_W, whereas the brightness temperature as observed by the satellite-borne radiometer is proportional to the product ϵ_W T_W, the oceans provide a convient background to the ESMR system, and this facilitated rainfall mapping over wide oceanic regions.

Calibration curves for interpreting ESMR brightness temperature in terms of rainfall rate were obtained from the model proposed by Wilheit, Chang, Rao, Rodgers, and Theon, which assumes a Marshall-Palmer distribution of raindrops, and permits the solution of the equation of radiative transfer considering both absorption and scattering. The theoretical curves were compared with (1) ground truth from radar and (2) the results of a specially designed ground-based experiment during which upward-viewing microwave brightness temperatures were compared over a period of several months with directly measured rain-rates. The agreement was good.

A number of problems presented themselves when an attempt was made to generate rainfall maps from satellite ESMR data. More than fifteen sources of error (including anomalous mode, saturation, over-sensitivity to freezing height level, inadequate sampling and field of view) became apparent. However, applying approximate corrections to these errors as far as possible, global oceanic maps were generated. These maps were compared with the best available climatological data. The results showed that notwithstanding the various short comings, it is possible to utilize ESMR data for studies on certain scales – studies involving large spatial and temporal averages.

With the objective of investigating the local characteristics in the GATE region a set of rainfall maps were generated for the rectangular area bounded by latitudes 25°N and 10°S and longitude 95°W and 15°E. The rain-rate data were averaged over 1 degree latitude by 1 degree longitude grid cells. Precipitation charts were produced separately for daytime and nighttime observations for each of the days of the GATE period viz. 15 June through 30 September 1974. Figure 1 reproduces the map of daytime precipitation for the first day and Figure 2 the nighttime precipitation for the same day.

Statistical analysis of these rainfall observations for the entire GATE period was made with a view to gaining insight into the day-night variations and other small time scale fluctuations in oceanic rainfall. Figure 3 represents the frequency of rainfall occurrence in the entire area as a function of time, separately for daytime and night-time precipitation. Similar curves for the average rainfall intensity in the region are presented in Figure 4. The figures reveal that in the tropical Atlantic, rainfall near local noon is higher both in frequency and in intensity than that near local midnight. The overall ratio of the day to night frequency of occurrence for the entire region and for the entire period of GATE is 1.4:1.0. The overall ratio of day to night rainfall intensity is 1.7:1.0.

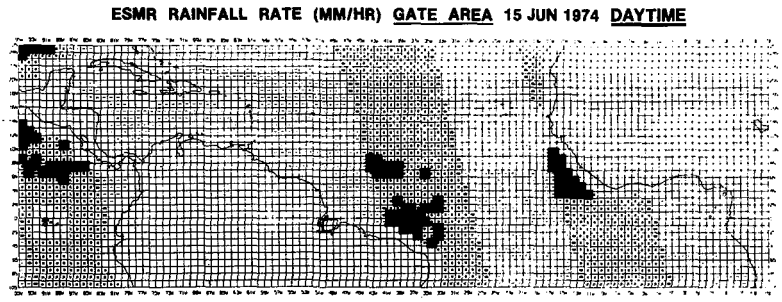

Fig. 1–Map of precipitation near local noon for the first day of GATE.

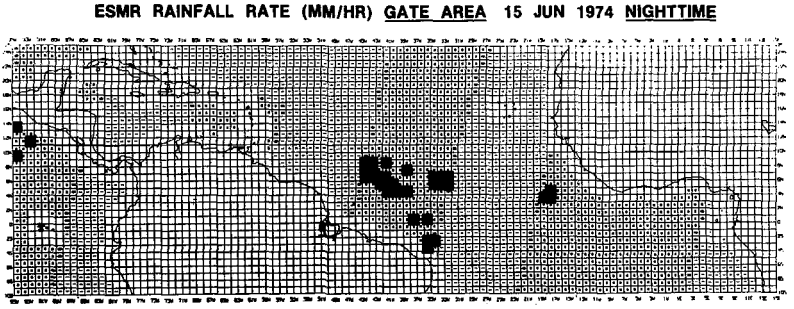

Fig. 2–Map of precipitation near local midnight for the first day of GATE.

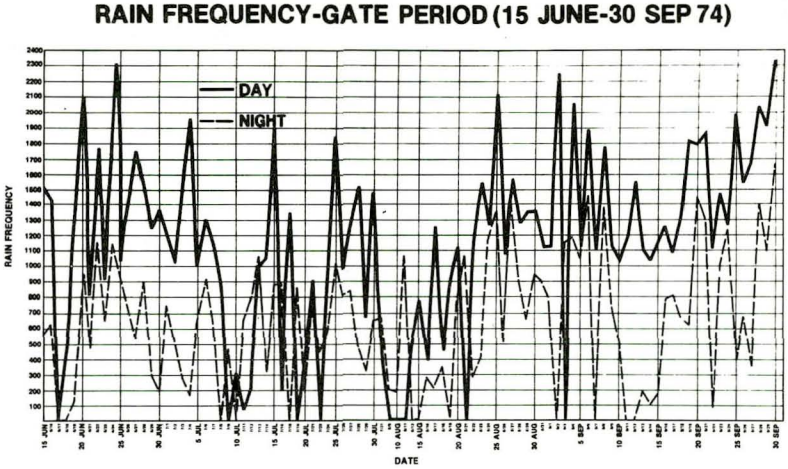

Fig. 3–Curves of frequency of rainfall occurrences vs. time (day and night).

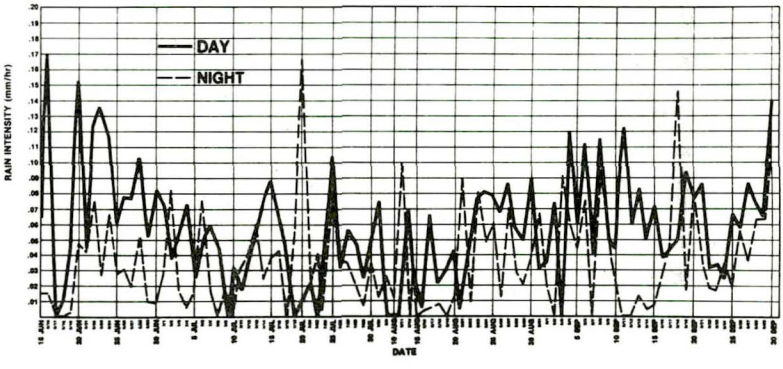

Fig. 4–Curves of average rainfall intensity vs. time (day and night).

Dynamical considerations do not favor such large variations being uniformly valid over all oceanic areas in general. For, precipitation is indicative of vertical motion, and ascending motion over large areas needs to be compensated by descending motion in other areas. It is therefore concluded that the observed diurnal variation is a location-dependent characteristic of the tropical Atlantic Ocean. It is possible that outside the tropical region the diurnal variation is opposite in phase.

The graphs in Figures 3 and 4 display an interesting small time-scale oscillation. Analysis of the curves reveals a fluctuation of periodicity 3.3 days in rainfall

occurrence as well as intensity. It is well known that easterly waves over Africa have a similar periodicity. Thus, the time scale of the oscillation observed in our analysis is consistent with easterly waves traveling from the African continent over the tropical Atlantic belt under study.

Paper No. 54

REMOTE SENSING OF SEASONAL DISTRIBUTION OF PRECIPITABLE WATER VAPOR OVER THE OCEANS AND INFERENCE OF BOUNDARY LAYER STRUCTURE

C. Prabhakara, *Goddard Space Flight Center, Greenbelt, Maryland 20771*

ABSTRACT

Over the oceans satellite infrared spectral measurements in the 18 μm water vapor band and the 11 μm window region have been used to derive precipitable water vapor, w, in the atmosphere and the sea surface temperature, SST. Seasonal maps of w on the oceans derived from these data reveal the dynamical influence of the large scale atmospheric circulation. With the help of a model for the vertical distribution of water vapor, the configuration of the atmospheric boundary layer over the oceans can be inferred from w when the information of SST is combined. The gross seasonal mean structure of the boundary layer inferred in this fashion reveals the broad areas of the trade wind inversion and the convectively active areas such as the intertropical convergence zones.

INTRODUCTION

The general circulation of the atmosphere displays some important climatological features over the oceans such as the subtropical anticyclones and the intertropical convergence zones. The circulation of the oceanic subtropical anticyclones extends to about 40°N and 40°S in the respective hemispheres. The equatorward trade winds associated with these anticyclones are instrumental in transporting the water vapor to intertropical convergence zones and thereby help to maintain the directly driven Hadley circulation in the tropics (Riehl, et al., 1954; and Malkus, 1956). A salient feature of the trade wind circulation in the lowest layers of the atmosphere is the trade wind inversion which is produced as a consequence of the large scale dynamics of the subtropical anticyclones. Furthermore the base of this inversion is found to slope upward along the down stream (NE to SW in the northern hemisphere) in response to the joint influence of small convective motions and large scale subsidence (Mak, 1976).

The intertropical convergence zone is produced by the convergence of trades in the low levels. The vertical rising motion generated by the surface convergence leads to significant upward transport of water vapor making the lower layers of the troposphere very humid.

The importance of the sea surface temperature (SST) anomalies has been pointed out by several studies (see for ex. Namias, 1978). The association between these anomalies and the strength of the trades in the Pacific Ocean has been revealed in a study by Reiter (1978).

From the above discussion we see that remote sensing of SST and the stratification of the atmosphere in the first few kilometers above the ocean surface could be valuable for investigating the regional and seasonal climate.

The SST can be estimated from a method developed by Prabhakara et al. (1974) called the 'split window technique' which requires two radiance measurements in the 11 μm window region. Applying this method to the Nimbus 4 Infrared Interferometer Spectrometer (IRIS) data, seasonal mean maps of SST for three seasons (1. April, May and June; 2. July, August and September; and 3. October, November and December of 1970) have been derived. The cloud contamination in the data is eliminated by means of the following criterion: When the measured 11 μm brightness temperature exceeds 290°, 285° and 280° in the latitudinal zones 0° - 20°, 20° - 30° and 30° - 45° respectively the data are accepted as cloud free.

Over the oceans the precipitable water vapor w can be remotely sensed when a radiance measurement in the 18 μm water vapor band is available. The difference between the surface temperature and the brightness temperature T_{18} in the 18 μm band gives a measure of w. In Figure 1 the w estimated from Nimbus 4 IRIS data

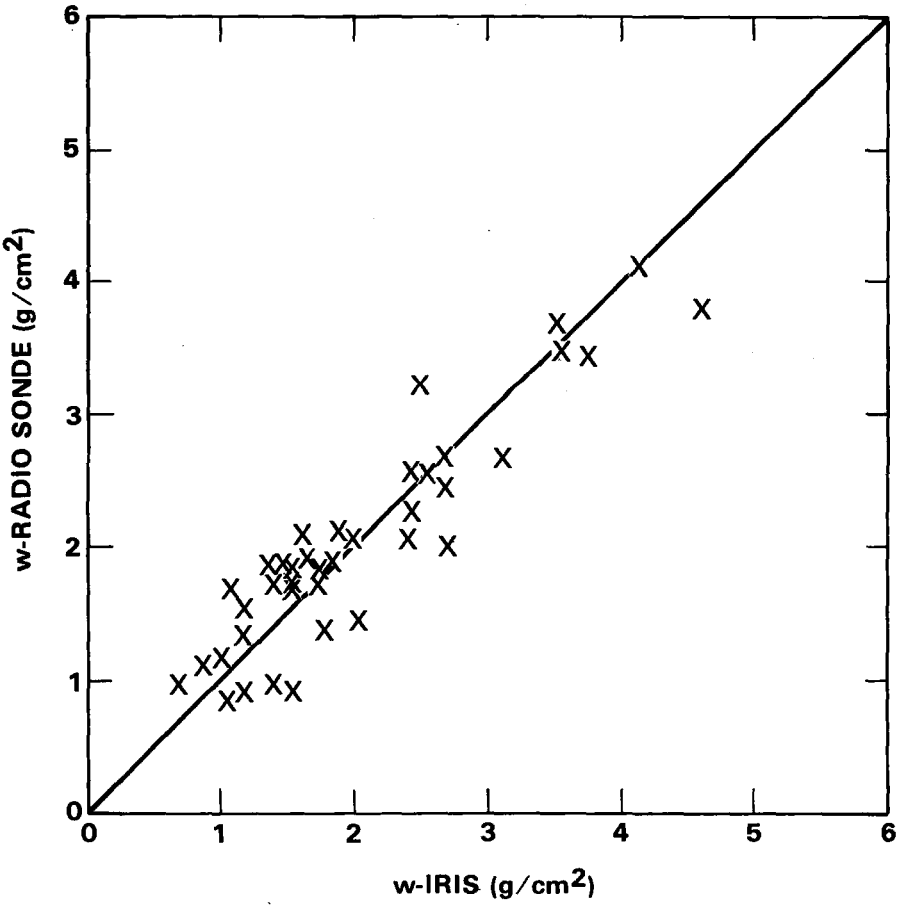

Fig. 1-Comparison between the water vapor content derived from the Nimbus 4 IRIS data and the water vapor content obtained from radiosonde data.

and the corresponding radiosonde measurements taken from 41 ship stations is compared. The standard error of estimation in w is about 0.4 g/cm^2. With the help of this method the w over the global oceans is estimated for the three seasons mentioned earlier. A map of the w over the oceans from about 45°N to 40°S for the period April, May and June 1970 derived in this fashion is shown in Figure 2.

The remotely sensed SST and w over the oceans can be used to infer the stratification of the atmosphere as shown in a study by Prabhakara et al., 1978. This is possible because on the average the vertical distribution of water vapor in the atmosphere above water bodies can be represented with a simple model. Then some average value of precipitable water $\overline{w}$ can be associated to a given surface temperature. The departure of the measured w from the corresponding $\overline{w}$ relates to the atmospheric stratification in the boundary layer. For instance w exceeds $\overline{w}$ when convective conditions, such as ITCZ, are present. When w is less than $\overline{w}$ stable conditions of inversions prevail.

The excess or deficit of w as mentioned above has been derived from IRIS data and a map of it is shown in Figure 3 for April, May and June 1970. The gross characteristics of the boundary layer over the oceans are seen in this map. The hatched areas showing excess of w correspond to ITCZ and the regions associated with the trade wind inversion on the north and south Atlantic and Pacific oceans as well as the Arabian sea are clearly seen.

REFERENCES

Mak, M. K., A Model Study of the Downstream Variation of the Lower Trade-Wind Circulation, Tellus, Vol. 28, n. 2, 97-107, 1976.

Malkus, J. S., On the Maintenance of the Trade Winds, Tellus, Vol. 8, n. 3, 335-350, 1956.

Namias, J., Multiple Causes of the North American Abnormal Winter 1976-77, Mon. Wea. Rev., Vol. 106, N. 3, 279-295, 1978.

Prabhakara, C., G. Dalu, and V. G. Kunde, Estimation of Sea Surface Temperature from Remote Sensing in the 11-13 μm Window Region, J. Geophys. Res., Vol. 79, 5039-5044, 1974.

Prabhakara, C., G. Dalu, R. Lo, and N. R. Nath, Inference of The Boundary Layer over the Oceans from Satellite Infrared Measurements, NASA Technical Memorandum 79653, pp. 55, 1978.

Reiter, E. R., The Interannual Variability of the Ocean-Atmosphere System, J. Atmos. Sci., Vol. 35, n. 3, 349-370, 1978.

Riehl, H., Tropical Meteorology, McGraw-Hill Book Co., Inc., New York, pp. 392, 1954.

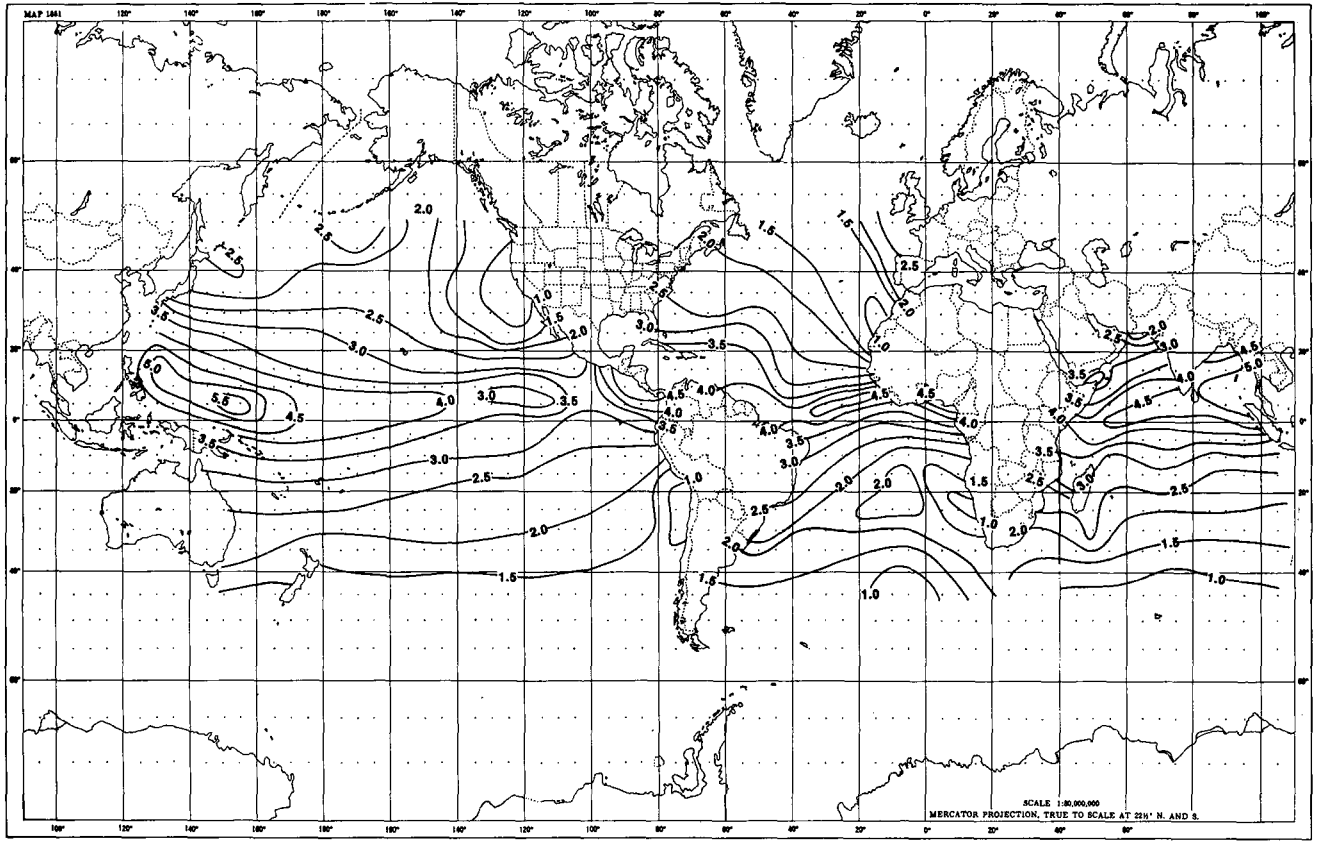

Fig. 2–Distribution of the total water vapor content (g/cm^2) over the global oceans (50°N to 40°S) derived from the Nimbus 4 IRIS data over the period April, May and June 1970.

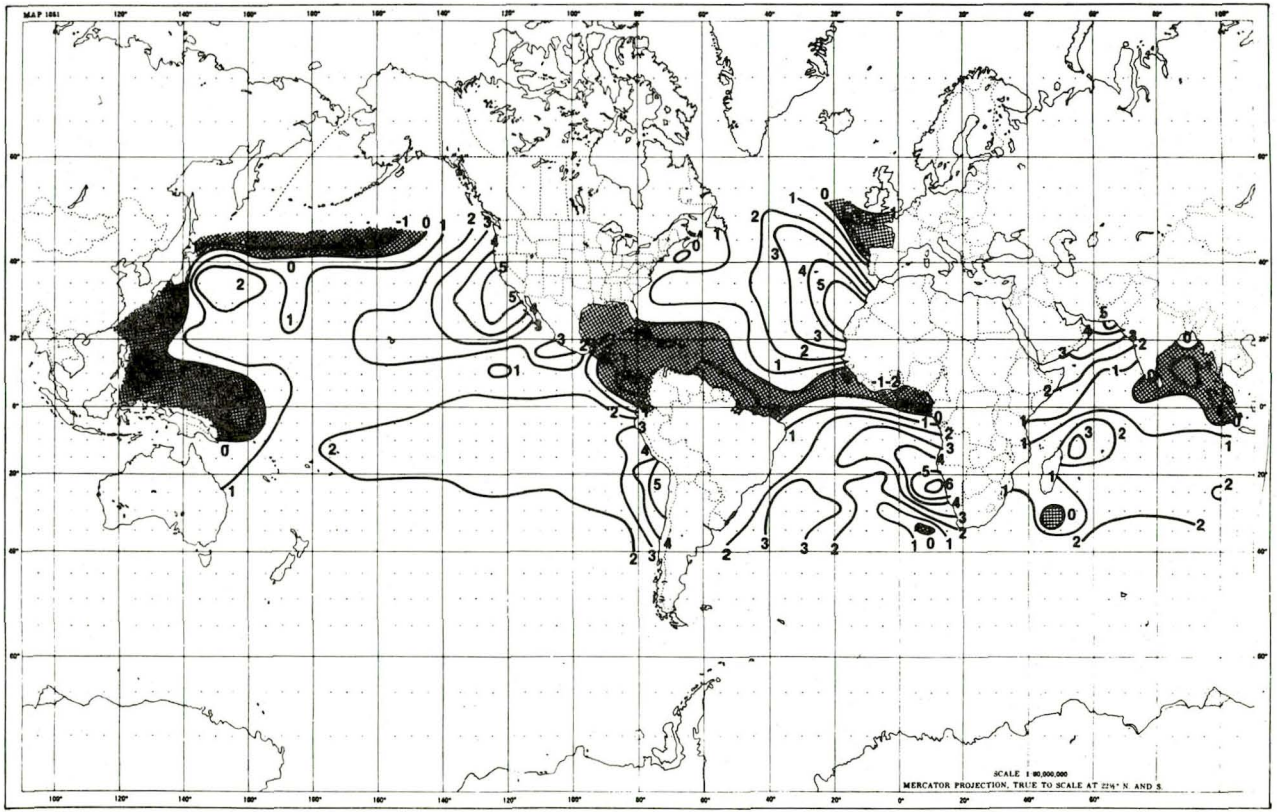

Fig. 3–Distribution of the index, $(\overline{w} - w)\overline{w} \times 10$, over the global oceans derived from the Nimbus 4 IRIS data for the period April, May and June 1970. Positive value of this index gives a measure of the temperature increase from bottom to top of trade wind inversion in °C. Negative values of the index are shown by shading.

Page intentionally left blank

Paper No. 55

SOME ASPECTS OF HYDROLOGY IN THE GLAS GCM

R. Godbole, *National Research Council, Washington, DC and Goddard Space Flight Center, Greenbelt, Maryland*

ABSTRACT

The response of hydrology in the GLAS GCM has been evaluated. The results show that the distribution of precipitation agrees fairly well with observations and that the model tends to maintain the hydrological balance.

INTRODUCTION

The performance of the GLAS GCM (Laboratory for Atmospheric Sciences General Circulation Model) in handling some of the hydrological parameters has been evaluated. Specifically, the distributions of precipitation and evaporation are examined in order to see how well they agree with each other and with observations, and in what manner, if any, they are associated with other related parameters such as cloudiness and vertical velocity. For the purpose of the present discussion, the results of one winter month, namely, February, are selected. With the initial state of the atmosphere as of January 1, 1975, the model has been run for the month of January and the run extended further through February.

Figure 1 shows the global distribution of precipitation as computed by the model. The observed distribution for winter (December-January-February) compiled by Schutz and Gates (1972) is represented in Figure 2. The precipitation associated with the ITCZ over the land and sea and also with Icelandic and Aleutian lows is very well reproduced. The model fails to produce the ITCZ rainfall over the Atlantic. Also, the computed precipitation appears to be overestimated, especially over the land mass. However, the monthly mean data for the period concerned from other independent sources do show a few individual land stations having high values of precipitation in the range of 14-16 mm/day.

Figure 3 shows the zonally-averaged distribution of two major types of precipitation, namely: a) the supersaturation precipitation and b) precipitation due to penetrative convection.

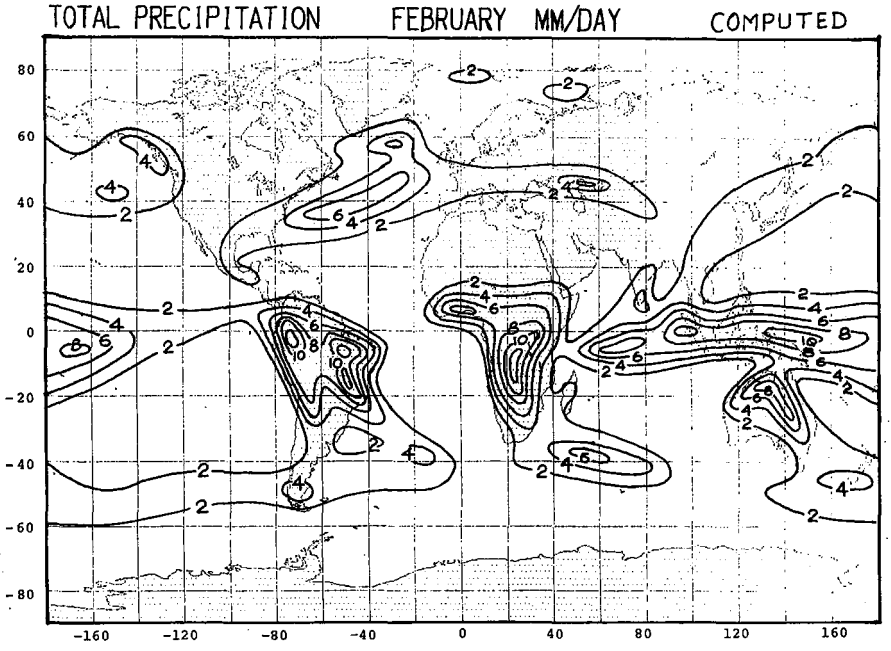

Fig. 1. Distribution of computed precipitation (mm/day) in February.

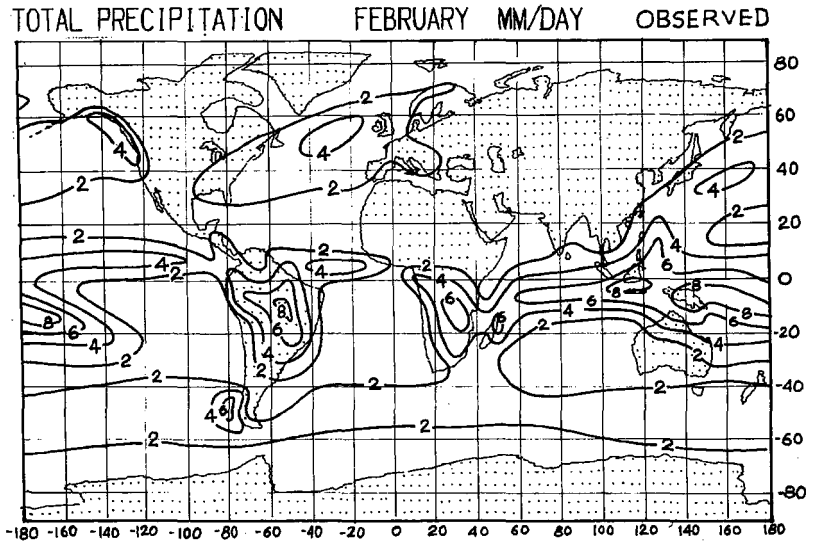

Fig. 2. Observed distribution of precipitation (mm/day) for winter (December-January-February).

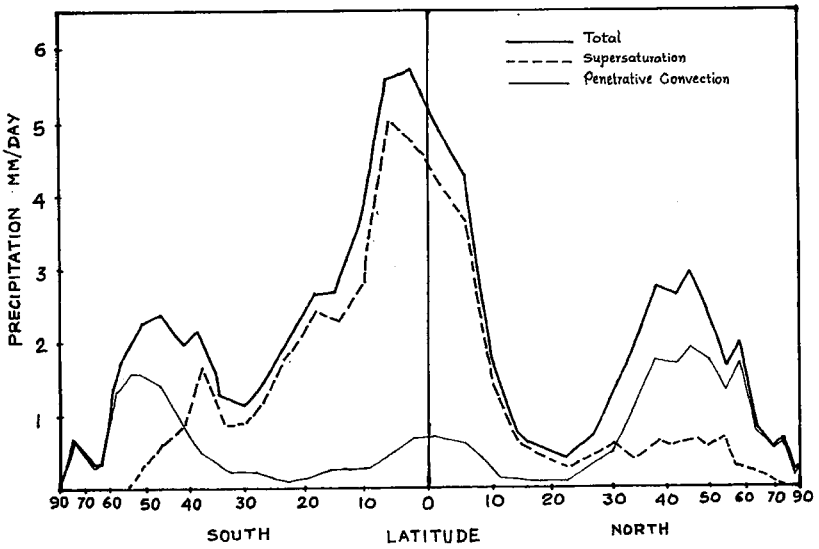

Fig. 3. Supersaturation precipitation (broken line) and penetrative convective precipitation (thin line) in relation to the total precipitation (thick line).

The zonally-averaged total precipitation is also shown in the figure. In the tropical belt where the atmosphere is convectively unstable, the penetrative convection dominates and accounts for most of the total precipitation. In the middle and high latitudes, the supersaturation processes overtake the convective processes. Supersaturation condensation arises largely due to the frontal systems which are more active in the winter hemisphere due to strong baroclinicity, a feature well reflected in the figure.

Figure 4 shows the distribution of various types of clouds generated by the model. Clouds are expressed as percentage of time they are present. It is interesting to observe that the frequency of the formation of the supersaturation clouds is very high at all the latitudes irrespective of the amount of its precipitation. On the contrary, the penetrative convective clouds form less frequently than the supersaturation clouds even in the tropical belt where its associated rainfall is maximum. This means that given the same amount of supersaturation and penetrative convective clouds, the actual realization of water from the former is less than that from the latter.

Figure 5 shows a relationship between precipitation, vertical velocity (p-coordinate) and cloudiness as a function of latitude. All the quantities are model generated. It is seen that between

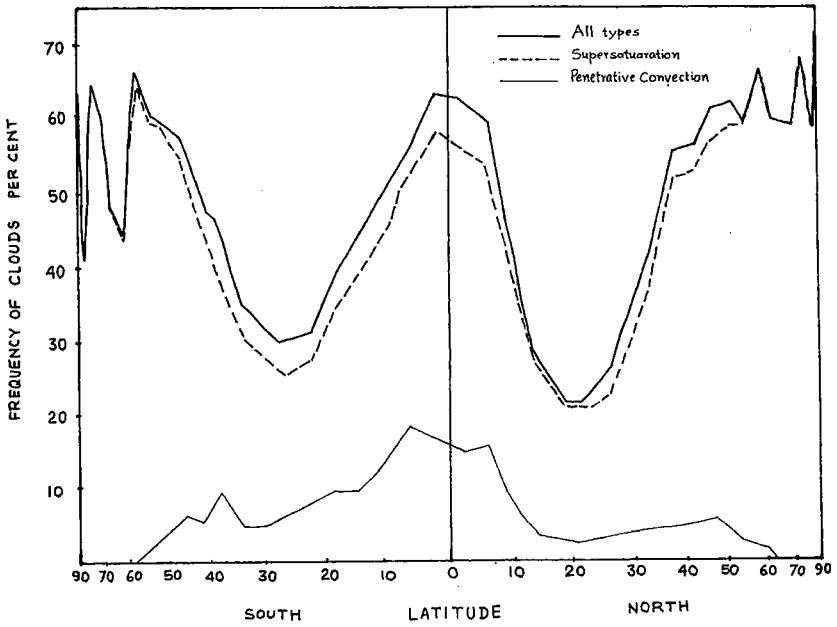

Fig. 4. Frequency of the formation of clouds; all types (thick line), supersaturation type (broken line) and penetrative convective type (thin line).

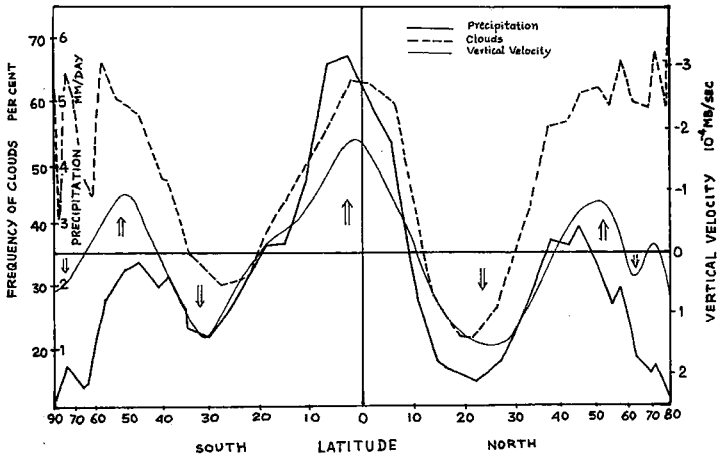

Fig. 5. Zonally-averaged distribution of precipitation, cloudiness and vertical velocity as computed by the model.

40N and 50S all three curves follow each other very closely, meaning thereby that the upward motion is associated with relatively more cloudiness and more precipitation and vice versa. Over the polar latitudes, this conventional relationship apparently does not hold good. Specifically, the relationship between cloudiness and precipitation is reversed, more cloudiness being associated with less precipitation. This is due to the fact that, over the polar latitudes, the almost saturation conditions would favor frequent formation of clouds, but the realization of moisture in the form of precipitation would be insignificantly small.

The computed surface evaporation is shown in Figure 6 along with the observed evaporation (for January) which is derived by Shutz and Gates (1971) indirectly on the basis of other hydrological data. The computed evaporation rate is largely underestimated except at the equator where it is comparable with observations. However, the point of some concern here is the failure of the model to reproduce the distribution pattern. The model shows peak in evaporation rate at the equator instead of a slight dip as observed. This aspect needs further examination which is under way.

Figure 7 shows the important result of the investigation, namely, the hydrological balance of the model. Five hourly values of precipitable water, evaporation, and precipitation were extract ed from the history tape and plotted as time series. The values represent the global mean. We find that the precipitation exceeds the evaporation and the difference between the two, which is very small, remains practically constant through the month of February. The global mean precipitable water of the atmosphere also remains constant with time. The model, therefore, tends to maintain the hydrological balance within a reasonable degree of accuracy.

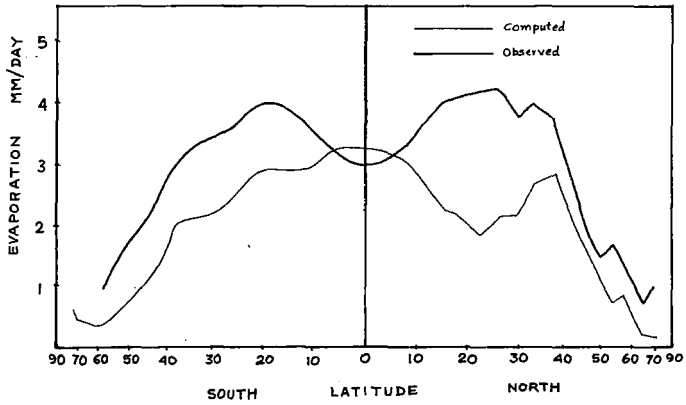

Fig. 6. Zonally-averaged surface evaporation (mm/day); computed (thin line), observed (thick line).

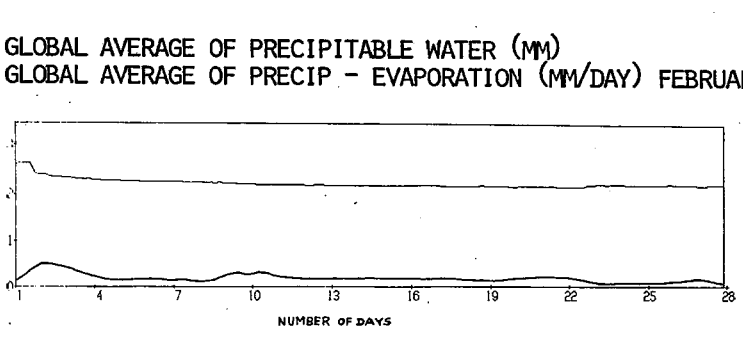

Fig. 7. Time series of global mean precipitable water (thin line) and precipitation minus evaporation (thick line).

REFERENCES

Schutz, C., and W. L. Gates, 1971: Global climate data for surface 800 mb, 400 mb: January. Report R-915-ARPA Rand., Santa Monica, Calif.

_____ and _____, 1972: Supplemental global climatic data: January. Report R-915/1-ARPA Rand., Santa Monica, Calif.

Paper No. 56

ANTARCTIC SEA ICE VARIATIONS 1973-75

H. J. Zwally, C. Parkinson, F. Carsey, P. Gloersen, *Laboratory for Atmospheric Sciences (GLAS), Goddard Space Flight Center, National Aeronautics and Space Administration, Greenbelt, MD 20771*
W. J. Campbell, *U.S. Geological Survey, Tacoma, WA 98416* 6
R. O. Ramseier, *Department of Environment, Ottawa, Canada K1A OH3*

ABSTRACT

Variations in the extent and concentration of sea ice cover on the Southern Ocean are described for the three-year period 1973-75 using information derived from the Nimbus-5 passive microwave imager (ESMR).

INTRODUCTION

Sea ice concentration (percent ice cover) is derived from the microwave brightness temperature and used to determine monthly averages of 1) total extent of ice-laden ocean (area having at least 15% ice cover) and 2) the area of ocean covered by highly concentrated ice (85-100% concentration). These areas of ice coverage are obtained for the entire Southern Ocean and for each of 5 sectors (Figure 1) into which the region has been divided.

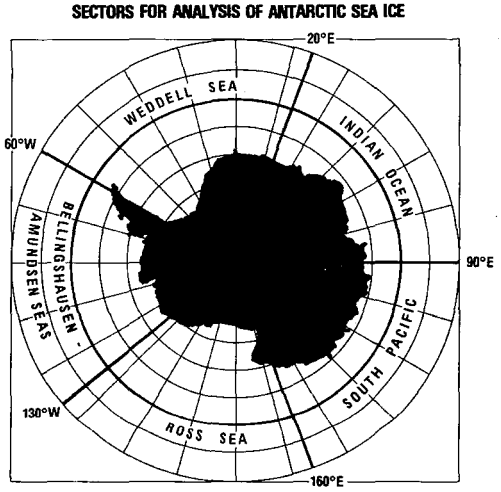

Figure 1

Most previous analyses of the seasonal and interannual variations of the sea ice cover have been limited to study of the position of the boundary between open ocean and the ice pack. Although the boundary is usually well-defined, such analysis does not consider changes in the actual area of ice versus open water within the ice pack. Because the heat exchange between the ocean and atmosphere is affected by the area of ice cover and its thickness, changes in the maximum extent of the ice pack alone might not be a significant indicator of changes in the climatic effects of the sea ice cover.

Ice concentration (C) is determined by taking the measured brightness temperature T_B to be a linear combination of the sea ice brightness temperature and open ocean brightness temperature (plus background) in proportion to the area covered by each as described by Zwally and Gloersen (1977):

$$C = \frac{T_B - 135K}{\epsilon_I T_O - 135K} \qquad (1)$$

where ϵ_I is the ice emissivity, T_O is the ice near-surface temperature, and 135K is the brightness temperature of sea water (120K at 1.55 cm wavelength plus 15K of atmospheric and cosmic background). The appropriate value of emissivity for first year sea ice at 1.55 cm wavelength is 0.92 (Zwally and Gloersen, 1977). This is also a good overall value for the Southern Ocean because only a small portion of the Antarctic sea ice exhibits a multiyear microwave signature. A significant improvement in the accuracy of the ice concentration results from estimating a T_O for each location for each month in contrast to using a constant T_O. The ice temperature is taken to be colder than the sea surface by 0.75 of the difference between the sea surface freezing point and the climatological air temperature (Taljaard et al., 1969) for air temperature below freezing. The value of 0.75 is supported by unpublished field measurements of the ice and air temperatures (Ramseier, private communication). The ice extent ($C \geq 15\%$) and the highly concentrated ice ($C \geq 85\%$) areas are obtained by summing the areas of resolution cells comprising the digital ice concentration maps created from T_B maps using Equation 1.

COMPLETE SOUTHERN OCEAN

The ocean area of the southern hemisphere affected by ice cover (15 - 100% concentration) decreases to a minimum of about 4×10^6 km^2 in February and increases

to a maximum of about 20 x 10^6 km^2 in September. Clearly the ice decay proceeds more rapidly than the February - September ice growth. Well over half the areal reduction of ice extent occurs within the 2 month period mid-November - mid-January.

The data show a mild trend toward less ice extent between 1973 and 1975, particularly during the growth season. However, they do not show a similar trend for the area of waters withhighly concentrated ice. In 1973 the maximum ice extent occurs in late September or early October, but is 2-4 weeks earlier in 1974 and 1975. Most of the interannual difference in total ice extent is due to the Weddell Sea sector where a major polynya formed in 1974 and 1975. There is a tendency for a decrease of ice in one sector to be compensated by an increase in another, as can be seen by comparing the Weddell and Ross Seas in 1973 and 1974.

The largest decrease in the area of highly concentrated ice occurs with a dramatic one month decrease of 6 x 10^6 km^2 from October - November of 1973 and with a slower two month decrease of slightly less total magnitude in October - December of 1974 and September - November of 1975. This decrease preceeds by about a month the largest decrease in total ice extent discussed above. This reduction of highly concentrated ice could be due to an increase in ice divergence or more likely to a decrease in new ice production in newly formed leads.

WEDDELL SEA SECTOR

Of the 5 sectors, the Weddell Sea contains the largest areal extent of sea ice. Roughly one-third of the Southern Ocean's sea ice area is within this region, and not surprisingly, its ice area also reaches a peak in September and descends to a minimum in February. In the Weddell Sea, however, the area of highly concentrated ice as well as the ice extent peaks consistently in September, and the magnitude of this peak is considerably greater in 1973 than in either of the other 2 years. The area of ice extent in the Weddell Sea is also greatest in 1973. A large area of open water surrounded by ice, a polynya, occurred in 1974 and 1975 but not in 1973. This highly significant feature accounted for nearly half the area difference in ice extent shown. Of the five sectors the Weddell Sea has the largest proportion, about half, of highly concentrated ice. This reflects the confining effect of the Antarctic Peninsula in reducing the ice divergence in comparison to more open seas.

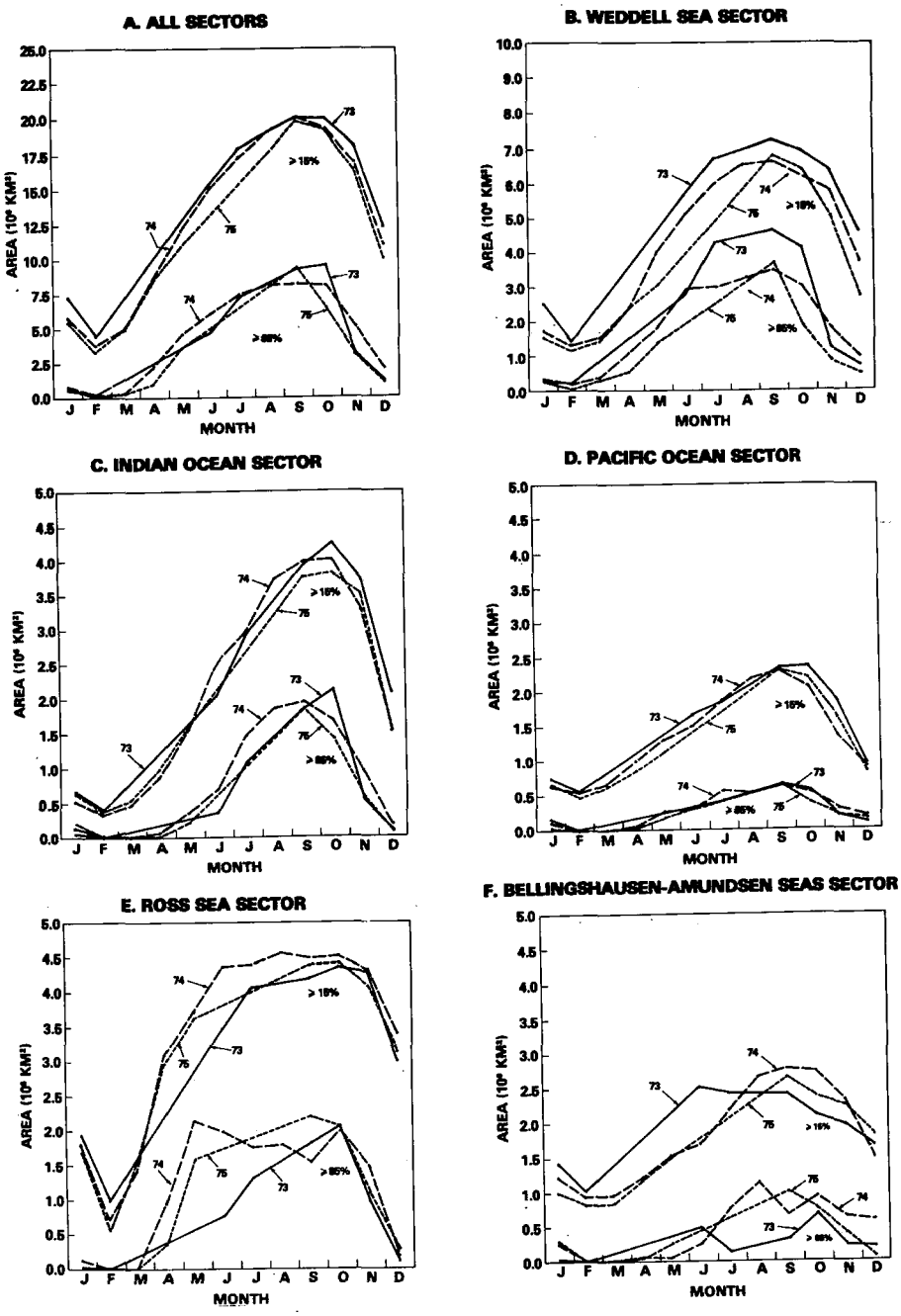

Fig. 2—Areal extent of ocean waters with sea ice concentration at least 15% and with sea ice concentration at least 85%

INDIAN OCEAN SECTOR

The month of peak ice extent in the Indian Ocean is October, not September as in the Weddell Sea, though the month of minimum extent is again February. The peak month for highly concentrated ice is also October for 1973 and 1974, though by October of 1975 the area of highly concentrated ice has decreased substantially from September. It is interesting that in this sector the winter of peak ice extent for the 3 years, in October 1973, is followed the next summer by the 3-year minimum, suggesting the difficulty of forecasting ice extent by persistence.

PACIFIC OCEAN SECTOR

With the Antarctic Continent extending equatorward to 67°S, the Pacific Ocean sector has the smallest sea ice extent of the 5 sectors. The ice extent peaked in September with a magnitude of about 2.3×10^6 km^2 in both 1974 and 1975. In 1973 the September areal extent was also 2.3×10^6 km^2, but in that earlier year the area increased very slightly during October. In all 3 years the area of highly concentrated ice peaked in September, and the minimum of both ice extent and highly concentrated ice occurred in February. The small interannual variations in the Indian Ocean and the Pacific Ocean reflect that the ice is principally influenced by temperature and is less affected by winds of the weaker synoptic systems in these regions.

ROSS SEA SECTOR

The data for the Ross Sea Sector reflect much variability among the 3 years. This is indicated particularly by the 3 contrasting curves for highly concentrated ice, which peak in October for 1973, in September for 1975, and much earlier, in May for 1974. The 1974 occurrence of a relative minimum of highly concentrated ice in September may be due to advection of ice as discussed in relation to the Bellingshausen-Amundsen Seas. The year 1974 also witnessed an unusually large expansion of the ice extent between February and June. A comparison between 1973 and 1974 shows that the summer with the lower minimum (1974) was followed by a rapid growth of ice area and a consequent higher maximum. As in the period October 1973 - February 1974 in the Indian Ocean Sector, this phenomenon is further evidence of the difficulty of forecasting by persistence.

BELLINGSHAUSEN - AMUNDSEN SEAS

As with the Ross Sea to the west, the Bellingshausen - Amundsen Seas show a highly variable cycle of sea ice over the 3 years. These facts could be interrelated. For example, the unusually high amount of ice in the Bellingshausen and Amundsen Seas in June of 1973 could reflect an unusually strong eastward transport of ice from the Ross Sea which had lesser ice at that time. Non-occurrence of such transport in the 2 succeeding years could account for the greater late-fall Ross Sea ice extents in those years.

CONCLUDING REMARKS

With data assembled for only a 3 year time period, it is only possible to point out some interesting suggestive evidence. Many more years of data are required before firm conclusions can be drawn on the nature of interannual variability of Antarctic sea ice. Some interannual variation is shown in the phase and amplitude of maximum and minimum in the curves for all sectors, but the curves for the individual sectors were much more variable. This suggests a large scale interaction among the regions. Also, the different sectors show varying proportions of highly concentrated ice, indicating regionally different meteorological and oceanographic processes.

REFERENCES

Zwally, H. J. and P. Gloersen, 1977: Passive Microwave Images of the Polar Regions and Research Applications. Polar Record 18, 431-450.

Taljaard, J. J., H. van Loon, H. L. Crutcher and R. L. Jenne, 1969: Climate of the Upper Air Part 1 - Southern Hemisphere, Vol. 1, Temperatures, Dew Points, and Heights at Selected Pressure Levels. A joint publication of National Center for Atmospheric Research, National Weather Records Center, and Department of Defense, 135 pp.

Paper No. 57

VARIATIONS OF THE EARTH'S MAGNETIC FIELD AND RAPID CLIMATIC COOLING: A POSSIBLE LINK THROUGH CHANGES IN GLOBAL ICE VOLUME

Michael R. Rampino, *Goddard Institute for Space Studies, New York, New York 10025*

ABSTRACT

A possible relationship between large-scale changes in global ice volume, variations in the earth's magnetic field, and short-term climatic cooling is investigated through a study of the geomagnetic and climatic records of the past 300,000 years. The calculations suggest that redistribution of the earth's water mass can cause rotational instabilities which lead to geomagnetic excursions; these magnetic variations in turn may lead to short-term coolings through upper-atmosphere effects. Such double coincidences of magnetic excursions and sudden coolings at times of ice-volume changes have occurred at 13,500, 30,000, 110,000, and 135,000 YBP.

Introduction. A relationship between variations in the earth's magnetic field and changes in climate has been suggested by many authors (e.g., Harrison and Prospero, 1974; Wollin et al., 1971). The low field strengths at the times of magnetic reversals or excursions should lead to an increase in the cosmic-ray flux in the upper atmosphere. It has been proposed that this might cause increased upper-atmosphere ionization and cloud formation or perhaps a catastrophic depletion of the ozone layer. These are conditions that could ultimately result in increased high altitude cloudiness and increased precipitation and cooling in the mid-latitudes (Harrison and Prospero, 1974; Reid et al., 1976).

It has also been suggested that long-term climatic changes which cause major fluctuations in global ice volume, and hence in the redistribution of water mass on the earth's surface, could lead to rotational instabilities and therefore result in changes in the magnetic field through core-mantle effects (Doake, 1977; Mörner, 1977). A glacio-eustatic sea level change of about 100 meters would cause a change in rotational energy of 1.9×10^{24} J. In this case, the fractional change in angular velocity, length of day and moment of inertia would be 10^{-5} (Doake, 1977). In the model of Doake, the changes in core energy involved are of the same order of magnitude (a rate of energy dissipation of 10^{12} W) as the energy required to drive the geodynamo. Doake (1978) has noted a statistical correlation between magnetic reversals and climatic change.

There is thus an indication in the geologic record of a correlation between long-term, large-scale changes in ice volume (and therefore sea level) and excursions of the earth's magnetic field. The magnetic excursions, which occupy a relatively short time span, may produce rapid climatic coolings. It is therefore worthwhile to search for a further co-

incidence; magnetic excursions which occur during a time of large-scale melting or growth of ice sheets may be accompanied by a significant cooling and short-term growth of ice sheets (Fig. 1).

Study of climatic and geomagnetic records. A first step in this problem is to examine the climatic and geomagnetic records of the past several hundred thousand years in search of evidence for such double coincidences of major ice/water redistributions, magnetic excursions, and rapid coolings. One such double coincidence at the time of the Gothenburg Magnetic Excursion ∿13,500 YBP, has been documented by Fairbridge (1977). This event came at about the midpoint of the melting of the latest Pleistocene northern hemisphere ice sheets. Furthermore, the magnetic excursion appears to correlate with a time of short-term rapid climate cooling and ice buildup. Sea level dropped more than 10 meters between 13,000 and 14,000 YBP and glaciers on North America readvanced over an area of some 500,000 square kilometers.

Several other magnetic excursions are reported to have occurred during the past 300,000 years. The two excursions considered to rest on the best supporting evidence are the Lake Mungo Excursion at∿30,000 YBP and the Blake Event at ∿110,000 YBP (Verosub and Banerjee, 1978). Furthermore, study of a core from Lake Biwa, Japan has indicated the presence of the Blake Event (dated at ∿110,000YBP) as well as two other magnetic excursions, estimated to date from ∿185,000 YBP (the Biwa I Event) and ∿295,000 YBP (the Biwa II Event) (Fig. 2). These excursions are coincident with pronounced lows in organic carbon in the Lake Biwa sediments (Fig. 3). The decrease in organic carbon is believed to be related to climatically controlled changes in the productivity of the lake (Kawai et al., 1975).

The Blake Event has previously been correlated with a time of quite sudden climatic cooling and ice buildup, following the large-scale melting of the ice sheets which marked a change from full-glacial to full-interglacial conditions (Mörner, 1977). A cooling at about 110,000 YBP might be expected from considerations of earth orbital variations (the Milankovitch mechanism) (Kukla, 1975). However, the actual cooling and glacier buildup was extremely rapid. Studies of changes in sea level (Matthews, 1972) and of changes in the oxygen-isotope ratios in deep-sea cores (Shackleton, 1976) indicate that sea level fell rapidly, 60-70 meters in a few thousand years. These rapid rates of change in global climate and ice volume might be explained as being a result of the alterations of atmospheric circulation and precipitation that have been suggested to accompany magnetic-field fluctuations (Fairbridge, 1977).

The Lake Mungo Excursion at ∿ 30,000 YBP was also associated with a time of apparent rapid cooling and glacier advance. This cooling came soon after the global warming and large-scale melting of ice associated with an interstadial interval. Evidence from Long Island, New York in the form of radiocarbon-dated marine deposits points to the possibility that the sea at ∿30,000 YBP rose to within 20 meters of modern sea level (MSL) and then dropped to more than -100 meters MSL by about 20,000 YBP (Rampino and Sanders, 1976). Pollen analyses from the same deposits indicate a very rapid cooling just after 28,000 YBP. Temperate-forest vegetation on Long Island was replaced by boreal type forests within a few hundred years. Ice sheets readvanced to the Long Island area by 23,000 YBP (Sirkin, 1977).

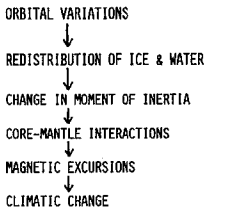

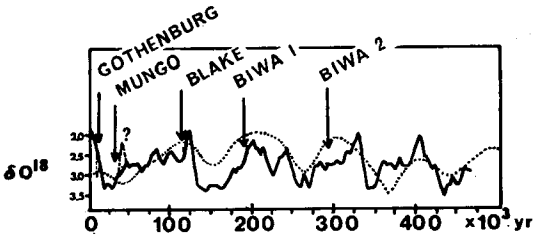

Fig. 1 (left). Diagram of possible relationships between the redistribution of global water mass, magnetic excursions, and short-term climatic cooling.

Fig. 2 (right). Record of global ice volume for the last 400,000 years as inferred from oxygen-isotope records in sub-Antarctic deep-sea cores (Hays et al., 1976). Low values of δO^{18} indicate small ice volumes; high δO^{18} values indicate large ice volumes. The dotted line is a plot of the eccentricity of the earth's orbit. The times of five reasonably well-established magnetic excursions are shown by arrows.

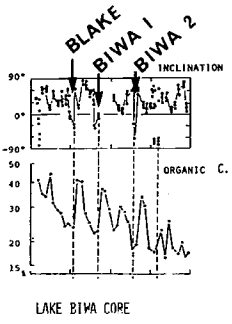

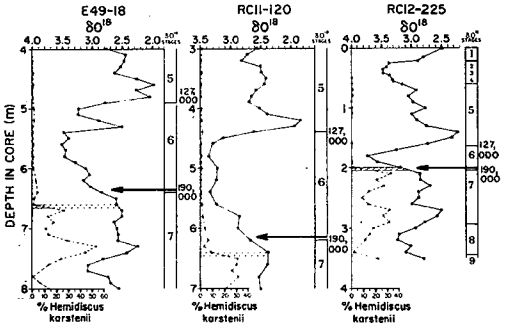

Fig. 3 (left). Magnetic inclination and percent organic carbon in the Lake Biwa sediment core. The positions of the Blake, Biwa I and Biwa II magnetic events are shown by arrows (Kawai et al., 1975).

Fig. 4 (right). Oxygen-isotope record (solid line) and percent abundance of the diatom Hemisdiscus karstenii in sections of sub-Antarctic deep-sea cores. The last appearance of H. karstenii is shown by the diagonal hatched areas (Burckle et al., 1978). The date of the Biwa I magnetic event, as inferred from the Lake Biwa core, is shown by arrows.

The sequence of events at ∿30,000 YBP could be an example of a climatic warming induced by changes in seasonal insolation (the Milankovitch mechanism) which was cut short by magnetically induced cooling. The original warming and melting of ice sheets led to changes in the earth's rotation and therefore to magnetic instabilities; the magnetic influences on climate in turn caused a pronounced short-term cooling.

The magnetic excursion estimated to have occurred at ∿185,000 YBP (the Biwa I Event) also appears to be correlated with a time of rapid growth of ice as indicated by oxygen-isotope records in deep-sea cores (Fig. 2). It is estimated that at about 190,000 YBP summer sea-surface temperatures in the sub-Antartic declined approximately 2° C (from 9° C to 7° C). This time also marked the last appearance of the diatom Hemidiscus karstenii in sub-Antarctic deep-sea cores (Burckle et al., 1978) (Fig. 4). This probable extinction might be related to the environmental stress generated by the climatic cooling, magnetic excursion, or some combination of the two.

The Biwa II Event at ∿295,000 YBP was apparently not accompanied by rapid changes in ice-volume as indicated by oxygen-isotope curves (Fig. 2), although the Lake Biwa Core shows a marked decrease in productivity, intepreted as a cooling of the climate at that time (Fig. 3). However, a very short period of rapid ice-sheet growth might be beyond the resolving power of the isotope record in most deep-sea cores.

Discussion. An association of events such as changes in global ice volume, magnetic excursions and short-term rapid cooling and glaciation of course does not prove that any cause and effect relationship exists. Several magnetic excursions that have been reported in the literature (including the Biwa II event mentioned here) are apparently not associated with times of ice-volume changes or rapid cooling as recorded in oxygen-isotope curves (for a review of reported excursions see Verosub and Banerjee, 1977). This argues against a one-to-one cause and effect relationship. However, some of these reported excursions are very likely spurious or poorly dated (Verosub and Banerjee, 1977). Furthermore, the climatic record in many deep-sea cores may have poor resolution of events shorter than a few thousand years, as a result of slow deposition, bioturbation and/or dissolution of calcium carbonate.

A more definitive answer to the question of possible relationships between magnetic excursions and climate change will depend upon further study of the response of the core and mantle to changes in the earth's rotation, and upon a better understanding of the possible effects that geomagnetic variations might have on climate through upper-atmospheric mechanisms. Further empirical tests of the validity of the relationship between magnetic excursions and short-term climate cooling can be obtained from analyses of sedimentary sequences with high rates of deposition, and from closely spaced paleomagnetic determinations in suitable materials.

Acknowledgements. The author is grateful to Dr. Rhodes Fairbridge for helpful discussions. This work was carried out while the author was a NAS-NRC Research Associate at the Goddard Institute for Space Studies.

REFERENCES

Burckle, L.H., Clarke, D.B., and Shackleton, N.J., "Isochronous last-abundant-appearance datum (LAAD) of the diatom Hemidiscus karstenii in the sub-Antarctic," Geology, 6, p. 243-246, 1978.

Doake, C.S.M., "A possible effect of ice ages on the earth's magnetic field," Nature, 267, 415-416, 1977.

_____, "Climatic change and geomagnetic field reversals: A statistical correlation" Earth and Planet. Sci. Letters, 38, 313-318, 1978.

Fairbridge, R.W., "Global climate change during the 13,500-b.p. Gothenburg geomagnetic excursion", Nature, 265, 430-431, 1977.

Harrison, C.G.A. and J.M. Prospero, "Reversals of the earth's magnetic field and climate changes," Nature, 250, 563-565, 1974.

Hays, J.D., Imbrie, J., and N.J. Shackleton, "Variations in the earth's orbit: Pacemaker of the ice ages," Science, 194, 1121-1132, 1976.

Kawai, N., Yasakawa, K., Nakajima, T., Torii, M., and N. Natsuhara, "Voice of geomagnetism from Lake Biwa," Paleolimnology of Lake Biwa and the Japanese Pleistocene, 3, 143-160, 1975.

Kukla, G.J., "Missing link between Milankovitch and climate," Nature, 253, 600-603, 1975.

Matthews, R.K., "Dynamics of the ocean-cryosphere system: Barbados data," Quaternary Research, 2, 368-373, 1972.

Mörner, N.A., "Eustasy and instability of the geoid configuration," Geologiska Fören. i. Stockholm Förhandl., 99, 369-376, 1977.

Rampino, M.R., and J.E. Sanders, "New stratigraphic evidence for major mid-Wisconsinan climatic oscillation and sea-level rise: "Interstadial" or "Interglacial"?", Geol. Soc. of America Abstracts with Programs, 8, 1059-1060 (abstract), 1976.

Reid, G.C., Isaksen, I.S.A., Holzer, T.E., and P.J. Crutzen, "Influence of ancient solar-proton events on the evolution of life," Nature, 259, 177-179, 1976.

Shackleton, N.J., "Oxygen isotope evidence relating to the end of the last interglacial at the substage 5e to 5d transition about 115,000 years ago," Geol. Soc. of America Abstracts with Programs, 8, 1099-1100 (abstract), 1976.

Sirkin, L.A., "Late Pleistocene vegetation and environments in the middle Atlantic region," N.Y. Acad. Sci. Annals, 288, 206-217, 1977.

Verosub, K.L. and S.K. Banerjee, "Geomagnetic excursions and their paleomagnetic record," Rev. of Geophys. and Space. Phys., 15, 145-155., 1977.

Wollin, G., Ericson, D.B., Ryan, W.B.F., and J.H. Foster, "Magnetism of the earth and climatic changes," Earth and Planet Sci. Letters, 12, 175-183, 1971.

Page intentionally left blank

Paper No. 58

STOCHASTIC MODELING OF THE TIME-AVERAGED EQUATIONS FOR CLIMATE DYNAMICS OR

J. A. Laurmann, *Div. of Appl. Mech., Stanford Univ.,*

Long Term Objectives

The grant study deals overall with long term, climatologically significant statistical properties of the atmospheric component of the climate system. Understanding should lead to an ability to correctly and efficiently incorporate this component into larger models for climate that include oceanic and cryospheric influences and deal realistically with climate replication. An immediately usefully and critically important consequence of successful completion of the study would be the ability to assess the magnitude of the unpredictable (noise) component of long term atmospheric behavior, and hence the potential for viable climatological forecasting.

Immediate Program Content And Objectives

The Stanford program in climate is new and in process of development. Both because of the relative novelty of our approach to the problem and because our students have minimal backgrounds in meteorology and atmospheric sciences, we have elected to start at a simple but fundamental level of analysis. Thus, the initial effort is concentrating on the use of Lorenz's "*minimum hydrodynamic equations*" as a *prototype for* describing at least some of the non-linear characteristics of long term atmospheric behavior that we believe are important for climate. We have two main thoughts in mind:

a) that techniques for closure of the moment equations *that arise from treating time averaged* climatic variables can be tested with the minimum equations. These do indeed exhibit the counter-gradient momentum transfer and vacilla-

tory behaviors that are known as essential features on the non-linear behavior of the atmosphere;

and b) in view of the fact that temporal response characteristics need to be known for developing atmospheric climate models, it is hoped that study of such properties of the minimum equations (hopefully with only minor modifications) will lead to a rationale for simplified atmospheric climate models via a subdivision into more easily treated sub-components. For example, we might consider long term, large scale changes to be describable in terms of a barotropic model that is driven baroclinically, perhaps by stochastic forcing via quasi-geostrophic turbulence, as well as by deterministic terms. The minimum equations would represent the simplest possible description for the barotropic component of such a model.

Accomplishments

We are advocating the introduction of time averaging for the treatment of climate questions. The approximations that then become possible (and, we suggest, necessary for practical viability of answering climate problems) will vary with the averaging time selected, which in term will vary with the particular climate question being addressed. In every case, however, the averaging process, when applied to the (non-linear) differential equations governing atmospheric motions, introduces new, statistically defined variables (moments and correlations) which are formally governed by an infinite set of equations. For large scale motions conventional turbulence theory approaches for closing these equations do not apply, and for the climatological case we must resort to other techniques, the nature of which we expect to discover only from better understanding of the atmospheric circulation system itself. The simplest model that incorporates the important counter-gradient transport of momentum, necessary for the maintenance of the atmospheric energy cycle, is represented in Lorenz's introduction of the "minimum hydrodynamic" system of equations. These represent the first three Fourier modes of a standing wave system for a rectangular domain, with β effect neglected, and their solution (available analytically) describes the temporal non-linear oscillations of the standing waves. The equations governing the time-

variation of the amplitudes of the three wave components, A_1, A_2, A_3, are

$$\frac{dA_1}{dt} = C_1 A_1 A_2 \; ; \; \frac{dA_2}{dt} = C_2 A_1 A_3 \; ; \; \frac{dA_3}{dt} = C_3 A_2 A_1 \; ; \qquad (1)$$

where $C_1 = -[\alpha(\alpha^3 + 1)]^{-1}$; $C_2 = \alpha^2(\alpha^2 + 1)^{-1}$, $C_3 = -(\alpha^2 - 1)/2\alpha$, and $\alpha = k/\ell$, the ratio of zonal to meridional wave number. Jacobian elliptic functions constitute the analytic solution to (1):

$$\begin{aligned} A_1 &= A_1^* \; dn(\overline{ht - t^*}, h_o^2) \\ A_2 &= A_2^* \; sn(\overline{ht - t^*}, h_o^2) \\ A_3 &= A_3^* \; cn(\overline{ht - t^*}, h_o^2) \end{aligned} \qquad (2)$$

for $\alpha > 1$ and $2k^2E/V < 1$, where E and V are the enstrophy and energy of the system. The parameters A_1^* , A_2^* , A_3^* , t^*, h and k_o are defined in terms of E and V and a phase angle.

The description and analysis can be simplified by a scaling transformation:

$$\begin{aligned} &X_1 = A_1/A_1^* \; , \; X_2 = A_2/A_2^* \; , \; X_3 = A_3/A_3^* \; , \\ &t' = ht = A_1^* \frac{\alpha}{2}\left(\frac{\alpha^2 - 1}{\alpha^2 + 1}\right)^{\frac{1}{2}} t \; . \end{aligned} \qquad (3)$$

to give

$$\begin{aligned} \dot{X}_1 &= -k_o^2 X_2 X_3 & X_1 &= dn(t' - t'^*, k_o^2) \\ \dot{X}_2 &= X_3 X_1 & X_2 &= sn(t' - t'^*, k_o^2) \\ \dot{X}_3 &= -X_1 X_2 & X_3 &= cn(t' - t'^*, k_o^2) \end{aligned} \qquad (4)$$

Provided we modify the conventional definition for the moment of a time-averaged variable from

$$M_{ij\cdots\ell}(t) = \frac{1}{T} \int_{t-T}^{T} [X_i(t') - \mu_i(t')]$$
$$[X_j(t') - \mu_i(t')]\cdots[X_\ell(t') - \mu_\ell(t')]dt'$$

to

$$M_{ij\cdots\ell}(t) = \frac{1}{T} \int_{t-T}^{t} [X_i(t') - \mu_i(t)]\,[X_j(t') - \mu_j(t)]\ldots[X_\ell(t') - \mu_\ell(t)]dt' \qquad (5)$$

moment equations for the time averaging interval T can be readily derived. It is this (infinite) system of equations that we need to solve for the climate case, and since the solutions (4) can be used to calculate the moments (5) exactly for the minimum equations, we are in position to evaluate the accuracy of any proposed closure scheme, at least as far as the properties of the minimum equations are concerned. Exact moments, for arbitrary values of averaging time T can in fact be derived in analytic, though rather cumbersome form, and this has been done up to the third order moments τ_{ijk}.

A possible approach for achieving approximate closure that has worked well in the case of stochastic dynamics weather forecasting, is linearisation of the moment equations. In our case, the linearisation would be made about an assumed known climatic state, which, for problems of the first kind would be based on observed records over the period $0 > t > -T$, and, for prediction of the second kind, would correspond to climatological mean estimates of statistically stationary states. Note that in the second case we need to treat ensemble as well as temporal means, as situation which leads to complications in the development of the moment equations which we are starting to look into. Tests on the efficacy of this concept of a linearised approximation are now being carried out by numerical solution of truncated forms of the (linearised) moment equations.

However, for the minimum equations we have discovered an unexpected property that indeed seems to obviate the need for devises such as linearisation for closing the moment equations. It turns out that for small values of the parameter

$$k_o^2 = \frac{1}{\alpha^4} \frac{A_2^{*2}}{A_1^{*2}} \qquad (6)$$

moments of the solutions (2) for the minimum equations tend to decrease with increasing order of the moment. In fact power series of the form

$$\dot{\mu}_i = \sum_{n=0}^{\infty} k_o^{2n} \mu_i^{(n)} \qquad [\mu_1^{(0)} = 1]$$

$$\dot{\sigma}_{ij} = k_o^{2(\delta_{1i} + \delta_{1j})} \sum_{n=0}^{\infty} k_o^{2n} \sigma_{ij}^{(n)} \tag{7}$$

$$\dot{\tau}_{ijk} = k_o^{2(\delta_{1i} + \delta_{ij} + \delta_{ik})} \sum_{n=0}^{\infty} k_o^{2n} \tau_{ijk}^{(n)}$$

when $\delta_{ab} = 0$ $a \neq b$, $\delta_{ab} = 1$, $a = b$, yield series of of differential equations for the moments which are automatically closed. For example, the lowest order equations in k_o^2 turn out to be

$$\dot{\mu}_1 = 0$$

$$\dot{\mu}_2 = \mu_3$$

$$\dot{\mu}_3 = -\mu_2$$

$$\dot{\sigma}_{22} = 2\sigma_{32}$$

$$\dot{\sigma}_{33} = -2\sigma_{32}$$

$$\dot{\sigma}_{32} = \sigma_{33} - \sigma_{22}$$

which can readily be shown to have solutions identically equal to those obtained from the exact solution (4), when the exact moments are expanded for $k_o^2 \ll 1$. Small values of k_o in fact correspond to mild vacillations of the zonal flow and, as discussed by Lorenz, represent the predominant mode of atmospheric vacillation phenomena. For k_o^2 close to 1 (which is the upper bound for k_o^2) , corresponding to large oscillations in the east-west wind, this approach does not appear to be

applicable.

The fact that closure of the time-averaged moment equations for the minimum equations is possible for physically reasonable values of parameters immediately brings to the fore the question of the applicability of moment equation closure procedures such as (7) to more realistic equations for atmospheric motions. It is our intent to enter at depth into this question, both by judging which properties of the minimum equations can be expected to hold more generally and by modifying the minimum equations to allow for clearly omitted features (such as β , or adding secular and stochastic forcing terms).

One of the important results looked for in the statistical approach we are trying to develop is the determination of the principal time-scaled components into which the atmospheric system can be subdivided. These separate, but coupled components are distinguished by their disparate time scales, and their content would surely vary with climatic average of concern; the aim is to obtain the simplest possible mode of description of the atmospheric portion of the climate system. Whether, or under what circumstances such a form of representation is possible is still at issue. Our investigations currently seek to evaluate the 'response time' for the minimum equations, so as to better understand how both long term forcing (e.g. seasonal variation) and rapid fluctuations (e.g. from two-dimensional turbulence) should be coupled to the equations. We are in process of determining how best to proceed with this problem, and we envisage that the coupling has at least in part to be stochastic, leading to variability in climate evolution as prescribed by the equations of currently unknown magnitude.

Bibliography

J. A. Laurmann. A small perturbation approximation for stochastic dynamic weather prediction. To appear in Tellus.

E. N. Lorenz. Maximum simplification of the dynamic equations. Tellus 12 243 1960

J. Paegle and E. Robl. The time dependent behavior of the probability density function of some simplified atmospheric flows. J. Atm. Sci. 34 979 1977

G. D. Robinson. Weather and climate forecasting as

problems in hydrodynamics. Month. Wea. Rev. 106 448 1978. Also comments on this paper by J. A. Laurmann, to appear in the Monthly Weather Review.

G. P. Williams. Planetary circulations: 1. Barotropic representation of Jovian and terrestrial turbulence. J. Atm. Sci. 35 1399 1978

Page intentionally left blank

Paper No. 59

A SLAB MODEL FOR COMPUTING GROUND TEMPERATURE IN CLIMATE MODELS

Sergej Lebedeff, Gary Crane and Gary Russell, *Goddard Institute for Space Studies, New York, NY 10025*

ABSTRACT

A method is developed for computing the ground temperature accurately over both the diurnal and annual cycles. The ground is divided vertically into only two or three slabs, resulting in very efficient computation. Seasonal storage and release of heat is incorporated, and thus the method is well suited for use in climate models.

Introduction. The ground temperature should be computed accurately over both the diurnal cycle and annual cycle in a climate model. The diurnal and seasonal cycles are important because of the highly nonlinear way in which latent and sensible heat fluxes from the surface depend upon temperature. Seasonal storage and release of heat is also important because it can amount to several watts per square meter and can significantly influence the ground temperature (Taylor, 1976).

The basic problem is to solve the one-dimensional heat conduction equation

$$\frac{\partial T}{\partial t} = \frac{\lambda}{c_g} \frac{\partial^2 T}{\partial z^2} = K_g \frac{\partial^2 T}{\partial z^2} , \qquad (1)$$

where c_g is the heat capacity of the ground per unit volume, λ is the thermal conductivity and K_g is the thermal diffusivity, subject to numerically specified heat flux at the upper boundary:

$$F(0) = F_{sw} - F_{lw} - F_h - F_q . \qquad (2)$$

F_{sw} is the absorbed solar radiation, F_{lw} the net thermal radiation, and F_h and F_q are the sensible and latent heat fluxes from the ground to the atmosphere.

A straightforward finite difference approach with computation of temperatures at several subsurface depths can yield accurate results. However, that method has the disadvantage of requiring (1) computation and storage of temperatures at several depths, and (2) a short time step, of the order of a few minutes or less.

Slab model. An approach requiring less resources, is to divide the ground into a small number of slabs and solve for the mean temperature of each slab. In this method we use the average temperature of the upper slab to simulate the surface temperature. That layer must be suf-

ficiently thin that its diurnal temperature response is representative of that for the upper skin of the ground; on the other hand, it should be thick enough to allow long time steps. The minimum number of ground layers that are needed for a climate model is two, since a deep lower layer is needed for seasonal heat storage.

The equations for our slab model are derived under the assumption that the heat capacity and conductivity are uniform in each slab, and with the temperature profile within each slab approximated as a quadratic function of depth:

$$T_i(z) = \alpha_i z^2 + \beta_i z + \gamma_i. \tag{3}$$

For two layers we obtain the six parameters from the six equations:

$$\lambda_1 \frac{\partial T_1}{\partial z}\bigg|_0 = F(0), \quad \frac{1}{z_1}\int_{-z_1}^{0} T_1 dz = \bar{T}_1, \quad T_1(-z_1) = T_2(-z_1)$$

$$\lambda_1 \frac{\partial T_1}{\partial z}\bigg|_{-z_1} = \lambda_2 \frac{\partial T_2}{\partial z}\bigg|_{-z_1}, \quad \frac{1}{z_2}\int_{-z_1-z_2}^{-z_1} T_2 dz = \bar{T}_2, \quad \lambda_2 \frac{\partial T_2}{\partial z}\bigg|_{-z_1-z_2} = 0. \tag{4}$$

Thus we require that no heat cross the $z = -z_1-z_2$ interface. The heat crossing the $z = -z_1$ interface is:

$$F(-z_1) = \frac{3\bar{T}_1 - 3\bar{T}_2 - \frac{1}{2}F(0)z_1/\lambda_1}{z_1/\lambda_1 + z_2/\lambda_2}. \tag{5}$$

The final equations for the mean temperatures of the two slabs are:

$$z_1 c_1 \frac{d\bar{T}_1}{dt} = F(0) - F(-z_1), \tag{6}$$

$$z_2 c_2 \frac{d\bar{T}_2}{dt} = F(-z_1). \tag{7}$$

We use a similar formulation for ocean ice but the no flux condition at $z = -z_1-z_2$ is replaced by:

$$T_2(-z_1 - z_2) = T_{fo}. \tag{8}$$

T_{fo}, the freezing point for ocean, is taken as 271.6 K. The heat crossing the $z = -z_1$ interface is

$$F(-z_1) = \frac{12\bar{T}_1 - 18\bar{T}_2 + 6T_{fo} - 2F(0)z_1/\lambda_1}{4z_1/\lambda_1 + 3z_2/\lambda_2}, \tag{9}$$

and the heat crossing the ice-ocean interface:

$$F(-z_1 - z_2) = 3\lambda_2 \frac{\overline{T}_2 - T_{fo}}{z_2} - \frac{F(-z_1)}{2} \quad . \tag{10}$$

The final equations for the two layer model for ocean ice are:

$$z_1 c_1 \frac{d\overline{T}_1}{dt} = F(0) - F(-z_1) \quad , \tag{11}$$

$$z_2 c_2 \frac{d\overline{T}_2}{dt} = F(-z_1) - F(-z_1 - z_2) \quad . \tag{12}$$

The equations for our three layer model are determined in a similar way.

The thicknesses of the layers were determined empirically by comparison with an exact periodic solution and an accurate 21 layer finite difference solution. For $K_g = 4 \times 10^{-7} m^2 s^{-1}$ the optimum depths for two layers were found to be $z_1 \sim 10$ cm, $z_2 \sim 4$ m, while for three layers $z_1 \sim 5$ cm, $z_2 \sim 25$ cm, $z_3 \sim 4$m. For other values of K_g these depths should be scaled in proportion to the square root of K_g. Note that for the particular thermal diffusivity which we employ the damping depth, at which the amplitude of the temperature variation is reduced by e^{-1} (cf. Sellers, 1972), is ~ 10 cm for the diurnal temperature wave and ~ 2 m for the annual temperature wave.

To illustrate the errors in the two and three layer models, we show the results of computations for the case $K_g = 4 \times 10^{-7} m^2 s^{-1}$ (the same as case 1 of Deardorff, 1978). For these tests we considered the simple case of no atmosphere above the ground ($F_h = F_q = 0$), with

$$F_{sw} = (1 - A_g) S_o \cos\theta_o \quad , \tag{13}$$

$$F_{lw} = \varepsilon \sigma T_1^4 \quad , \tag{14}$$

ground albedo $A_g = 0.24$, solar constant 1.354×10^3 W m^{-2} and ground emissivity $\varepsilon = 0.9$; θ_o is the solar zenith angle and σ the Stefan-Boltzmann constant. This idealized case yields unrealistic temperature variations at the surface, but it simplifies the computations and their interpretation.

Fig. 1 compares the diurnal and annual surface temperature variations computed with several different models. The computations are for the simplified case of no atmosphere described above. Our two layer and three layer results are about equally accurate for the annual temperature variation, as expected since both models use one deep layer for annual heat storage. Three layers are clearly needed if it is desired to represent both the amplitude and phase of the diurnal ground temperature variations, as well as the seasonal heat storage. We emphasize that the Arakawa (1972) and Deardorff(1978) schemes were not designed for use in climate models, and we have included them only to illustrate the necess-

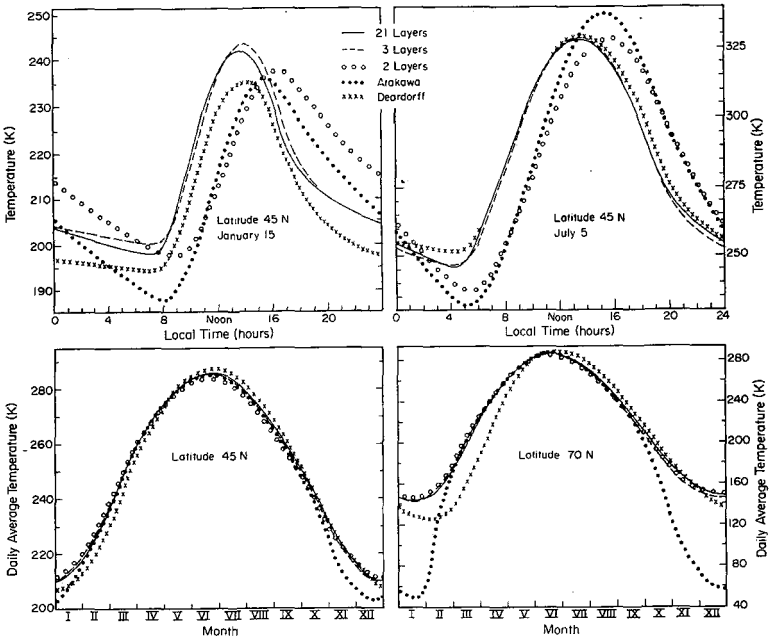

Fig. 1 Diurnal and annual surface temperature variations computed with several different models for the simple case of no atmosphere and thermal diffusivity $K_g = 4 \times 10^{-7} m^2 s^{-1}$. The Arakawa (1972) and Deardorff (1978) schemes were not designed for use in climate models, and are included here only to illustrate the necessity of having a deep layer for annual heat storage.

ity of having a deep layer for annual heat storage. Arakawa's scheme has one layer which is used to represent the diurnal temperature variation. Deardorff's method has two layers, with the lower layer damping the upper layer so as to give a realistic phase to the diurnal temperature variation.

Fig. 2 compares the diurnally averaged heat flux into the ground for the same models as in Fig. 1. The Arakawa (1972) model has a negligible diurnally averaged flux, since it consists of a single thin layer with a zero flux lower boundary condition. Although the two layers in the Deardorff (1978) model are thin, there can be a substantial diurnally averaged heat flux into (or out of) the ground because the method does not employ a zero flux lower boundary condition.

Discussion. The ground temperature model we have presented permits efficient and accurate computation of both diurnal and seasonal temperature variations with a minimum number of layers. It is therefore well suited for use in global climate models.

The diurnally averaged heat flux into the ground is usually small in comparison to typical radiative, latent and sensible heat fluxes, even

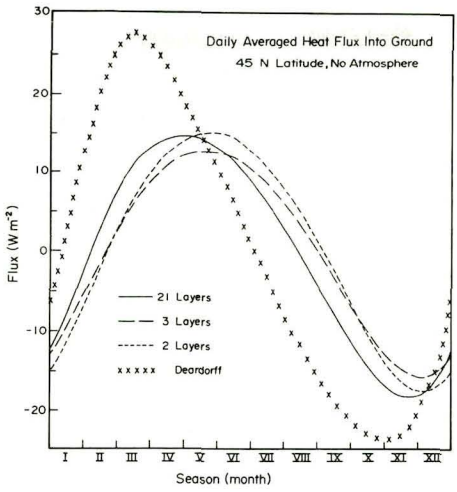

Fig. 2 Diurnally averaged heat flux into the ground for the same models as in Fig. 1. The calculations are for the simple case of no atmosphere at 45 N latitude, as described in the text. Arakawa's model, since it is a single thin layer with zero flux lower boundary condition, has negligible diurnally averaged heat flux.

for this idealized case in which the moderating effects of the atmosphere are excluded. Thus a large impact of seasonal heat storage on short time scales should not be expected, but the cumulative effect on seasonal time scales may be significant. Specific tests of the impact will be included in the three-dimensional climate model described elsewhere in these proceedings. A previous test has been made in a general circulation model by Delsol et al. (1971), who used a ground thickness of 5 m with a lower boundary condition of T=280 K; however, they ran the model only 14 days which is too short for an adequate test.

REFERENCES

Arakawa, A., Tech. Rep. 7. Dept. of Meteorol., Univ. of Calif., Los Angeles, 103, 1972.

Deardorff, J.W., J. Geophys. Res., 83, 1889-1903, 1978.

Delsol, F., K. Miyakoda, and R.H. Clarke, Quart. J.R. Meteor. Soc., 97, 181-208, 1971.

Sellers, W.D., Physical Climatology, Chicago, Univ. of Chicago Press, 272 pp., 1965.

Taylor, K., J. Appl. Meteor., 15, 1129-1138, 1976.

Page intentionally left blank

Paper No. 60

INCORPORATION OF SURFACE ALBEDO-TEMPERATURE FEEDBACK IN A ONE-DIMENSIONAL RADIATIVE-CONVECTIVE CLIMATE MODEL

Wei-chyung Wang, *Goddard Institute for Space Studies, NY, NY 10025*
Peter H. Stone, *Department of Meteorology, MIT, Cambridge, MA 02139*

ABSTRACT

The feedback between ice-snow albedo and temperature is included in a one-dimensional radiative-convective climate model. The effect of this feedback on sensitivity to changes in solar constant is studied for the current values of the solar constant and cloud characteristics. The ice-snow albedo feedback amplifies global climate sensitivity by 33% and 50%, respectively, for assumptions of constant cloud altitude and constant cloud temperature.

Introduction. One-dimensional radiative-convective models which determine the thermal structure of the atmosphere as a result of the balance between the radiative flux and a parameterized convective flux are useful tools for climate studies. Such models, which can include realistic vertical distributions of radiatively-important atmospheric constituents, can be used to examine the role that these constituents play in determining the global mean temperature structure. One major drawback of these models is their lack of the ice-snow albedo-temperature feedback which is of great importance because of the large difference in albedo between ice and ice-free areas. The present work describes a simple method of incorporating the albedo-temperature feedback in a one-dimensional radiative-convective climate model. In addition the effect of this feedback on the sensitivity of the climate to changes in solar constant is studied and compared with the sensitivity found in other models.

Analysis. The one-dimensional radiative-convective model described in Wang and Lacis (1979) is used in the present study. In order to incorporate the ice-snow albedo-temperature feedback in a global model, it is necessary to know the response of the global mean surface albedo to changes in the ice-snow line as a result of changes in global mean surface temperature.

We assume first the zonal mean surface albedo α_s has a simple form

$$\alpha_s = \begin{cases} a & 0 \leq x < x_s \\ b & x_s \leq x \leq 1 \end{cases} \qquad (1)$$

where a and b are constants characterizing the ice-free and ice-covered surface albedos, respectively, and x_s is the sine of the latitude of the edge of the ice sheet. For the ice-sheet edge, the prescription by Budyko (1969) is adopted, i.e., if the zonal mean surface temperature T_s is less than -10° C, ice will be present. We will further use the simple formu-

lation of the latitudinal temperature structure used by North (1975). In this formulation the temperature structure is approximated by the first two Legendre polynomials in a series expansion, i.e.,

$$T_S(x) = \overline{T}_S + T_2 P_2(x) \tag{2}$$

where $P_2(x) = (3x^2-1)/2$. The first term $\overline{T}_S$ is the global mean surface temperature since the second term vanishes upon integration from 0 to 1. This two-mode approximation with $T_2 = -28.40$ C yields a reasonably good temperature distribution compared with observations.

In the atmosphere T_2 varies with the tropospheric lapse rate because of the effect of large scale eddies (Stone, 1978). Since the tropospheric lapse rate is essentially constant in the radiative-convective model, we can adopt the simple parameterization suggested by Stone (1978) for taking into account the effect of the eddies on temperature structure in climate calculations, i.e., T_2 = constant = -28.4 C. Then setting $x = x_S$, $T = T_S = -10^\circ$ C in Equation (2) we obtain

$$x_S = (0.5681 + 0.02347\ \overline{T}_S)^{\frac{1}{2}} . \tag{3}$$

This equation describes how the extent of the polar ice cap changes as the global mean surface temperature changes.

Next, we wish to determine the relationship between the global mean surface albedo $\overline{\alpha}_S$ and x_S. Employing Equation (1), we obtain

$$\overline{\alpha}_S = \int_0^1 S_S(x,x_S)\ \alpha_S(x,x_S)dx \ / \int_0^1 S_S(x,x_S)dx \tag{4}$$

where S_S is the zonal mean solar radiation received at the surface. S_S is a complicated function, which depends on solar zenith angle and atmospheric transmissivity. As an initial calculation, to test the method, we assume that S_S has the same latitudinal distribution as the solar insolation at the top of the atmosphere, S_O. This approximation will be relaxed ultimately. Also we will use North's (1975) two mode approximation for S_O, i.e., we choose

$$S_S(x,x_S) = [\,1 + S_2 P_2(x)\,]\ \overline{S} \tag{5}$$

where $\overline{S}$ is the mean value of S_S and $S_2 = -0.482$. Substituting Equations (1) and (5) into (4), we obtain the following expression

$$\overline{\alpha}_S = [b(1-x_S) + ax_S\,] + S_2(b-a)(x_S - x_S^3)/2 \tag{6}$$

where the first term is the geometrical albedo. Equations (3) and (6) when coupled give a highly non-linear relation describing the feedback between ice-snow albedo and temperature.

Results and discussion. First we examine the sensitivity of the present radiative-convective model with and without the surface albedo-temperature feedback. A convenient measure of the sensitivity of the

Table 1. Comparison of the model sensitivity parameter β_0 and the ice-snow albedo amplification parameter γ for several climate models. C_T is the dependence of zonal surface-atmosphere albedo upon zonal mean surface temperature (cf., Sellers, 1969).

MODEL	β_0 (°C)	γ
A. Energy balance models		
Budyko (1967)	155	1.58
Lian and Cess (1977)	147	
$C_T = C_T(x)$		0.25
$C_T = 0.009$		1.68
$C_T = 0.004$		0.27
Sellers (1969)	150	
$C_T = 0.009$		1.17
Gal-chen and Schneider (1976)	134	
$C_T = 0.009$		0.98
$C_T = 0.004$		0.22
B. Radiative-convective models		
Wetherald and Manabe (1975)		
I	128	
II*	114	
Present model		
FCA†	112	0.33
FCT†	140	0.49

*Uses the radiation scheme of Rodgers and Walshaw (1966).
† FCA denotes fixed cloud altitude, FCT denotes fixed cloud temperature.

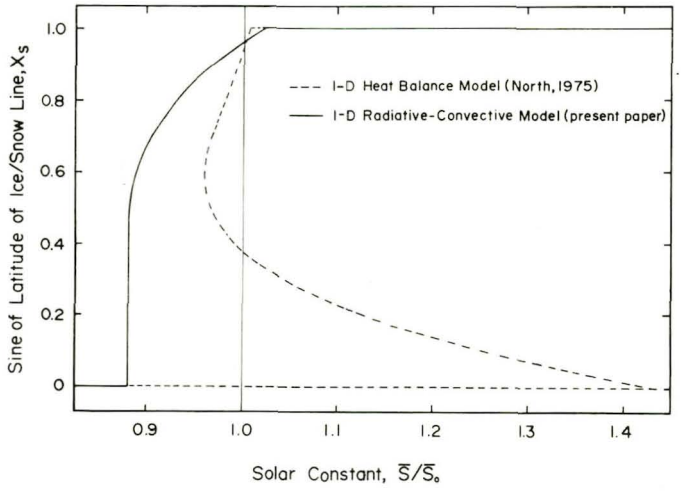

Fig. 1. Position of the edge of the polar ice cap as a function of the solar constant, as determined by the present model (solid curve) and by North (dashed curve).

global climate model is the parameter defined as

$$\beta = \bar{S} \frac{d\bar{T}_S}{d\bar{S}} \quad . \tag{7}$$

The enhancement in global sensitivity due to surface albedo-temperature feedback can be described by the amplification parameter,

$$\gamma = \frac{\beta - \beta_o}{\beta_o} , \tag{8}$$

where β_o is the model sensitivity in the absence of the surface albedo-temperature feedback. Values of β_o and γ for the present model and several other climate models are given in Table 1. In the calculations the present value of the solar constant S was chosen to be 1365 $W m^{-2}$ and values of a and b were chosen to be 0.09 and 0.6, respectively. The characteristics of the model corresponding to the present climate are: $\bar{\alpha}_S = 0.1$, $x_S = 0.964$, $\bar{T}_S = 15.37^\circ$ C and global mean planetary albedo 0.306.

In general, radiative-convective models yield smaller values of β_o than energy balance models, since the former do not include the $\alpha_s - T_s$ positive feedback. The most accurate values of β and γ are those given by Lian and Cess (1977) for $C_T = C_T(x)$, whose calculations included the most realistic parameterizations of this feedback. The results of our model with this feedback included are also listed in Table 1. The enhancement of the model's sensitivity is in good agreement with Lian and Cess' results, although the magnitude of the enhancement is subject to modification when a more accurate representation of S_S is used.

We also calculated the variation of the ice line with solar constant in the radiative-convective model. The solution is illustrated in Fig. 1. The qualitative behavior is similar to that in the 1-D heat balance models. As the solar constant is decreased, a point is reached at which the ice cap is unstable and will grow spontaneously until it covers the whole earth. For the approximation to S_S we have used, this occurs when the solar constant has decreased by 12%.

We conclude that the surface albedo-temperature feedback can be included in a one-dimensional radiative-convective climate model in a qualitatively realistic way. This addition represents a significant improvement in the ability of such models to simulate the effects of radiative perturbations on climate in a realistic way.

REFERENCES

Budyko, M.I., "The effect of solar radiation variations on the climate of the earth," Tellus, 21, 611-619, 1969.

Gal-chen, T., and S.H. Schneider, "Energy balance climate modeling: comparison of radiative and dynamic feedback mechanisms," Tellus, 28, 108-121, 1976.

Lian, M.S., and R.D. Cess, "Energy balance climate models: a reap-

praisal of ice-albedo feedback, J. Atmos. Sci., 34, 1058-1062,1977.

North, G.R., "Theory of energy-balance climate models, J. Atmos. Sci., 32, 2033-2043, 1975.

Rodgers, C.D., and D.C. Walshaw, "The computation of infrared cooling rate in planetary atmospheres," Quart. J. Roy. Meteor. Soc., 92, 67-92, 1966.

Sellers, W.D., "A global climate model based on the energy balance of the earth-atmosphere system," J. Appl. Meteor., 8, 392-400, 1969.

Stone, P.H., "Baroclinic adjustment," J. Atmos. Sci., 35, 561-571, 1978.

Wang, W., and A.A. Lacis, "A one-dimensional radiative-convective model of the earth's atmosphere for climate applications," Preprint, 1979.

Wetherald, R.T., and S. Manabe, "The effects of changing the solar constant on the climate of a general circulation model, " J. Atmos. Sci., 32, 2044-2059, 1975.

Page intentionally left blank

Paper No. 61

A GCM SIMULATION OF THE EARTH-ATMOSPHERE RADIATION BALANCE FOR WINTER AND SUMMER

M. L. C. Wu, *National Research Council, Washington, DC and Goddard Space Flight Center, Greenbelt, Maryland*

ABSTRACT

The radiation balance of the earth-atmosphere system simulated by using the general circulation model (GCM) of the Laboratory for Atmospheric Sciences (GLAS) is examined in regards to its geographical distribution, zonally-averaged distribution, and global mean. Most of the main features of the radiation balance at the top of the atmosphere are reasonably simulated, with some differences in the detailed structure of the patterns and intensities for both summer and winter in comparison with values as derived from Nimbus and NOAA (National Oceanic and Atmospheric Administration) satellite observations. Both the capability and defects of the model are discussed.

INTRODUCTION

The GLAS GCM simulates the general features of climatology reasonably well (Halem et al., 1978). Climatological elements, such as the mass distribution, geopotential height, and oceanic rainfall rates generally are in reasonable agreement with observations. Here, we examine the primary driving force, radiation balance, of the circulation system. The GLAS GCM has the feature that the important thermodynamic variables, such as cloud types and cloud heights, atmospheric and ground temperatures, and specific humidity, are interactive with model dynamics, which allows this study to be meaningful. Through a complicated interactive process, in order for the simulated radiation balance at the top of the atmosphere to be right, the kinematics, dynamics, and thermodynamics of the model have to be right. The geographical distribution of the earth-atmosphere system radiation balance from satellite measurements provides a valuable check on our diagnostic studies of the circulation system of the GLAS GCM.

The winter (summer) simulations, starting from real data for 1 January 1975 (15 May 1974), were integrated for 60 days (105 days), and the last 30-day mean was used for comparison with geographical distribution of the radiation balance as derived from Nimbus 3 measurements, for the 14-day (16-day)

mean, starting from 21 January 1970 (16 July 1969). The zonal mean of the radiation balance was compared with both Nimbus 3 and NOAA SR measurements (January 1975).

It should be noted that the periods used for comparison are different since Nimbus 3 data was not available for the exact period of years for which the model had equilibrated. It should also be noted that the satellite measurement instrument is not calibrated on board for shortwave measurement; and it is a sun-synchronous orbit.

The Geographical Distribution of the Radiation Balance of the Earth-Atmosphere System

Global patterns of the radiation balance and its associated components, absorbed solar radiation, and outgoing longwave radiation, are shown for winter in Figs. 1, 2, and 3, respectively. Similar distributions for summer are shown in Figs. 4, 5, and 6. For comparison, values as derived from Nimbus 3 measurement are displayed in Figs. 1a-6a, and values as simulated from the model are displayed in Figs. 1b-6b.

Overall, there is reasonably good agreement between the simulated and the observed radiation balance patterns, particularly for the major energy gain areas over the subtropical minimum cloudiness regions in both summer hemisphere oceans, for local minima over the continents in summer hemispheres, and for the zonal pattern of deficit in the winter hemispheres. For all of these features there is general agreement in patterns, which indicates that the GLAS GCM is capable of simulating the general climatology to the accuracy of the zeroth order. The differences are in the intensities and in the detailed structure of the patterns. It is from these differences that we are able to diagnose some of the model defects.

In winter, the simulated zero-balance isoline is around 30N without a southward dip off the west coast of North America, probably because the model does not generate low stratus clouds, and with a relatively small southward shift of the zero-balance isoline over North Africa, probably because the model generates slightly more cloudiness over Africa especially on the equatorward side of North Africa. The simulated period is February, whereas the observed period is the last two weeks of January. Due to the sun's declination, there should be about 5° northward shift of the zero-balance isoline. The cause of the remaining latitudinal difference may be due to the following reasons. Generally speaking, the model overestimates total absorbed solar radiation in the winter hemisphere in comparison with observation (Fig. 2). In addition, the model systematically underestimates outgoing longwave radiation (Fig. 3). For example, around 20N, the simulated value is about .36 cal/cm^2/min, whereas the value as derived from observation is about .42 cal/cm2/min.

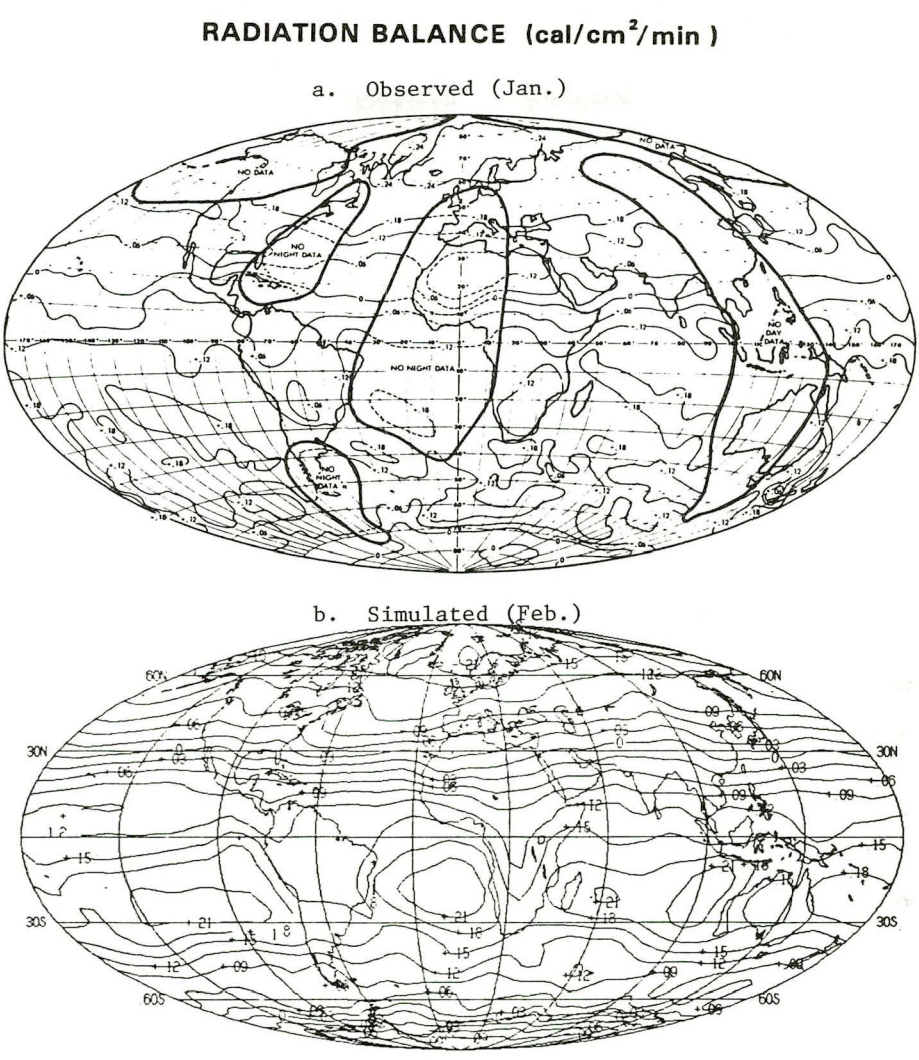

Fig. 1. Net radiation balance of the earth-atmosphere system

a. as derived from Nimbus 3 observations during the period 21 January to 3 February 1970.

b. as simulated from the GLAS GCM for February.

TOTAL ABSORBED SOLAR RADIATION (cal/cm^2/min)

a. Observed (Jan.)

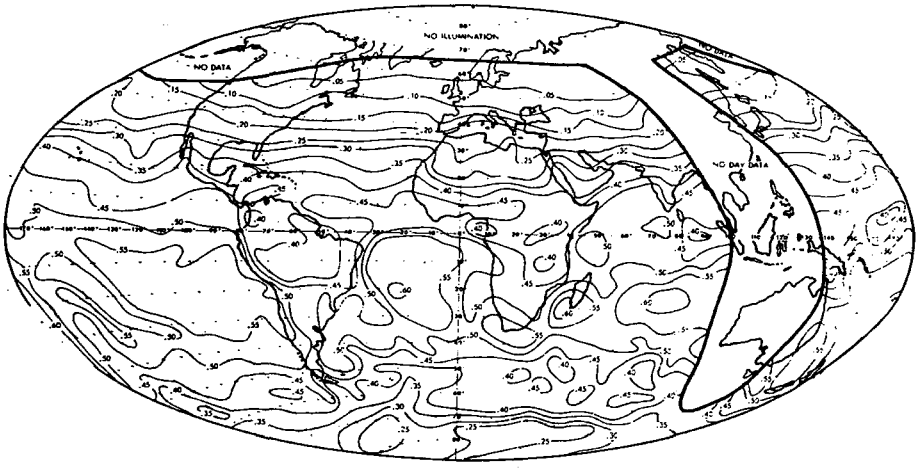

b. Simulated (Feb.)

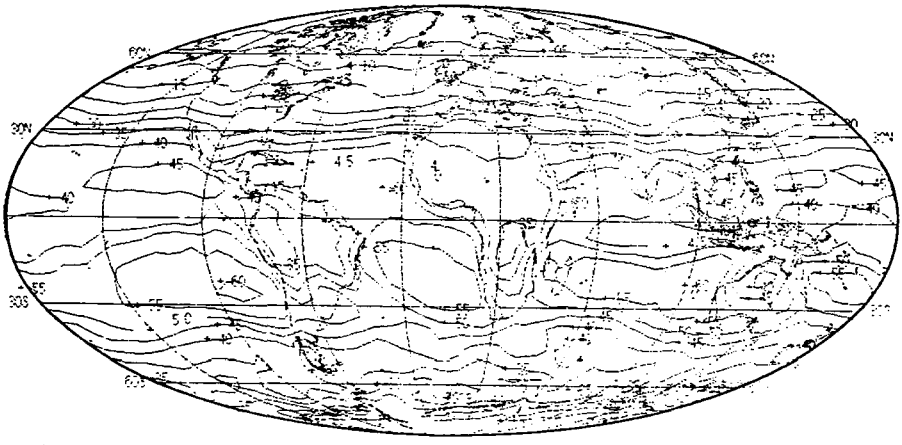

Fig. 2. Total absorbed solar radiation in the earth-atmosphere system

a. as derived from Nimbus 3 measurements during the period 21 January to 3 February 1970.

b. as simualted from the GLAS GCM for February.

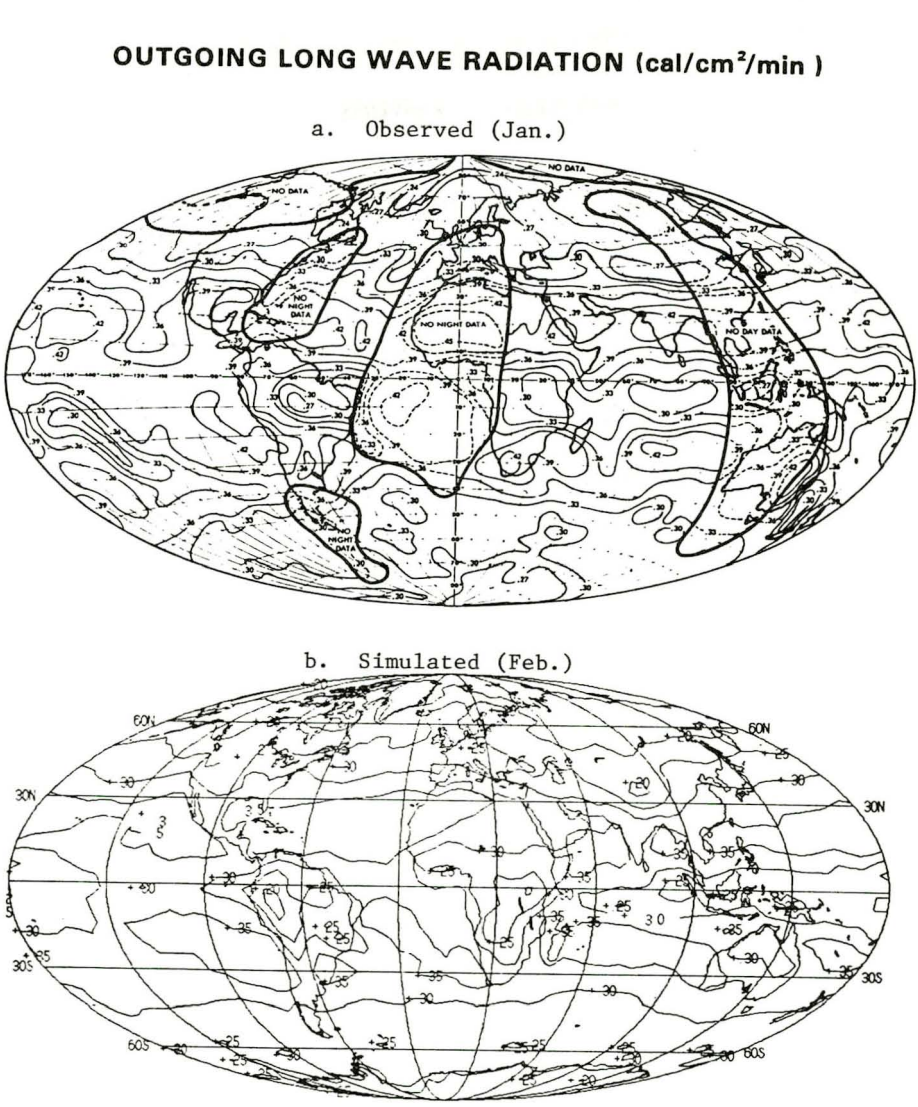

Fig. 3. Outgoing longwave radiation emitted from the earth-atmosphere system to space

a. as derived from Nimbus 3 measurements during the period 21 January to 3 February 1970.

b. as simulated from the GLAS GCM for February.

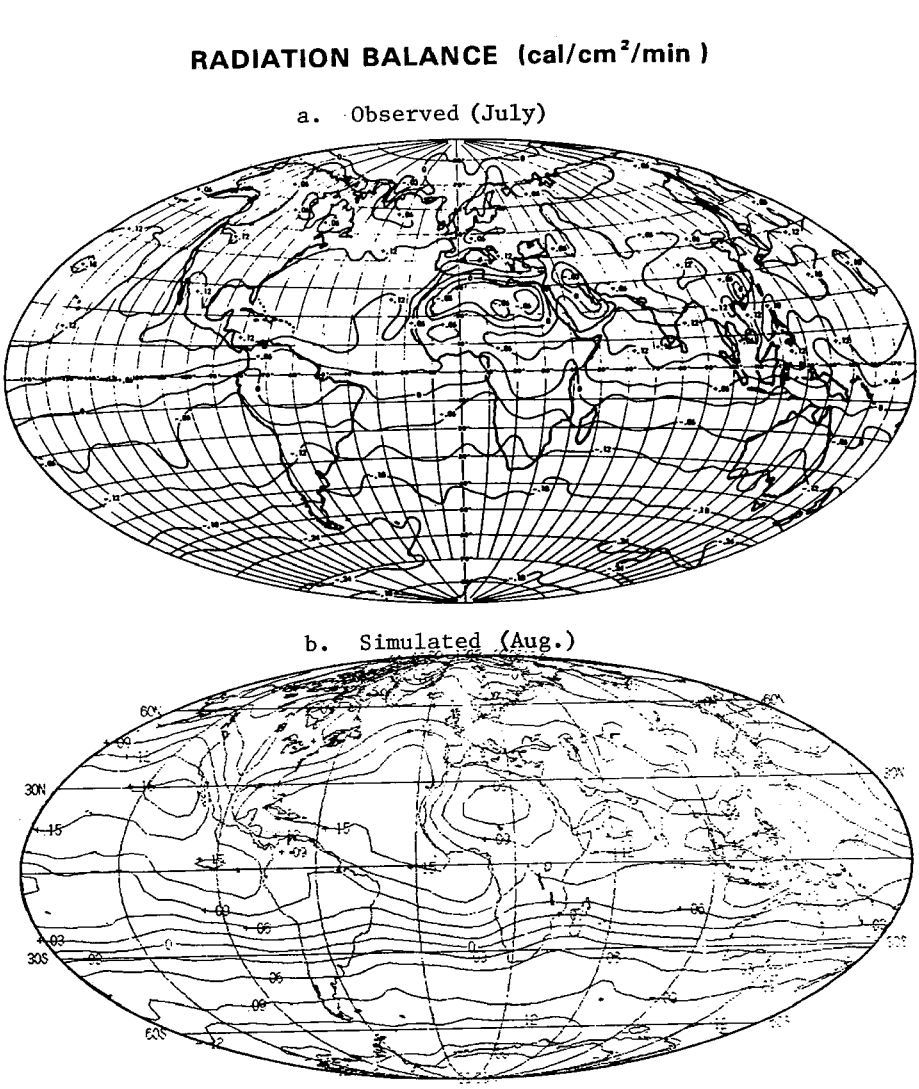

Fig. 4. Net radiation balance of the earth-atmosphere system

a. as derived from Nimbus 3 measurements during the period 16 to 31 July 1969.

b. as simulated from the GLAS GCM for August.

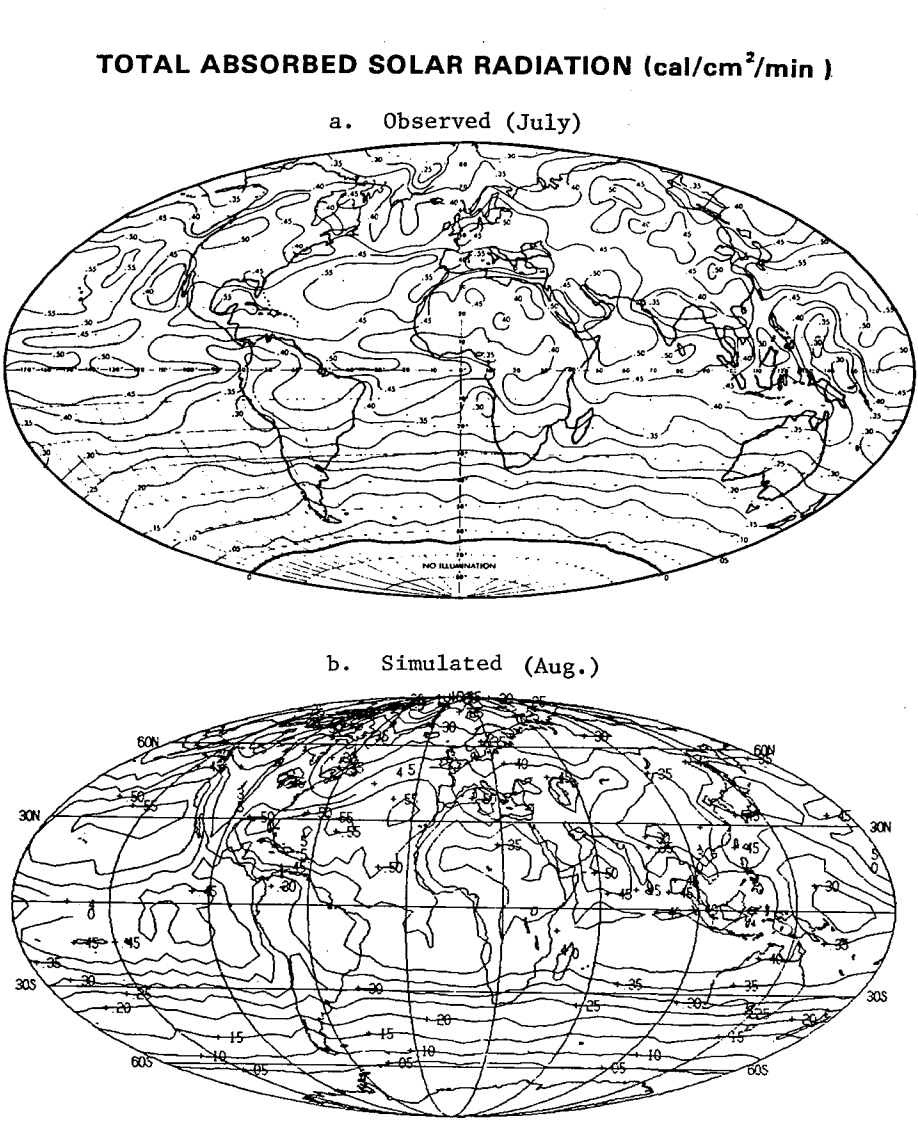

Fig. 5. Total absorbed solar radiation absorbed in the earth-atmosphere system

a. as derived from Nimbus 3 measurements during the period 16 to 21 July 1969.

b. as simulated from the GLAS GCM for August.

OUTGOING LONG WAVE RADIATION (cal/cm^2/min)

a. Observed (July)

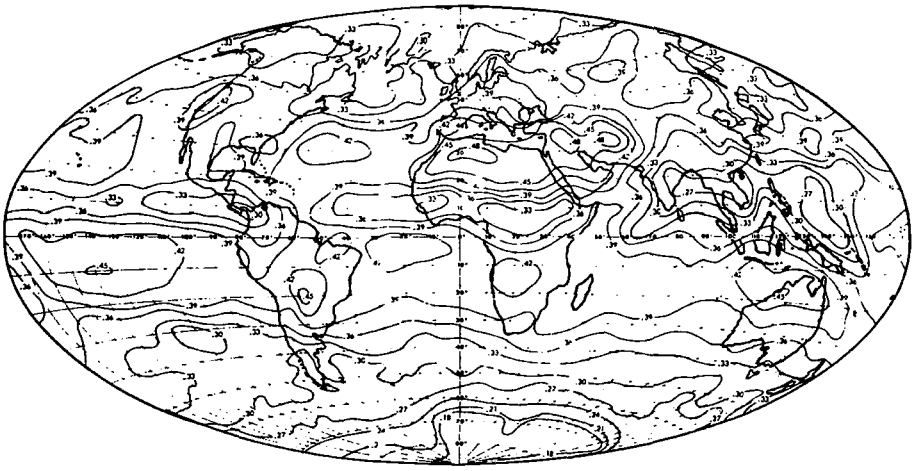

b. Simulated (Aug.)

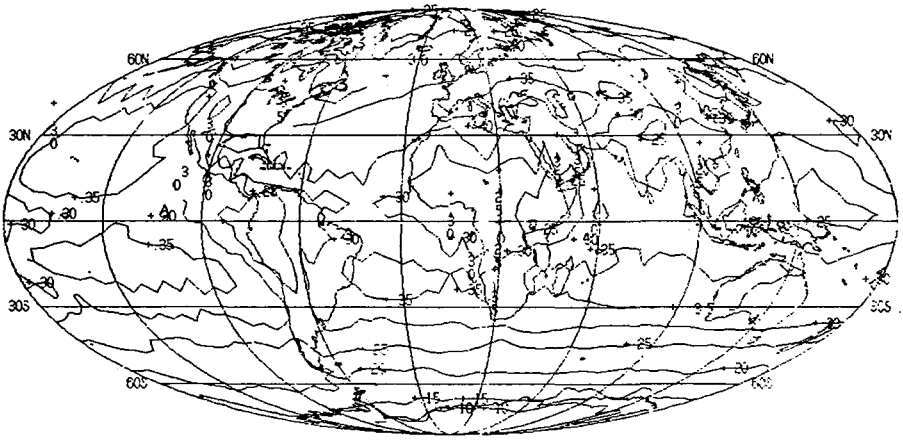

Fig. 6. Outgoing longwave radiation emitted from the earth-atmosphere system to space

a. as derived from Nimbus 3 measurements during the period 16 to 21 July 1969.

b. as simulated from the GLAS GCM for August.

The major energy gain area is over the Southern Hemisphere with maxima over the oceans in connection with subtropical cloudiness minima, and local minima over continents associated with a heavy ITCZ cloudiness over South America and South Africa around latitude 0 to 20S. The model reproduces maxima over the oceans, because the model simulates subtropical anti-cyclones reasonably well, as well as local minima over the continents.

As would be expected from seasonal change in solar heating, the major energy gain areas are moved to the northern summer for July and August with maximum over the oceans. One striking feature appearing in the summer observations is a deficit in the energy budget over the Sahara and Saudi Arabia. The model produces a more localized minimum over the Sahara, in agreement with the wide-angle radiative balance for August measured with the Earth Radiation Budget (ERB) instrument in Nimbus 6, which also does not show a negative deficit as in the earlier Nimbus 2 and 3 observations. This suggests that part of the discrepancy may be due to the coarseness of resolution of the model. When we examine the separate components of the radiation balance, we find that the deficit is due to high surface albedo and high outgoing longwave radiation. But the particular reason for the deficit to be over the northernmost part of Africa, between 30N and 40N, can be found by examining Figs. 5a and 6a. Fig. 6a is a display of the outgoing longwave radiation. The cloudiness associated with the ITCZ and summer monsoon system are reasonably well revealed in this figure. Fig. 5a shows that the absorbed solar radiation has a more or less uniform distribution with a value of about .4 cal/cm^2/min over North Africa, whereas the outgoing longwave radiation has a strong gradient, starting with a minimum over the equatorward side of north Africa associated with high level clouds over the ITCZ and increasing northward with a maximum on the northernmost part of Africa associated with high surface temperature in a clear area. Thus, a deficit is formed over the northernmost part of Africa. The outgoing longwave radiation in the model does not show a sharp northward gradient over this area and the values over this area are not large enough to produce a deficit. Among the possible reasons are the model-generated cloudiness associated with ITCZ and monsoon system extends too far north and that clouds are assumed to be black emitters and to fill an entire grid area as mentioned above.

More clearly than for winter, some of the differences in the detailed structure of the pattern may be due to the failure of the model to generate low stratus and strato-cumulus clouds over the west coasts of North America, South America, and Africa. For example, instead of a local minimum, the model generates a local maximum over the west coast of North America. The model-generated local maxima with values larger than .12 cal/cm$_2$/min extend too far south and extend into the

Southern Hemisphere over both the eastern Pacific and eastern Atlantic. Moreover, the model-generated cloudiness associated with the ITCZ system over the Atlantic extends too far south. These effects can be seen from Figs. 5b and 6b. Fig. 5b indicates cates that the local maxima with values larger than .45 cal/cm^2/min of the absorbed solar radiation extend too far south into the eastern south Pacific. Fig. 6b indicates that the simulated local maxima outgoing longwave radiation over the south Atlantic is too far south in comparison with observations. The local maxima with values larger than .12 cal/cm^2/min over the Northern Hemisphere also extend too far north (to 40N) over the eastern Pacific and eastern Atlantic, because the model-generated subtropical minimum cloudiness system extends too far north. In other words, cyclonic activities are shifted too far north in the model.

The model does not simulate a deep northwestward dip north of New Guinea, because the cloud systems generated by the model are shifted too far east and have broader structures. The observed zero-balance isoline on the winter hemisphere is around 10S with northward dips over the east and west coasts of both South America and south Africa. The dips over the west coast may be related to the stratus clouds and cloudiness associated with the ITCZ over these regions. The dips over the east coasts may also be related to the clouds over that area. The simulated zero-balance isoline is around 28S. The difference in solar radiation accounts for about an 8° difference in latitudes, but this still leaves a residue difference of about 10°.

As far as the pattern is concerned, the maximum outgoing longwave radiation is confined between 10S and 30S, because the model-generated subtropical minimum cloudiness is located around 10S and 30S. There seems to be a coincidence of the zero-balance isoline with the poleward side of the maximum outgoing longwave radiation for both winter and summer, which appears in both simulated and observed distributions. As for the intensity, we did not take the cloud fraction and cloud transmittance into account in our longwave radiation parameterization, with the result that we tended to underestimate the outgoing longwave radiation.

On the whole, the differences in the detailed structure of the patterns and intensities are either due to: The model failing to generate low-level stratus clouds over the west coasts of North America, South America, and Africa; or differences in detailed structure of the cloud distribution patterns; or the assumption that clouds are black in infrared emission and absorption spectra, and fill an entire grid area. Of course, some of the differences are due to the natural variability of the atmosphere. The above comparison is based on an assumption that values as derived from Nimbus 3 measurement are correct.

Zonally-Averaged Distributions and Global Mean

The zonally-averaged distributions of net heat surplus and deficit with latitude, which are important for the meridional energy transport, are plottted in Fig. 7 for winter comparison. The values as derived from satellite measurement are for January; the values as simulated by model are for February. It should be noted that the observations are taken near 11:30 a.m. (9 a.m.) and 11:30 p.m. (9 p.m.) local standard time for Nimbus 3 (NOAA SR) measurements. Because the model systematically underestimates outgoing longwave radiation, the net radiation balance is overestimated in comparison with results of NOAA SR measurements, but it is overestimated only in the winter hemisphere in comparison with Nimbus 3 measurements.

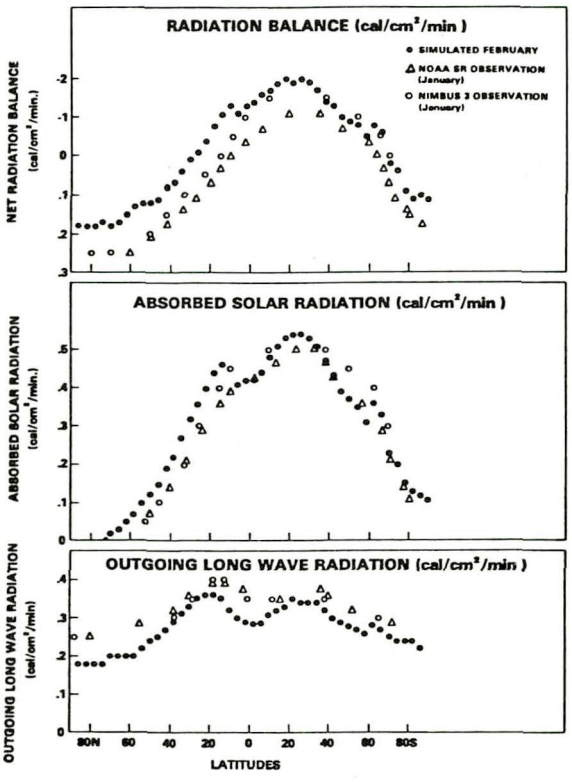

Fig. 7. Zonally-averaged radiation balance.

The global radiation balance is tabulated in Table 1. Because the model-generated longwave radiation is systematically lower than values derived from Nimbus 3 measurements, the model produces a large unbalanced radiation. We have noted above that the overestimated cloud amount and cloud emissivity might account for much of the low outgoing longwave radiation. In addition, the simulated temperature is colder than that of observation; for example, it is almost 10°C to 20°C too cold in polar regions which will also tend to underestimate outgoing longwave radiation.

Table 1. Global radiation budget of the earth-atmosphere system

	Solar radiation cal $cm^{-2}min^{-1}$			Outgoing Longwave radiation cal $cm^{-2}min^{-1}$	Radiation balance cal $cm^{-2}min^{-1}$
	Incoming	Absorbed	Albedo		
Observed (Jan. 21-February 3, 1970)	.501	.361	.283	.337	.024
Simulated (February)	.513	.356	.305	.295	.061
Observed (July 16-July 31, 1969)	.472	.339	.281	.354	-.015
Simulated (August)	.488	.334	.315	.294	.040

Since the sea surface temperature is fixed in the model, we suspect that most of the excess of the unbalanced radiation is lost to the oceans. This can be seen from Table 2, in which the heat balance of the ice-free ocean surface is tabulated. In the model, the sea surface temperature does not change whether the heat balance at the ocean surface is positive or negative. The sensible heat flux, moisture flux, and net longwave radiation flux in the model depend on the prescibed sea surface temperature. Calculations, results of which are shown in Table 2, indicate that heat loss due to the above fluxes is less than heat gain due to solar flux by .083 cal/cm^2/min (.064 cal/cm^2/min) for February (August) simulations. The global mean, i.e., the above values weighted by fraction of the ice-free ocean (about 66%) is compatible with values of the unbalanced radiation at the top of the atmosphere.

Table 2. Heat balance of the ice-free ocean surface (cal $cm^{-2}min^{-1}$).

	Net solar radiation absorbed by oceans	Net loss through longwave radiation	Loss through sensible heat flux	Loss of heat through evaporation	Net heating of ocean	Global ice-free ocean surface balance
February	.275	.073	.033	.086	.083	.055
August	.168	.042	.018	.044	.064	.042

On an overall basis, the radiation balance of the earth-atmosphere system simulated by using the GLAS GCM is compatible with results as derived from Nimbus 3 observations in geographical distribution of the patterns but with differences in detailed structure of the patterns and in intensities. We think we know some of the causes of these discrepancies and are in the process of trying to eliminate them.

REFERENCES

Gruber, A. 1977: Determinations of the earth-atmosphere radiation budget from NOAA satellite data. NOAA Tech. Rep. NESS 76, Washington, DC.

Halem, M., J. Shukla, Y. Mintz, M. L. Wu, R. Godbole, G. Herman, and Y. Sud, 1978: Comparison of observed seasonal climate features with a winter and summer numerical simulation produced with the GLAS general circulation model. Proceedings of the JOC Study Conf. on Climate Models, April 1978, Washington, DC.

Miller, D. B., 1971: Global atlas of relative cloud cover, 1967-70, U. S. Dept. of Commerce and U. S. Air Force, Washington, D C.

Raschke, E., T. H. Von der Haar, M. Pasternik, and W. R. Bandeen, 1973: The radiation balance of the earth-atmosphere system from Nimbus-3 radiation measurements. NASA TN D-7249, NASA, Washington, DC.

_____, and W. R. Bandeen, 1970: The radiation balance of the planet earth from radiation measurements of the satellite Nimbus II. J. Appl. Meteor., 9, 215-238.

Sadler, J. C., 1968: Average cloudiness in the tropics from satellite observations. East-West Center Press, Honolulu.

Winston, J. S., 1977: Global distribution of cloudiness and radiation as measured from weather satellites. World Survey of Climatology, 6, 247-280.

Page intentionally left blank

Paper No. 62

MAINTENANCE OF QUASI-STATIONARY WAVES IN A 2-LEVEL QUASI-GEOSTROPHIC SPECTRAL MODEL WITH TOPOGRAPHY

Mao-Sung Yao, *Goddard Institute for Space Studies, New York, New York 10025*

ABSTRACT

The maintenance of the quasi-stationary waves obtained through numerically integrating a 2-level quasi-geostrophic spectral model on a β-plane is investigated. An idealized topography which has only wavenumber n in the zonal direction and the first mode in the meridional direction is used to force the quasi-stationary waves. It is shown that the topographical forcing is not necessarily the mechanism for maintaining the quasi-stationary waves.

Introduction. The earth's topographical forcing is one of the major mechanisms for producing quasi-stationary waves in the atmosphere. Many studies have been made on the role of the topography in forcing these waves, such as Charney and Eliassen (1949), and Derome and Wiin-Nielsen (1971). Saltzman (1968) gives a general review of this kind of study.

There have also been some observational studies on the maintenance of the quasi-stationary component of the atmospheric circulation. Holopainen (1970) studied the energy balance of the quasi-stationary disturbances in the northern hemisphere. He concluded that in winter the quasi-stationary disturbances are usually baroclinic waves which extract available potential energy from the zonally averaged mean flow. These waves then convert part of their potential energy into kinetic energy to offset the destruction of the latter by small-scale turbulent friction, large-scale transient motion and conversion into zonally-averaged mean motion. As far as the energy balance of the quasi-stationary waves is concerned, the effect of mountains seems to be very small. In summer the stationary disturbances appear to form a thermally-driven system.

Thus it is not obvious how the theoretically calculated stationary waves are related to the observed quasi-stationary waves. Our objective is to examine the maintenance of the quasi-stationary waves produced by a simple 2-level quasi-geostrophic truncated spectral model, in which the dependence of the mechanism for maintaining the waves upon parameters, such as the wavenumber n, the imposed thermal equilibrium temperature gradient ΔT_e, and damping coefficients, can be readily obtained.

Two-level quasi-geostrophic truncated spectral model. The planetary-scale waves forced by topography and the cyclone-scale transient waves can be described by the quasi-geostrophic system of equations on a β-plane. We assume that the motion takes place in a cyclic

zonal channel of width Y_o in the y (meridional) direction and of a length X_o in the X (zonal) direction. Then, we have the following governing equations in p-coordinates:

$$\left(\frac{\partial}{\partial t} + \underset{\sim}{v}_g \cdot \underset{\sim}{\nabla}\right) \zeta_g + \beta v_g - f_o \frac{\partial \omega}{\partial p} = -g \frac{\partial}{\partial p} \underset{\sim}{k} \cdot \underset{\sim}{\nabla} \times \underset{\sim}{\tau}, \tag{1}$$

$$\left(\frac{\partial}{\partial t} + \underset{\sim}{v}_g \cdot \underset{\sim}{\nabla}\right) \frac{\partial \phi}{\partial p} + S_p \omega = -\frac{R}{C_p P} \dot{Q}, \tag{2}$$

$$\underset{\sim}{\nabla} \cdot \underset{\sim}{v} + \frac{\partial \omega}{\partial p} = 0, \tag{3}$$

$$\frac{\partial \phi}{\partial p} = -\alpha, \tag{4}$$

where S_p is static stability, $\underset{\sim}{\tau} = -g\rho_s^2 \nu (\partial \underset{\sim}{v}_g / \partial p)$ the frictional stress, ρ_s horizontally averaged density, ν kinematic coefficient of turbulent eddy viscosity, $Q = -\mu C_p(T-T_e)$ diabatic heating, T_e the imposed thermal equilibrium temperature, and μ a constant. Other variables have their usual meaning.

The static stability S_p is assumed to be a constant. The diabatic heating is in the form of Newtonian cooling, where T_e is a function of y only. We assume the following boundary conditions:

$$v_g = v = 0 \qquad \text{at } y = 0, Y_o$$

$$\underset{\sim}{\tau}_T = 0, \ \omega_T = 0 \qquad \text{at } p = p_T, \text{ the top of the model atmosphere,}$$

$$\underset{\sim}{\tau}_B = \rho_B C_D \underset{\sim}{v}_g, \ \omega_B = -\rho_B g \underset{\sim}{v}_g \cdot \nabla h \qquad \text{at } p = p_B, \text{ the bottom of the model atmosphere}$$

where C_D is the drag coefficient, h the topographic function and ρ_B a standard air density at the bottom of the atmosphere.

In the vertical direction, we divide the mass of the atmosphere into two equal layers. We carry ϕ and $\underset{\sim}{v}$ at levels 1 (250 mb) and 3 (750 mb), ω and $\underset{\sim}{\tau}$ at the top (0 mb) and bottom of the atmosphere, and ω, $\underset{\sim}{\tau}$ and α at the middle level (500 mb).

Horizontally we expand variables in terms of double Fourier series. The detailed mathematical treatment is given by Yao (1977). In the results discussed below we restrict ourselves to some highly truncated cases where only the first three meridional modes and wavenumbers n and 2n are allowed. n is the lowest existing eddy wavenumber in the x-direction, as well as the wavenumber of the topography. We only have first mode for the topography and the imposed thermal equilibrium temperature. We will restrict ourselves to the cases n = 2 and n = 3, so that both topographical forcing and baroclinic instability are significant,

and occur at realistic wavenumbers.

The spectral model was integrated initially to determine the quasi-equilibrium state. Unless otherwise mentioned, we used the following parameter settings: $X_o = 2\pi R_e \cos 45°$, where R_e is the earth's radius, $Y_o = 60°$ latitudinal length, $S_p = 0.03\ m^2 mb^{-2} sec^{-2}$, $f_o = 10^{-4} s^{-1}$, $\beta = 1.6 \times 10^{-11} m^{-1} s^{-1}$, $k_B = 4k_I$, $\mu = 2k_I$, where $k_B \equiv \rho_B g C_D / \Delta p$ and $k_I \equiv g^2 \rho_s^2 \nu / \Delta p^2$. The amplitude used for the topography is 750 m. The densities at level 2 and at the surface are based on $T_{s2} = 250$ K and $T_B = 280$ K, respectively. We define $\Delta T_e = T_e(0) - T_e(Y_o)$.

Maintenance of quasi-stationary waves. In considering the energy balance of the atmospheric flow we employ the kinetic energy and the available potential energy of time-averaged zonal mean flow K_Z and A_Z, of time-averaged eddies (K_S and A_S) and of transient flow (K_T and A_T). Fig. 1 shows the energy exchange processes in an energy cycle diagram. The arrows indicate the direction of the energy conversions when they are positive. $CB(K_Z, K_S)$ is the energy conversion due to topographic effect. This topographical effect is in the form of vertical geopotential flux at the surface.

Case n = 3. Fig. 2 is the stability diagram for n=3. The curve defining the transition between the Hadley and the Rossby regimes is obtained by a stability study (Yao 1977). In the indicated Rossby regime I, the kinetic energy of quasi-stationary waves (K_S) is maintained mainly by the topographical forcing, whereas in the Rossby regime II, K_S is maintained mainly through the energy conversion $A_S \rightarrow K_S$. In both Rossby regimes I and II, the available potential energy of the quasi-stationary waves (A_S) is maintained by the energy conversion $A_Z \rightarrow A_S$. When ΔT_e or $1/K_I$ is sufficiently large, the model's motion becomes highly irregular and a clear distinction between different Rossby regimes can not be made; however, when ΔT_e or $1/K_I$ is very large the assumption of a constant static stability is invalid.

As an example from Rossby regime II, Fig. 3 shows the time-averated energy cycle diagram from the results of integration for the combination $\Delta T_e = 38$ K and $1/k_I = 26$ days. A_S is maintained by the energy conversion $A_Z \rightarrow A_S$. A portion of A_S is then converted to the kinetic energy of quasi-stationary waves, K_S. K_S is also produced from the conversion $K_Z \rightarrow K_S$ through the topographical effect. It can be seen that $C(A_S, K_S)$ is considerably larger than $CB(K_Z, K_S)$. We conclude that for this case the kinetic energy of the quasi-stationary waves is maintained mainly by the energy conversion $A_S \rightarrow K_S$. This is consistent with the findings of Holopainen (1970) for winter.

As an example from Rossby regime I, Fig. 4 shows the energy cycle diagram for the combination of $1/k_I = 26$ days and $\Delta T_e = 34$ K. It is apparent in this case that the quasi-stationary waves are maintained by the topographical effect $CB(K_Z, K_S)$, rather than by the conversion $C(A_S, K_S)$.

Case n = 2. For n = 2 a delineation between different Rossby

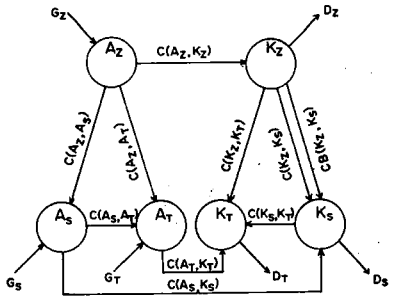

Fig. 1. Energy cycle diagram. The arrows indicate the positive direction of individual processes as defined.

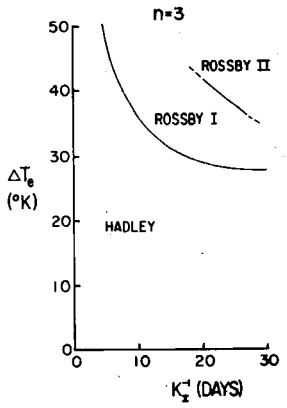

Fig. 2. Stability diagram for the case n = 3.

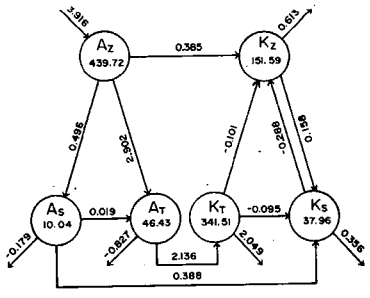

Fig. 3. Energy cycle of the quasi-steady state with n = 3, $1/K_I$ = 26 days and ΔT_e = 38 K. Energy is in m^2/s^2, while conversion rates are in $10^{-4} m^2 s^3$.

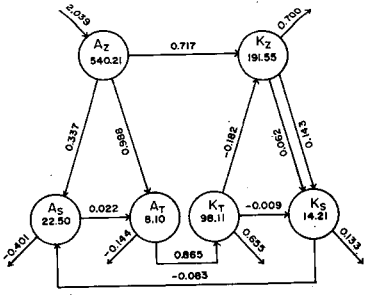

Fig. 4. Same as Fig. 3, but with ΔT_e = 34 K.

regimes is not well defined. For relatively small values of ΔT_e and $1/K_I$, typical of atmospheric values, K_S in the Rossby regime is maintained by topographical forcing, whereas A_S is maintained by energy conversion $A_Z \rightarrow A_S$. When ΔT_e or $1/K_I$ is sufficiently large, the motion becomes highly irregular and no systematic change of regimes is observed.

Discussion. The finding that quasi-stationary waves are maintained by energy conversions $A_Z \rightarrow A_S$ and $A_S \rightarrow K_S$ when n=3 with ΔT_e and $1/K_I$ moderately large implies that in Rossby regime II these quasi-stationary waves are generated mainly by baroclinic instability. However, the baroclinic waves generated are also stationary. According to Stone (1977), this is a plausible explanation of the baroclinic nature associated with quasi-stationary waves as observed by Holopainen (1970) in winter. It is noted, though, that topography is needed to trigger the generation of available potential energy A_S; if there is no topography $C(A_Z, A_S)$ is negligible.

Acknowledgements. The paper reported here is an extension from the author's Ph.D. dissertation (Yao, 1977). He is indebted to Professor Akio Arakawa of the University of Los Angeles, for his guidance through that dissertation work.

REFERENCES

Charney, J.G. and A. Eliassen, Tellus, 1, 38-54, 1949.

Derome, J., and A. Wiin-Nielson, Mon. Wea. Rev., 99, 564-576, 1971.

Holopainen, E.O., Quart. J. Roy. Meteor. Soc., 96, 626-644, 1970.

Saltzmann, B., Meteor. Monogr., 8, Amer. Meteor. Soc., 4-19, 1968.

Stone, P.H., Contribution of the U.S. Delegation to the Yalta Polymode Theoretical Institute. P. Rhines, ed., U.S. Polymode Organizing Committee, Cambridge 22 pp. (Available from the US PMOC).

Yao, M.-S., Ph.D. Thesis, University of California, Los Angeles, 161 pp.

Page intentionally left blank

Paper No. 63

USE OF GLOBAL ATMOSPHERIC DATA SETS TO TEST QUASI-GEOSTROPHIC EDDY MOMENTUM FLUX CONVERGENCE

W. J. Heck, *Goddard Institute for Space Studies, New York, NY 10025*

ABSTRACT

The quasi-geostrophic relation between the fluxes of momentum, potential vorticity, and potential temperature is tested with global sets of atmospheric wind and temperature data by computing the convergence of momentum flux as a residual of the potential temperature and potential vorticity flux and comparing it to the momentum flux convergence computed directly. It is shown that in the troposphere between 18°N and 74° N the observed momentum flux convergence differs from the quasi-geostrophic convergence by 25%-60%, with the larger errors only occurring where the convergence is small. These results indicate that momentum flux convergence obtained from quasi-geostrophic theory is adequate for qualitative studies of the general circulation, and is comparable in accuracy to values obtained in general circulation models. For simple climate models and qualitative process studies, it can thus provide a useful approach.

Introduction. The poleward eddy transport of westerly momentum, crucial to the maintenance of the zonally averaged distribution of zonal winds, is to a large extent directed against the gradient of zonally averaged angular velocity. This countergradient flux cannot be described by the "diffusion" or "mixing" hypothesis because such a formulation either yields downgradient fluxes, or, if one insists upon countergradient fluxes, negative values of the exchange coefficients. The first option does not fit the data and the second is objectionable on physical grounds.

Various parameterizations of the momentum flux have been propsed. Williams and Davies (1965) parameterized the momentum flux in terms of the mean meridional temperature gradient using an eddy viscosity as the constant of proportionality. From their numerical results they concluded that this type of relation satisfactorily represented the main functions of the large eddies. Saltzman and Vernekar (1968) suggested a more elaborate expression based on the tilting of the trough lines in barotropic flow and a balance between the rate of convergence of momentum and its removal by friction. Their formulation also gave satisfactory agreement with observation.

A different approach to parameterizing the poleward eddy transport of westerly momentum is discussed by Green (1970). The chief characteristic of his theory is that the concept of "mixing" is avoided by finding the transfer of quantities, conserved during the eddy-lifetime,

directly in terms of trajectories. He shows that the transfer of entropy is related to the mean gradient and that this transfer can be formalized in terms of observable mean quantities.

An aspect of Green's parameterization that has not been tested is the quasi-geostrophic relation between the fluxes of momentum, potential vorticity and potential temperature. This relation forms the heart of Green's parameterization. It is not clear to what extent it is satisfied in the atmosphere or in a primitive equation model of the atmosphere in which the large-scale eddy motion is explicit. The numerical calculations of Simmons and Hoskins (1976), for example, do show substantial differences between the quasi-geostrophic and primitive equation momentum fluxes accompanying the most unstable baroclinic waves.

Our purpose is to test the quasi-geostrophic relation for atmospheric data by computing the convergence of momentum flux as a residual of the potential temperature and potential vorticity fluxes and comparing it to the momentum flux convergence computed directly. If the large-scale eddy fluxes are nearly quasi-geostrophic, the convergence of momentum flux, computed as a residual of the potential temperature and potential vorticity fluxes, should equal the convergence of eddy momentum flux computed directly.

Equations. From the quasi-geostrophic potential vorticity equation on a β-plane and the geostrophic approximations, one obtains an expression for the convergence of eddy momentum flux as a function of the potential vorticity and potential temperature flux:

$$\frac{\partial \overline{u'v'}}{\partial y} = -\overline{v'q'} + f_0^2 \frac{\partial}{\partial p}\left(\overline{\frac{v'}{\sigma}\frac{\partial \psi'}{\partial p}}\right) \qquad (1)$$

where q is the quasi-geostrophic potential vorticity.

To test this relationship we must evaluate q in terms of observable quantities. We denote by Q the potential vorticity computed from the observed eastward wind speed, U, and the observed northward wind speed, V. For quasi-geostrophic flow we obtain the following expression which allows us to test the quasi-geostrophy of the momentum flux in terms of observable quantities:

$$\frac{\partial \overline{u'v'}}{\partial y} = \frac{\partial \overline{U'V'}}{\partial y} - \overline{U'\frac{\partial V'}{\partial y}} - f_o\overline{\frac{\alpha'}{\sigma}\frac{\partial V'}{\partial p}} \qquad (2)$$

We will refer to the terms in these equations in their β-plane formulation, although our numerical calculations were performed in spherical coordinates.

Global data set. The basic data set, covering the period July 1976 through June 1977, consists of twice daily (0000 and 1200 GMT) analyses of the wind and temperature fields for the Northern Hemisphere, as made by the U.S. National Meteorological Center (NMC). A set of this data has been obtained for climate studies at GISS from the archive at the National Center for Atmospheric Research (NCAR). The analyses are based on Flattery's global analysis scheme with 12 h operational forecasts used as the first guess field. With the exception of the

zonally averaged meridional wind (which is forced to zero), the values produced by Flattery's analysis are presumed unbiased.

The values of $\partial \overline{U'V'}/\partial y$, $\overline{U'\partial V'}/\partial y$ and $f\overline{\alpha'\partial V'}/\sigma\partial p$ were computed for a 4° x 5° latitude-longitude grid resolution for pressure levels 200, 300, 400, 550 and 700 mb, and then averaged for levels 200 to 400 mb and 400-700 mb.

Results. The main computational results will be presented in terms of seasonal averages: winter (December, January, February), spring (March, April, May), summer (June, July, August), and fall (September, October, November).

Fig. 1a shows the observed and quasi-geostrophic momentum flux convergences as a function of latitude and pressure for pressure levels A for winter. Qualitatively, the observed and quasi-geostrophic convergences are similar during all seasons for both the mid(400 mb - 700 mb) and upper (200 mb - 400 mb) troposphere. Quantitatively, the difference between the observed and quasi-geostrophic momentum flux convergence is largest at latitudes where the convergence is a maximum.

The numerical difference between the observed and quasi-geostrophic momentum flux convergence is given by the sum of the last two terms on the RHS of (2). When these terms are small, the observed momentum flux convergence is quasi-geostrophic. Each of these terms is shown as a function of latitude and pressure in Fig. 1b for winter. During all seasons, the terms are of opposite sign at most latitudes south of 60; at some latitudes between 45° and 25° the terms are both opposite in sign and equal in order of magnitude. By examining only the

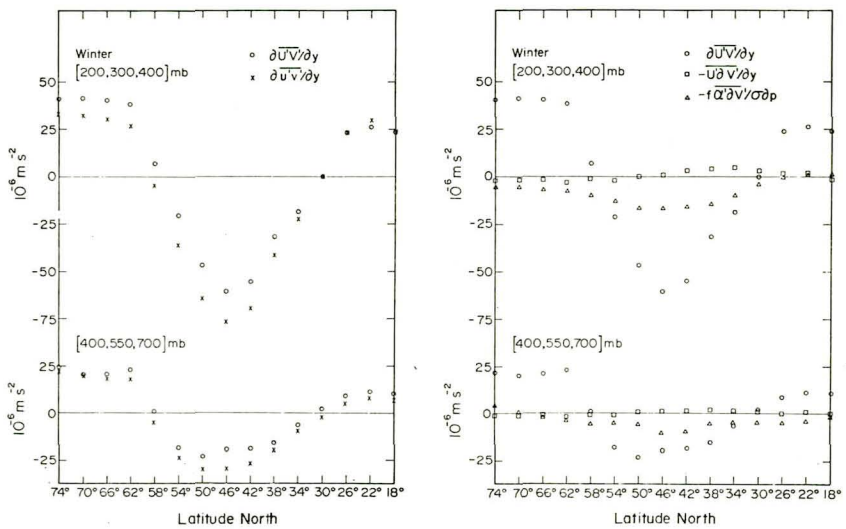

Fig. 1 (a) The winter average of the observed and quasi-geostrophic momentum flux convergence as a function of latitude for the indicated pressure levels. (b) The winter average of the terms in (2) as a function of latitude for the indicated pressure levels.

sum of these terms, we could falsely conclude that the observed fluxes are more quasi-geostrophic than they actually are. We use $|\alpha' \overline{\partial v'/\sigma \partial p}| / |\partial \overline{U'V'}/\partial y|$ as a measure of the degree of quasi-geostrophy, and define the relative error as the ratio $|\alpha' \partial V'/\sigma \partial p|_{Max} / |\partial U'V'/\partial y|_{Max}$ and the absolute error as $|\alpha' \partial V'/\sigma \partial p|_{Max}$. The subscript "Max" refers to the maximum values of these quantities for a given tropospheric level and season.

The relative and absolute errors for pressure levels A are listed as a function of tropospheric level and season in Table 1. As can be seen, the degree of quasi-geostrophy of the observed momentum flux convergence, as measured by the relative error, ranges from 25%-41% in the upper troposphere and 26%-60% in the mid troposphere. In the upper troposphere the relative error for winter, spring, and fall is about 30% less than for summer. A comparison of mid and upper tropospheric relative errors indicates that the relative errors in the mid troposphere are 50% greater than the relative errors of the upper troposphere during all seasons except winter. However the relative errors only exceed 30% at levels or in seasons when the momentum convergence is small and relatively unimportant.

SEASON / PRESSURE		Winter		Spring		Summer		Fall		Annual	
		Abs. Error 10^{-6} m s^{-2}	Rel. Error	Abs. Error 10^{-6} m s^{-2}	Rel. Error	Abs. Error 10^{-6} m s^{-2}	Rel. Error	Abs. Error 10^{-6} m s^{-2}	Rel. Error	Abs. Error 10^{-6} m s^{-2}	Rel. Error
Pressure levels A	200,300,400	17	.29	10	.25	9	.41	11	.26	11	.29
	400,550,700	6	.26	8	.38	6	.60	7	.41	5	.29
Pressure levels B	150,200,250	11	.17	6	.16	4	.20	10	.25	7	.18
	200,250,300	14	.20	11	.24	10	.40	9	.19	10	.24
Pressure levels A with constant σ	200,300,400	17	.29	6	.15	7	.32	8	.19	7	.18
	400,550,700	8	.35	5	.24	5	.50	5	.29	4	.24

Table 1. Relative and absolute errors as a function of season for pressure levels A, B and pressure levels A with constant σ.

In the numerical calculations above, the term $\alpha' \partial V'/\sigma \partial p$, which has been a measure of quasi-geostrophy, was computed with a pressure dependent σ. In quasi-geostrophic theory, however σ is often assumed independent of pressure. Thus $\alpha' \partial V'/\sigma \partial p$ was also computed from pressure levels A data with σ artificially fixed at its mid-tropospheric value of $3.4 \times 10^{-6} m^4 s^2 kg^{-2}$. Table 1 shows that in the mid and upper troposphere the absolute error for constant σ is less than for the corresponding variable σ values in the annual mean and during all seasons except winter. The constant σ results are the same as those with variable σ in the sense that mid-tropospheric relative errors are still 50% greater than the upper-tropospheric relative errors during spring, summer, and fall.

To determine the sensitivity of the momentum flux convergence

to the horizontal resolution, the NMC data were interpolated to an $8° \times 10°$ latitude-longitude grid. The results were identical to those described above and are thus not shown here.

Summary. With our measure of relative error we have shown that the observed momentum flux convergence averaged seasonally is quasi-geostrophic within 25%-40% in the upper troposphere and within 25%-60% in the mid troposphere. The observed momentum flux convergence averaged annually is quasi-geostrophic within 30% in the mid and upper troposphere. The degree of quasi-geostrophy is slightly greater for a constant static stability than for a static stability dependent on pressure.

Since the relative errors do not exceed 30% except when the absolute values are small and relatively unimportant, the momentum flux convergence computed from quasi-geostrophic theory is a satisfactory approximation for qualitative studies of the general circulation. In fact, the accuracies are as good as provided by current general circulation models. It thus can be usefully employed in simple climate models and qualitative process studies.

Acknowledgements. I wish to express my gratitude to Dr. Peter Stone for his helpful suggestions. The research was supported through a NAS-NRC Resident Research Associateship at GISS.

REFERENCES

Green, J.S.A., "Transfer properties of the large-scale eddies and the general circulation of the atmosphere," Quart. J. Roy. Meteor. Soc., 96, 157-185, 1970.

Saltzmann, B. and Vernekar, "A parameterization of the large-scale transient eddy flux of relative angular momentum," Mon. Wea. Rev., 96, 854-857, 1968.

Simmons, A.J. and B.J. Hoskins, "Baroclinic instability on the sphere: Normal modes of the primitive and quasi-geostrophic equations," J. Atmos. Sci., 33, 1454-1477, 1976.

White, A.A., "The surface flow in a stratified climate model - a test of a parameterization of large-scale momentum fluxes. Quart. J. Roy. Meteor. Soc., 103, 93-119, 1977.

Williams, G.P. and D.R. Davies, "A mean motion model of the general circulation," Quart. J. Roy. Meteor. Soc., 91, 471-489, 1965.

Page intentionally left blank

Paper No. 64

SPATIAL AND TIME DOMAIN SPECTRAL ENERGETICS IN THE GLAS GENERAL CIRCULATION MODEL

J. Tenenbaum, *State University of New York, Purchase, New York*

ABSTRACT

Zonally averaged eddy kinetic energies and time domain energetics spectra have been calculated for the new GLAS general circulation model. The spatial results show significant improvements in the magnitude and distribution of the eddy kinetic energy. The spectral results provide a technique for tracing when and where the model predictions diverge from observations.

Introduction

Three major approaches are used to check agreements between general circulation models and the real atmosphere: synoptic comparisons, climate mean statistics, and time domain analyses. All three attempt to quantify the model's success and identify the details of its failure. Time domain analyses also permit one to study how to extract the maximum possible information at times approaching the predictability limit. The usual example here is one's intuitive belief that some skill should remain in the low wave number spectral coefficients even after grid point values have approached the noise level. Since only limited success has been obtained in this regard, a related question is where, in detail, is the model going wrong.

Method

Energetics calculations involve subdividing atmospheric energy into four components: zonal kinetic energy (KO), eddy kinetic energy (KE), zonal potential energy (PE). The eddy energies may be further subdivided by calculating the one-dimensional Fourier transforms around each latitude circle, P(n) and K(n). Further details of the calculations are given in Tenenbaum, 1976. In this report, we use the formulas given there to evaluate new model and observational runs for January 1975 and 1977 (Halem et al., 1978). The domain of comparison is the northern hemisphere troposphere.

Spatial Results

The primary improvement in the new model occurs in the magnitude and distribution of KE. Fig. 1 shows the zonally averaged KE for the model, the corresponding observations, and a climatic mean. The model distribution is significantly less diffuse than previous results (Tenenbaum, 1976, Fig. 15). The qualitatively incorrect behavior of the conversion from KE to KO has also been eliminated and one now obtains the characteristic dipole structure (Tenenbaum, 1976, Fig. 17).

Time Domain Spectra

An excellent example of the model following the behavior of

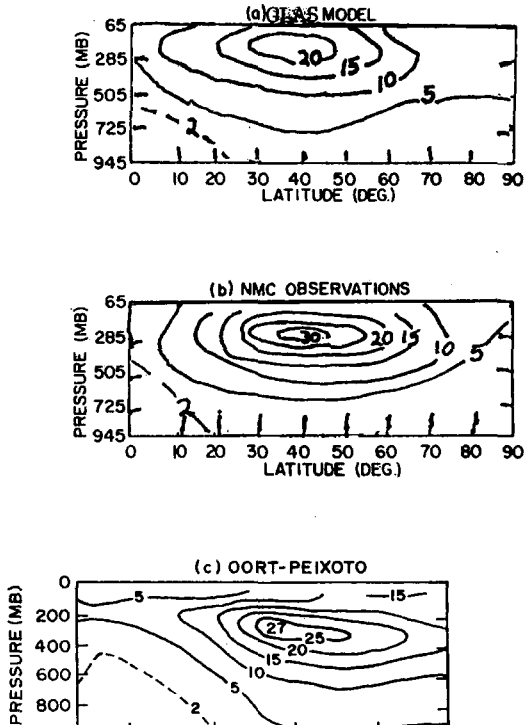

Fig. 1. (a) Spatial distributions of the eddy kinetic energy, KE. Data are for the northern hemisphere troposphere, January 1975, for the GLAS model. (b) NMC observations. (c) Climatic means from Peioxto and Oort (1974). Units: 10^5 J/(m^2 bar).

the atmosphere for almost two weeks is given in Fig. 2a (January 1977). Significant skill is maintained for a highly averaged quantity, KE, right out to the predictability limit. Fig. 3a (January 1975) shows another example where a discrepancy occurs after only 5 days. An important value of time dependent spectral techniques is to let us pursue the cause of the discrepancy in Fig. 3a. Most KE is contained in the lowest few wave numbers, and on comparing model and observation wave number by wave number we find that the primary difference is in wave number 3. This quantity is shown in Fig. 3b for the first 15 days of the model run. Note that the major portion of the KE discrepancy for days 5 through 10 is explained by the elevated values of K(3) during this period. Just previous to this period the fall of K(3) was compensated for by small contributions from many other wave numbers.

Time domain spectral techniques permit us to analyze the disagreements further by examining all of the conversions to and from K(3). These are: conversions from PE and all other K(n) and conversions to KO and sub-grid scales (dissipation). For this case only the conversion from P(3) to K(3) has major disagreements between model and observations (Fig. 3c). Note that the positive and negatives excursions of the model's K(3) seem causally linked to this conversion.

A spectral analysis also permits us to verify whether the model is accurately predicting the time dependence of each K(n) even when it is properly calculating the sum. Although the KE predictions in Fig. 2a are quite good, Fig. 2b and 2c show that the sum masks an erroneous distribution between K(1) and K(3).

Conclusions

Time domain spectral energetics provides a tool which deals with quantities displaying significant skill over periods comparable to the predictability limit. More importantly, we can (1) pinpoint the specific times and conversions which appear causally correlated with departures between model and observations; and (2) isolate cases where apparently correct predictions of KE mask major errors in its spectral components. By examining the spatial dependence of both the spectral components and conversions, we may seek linkages with erroneous physical processes in the model.

References

Halem, M., J. Shukla, Y. Mintz, M.L. Wu, R. Godbole, G. Herman, and Y. Sud, 1978: Climate comparisons of a winter and summer numerical simulation with the GLAS general circulation model. Proceedings of the JOC Study Conference on climate models, April 1978, Washington, D.C.

Peixoto, J.P., and A.H. Oort, 1974: The annual distribution of atmospheric energy on a planetary scale. J. Geophys. Res., 79, 2149-2159.

Tenenbaum, J., 1976: Spectral and spatial energetics of the GISS model atmosphere. Mon. Wea. Rev., 104, 15-30.

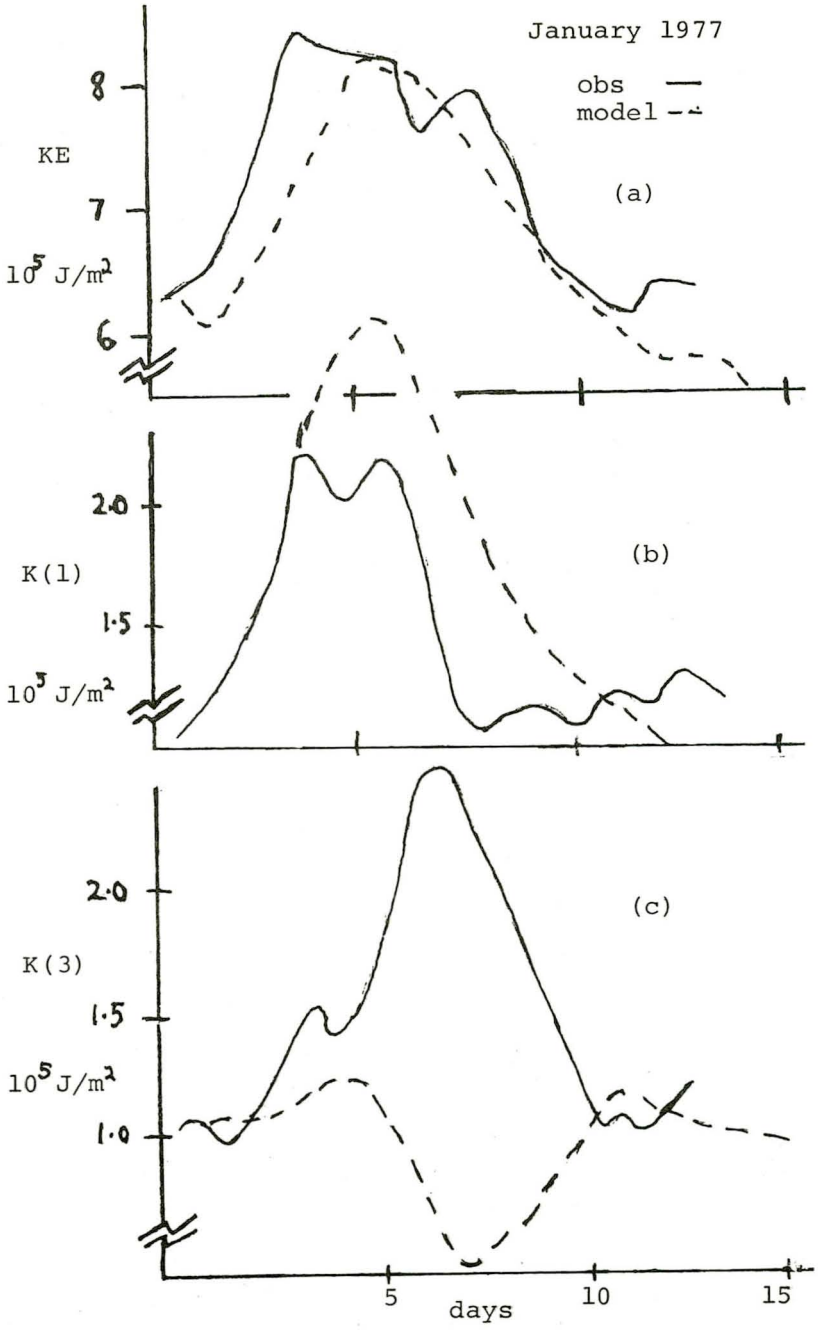

Fig. 2. (a) KE, (b) K(1), and (c) K(3) for January 1977 over the northern hemisphere troposphere.

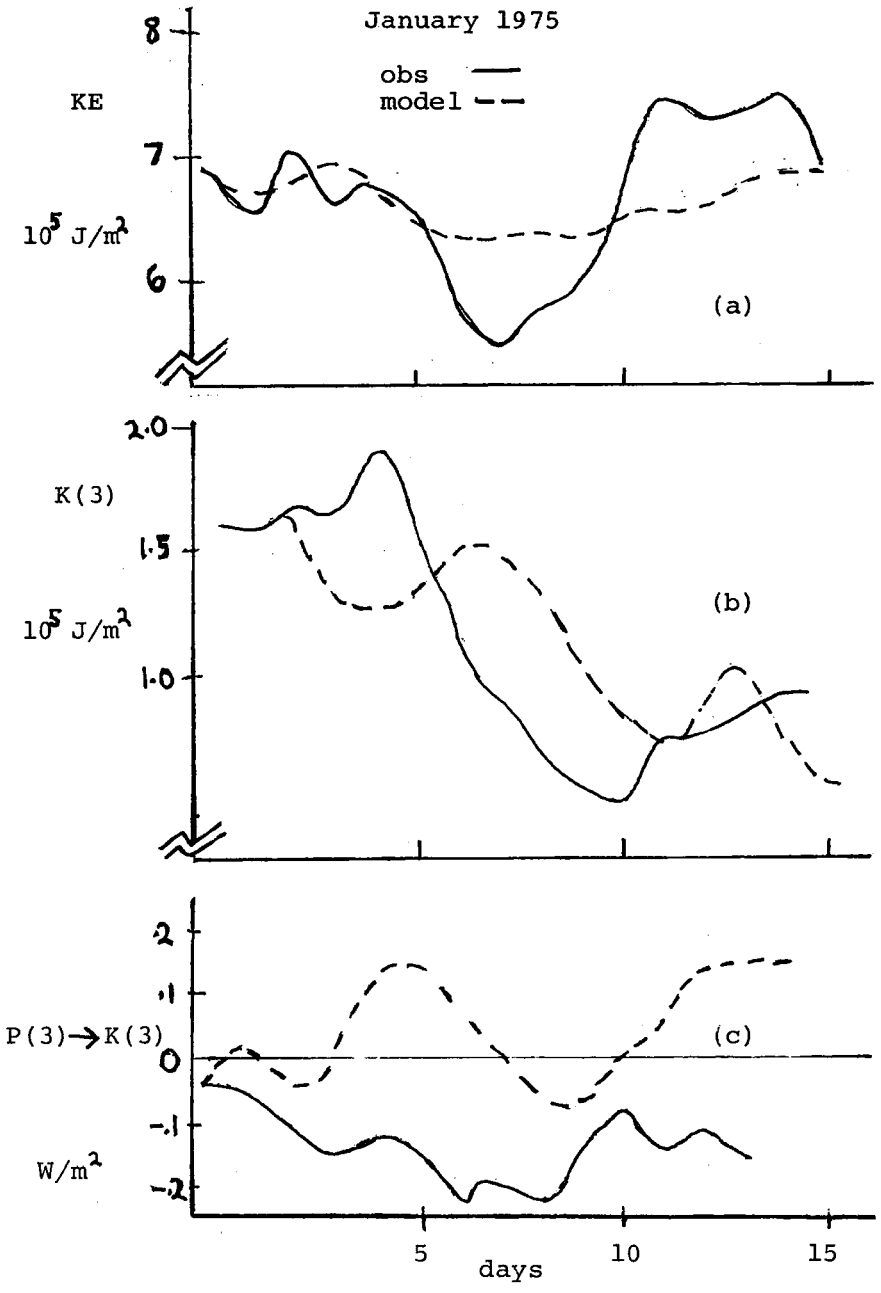

Fig. 3. (a) KE, (b) K(3), and (c) P(3) K(3) for January 1975 over the northern hemisphere troposphere.

Paper No. 65

LONG-TERM MIGRATION OF THE SOLAR SECTOR STRUCTURE

C. L. Wolff and D. F. Heath, *Goddard Space Flight Center, Greenbelt, MD*

INTRODUCTION

Periodicities are often seen in weather records and immediately dismissed as not due to solar variability because the period is not a simple multiple of 27 days or 11 years. This is wrong because solar observations of the last few centuries show numerous other periodicities ranging from many months to many years. A theory is now under development which can predict the values of these periods and which will put this subject on a sound physical basis if the theory continues to be successful. Weather records can then be analyzed in a more comprehensive and respectable manner because the variable solar input will be more rigorously modelled.

The magnetic sector boundaries on the sun and in the solar wind have a high correlation with winter low pressure systems on earth. Roberts and Olson (1973) and Wilcox, et al. (1974) found that the vorticity-area index typically declines by about 10% during several days centered on the time when a sector boundary sweeps past the earth. The physical connection between these two events is not established. A whole group of other correlations exists between weather and solar activity (Goldberg and Herman, 1978). Again, much of the detailed physics is in doubt. Progress in understanding these phenomena is slow, partly because there are a very large number of possible explanations--each with its free parameters--and a relatively modest number of truly independent observational results. This paper is part of a continuing attempt to reduce the degrees of freedom available to sun-weather theories and, perhaps, to discover some more fundamental inputs to those theories. In what follows, we present new evidence that BOTH the sector structure and solar activity levels can be understood as being under the influence of the same regular, internal solar mechanism. Because of this, long-term predictions of each phenomenon may ultimately be possible.

Observed Position of Sector Boundaries

There are now available 50 years of observations of the magnetic sector boundaries, both those detected by spacecraft and those inferred from high latitude geomagnetic records. Svalgaard and Wilcox (1975) published the data for the predominant 4-sector pattern. The whole pattern is defined by giving the solar longitude of one of the boundaries and their result appears at the top of Figure 1. Each short horizontal dash on the figure represents the longitude of the boundary, averaged over 37 solar rotations. However, a new average is made every 6 rotations, forcing the graph to be fairly smooth. Approximately then, their graph displays 3 year averages of boundary locations updated every one-half year. Svalgaard and Wilcox concentrated on trends lasting for many years and pointed out these two tendencies: Prior to each minimum of sunspot activity the boundary migrates toward larger longitudes (corresponding to a rotation period of about 27.15 days) and after the minimum it migrates toward smaller longitudes (period ≈26.85 days). For our purposes, more information can be obtained by considering the many shorter-term trends which could also have been defined by this data. We have identified with the broken curve all trends lasting more than half a year, in the raw data. For clarity, the broken curve is displaced downward by 4 days of longitude relative to the raw data on Figure 1. The slope of each segment of the broken curve gives the mean drift of the sector boundary in that time interval. We will now compare these 27 drift rates with theoretical expectations.

Comparison with Theory

First, we give a very brief summary of the theory which has been developed in a series of papers during the last four years. It is based on the normal modes of oscillation of a star, those whose amplitudes are large in the interior but small at the surface. Astronomers call these g-modes. Oscillation periods appropriate for these modes have already been seen in the sun by groups in Arizona and the Soviet Union (Hill, 1977). Once these modes are excited in a slowly rotating star like the sun, their rotation periods are one of the more reliably predictable properties. Each mode has a rotation period which is a simple function of its angular harmonic number if the lowest radial harmonics are ignored. Precise beat periods are also calculable as the antinodes of various modes rotate into temporary alignment with each other. The beat periods range from many years down to fractions of a year. The pattern containing many of these beat periods has already been detected to a high degree of certainty in records of sunspot activity for the last two and one-half centuries (Wolff, 1976). In summary, beats occurring deep inside the sun appear to be causing the main episodes (lasting many months) of solar activity. We now ask the question: Do these same beats have any demonstrable effect on the migration of sector boundaries?

The beat and its associated convective upwelling will be assumed to have a significant physical interaction with the sector structure at the surface. It follows that there must be a relative alignment between the longitude of the beat and the longitude of a sector boundary which minimizes their interaction energy. This is the stable configuration. (Probably, boundaries caused by upwelling fluid will prefer to be at the same longitude as the beat.) When a new beat develops at some other longitude, it should accelerate the appropriate sector boundary toward it. Figure 2 shows the torque which we expect the oscillation modes to exert in each one-half year interval into which Svalgaard and Wilcox subdivided their observations. A positive torque is one pulling the sector boundary toward higher Bartels longitude. The torque was modelled very simply by the function,

$$\sum_{i} A \sin \left[B(L_i - L_{sb})\right]$$

where L_i is the longitude of the i^{th} beat occurring in the time interval, L_{sb} is the observed longitude of the sector boundary, and A is an unknown proportionality constant taken as unity. For our unit of longitude which ranges from 0 to 27 days, B = (4 π radians)/(27 days) which is the proper value for a pattern of 2 sector boundaries of upwelling and 2 of subsidence. It is clear from Figure 2 that many rapid changes are to be expected in the direction of migration of the sector structure. Unfortunately, the observations were heavily smoothed and have lost much of this detail. But, by averaging the theory over intervals longer than one-half year increments of Figure 2, a valid comparison becomes possible. We computed the mean theoretical torque in each of the 27 time intervals corresponding to segments of the broken curve identifying trends in the observations. Then we plotted these against the mean observed drift in the same intervals, Figure 3 is the result and it shows a significant correlation which we have fitted with the straight line. This figure shows that, over its 50 year history, this sector boundary has tended to drift towards the longitudes where beats between oscillation modes were located.

Figure 3 is our first preliminary view of this correlation. The points have a rather large scatter which can be reduced in the future by several improvements. First, the observers can be encouraged to shorten or remove the 3 year smoothing of their observations to permit more of the expected detailed motions to appear. Secondly, the theory can be upgraded by taking into account the known lifetimes of each individual beat and the varying strengths of the oscillation modes. Up to now, the theory has been used in its most primitive form so as to eliminate virtually all free parameters except for an essential statement of how many oscillation modes are being considered. In this paper, we used all the modes from spherical harmonics ℓ = 4 to ℓ = 9 in equal strength. This is similar to the range found appropriate in earlier work for matching periodicities in solar activity.

References
J.R.Herman and R.A.Goldberg 1978, "Sun, Weather, and Climate", NASA SP-426.
H.A.Hill 1977, In "The New Solar Physics", ed. J.A.Eddy, (AAAS, Washington).
W.O.Roberts and R.H.Olson 1973, J. Atmos. Sci., 30, 135.
L.Svalgaard and J.M.Wilcox 1975, Solar Physics, 41, 461.
C.L.Wolff 1976, Astrophysical J., 205, 612.

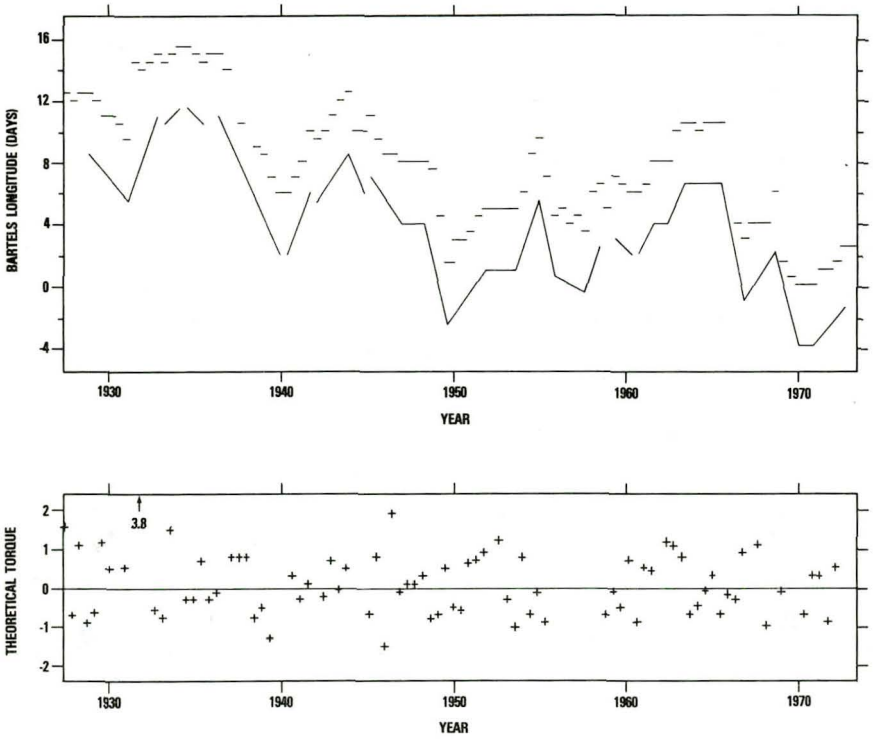

Fig. 1--(upper graph) History of the solar sector boundary migration since the year 1926. Short horizontal dashes locate the boundary longitudes determined by Svalgaard and Wilcox for each interval of 6 solar rotations ($\simeq \frac{1}{2}$ year). Pronounced trends in the observations, lasting from one to four years, are emphasized by the diagonal line segments just below.

Fig. 2--(lower graph) The torque expected to be exerted upon the sector structure by beats between the theoretical system of solar oscillation modes.

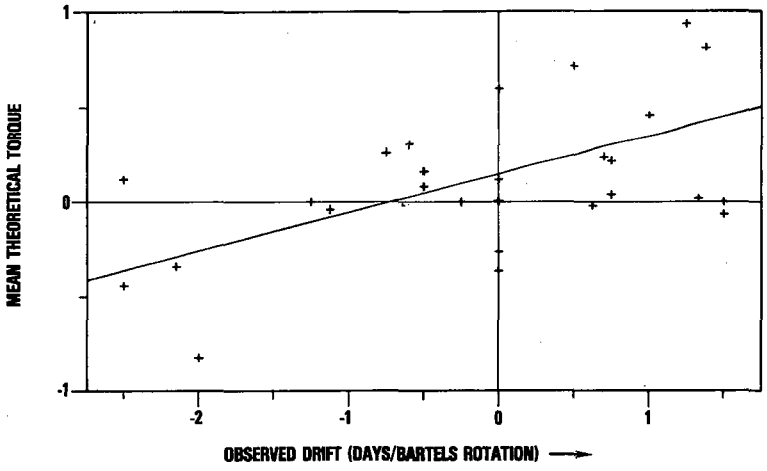

Fig. 3--The torque exerted by solar beat phenomena is compared to the observed drift in longitude of the magnetic sector structure. Each point corresponds to one of the 27 pronounced trends marked on Figure 1. The positive correlation shown on this graph indicates that the beats are influencing the location of the sector boundaries.

Page intentionally left blank

AUTHOR INDEX

NASA WEATHER AND CLIMATE PROGRAM
SCIENCE REVIEW

ATTENDEES

Robert F. Adler
Goddard Space Flight Center
Code 914
Greenbelt, MD 20771
(301) 344-7885

Suraiya Ahmad
Systems & Applied Sciences Corp.
6811 Kenilworth Avenue
Riverdale, MD 20840
(301) 699-5400

Ziauddin Ahmad
Systems & Applied Sciences Corp.
6811 Kenilworth Avenue
Riverdale, MD 20840
(301) 699-5400

M. A. Alaka
NOAA/NWS
8060 13th Street
Silver Spring, MD 20910
(301) 427-7772

Richard W. Anthony
GE/MATSCO
5050 Power Mill Road
Beltsville, MD 20705
(301) 932-3500

Albert Arking
Goddard Space Flight Center
Code 915
Greenbelt, MD 20771
(301) 344-7208

George D. Ashton
U.S. Army
Cold Regions Research & Engr. Lab.
Hanover, NH 03766
(603) 643-3200

David Atlas
NASA, Lab. for Atmospheric Sciences
Code 910
Goddard Space Flight Center
Greenbelt, MD 20771
(301) 344-6925

Robert M. Atlas
Goddard Space Flight Center
Code 911
Greenbelt, MD 20771
(301) 344-7519

Ferdinand Baer
University of Maryland
Meteorology Program
College Park, MD 20742
(301) 454-2708

Wayman E. Baker
NRC/GLAS
Goddard Space Flight Center
Code 911
Greenbelt, MD 20771
(301) 344-7509

William R. Bandeen
Goddard Space Flight Center
Code 910
Greenbelt, MD 20771
(301) 344-8406

Jon F. Bartholic
101 Agr. Hall
Michigan State University
E. Lansing, MI 48824

William L. Barnes
Goddard Space Flight Center
Code 941
Greenbelt, MD 20771
(301) 344-8117

E. Stanley Batten
Jet Propulsion Laboratory
4800 Oak Grove Drive
Pasadena, CA 91103
(213) 354-7151

Thomas D. Bess
Langley Research Center
Hampton, VA 23665
(804) 827-3431

P. K. Bhartia
SAS/OPT
Goddard Space Flight Center
Code 931.6, Bldg. 18
Greenbelt, MD 20771
(301) 344-7285

William P. Bishop
NASA, HQS. Code EB8
Washington, DC 20546
(202) 755-8617

Walter T. Blackshear
Langley Research Center
Hampton, VA 23665
(804) 357-3270

Frank D. Carsey
Goddard Space Flight Center
Code 913
Greenbelt, MD 20771
(301) 344-8513

Wen-Yuan W. Chen
NOAA/EDIS/CEAS
10525 Farnham Dr.
Bethesda, MD 20014
(202) 634-7288

Chieh-San Cheng
OAO Corp.
5050 Powder Mill Road
Beltsville, MD 20705
(301) 937-3090

John P. Claybourne
John F. Kennedy Space Center
Code SA
Kennedy Space Center, FL 32899
(305) 867-4541

Robert C. Costen
Langley Research Center
Code 423
Hampton, VA 23665
(804) 827-3431

Norman L. Crabill
Langley Research Center
Code 247
Hampton, VA 23665
(804) 827-3274

C. David Crandall
Naval Research Lab. Bldg. 209
Code 7006
Washington, DC 20375
(202) 767-3848

Howard J. Curfman, Jr.
Langley Research Center
Code M.S. 422
Hampton, VA 23665
(FTS) 928-2717

Paul C. Dalrymple
Dept. of Army
Engineer Topographic Labs.
Ft. Belvoir, VA 22060
(703) 664-1561

Giuseppe Dalu
Goddard Space Flight Center
Code 915
Greenbelt, MD 20771
(301) 344-8724

Paul A. Davis
Systems & Applied Sciences Corp.
6811 Kenilworth Ave. Suite 610
Riverdale, MD 20840
(301) 864-4157

Bernard C. Diesen
NSSDC
Goddard Space Flight Center
Code 601
Greenbelt, MD 20771
(301) 344-8556

James C. Dodge
NASA, HQS
Code EBT-8
Washington, DC 20546
(202) 755-8596

Currie S. Downie
NSF
1800 G Street, N.W. Rm. 644
Washington, DC 20550
(202) 632-4297

Leland L. DuBach
Goodard Space Flight Center
Code 901
Greenbelt, MD 20771
(301) 344-5056

Jerome Eckerman
Goodard Space Flight Center
Code 946
Greenbelt, MD 20771
(202) 344-6781

Daniel L. Endres
Goddard Space Flight Center
Code 942
Greenbelt, MD 20771
(301) 344-8670

Francis E. Fendell
TRW(R1/1038)
1 Space Park
Redondo Beach, CA 90278
(213) 536-1624

Douglas D. Fenn
GE/MATSCO
5050 Powder Mill Road
Beltsville, MD 20705
(301) 344-6351

George H. Fichtt
Marshall Space Flight Center
Code ES82
Huntsville, AL 35803
(FTS) 872-0875

James L. Foster
Goddard Space Flight Center
Code 913
Greenbelt, MD 20771
(301) 344-8741

Robert S. Fraser
Goddard Space Flight Center
Code 915
Greenbelt, MD 20771
(301) 344-5786

Paul O. Frederickson
Goddard Space Flight Center
Code 911
Greenbelt, MD 20771
(301) 344-4695

John E. Geisler
University of Miami
4600 Rickenbacker Causeway
Miami, FL 33149
(305) 350-7257

Richard A. Goldberg
Goddard Space Flight Center
Code 912
Greenbelt, MD 20771
(301) 344-8603

James R. Greaves
Goddard Space Flight Center
Code 910.2
Greenbelt, MD 20771
(301) 344-7624

Bruce W. Guenther
Goddard Space Flight Center
Code 912
Greenbelt, MD 20771
(301) 344-8538

Isidore M. Halberstam
Jet Propulsion Laboratory
4800 Oak Grove Drive
Pasadena, CA 91103
(213) 354-2394

Milton Halem
Goddard Space Flight Center
Greenbelt, MD 20771
(301) 344-7482

Harshvardhan
University of Maryland
Goddard Space Flight Center
Code 915
Greenbelt, MC 20771
(301) 344-6360

Arthur F. Hasler
Goddard Space Flight Center
Code 914
Greenbelt, MD 20771
(301) 344-7885

Donald F. Heath
Goddard Space Flight Center
Code 912
Greenbelt, MD 20771
(301) 344-6421

Gerald F. Herman
University of Wisconsin
Dept. of Meteorology
1225 W. Dayton St.
Madison, WI 53706
(600) 263-2487)

Ernest Hilsenrath
Goddard Space Flight Center
Code 912
Greenbelt, MD 20771
(301) 344-5754

Laurence T. Hogarth
Goddard Space Flight Center
Code 903
Greenbelt, MD 20771
(301) 344-7497

A. C. Holland
Wallops Flight Center
Code DAS/E106
Wallops Island, VA 23337
(804) 824-3411

Lee R. Hoxit
NOAA/ERL
Atmospheric Physics & Chem. Lab.
Boulder, CO 80302
(303) 499-1000

Donald H. Hunt
NOAA/HQS, RDI
6010 Executive Blvd.
Rockville, MD 20852
(301) 443-8971

Edward J. Hurley
Goddard Space Flight Center
Code 941
Greenbelt, MD 20771
(301) 344-6233

Wilber B. Huston
OAO Corp.
5050 Powder Mill Road
Beltsville, MD 20705
(301) 937-3090

Karl R. Johannessen
NOAA/NWS
8060 13th Street
Silver Spring, MD 20910
(301) 427-7700

Winthrop T. Johnson
Goddard Space Flight Center
Code 911 - Bldg. 22
Greenbelt, MD 20771
(301) 344-7438

James B. Jones
NOAA/NWS
Code W12
8060 13th Street
Silver Spring, MD 20910
(301) 427-7704

Bert B. Katz
University of Maryland
Dept. of Meteorology
Space Sciences Bldg.
College Park, MD 20742
(301) 454-5199

Ashok Kaveeshwar
Systems & Applied Sciences Corp.
Goddard Space Flight Center
Code 931.6 Bldg. 18
Greenbelt, MD 20771
(301) 344-7285)

Vernon W. Keller
Marshall Space Flight Center
Atmospheric Science Div.
Code ES 83
Huntsville, AL 35812
(205) 453-0941

Stanley Q. Kidder
Colorado State University
Dept. of Atmospheric Science
Fort Collins, CO 80521
(303) 491-8484

James King, Jr.
Jet Propulsion Laboratory
4800 Oak Grove Drive
Pasadena, CA 91103
(213) 354-7546

Larry J. King
Goddard Space Flight Center
Code 946
Greenbelt, MD 20771
(301) 344-8949

Kenneth F. Klenk
Systems & Applied Sciences Corp.
6811 Kenilworth Ave.
Riverdale, MD 20840
(301) 864-4150

Earl R. Kreins
Goddard Space Flight Center
Meteorology Program Office
Code 901
Greenbelt, MD 20771
(301) 344-5056

Andrew A. Lacis
Goddard Institute for Space Studies - 2880 Broadway
New York, NY 10025
(212) 678-5595)

W. Roger Lambertson
Naval Air Systems Command
Code Air 370G
Washington, DC 20361
(202) 692-7414

Charles R. Laughlin
Goddard Space Flight Center
Code 901
Greenbelt, MD 20771
(301) 344-6291

John A. Laurmann
Stanford University
Division of Applied Mechanics
Stanford, CA 94305
(415) 497-2173

David Lee
Systems & Applied Sciences Corp.
Goddard Space Flight Center
Code 931.6
Greenbelt, MD 20771
(301) 344-7137

Jules Lehmann
NASA/HQS
Code ERC-2
600 Independence Ave. SW
Washington, DC 20546
(202) 755-8628

Hendricus G. Loos
Laguna Research Lab.
21421 Stans Lane
Laguna Beach, CA 92651
(714) 494-7858

Daniel H. Lufkin
NOAA/OA3
Rockville, MD 20852
(301) 443-8734

Louis A. Mayo
Systems & Applied Sciences Corp.
9601 Lorain Ave.
Silver Spring, MD 20901
(301) 588-8185

Raymond A. Minzner
Goddard Space Flight Center
Code 914
Greenbelt, MD 20771
(301) 344-5786

Dudley G. McConnell
NASA/Natl. Climate
Program Office
6010 Executive Blvd.
Rockville, MD 20852
(301) 443-8981

Andrew W. McCulloch
Goddard Space Flight Center
Code 480
Greenbelt, MD 20771
(301) 344-8079

William J. McKechney
USAF/AFOSR/MC
Bolling AFB, DC 20332
(202) 767-4963

Ernest A. Neil
Goddard Space Flight Center
Code 901
Greenbelt, MD 20771
(301) 344-6291

Henry Newhouse
NOAA/NWS
8060 13th St. (W411)
Silver Spring, MD 20910
(301) 427-7781

James R. Norton
Systems & Applied Sciences
Corp. Suite 610
6811 Kenilworth Ave.
Riverdale, MD 20840
(301) 699-5400

Vincent J. Oliver
NOAA/NESS
World Weather Bldg.
Camp Spring, MD 20023
(301) 763-8282

Hugh M. O'Neil
NOAA/NWS (W413)
8060 13th St. N.W.
Silver Spring, MD 20901
(301) 427-7780

Stephen P. Palm
University of Maryland
4505 Ronlon St. Apt. 104
Beltsville, MD 20705
(301) 937-3792

John J. Park
National Research Council
Resident Research Associate
Code 913
Goddard Space Flight Center
Greenbelt, MD 20771
(301) 344-5377

William A. Pearce
EG&G/ Washington Analytical
Services Center
6801 Kenilworth Ave.
Riverdale, MD 20840
(301) 779-2800 X247

Cynthia A. Peslen
Goddard Space Flight Center
Lab. of Atmospheric Sciences
Code 914
Greenbelt, MD 20771
(301) 344-6360

Serhij Pilipowskyj
USAF/AFSC/WE
Andrews AFB, MD 20331
(301) 951-2743

Cuddapah Prabhakara
Goddard Space Flight Center
Code 915
Greenbelt, MD 20771
(301) 344-6369

J. Purdom
NOAA/NESS
World Weather Bldg. Rm. 601
Suitland, MD 20023
(301) 763-8282

Robert M. Rados
Goddard Space Flight Center
Code 901
Greenbelt, MD 20771
(301) 344-6291

Michael R. Rampino
Goddard Institute for Space Studies
2880 Broadway
New York, NY 10025
(212) 678-5573

Mirle S.V. Rao
Systems Applied Sciences Corp.
7800 Hanover Pkwy #202
Goddard Space Flight Center
Code 911
Greenbelt, MD 20770
(301) 365-5577

P. K. Rao
NOAA/NESS
World Weather Bldg. Stop G
Washington, DC 20233
(202) 763-8031

James L. Raper
Langley Research Center
Code 271
Hampton, VA 23665
(804) 827-2977

Ichtiaque S. Rasool
NASA/HQS
Chief Scientist, Code E
Office of Space & Terrestrial Applications
Washington, DC 29546
(202) 755-8734

Francis P. Richards
NOAA/EDIS/CEAS
3300 Whitehaven St. N.W.
Washington, DC 20235
(202) 634-7340

Edward B. Rodgers
Goddard Space Flight Center
Code 914
Greenbelt, MD 20771
(301) 344-6360

Ariel Rosenberg
Sigma Data Services
Goddard Space Flight Center
Code 911
Greenbelt, MD 20771
(301) 344-8721

Robert I. Rosenberg
Sigma Data Services
6015 Springhill Dr. #103
Greenbelt, MD 20770
(301) 474-3025

Robert A. Schiffer
NASA/HQS
Code EBT-8
Washington, DC 20546
(202) 755-8596

Barry M. Schlesinger
Systems & Applied Sciences Corp.
6811 Kenilworth Ave.
Riverdale, MD 20840
(301) 864-4150

Francis J. Schmidlin
Wallops Flight Center
Wallops Island, VA 23337
(804) 824-3411 X618

Howard W. Shaffer
NASA/HQS
Code ESI-5
Washington, DC 20546
(202) 755-8576

Omar H. Shemdin
Jet Propulsion Laboratory
4800 Oak Grove Dr.
Pasadena, CA 91103
(213) 354-2447

Jagadish Shukla
Goddard Space Flight Center
MIT Code 911
Greenbelt, MD 20771
(301) 344-7413

Honnappa Siddalingaiah
Goddard Space Flight Center
Code 946
Greenbelt, MD 20771
(301) 344-5774

Jospeh W. Siry
Goodard Space Flight Center
Code 900
Greenbelt, MD 20771
(301) 344-6662

G. Louis Smith
Langley Research Center
Code M/S 423
Hampton, VA 23665
(804) 827-3431

William A. Sprigg
NOAA/National Climate
Program Office
6010 Executive Blvd.
Rockville, MD 20852
(301) 443-8861

Francis L. Stetina
Goodard Space Flight Center
Code 903
Greenbelt, MD 20771
(301) 344-7626

Richard W. Stewart
Goodard Space Flight Center
Code 912
Greenbelt, MD 20771
(301) 344-8895

Richard S. Stolarski
Goodard Space Flight Center
Greenbelt, MD 20771
(301) 344-5485

Frank S. Stone
OAO Corporation
5050 Powder Mill Road
Beltsville, MD 20705
(301) 937-3090

Max Suarez
UCLA
1114 12th St. 103 SM
Los Angeles, CA 90813
(213) 825-9205

Yogesh Sud
Sigma Data Services
Code 911
Building 22
Goddard Space Flight Center
Greenbelt, MD 20771
(301) 344-8339

Joel Susskind
Goddard Space Flight Center
Code 911
Greenbelt, MD 20771
(301) 344-7210

Robert A. Sutherland
University of Florida
1172 McCarty Hall
Gainesville, FA 32611
(904) 392-4711

John T. Suttles
Langley Research Center
Mail Stop 423
Hampton, VA 23665
(804) 827-3431

Joel Tenenbaum
SUNY Purchase
Division of Natural Sciences
Purchase, NY 10577
(914) 253-5156

Morris Tepper
Goodard Space Flight Center
Code 910.2
Greenbelt, MD 20771
(301) 344-5056

Robert G. Terwilliger
NASA/HQS Code ERC-2
Washington, DC 20546
(202) 755-8596

John S. Theon
NASA/HQS
Code EBT-8
Washington, DC 20546
(202) 755-8619

Otto W. Thiele
Goddard Space Flight Center
Code 910.1
Greenbelt, MD 20771
(301) 344-7624

Charles E. Thienel
Goddard Space Flight Center
Code 480
Greenbelt, MD 20771
(301) 344-6084

Robert W. L. Thomas
EG&G/WASC
6801 Kenilworth Ave.
Riverdale, MD 20804
(301) 779-2800

Shelby G. Tilford
NASA/HQS
Code EBT-8
Washington, DC 20546
(202) 755-8617

Owen B. Toon
Ames Research Center
Code MS 245-3
Moffett Field, CA 94087
(415) 965-5971

Arnold L. Torres
Wallops Flight Center
Wallops Island, VA 23337
(804) 824-3411

Louis W. Uccellini
Goodard Space Flight Center
Bldg. 22 - Code 914
Greenbelt, MD 20771
(301) 344-7519

William W. Vaughan
Marshall Space Flight Center
Code ES-81
Atmospheric Sciences Div.
Huntsville, AL 35812
(205) 453-3100

Friedrich O. Vonbun
Goddard Space Flight Center
Code 900
Greenbelt, MC. 20771
(301) 344-5201

Wei-Chyung Wang
Goddard Institute for Space Studies
2880 Broadway
New York, NY 10025
(212) 678-5589

Robert T. Watson
Jet Propulsion Laboratory
Bldg. 183-601
4800 Oak Grove Drive
Pasadena, CA 91103
(213) 354-2231

William L. Weaver
Langley Research Center
Code MS 271
Hampton, VA 23666
(804) 827-2977

Adolf Werbowetzki
NOAA/NESS
Code F.B. 4
Suitland, MD 20233
(201) 763-5905

Thomas T. Wilheit
Goddard Space Flight Center
Code 946
Greenbelt, MD 20771
(301) 344-5105

Gregory S. Wilson
Marshall Space Flight Center
1023 Antietam Rd. S.E.
Huntsville, AL 35803
(205) 881-6158

Charles V. Woerner
Langley Research Center
Mail Stop 158
Hampton, VA 23665
(804) 827-2303

Mary A. Woerner
Langley Research Center
Hampton, VA 23665
(804) 827-3431

Man-Li C. Wu
Goddard Space Flight Center
Greenbelt, MD 20771
(301) 344-7509

Henry J. Yotko
NOAA/NESS
World Weather Bldg. Rm. 810
Camp Springs, MD 20233
(301) 763-8007

H. Jay Zwally
Goddard Space Flight Center
Code 913
Greenbelt, MD 20771
(301) 344-7895)

BIBLIOGRAPHIC DATA SHEET

1. Report No. NASA CP	2. Government Accession No.	3. Recipient's Catalog No.
4. Title and Subtitle Fourth NASA Weather and Climate Program Science Review-Proceedings of a review held January 24-25, 1979 at the NASA Goddard Space Flight Center, Greenbelt, Maryland.		5. Report Date January 24-25, 1979 6. Performing Organization Code
7. Author(s) Editor, Earl R. Kreins		8. Performing Organization Report No.
9. Performing Organization Name and Address NASA Goddard Space Flight Center Greenbelt, Maryland 20771		10. Work Unit No. 11. Contract or Grant No. 13. Type of Report and Period Covered Fourth Science Review, FY 1978
12. Sponsoring Agency Name and Address Earl R. Kreins Meteorology Program Office, Code 901 NASA Goddard Space Flight Center Greenbelt, Maryland 20771		14. Sponsoring Agency Code

15. Supplementary Notes

16. Abstract

This was the fourth in an annual series of reviews of the principal research accomplishments made within the Weather and Climate Program of the NASA Office of Space and Terrestrial Applications. The review was held to evaluate program progress, provide a basis for the definition of future activities, and exchange information with the meteorological community. These proceedings contain 65 papers covering three general areas: severe storms and local weather research, global weather research, and climate research. Thirty-seven of these papers were presented orally during the review. These papers are denoted by an asterisk in the Table of Contents.

17. Key Words (Selected by Author(s))	18. Distribution Statement
Weather, Climate, Severe Storms, Global Weather, Meteorological Research	

19. Security Classif. (of this report)	20. Security Classif. (of this page)	21. No. of Pages	22. Price*
Unclassified	Unclassified		

*For sale by the National Technical Information Service, Springfield, Virginia 22151.